NASA-CR-200873

TRANSITION STUDIES ON A SWEPT-WING MODEL

Final Technical Report
Full Award Period 1/6/89 - 5/14/94

SPONSOR AWARD # NAG-1-937

NASA-Langley Research Center
FLDMD
Mail Stop 163
Hampton, VA. 23681-0001

Attention:
Michael J. Walsh

APRIL 1996

Submitted by

WILLIAM S. SARIC

Mechanical and Aerospace Engineering
College of Engineering and Applied Science
Arizona State University
Tempe, AZ 85287-6106

Janice D. Bennett, Director
Office of Research Creative Activity
(602) 965-8239

TABLE OF CONTENTS

LIST OF TABLES

LIST OF FIGURES

NOMENCLATURE

A	disturbance amplitude
A_o	disturbance amplitude at initial point of instability
C	airfoil streamwise chord (along X coordinate)
C_p, C_{p_3}	swept pressure coefficient
C_{p_2}	unswept pressure coefficient
C_{p_s}	streamwise pressure coefficient, measured by hot-wire probe
c	airfoil chord, measured normal to leading edge
D	diameter of a circular roughness element
f	frequency
h_{10}	height of 2^{nd} 10% point in crossflow velocity profile
$\mathbf{k}$	wave vector of crossflow disturbances
k	roughness height [μm]
$\|k\|$	magnitude of wave vector (wavenumber)
M	number of averages in FFT
m	stationary crossflow mode number, based on roughness spacing s
N	$= \ln(A/A_o)$, amplification factor; number of samples
N_{max}	maximum amplification factor for a crossflow mode
n	number of elements in a spanwise roughness array
Re_c	$= U_\infty C/\nu$, chord Reynolds number
Re_{cf}	$= h_{10}\|w_{t_{max}}\|/\nu$, crossflow Reynolds number based on height of 2^{nd} 10%-point in crossflow velocity profile, maximum crossflow velocity, and viscosity

Re_k	$= k\|u\|(k)/\nu$, Reynolds number based on roughness height and velocity at top of roughness
Re_θ	$= w\theta/\nu$, Reynolds number based on attachment-line edge velocity and momentum thickness
S	total span covered by a data set
σ	dimensionless growth rate
U_e	boundary-layer edge velocity
U_∞, U_{∞_3}	freestream velocity
U_{∞_2}	x component of freestream velocity
u, v, w	velocity field in global coordinates
u_n, v_n, w_n	velocity field in model-oriented coordinates
$\|u\|$	$= (u^2 + w^2)^{1/2}$, magnitude of total velocity
u_t, v_t, w_t	velocity field in boundary-layer coordinates
u', v', w'	disturbance velocity field, normalized by U_∞
X, Y, Z	global test-section coordinates: X is along flow axis, Y is normal coordinate, Z is unswept spanwise coordinate (positive down)
x, y, z	model-oriented coordinate system: x is chordwise, y is in thickness direction, z is spanwise
x_t, y_t, z_t	boundary-layer coordinate system: x_t is along outer streamline (tangential direction), y_t is along y, z_t is crossflow direction
$(x/c)_o$	initial point of instability
α	airfoil angle of attack; x component of wave vector
α_i	imaginary part of chordwise wavenumber
α_r	real part of chordwise wavenumber
β	spanwise component of wave vector

Δ	sampling interval
δf	frequency spacing
Λ	$= 45°$, airfoil sweep angle
λ	wavelength [mm]
λ_{cf}	crossflow disturbance wavelength measured normal to vortex axis
λ_s	crossflow disturbance wavelength measured in spanwise direction

1. INTRODUCTION

1.1. Background and Motivation

One of the most important unsolved problems in fluid mechanics is the prediction and understanding of the processes which lead to boundary-layer transition and turbulence. This problem is important not only from a theoretical point of view, but also because it has many practical applications. Many engineering design problems are critically dependent on the state of the boundary layer. Several examples include heat-transfer characteristics and material requirements for turbomachinery and hypersonic vehicles, performance and detection of submerged vehicles, and separation and stall characteristics of low-Reynolds-number airfoils. Of particular interest here is the effect of boundary-layer transition on the drag characteristics of airfoils. It has been estimated that if laminar flow could be maintained on the wings of a large transport aircraft, a fuel savings of up to 25% would be obtained (Pfenninger 1977; Thomas 1984; Saric 1994b). The process of maintaining laminar flow on an airfoil is referred to as Laminar Flow Control (LFC). This can be accomplished through several active means, including wall suction and cooling, or through passive means, such as careful shaping of the pressure distribution. A great deal of progress has been made towards this goal, but a greater understanding of the details of the transition process is necessary in order to solve some of the remaining problems.

The process of boundary-layer transition is usually divided into three phases. The first phase involves the mechanisms by which disturbances are introduced into the boundary layer. This process is called *receptivity* (Morkovin 1969). External disturbances, due to acoustical or vortical freestream fluctuations, surface imperfections, or vibration enter the boundary layer as small fluctuations in the basic-state flow. This process is not well understood, but it plays a central role in the transition process

by providing the initial conditions for the unstable waves which lead to transition. Several different types of instability may be present in the boundary layer, and the details of transition can be strongly influenced by the relative receptivity of the flow to these various modes.

The next part of the transition process involves the initial growth of the small disturbances. This stage of development is governed by *linear stability theory*, which has been very successful in describing certain types of instabilities. The flow is modeled by the linearized, unsteady Navier-Stokes equations. For parallel-flow basic states this leads to the well-known Orr-Sommerfeld equation, which has been used with great success in describing the Tollmien-Schlichting (T-S) and crossflow instabilities.

The final stage of the transition process occurs when the disturbances grow large enough to distort the basic-state flow or interact with each other. Nonlinear interactions lead to a complicated cascade of three-dimensional instabilities which quickly cause transition and turbulence. Basic-state distortions can lead to secondary inflectional instabilities with very high growth rates which also cause very rapid breakdown.

This simplified view of the transition process is a satisfactory model in most cases. However, for some instances with very high initial-disturbance levels, the conventional linear stability stage is bypassed, and the boundary layer becomes turbulent immediately after the source of the large disturbance. This phenomenon is not well understood, but is discussed by Morkovin (1969, 1993). It is usually observed in cases with high freestream turbulence or very large roughness. Since roughness is used in the present investigation, appropriate care must be used to avoid this type of transition.

Even with limited knowledge of the receptivity and breakdown processes, effective engineering methods for transition prediction can be developed in many cases. Be-

cause the nonlinear breakdown phase occurs on very short convective length scales, the details of this process have only a small effect on the transition location. The linear stability behavior has a much longer length scale, and is much easier to solve. Thus, transition-prediction schemes are very often based on linear stability theory. The most widely used tool is the e^N method, developed by Smith and Van Ingen (Smith & Gamberoni 1956; Van Ingen 1956), and most recently reviewed by Saric (1992a) and Arnal (1992, 1993). With this method, the linear-stability growth rates are integrated to obtain a total amplification factor A/A_o, starting from the point of initial instability. The natural log of this ratio is called the N-factor. Measured transition locations in controlled experiments are correlated with computed N-factors, and the resulting transition N-factor can be used to predict transition in similar flow configurations. Typical N-factors at transition are usually in the 9–11 range (Arnal 1992).

The e^N method must be used with caution because of several limitations. Care must be used in selecting which correlations to use for any given flow, since stability and transition behavior can strongly depend on the details of the flow. Without a clear understanding of the detailed physics and which instabilities are responsible for transition, incorrect results are obtained. Other complications arise in integrating the linear-stability growth curves. For example, with the crossflow instability, it is unclear whether one should integrate the growth of the mode with the highest local amplification rates (envelope method), or track the growth of a single mode. An even more serious deficiency is the fact that the e^N method entirely ignores the effect of receptivity on the transition process. Higher initial disturbance amplitudes will certainly lead to earlier transition. Radeztsky *et al.* (1993a) indicate a change of almost 5 in the transition N-factor for stationary crossflow as a result of changing the

surface-roughness characteristics of a swept airfoil. Arnal (1993) indicates that the e^N method works very well under some conditions in two-dimensional boundary layers, but clearly this depends very strongly on the detailed conditions of the experiment. It is not so successful for three-dimensional boundary layers. Successful transition-prediction schemes must be based on a thorough understanding of all aspects of the transition process.

1.2. Swept-Wing Flows

The present investigation is concerned with the three-dimensional boundary layers found in swept-wing flows. These flows exhibit a rich variety of instabilities. Four fundamental instabilities—attachment line, streamwise (Tollmien-Schlichting), centrifugal (Görtler) and crossflow—contribute to the breakdown of the boundary layer. The attachment-line instability can develop under some conditions on wings with a large leading-edge radius (Poll 1984). The streamwise instability is governed by the three-dimensional equivalent of the Orr-Sommerfeld equation, and is fairly well understood. Concave regions on the lower surface of an airfoil may develop centrifugal instabilities in the form of Görtler vortices (Saric 1994a). Finally, crossflow instabilities develop due to a combination of sweep and pressure gradient and are at the heart of the present investigation.

The model for this experiment is designed to concentrate on the crossflow and streamwise instabilities. The leading edge is subcritical to attachment-line instabilities, and convex curvature prevents Görtler vortices. Streamwise instabilities can be controlled by changing the angle of attack, which influences the pressure distribution of the model. For the present experiment, the design angle of attack of 0° allows weak T-S growth. At the same time, the crossflow instability is also amplified. The combination of sweep and pressure gradient deflects the inviscid streamlines as

they pass over the airfoil. Because of viscosity, this deflection is greater within the boundary layer. Thus a component of velocity, parallel to the surface and perpendicular to the inviscid streamlines, exists and is called the *crossflow* velocity. Since the profile must have a zero at the wall, have an extremum within the boundary layer, and asymptotically go to zero at the boundary-layer edge, a curvature change and hence an inflection point is present. This inflectional crossflow profile is subject to a dynamic instability which results in unstable crossflow waves. These disturbances take the form of co-rotating vortices aligned roughly in the streamwise direction.

1.3. Current Issues

Crossflow-dominated transition is a very complicated phenomenon which is influenced by many factors. Recent research has identified a number of key issues which must be resolved before this problem is completely understood. This section will give an overview of these issues, while Chapter 2 will give a review of the current literature on the subject.

1.3.1. *Stationary Waves*

One of the key features of the crossflow instability is that both stationary and travelling waves are possible. The two types of waves seem to be influenced by different factors, and cause transition in different ways. Both types of waves are observed in most experiments (Dagenhart *et al.* 1989; Arnal *et al.* 1990; Müller & Bippes 1989; Bippes & Müller 1990; Bippes 1991), but some experiments are dominated by stationary waves while others are dominated by the travelling waves. As might be expected, this difference is related to receptivity (discussed below). When transition is dominated by stationary waves, the transition front is very jagged, and is fixed relative to the model. The transition front is more uniform when travelling waves dominate.

Most of the interesting features of stationary waves are due to the fact that they are fundamentally nonlinear. A weak stationary vortex will produce very large changes in the basic-state flow by convecting low-speed fluid away from the surface in the regions with $v' > 0$, and high-speed fluid towards the surface in regions with $v' < 0$. As soon as the stationary vortices are strong enough to be measured, the basic state has already been changed enough that the assumptions of linear stability theory have been violated (Dagenhart 1992; Dagenhart *et al.* 1989; Bippes & Müller 1991). One should not expect the development of these vortices to be accurately predicted by linear theory. Essentially, linear theory is computing the stability of profiles which no longer exist.

Another effect of the basic-state distortions is the development of secondary instabilities. Stationary crossflow waves cause strong spanwise variations of the streamwise velocity profiles, with alternating inflected, accelerated, and decelerated profiles. The inflected profiles are vulnerable to a high-frequency secondary instability which quickly leads to local early transition (Kohama *et al.* 1991). This can occur well before the more-amplified travelling waves have had a chance to grow to transitional amplitudes.

There is some confusion in the literature as to which stationary wavelengths will be observed as the boundary layer develops. Linear theory predicts that short wavelengths are amplified at small x/c, while longer wavelengths (larger vortex spacing) will dominate at larger x/c. Some experiments show an evolving vortex pattern with vortices merging at downstream locations as the observed spacing increases. Other experiments show a fixed vortex spacing with no evidence of vortices merging or dropping out. This discrepancy may be related to whether or not the flow is spanwise uniform. There is a corresponding lack of agreement over which constraints should be

applied in solving the stability equations. Some researchers use the envelope method, while others constrain the solution to a constant vortex spacing, and some use a constant spanwise wavenumber.

1.3.2. *Receptivity*

One of the surprising discoveries in recent crossflow experiments is that the stationary waves seem to be dominant in low-turbulence environments, while travelling waves are dominant in a high-turbulence environment (Müller & Bippes 1989; Bippes 1991). According to linear theory, the travelling waves are much more amplified than the stationary waves, and would be expected to dominate the flow. Since the low-turbulence environment is more likely in flight, these results cast some doubt on the applicability of simple transition-prediction schemes to swept-wing flows. The answer to this puzzle is found not only in a study of the nonlinear aspects of the crossflow instability, but also of the other major component of the problem—receptivity. Recent theoretical work (see Chapter 2) suggests that the travelling disturbances are introduced via an interaction of freestream disturbances and surface roughness. The small amplitude of the freestream disturbances in a low-turbulence environment leads to very low initial amplitudes of the travelling crossflow modes. The stationary disturbance is thought to be introduced by direct modification of the basic state as it flows over surface roughness.

Experimentally, preliminary results from the current investigation, reported by Radeztsky *et al.* (1993a) indicate a very strong sensitivity to roughness for stationary crossflow in a low-turbulence environment. These results will be reviewed in Chapter 6.

1.4. Experimental Objectives

The goal of the present investigation is to cast some light on some of the issues outlined above, in order to gain a better understanding of the fundamental physics of the crossflow problem. A detailed set of measurements is needed to provide a benchmark for theoretical investigations.

Specifically, the present experiment concentrates on the details of the development of roughness-induced stationary crossflow vortices. Previous investigations at Arizona State University have suggested a sensitivity of stationary crossflow to surface roughness, and a nonlinear saturation of stationary vortices at high amplitudes. The current experiment investigates these issues through several modifications of the ASU swept-wing model. First, the surface finish of the model is carefully documented, and the model is hand-polished to produce a mirror-like finish with a typical roughness height of $k_{rms} < 0.25$ μm. This provides a suitable surface for investigating the effect of controlled roughness distributions. Second, after a preliminary investigation of the effect of surface roughness in a crossflow-dominated environment with high-amplitude stationary vortices, the angle of attack of the model is changed to $\alpha = 0°$. This reduces the amplification rates for crossflow instabilities, allowing the study of stationary crossflow waves at much lower amplitudes. A detailed comparison of experimental and theoretical growth rates under these conditions will provide a valuable test of the applicability of linear stability theory to swept-wing flows.

This combination of modifications provides an excellent environment for sensitive roughness experiments. Without any artificial roughness, the combination of low receptivity and low growth rates results in no measurable stationary or travelling crossflow waves, giving a perfect baseline for controlled experiments. As in the previous ASU experiments, the basic-state flow is carefully controlled through the use

of end liners in the test section, which produce an effective simulation of an infinite-span model. Basic-state and stability calculations are performed as part of the design process.

Stationary vortices are introduced by applying spanwise arrays of circular roughness elements near the attachment line. These elements produce well-defined initial conditions, providing input for theoretical studies of receptivity issues.

The investigation of low-amplitude DC velocity fluctuations requires a refinement of measurement techniques. In addition to the modifications of the swept-wing model, a new high-resolution traverse mechanism is installed at the Unsteady Wind Tunnel. This computer-controlled four-axis system allows a new level of precision in boundary-layer measurements. Using this new traverse, detailed measurements reveal the structure of stationary vortices in very thin boundary layers near the attachment line. Spanwise scans extending to 24 wavelengths permit improved wavelength discrimination so that multiple crossflow modes may be separated and individually tracked. As a result, detailed comparisons are possible with single-wavelength stability calculations.

1.5. Outline

The remaining chapters describe the details of the experiment. Chapter 2 gives a review of recent experimental and theoretical developments related to this investigation. The ASU Unsteady Wind Tunnel facility is described in Chapter 3. Details of the new traverse system and data-acquisition equipment are included. Chapter 4 covers the design issues for the experiment, and presents the basic-state and linear stability calculations which are compared with the measured data. Chapter 5 introduces the experimental and analytical techniques which are used in gathering and processing the data. In Chapter 6, the preliminary tests of the sensitivity of stationary crossflow to surface roughness are presented. Chapter 7 presents the ex-

perimental data, including extensive boundary-layer surveys and spanwise scans. The data are carefully compared with the predictions of stability theory. Chapter 8 gives the conclusions.

2. REVIEW OF RECENT RESULTS

A great deal of knowledge has been obtained in recent years concerning the stability of three-dimensional boundary-layer flows, but there are still many aspects of the problem which are not yet well understood. The combination of complicated geometries and nonlinear effects has made this a difficult problem to master. A vast amount of theoretical effort has been expended in trying to understand these problems, but detailed experiments have been few in number.

2.1. Review of Early Results

Excellent reviews of transition and stability research in three-dimensional boundary layers can be found in Reed & Saric (1989), Arnal (1992) and Dagenhart (1992). Instead of duplicating the same information here, the reader is referred to these reviews for information concerning the basic development of early theoretical and experimental efforts. Reed & Saric (1989) include a tutorial on the basic ideas of three-dimensional stability theory, as well as a thorough documentation of the historical development of this branch of fluid mechanics. Material is included for swept-wing flows, rotating disks, and rotating cones and spheres. Arnal (1992) and Dagenhart (1992) concentrate on the swept-wing problem, and include later references not found in the 1989 work. Reviews of earlier work on stability and transition can be found in Mack (1984), Arnal (1984, 1986), and Poll (1984). This chapter will instead concentrate on the theoretical and experimental developments directly related to the present experiment.

2.2. Theoretical Developments

A substantial amount of theoretical and computational work has been produced in recent years. These efforts contribute to an understanding of several issues outlined in Chapter 1.

2.2.1. *Stability Theory and Transition Prediction*

It is clear that for complicated flow geometries, methods beyond traditional linear stability theory must be developed. Even for simple situations, current methods of transition prediction often fall short. Saric (1994b) points out that for a simple zero-pressure-gradient flat plate, no method exists which can accurately predict the transition location.

The first stage of modifications to linear theory is accomplished by considering corrections due to nonparallel effects, streamline curvature, and surface curvature. Examples of nonparallel corrections for three-dimensional boundary layers include Padhye & Nayfeh (1981), Nayfeh (1980a,b), El-Hady (1980), and Reed & Nayfeh (1982). The older nonparallel analyses have been obviated by newer calculations using parabolized stability equations. Herbert (1993) gives a description of PSE methods. These results show that nonparallelism is not important. Viken *et al.* (1989), Müller, Bippes & Collier (1990), Collier & Malik (1990), Lin & Reed (1992), and Malik & Balakumar (1993) investigate the effects of streamline and surface curvature on crossflow instabilities. There is currently some disagreement over the importance of these effects. Reed (1994) indicates that surface curvature has a stabilizing effect, while streamline curvature is slightly destabilizing. Both of these effects are very small.

One of the more important recent advances has been the introduction of nonlinear techniques, such as PSE analysis and direct numerical simulation (DNS). These methods allow a more accurate investigation of large-amplitude stationary vortices, by including changes in the basic state as the flow evolves. Spalart (1989) shows the development of both stationary and travelling crossflow vortices by solving the spatial Navier-Stokes equations for a swept Heimenz flow. He finds evidence of non-

linear saturation at large vortex amplitudes, in agreement with the trends found in experiments. Recently, Malik & Li use linear and nonlinear PSE to investigate the same flow, and find similar results. The vortex growth saturates at levels well below the linear result. Reed & Lin (1987) and Lin (1992) perform numerical simulations of the flow over a swept-wing configuration similar to the ASU experiments. Meyer & Kleiser (1988, 1989), Singer, Meyer & Kleiser (1990), Meyer (1990) and Fischer (1991) conduct numerical simulations of nonlinear vortex growth and of the interaction between stationary and travelling waves. Falkner-Skan-Cooke similarity profiles are used for the basic state. These simulations are compared with the experimental results from DLR using a swept flat plate. A nonlinear saturation of the stationary vortices is observed for large amplitudes.

Another nonlinear effect is the development of secondary instabilities. Examples of research in this direction include Balachandar *et al.* (1992), Reed (1988), Reed & Fuciarelli (1991), and Fischer & Dallmann (1987, 1988, 1991), who were motivated by the wave-interaction results of Saric & Yeates (1985) and Bippes & Nitschke-Kowsky (1987).

2.2.2. *Receptivity*

The other area of research which is very relevant to the current investigation is receptivity. Recent contributions concerning crossflow receptivity include Balakumar *et al.* (1991), Choudhari (1993), Choudhari & Street (1990), Crouch (1993), Mack (1985), and Manuilovich (1990).

Mack (1985) attributes the vortex pattern on a rotating disk to wave patterns produced by small surface imperfections. Balakumar *et al.* (1991) investigated the receptivity of a rotating-disk flow to high-frequency fluctuations and surface imperfections, and found unsteady crossflow waves. Choudhari & Streett (1990) investigated

the effects of roughness and suction on the same flow, and argued for the importance of stationary waves. Manuilovich (1990) examined the receptivity of boundary layers near the attachment line and found extremely small receptivity effects due to surface roughness.

Crouch (1993) investigates crossflow receptivity using Falkner-Skan-Cooke (F-S-C) profiles as the basic state. He introduces disturbances via perturbations of the surface height and freestream acoustic waves. Initial crossflow amplitudes are formulated as a product of the disturbance parameters and a *response residue.* A principal result is a comparison of stationary and travelling receptivity coefficients. He finds that even though the response residue is much greater for the travelling waves, the initial amplitudes for stationary waves are likely to be larger when the extremely low acoustic levels found in flight are considered. This result is consistent with the observations of Müller & Bippes (1989) and the ASU experiments (Kohama *et al.* 1991; Radeztsky *et al.* 1993a).

Choudhari (1993) investigates the receptivity of F-S-C profiles using similar techniques. He numerically investigates a wide set of parameters, including single and multiple elements in spanwise and skewed arrays, random distributions, roughness diameter, acoustic-wave orientation, and F-S-C parameter changes. The results for a single roughness element are found to be in agreement with the preliminary results of this investigation (Radeztsky *et al.* 1993a). Choudhari also finds that for typical acoustic amplitudes in flight, the receptivity to stationary modes can be larger than the receptivity to travelling modes. It is unclear whether this larger initial amplitude is enough to compensate for the larger growth of the travelling modes. Finally, Choudhari points out a need for investigations of the receptivity of three-dimensional

boundary layers with large roughness heights. Such work would be useful in the interpretation of the present experiment.

2.3. Transition and Stability Experiments

Modern experimental investigations of crossflow-dominated flows on airfoils begin with Saric & Yeates (1985), Poll (1985), and Michel *et al.* (1985). These experiments illustrate the various techniques for producing swept-wing boundary layers in the laboratory. Poll (1985) uses a long cylinder with a variable sweep angle. Saric & Yeates (1985) introduce the technique of using a swept flat-plate model, with a favorable pressure gradient imposed by a wall bump. This technique is also used by Kachanov & Tararykin (1990), and for the DLR experiments (see below), which use an airfoil to produce the pressure gradient. Dagenhart (1992) points out that the swept flat-plate experiments allow for easy probe access, but do not have a proper leading-edge shape. Michel *et al.* (1985) use a high-aspect-ratio swept airfoil model. A low-aspect-ratio swept airfoil is used for all of the ASU experiments, including the present investigation.

Many of the important recent results come from the DLR experiments in Germany. These results are found in Bippes & Nitschke-Kowsky (1987), Nitschke-Kowsky (1986), Nitschke-Kowsky & Bippes (1988), Bippes (1990, 1991), Müller (1990), Bippes & Müller (1990), Bippes *et al.* (1991), and Deyhle *et al.* (1993). As in most crossflow experiments, Bippes and co-workers find both stationary and travelling waves. Bippes *et al.* (1991) report that the details of the transition process and observed features strongly depend on the environmental conditions. When the experiment is performed in a low-turbulence tunnel, the stationary vortices are dominant and reach relatively large amplitudes. In a high-turbulence environment, the travelling waves dominate the transition process, and the stationary waves are suppressed. These results provide

important clues about the central role of receptivity and nonlinear processes in the crossflow problem. The stationary waves exhibit growth rates that agree with linear theory at low amplitudes, but a nonlinear saturation is observed at higher amplitudes. The saturation level seems to depend on the freestream turbulence level. They find that the behavior of the stationary waves is in better agreement with linear theory in the low-turbulence tunnel. Observed wavelengths for both stationary and travelling waves are in the amplified range according to linear theory, but the dominant wavelengths are not always in agreement with the most-amplified linear solutions. Not surprisingly, the band of amplified travelling waves has a different range depending on the turbulence level of the tunnel. Other nonlinear effects include a spanwise modulation of the travelling-wave amplitude, indicating an interaction with the stationary modes.

Through the use of several innovative experimental techniques involving rotating probes, the DLR group has contributed to the database on travelling disturbances by measuring phase and group velocities, wavelengths, and directions of propagation. Deyhle *et al.* (1993) report that phase velocities and wavelengths are in agreement with linear theory, while the group velocity shows a significant difference. Again, the results are affected by nonlinear interactions.

Another important result reported by Müller & Bippes (1988) has significant implications concerning receptivity. The pattern of stationary vortices is fixed relative to the model so that if the model is shifted in the tunnel, the stationary pattern moves with the model. This provides evidence that the stationary vortices are sensitive to the surface of the model rather than freestream disturbances. They also note that under natural conditions, the observed stationary wavelength is unaffected by changes in surface roughness. The wavelength selection mechanism under conditions

of random natural roughness is unclear, but may be related to selectivity based on the most-amplified wave.

Another significant result is reported by Arnal *et al.* (1984). In this swept-wing experiment, the stationary vortex pattern evolves with increasing downstream distance, with larger wavelengths observed downstream. This is accompanied by a merging or vanishing of individual vortices to accommodate the growth in wavelength. Most other experiments with a careful simulation of swept-wing flow (Dagenhart 1992) show a fixed-wavelength vortex pattern. Later swept-wing experiments by Arnal's group include Arnal & Juillen (1987) and Arnal *et al.*(1990).

The set of experiments at Arizona State University represents another major source of data. The design of these experiments is described by Saric *et al.* (1990). The data are reported by Dagenhart *et al.* (1989, 1990), and by Dagenhart (1992), who reports all the initial detailed measurements of stationary and travelling waves in a crossflow-dominated flow. The ASU experiments are in a low-turbulence tunnel, so transition is dominated by stationary waves. Dagenhart's experiments report stationary growth rates below those predicted by linear theory, and the observed wavelengths are smaller than predicted by theory. Dagenhart compares his measurements with stability calculations performed on the exact airfoil used in the experiment.

Later work by Kohama *et al.* (1991) identifies a high-frequency secondary instability that leads to transition. This instability first appears near the highly inflected profiles produced by the stationary vortices. This result is consistent with earlier work by Kohama on a swept cylinder. In light of this experiment, the observation of high-frequency disturbances near the point of transition by Poll (1985) appears to be an example of this secondary instability. Saric (1994b) gives a review of these secondary-instability measurements and their impact on transition prediction.

2.4. Summary

Several important themes dominate current investigations into the fundamental nature of the crossflow instability. Receptivity has been shown to be as important as linear stability in determining transition locations. Nonlinear effects and secondary instabilities also play a key role in the transition process. It is clear that for swept-wing flows, transition-prediction methods based on linear theory fail to capture the essential elements of the process. Further progress requires a better understanding of the receptivity and nonlinear aspects associated with stationary vortices.

The goal of the present investigation is to continue the development of these ideas by providing detailed measurements of stationary vortices. By lowering the growth rates and surface-roughness levels below those found in the Dagenhart and DLR experiments, stationary vortices can be studied under carefully controlled conditions. With no natural vortices present, artificial roughness distributions create well-defined initial conditions. High-resolution measurements of disturbance details will provide a database for comparison with new theoretical and numerical results.

3. EXPERIMENTAL FACILITY

3.1. Unsteady Wind Tunnel

All of the experiments are performed in the Arizona State University Unsteady Wind Tunnel (Figure 3.1). This facility is a low-speed, low-turbulence, closed-circuit tunnel with a unique double-duct design. Originally built at the National Bureau of Standards in Gaithersburg, Maryland, it was moved to Arizona State University in 1984 and extensively rebuilt. It became operational in its present configuration in 1987. A detailed description of the tunnel is given by Saric (1992b).

The tunnel is driven by a 150 hp variable-speed DC motor and a single-stage axial fan. The fan has 9 adjustable blades, followed immediately by 11 stators. The diameter is 1.8 m. An analog controller maintains rotation speeds within 0.1%. For the test section used in this experiment, speeds are continuously variable and accurately controlled between 5 m/s and 38 m/s.

The Unsteady Wind Tunnel has several features designed to produce exceptionally low turbulence levels. The length of the tunnel is extended by 5 meters compared with the original design. This allows an extension of both the primary diffuser downstream of the fan and the return-leg diffuser after the test section. This reduces low-frequency fluctuations in the tunnel. A new nacelle is installed on the fan. All corners of the tunnel have steel turning vanes with a 50 mm chord and 40 mm spacing (item *a* in Figure 3.1). The new contraction cone is manufactured from 3.2 mm thick steel with 25 mm steel angle reinforcements, and has a contraction ratio of 5.33:1. The sides of the contraction cone follow a 5^{th}-order polynomial to eliminate curvature discontinuities at the ends. Upstream of the contraction, the flow is conditioned by a 76 mm aluminum honeycomb section (item *b* in Figure 3.1) and seven stainless steel screens (item *c* in Figure 3.1). The honeycomb has a cell size of 6.35 mm. The

screens are 2.7 × 3.7 m, and are separated by 230 mm. The first five screens have an open area ratio of 0.7, and the last two are seamless, with an open area ratio of 0.65. They are constructed from 0.165 mm wire on a 30/inch mesh. The screens are followed by a settling chamber, where viscous damping removes any remaining small-scale fluctuations. Other screens are placed around the tunnel in order to avoid diffuser stall.

Several mechanical features also contribute to the low-noise environment. The fan section is isolated from the tunnel by a flexible coupling which reduces transmitted vibrations. The fan housing rests on an isolated concrete pad. The test section is isolated in a similar manner. The wind-tunnel building is divided into two rooms, with the test section and fan on opposite sides of a sound-insulated wall.

These features combine to produce excellent flow conditions. Measured u' turbulence levels with a flat-plate test section are below 0.02% (20 m/s, 2 Hz high-pass). Further information on freestream turbulence measurements is given by Saric *et al.* (1988) and Rasmussen (1992).

The secondary duct of the Unsteady Wind Tunnel allows an unsteady mode of operation. A set of rotating shutters is located downstream of the test section. Another set of shutters in the secondary duct rotates with a 180° phase lag. This allows up to 100% velocity fluctuations with frequencies up to 25 Hz, while minimizing unsteady loading on the fan. For steady operation, as in the present experiment, the primary shutters are locked open, and the secondary duct is sealed off.

The Unsteady Wind Tunnel features a multiple test-section arrangement which improves operational efficiency. Each experiment has a dedicated test section measuring 1.4 m × 1.4 m × 4.9 m. The test section is connected to the tunnel only by a flexible coupling, and can easily be rolled out on castors when necessary. While one

experiment is in the tunnel, another model can be prepared in the work area of the tunnel building.

3.2. Instrumentation

Static and dynamic pressures are measured with two temperature-compensated transducers, MKS type 390HA-0100SP05. The 1000 torr absolute transducer is open to the atmosphere. The 10 torr differential transducer is connected to a Pitot-static probe near the test-section entrance. The transducers are connected to two MKS 270B 14-bit signal conditioners. These provide continuous digital displays, along with digital and analog signals for the data-acquisition system. Test-section temperatures are measured by a thin-film RTD. The calibrated bridge output is interfaced directly with the data-acquisition system.

Accurate velocity measurements are provided by two Dantec 55M01 constant-temperature anemometers using 55M10 CTA standard bridges. The sensors are Dantec 55P15 and 55P05 miniature boundary-layer probes. The P15 probes use 5 μm platinum-plated Tungsten wires, and the P05 probes use Gold wires. The wires are 1.25 mm long. The probe tines are 8 mm long, and are offset 3 mm from the probe axis for easy boundary-layer access. Standard 4 mm probe supports are attached to the instrumentation sting and traverse system (described below).

A two-color, two-velocity-component laser-doppler velocimeter is used for mean-flow measurements. This system includes an 8 W Argon-Ion laser, 3-D traverse, and detection optics and electronics.

AC signals are processed with a two-channel, computer-controlled filter-amplifier system, Stewart type VBF44. This versatile device provides several filter responses with cutoffs ranging from 1 Hz to 255 kHz, and provides gain of up to 70 dB. It is interfaced to the data-acquisition computer with an RS-232 line. Additional filtering is

provided by a 3-channel Tektronix filter-amplifier and several in-house-built antialias filters.

All analog voltage signals are digitized with an Iotech AD488/8SA A/D converter. This unit provides 8 16-bit differential input channels with simultaneous sample and hold. The maximum aggregate sampling rate is 100 kHz. It is interfaced to the data-acquisition computer with a high-speed GPIB. A GPIB-controlled multiplexer unit increases the capacity to 32 differential input channels.

Phase and amplitude measurements are obtained with a GPIB-controlled Stanford SR530 lock-in amplifier. Voltages are also monitored with an 8-channel Tektronix 5440 oscilloscope and Fluke 8050A digital multimeters.

3.3. Computer System

The primary data-acquisition computer at the Unsteady Wind Tunnel is a PC compatible with a 50 MHz 80486DX microprocessor and 20 MB of RAM. Primary storage is provided by a 425 MB SCSI hard disk with an ADAPTEC 1542 SCSI controller. A 2 GB, 4 mm DAT drive is used for system backups and data archiving. The graphics system includes a Trident 8900 SVGA card and a 17 inch Viewsonic monitor with 1024×768 resolution. A National Instruments GPIB card provides a general interface for a variety of external data-acquisition equipment. This modular arrangement separates the computer from the acquisition hardware, which produces several benefits. Signal noise is reduced, since the acquisition hardware is placed close to the experiment. Data are sent to the main computer over the digital GPIB, eliminating the need for long analog signal cables between the control room and the wind-tunnel room. Overall system reliability is improved, as any defective equipment can be removed for repair without affecting the rest of the system. Many components, including the main computer, can be easily upgraded or replaced without rendering

the remainder of the system obsolete. Finally, the GPIB allows for much greater expansion than would be possible with an internal acquisition system.

The acquisition PC runs the SCO UNIX operating system. This multiuser, multitasking system allows simultaneous data acquisition, analysis, and program development. The X-windows graphics system provides a modern user interface. All acquisition and analysis codes are written in C.

The backup data-acquisition computer is a Concurrent 5600 real-time UNIX system. This unit includes a 12-bit, 16 channel, 1 MHz A/D board, 8 channels of D/A at 500 kHz, and high-speed parallel and GPIB interfaces. The graphics system includes a 19 inch 1152×910 color monitor.

High-speed data analysis and additional storage are provided by a DECstation 5000/200, which includes a 25 MHz MIPS R3000/3010 processor, 16 MB RAM, high-resolution gray-scale monitor, two 330 MB SCSI hard disks, and a 100 MB TK50 SCSI tape system.

An AT-compatible PC is dedicated to wind-tunnel speed control. Equipped with Metrabyte A/D and D/A boards, this system monitors temperature, static and dynamic pressures, fan motor speed, and continuously updates the motor speed to maintain the desired conditions in the test section. The analog motor controller is interfaced with the computer via a 4-20 mA current loop. The wind-tunnel speed-control program (also called "cruise control") allows several control modes, including constant speed, constant dynamic pressure, and constant Reynolds number. The constant Reynolds number mode becomes important during extended runs, because the temperature can change significantly during the experiment.

All wind-tunnel computers are connected to a local Ethernet, which is in turn connected to the campus network, and ultimately to the global Internet. Additional

computer facilities at the Unsteady Wind Tunnel include several personal computers, a 600 dpi Hewlett-Packard laser printer, Digital LA50 dot-matrix printer, Seiko color hard copier, and a Hewlett-Packard 7475A pen plotter.

3.4. Traverse System

A new three-dimensional traverse system provides the extremely precise probe positioning required by this experiment. Drawings are included in Figures 3.2 and 3.3.

The traverse mechanism consists of several components. A steel carriage (detailed in Figure 3.3) is supported by two stainless steel rails (item *c* in Figure 3.2) and is driven by a 3.65 m precision lead screw (item *b* in Figure 3.2) in the X direction. This system replaces the old chain drive, and provides much greater accuracy and stability. In the Y (wall-normal) direction, the Aluminum sting strut is attached to a small Aluminum carriage (item *d*), which rides on two parallel rails for maximum accuracy. The carriage is driven by a single center-mounted precision lead screw. The entire Y subsystem is attached to the X carriage with two steel rails to provide motion in the Z (vertical) direction. Two independently-driven precision lead screws drive this mechanism. These lead screws and rails are shown as items *b* and *c* in Figure 3.3.

All lead screws are driven by Compumotor microstepping motors (items *a*), which have an extremely high resolution of up to 50,000 steps per turn. 1000-line Renco digital encoders with quadrature provide continuous position information. The motors are controlled with a Compumotor CM4000 4-axis microprocessor-based motion controller, connected to the main computer by the GPIB. This system allows simultaneous coordinated moves in all three directions with guaranteed accuracy through a feedback system using the digital encoders. Since the controller internally handles all details of the motion process, the main computer need only provide the requested

position, and can then move on to other activities. This improves overall system performance.

The entire traverse mechanism is located in a steel and plexiglass enclosure which forms the outer pressure wall of the tunnel (item *f* in Figure 3.2). This design offers several advantages. The outer wall supports the pressure difference between the test-section interior and the atmosphere, eliminating most of the mass flow through the inner wall which must contain a gap for probe access. Since the traverse machinery is not inside the test section, potentially serious flow-interference effects are eliminated. The importance of this should not be underestimated. Saric (1990) indicates that traverse interference can be a major problem in stability experiments, and that great care must be used in designing a traverse system. In addition to local pressure gradients, the presence of a moving traverse in a test section can cause global flow-field adjustments which can change the results of stability measurements.

The inner wall of the test section contains a sliding plexiglass panel with a horizontal slot for probe access. The panel is moved vertically by a lead screw and steel-rail arrangement, with a maximum range of 175 mm. This motion is carefully synchronized with the vertical motion of the traverse so that the probe-support sting is centered in the slot at all times. The slot is sealed with a zipper which automatically opens and closes around the sting as it moves, leaving the smallest possible gap in the inner wall.

Hot-wire probes are attached to the probe-support sting (Figure 3.4) which enters the test section through the slot in the sliding panel. The sting consists of a tapered composite element and an Aluminum strut. The composite portion is streamlined, 5 mm thick and 425 mm long. The chord varies from 64 mm at the base to 50 mm at the tip. Standard Dantec 165 mm probe-support tubes are connected to the

sting with adjustable attachment brackets. The attachment bracket at the tip of the sting allows the tube angle to be adjusted for easy boundary-layer access on three-dimensional models. For a swept-wing model, both the probe rotation about the X axis and the support-tube orientation in the (X, Y) plane must be adjusted at each chord location to enable accurate positioning in thin boundary layers. The composite sting is supported by an Aluminum strut with dimensions 13 mm $\times$ 75 mm $\times$ 268 mm. The strut reaches through the sliding window and attaches directly to the traverse mechanism.

Sting-design procedures at the Unsteady Wind Tunnel concentrate on minimizing flow interference. The combination of long, thin airfoil sections and long probe tubes is selected to reduce the local pressure coefficient due to the sting below 0.005 at the probe location. Sting influence is tested using the sensitive procedure suggested by Saric (1990). A fixed hot-wire probe is installed on a flat plate at $u/U_e = 0.3$. A controlled T-S wave is introduced, and the wave amplitude is carefully measured. A sting-mounted probe is moved close to the fixed probe, and any changes in the measured T-S amplitude are recorded. This procedure works very well because T-S waves are very sensitive to pressure gradients.

One negative effect of the ASU traverse and sting design is due to the long span of the sting. Small vibrations of the sting produce false signals in the boundary-layer probe because the probe moves slightly in the boundary-layer velocity profile. This does not cause any difficulty in the present experiment, which concentrates on DC measurements, but it can be a significant factor in AC measurements. The vibration problem is eliminated through several means. The carbon-composite sting is very stiff, which keeps vibration amplitudes to a minimum. Remaining vibration contamination

is removed through signal processing techniques (Spencer 1992; Rasmussen 1993) and by choosing experimental parameters which avoid the natural frequencies of the sting.

The new traverse system allows a new level of precision in boundary-layer measurements. System capabilities are summarized in Table 3.1.

Table 3.1. Traverse Specifications

	X (streamwise)	Y (normal)	Z (vertical)
Total Travel	1.25 m	100 mm	175 mm
Minimum Step	11.9 μm	0.64 μm	1.27 μm

4. DESIGN OF THE EXPERIMENT

This chapter covers the design issues for the experiment. A description of the airfoil model is given, and the design and construction of test-section liners is presented. Pressure distributions and stability calculations are presented, and appropriate test conditions are selected. Crossflow-producing artificial roughness elements are described.

4.1. Model

4.1.1. *Airfoil*

This experiment uses the existing NLF(2)-0415 airfoil (Somers & Horstmann, 1985), which has been in use at the Unsteady Wind Tunnel since 1988 in an ongoing investigation of stability and transition in three-dimensional boundary layers. The NLF(2)-0415 is actually designed for laminar flow in unswept applications on general aviation aircraft. As a natural laminar flow airfoil, it minimizes drag by maintaining laminar flow as long as possible through careful shaping of the pressure gradient. The airfoil shape and design pressure distribution are shown in Figure 4.1. The favorable pressure gradient region extending from the attachment line to $x/c = 0.71$ minimizes the Tollmien-Schlichting instability growth over most of the upper surface.

For the experiments at ASU, the airfoil is swept 45°, changing the stability situation considerably. The sustained region of negative dp/dx is now ideal for generating crossflow, particularly at negative angles of attack. The swept NLF(2)-0415 is an excellent platform for studying a wide variety of stability and transition scenarios. For $\alpha < 0°$, the crossflow instability is strongly amplified over the upper surface, while the Tollmien-Schlichting instability is suppressed by the favorable pressure gradient. This condition was used for previous investigations of crossflow-dominated transition (Saric *et al.* 1990; Dagenhart *et al.* 1989, 1990; Kohama *et al.* 1991; Dagen-

hart 1992; Radeztsky *et al.* 1993a). At small positive angles of attack, the pressure gradient is flat or decelerating on the upper surface, leading to the growth of strong Tollmien-Schlichting waves. At the design angle of attack of 0°, the weak favorable pressure gradient leads to the formation of moderate crossflow disturbances, as well as weakly-amplified Tollmien-Schlichting waves. This condition is chosen for the present experiment. Additional flexibility in the pressure gradient is achieved through the addition of a 20%-chord flap, with a maximum deflection of ±20°. The flap is set at 0° for this experiment. A complete review of the range of operating conditions for this airfoil is given by Dagenhart (1992).

The small leading edge radius of the NLF(2)-0415 eliminates the attachment-line instability mechanism for moderate Reynolds numbers. For example, at $Re_c = 3.6 \times 10^6$, the attachment-line Reynolds number is 38. The Görtler instability is also not present because there are no concave regions on the test (upper) side of the airfoil.

4.1.2. *Test Section*

The airfoil model is installed in a test section that is dedicated to this experiment. The test section consists of a steel frame with plywood and plexiglass wall panels and was modified in 1992 to include a steel and plexiglass enclosure around the traverse mechanism. This enclosure forms a rigid, airtight wall which supports any pressure differences between the test-section interior and the outside air. This eliminates most of the mean mass flow through the slotted interior wall of the test section, although some mass exchange still occurs due to the local pressure gradients over the airfoil surface. Test-section gauge pressures are minimized by venting the tunnel aft of the test section, where the cross-sectional area is only slightly larger than the test section.

The model is supported by a thrust bearing attached to the test-section frame at the floor of the test section. The bearing is centered 610 mm from the front wall and

760 mm from the rear wall, and is designed to allow the two-dimensional angle of attack to vary between $-4°$ and $+4°$ in $1°$ increments.

4.2. Test Conditions

The sensitive nature of stability experiments requires that the test conditions are carefully documented. If the flow conditions are off even slightly from the design conditions, it will be difficult to obtain meaningful results and to compare with theoretical predictions. This section describes the calculations and design issues for this experiment.

4.2.1. *Inviscid Flow*

The inviscid flow field is computed with a modified version of the two-dimensional MCARF airfoil code (Stevens *et al.* 1971; Dagenhart 1992). This code computes the flow over a two-dimensional airfoil in a two-dimensional duct, and has been modified to compute pressure coefficients for swept configurations (Dagenhart 1992).

The goal of producing infinite swept-wing flow is complicated by the presence of walls in the test section. This problem is dealt with by installing liners on the walls which follow the inviscid streamlines for infinite swept-wing flow. If liners are installed on all four walls, access to the model is severely limited, so a two-liner system is used instead. The front and back walls of the test section are left flat. This simplifies visual and probe access to the model, but has a significant effect on the flow field. The top and bottom walls are contoured to match the flow. With the model mounted vertically, this allows a spanwise-invariant flow field.

With a properly computed wall-liner system installed, it is not expected that the basic-state flow will be perfect in every respect. The primary purpose of the liner system is to eliminate most of the spanwise variations in the basic state. It is impossible to accurately predict all effects of differential blockage, probe-support systems, and

wall gaps for instrumentation access. Moreover, the test section has a finite length, while the calculations are performed in a very long duct. It is expected that the actual flow field will differ slightly from the theoretical predictions. After the liners are installed, detailed basic-state measurements are performed so that corrections may be applied to the boundary-layer and stability calculations. These measurements and corrections are described in Chapter 7.

With these ideas in mind, design calculations begin with computing the inviscid flow field over the model, including the effect of the flat front and rear test-section walls, but assuming infinite span. The flow is first computed using the two-dimensional MCARF code. The actual flow over an infinite-span swept wing is obtained by adding a constant velocity component $U_\infty \sin\Lambda$ in the spanwise direction. The two-dimensional C_{p_2} from the MCARF code is converted to a swept C_p by the formula

$$C_{p_3} = C_{p_2} cos^2\Lambda \tag{4.1}$$

where Λ is the sweep angle of 45°.

The MCARF code is run without any viscous corrections. Displacement thickness effects are accounted for by tilting the test-section floor slightly downward, which opens the cross-sectional area enough to account for boundary-layer growth on the model and test-section walls. This correction is only approximate, and is technically optimal only for one operating condition, but it has been shown to be sufficiently accurate for this model (Dagenhart 1992).

The computed pressure coefficient for the 45° swept NLF(2)-0415 at 0° angle of attack and 0° flap deflection in the Arizona State University Unsteady Wind Tunnel is shown in Figure 4.2. The major difference between Figures 4.1 and 4.2 is that

Figure 4.2 is for the swept airfoil, so the C_p is modified as in Equation 4.1. The minimum C_p in the unswept case is -1.123. In the swept case, the minimum C_{p_3} is -0.5617. Several significant effects of the wind-tunnel walls are observed. Both the upper and lower surface accelerate to lower pressures in the tunnel due to the side-wall effect. The effect is stronger on the thicker upper side of the airfoil, so the lift is increased substantially over the free-air value. The shape of the upper-surface C_p is also changed. In free air, the pressure is almost flat from $x/c = 0.05$ to $x/c = 0.20$. In the wind tunnel, the upper surface shows a continuous mild acceleration from the attachment line at $x/c = 0.0$ to $x/c = 0.71$. This is an ideal distribution for observing the development of crossflow disturbances with mild growth rates. The pressure minimum is followed by a moderate recovery until $x/c = 0.80$, followed by a plateau until $x/c = 0.95$, and a final rapid recovery to the trailing edge.

4.2.2. *Test-Section Liners*

Upper and lower wall liners are constructed to follow the inviscid streamlines for infinite swept-wing flow. Streamlines are computed from the MCARF solution by a program called TRAC. The two-dimensional velocity field is modified by the addition of a constant spanwise component equal to U_{∞_2}, giving a total incoming velocity of

$$U_{\infty_3} = U_{\infty_2} / \cos \Lambda. \tag{4.2}$$

Streamlines are computed from this total velocity field using an array of starting positions with Y varying across the test section width, and $X/C = -0.5$. A total of 25 streamlines are computed, with a greater concentration near the model where the streamline deflection is greatest. Figures 4.3 and 4.4 show projections of these streamlines in the (X, Y) and (X, Z) planes for the $\alpha = 0$ case. Several important

features of the flow are evident in these plots. In Figure 4.3, $Y = 0$ corresponds to the wing-chord plane, and positive Y is towards the front of the test section. The streamlines are consistent with typical low-speed flow over a lifting airfoil. The streamlines near the model deflect significantly, while those near the walls are almost straight. The stagnation streamline is parallel to the X axis a short distance upstream and downstream of the model, but approaches and leaves the model with slightly negative Y-values. The significant negative deflection downstream of the model adds some complexity to the liner construction because there is a discontinuity in the stream surface at this location.

The (X, Z) projection in Figure 4.4 is much more dramatic, showing the combined effects of lift and sweep. Here, X is the global streamwise coordinate in the test section. Because Y is positive away from the model, the vertical coordinate Z must be positive downward for a right-handed coordinate system. A comparison of the various wind-tunnel coordinate systems is given in Figure 4.9. The streamlines are clearly divided into two groups. Those passing over the suction side of the airfoil are accelerated, acquiring significant additional velocity in the x-direction. Since the wing is swept, this corresponds to an upward deflection in the (X, Z) plane. The streamlines passing on the pressure side of the airfoil are not strongly accelerated, and remain fairly flat. The streamlines passing near the model come close to the attachment line, where the flow is purely spanwise. This loss of x-velocity corresponds to a downward curvature of the streamlines. These effects produce a very complex stream surface. The sharp discontinuity in Z between the two groups of streamlines begins after the attachment line, but continues downstream of the airfoil, creating a significant step in the liner surface.

The streamlines are started at $X/C = -0.5$ because there is slightly more than $0.5c$ between the leading edge of the airfoil and the test-section entrance at the upper end of the model. At the lower end of the model, the sweep of the airfoil provides a greater distance between the test-section entrance and the model. The lower liner also begins at $X/C = -0.5$, and the extra distance to the test-section entrance is used for a flat platform with an access door. This gives the experimenter convenient physical access for probe and roughness installation, and model cleaning and maintenance. On the downstream side, the liners extend to the test-section exit.

The final liner coordinates are computed by a program called *liners*, which converts the streamlines from the wing-oriented coordinates of MCARF to the global (X, Y, Z) system. The stream surface is then interpolated to lines of constant Y, to be used as templates for liner construction. The stream surface is also extrapolated to the wing surface, and to the dividing streamline at the discontinuity. The resulting coordinates are sent to a digital plotter, producing continuous paper templates to be used for construction of the liners. The Y-spacing of the templates is 152 mm in the regions away from the model, but is reduced to 51 mm near the model for a more accurate representation of the highly-curved regions of the liner surface.

The liners are constructed from blocks of polystyrene foam in a manner similar to Dagenhart (1992). The foam blocks are pre-cut with a length of 1.22 m in the X direction and widths varying from 152 mm to 51 mm in the Y direction. The blocks are sliced along the stream-surface coordinates with a heated-wire device. The lower portion of the block forms the lower liner, and the complementary upper portion is used for the upper liner. Figure 4.4 shows that the upper liner must be over 200 mm thick at the test-section entrance in order to accommodate the dramatic upward sweep of the suction-side streamlines. If the lower liner has the same upstream thickness, it

will be over 400 mm thick at the downstream end of the test section. This extremely thick liner is rejected. Instead, an asymmetric liner system is designed. The lower liner has very small downward deflections, allowing a minimum entrance thickness as low as 50 mm. With this in mind, a total block thickness of 305 mm (12 in) is used. The blocks are sliced to produce a 216 mm upper-entrance thickness and a 89 mm lower-entrance thickness.

The rough-cut blocks are assembled into groups and attached to a 3.2 mm fiberboard backing material to produce several large slabs. The wing shape and stream-surface discontinuity are carefully cut into the slabs. These large blocks are then carefully sanded until the surface is smooth and accurately matches the template contours. This final surface is then painted and sealed in a thin plastic coating for protection. The slabs are then carefully aligned and attached to the test-section floor and ceiling to produce the liner shape. All seams are sealed and painted to produce a continuous airtight surface. Figure 4.5 shows the upper and lower liner shapes with the airfoil model in place.

The finite thickness of the liners at the entrance of the test section requires additional fairings in the contraction cone in order to smoothly match the existing contraction shape to the new smaller effective entrance. These fairings are designed with a 5^{th}-degree polynomial shape to avoid any curvature discontinuities. The fairings begin at the inflection point of the original contraction, and are numerically cut from a single large block of foam.

The asymmetric liner and fairing thickness produce a skewed contraction which is tested with an empty test section. Adverse effects on the entrance flow are minimized by the small contraction ratio and relatively large size of the test section. The velocity skew is limited to 2% and no separation or additional turbulence is detected.

4.2.3. *Boundary-Layer Basic State*

In preparation for stability calculations, the basic-state boundary layer for this configuration is computed using the Kaups-Cebeci code (Kaups & Cebeci, 1977). This code is designed for swept and tapered wings. For this untapered wing, the taper parameter is set to a negligibly small value. The edge conditions are supplied by the three-dimensional extension of the MCARF solution (Figure 4.2). The resulting basic-state boundary-layer profiles are shown in Figures 4.6–4.8. The interpretation of these profiles depends on the coordinate systems shown in Figures 4.9 and 4.10. In Figure 4.9, X and Z represent the right-handed global test-section coordinate system. X is along the flow axis and is called the *streamwise* direction. Z is the global spanwise coordinate and is positive down. Y is the wall-normal coordinate. In the airfoil-oriented coordinate system, x is in the chordwise direction and z is parallel to the leading edge. y is in the same direction as Y. The boundary-layer coordinate system (x_t, y_t, z_t) is shown along with a representation of an inviscid streamline over the model. In this system, x_t points along the inviscid streamline at the edge of the boundary layer, and is called the *tangential* direction. y_t points along Y and y. z_t is orthogonal to x_t and y_t in a right-handed sense and is called the *crossflow* direction. A more detailed picture of the boundary-layer coordinate system is shown in Figure 4.10, which gives a schematic representation of a swept-wing boundary layer. The tangential and crossflow velocity components combine to produce a twisted and inflectional total-velocity profile. Notice that for the positive sweep angle Λ defined in Figure 4.9, the crossflow velocity component is negative.

The laminar boundary-layer solutions for the NLF(2)-0415 model are typical for swept wings. Figures 4.6 and 4.7 show a family of boundary-layer solutions for a chord Reynolds number of 3.0×10^6 and an angle of attack of 0°. The x/c range covers the

complete region of interest, from the attachment line near $x/c = 0.0$ to just beyond the pressure minimum at $x/c = 0.71$. The tangential velocity component shows strong acceleration near the leading edge, followed by mild acceleration and continuous growth to the pressure-minimum location. The final profile at $x/c = 0.73$ is dramatically thicker and has a characteristic decelerated shape. The crossflow velocity component reaches a sharp maximum of just over 10% in the rapid acceleration region near the attachment line. It then falls to a minimum of 1.8% near $x/c = 0.02$. This is followed by a continuous growth to a final value of 3.3% at the pressure minimum. The final profile in the recovery region shows a reversal of the crossflow component near the wall, as expected. The boundary-layer thickness varies from 0.14 mm at the attachment line to 4 mm at the pressure minimum. The relatively thick boundary layers over most of the wing allow extremely detailed measurements with the high-accuracy traverse mechanism. Crossflow Reynolds numbers (Re_{cf}) reach a maximum of 68 at $x/c = 0.029$, fall to 56 at $x/c = 0.1$, and rise smoothly to 185 at $x/c = 0.7$. Figure 4.8 shows the streamwise (u) velocity component for the same conditions. This is the component measured by the hot-wire probes.

4.2.4. *Linear Stability Calculations*

Boundary-layer stability calculations are made before the experiment is performed in order to provide guidance in choosing the experimental condition. After the experiment, the computations are compared with the data in order to gauge the effectiveness of linear stability theory in describing swept-wing flows. Two primary codes are chosen for these computations—MARIA (Dagenhart 1981, 1992) and SALLY (Srokowski & Orszag 1977). These codes compute the stability characteristics of the laminar boundary-layer solutions provided by the Kaups-Cebeci code. They both ignore any changes in the basic state caused by the presence of stationary waves. The

MARIA code is designed strictly for the stationary crossflow modes, and is not a typical eigenvalue solver. Instead, it estimates growth rates by comparing the basic-state profile to a catalog of crossflow profiles. The SALLY code is an eigenvalue solver. It is designed mainly for travelling crossflow disturbances, but stationary modes are computed as the limit of very low frequency. Results for a spanwise wavelength of 12 mm are also compared with Orr-Sommerfeld and linear PSE computations (Arnal *et al.* 1994).

Three-dimensional linear-stability codes typically require a constraint on the complex wavenumber in order to produce a solvable eigenvalue problem (Dagenhart 1992). Following Dagenhart, the constant-wavelength constraint is used for this experiment. This is appropriate for several reasons: Repeated flow-visualization and hot-wire measurements indicate that for infinite swept-wing flows the stationary crossflow structure develops with a constant wavelength (Dagenhart 1992; Radeztsky *et al.* 1993a). The present experiment uses specific arrays of roughness as receptivity elements. This produces a sharply-defined Fourier spectrum of crossflow disturbances. The development of these specific modes is of primary interest here. Finally, the high-resolution measurements presented here allow spectral analysis and identification of specific crossflow modes, permitting direct comparison with single-wavelength crossflow computations.

For *spatial* stability analysis with an eigenvalue solver, a basic state boundary-layer solution is provided as input, along with global flow parameters, a real frequency (zero for stationary waves), and a wavevector constraint. The code computes the corresponding complex wavevector, given by

$$\mathbf{k} = (\alpha, \beta) \tag{4.3}$$

where α and β are the complex wavenumbers in the chordwise and spanwise directions. The imaginary component of the chordwise wavenumber, α_i, gives the local chordwise spatial growth rate, where negative α_i indicates growth. This solution is only valid locally, so the process must be repeated for each chord position, using the local conditions for each x/c as input values.

The global amplification of a disturbance is computed by integrating the growth rate over x/c. At any position x/c, the disturbance amplitude is compared with the amplitude at the initial position of instability. The resulting amplitude ratio is given by

$$\frac{A}{A_o} = e^N \tag{4.4}$$

where the integrated growth rate is called the N-factor and is given by

$$N(x/c) = \int_{(x/c)_o}^{(x/c)} -\alpha_i \, d(x/c). \tag{4.5}$$

Details of amplitude-ratio calculations and e^N methods are given by Saric (1992a) and Arnal (1992).

The maximum growth for a particular mode is obtained by integrating α_i from the neutral point to the end of the growth region, which usually occurs near the pressure minimum on this model (Dagenhart 1992). The primary method of presenting stability computations is then to give N as a function of x/c on the wing. A summary of the stationary crossflow behavior is obtained by presenting N_{max} as a function of disturbance wavelength.

When SALLY calculations are performed, one must be careful to avoid a potential source of error involving the wave orientation angle, which is given by

$$\varphi_k = \arctan\left(\frac{\beta_r}{\alpha_r}\right). \tag{4.6}$$

SALLY searches for unstable solutions only within a finite range of wave orientations input by the user. If the orientation of the unstable solution initially falls outside of the given range, the mode may not be detected. At larger x/c, the wavevector may change directions so that the orientation falls in the selected range. The result will be an incorrect growth curve which shows a delayed initial-growth position.

Another possible source of error occurs because SALLY is not able to track a disturbance mode through a region of stability. If two unstable ranges of x/c are separated by a stable region, N-factor calculations are suspended through the stable region, and resumed in the second unstable region. This results in incorrect total N-factors.

These problems can only be detected and solved through a careful manual examination of the lengthy SALLY output files, which in most implementations are presented in an overly verbose format. SALLY calculations must be performed with great care, and it should be noted that the experience and training of the user can have an effect on the results.

4.2.5. *Stability Predictions*

Stability calculations are performed for the NLF(2)-0415 installed in the ASU Unsteady Wind Tunnel at an angle of attack of 0°. Figures 4.11–4.12 give N as a function of x/c for chord Reynolds numbers of 3.0×10^6 and 3.6×10^6, as computed by the SALLY code. In these plots, λ_{cf} is the crossflow wavelength, $2\pi/|k|$, and λ_s

is the spanwise wavelength. The spanwise wavelength is given because it is directly measured by most of the experimental methods used here. These results show typical behavior for stationary crossflow modes on a swept wing. Short wavelengths are amplified at small values of x/c, but quickly reach a second neutral point. Longer wavelengths are amplified at larger values of x/c, and the growth is sustained for a longer distance. The wavelengths with the largest total N-factors are those which begin growing fairly early, but are not short enough to reach a second neutral point before the pressure minimum. This behavior is consistent with the fact that the boundary layer provides a fundamental length scale at any given chord position. Since the boundary layer grows quickly at first, and then more slowly, small wavelengths are in the growth range for only a very short time, while longer wavelengths can grow for a comparatively longer time. Comparing the plots for various values of Re_c shows that chord Reynolds number has the expected effect of shifting the amplification to slightly shorter wavelengths while generally increasing the growth rates. For example, at $Re_c = 3.0 \times 10^6$, the most amplified stationary wave has a spanwise wavelength of 12 mm, while at $Re_c = 3.6 \times 10^6$ the most amplified wavelength is between 10 mm and 12 mm.

SALLY computations are also performed for $Re_c = 3.2 \times 10^6$ and 3.4×10^6. As expected, the growth curves fall smoothly between those in Figures 4.11 and 4.12. In addition, MARIA calculations are performed for the same set of Reynolds numbers. The results agree very well with the SALLY calculations. At $Re_c = 3.0 \times 10^6$ and $\alpha = 0°$, the largest N is obtained for $\lambda_s = 12$ mm.

In Chapter 7, it is shown that a small correction of the angle of attack is needed to compensate for a slight misalignment of the flow. Therefore, a full set of MARIA and SALLY calculations are performed for $\alpha = -1°$. The growth curves are similar

in appearance to those at $\alpha = 0°$, but the amplification is much larger in this case, and the range of amplified wavelengths is extended. The maximum N-factor for this case is 6.0. The curves for $Re_c = 3.0 \times 10^6$ and 3.6×10^6 are shown in Figures 4.13 and 4.14.

Additional stability calculations using both Orr-Sommerfeld and linear PSE methods are provided by Arnal *et al.* (1994) for comparison. Figure 4.15 shows a comparison of SALLY, MARIA, Orr-Sommerfeld and linear PSE N-factor predictions for $\lambda_s = 12$mm. As expected, Arnal's Orr-Sommerfeld solver agrees almost exactly with the SALLY results. The PSE code predicts somewhat greater growth, especially near $x/c = 0.1$, so the total N is slightly higher. One can see that there is no essential difference between these techniques except that the PSE calculation gives a representation of the nonparallel effects. It should be mentioned that body curvature is ignored in these calculations since no essential trends in the stability characteristics will change for this configuration.

4.2.6. *Tollmien-Schlichting Waves*

The SALLY code also computes growth rates and N-factors for Tollmien-Schlichting disturbances. Figure 4.16 shows maximum N-factors for T-S waves for angles of attack of 0°, 2°, and 4°, with $Re_c = 3.8 \times 10^6$. At 0°, the favorable pressure gradient stabilizes T-S waves over most of the upper surface. The maximum N-factor is 3, for waves in the 500 Hz range. For negative angles of attack, T-S waves are subcritical over the accelerated region from the attachment line to the pressure minimum. This condition was used for previous crossflow-dominated experiments. At positive angles of attack, the flat pressure gradient allows substantial T-S growth over the upper surface. The maximum N-factor is over 14, and the most unstable frequency is near 2 kHz.

4.2.7. *Reynolds-Number Selection*

Reynolds-number selection is influenced by a combination of theoretical and practical issues. The selected angle of attack of 0° produces small growth rates for both crossflow and Tollmien-Schlichting disturbances. To compensate for this, reasonably large Reynolds numbers are required in order to maximize the disturbance amplitudes. The maximum achievable chord Reynolds number (Re_c) for the Unsteady Wind Tunnel with this model is 4.0×10^6, but this is only for operating temperatures below 35 C. The measurement techniques for this experiment require very long run times, and the tunnel temperature often rises above 50 C during long runs. This limits the practical Reynolds-number range to 3.6×10^6. Therefore, the measurements are made with Reynolds numbers varying between 3.0×10^6 and 3.6×10^6. This range is high enough to produce significant disturbance amplitudes, but low enough to avoid excessive heating of the tunnel.

4.3. Roughness Elements

The linear-stability behavior of boundary-layer disturbances is only one part of the transition process. Initial conditions are equally important in determining the nature and location of transition. The primary source of initial conditions for stationary crossflow waves is microscopic roughness near the attachment line (Radeztsky *et al.* 1993a), while moving crossflow waves are generally influenced by freestream disturbances (Bippes & Müller 1990; Bippes 1991). Chapter 6 presents the results of preliminary experiments at $\alpha = -4°$ which form the foundation for the present experiment and establish the importance of roughness. One of the major goals of this experiment is to carefully document the development of stationary crossflow disturbances with controlled initial conditions. Hence, the surface-roughness distribution must be carefully defined.

The airfoil used in this experiment has a highly-polished surface. Figure 4.17 shows a measurement of the surface finish in the mid-chord region. Measurements presented in Chapter 6 indicate that the roughness level is 0.25 μm rms near the attachment line. When this very smooth surface is combined with the weak amplification of stationary crossflow at $\alpha = 0$, the boundary-layer disturbances are reduced below measurable levels. The flow remains laminar well beyond the pressure minimum. More details can be found in Chapter 7. This is an ideal environment for the study of roughness-induced crossflow.

It is also shown in Chapter 6 that artificial roughness is a very effective crossflow generator. Under conditions of strong amplification, extremely small roughness heights can have a significant impact on transition location. Roughness heights are measured in terms of a Reynolds number, defined by

$$Re_k = \frac{k|u|(k)}{\nu} \tag{4.7}$$

where k is the roughness height and $|u|(k)$ is the velocity at the top of the roughness element. In previous experiments on the NLF(2)-0415 airfoil at an angle of attack of $-4°$, roughness elements had heights between 6 μm and 36 μm, and were placed in a narrow region between $x/c = 0.005$ and $x/c = 0.045$. At this location, the roughness corresponds to less than 5% of the boundary-layer thickness. The Re_k values are between 0.1 and 10.

For the present experiment, much higher roughness elements are needed, due to the low amplification rates. Two primary elements are chosen. The first type are circular plastic file marking dots, Avery #5796. These have a very uniform height of 73 μm, very clean edges, and are easy to apply and remove. The dots have a diameter

of 6.2 mm (1/4 inch). They are easily stacked to produce a height of 146 μm. The second type is a similar dot made from paper, Avery #TD-5730. The paper dots are also 6.2 mm in diameter. The height is less uniform, depending on the application technique, and is found to be 112 μm $\pm 2\,\mu$m. These dots are more difficult to apply and remove, and the edges are less smooth. Therefore, the plastic dots are preferred for most situations. Dot heights are directly measured with a micrometer. A flat steel plate is cleaned with alcohol and measured with the micrometer. The dot is carefully applied, and the thickness is measured again. This procedure is repeated many times by multiple persons.

Roughness Re_k values will vary depending on the operating condition. Figure 4.18 shows Re_k as a function of dot height k at $x/c = 0.005$ for the range of freestream speeds encountered in the present experiment. These Re_k values are computed with $\alpha = 0°$, but the results are almost identical for $\alpha = -1°$. The values are computed using the theoretical boundary-layer solutions, since the boundary layer is too thin for direct measurement at this chord position. The Re_k values for several roughness types are given in Table 4.1. With these high Re_k values, one must be careful to avoid

Table 4.1. Roughness Re_k Values at $x/c = 0.005$

		Chord Reynolds Number			
Roughness Type	k [μm]	3.0×10^6	3.2×10^6	3.4×10^6	3.6×10^6
Paper, 1 Layer	112	94	103	112	122
Plastic, 1 Layer	73	42	47	51	55
Plastic, 2 Layers	146	152	166	180	195

the direct tripping mechanism associated with three-dimensional roughness elements (von Doenhoff & Braslow 1961; Juillen & Arnal 1990). This effect occurs at high Re_k values ($\gg 100$) and is distinguished by a transition wedge beginning immediately behind the roughness element, due to an instability of the wake behind the element.

In contrast, crossflow transition wedges occur at some distance behind the roughness element, after a region of vortex growth. The direct-trip mechanism appears to depend as much on the character of the edges of the roughness element as on the height of the element, since the plastic dots are routinely stacked to Re_k well over 100 without causing a transition wedge. The rougher paper dots cause transition at lower Re_k values.

The dots are applied either individually or in spanwise arrays. There is some disagreement as to which arrangement is more fundamental. If the receptivity mechanism is through a local injection of streamwise vorticity, then a single dot is the most basic disturbance source. If the roughness is viewed as a wavelike pressure disturbance, then a uniform array with a simple Fourier decomposition is the most basic. The dot locations are determined by measurement along the airfoil surface and verified by calibrated traverse movements with a probe over the target area. The wing surface is carefully cleaned with alcohol and window cleaner before application of the roughness. Each element is individually applied, rubbed for uniform thickness, and carefully inspected. The dots have a fixed diameter of 6 mm, but changes in dot spacing change the fundamental wavelength of the roughness array. Effective arrays with wavelengths as low as 9 mm are easily produced. Widely-spaced arrays approach the limit of isolated roughness elements.

5. EXPERIMENTAL TECHNIQUES

High-resolution hot-wire measurements over large spanwise distances require a careful development of experimental techniques. Several aspects of the measurement and analysis process are described here.

5.1. Hot-Wire Signal Processing

The analysis of hot-wire signals is a complex subject. Many different techniques have been developed over the years, each having advantages and disadvantages. The analysis approach at the Unsteady Wind Tunnel emphasizes the use of computerized calibration techniques which eliminate the need for external hardware at the expense of additional software development. This technique is relatively independent of any particular physical model of the heat transfer characteristics of hot-wires, and concentrates on empirical accuracy as the primary concern. Perry (1982) indicates that simple polynomial calibration is often at least as accurate as very sophisticated flow models.

The basic analysis technique is outlined in Dagenhart (1992), and extended to include software temperature compensation by Radeztsky *et al.* (1993b). In general (Perry 1982), the voltage response of a constant-temperature anemometer is a function of density, velocity, and total temperature:

$$E = F(\rho, U, T_o). \tag{5.1}$$

For a low-speed wind tunnel, the density dependence is negligible, and the response is dominated by the velocity and temperature response. The velocity response is by far the largest component. If the temperature is held constant, a very accurate calibration is obtained by fitting a low-order polynomial to a modest number of

velocity-voltage pairs. Usually a 4^{th}-order fit is chosen because it can model the dominant King's law behavior, but it must be emphasized that a polynomial fit is more general than King's law and will more accurately fit a given set of points within the velocity range of those points. Outside of that range, the polynomial fit may deviate significantly from the behavior of the anemometer. For boundary-layer work, the calibration points must cover the full velocity range from the pressure-minimum edge velocity to the minimum boundary-layer measurement. The practical lower limit for constant-temperature anemometers is about 1 m/s (Perry 1982). The calibration points are obtained with the hot-wires positioned at a standard location near the pressure minimum so that the wires may sample the highest possible velocities. The C_p difference between this location and the reference Pitot-static probe is included in the calibration calculations.

In low-speed flows, the temperature response is large in the sense that it may not be ignored, but small in a perturbation sense. In other words, the temperature dependence of the anemometer may be treated as a correction to the dominant velocity behavior, without resorting to complicated models. Radeztsky *et al.* (1993b) point out that for the temperature ranges encountered at the Unsteady Wind Tunnel, the temperature drift of the hot-wire voltage is modeled very well by a linear correction term. This coefficient is obtained before calibration, while the tunnel is being pre-heated. The pre-heating brings the tunnel to an approximate equilibrium, minimizing temperature changes during the experiment. The temperature coefficient actually is not a constant, but depends on the velocity. For the small temperature changes encountered during a typical experiment, this additional effect is ignored. Recent versions of the analysis software include this correction as well. The temperature-drift

coefficient is applied even during the calibration to eliminate any small temperature changes during the calibration.

The other major effect of temperature changes in low-speed wind tunnels is on the unit Reynolds number. This is compensated at the Unsteady Wind Tunnel by a computer-based "cruise-control" system which constantly monitors flow conditions in the test section. The velocity setting of the motor controller is continuously updated to maintain constant Reynolds number in the test section. This is the most appropriate control mode for boundary-layer stability experiments. The velocity changes are eliminated by using normalized velocities in all results. A reference hot-wire is located in the freestream near the boundary-layer probe.

Accurate mean-flow measurements require time-averaging over several seconds in order to eliminate the effect of low-frequency tunnel fluctuations. Fluctuation measurements require a large number of samples to satisfy the Nyquist requirements of the desired signal components. In either case, thousands of separate samples must be processed to obtain a single result. With the introduction of the new high-speed acquisition computer, the standard processing technique is changed. Each voltage sample is now processed through the temperature-correction and calibration polynomials. The resulting velocities are then averaged to obtain the mean velocity. The older method averaged the voltages first, and then processed the single average voltage. The new technique eliminates errors from the local nonlinearity of the calibration curve with negligible time penalties due to the extremely fast floating-point capabilities of modern computers.

All acquisition programs used in this experiment employ the above techniques through a standard library of routines. This simplifies the programming process, and allows modular acquisition programs to be developed and updated efficiently.

5.2. Spectral Analysis

A primary goal of this experiment is to obtain measurements of stationary crossflow disturbances with sufficient resolution for quantitative analysis. Analysis is complicated by the fact that no practical roughness distribution forces a single crossflow mode. Methods which simply characterize the amplitude variations of the total disturbance are inaccurate because all stationary modes which are present in the flow are lumped together. Some of the disturbance energy may belong to decaying short-wavelength modes. Interpretation is simplified if the measurements are sufficiently dense to allow the application of spectral methods. If a single mode can be extracted from the total signal, comparisons with linear stability theory will be much more meaningful. This section describes several issues influencing the use of spectral methods for this experiment. A complete explanation of discrete spectral methods can be found in Press *et al.* (1988), and in many other places. Therefore, only those issues related to their use in this experiment will be explained here.

5.2.1. *Wavelength-Resolution Issues*

Spectral methods are usually applied in the time domain in order to separate various frequency components from a measured time series. They are, of course, equally effective in resolving different wavelength components from a spatially-varying signal. When an experiment is set up, a primary concern is choosing sampling parameters appropriately so that the desired spectral resolution is achieved. These parameters are usually given in terms of "frequency," which in a spatial spectrum corresponds to inverse wavelength. A translation of these parameters to a wavelength representation reveals the necessary constraints on the measurement.

A typical measurement for this experiment consists of N disturbance velocities spaced evenly along a spanwise distance S. The sampling interval Δ is defined by

$$S = (N-1)\Delta. \tag{5.2}$$

When a discrete Fourier transform (using the FFT) is applied to N data points, amplitude information is obtained at N frequencies given by

$$f_k = \frac{k}{N\Delta}, \quad k = \frac{-N}{2}, \ldots, 0, \ldots, \frac{N}{2}. \tag{5.3}$$

The amplitudes at the most negative and positive frequencies are the same, so there are really only N independent quantities. The power spectrum is computed by squaring the amplitudes and folding the negative-frequency information over to the corresponding positive frequencies. The power spectrum is then defined at the $N/2+1$ frequencies

$$f_k = \frac{k}{N\Delta}, \quad k = 0, \ldots, \frac{N}{2}. \tag{5.4}$$

The frequency spacing is then given by $\delta f = 1/N\Delta$. In a spatial spectrum, f corresponds to $1/\lambda$, so we have power estimates at $N/2+1$ wavelengths

$$\lambda_k = \frac{N\Delta}{k}, \quad k = 0, \ldots, \frac{N}{2}. \tag{5.5}$$

The wavelength estimates are not evenly spaced in λ, so the wavelength resolution is a function of λ. The best estimate of the wavelength resolution is obtained by treating λ and f as continuous functions. Then the λ spacing is given by $\delta\lambda = (d\lambda/df)\delta f$, so

we have

$$|\delta\lambda| = \frac{\lambda^2}{N\Delta} \approx \frac{\lambda^2}{S}. \tag{5.6}$$

This equation becomes more accurate as the number of samples is increased. We see that the wavelength resolution is entirely determined by the total span of the measurement. Simply increasing the number of samples N for a given span does not decrease $\delta\lambda$ because Δ will decrease. Therefore, for maximum wavelength resolution we must cover the largest possible span. The sampling interval is determined by the shortest desired wavelength, given by $\lambda_c = 2\Delta$.

For the conditions of this experiment, the most amplified wavelengths are centered around $\lambda = 12$ mm. The maximum spanwise distance for the traverse mechanism is 240 mm. If 256 samples are obtained along this span, then at $\lambda = 12$ mm we have $\delta\lambda = 0.6$ mm. The lowest and highest resolvable wavelengths will be 1.9 mm and 240 mm. The sampling interval $\Delta = 0.94$ mm is also a reasonable value for producing accurate representations in the spatial domain. It is also an appropriate lower limit, since the length of the hot-wire sensor is 1.25 mm. Information at shorter spanwise intervals is effectively filtered out by the probe. Therefore, all hot-wire scans for which spectral information is desired will cover the full span of 240 mm with a spacing of 0.94 mm. If only a spatial representation is desired, a shorter span of 1 or 2 wavelengths will be sufficient.

5.2.2. *Fast Fourier Transform*

Of the many spectral analysis techniques available (Kay & Marple 1981), the FFT is by far the most common. All spectral techniques exhibit a set of strengths and weaknesses, and the FFT is no exception. FFT estimates suffer greatly when the number of samples is limited, which is often the case for spatial measurements. Unlike

the theoretician who expresses a function as an exact combination of Fourier modes, the experimentalist is approximating an existing continuous function of unknown spectral content as a combination of discrete modes. The result is a high error in the spectral estimates, and significant leakage of spectral peaks into nearby frequency bins. The well-known remedies for these problems are data windowing and averaging (Press *et al.* 1988). Many window functions are in common use, each with its own set of trade-offs. The Hanning window is used for this experiment. Averaging is usually accomplished by breaking a long data stream into several segments, computing a power spectrum on each segment, and then averaging the results to produce the final power spectrum. This works fine for the time domain, where a long data stream is easily obtained by extending the sampling time. For the present spatial experiment, the data stream is already as long as possible, i.e. the full traverse span. Breaking the spanwise scan into segments will compromise the sampling parameters, rendering the resulting spectrum useless. For this case, the averages must be obtained by repeating the experiment multiple times. This option is not always practical, as each repetition includes significant overhead time. The experiment may exceed available time limits. As a compromise, multiple averages are obtained for this experiment by increasing the number of samples N by a factor of M, the desired number of averages. These samples are not useful for increasing the resolution of the FFT, due to the restrictions outlined in the previous section, but the measurements can be demultiplexed to produce M data sets, each of length N and covering the total span S. The data sets will differ slightly in phase, but this will not affect the squared power spectrum. This scheme may also help to remove any systematic traverse errors by obtaining the data sets at slightly different positions.

Another problem encountered with FFT estimates is the considerable number of normalization schemes in common use. Often this issue is "swept under the rug," and power spectra are presented without appropriate units. The normalization must be clearly understood if quantitative information is to be extracted.

The major normalization issue is whether the "summation" or "integration" convention is used for the total power. The summation convention recognizes the FFT as yielding a discrete spectrum, and specifies that the total power is simply the sum of the power estimates. The integration convention views the FFT as an approximation of the underlying continuous spectrum. The power estimates are divided by the frequency spacing so that the spectrum must be integrated to obtain the total power. For sufficiently-large numbers of samples, this method has the advantage that the power spectrum will not change much if the sampling parameters are changed. The discrete spectrum will change in amplitude if the number of bins is changed. On the other hand, the integral convention is confusing when the spectrum is plotted as a function of wavelength instead of frequency for spatial data. One must decide whether to preserve the values of the spectrum while simply inverting the frequencies, or to divide the spectral estimates by λ^2 so that power integration may be performed in the power vs. λ plane. All FFT power spectra reported here will follow the summation convention, and will be plotted with λ as the independent variable. For power spectra of dimensionless disturbance velocities, the dependent coordinate will then be dimensionless.

5.2.3. *Maximum Entropy Method*

The maximum entropy method (MEM) of spectral estimation models the power spectrum as a Laurent series and allows singularities. It is thus very good at finding sharp spectral peaks. However, Press *et al.* (1988) point out that all spectral methods

suffer from inherent flaws and one must be careful about overstating the effectiveness of any technique. The MEM techniques suffer from the fact that the user must choose the number of poles to allow in the spectrum. A sufficient number must be used to reveal all spectral features. Too many poles will cause spurious peaks to appear, and a single sharp peak will often be split. This creates serious problems with automated techniques for integrating the power under sharp peaks. For small numbers of samples, the spectral peaks can change frequency depending on the phase of the signal. These features require that the MEM be applied with great care. The number of poles must usually be chosen interactively, according to the subjective impressions of the user.

Fortunately, the integrated power under a spectral peak is fairly insensitive to the number of poles, even though the actual height of the peak may vary considerably. In spite of the above cosmetic difficulties, the MEM can be used very successfully to track amplitudes of dominant spectral features. It will often follow small peaks in cases where the FFT can not resolve the desired features.

The MEM produces continuous spectra, so the summation convention is not an option in this case. The normalization issue revolves around whether the spectral values should be divided by λ^2 when the spectrum is plotted as a function of λ. For MEM spectra presented here, the data are not normalized with λ^2. All power integrations take place in the dimensionless frequency domain, and the visual presentation of the spectrum as a function of λ is viewed as a matter of convenience. This method of presentation gives the dependent variable the same units as the independent variable for a power spectrum of dimensionless velocities.

5.3. Traverse Alignment

The measurement constraints outlined in the previous sections require long spanwise scans with precise positioning. In the worst-case scans at $x/c = 0.05$, the

boundary layer is only 1 mm thick, and accurate positioning must be maintained over a span of 240 mm. This precision must be achieved at all positions on a model with a chord of nearly 2 m, while reaching through a window 0.6 m away from the model. This level of accuracy is not possible with simple mechanical adjustments of the traverse system. Instead, a software alignment system is used.

Before experiments are started, the traverse is roughly aligned with the wing-chord plane by carefully measuring the distances between the support rails and the wing. This allows gross movements of the traverse over the model to be accomplished with reasonable confidence.

At this point, when a spanwise scan is attempted in the boundary layer, the hot-wire drifts significantly, finishing the scan at a completely different relative position in the boundary layer. In some cases, the wire may drift completely out of the boundary layer, or may hit the airfoil. A more precise alignment is achieved experimentally. At each chord position between $x/c = 0.05$ and $x/c = 0.60$, with $0.05c$ spacing, a special spanwise scan is performed with the wind tunnel operating at $Re_c = 3.0 \times 10^6$. No roughness is placed on the model, so the boundary layer is completely laminar with no spanwise variations. The traverse takes 1 mm steps in the spanwise direction. At each position, the y coordinate of the traverse is moved until a relative velocity of $u/U_e = 0.5$ is achieved. The convergence is accelerated using Newton's method. The required y coordinate is recorded. The resulting data set of y vs. span is modeled with a linear least-squares fit. This produces a linear traverse drift coefficient at each chordwise position.

The traverse drift coefficients are stored in the computer. All traverse motions are controlled by the computer, which always knows the exact position of the boundary-layer hot-wire probe. When spanwise moves are requested, the computer applies an

appropriate y-correction to remove the traverse drift. This method is accurate enough to allow large spanwise motions with no danger of striking the airfoil surface with the hot-wire probe. The spanwise scanning methods outlined in the following sections employ additional procedures to guarantee precise alignment of spanwise data.

5.4. Spanwise Scans

The software alignment system described above is not sufficiently accurate for detailed measurements of stationary vortices. Each of the scanning methods needs additional alignment techniques to assure accuracy. This extreme precision is necessary because the disturbance velocity is a strong function of y. A slight drift in y during a scan can cause large errors in the measured disturbance velocity.

One of the useful measurement techniques is a simple spanwise hot-wire scan. This type of scan is useful where detailed spectral and amplitude information is desired, but a complete picture of the disturbance modes is not needed.

Since the disturbance velocity depends on y, a consistent method is needed for determining the proper location for the scans. Examination of theoretical solutions and detailed boundary-layer scans reveals that the maximum disturbance amplitude is always found approximately where $u/U_e = 0.75$ in the mean velocity profile. Since the disturbance profile is nearly flat near the maximum point, small errors in y can be tolerated at this point in the boundary layer more than at others. For this reason, all spanwise scans are conducted at a mean velocity of 0.75 in the boundary layer.

Tracking the target location in the boundary layer is complicated by several factors. The surface of the model is not completely flat in the spanwise direction. The required path to maintain a mean velocity is therefore not a straight line. The software drift correction follows the best straight-line fit through the desired path. For spanwise scans, the actual path must be determined. Temperature changes cause

expansion of the various traverse components and the airfoil model during long runs. The proper path must be determined at the time of the scan, and the scan must be completed in a short time period. Finally, the presence of the stationary vortices causes mean flow distortions which show up as variations in u/U_e. Indeed, the purpose of the spanwise scan is to detect and measure these distortions. The path-finding algorithm must not be so detailed that it actually causes the traverse to follow the distortions, yielding a null result!

Keeping these restrictions in mind, the proper traverse path is located as follows: With the wind tunnel warmed up and operating at the desired Re_c, the calibrated hot-wire is placed near the boundary-layer edge at the starting position for the scan. The reference probe is positioned in the freestream at the same x/c and spanwise position. An initial velocity reading is performed at this position. This reading verifies that the probe is actually outside the boundary layer, and establishes the velocity ratio between the two wires, which will have slightly different readings due to the velocity field over the wing. All subsequent freestream readings are divided by this ratio. This allows the freestream probe to monitor freestream variations while normalizing the boundary-layer readings to 1.0 at the edge. The probe is then moved in until the normalized velocity is 0.75. This position is influenced by the local phase of the stationary crossflow, but for low-amplitude disturbances, the resulting offset on the final curve is sufficiently small. The probe is then stepped along the span in 1 mm steps. At each location, the y position is varied until the normalized velocity is 0.75, and the location is recorded. The resulting path follows the desired averaged path, but with deviations due to the stationary crossflow. This path is obtained in about 15 minutes, which is short enough to avoid significant temperature changes. Figure 5.1 shows a typical alignment scan. Several features are apparent. The path

has a significant slope due to the mechanical misalignment of the traverse. The path is slightly curved due to slight curvature of the wing surface. The path shows short-wavelength deviations because of the stationary crossflow. The desired mean path will follow the slope and large-scale curvature, but will ignore the short-wavelength deviations. This desired path is produced by fitting a low-order polynomial to the raw traverse path. A 4^{th}-order fit is usually appropriate. Figure 5.1 shows this path along with the original traverse path. This path has the desired characteristic of following the average position of $u/U_e = 0.75$ in the boundary layer. After this initial pathfinding scan the probes are returned to the starting position in preparation for the actual spanwise scan.

To begin the the spanwise scan, an array of traverse positions is prepared from the required path. These points are on the fine grid required for obtaining many averages for spectral analysis. Usually, 2048 points are measured. This provides 8 averages, each with 256 points covering the full span of 240 mm. Before the scan, an additional reference point is obtained outside of the boundary layer. The traverse is then quickly moved to each of the 2048 points on the averaged path, and a velocity sample is acquired. Figure 5.2 shows the resulting plot of normalized velocity as a function of span. The probe successfully follows the proper constant-height line while accurately measuring the stationary crossflow distortions at the maximum of the mode shape.

5.5. Multiple Boundary-Layer Scans

The spanwise scans described in the previous section have several distinct advantages. They can be completed in the relatively short time span of about 30 minutes. They do not require the hot-wire probe to approach the model surface, so they are

easy to perform in thin boundary layers. However, when a complete picture of the stationary vortices is desired, a full two-dimensional scan must be completed.

One method for producing a full two-dimensional profile would be to perform spanwise scans at many y-positions in the boundary layer, and then assemble these scans to form the image. This procedure does not work well because it is difficult to establish a common reference frame for the scans. Temperature changes over the long time period required for the scans change the traverse alignment slightly. Instead, a sequence of wall-normal scans (boundary-layer scans) is assembled to create the full profile.

Constructing a full two-dimensional scan from individual boundary-layer scans has several advantages. A boundary-layer scan is extremely simple to perform, and can be completed in less than 1 minute. A boundary-layer scan is self-aligning, because the wall can be located directly from the measurements. For the mild favorable pressure gradients found on this model, the slight curvature of the profile near the wall may be ignored. The velocity profile is approximated by a straight line for a significant region near the wall. A linear extrapolation to zero velocity will accurately locate the wall. This wall-location procedure is well-established, and has been used with remarkable success (Rasmussen 1993; Spencer 1992; Dagenhart 1992). As long as temperature drifts are small within each scan, many scans may be completed over a very long time period. The wall is located for each scan, providing a global reference frame in which to assemble the two-dimensional profile.

A full set of 2048 spanwise points would take a prohibitive amount of time to complete. Therefore, only 256 spanwise positions are used for this type of measurement. The major goal is to produce a full image of the crossflow vortices, and this resolution is sufficient. However, a spanwise set of velocities at any altitude can be

extracted from the full two-dimensional profile for comparison with the full spanwise scans.

A standard boundary-layer scan is performed with a nonuniform step size. An appropriate step size is chosen at the outer edge, based on the expected thickness of the boundary layer. After acquiring a reference point at the edge of the profile, the probe is stepped towards the wall, acquiring velocities at each point. As the probe moves in, the step size is scaled with u/U_e. This gives better resolution near the surface, and prevents the probe from accidently striking the model. This conservative procedure gives a high-resolution profile, usually containing about 45 points. An example is shown in Figure 5.3.

Even for only 256 scans, the above procedure will take too much time to complete. Instead, a list of 18 to 24 desired velocity positions is compiled, depending on the size of the boundary layer. The first boundary-layer scan is completed in the conventional manner. For each subsequent spanwise position, the data from the previous scan are used to estimate the y-position of the desired velocity points. The linear traverse correction is applied to the estimates. Several points are taken outside the estimated edge of the boundary layer to guarantee a complete profile. Several extra points are acquired near the wall to insure a good extrapolation to the wall. The y-estimates do not need to be completely accurate. As long as a sufficiently complete profile is obtained at each spanwise position, the procedure can proceed indefinitely. This procedure reduces the total sampling time for a two-dimensional profile to approximately 3 hours, depending on the size of the boundary layer. The method is very robust, and is used effectively in boundary layers as thin as 1 mm across the full span of 240 mm.

After the scan is complete, the boundary-layer profiles are assembled to produce the full two-dimensional picture. The data are interpolated to a uniform grid for

later processing. Any desired contour plots, disturbance mode shapes, and spanwise profiles may then be extracted from the interpolated data set.

6. PRELIMINARY EXPERIMENTS

A set of preliminary experiments are conducted at $\alpha = -4°$ in order to determine the role of roughness in crossflow-dominated flows. These experiments are documented in detail by Radeztsky *et al.* (1993a). A review of important results from these experiments will be given here.

6.1. Introduction

At small negative angles of attack, the NLF(2)-0415 airfoil has a favorable pressure gradient until $x/c = 0.71$ on the upper surface. Under these conditions, the boundary layer is subcritical to T-S waves but produces considerable crossflow amplification. Figures 6.1–6.3 show MARIA stability results for the range of chord Reynolds numbers used in this test. The maximum N-factors for stationary crossflow vary from 11 to 14 at a crossflow wavelength of about 10 mm. For travelling waves, SALLY calculations show that the maximum N-factor is 16 at $f = 200$ Hz. These N-factors are high enough so that transition is expected well ahead of the pressure minimum (Dagenhart 1981).

The basic-state flow and stability results for this configuration have been thoroughly documented (Saric *et al.* 1990; Dagenhart *et al.* 1989, 1990; Dagenhart 1992). The pressure distribution and boundary-layers match the design predictions except for a small angle-of-attack correction similar to the correction found in the present experiment. Boundary-layer measurements reveal the presence of both travelling and stationary crossflow waves, as predicted by linear theory.

Even though the travelling wave is predicted to be more unstable, the transition process in a low-disturbance environment is controlled by the stationary wave (Kohama *et al.* 1991). Mean-flow distortions produced by the stationary wave give rise to a high-frequency secondary instability which leads to transition. The transition

front has a jagged form which is fixed relative to the stationary crossflow pattern. The initial transition point is always located near regions where the basic-state has been distorted to produce highly-inflected profiles.

Linear stability is only one factor in predicting transition. The other key ingredient is *receptivity*, which is not as well-understood as the stability problem. The receptivity problem for stationary vortices is related to sources of streamwise vorticity. Even at very low Re_k values, the flow around a three-dimensional roughness element in a shear flow can be a source of streamwise vorticity (Saric *et al.* 1990b). It is clear that surface roughness plays a major role in the receptivity process for stationary crossflow. This set of experiments is designed to quantify this effect.

6.2. Results

6.2.1. *Initial Flow-Visualization Observations*

For previous crossflow experiments at $\alpha = -4°$, the NLF(2)-0415 model was covered with a layer of black paint for LDV work. Naphthalene flow-visualization measurements with this painted surface provided some of the initial clues about the importance of surface roughness. The naphthalene-visualization technique is described in Chapter 7. Figure 6.4 shows a typical visualization of the transition pattern for $Re_c = 2.6 \times 10^6$. The flow is from left to right, and x/c locations are marked with diagonal lines parallel to the leading edge, which can be seen at the lower left of the figure. The jagged transition front is clearly visible as a change from light to dark near $x/c = 0.5$ (marked with '50' in the figure). This location is well ahead of the pressure minimum, as anticipated by linear theory. Strong stationary crossflow vortices are observed as streaks in the naphthalene, running at a slight angle above the horizontal direction. For similar flow parameters, the "saw-tooth" transition pattern is always the same, even if the experiment is repeated weeks or months later. If the swept-wing

test section is removed and re-installed after several months of flat plate experiments, or even if the flow-conditioning screens are removed, cleaned and installed in a different order, the transition pattern on the airfoil will appear at the same locations. This provides very strong evidence that the stationary crossflow pattern is influenced by the model rather than by freestream disturbances.

The initial indications of the importance of roughness come from an examination of the transition wedges which begin at the smallest value of x/c. If a streamline is traced from the apex of the earliest wedges to the leading-edge region, a small paint imperfection is usually found. If this paint speck is sanded smooth, the corresponding transition wedge moves back to larger x/c. It is clear that very small roughness near the attachment line has a significant effect on transition. The results in this section provide a quantitative measurement of this effect.

6.2.2. *Measurement of Roughness Heights*

One of the major challenges associated with roughness experiments is the measurement of roughness characteristics. Roughness heights are often in the micron range, while the lateral scales can be anywhere from several microns to tens of millimeters. The surface to be measured is that of a 620 kg solid-aluminum wind-tunnel model which can not easily be moved.

A partial solution to these problems is implemented for this set of experiments. The surface of the airfoil is duplicated in a portable medium by taking castings with a *dental pattern resin.* This material is applied to the surface in liquid form, and it dries to form a hard, rigid imprint of the surface. This casting is accurate to submicron levels. It can be measured with a profilometer, which traces the surface using a diamond stylus with a 4 μm diameter, producing a calibrated voltage signal which is

directly acquired by a computer. The result is a highly-detailed image of the original surface finish. Figures 6.5–6.7 show several examples of these surface measurements.

There are several complications which prevent this measurement technique from being ideal. The finite diameter of the stylus limits the ability of the profilometer to follow very tiny details on the surface. The surface profiles shown here are filtered at 20 μm to reflect this limitation. These extremely small features are not at lateral scales comparable to the crossflow instability, and do not seem to be important in the receptivity process, according to these experiments. A more serious problem occurs at the long-wavelength end of the roughness spectrum. The resin castings tend to warp as they are removed from the original surface. If the sample is left to dry for a longer period of time to avoid this problem, it becomes difficult to remove and is often shattered during removal. These problems limit the effective maximum sample size to about 30 mm. On most samples, the profilometer data is contaminated by false long-wavelength signals due to the warping. Data are typically filtered at around 1500 μm to eliminate this contamination. However, this wavelength is not long enough to include the most important roughness scales (those on the order of the most-amplified crossflow waves). Thus, the roughness samples are only used as method of characterizing the general quality of a surface. This technique works very well in tracking surface improvements due to polishing. Careful polishing would be expected to remove roughness at length scales well beyond the limit of the profilometer technique, and this seems to be true based on the dramatic effect polishing has on crossflow-dominated transition (see below).

The profilometer technique is also useful for measuring the height of the artificial roughness elements used in these tests. In this case, the measurement is over a small span, and the wavelength limitations do not apply.

Artificial roughness elements are also measured directly with micrometer-based instruments. The results are consistent with those of the profilometer technique.

6.2.3. *Distributed Roughness*

The effect of distributed roughness on crossflow-dominated transition is documented with naphthalene flow visualization. For the original painted surface, Figure 6.8 shows that the average transition location is very early. For example, at $Re_c = 3.0 \times 10^6$, the average transition location is at $x/c = 0.33$. Profilometer measurements (Figure 6.5) indicate a peak-peak roughness height of about 10 μm, which would normally be considered very smooth. Roughness Reynolds numbers (Re_k) are about 0.3, well below the usual limits for transition effects.

After the surface is carefully measured, the paint is removed and the aluminum surface is carefully polished. The resulting finish is shown in Figure 6.6. The rms roughness height is reduced to 0.509 μm. A second treatment with careful hand polishing reduces the roughness to the conditions shown in Figure 6.7. The final surface finish is about 0.25 μm near the attachment line and 0.12 μm in the mid-chord region.

Transition measurements are conducted over a range of Re_c at the different stages of the polishing process. The results are shown in Figure 6.8. The transition location is shown to increase with higher levels of polishing. This measurement shows very dramatically the effect of surface finish on crossflow-dominated transition. For example, at $re_c = 2.7 \times 10^6$, transition is moved from 40% chord to 62% chord. Thus, a 50% increase in the laminar-flow region results from paint removal. The fact that even an improvement in surface finish from 0.5 μm to 0.25 μm produces a substantial change in transition location is also remarkable.

6.2.4. *Isolated Roughness Elements*

The effect of surface roughness is systematically examined by introducing isolated roughness elements on the polished wing surface. The elements are created by applying "rub-on" symbols from dry transfer sheets commonly used in the graphic arts industry. The elements have been carefully measured to produce a reliable height of 6 μm, and are available in a variety of diameters.

A single 6 μm roughness element applied at $x/c = 0.023$ with $Re_c = 2.6 \times 10^6$ causes a distinct, repeatable transition wedge to appear, with the apex of the wedge near $x/c = 0.4$. This location is near the average transition location for the painted surface under these conditions. The wedge is accompanied by a strong vortex signature in the naphthalene between the roughness element and the wedge, indicating that the roughness has a strong effect on the stationary vortex originating near it.

The diameter and height of the roughness element are systematically varied over a wide range. Figure 6.9 shows the transition location obtained with these elements. As expected, higher roughness has a stronger effect on transition, moving the wedge closer to the leading edge. A more significant effect is discovered from the diameter variations. As the roughness diameter is reduced below $\lambda_{cf}/10$, the transition wedge vanishes. This remains true even as the roughness height is increased. This may be because the smaller roughness elements introduce no net streamwise vorticity on the scale of the crossflow vortices. The effect of roughness diameter is measured at three different values of Re_c, with the results shown in Figure 6.10. As D/λ_{cf} is reduced below 0.1, the transition Reynolds number returns to the undisturbed value. These results indicate the importance of spanwise scale in determining the effect of roughness on stationary crossflow.

If a spanwise strip of roughness is introduced at $x/c = 0.023$, a pair of transition wedges appear in the regions behind the ends of the strip, but the transition location is unaffected in the center of the strip. This again confirms the importance of spanwise scale, and illustrates the three-dimensional nature of the receptivity process. These elements would normally be classified as two-dimensional from a traditional geometric point-of-view, because $D/k \gg 1$, but they are three-dimensional from a receptivity point-of-view, because all three dimensions are important in the receptivity process.

The effect of roughness location is investigated by varying the position of the roughness element from $x/c = 0.005$ to $x/c = 0.045$. For this configuration, the attachment line is at $x/c = 0.007$, and the crossflow neutral point is at $x/c = 0.02$. These measurements (Figure 6.11) show that the effect of roughness is limited to a very narrow region near the leading edge. If the roughness element is moved in front of the neutral point, or too far downstream, transition returns to the undisturbed position. This justifies the use of naphthalene as a nonintrusive visualization technique.

6.2.5. *Hot-Wire Measurements*

The effect of roughness on the stationary vortices is clarified by hot-wire measurements taken directly behind the roughness element. These measurements are similar to the spanwise scans described in Chapter 5, and measure the large distortions in the streamwise velocity profiles caused by the convective action of the weak stationary vortices. These scans are made at four chord positions and three heights in the boundary-layer.

Figure 6.12 shows the results at $x/c = 0.35$. A periodic modulation of the streamwise velocity is evident over the entire scan. A region of very strong modulation occurs in the area directly affected by the roughness element. This is consistent with

the enhanced vortex tracks observed with naphthalene flow visualization. The variations are present at all heights in the boundary layer. A spatial power spectrum reveals a spanwise wavelength of about 10 mm, corresponding to $\lambda_{cf} = 8$ mm, in agreement with the spacing observed via flow visualization.

The streamwise growth of the vortices is documented in Figure 6.13, which displays the spanwise scans at all four chord positions for one height in the boundary layer. The enhanced vortices behind the roughness element grow in amplitude all the way back to $x/c = 0.4$, which is near the tip of the transition wedge. It is important to note that the undisturbed stationary vortices do not appear to be growing, even though linear theory predicts substantial growth in this region. This apparent saturation is most likely due to nonlinear effects, and is one of the reasons for conducting the main set of measurements (Chapter 7) at much lower stationary crossflow amplitudes.

6.3. Conclusions

These preliminary measurements show that micron-sized roughness has a profound effect on the development of stationary crossflow waves, and on crossflow-dominated transition. The effect of roughness height and diameter is quantified. It is found that roughness with $D = \lambda_{cf}/2$ has a large effect on transition, while roughness with $D < \lambda_{cf}/10$ has no effect. The effect of roughness is limited to a narrow region near the leading edge.

In a low-disturbance environment like that found in flight, the stationary crossflow vortex dominates the transition process. Any attempt to understand and predict transition under these conditions must take into account the receptivity process, and the role of surface roughness in providing initial conditions for stationary crossflow vortices.

These measurements set the stage for the more extensive measurements in Chapter 7. Roughness can be used to induce carefully-controlled stationary crossflow vortices for detailed measurements of vortex development and growth.

7. EXPERIMENTAL RESULTS

7.1. Flow Quality

The Unsteady Wind Tunnel has very low freestream turbulence levels. Dagenhart (1992) indicates that the turbulence level depends somewhat on the particular model and liner configuration. With the swept-wing model at $\alpha = 0°$, measurements of the u' fluctuations in the freestream at the test-section entrance are conducted with several band-pass settings. Figure 7.1 shows the disturbance spectrum with a filter pass band of 1–1000 Hz, for a freestream speed of 18 m/s. Most of the disturbance energy is concentrated in the lowest frequencies. The fluctuation level u'/U_∞ is measured to be 0.038%. With a pass band of 10–1000 Hz, the value for u'/U_∞ is 0.015%.

7.2. Flow Visualization

Previous experiments with the model in a crossflow-dominated configuration use naphthalene flow visualization as the standard vortex-location technique (Dagenhart 1992; Radeztsky *et al.* 1993a). A naphthalene/1,1,1-trichloroethane mixture is sprayed on the wing surface, leaving a visible white naphthalene layer. The sublimation rate of the naphthalene is sensitive to the local shear stress. The distortions caused by stationary crossflow leave visible streaks parallel to the vortex tracks. Transition is clearly detected as well by the complete absence of naphthalene.

The present configuration limits the stationary crossflow waves to very small amplitudes, and hence the naphthalene technique is not as effective. Figure 7.2 shows a photograph of stationary crossflow streaks for the present experiment. The chord Reynolds number is 3.0×10^6, and a full-span array of 146 μm roughness with 10 mm spacing is located at $x/c = 0.005$. This condition produces the largest possible stationary crossflow as indicated by hot-wire measurements. The vortex tracks are very weak because the periodic shear stress variations are very small. The difference

in sublimation only becomes apparent as the last traces of naphthalene disappear. With no roughness elements on the wing, there is no trace of stationary crossflow streaks at any Reynolds number. This makes the naphthalene technique unsuitable for tracking the locations of individual vortices. For this experiment, the vortices must be located with hot-wire surveys, which takes considerably longer.

Since the crossflow is too weak to cause transition even at the maximum chord Reynolds number, there is no visible jagged transition front as in the previous experiments. Turbulent wedges are sometimes visible starting from several of the access panels on the model surface. These panels are in areas which do not interfere with the central test region.

7.3. Outline of Hot-Wire Data

The majority of the data for this experiment consists of extensive spanwise hot-wire surveys covering a wide variety of conditions. This section presents an overview of the various scans and roughness configurations. A naming scheme for the data sets is described, and a table of data sets is presented. This provides a guide for the remaining sections of this chapter.

The hot-wire data are divided into 18 distinct run conditions and 24 data sets. The run conditions are distinguished with lowercase letters a through r. The data sets are labeled with uppercase letters A through X. The majority of the data sets falls into two major types. The first major scan type is the spanwise scan described in section 5.4. The other major type is the detailed array of boundary-layer scans described in section 5.5. A particular run condition may have several data sets associated with it, because both spanwise and boundary-layer scans are performed. Therefore, there is not a one-to-one correspondence between run condition names and data set names. The tables should always be consulted to avoid any confusion. In Table 7.1, n is the

Table 7.1. Major Configurations and Data Sets

	Conditions				Data Sets	
Name	n	k [μm]	λ [mm]	$Re_c/10^6$	*Span*	*BL*
a	10	117	12	3.2	-	*A*
b	∞	117	12	3.0	-	*B*
c	∞	73	12	3.0	*E*	*C*
d	∞	146	12	3.0	*F*	*D*
e	∞	146	12	3.2	*G*	-
f	∞	146	12	3.4	*H*	-
g	∞	146	12	3.6	*I*	*J*
h	∞	146	10	3.0	*K*	*L*
i	∞	73	15	3.0	*M*	-
j	∞	73	18	3.0	*N*	*O*
k	∞	146	18	3.0	*Q*	*P*
l	∞	73	21	3.0	*R*	-
m	∞	73	24	3.0	*S*	-
n	∞	146	24	3.0	*T*	-
o	∞	146	36	3.0	*U*	-
p	1	146	-	3.0	*V*	-
q	0	-	0	2.5–3.5	*W*	-
r	*	*	*	3.2	*X*	-

spanwise number of roughness elements, where ∞ indicates a full spanwise roughness array and $*$ indicates multiple arrays. The k column shows the roughness height, and λ is the spanwise roughness spacing. A letter in the *Span* column indicates the data set number for spanwise scans. A letter in the *BL* column indicates a data set for boundary-layer scans.

The data sets cover a wide range of parameters, allowing investigations of Reynolds number, roughness height, number, and spacing effects. Data set *V* (*p*) follows the influence of a single roughness element, and can be used for following the vortex tracks. Data set *A* contains vortex tracking information for a multiple-dot configuration. Data set *W* (*q*) provides a no-roughness baseline scan, revealing a signal due to

Table 7.2. Wing Coverage of Data Sets

Data Set	Span	$100x/c$											
		5	10	15	20	25	30	35	40	45	50	55	60
A	24	•	•	•	•	•	•	•	•	•	•	•	•
B	240	•	•	•	•	•	•	•	•	•	•	•	•
C	240	•	•	•	•	•	•	•	•	•	•	•	•
D	240						•		•		•		•
E	240	•	•	•	•	•	•	•	•	•	•	•	•
F	240						•		•		•		•
G	240						•		•		•		•
H	240						•		•		•		•
I	240				•		•		•		•		•
J	48				•		•		•		•		•
K	240		•		•		•		•		•		•
L	48		•		•				•				•
M	240				•				•				•
N	240				•				•				•
O	50												•
P	50												•
Q	240				•				•				•
R	240				•				•				•
S	240				•				•				•
T	240												•
U	240				•				•				•
V	240						•		•		•		•
W	240	•			•				•				•
X	240						•						•

traverse imperfections. Data set *X* (*r*) is a special multiple dot-array scan to detect any upstream influence of roughness elements.

Most of the data sets cover the full 240 mm reachable span of the wing, while others cover a limited range. The full-span measurements are suitable for spectral analysis. The data sets also cover varying chordwise positions on the wing. Table 7.2 shows the wing coverage for each of the major data sets.

7.4. Basic State

The validity of comparisons with linear stability theory depends on the accuracy of the basic-state flow field over the model. The discussion in Chapter 4 suggests that small basic-state discrepancies are expected in any real experiment, and these effects must be included in the calculations. The basic state is checked in several ways. At the beginning of the experiment, the pressure coefficient is measured with a hot-wire probe just outside the boundary layer. This provides an initial check of the flow field and verifies that the liner configuration is sufficiently accurate. Later, when the detailed boundary-layer scans have been obtained, they are compared with the Kaups-Cebeci calculations. This gives a much more accurate picture of the basic state and detects any small discrepancies between the theoretical and experimental flow fields.

7.4.1. *Preliminary Pressure Coefficient Measurements*

Measurements of the pressure coefficient near the model surface are conducted with a calibrated hot-wire probe. This allows the measurement to take place at the center of the span of the model, which is the location of all crossflow measurements. This method also includes the effect of the sting and slotted window on the C_p. The hot-wire is moved along a path from $x/c = 0.0$ to $x/c = 0.70$, staying as close as possible to the model. The exact path is determined by several constraints. With a probe-angle setting appropriate for all chord positions, the probe cannot reach the model near the attachment line. For intermediate positions, the sting must clear the wing surface. For later chord positions, the probe path follows the closest computed streamline from the MCARF code. This keeps the probe outside of the boundary layer, and avoids extrapolation of the theoretical stream data. At each streamwise location, the velocity is measured and a streamwise pressure coefficient is computed

using

$$C_{p_s} = 1 - \frac{u^2}{U_\infty^2}. \tag{7.1}$$

The results are shown in Figure 7.3 for a freestream speed of 30 m/s.

The theoretical C_p is computed directly from the streamline traces used for the liner design (Figure 4.3). The surface C_p cannot be used because the measurements are made above the surface. Since the hot-wire is sensitive to the u and v velocity components, but not to the w component, the appropriate components are extracted from the stream data. The theoretical data are also corrected for the fact that the Pitot probe is located in a region with nonzero C_p. The main effect of this problem is that the the speeds in the test region are slightly higher than those indicated by the Pitot probe. An additional offset is also needed to bring the curves in line. The required offset corresponds exactly to the measured velocity skew at the test-section entrance due to the presence of the model.

The resulting theoretical C_{p_s} is shown along with the experimental data in Figure 7.3. The theoretical and experimental C_{p_s} values show good agreement at all chord positions. The overall shape is very similar, and the pressure gradient is in close agreement. The comparison shows that the experimental pressure distribution is close to that predicted by the theoretical codes, but the required combination of offsets and corrections leaves some uncertainty as to whether exact agreement has been achieved. A more careful comparison using boundary-layer measurements gives a better indication of the basic-state flow.

7.4.2. *Boundary-Layer Scans*

Data set A contains a spanwise array of boundary-layer scans at $x/c = 0.6$, along with single boundary-layer scans at other chord positions, with no roughness on the

wing. These measurements are for direct comparison with the other scans of data set A, for which a spanwise array of 117 μm roughness is installed. These scans, along with the corresponding spanwise scans, indicate a very clean basic state with no measurable stationary crossflow, in agreement with the flow-visualization results. Figure 7.4 shows a plot of the boundary-layer profiles at $x/c = 0.60$. What appears to be a single profile is actually a set of 25 profiles covering a span of 24 mm, or approximately 2 wavelengths of the expected natural crossflow waves. The profiles are nearly identical, and show no indication of any spanwise variations from either crossflow waves or spanwise changes of the basic state. The profiles can also be viewed as a contour plot, which is shown in Figure 7.5. The velocity profile is very uniform, with only very small random variations. Thus, the primary goal of establishing a spanwise-invariant flow with wall liners has been achieved.

A more sensitive measure of any natural disturbances is obtained by subtracting the spanwise mean velocity profile from each of the profiles in Figure 7.5. The resulting disturbance profiles are shown in Figure 7.6, and the corresponding disturbance velocity contours are shown in Figure 7.7. The disturbance profiles show only small random fluctuations with amplitudes below 1%. There is no indication of any crossflow disturbance profile, and the disturbance contours do not contain any organized spanwise variations.

7.4.3. *Shape-Factor Comparisons*

The preliminary pressure measurements leave some amount of uncertainty in the proper Reynolds number to use for comparisons between theory and experiment. The model has some effect on the incoming freestream flow, while the theoretical calculations assume a very long wind tunnel. In addition, Dagenhart (1992) observes a slight misalignment of the freestream flow. Since even small basic-state changes can

cause large differences in stability behavior, an effort must be made to identify any Reynolds number or angular corrections before any conclusions are drawn from the disturbance measurements.

The spanwise arrays of boundary-layer scans are very effective for comparing the experimental basic state with that predicted by theory. An analysis of the theoretical boundary-layer profiles shows that the shape factor is sensitive to pressure-gradient changes caused by angle-of-attack deviations, but relatively insensitive to Reynolds number changes. In contrast, the displacement thickness depends on both the pressure gradient and the Reynolds number. The proper parameters can then be obtained by first comparing the experimental shape factors with theoretical profiles at different angles of attack. The Reynolds number is then determined by comparing displacement thickness with varying theoretical Reynolds number, while holding the angle of attack constant.

Data set A is most easily used for this comparison, since it contains some boundary-layer scans with no roughness on the wing. Because there is some scatter in the data, additional data sets with roughness are used in the comparison. Data sets B, C, D, J, and L contain spanwise arrays of boundary-layer scans with roughness on the wing. Because the disturbance levels are small, a spanwise average of these data gives an approximation of the basic-state flow. In all cases the streamwise (X) velocity component is extracted from the theoretical profiles before boundary-layer parameters are computed.

Figure 7.8 shows shape factor as a function of x/c for data sets A, B, C, D, J, and L. Theoretical shape factors for $\alpha = 0°$, $-1°$, and $-2°$ are included for comparison. There are some slight discrepancies in the development of the shape factor with x/c, but the experimental data points generally follow the theoretical curves. This comparison

definitely shows that there is a slight flow misalignment. The best agreement with theory occurs for $\alpha = -1°$. This is consistent with Dagenhart (1992), where a similar adjustment was necessary.

With the angle of attack set at $-1°$, the Reynolds number is varied and the displacement thickness is compared with the experimental data. Figure 7.9 shows that a slight adjustment in Reynolds number is necessary for agreement between theory and experiment. The best basic-state agreement is obtained with a Reynolds number of 3.2×10^6 for data taken at $Re_c = 3.0 \times 10^6$.

7.4.4. *Spanwise Scans Without Surface Roughness*

Spanwise hot-wire scans are made with no artificial roughness on the wing, providing a baseline measurement against which roughness configurations may be compared. This measurement also gives an indication of the noise levels in the measurement process, and detects any imperfections in the traverse hardware.

Figures 7.10–7.13 show spanwise hot-wire surveys of the normalized streamwise velocity at $x/c = 0.05$, 0.20, 0.40, and 0.60. These scans are from data set *W*, and contain 2048 points covering 240 mm of span. This high resolution allows accurate spectral analysis.

The data at $x/c = 0.05$ show the difficulty of making accurate measurements in a thin boundary layer. At this position, the boundary layer is only 1 mm thick. The rms fluctuation level is 3.5%, and is computed after subtracting the average velocity from all of the data points. Any small features due to roughness in later measurements could easily be obscured by this noise level. Fortunately, spectral techniques can extract low-level waves from this background. The noise level diminishes consistently at larger chord positions. At $x/c = 0.6$, the rms fluctuation level is only 0.18%. The overall flatness of the scan shows that the traverse-alignment techniques outlined in

section 5.4 are operating correctly. The fine-scale jaggedness in Figure 7.13 indicates the level of random acquisition errors for this scanning technique. The errors are due to electrical noise, digitization errors, and small random velocity fluctuations in the flow. These tiny errors could be reduced even more by increasing the sampling time for each data point, but this would create unnecessary time penalties. The random noise is already small enough that it is not a factor in these measurements.

The larger-scale fluctuations observed at small x/c are the major component of the background signal, and must be explained in greater detail. Recalling that these are time-averaged measurements, and that the size of the random sampling errors has been determined, the remaining signal either indicates a real stationary structure in the flow, or imperfections in the traverse mechanism. A spectral analysis of the signal resolves this ambiguity. Figure 7.14 shows maximum-entropy spectra of the spanwise data in Figures 7.10–7.13. A description of the maximum-entropy method is given in Chapter 5. The overall signal level decreases dramatically as x/c increases. The main feature at all chord positions is a strong peak at $\lambda = 7.2$ mm. At $x/c = 0.05$, this peak contains 53% of the total rms signal. Even though this wavelength is in the amplified region for these conditions, the wave is determined to be due to a traverse imperfection for the following reasons. The precision lead screws for Z motion of the traverse have exactly 5 turns per inch. This corresponds to a distance of 5.08 mm per turn. This Z distance is equivalent to 7.18 mm along the span, in exact agreement with the observed wavelength. A small imperfection in the Z motion may lead to slight variation of the probe height as the traverse is moved. Small height variations will be observed as periodic velocity fluctuations. The chordwise variation of the disturbance amplitude is consistent with this mechanism, since a

probe motion of constant amplitude will produce larger velocity fluctuations in the very thin boundary layers at small x/c.

The traverse periodicity is confirmed by careful visual observation of the probe during long spanwise moves. A final confirmation is obtained by conducting measurements at $x/c = 0.2$ for different Reynolds numbers. Figure 7.15 shows a magnified view of the 7 mm peak from scans at $Re_c = 2.5 \times 10^6$, 3.0×10^6, and 3.5×10^6. If the peak is due to a natural crossflow disturbance, the wavelength would be expected to vary with Reynolds number (Dagenhart 1992). The wavelengths for all three Reynolds numbers agree very well, so the disturbance is not due to a natural feature in the flow.

7.5. Spanwise Scans

The majority of data sets are full spanwise hot-wire scans at constant nominal relative velocity, with full spanwise arrays of roughness at $x/c = 0.005$. The details of this type of scan are given in Section 5.4. All scans are made at an average relative velocity of 0.75. This position is justified by examining the disturbance profiles obtained from the full boundary-layer scans. At all chord positions measured, $u/U_e = 0.75$ is very close to the maximum-amplitude position. Since the profile is flat near the maximum, some tolerance is possible. Only one u/U_e position is chosen because of time constraints, and because the full boundary-layer scans yield profile information. The spanwise scans are primarily used for amplitude and spectral information.

7.5.1. *Disturbance Measurements*

Since the single-wire probes used in this experiment are mainly sensitive to the streamwise (X) velocity component, the spanwise scans measure the u' component of the stationary crossflow disturbance. The basic plot from this type of scan shows

u/U_e as a function of span. Figures 7.16–7.64 show these plots for the spanwise scans in data sets E through U. The plots are all shown with a u/U_e range from 0.5 to 1.0, so amplitudes can be easily compared. In most cases, the automatic probe-alignment scheme works very well, and the signal tracks the nominal $u/U_e = 0.75$ position accurately.

Several features are evident in the plots. In all cases, the disturbance amplitudes are largest at small values of x/c, where the signal is dominated by short-wavelength components. At larger values of x/c, the shorter components are damped, and the signal looks much cleaner as the remaining longer components become dominant. The overall noise level is very good except at the smaller chord positions, where the traverse imperfections produce a strong component with a wavelength of about 7.2 mm.

At larger chord positions, the dominant stationary crossflow signal is very clear, and is seen as a wavelike signal varying roughly sinusoidally with span. The dominant wavelength usually corresponds to the spanwise spacing of the roughness array, except in cases where the roughness spacing is substantially larger than the most-amplified stationary wave. In these cases (for example, Figure 7.64) the crossflow signal consists of several dominant components corresponding to the various Fourier components of the roughness distribution. Crossflow modes are observed at the primary roughness spacing s, and at wavelengths s/m, where m is a small integer. For moderate roughness spacings in the 10–15 mm range, only a small number of modes are clearly observed, usually only the $m = 1$ and $m = 2$ modes. For larger roughness spacings, more modes are observed. For example, in Figure 7.64, at least 5 modes are visible. In this case, some of the higher modes have higher growth rates than

the primary mode, so the signal is dominated by these components even though the roughness should put in the strongest initial signal at the primary wavelength.

7.5.2. *Spectral Analysis*

An examination of the spanwise scans clearly shows that global amplitude estimates using rms or peak-peak methods will be inaccurate when compared with single-wavelength theoretical estimates, because the crossflow signal consists of several components. The spanwise scans are designed with this in mind, and are conducted with sufficient span and resolution to allow successful spectral analysis.

Figure 7.65 shows a typical maximum-entropy spectrum for a case where the signal is dominated by a 12 mm component. The corresponding spanwise scan is shown in Figure 7.27. The maximum entropy method is very good for extracting peaky spectra from signals of this type. In this case, the bulk of the crossflow energy is contained in the peak (note the logarithmic scale), and there is not much difference between the global rms and the integrated peak. In contrast, Figure 7.66 shows a case where many components are present in the signal. This spectrum is computed from the spanwise scan shown in Figure 7.64. In this case, a global rms is not as useful, so the spectral components must be separately integrated to obtain meaningful results. Even in this complicated case, the spectrum has sufficient resolution to clearly distinguish the crossflow modes at 36, 18, 12, 9, and 7.2 mm. Of course, the 7.2 mm component must be viewed with some caution since it is near the wavelength of the traverse contamination. In this case, however, the scan is at $x/c = 0.6$, where the traverse contamination is vanishingly small.

Figures 7.67–7.78 show the maximum entropy spectra for the major spanwise scans. When examining the spectrum plots, one should be careful to consider the fact that the x-axis is inverted in the plots, so the peaks are distorted. Accurate

amplitudes are obtained only when the peaks are integrated numerically in the proper dimensionless inverse wavelength domain. Also, since the maximum entropy spectrum is continuous and is plotted with the integral normalization convention, the relative maximum heights of the peaks do not always indicate the proper relative energy content.

The spanwise scans can also be analyzed with the more traditional FFT spectrum. Figure 7.79 shows the FFT spectrum corresponding to the scan in Figure 7.27. The dominant 12 mm peak is also clearly seen in the FFT spectrum, but the spectrum is not as clean. This is due to the typical characteristics of the FFT under marginal sampling conditions. Figure 7.80 shows an FFT spectrum of the multiple-wavelength scan in Figure 7.64. In this case, the FFT cannot easily distinguish all of the components in the signal, due to the severe leakage and contamination in the presence of large spectral peaks. Because of these difficulties, the maximum entropy spectra are used for all quantitative estimates in the following section.

Figures 7.81–7.92 show the FFT spectra for all of the major spanwise scans. Since the FFT is a discrete spectrum, the amplitudes will not match those in the maximum entropy spectra. Amplitudes of spectral peaks are obtained by adding the values of the discrete points lying in the peaks.

7.5.3. *Amplitudes*

Stationary crossflow amplitudes for the u velocity component are obtained by integrating the components of the maximum entropy spectra. All integrations are performed in dimensionless frequency (inverse wavelength) space. The integration bounds are determined by locating the appropriate minima in the spectrum at the edges of the desired peaks.

Figures 7.93–7.104 show the crossflow amplitudes extracted from the spanwise scans. The amplitudes are plotted as a function of x/c so the development of the various components can be followed for comparison with stability theory. For each case, the total rms of the spanwise scan is plotted first. This is obtained either directly from the spanwise scan or by integrating the entire maximum-entropy spectrum, which yields the total squared power in the signal. For each data set, curves are also plotted for any spectral components which can be clearly distinguished in the spectrum. For many of the cases, some components are only visible for a limited range of x/c, so the curves are not always complete.

Amplitudes are generally largest near the leading edge, and decay at larger values of x/c. The largest measured stationary disturbance amplitude is 6.7% at $x/c = 0.1$. For $x/c \geq 0.2$, the total rms amplitude is less than 4%. These levels are much lower than the $\pm 20\%$ amplitudes measured by Dagenhart (1992).

7.5.4. *N-Factor Comparisons*

The amplitude information from the spanwise scans can be processed to obtain growth rates and N-factors. This information can then be directly compared with the predictions of the MARIA and SALLY codes for specific stationary modes.

A complication arises when comparing the experimental data with N-factors from linear stability codes. The theoretical codes compute N relative to the initial point of instability $(x/c)_o$ for a particular stationary mode. This position varies with wavelength. The N-factor remains at zero until $(x/c)_o$ and is then positive throughout the region of growth. Experimental N-factors are computed from amplitude data at a limited set of points which often does not include the position of initial instability. Because N-factors are relative, they can be shifted by an arbitrary offset. An obvious solution is then to offset either the theoretical or experimental data so that

the two curves agree at some appropriate base point. For the data presented here, the theoretical and experimental curves will be shifted so that $N = 0$ at the first experimental data point. Since the theoretical curves often show significant growth before the initial experimental point, the initial theoretical N-factors for small x/c will be negative.

With the data plotted as described above, the curves all converge to $N = 0$ at the initial experimental point. The theoretical N-factor curves approach this point from $N < 0$, indicating growth. The fact that the experimental and theoretical data both show $N = 0$ at the first experimental point does not indicate better agreement at that point, but merely reflects the choice of base point.

Figures 7.105–7.118 show the N-factor comparisons for the major spanwise data sets at $Re_c = 3.0 \times 10^6$. The data are plotted separately for each of the 14 distinct wavelengths measured. These range from 5 mm to 36 mm. Several wavelengths (9.0, 12.0, and 18.0 mm) are associated with multiple data sets. For these cases, the average N-factor is plotted. In all other cases, the appropriate experimental data set is indicated in the plot. The MARIA and SALLY results are computed for $Re_c = 3.2 \times 10^6$ and $\alpha = -1°$. In most cases, there is a significant disagreement between the experimental and theoretical growth curves, with the linear stability results severely overpredicting the growth of the stationary disturbance. In fact, the experimental data typically show weak decay over most of the airfoil, while the stability codes predict substantial growth. The best agreement is for $\lambda_s = 36$ mm, the longest wavelength measured.

For all wavelengths, the MARIA and SALLY codes show slight discrepancies, but the agreement is generally very good. Any differences are much smaller than the disagreement with the experimental data.

For the primary design wavelength of 12 mm, linear PSE and Orr-Sommerfeld calculations are performed (Arnal *et al.* 1994). Figure 7.119 shows experimental and computed N-factors relative to $x/c = 0.05$. This clearly shows the large difference in growth rates between linear theory and experiment. Clearly, a nonlinear calculation is needed for correct prediction of stationary crossflow growth.

7.5.5. *Growth Rates*

The local dimensionless growth rate is estimated by the formula

$$\sigma = \frac{1}{A}\frac{dA}{d(x/c)}. \tag{7.2}$$

For simplicity, experimental growth rates are computed as simple central differences between pairs of amplitudes, and the resulting σ will be associated with the x/c location midway between the two data points. The local amplitude A will be given by the average of the two experimental amplitudes. The experimental estimates cannot always reveal fine details, and are slightly nonlocal, due to the wide spacing of the data points. Otherwise, there is no essential difficulty in computing the growth rates, and there is no base-point ambiguity as with the N-factors, because the growth rates are a local quantity.

A slight problem exists for the theoretical data at long wavelengths and small x/c (for example, Figure 7.133), where the theoretical curves indicate $\sigma = 0$. These regions are actually stable, but the codes are designed to only report growth in regions of instability. Any confusion can be resolved by referring to the N-factor results in Figures 4.13 and 4.14. Also, for $\lambda_s = 5$ mm (Figure 7.120), SALLY data do not exist beyond $x/c = 0.1$, because SALLY does not track the disturbance through regions of negative growth. MARIA is able to follow this mode to $x/c \geq 0.25$.

Figures 7.120–7.133 show growth rate comparisons for the same 14 wavelengths included in the N-factor results. In all cases, the experimental data lie well below the linear-stability predictions. However, the curves seem to follow similar shapes, indicating a consistent magnitude of the overprediction throughout the region of study.

7.5.6. *Wavelength Sensitivity*

Another important quantity obtained from the experimental data is the sensitivity to wavelength. The deliberately vague term "sensitivity" is used here to emphasize the qualitative nature of this measurement. The data are obtained with widely varying roughness configurations, and it is unclear whether the receptivity to stationary modes is comparable in all cases. Some of the wavelengths measured are at the primary roughness spacing, while some are at higher modes ($m = 2$ or 3). The roughness height is 146μm in some cases and 73μm in others. Also, it can be argued that, for example, an array of 6 mm-diameter roughness spaced 21 mm apart is not the appropriate 21 mm roughness array for comparison with 6 mm roughness spaced 12 mm apart. Obviously, one would like to find 10.5 mm elements to produce 50% coverage. In spite of these difficulties, with appropriate care the data can be processed to answer the simple question: "Given a 'similar' roughness array at various primary spacings near the leading edge, which spacing will produce the largest signal at $x/c = 0.6$?" The answer to this question will be at least qualitatively related to the relative stability of the various wavelengths, and can be compared with the predicted most unstable wavelength according to linear theory.

Figure 7.134 shows the experimentally measured stationary crossflow amplitude at $x/c = 0.6$ for the 14 measured wavelengths between 5 mm and 36 mm. The data have been divided into 6 distinct groups according to roughness height s and mode number

m. For example, the curve with $s = 146$ and $m = 1$ includes all data points with 146 μm roughness for which the measured crossflow component is at the primary roughness spacing. The two curves with $m = 2$ correspond to measured crossflow components with a wavelength equal to half the primary roughness spacing. This method of segregating the data accounts for the first two complications described above, but not the third. The effect of fixing the roughness diameter is difficult to quantify without a detailed understanding of the receptivity process, although some information is available in the preliminary measurements of Radeztsky *et al.* (1993a). For the data used in this comparison, the ratio of roughness diameter to crossflow wavelength varies between 1.24 at $\lambda_s = 5$ mm and 0.17 at $\lambda_s = 36$ mm. Results obtained without accounting for this variation would not be expected to be accurate, particularly near the extremes of this range. However, if this difficulty is ignored, an examination of Figure 7.134 shows that all of the data sets show a maximum near $\lambda_s = 10$mm. For λ_s between 8 and 15 mm, the roughness diameter to crossflow wavelength ratio varies only between 0.78 and 0.41. Radeztsky *et al.* (1993a) show that the effect of roughness diameter variation is minimal for ratios near 0.5, so this local peak is likely to be related to stability and not to roughness diameter effects.

Forging ahead under these assumptions, we note that 5 of the 6 groups of data contain a point at $\lambda_s = 12$ mm. This fact can be used to unify the data sets into a single curve as follows. If each data point is divided by the amplitude at $\lambda_s = 12$ mm within the *same* data group, we obtain 5 normalized amplitude curves which all pass through 1 at $\lambda_s = 12$ mm. The result is shown in Figure 7.135. Since the 5 curves have now been properly normalized, the data may be directly compared, even between groups.

We now take the natural logarithm of each data point to obtain an N-like quantity for comparison with the linear stability predictions. For simplicity, the data points are joined into a single curve by averaging any duplicate points at the same wavelength. The result is shown in Figure 7.136 along with an N-factor vs. λ_s curve from SALLY. The SALLY curve has been shifted to match $N = 0$ at $\lambda_s = 12$ mm. The agreement in position of the maximum is remarkable. Both SALLY and the experiment show a maximum at exactly 10 mm. Even the shape of the amplitude curve near the peak is similar. The amplitude drops off more rapidly at short wavelengths and more slowly at longer wavelengths.

This result suggests that although linear stability theory does not accurately predict the growth rates of stationary crossflow disturbances, some aspects of the linear theory are correct. The most-amplified wavelength appears to agree with experiment.

7.5.7. *Reynolds-Number Variation*

The data in sets *F*, *G*, *H*, and *I* include identical roughness configurations measured at chord Reynolds numbers between 3.0×10^6 and 3.6×10^6. The growth of 12 mm stationary crossflow waves can be compared under these varying conditions.

Figure 7.137 shows N-factor as a function of x/c for the four experimental chord Reynolds numbers. The N-factors are computed as in the previous section, and are referenced to the initial experimental data point at $x/c = 0.3$. MARIA and SALLY computations are included for comparison. The theoretical curves are computed for $\alpha = -1°$, and with slightly higher Reynolds numbers due to the flow corrections described in Section 7.4.

The most striking feature in the data is of course the great amount of disagreement between the theoretical and experimental data. The linear stability codes show much higher growth rates at all of the Reynolds numbers. However, the dependence on

Reynolds number is in agreement, with both theory and experiment showing a slight increase in total amplification with increasing Re_c.

Figure 7.138 shows the local growth rates corresponding to the data in Figure 7.137. The results are as expected, showing a slight increase in growth with increasing Re_c, and a significant overprediction of growth rate by the linear stability codes.

7.5.8. *Single Roughness Element*

The preliminary experiments at $\alpha = -4°$ show significant growth of roughness-induced stationary vortices even when the background natural stationary disturbances appear to be saturated. Since the present measurements indicate growth rates well below those predicted by linear stability theory, an obvious question arises. Is there something inherently different about the development of stationary vortices which have been influenced by a single roughness element, when compared with vortices caused by a full spanwise array of roughness?

To answer this question, a single 146μm roughness element with a diameter of 6 mm is installed at $x/c = 0.005$. The element is placed in a spanwise position such that its region of influence can be observed at all chord positions. This is called roughness configuration p, and the resulting measurements form data set V.

Spanwise scans are performed at a nominal u/U_e value of 0.75 at $x/c = 0.3$, 0.4, 0.5, and 0.6. These scans are shown in Figures 7.139–7.142. The background portions of these scans look very similar to the no-roughness scans, showing a low level of background noise including the traverse contamination signal. This background noise level decreases as x/c increases, becoming negligibly small at $x/c = 0.6$. At $x/c = 0.3$, a small region between 120 mm and 160 mm along the span shows evidence of a localized stationary crossflow structure. At later chord position, this crossflow vortex

moves to different span positions because the vortex path is not aligned directly along the X axis. The vortex also becomes more clearly defined as the background noise subsides. The vortex amplitude does not appear to increase significantly between $x/c = 0.3$ and $x/c = 0.6$.

It is difficult to quantify the amplitude of this isolated crossflow vortex pattern using the standard spectral techniques, but it is obvious that this isolated vortex does not show a growth rate substantially higher than seen with full-span roughness arrays. Some other explanation is necessary for the unusual growth rate results of the preliminary experiment. The preliminary data were obtained with a lower-resolution traverse system for which the noise signature was not as well defined. It is possible that the measurements of the natural background vortices were not sufficiently resolved.

7.6. Boundary-Layer Scans

The majority of the remaining data sets consists of full arrays of boundary layer scans of the type described in section 5.5. Tables 7.1 and 7.2 show the conditions and roughness configurations for these scans. Data set A covers only two wavelengths of the dominant vortex, but follows the same set of vortices throughout the set of scans. Data sets B, C, and D cover the maximum spanwise range of 240 mm at several chord positions, while data sets J, L, O and P cover shorter spans. The major goals for these scans are to observe the details of the vortex motion, to obtain mode shapes, and to verify the growth rate results of the spanwise scans.

7.6.1. *Detailed Vortex Evolution*

Data set A is obtained with a spanwise array of 10 circular roughness elements with a height of 117 μm, a diameter of 6.2 mm, and a spacing of 12 mm. This limited roughness array covers a large enough span that the stationary vortices near the center

of the region of influence may be representative of vortices influenced by a full spanwise array. This may be verified by comparing the results of these measurements with those obtained with a full spanwise array of roughness. On the other hand, the roughness array is limited enough that the edges of the region of influence may be detected using full spanwise scans as in data set *V* and the preliminary investigations with single roughness elements (Radeztsky *et al.* 1993a). Figure 7.143 shows a typical spanwise scan with roughness configuration *a* in place. The region of influence is clearly seen as a distinct set of distortions in an otherwise quiet background. Since the region of influence is of finite extent, the individual peaks and valleys may be identified at different chord positions, allowing precise alignment of the arrays of boundary-layer scans and successful tracking of the same set of vortices over the entire wing. The peaks in the spanwise scan correspond to regions where high-momentum fluid has been convected into the boundary-layer due to the local negative w' component of the stationary vortex. The valleys correspond to regions of velocity deficit due to the convection of low-momentum fluid away from the wall. The starting point for the array of boundary-layer scans is aligned with the peak near $s = 55$ mm in Figure 7.143. The scans cover a spanwise distance of 24 mm, or two cycles of the dominant 12 mm vortex. Thus, one would expect to see regions of excess u velocity at the edges and at the center of the scan array, and regions of velocity deficit between these regions.

Figures 7.4–7.7 provide a reference point for analyzing the results of these measurements. With no roughness in place, the spanwise array of 25 boundary-layer scans appears as a single line when plotted on the same graph, indicating that no measurable distortions are present. A velocity contour plot shows a uniform boundary-layer profile across the entire span of the measurement. Figures 7.6 and 7.7 are disturbance

plots obtained by subtracting the mean u velocity at each y position in the boundary layer. These plots show no significant deviation from the mean, and no evidence of any stationary structure.

In dramatic contrast to the clean-surface case, Figure 7.144 shows a spanwise array of 25 boundary-layer scans measured at the same position ($x/c = 0.6$, same span location) as those in Figure 7.4, but with roughness configuration a in place. In this case, significant boundary-layer distortions are present, as indicated by the wildly-varying shapes of the boundary-layer profiles. Many important results are evident even from this single plot:

1. The boundary-layer scans are well-aligned at the wall and at the outer edge, indicating that the wall-location and alignment techniques are working properly even in the presence of distortions.

2. The region near the wall is sufficiently linear to allow wall location through extrapolation.

3. The individual profiles are very clean and smooth, indicating a low background noise level.

4. The measurements are time-averaged. This means that the measured distortions are stationary structures.

5. The distortions show no evidence of an interior node point, so the span-averaged rms disturbance mode shape will have a single lobe, consistent with theoretical predictions and previous experimental results.

6. The maximum spread in the profiles occurs near $u/U_e = 0.75$, validating the choice of this position for spanwise scans.

7. The scans cover a spanwise distance of only 24 mm but show significant variation, so nontrivial structure exists on scales comparable to the roughness spacing.

8. The crossing of profiles near the region of maximum distortion shows that the phase of the distortion depends on both span and y. Thus, any observed vortices will be slightly skewed.

9. The presence of inflected profiles suggests that the stability characteristics of this boundary layer will differ significantly from those of the undisturbed boundary layer, even though the disturbance levels are only a few percent.

Disturbance profiles are obtained by subtracting the spanwise mean profile from each of the profiles. The result is shown in Figure 7.145, which should be compared with the no-roughness scan in Figure 7.6. A consistent scale of 0 to 3 mm in y and $\pm 10\%$ for the disturbance amplitude will be used for all plots in this sequence for data set A. The disturbance profile shapes are clearly visible in this plot. Smooth phase changes are observed, indicating a wavelike disturbance. Even with a stationary structure, moving along the span produces wavelike phase changes. The disturbance level reaches a maximum of over 6% near $y = 1.25$ mm, which corresponds to $u/U_e = 0.75$ for this boundary layer. A slight asymmetry is observed. This is probably due to the limited number of spanwise positions, and the fact that the spanwise spacing of the scans is rationally related to the spanwise vortex wavelength, so that only a limited number of phase positions are sampled. Better results would be obtained with a longer span range, more profiles, and a slightly different spacing between the profiles. The current results, however, are sufficient for extracting mode shapes and flow details.

Velocity contour plots corresponding to the profiles in Figures 7.144 and 7.145 are shown in Figures 7.146 and 7.147, respectively. These plots show the entire velocity field in the (y, z) plane for the u component and the stationary disturbances. The edges of these plots correspond to regions of maximum velocity surplus, indicating that the scan alignment is successful. In all contour plots of this type, the mean flow is toward the reader, and the stationary vortices are turning counterclockwise (right-handed orientation). The span axis is inverted for consistency with the right-handed coordinate system used in this experiment. Since the plane of the plot is oriented in the spanwise direction, it is not cutting directly across the vortices, so observed wavelengths must be corrected for the vortex orientation. The observed *spanwise* spacing of 12 mm corresponds to the 12 mm spanwise spacing of the roughness array. A slight asymmetry is visible in Figure 7.146, indicating the beginning of the "rolling over" motion observed by Dagenhart (1992) at larger amplitudes. This motion is produced by the right-handed rotation of the stationary vortices.

Figure 7.147 clearly shows the alternating regions of velocity surplus and deficit caused by convection of fluid due to the stationary crossflow vortex pattern. The dark velocity deficit regions are caused by upwelling of slow fluid from the wall due to the weak v' and w' vortex components. Similarly, high-speed fluid in the light regions is carried downward by the vortex. Several important points should be noted when examining Figure 7.147:

1. The contours should not be misinterpreted as vorticity contours, directly showing the intensity of a row of alternating vortices. The contours indicate disturbance velocity levels.

2. The rotational motion of the vortices produces a skew in the profiles, bringing high-speed fluid under regions of low-speed fluid. This corresponds to the asymmetry in Figure 7.146 and the inflected profiles in Figure 7.144.

3. For clarity, the y axis is stretched with respect to the span axis. When viewed at the proper aspect ratio, the skewing of the velocity contours is much more apparent. Figure 7.148 shows the same disturbance contours as Figure 7.147, but with the proper aspect ratio. The inversion of high- and low-speed fluid is clearly visible.

Figures 7.149–7.159 show velocity profiles for chord positions between $x/c = 0.05$ and $x/c = 0.55$, at 5% chord intervals. Disturbance profiles for these scans are shown in Figures 7.160–7.170. Figures 7.171–7.181 and 7.182–7.192 show the corresponding velocity contour plots. At each chord position, the scans are aligned so that the same set of vortices is tracked. For positions with $x/c < 0.2$, this tracking is less accurate due to the complicated nature of the disturbances.

The data at $x/c = 0.05$ illustrate the capabilities of the new traverse system and scanning methods. Here, the boundary layer is only 1 mm thick, but a complete set of aligned boundary-layer profiles is obtained over a large spanwise distance. Several other data sets (B, C) contain boundary-layer arrays at $x/c = 0.05$ covering the full span of 240 mm. This corresponds to over 5000 time-averaged data points acquired over a three-hour time period.

The disturbance contours at larger chord positions ($x/c > 0.4$) show a very clean 12 mm vortex structure. At earlier positions, the picture is more complicated. A review of the data from the spanwise scans indicates that at these low values of x/c, additional crossflow components have a significant amplitude. In particular, a 6 mm

component is to be expected. This multi-component disturbance produces a complicated contour plot, but some basic features can be extracted. At $x/c = 0.05$, the disturbance intensities are very large, and smaller scales dominate the picture. Even though later positions show a clear right-handed rotation as expected, the obvious visual pairing of the most intense contours at $x/c = 0.05$ would correspond to a left-handed motion. This is very unusual. Moving to $x/c = 0.15$, the most intense distortions are paired in a right-handed manner. This pairing persists for the remainder of the wing, until at the largest chord positions the symmetry of the distortions makes such distinctions impossible. At these locations, however, the direction of rotation is obvious from the skewed profiles. The overall scale of the disturbance motion increases as the boundary layer grows and larger wavelengths begin to dominate. In all cases, the disturbances are limited to within the boundary layer. At chord positions beyond $x/c = 0.4$, only the dominant 12 mm structure is observed. The overall disturbance intensity decreases up to $x/c = 0.4$, but increases again once this dominant structure emerges.

7.6.2. *Disturbance Profiles*

Mean disturbance mode shapes are obtained by combining the individual disturbance profiles. Several methods are available for this procedure. The first method obtains the mode shape by computing a spanwise rms at each y position in the boundary-layer. For a stationary wave, this is equivalent to a typical rms profile obtained from a time-series measurement of a travelling disturbance. The second method records the magnitude of the largest measured disturbance velocity at each y position, producing an envelope of the disturbance motion. The rms method will produce smoother profiles when computed from a limited number of scans.

Figure 7.193 shows a set of profiles for data set A obtained with the rms method. The profiles generally follow the shapes predicted by linear theory (Dagenhart 1992), with a single lobe near the center of the boundary layer. The position of the maximum increases as the boundary layer grows. The maximum rms amplitude is 7% for the measurement at $x/c = 0.05$. The amplitude decays with x/c to a minimum at $x/c = 0.3$. The amplitude grows from this point back to the last measurement station at $x/c = 0.6$.

Figure 7.194 shows a set of stationary profiles computed using a linear PSE code (Arnal *et al.* 1994). These profiles show the same shape as the experimental data, but grow at a much higher rate, reflecting the general overprediction of the growth rate by linear codes. Figure 7.195 shows a direct comparison of mode shapes. In this plot, the PSE results have been scaled to match the experimental amplitudes at each chord position. The agreement is excellent. This indicates that linear theory accurately predicts the expected mode shapes, and also verifies that the measured stationary structures in the experiment are indeed crossflow waves.

Figure 7.196 shows a set of profiles obtained using the second method (disturbance envelope). The amplitudes are of course much higher using this method, with a peak value of 18% for $x/c = 0.05$. These profiles are not as smooth as those obtained with the rms method. The rms method will be used for further amplitude computations.

7.6.3. *Amplitudes*

The disturbance profile data can be used to obtain amplitude estimates for the stationary crossflow vortices. Following Dagenhart (1992), three methods are used for specifying disturbance amplitudes. The first method measures the maximum of the rms disturbance profile at each chord position. The second method computes an rms of the disturbance profile in the y direction. Recall that the mean profiles

are produced by computing an rms in the span direction, so this method essentially results in a two-dimensional rms of the disturbance. The third method computes an average over y instead of an rms, and is similar to the second method.

Figure 7.197 shows amplitude as a function of x/c for each of these methods for data set A. The 'maximum' method of course produces larger amplitude estimates, but the three methods otherwise are in very good agreement, particularly with respect to growth behavior. These amplitude data may be converted to N-factors, providing a good method for checking the N-factor results from the spanwise scans. Figure 7.198 shows N-factor as a function of x/c for the three amplitude measures. The three curves collapse beautifully into a single path. This figure may be compared with Figure 7.113, which shows the N-factor results for the 12 mm component measured with spanwise scans. The agreement between the two methods is excellent. The data in Figure 7.198 are not a pure 12 mm crossflow component, but for the case of 12 mm roughness, the spanwise scans show that the 12 mm component dominates the signal.

This result indicates that these experimental measurements of stationary crossflow waves are very accurate and repeatable, even when measured using different scanning techniques.

7.6.4. *Full Spanwise Arrays*

Data sets B, C, and D contain arrays of boundary-layer scans covering the full 240 mm span of the traverse system. For these data sets, complete arrays of roughness with 12 mm spacing and several different heights are used.

The extremely large amount of data in these scans presents some difficulty in creating plots. For simplicity, only contour plots will be shown for the total and disturbance velocities. Even though the scans extend for a spanwise distance of

240 mm, only 100 mm of span are shown in the plots, because the aspect ratio distortions are too severe if the entire data set is shown.

Figures 7.199–7.209 show the total u velocity contours for data set B. The characteristics are similar to those of data set A, but with more wavelengths shown. Intensities are highest near the leading edge, and the pattern settles down to a dominant 12 mm wave at larger chord positions. The growth of the boundary layer is also clearly visible.

Figures 7.210–7.220 show the corresponding disturbance contours for data set B. Figure 7.221 shows rms disturbance profiles computed from the entire set of 256 boundary-layer scans of data set B. The stationary profiles are similar to those of data set A. Figure 7.222 shows the disturbance amplitude computed by the 'maximum', 'average', and 'rms' methods. Several chord positions have been omitted because some of the boundary-layer scans at those positions contain errors due to a loss of calibration. It is difficult to continuously acquire data for several hours without experiencing technical problems. Fortunately, these problems are easily detected in the data files, and they can be filtered from the final results. The trends in Figure 7.222 agree with both the spanwise scans and data set A. The amplitudes are lower for data set B because Re_c is lower.

Figures 7.223–7.234 show the total velocity contours for data set C, while Figures 7.235–7.246 show the corresponding disturbance contours. Figure 7.247 shows the disturbance profiles, while Figure 7.248 shows the amplitude estimates. This data set agrees with the others, but the amplitudes are very small due to the small roughness height of 73μm.

Data set D contains complete spanwise arrays, but for a smaller selection of chord positions. The roughness heights are 146μm for this case. Figures 7.249–7.252 con-

tain the total velocity contours, and Figures 7.253–7.256 contain disturbance velocity contours. Figure 7.257 shows the disturbance profiles, and Figure 7.258 shows the amplitude estimates.

Data set *J* contains boundary-layer scans covering a smaller spanwise distance of 50 mm, but at a chord Reynolds number of 3.6×10^6. The roughness configuration is the same as for data set *D*. The total velocity contours are shown in Figures 7.259–7.262, and the disturbance velocity contours are in Figures 7.263–7.266. Figure 7.267 shows the disturbance profiles, and Figure 7.268 shows the amplitudes. The disturbance levels are high for this data set because the roughness height is large, and the chord Reynolds number is high.

7.6.5. *Multiple-Component Contours*

Data set *L* contains boundary-layer scans for roughness configuration *h*, the same case studied in the spanwise scans of data set *K*. The roughness has a spanwise spacing of 10 mm, corresponding to the most-amplified wavelength. The measured amplitudes are large in this case, and a clearly defined 5 mm crossflow component is detected in the spanwise scans at early x/c locations.

The total velocity contours and disturbance contours for this case are shown in Figures 7.269–7.276. Figure 7.269 shows a good example of velocity contours in the presence of two dominant crossflow components.

The Disturbance profiles and amplitude estimates are shown in Figures 7.277 and 7.278.

7.7. Tollmien-Schlichting Destabilization

It is obvious from the arrays of boundary-layer scans that the stationary crossflow disturbance significantly distorts the steady-state boundary-layer profiles, even at low amplitudes. These distortions have a strong spanwise variation. Figure 7.144 shows

that with over a spanwise distance corresponding to the stationary crossflow wavelength, the boundary-layer profiles take on a full range of different shapes, ranging from inflected to strongly accelerated.

With strong steady deviations from the undisturbed basic state, the boundary layer will exhibit strong local changes in stability characteristics. For example, it is well known that under conditions where stationary crossflow dominates the transition process, turbulent wedges first appear near the region of the stationary vortex containing inflected profiles (Kohama *et al.* 1991). A high-frequency signal is detected at these positions, probably due to a secondary instability. It is expected that if other types of waves are present, the stationary structure will affect the stability of these waves as well.

The present experiment operates at $\alpha = 0°$, where Tollmien-Schlichting disturbances are slightly amplified (See Figure 4.16). The weak favorable pressure gradient produces slightly accelerated basic-state profiles which prevent significant T-S growth. If a stationary crossflow structure changes this basic state and produces locally decelerated profiles, the growth of Tollmien-Schlichting waves may be enhanced.

Figure 7.279 shows two selected basic-state profiles from data set *A*. These profiles are located at span positions differing by only 6 mm, or one half of the dominant 12 mm vortex spacing. The stationary crossflow amplitude is only 2.5% rms at this location, but the profiles have markedly different shapes. The boundary layer at a span position of 17 mm is significantly decelerated. It is expected that Tollmien-Schlichting disturbances will be locally destabilized at this location. The profile at 11 mm shows an inflected shape. At larger amplitudes, a profile of this type is a likely location for development of secondary instabilities.

Figure 7.280 is a power spectrum of the time-dependent portion of the velocity at the position of the decelerated profile in Figure 7.279. The probe is placed at $u/U_e = 0.75$ and held fixed under constant flow conditions. The fluctuating portion of the hot-wire signal is amplified, filtered, and acquired using the high-speed 16-bit data-acquisition system described in Chapter 3. Details of the signal processing techniques used for AC hot-wire signals are found in Radeztsky *et al.* (1993b). The power spectrum in Figure 7.280 is computed with the same FFT routines used for the spatial spectra of spanwise scans. For this time series data, the sampling parameters are chosen so that the FFT-based power spectrum has sufficient resolution. The sharp decline in signal strength below 500 Hz is due to the high-pass filter applied to the hot-wire signal. The low-pass filter setting is 5000 Hz, so the high-frequency cut-off is not visible on the scale of this plot. The spectrum shows a large amount of energy in the 500–1000 Hz range, which indicates a rich spectrum of various travelling disturbances. Of course, the type of these disturbances is not certain without additional measurements, but they are possibly travelling crossflow modes. For this investigation, we will concentrate on the higher-frequency peak between 1750 and 1850 Hz. For the decelerated conditions at $\alpha = 4°$ in Figure 4.16, at a slightly higher Reynolds number, the most amplified T-S disturbances are found in this frequency range. Confirmation of this peak as a T-S mode will require additional measurements which have not been performed here.

Figure 7.281 shows a similar power spectrum obtained at the position of the inflected profile of Figure 7.279. Here, the peak at 1750–1850 Hz has a much lower amplitude. This suggests that this mode is more unstable in the decelerated region than in the inflected region.

The distorted basic state at $x/c = 0.6$ under these conditions is dominated by the 12 mm stationary vortex. The mean boundary-layer profiles smoothly change between the two profiles shown in Figure 7.279 in a regular repeating pattern. The amplitude of the T-S-like mode observed above should modulate in a regular pattern if a spanwise scan is performed. Figure 7.282 shows the integrated mean square power in the 1750–1850 Hz range at each spanwise position for data set *A*. The amplitude of this peak modulates exactly as expected, changing amplitude by a factor of two between the accelerated and inflected regions.

This preliminary evidence suggests that the stability of Tollmien-Schlichting-type disturbances is locally influenced by the distorted profiles produced by stationary crossflow waves. This effect can have a significant impact on the accuracy of transition prediction under appropriate conditions. Further investigation will be required to verify the nature of the observed high-frequency disturbances, and to more accurately quantify this effect.

8. CONCLUSIONS

8.1. Overview

Stability experiments are conducted on a swept-wing model in the Arizona State University Unsteady Wind Tunnel. The model is a 45-degree swept NLF(2)-0415 airfoil which is part of an ongoing crossflow experiment. The model is installed in a dedicated test section at the unsteady wind tunnel, with a 0° angle of attack. Basic-state flow calculations including wall effects are used to design a set of end liners, producing a simulation of infinite-span flow. As part of the design process, extensive stability calculations are performed. Under the conditions of this experiment, crossflow and Tollmien-Schlichting instabilities are weakly amplified. The surface of the model is carefully polished to produce a mirror-like finish. With this combination of low growth rates and clean initial conditions, no measurable crossflow disturbances are present. Carefully documented arrays of roughness are installed near the attachment line to provide a receptivity mechanism for stationary crossflow vortices. Extensive hot-wire measurements provide an extremely detailed map of the resulting disturbances. Comparisons are made with the predictions of stability theory, including amplitudes, growth rates, observed spectral distributions, and disturbance profiles.

Measurement techniques include long spanwise scans and large arrays of coordinated boundary-layer profiles. The spanwise scans are detailed enough to permit high-resolution spectral analysis, which can be used to isolate individual spectral components of the stationary waves. Direct comparisons are made with single-wavelength stability calculations. The arrays of boundary-layer profiles reveal details of the stationary vortex structure, which are presented in velocity contour plots. The mean flow is subtracted from these contours, producing disturbance-velocity profiles. Spanwise averaging of these profiles generates disturbance mode shapes, which are directly com-

pared with theoretical predictions. A measurement of unsteady fluctuations in the distorted boundary layer reveals a nonlinear modulation of travelling disturbances.

A preliminary set of measurements at $\alpha = -4°$ establishes the importance of roughness in providing the initial conditions for stationary crossflow vortices. Flow-visualization and hot-wire measurements document transition locations and vortex growth.

8.2. Specific Results

8.2.1. *Effect of Roughness on Transition*

The flow-visualization measurements described in Chapter 6 show a dramatic change in transition location with different leading-edge roughness characteristics. In a low-disturbance environment like that found in flight, stationary vortices can dominate the transition process, and because of the strong effect of roughness, the receptivity process can be the *primary* factor in determining the transition location. This causes major problems with using the e^N method for transition prediction.

8.2.2. *Effect of Roughness on Stationary Vortices*

Hot-wire measurements reveal that the presence of micron-sized roughness can dramatically affect the stationary vortex pattern even in cases where natural crossflow is very strong. Although the naturally occurring vortices are saturated over most of the airfoil, those vortices which are directly behind the applied roughness elements continue to grow, reaching rms amplitudes well over 10% of the edge velocity.

8.2.3. *Basic State*

Hot-wire measurements indicate that the pressure distribution on the model is close to that predicted in the design calculations. Detailed comparisons of boundary-layer shape factors and displacement thicknesses indicate the need for a slight correc-

tion in the angle of attack and freestream Reynolds number. These corrections are considered in the stability calculations used for comparison with the data.

Detailed boundary-layer scans show that without applied roughness, the boundary layer shows no sign of naturally-occuring stationary or travelling crossflow waves. This creates an unprecedented platform for the study of controlled stationary disturbances.

8.2.4. *Spanwise Scans*

Spanwise arrays of roughness placed near the attachment line introduce controlled stationary crossflow disturbances. As predicted by Choudhari (1993), spanwise scans reveal the presence of a discrete spectrum of stationary modes including the primary roughness spacing and its harmonics. Measured amplitudes are much lower than those found in previous experiments, and are typically around 2% rms, which is within the range that would be expected to display linear behavior.

The presence of these roughness-induced waves indicates that the stationary crossflow pattern is not predetermined by external conditions, but can be completely controlled by the surface conditions. Any wavelength in the unstable range can be produced with an appropriate roughness pattern.

Spectral analysis is used to separate individual modes from the roughness-induced crossflow spectrum. Amplitudes are obtained by integrating power in the peaks of the maximum-entropy spectrum.

Direct comparisons are made with linear-stability calculations performed for the basic state found on the model. Comparisons of predicted and measured N-factors show that linear stability theory does not properly predict the growth of stationary vortices even at amplitudes which would be expected to fall in the linear range. The differences between theory and experiment are quite dramatic, and in most cases the

sign of the growth is even incorrect. The differences are largest at smaller wavelengths, while better agreement is obtained at the largest wavelengths.

An analysis of measured amplitudes at the largest chord position suggests that the range of unstable wavelengths predicted by linear theory is roughly correct. This conclusion can be clarified with an analysis of receptivity coefficients.

Reynolds-number variations have the expected effect of increasing the observed amplitudes. The stationary crossflow amplitude is also sensitive to roughness height, as expected.

Spanwise scans behind a single roughness element do not indicate any substantial increase in the observed amplitudes when compared to the full-span arrays. This should be contrasted with the results of the preliminary measurements with high growth rates, which show a strong change in the stability behavior of stationary crossflow vortices behind an isolated roughness element.

8.2.5. *Boundary-Layer Scans*

Large arrays of boundary-layer scans reveal the structure and evolution of stationary vortices under several applied roughness distributions. Contour plots of total and disturbance velocities clearly show the vortex motion, with an exchange of high- and low-momentum fluid. A skew in the disturbance profiles shows the beginning of the "rolling-over" motion detected by Dagenhart (1992) at larger amplitudes.

Disturbance contours near the leading edge show a complicated structure including large amplitudes and many spectral components. As the pattern develops, smaller wavelengths disappear and the dominant, least-stable modes emerge. The primary spacing of the pattern remains fixed at the roughness spacing. There is no evidence of a smooth shift in wavelength at larger chord positions, and the observed evolution is due to the amplitude variations of the discrete modes already present.

Spanwise averages of the rms disturbance profiles show the mode shape of the stationary crossflow waves. The mode shapes are compared with the predictions of a linear PSE calculation (Arnal 1994). This important comparison shows that even though the roughness amplitudes are large, the detected disturbances are definitely crossflow waves. The agreement with theory is excellent, even though the linear PSE code was not able to correctly predict the growth rates. This observation, combined with the observed wavelengths found with the spanwise scans, indicates that the failure of linear theory is not complete. The expected mode shapes and wavelengths are observed in the experiment; only the growth rates are wrong. Nonlinear modifications of stability theory should be expected to show improved performance.

Amplitude information extracted from the spanwise scans agrees with the information obtained with spanwise scans.

8.3. Summary

The present investigation contributes to the understanding of boundary-layer stability and transition by providing detailed measurements of carefully-produced stationary crossflow vortices. It is clear that a successful prediction of transition in swept-wing flows must include an understanding of the detailed physics involved. Receptivity and nonlinear effects must not be ignored. Linear stability theory correctly predicts the expected wavelengths and mode shapes for stationary crossflow, but fails to predict the growth rates, even for low amplitudes. As new computational and analytical methods are developed to deal with three-dimensional boundary layers, the data provided by this experiment will serve as a useful benchmark for comparison.

REFERENCES

ARNAL. D. 1984 Description and prediction of transition in two-dimensional incompressible flow. *Special Course on Stability and Transition of Laminar Flows, AGARD Report No. 709.*

ARNAL, D. 1986 Three-dimensional boundary-layers: Laminar-turbulent transition. *Special Course on Calculation of Three-Dimensional Boundary Layers with Separation, AGARD Report No. 741.*

ARNAL, D. 1992 Boundary-layer transition: Prediction, application to drag reduction. In *Special Course on Skin Friction Drag Reduction, AGARD Report No. 786.*

ARNAL, D. 1993 Predictions based on linear theory. In *Special Course on Transition Modelling, AGARD Report No. 794.*

ARNAL, D., CASALIS, G. & COPIE, M. 1994 *Personal communication.*

ARNAL, D., CASALIS, G. & JUILLEN, J.C. 1990 Experimental and theoretical analysis of natural transition on infinite swept wing. In *Laminar-Turbulent Transition, Vol. III* (eds. D. Arnal & R. Michel). Springer.

ARNAL, D., COUSTOLS, E. & JUILLEN, J.C. 1984 Experimental and theoretical study of transition phenomena on an infinite swept wing. *Rech. Aérosp. No. 1984-4.*

ARNAL, D. & JUILLEN, J.C. 1987 Three-dimensional transition studies at ONERA-CERT. *AIAA Paper 87-1335.*

BALACHANDAR, S., STREET, C.L. & MALIK, M.R. 1992 Secondary instability in rotating-disk flow. *J. Fluid Mech.* **242**, pp. 323–348.

BALAKUMAR, P., HALL, P. & MALIK, M.R. 1991 On the receptivity and nonparallel stability of travelling disturbances in rotating disk flow. *Theor. Comp. Fluid Dyn.* **3**, 3, pp. 125–140.

BIPPES, H. 1990 Instability features appearing on swept-wing configurations. In *Laminar-Turbulent Transition, Vol. III* (eds. D. Arnal & R. Michel). Springer.

BIPPES, H. 1991 Experiments on transition in three-dimensional accelerated boundary layer flows. In *Proc. R.A.S. Boundary-Layer Transition and Control*, Cambridge, UK.

BIPPES, H. & MÜLLER, B. 1990 Disturbance growth in an unstable three-dimensional boundary layer. In *Numerical and Physical Aspects of Aerodynamic Flows IV* (ed. T. Cebeci). Springer.

BIPPES, H., MÜLLER, B. & WAGNER, M. 1991 Measurements and stability calculations of the disturbance growth in an unstable three-dimensional boundary layer. *Physics of Fluids A* **3**, 10, pp. 2371–2377.

BIPPES, H. & NITSCHKE-KOWSKY, P. 1987 Experimental study of instability modes in a three-dimensional boundary layer. *AIAA Paper 87-1336.*

CHOUDHARI, M. 1993 Roughness-induced generation of crossflow vortices in three-dimensional boundary layers. *High Technology Report No. HTC-9301.*

CHOUDHARI, M. & STREETT, C.L. 1990 Boundary layer receptivity phenomena in three-dimensional and high-speed boundary layers. *AIAA Paper 90-5258.*

COLLIER, F.S. JR. & MALIK, M.R. 1989 Curvature effects on the stability of laminar three-dimensional boundary layers. In *Fluid Dynamics of Three-Dimensional Turbulent Shear Flows and Transition, AGARD CP-438.*

CROUCH, J.F. 1993 Receptivity of three-dimensional boundary layers. *AIAA Paper 93-0074.*

DAGENHART, J.R. 1981 Amplified crossflow disturbances in the laminar boundary layer on swept wings with suction. *NASA TP-1902.*

DAGENHART, J.R. 1992 Crossflow stability and transition experiments in a swept-wing flow. PhD Thesis, V.P.I. & S.U., Virginia. Also *NASA-TM-108650*, December 1992.

DAGENHART, J.R., SARIC, W.S., MOUSSEUX, M.C. & STACK, J.P. 1989 Crossflow-vortex instability and transition on a 45-degree swept wing. *AIAA Paper 89-1892.*

DAGENHART, J.R., SARIC, W.S., HOOS, J.A. & MOUSSEUX, M.C. 1990 In *Laminar-Turbulent Transition: Proc. IUTAM Symp.* Toulouse, France, 1989 (ed. D. Arnal), pp. 369–380. Springer.

DEYHLE, H., HÖHLER, G. & BIPPES, H. 1993 Experimental investigation of instability wave propagation in a 3-D boundary-layer flow. Submitted to AIAA J.

VON DOENHOFF, A.E. & BRASLOW, A.L. 1961 The effect of distributed roughness on laminar flow. In *Boundary-Layer Control, Vol. II* (ed. Lachmann), Pergamon.

EL-HADY, N.M. 1980 On the stability of three-dimensional, compressible nonparallel boundary layers. AIAA Paper 80-1374.

FISCHER, T.M. 1991 A mathematical-physical model for describing transitional boundary layer flows. Volume 1: The linear and nonlinear disturbance differential equations. *ESA-TT-1242.*

FISCHER, T.M. & DALLMANN, U. 1987 Theoretical investigation of secondary instability of three-dimensional boundary layer flows. *AIAA Paper 87-1338.*

FISCHER, T.M. & DALLMANN, U. 1988 Theoretical investigation of secondary instability of three-dimensional boundary layer flows with application to the DFVLR-F5 model wing. *DFVLR-FB-87-44.*

FISCHER, T.M. & DALLMANN, U. 1991 Primary and secondary stability analysis of a three-dimensional boundary-layer flow. *Phys. Fluids A* **3**, pp. 2378-2391.

HERBERT, T. 1993 Parabolized stability equations. In *Special Course on Transition Modelling, AGARD Report No. 794*

JOSLIN, R. & STREET, C.L. 1992 Crossflow disturbance evolution on swept wings computed by spatial DNS. *Bull. Am. Phys. Soc.* **37**, 8.

JUILLEN, J.C. & ARNAL, D. 1990 Etude expérimentale du déclencement de la transition par rugosités et par ranier sur de bord d'attaque d'une aile en flèche en èncoulement incompressible. *CERT/ONERA Rapport Final 51/5018.35.*

KACHANOV, Y.S. & TARARYKIN, O.I. 1990 The experimental investigation of the travelling waves in a three-dimensional boundary layer. In *Laminar-Turbulent Transition, Vol. III* (eds. D. Arnal & R. Michel). Springer.

KAUPS, K. & CEBECI, T. 1977 Compressible laminar boundary layers with suction on swept and tapered wings. *Journal of Aircraft* **14**, 7.

KAY, S.M. & MARPLE, S.L. JR. 1981 Spectrum analysis—a modern perspective. *Proc. IEEE* **69**, 11.

KOHAMA, Y., SARIC, W.S. & HOOS, J.A. 1991 A high-frequency secondary instability of crossflow vortices that leads to transition. In *Proc. R.A.S. Boundary-Layer Transition and Control*, Cambridge, UK.

LIN, R.S. 1992 Stationary crossflow instability on an infinite swept wing. PhD Dissertation, Arizona State University, Arizona.

LIN, R.S. & REED, H.L. 1993 Effect of curvature on stationary crossflow instability of a three-dimensional boundary layer. *AIAA J.* **31**, 9, pp. 1611–1617.

MACK, L.M. 1984 Boundary-layer stability theory. *Special Course on Stability and Transition of Laminar Flows, AGARD Report No. 709.*

MACK, L.M. 1985 The wave pattern produced by a point source on a rotating disk. *AIAA Paper 85-0490.*

MALIK, M.R. & BALAKUMAR, P. 1993 Linear stability of three-dimensional boundary layers: effects of curvature and nonparallelism. *AIAA Paper 93-0079.*

MANUILOVICH, S.V. 1990 Disturbances of a three-dimensional boundary layer generated by surface roughness. *Fluid Dynamics*, pp. 764–769, Mar. 1990.

MEYER, F. 1990 Numerical simulation of transition in three-dimensional boundary layers. PhD Thesis, Karlsruhe University, Germany.

MEYER, F. & KLEISER, L. 1988 Numerical simulation of the nonlinear evolution of a perturbation in a three-dimensional boundary layer. In *DGLR, Flows with Separation*, pp. 39-40. Germany.

MEYER, F. & KLEISER, L. 1989 Numerical simulation of transition due to crossflow instability. In *Laminar-Turbulent Transition: Proc. IUTAM Symp.* Toulouse, France, 1989 (ed. D. Arnal). Springer.

MICHEL, R., ARNAL, D., COUSTOLS, E. & JUILLEN, J.C. 1985 Experimental and theoretical studies of boundary-layer transition on a swept infinite wing. In *Laminar-Turbulent Transition* (ed. V. Koslov), pp. 553–561. Springer.

MORKOVIN, M.V. 1969 *Viscous Drag Reduction*, pp. 1–31. Plenum.

MORKOVIN, M.V. 1993 Bypass-transition research: Issues and philosophy. In *Instabilities and Turbulence in Engineering Flows* (ed. D. Ashpis, T. Gatski, R. Hirsh). Kluwer Academic.

MÜLLER, B. 1990 Experimental study of the travelling waves in a three-dimensional boundary layer. In *Laminar-Turbulent Transition: Proc. IUTAM Symp.* Toulouse, France, 1989 (ed. D. Arnal). Springer.

MÜLLER, B. & BIPPES, H. 1989 Experimental study of instability modes in a three-dimensional boundary layer. In *Fluid Dynamics of Three-Dimensional Turbulent Shear Flows and Transition, AGARD CP-438.*

MÜLLER, B., BIPPES, H. & COLLIER, F.S. JR. 1990 The stability of a three-dimensional laminar boundary layer over a swept flat plate. In *Instability and Transition: Proc. ICASE/NASA LaRC Workshop.* Springer.

NAYFEH, A.H. 1980a Stability of three-dimensional boundary layers. *AIAA J.* **17**, 10, pp. 1084–1090.

NAYFEH, A.H. 1980b Three-dimensional stability of growing boundary layers. In *Laminar-Turbulent Transition* (ed. R. Eppler, H. Fasel), pp. 201–217. Springer.

NITSCHKE-KOWSKY, P. 1986 Experimental investigations on the stability and transition of three-dimensional boundary layers. *ESA-TT-1026 DFVLR-FB-86-24.*

NITSCHKE-KOWSKY, P. & BIPPES, H. 1988 Instability and transition of a three-dimensional boundary layer on a swept flat plate. *Physics of Fluids* **31**, pp. 786–795.

PADHYE, A.R. & NAYFEH, A.H. 1981 Non-parallel stability of three-dimensional flows. *AIAA Paper 81-1281.*

PERRY, A.E. 1982 *Hot-Wire Anemometry*, Oxford University Press, New York.

PFENNINGER, W. 1977 Laminar flow control—Laminarization. *Special Course on Drag Reduction, AGARD Report No. 654.*

POLL, D.I.A. 1984 Transition description and prediction in three-dimensional flows. *Special Course on Stability and Transition of Laminar Flows, AGARD Report No. 709.*

POLL, D.I.A. 1985 Some observations of the transition process on the windward face of a long yawed cylinder. *J. Fluid Mech.* **150**, 329.

PRESS, W.H., FLANNERY, B.P., TEUKOLSKY, S.A. & VETTERLING, W.T. 1988 *Numerical Recipes in C*, Cambridge University Press, New York.

RADEZTSKY, R.H. JR., REIBERT, M.S. & SARIC, W.S. 1993a Effect of micron-sized roughness on transition in swept-wing flows. *AIAA Paper 93-0076.*

RADEZTSKY, R.H. JR., REIBERT, M.S. & SARIC, W.S. 1993b A software solution to temperature-induced hot-wire voltage drift. In *Proc. Third International Symp. on Thermal Anemometry*, ASME-FED, Washington, DC.

RASMUSSEN, B.K. 1993 Boundary-layer receptivity: freestream sound on an elliptical leading edge. MS thesis, Arizona State University, Arizona.

REED, H.L. 1988 Wave interactions in swept-wing flows. *Phys. Fluids* **30**, 11, pp. 3419–3426.

REED, H.L. 1994 *Personal communication.*

REED, H.L. & FUCIARELLI, D.A. 1991 Analysis of high-frequency secondary instabilities in three-dimensional boundary layers. *Bull. Am. Phys. Soc.* **36**, p. 2630.

REED, H.L. & LIN, R.S. 1987 Stability of three-dimensional boundary layers. *SAE Paper 87-1857.*

REED, H.L. & NAYFEH, A.H. 1982 Stability of compressible three-dimensional boundary-layer flows. *AIAA Paper 82-1009.*

REED, H.L. & SARIC, W.S. 1989 Stability of three-dimensional boundary layers. *Ann. Rev. Fluid Mech.* **21**, pp. 235–284.

SARIC, W.S. 1990 Low-speed experiments: Requirements for stability measurements. In *Instability and Transition, Vol. I* (eds. M.Y. Hussaini & R.G. Voight), pp. 162–174. Springer.

SARIC, W.S. 1992a Laminar-turbulent transition: Fundamentals. In *Special Course on Skin Friction Drag Reduction, AGARD Report No.* 786, Von Karman Inst., Belgium.

SARIC, W.S. 1992b The ASU Transition Research Facility. *AIAA Paper 92-3910.*

SARIC, W.S. 1994a Görtler vortices. *Ann. Rev. Fluid Mech.* **26**, pp. 379.

SARIC, W.S. 1994b Low-speed boundary-layer transition experiments. In *Aspects of Transition to Turbulence: Experiments, Theory & Computations* (ed. M. Hussaini, T. Corke). Oxford.

SARIC, W.S., DAGENHART, J.R. & MOUSSEUX, M.C. 1990 Experiments in swept-wing transition. In *Numerical and Physical Aspects of Aerodynamic Flows IV* (ed. T. Cebeci), pp. 359–415. Springer. (First appeared 1989.)

SARIC, W.S., KRUTCKOFF, T.K. & RADEZTSKY, R.H. JR. 1990b Visualization of low-Reynolds-number flow fields around roughness elements. *Bull. Am. Phys. Soc.* **35**, p. 2262.

SARIC, W.S., TAKAGI, S. & MOUSSEUX, M.C. 1988 The ASU Unsteady Wind Tunnel and fundamental requirements for freestream turbulence measurements. *AIAA Paper 88-0053.*

SARIC, W.S. & YEATES, L.G. 1985 Experiments on the stability of crossflow vortices in swept-wing flows. *AIAA Paper 85-0493.*

SINGER, B.A., MEYER, F. & KLEISER, L. 1990 Nonlinear development of crossflow vortices. In *Instability and Transition: Proc. ICASE/NASA LaRC Workshop.* Springer.

SMITH, A.M.O. & GAMBERONI, N. 1956 Transition, pressure gradient, and stability theory. *Douglas Aircraft Company, Inc. ES 26388.*

SOMERS, D.M. & HORSTMANN, K.H. 1985 Design of a medium-speed natural-laminar-flow airfoil for commuter aircraft applications. *DFVLR-IB*/29-85/26.

SPALART, P.R. 1989 Direct numerical study of crossflow instability. In *Laminar-Turbulent Transition: Proc. IUTAM Symp.* Toulouse, France, 1989 (ed. D. Arnal). Springer.

SPENCER, S.A. 1992 Boundary-layer receptivity: freestream sound with three-dimensional roughness. MS Thesis, Arizona State University, Arizona.

SROKOWSKI, A.J. & ORSZAG, S.A. 1977 Mass flow requirements for LFC wing design. *AIAA Paper 77-1222.*

THOMAS, A.S.W. 1985 Aircraft drag reduction technology. In *Aircraft Drag Prediction and Reduction, AGARD Report No. 723.*

STEVENS, W.A., GORADIA, S.H. & BRADEN, J.A. 1971 A mathematical model for two-dimensional multi-component airfoils in viscous flow. *NASA CR-1843.*

VAN INGEN, J.L. 1956 A suggested semi-empirical method for the calculation of the boundary-layer transition region. *Rep. Nos. VTH 71 & 74*, Dept. Aeronaut. Eng., Univ. Technol., Delft, Neth.

VIKEN, J., COLLIER, F.S. JR., WAGNER, R.D. & BARTLETT, D.W. 1989 On the stability of swept wing laminar boundary layers including curvature effects. In *Laminar-Turbulent Transition: Proc. IUTAM Symp.* Toulouse, France, 1989 (ed. D. Arnal). Springer.

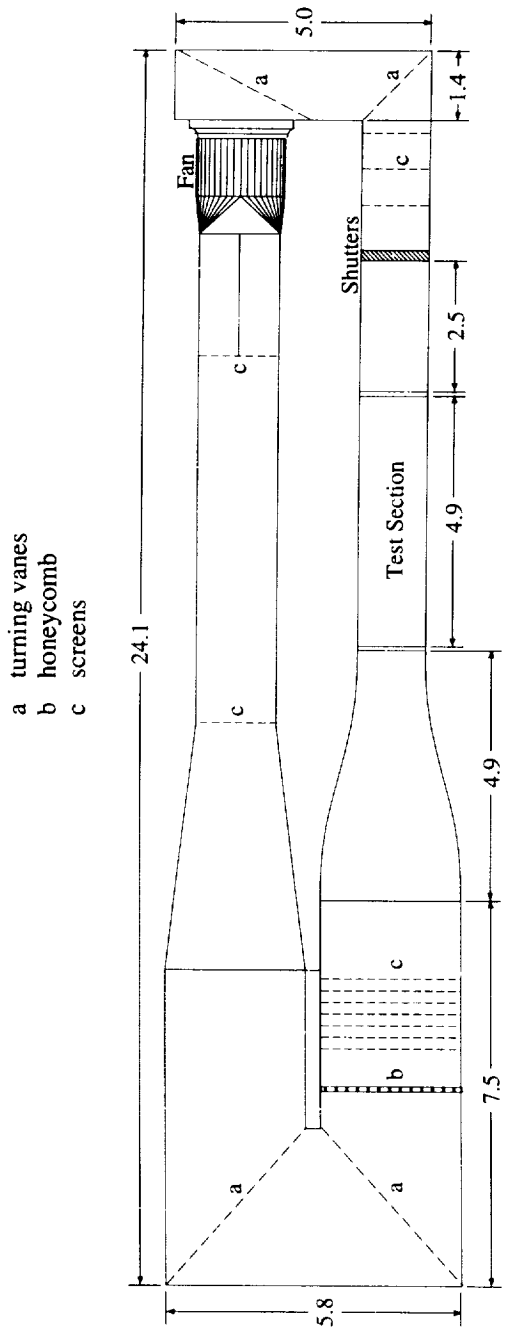

Figure 3.1. Plan view of Arizona State University Unsteady Wind Tunnel. All dimensions in meters.

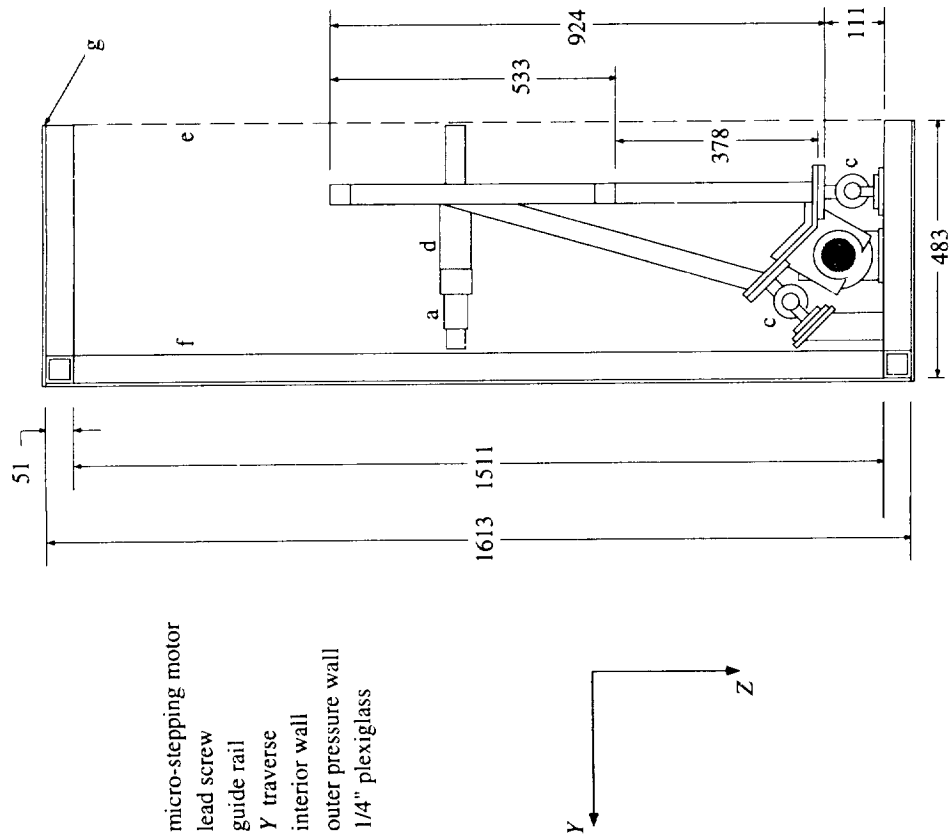

Figure 3.2. Side view of traverse mechanism. All dimensions in millimeters.

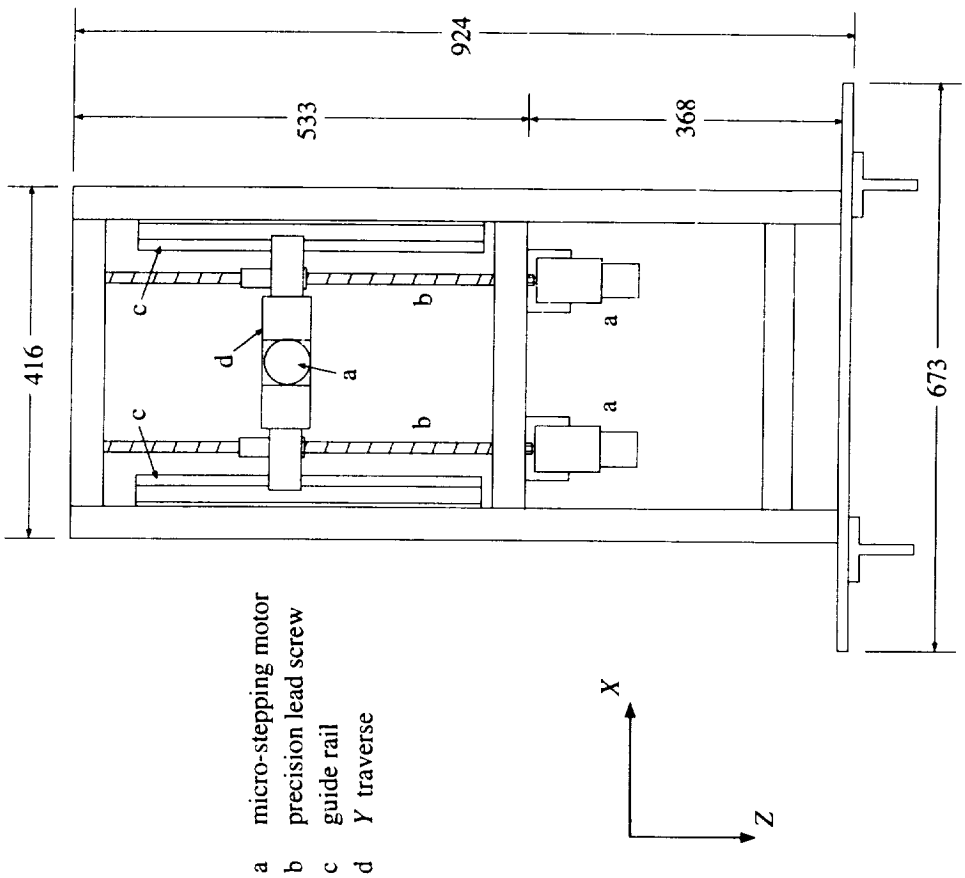

Figure 3.3. Front view of traverse mechanism. All dimensions in millimeters.

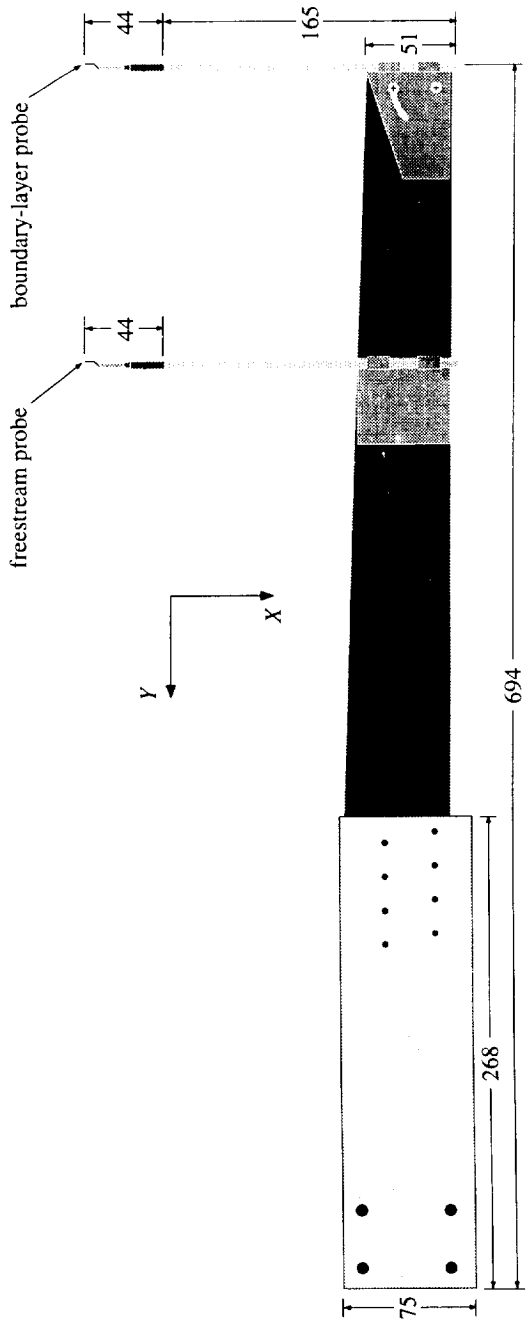

Figure 3.4. Plan view of hot-wire sting. All dimensions in millimeters.

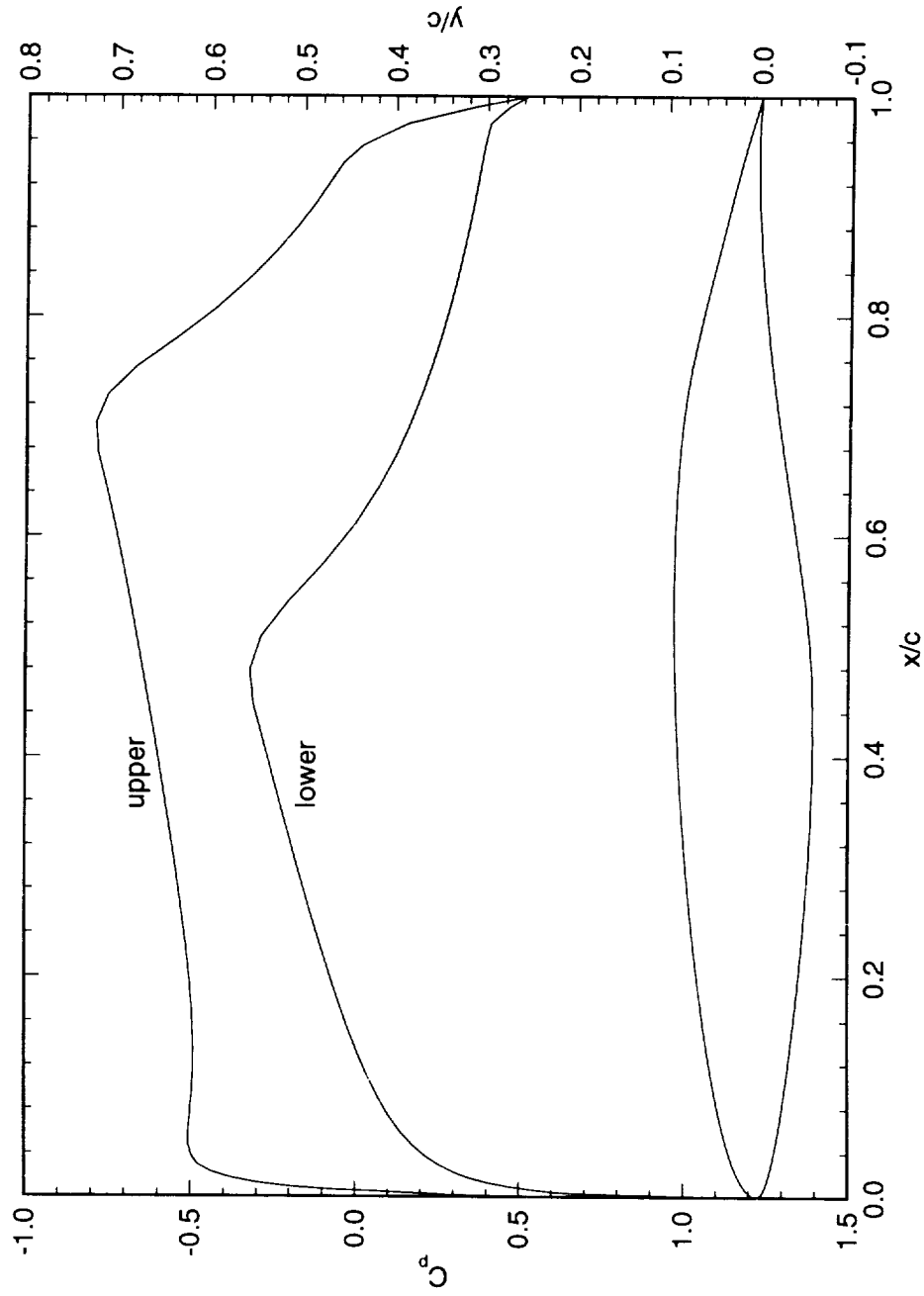

Figure 4.1. Unswept NLF(2)-0415 airfoil coordinates and design C_p at $\alpha = 0°$.

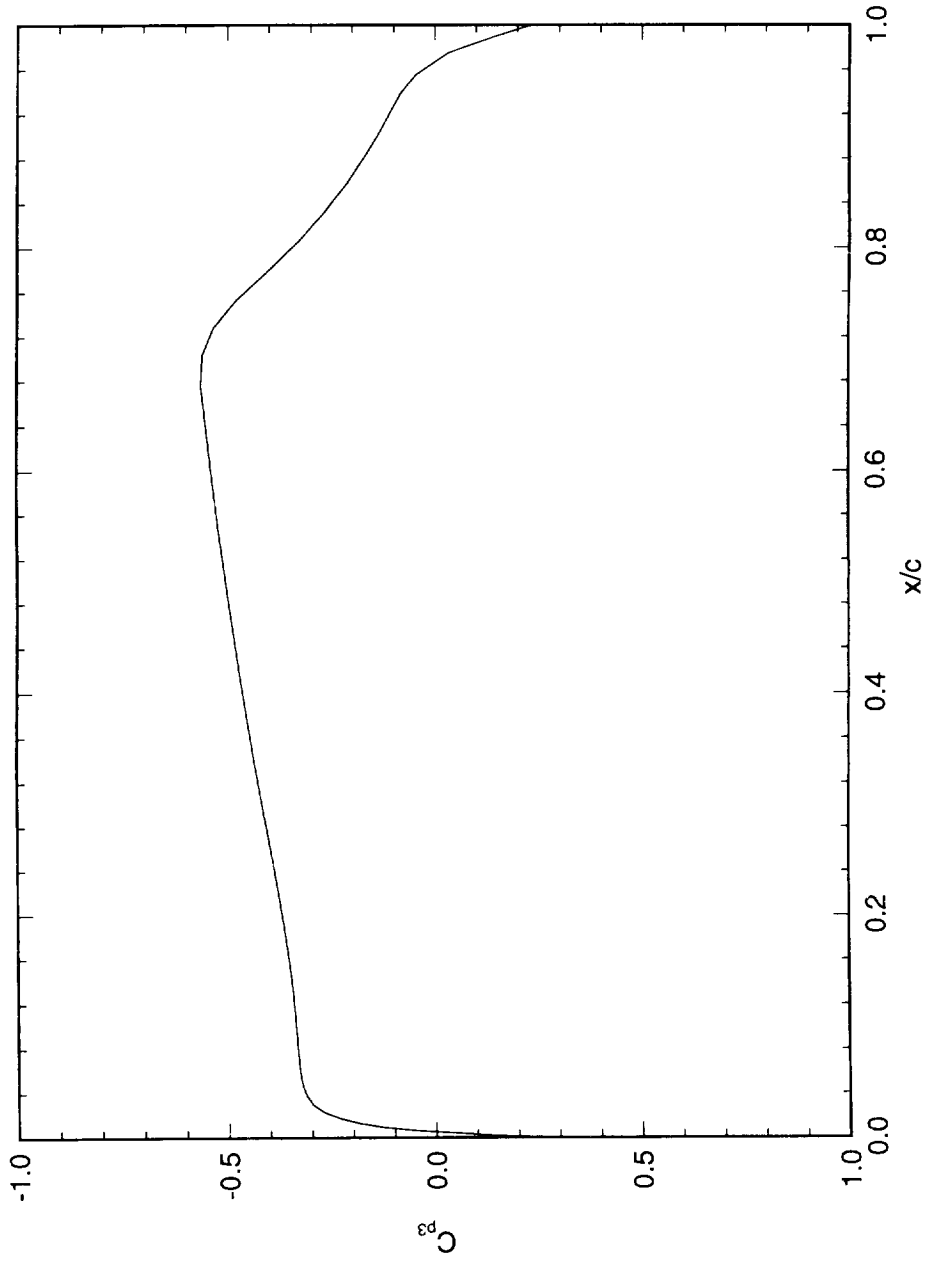

Figure 4.2. Swept NLF(2)-0415 pressure distribution in UWT. $\alpha = 0°$, flap angle $= 0°$.

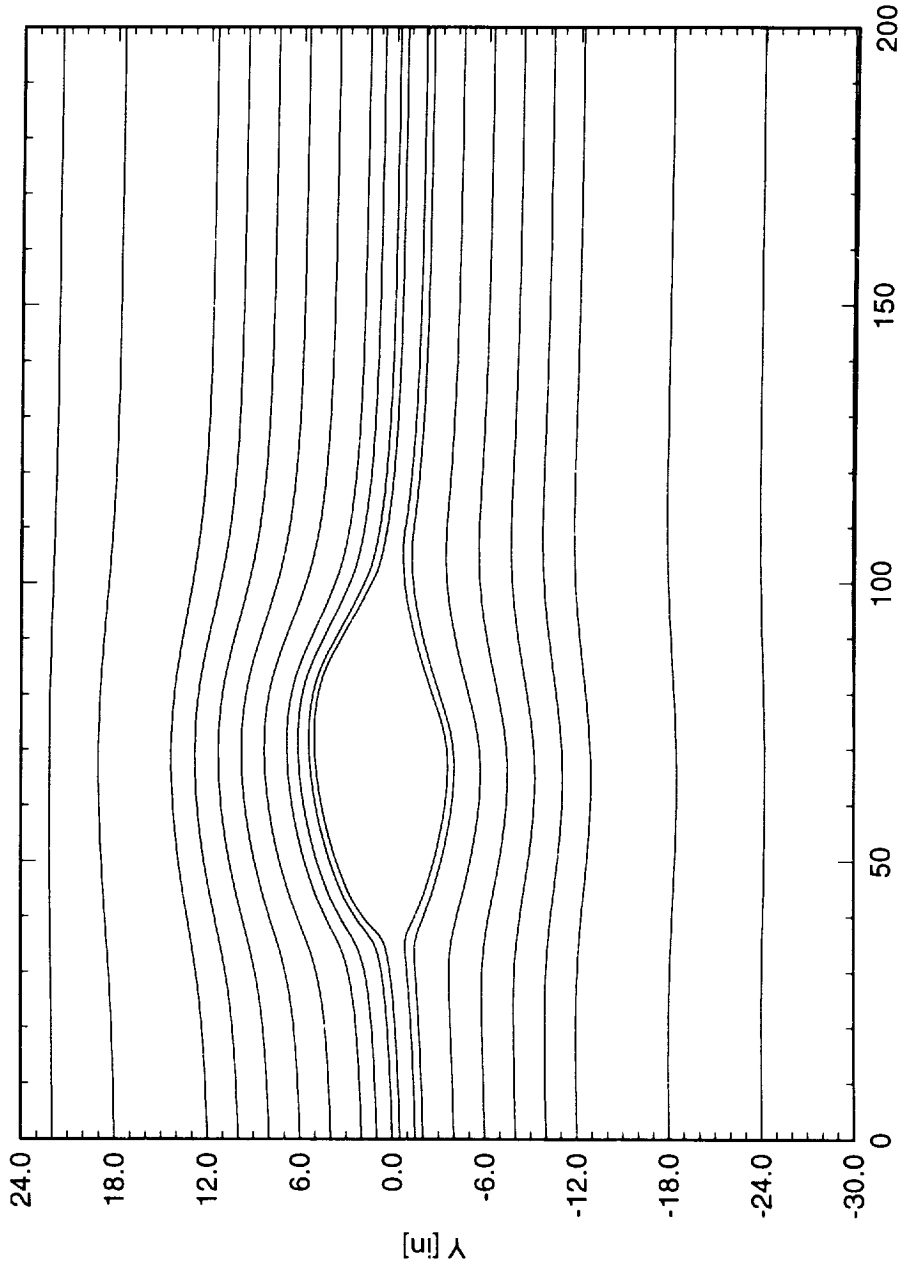

Figure 4.3. Streamlines for liner construction with $\alpha = 0°$. Projection in (X, Y) plane.

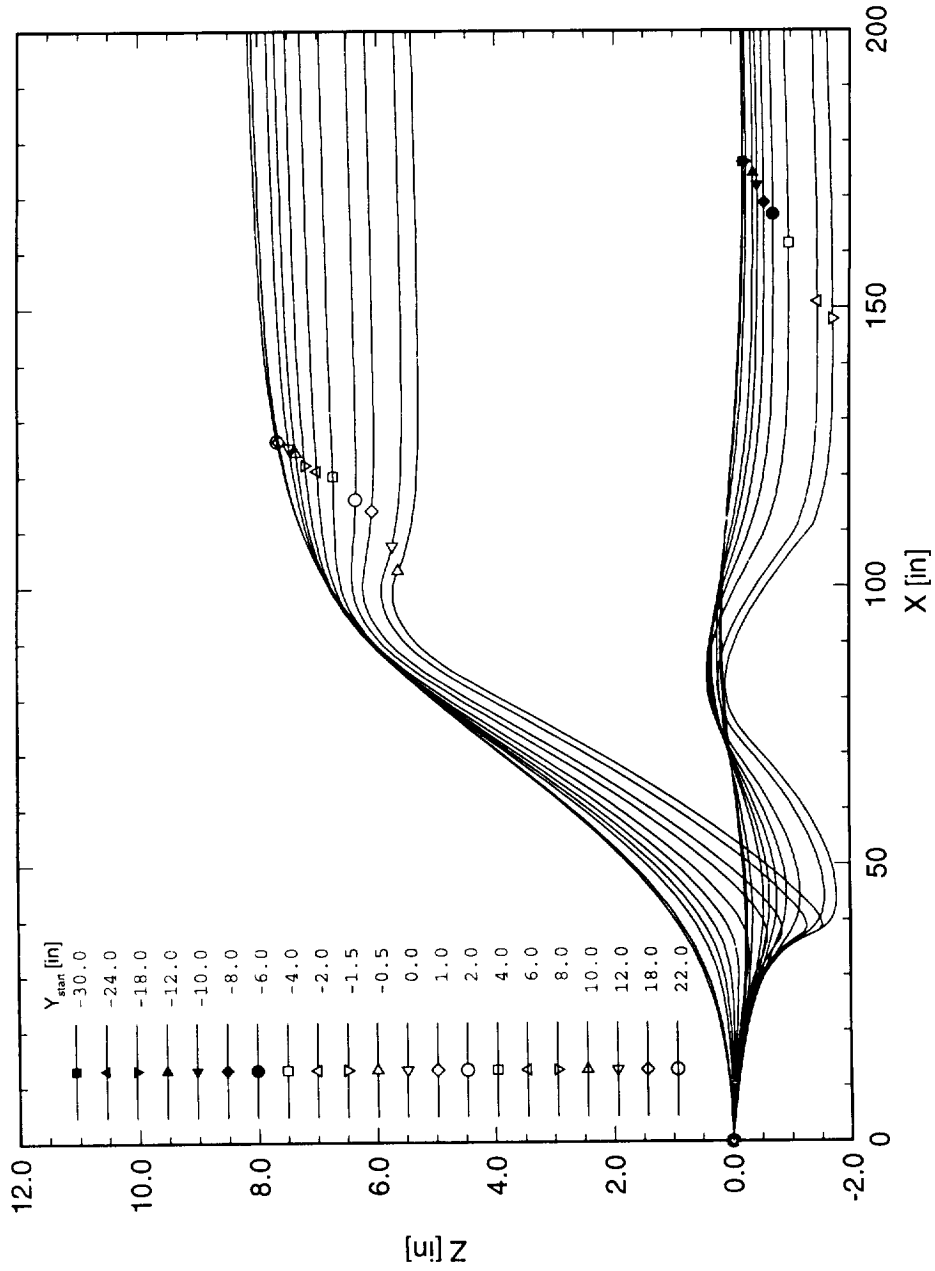

Figure 4.4. Streamlines for liner construction with $\alpha = 0°$. Projection in (X, Z) plane.

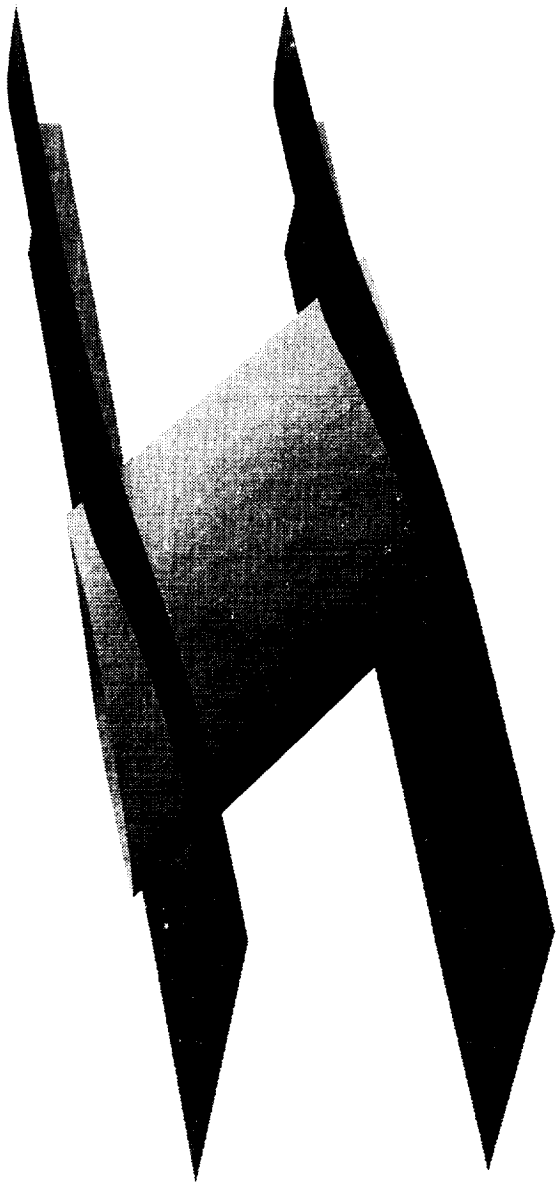

Figure 4.5. Test-section liners with airfoil installed at $\alpha = 0°$.

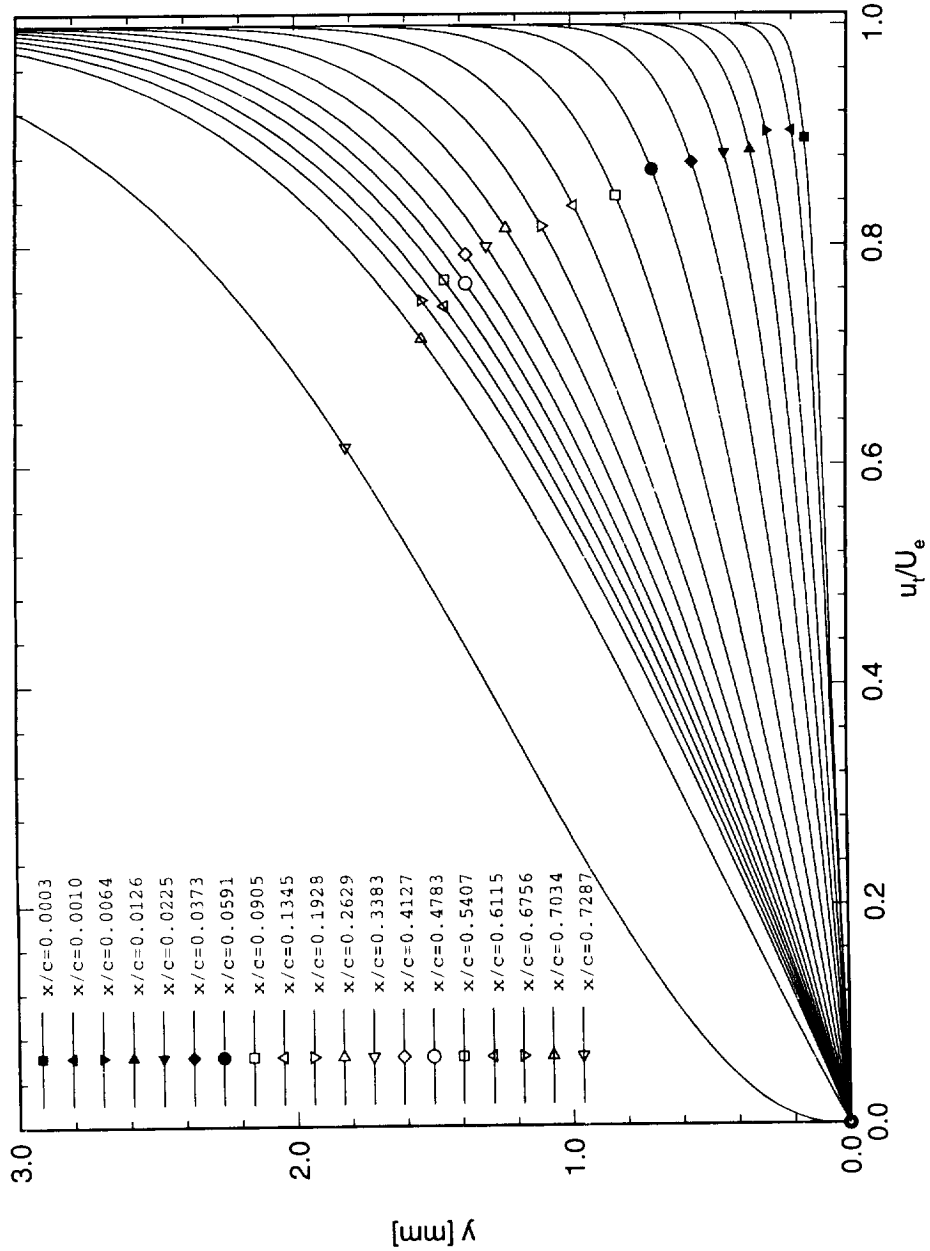

Figure 4.6. Theoretical boundary-layer profiles for $Re_c = 3.0 \times 10^6$ and $\alpha = 0^\circ$. Tangential component.

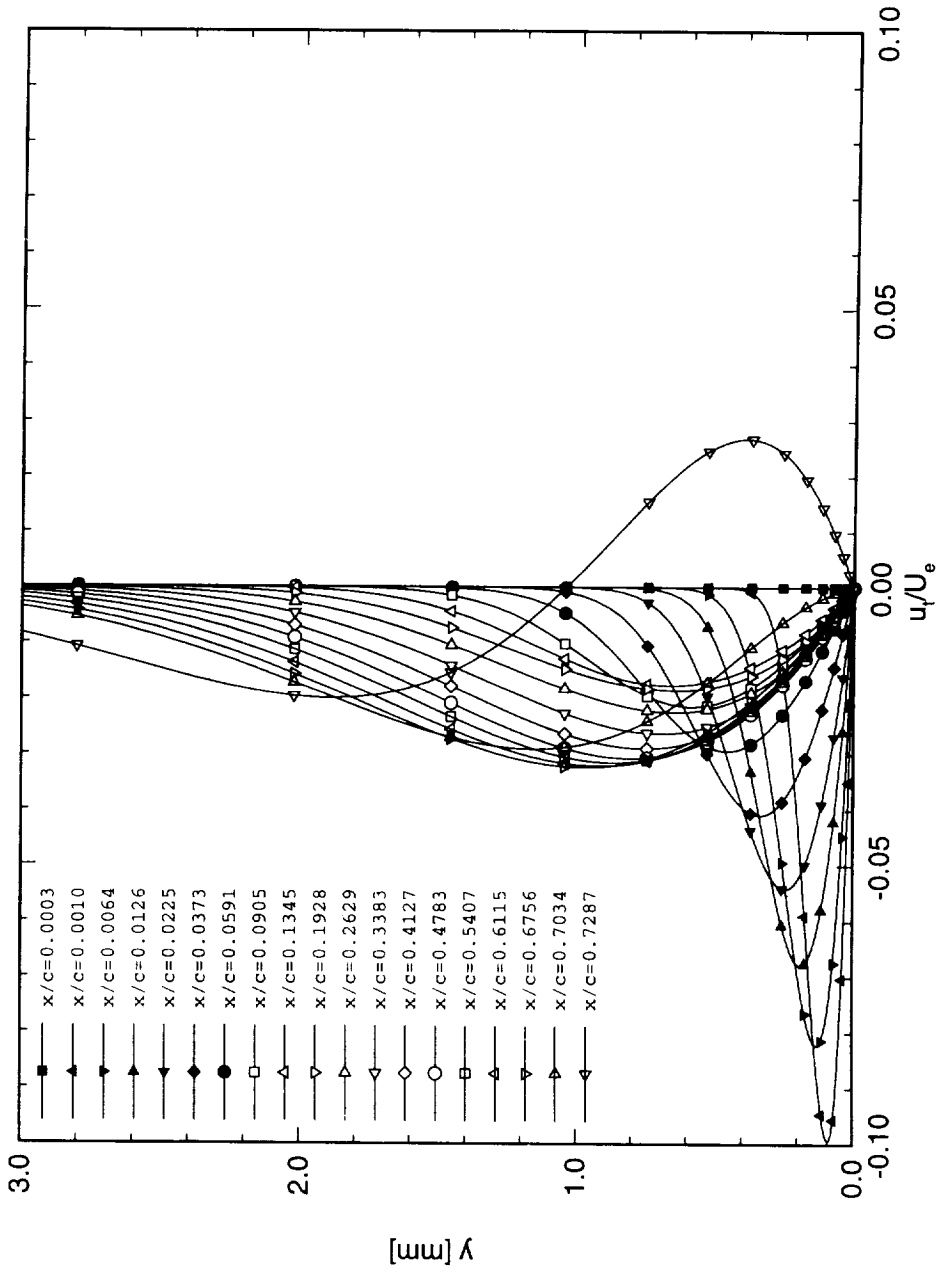

Figure 4.7. Theoretical boundary-layer profiles for $Re_c = 3.0 \times 10^6$ and $\alpha = 0°$. Crossflow component.

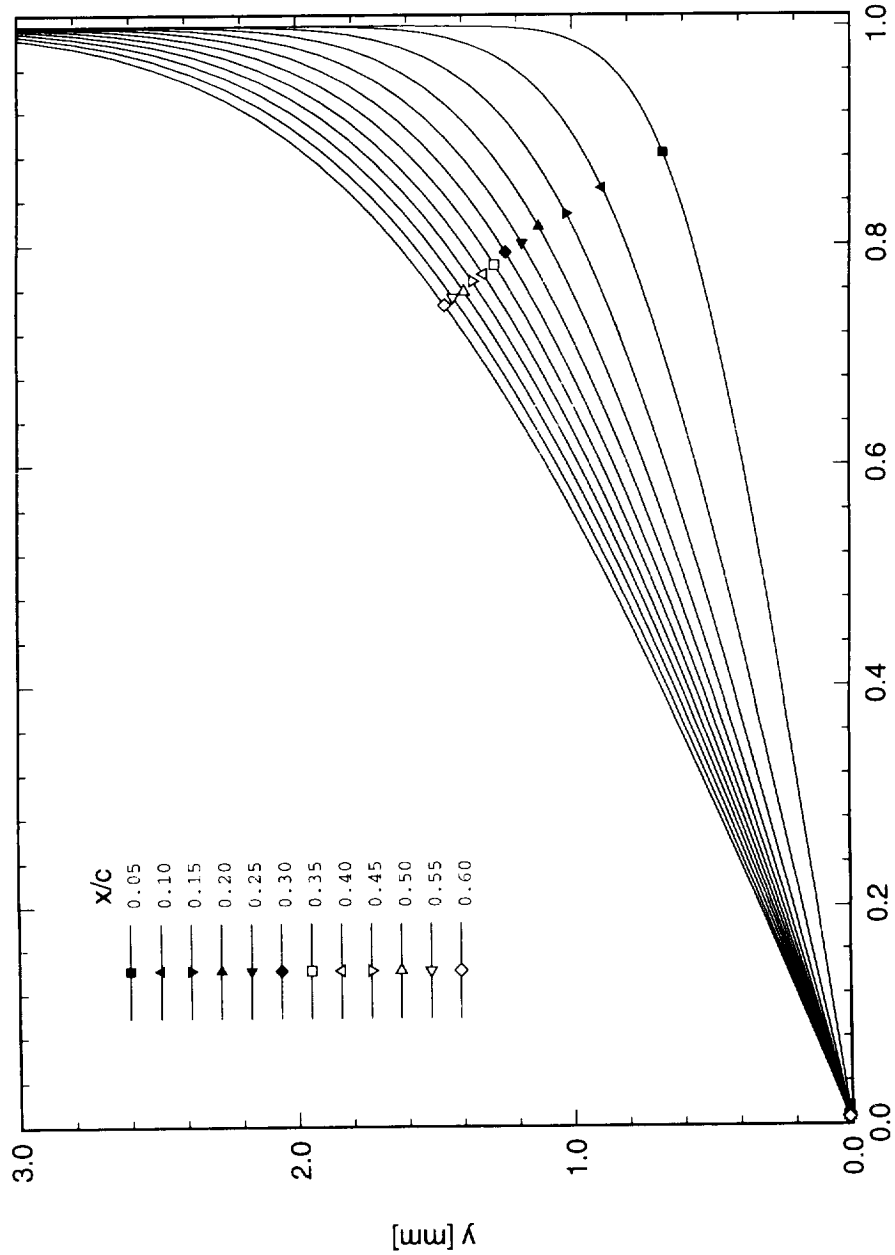

Figure 4.8. Theoretical boundary-layer profiles for $Re_c = 3.0 \times 10^6$ and $\alpha = 0°$. Streamwise component.

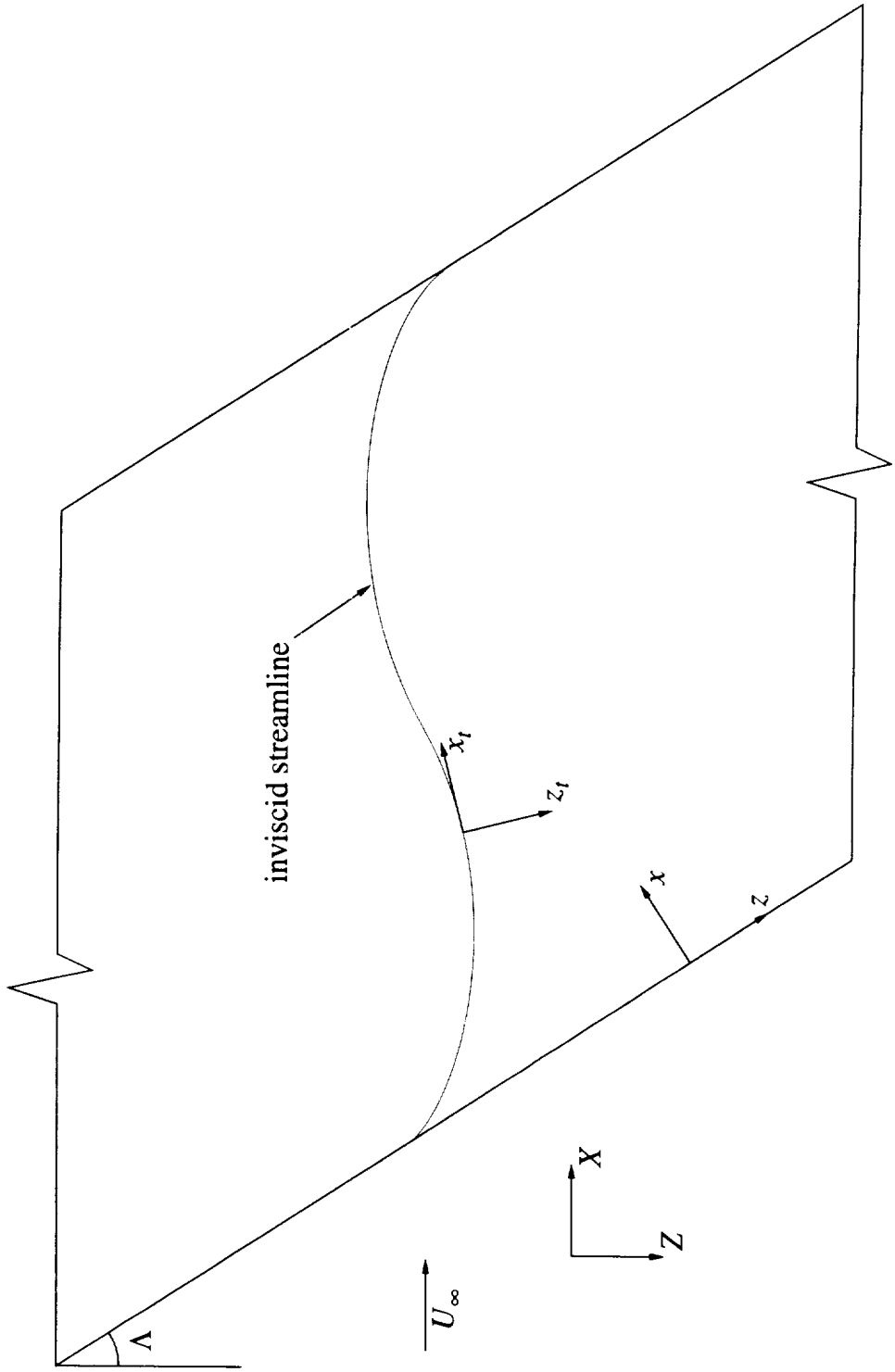

Figure 4.9. Swept airfoil showing coordinate systems and curved inviscid streamline.

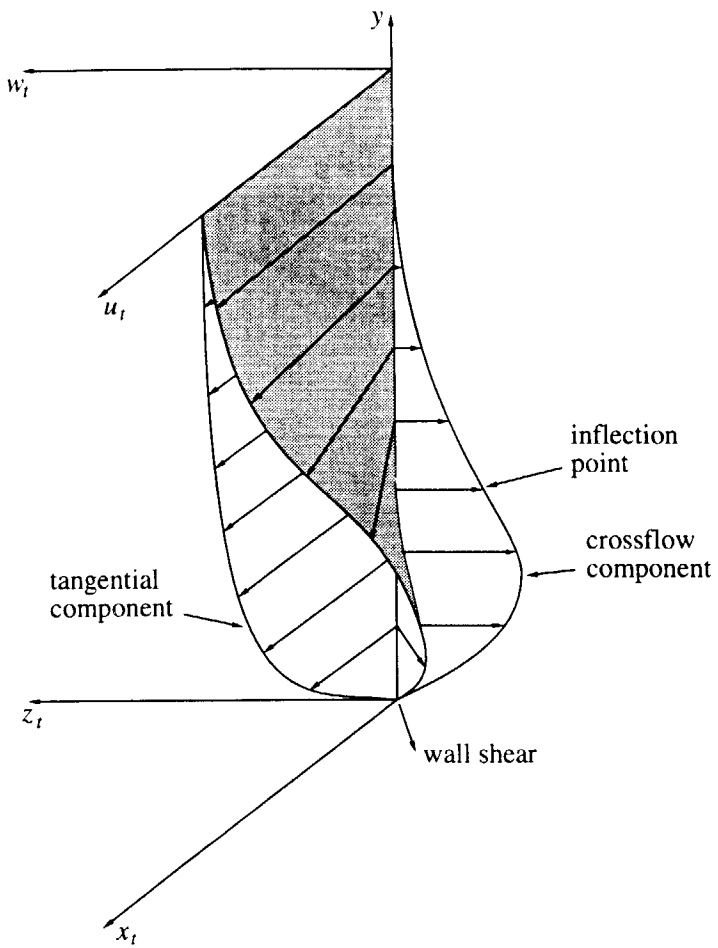

Figure 4.10. Swept-wing boundary-layer profile showing tangential, crossflow, and total velocity components.

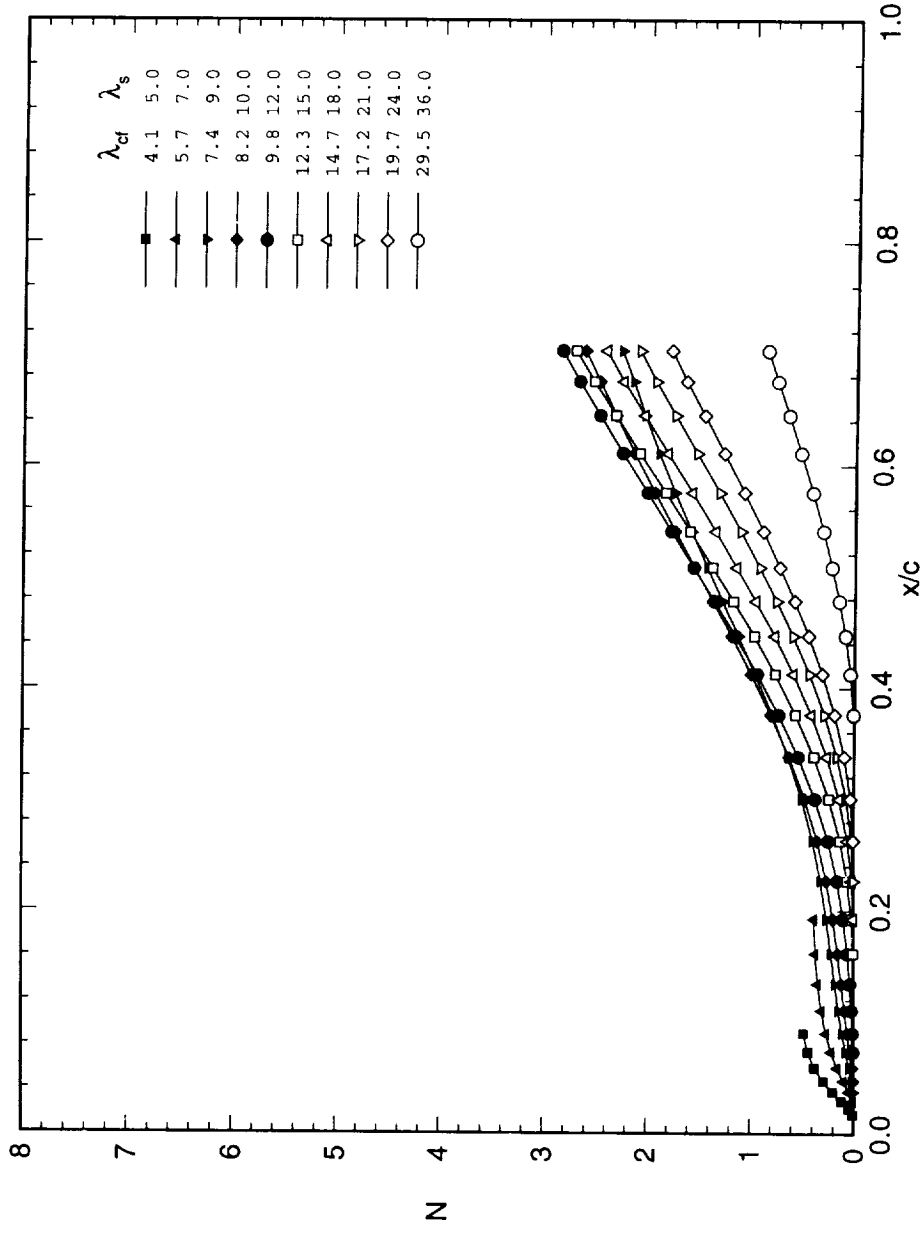

Figure 4.11. SALLY N-factors for stationary crossflow vortices at $\alpha = 0°$, $Re_c = 3.0 \times 10^6$.

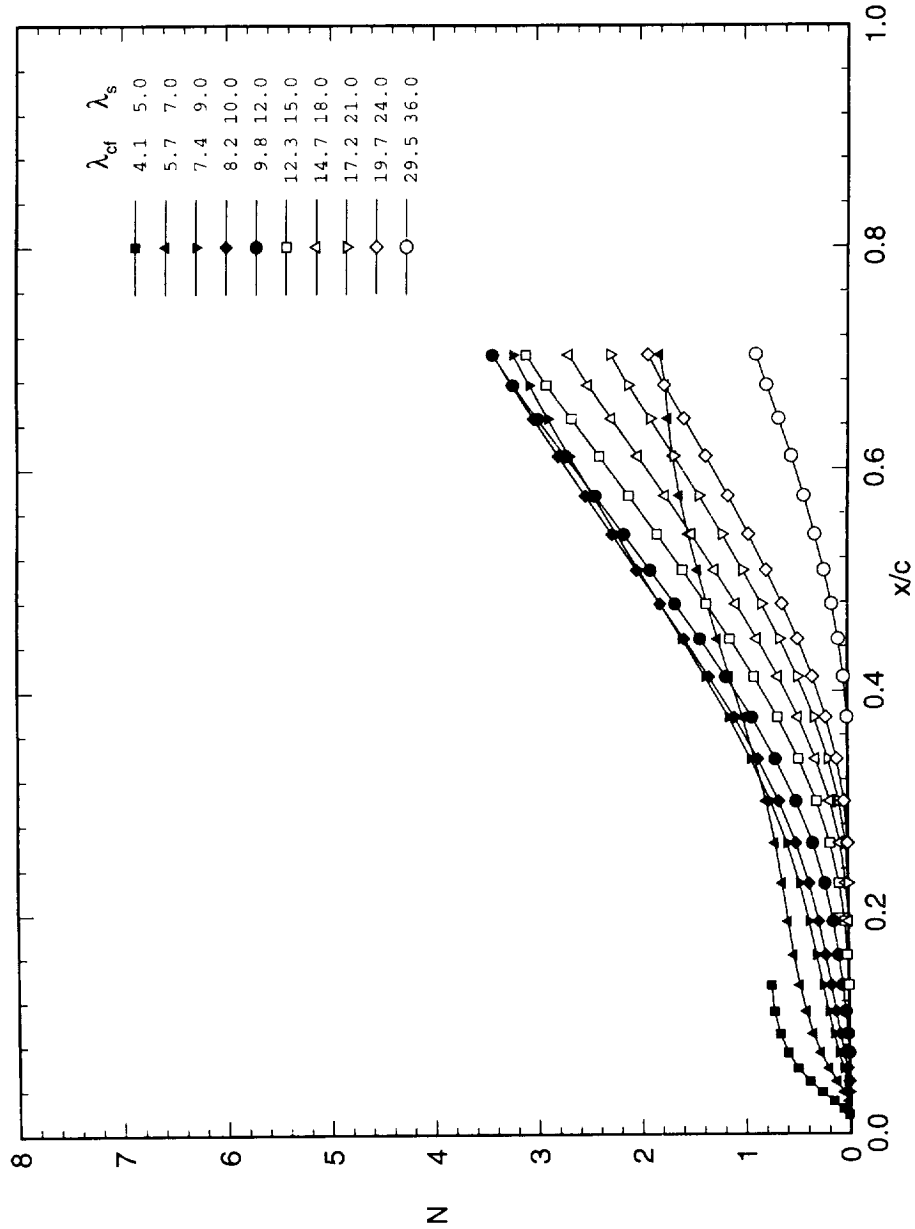

Figure 4.12. SALLY N-factors for stationary crossflow vortices at $\alpha = 0°$, $Re_c = 3.6 \times 10^6$.

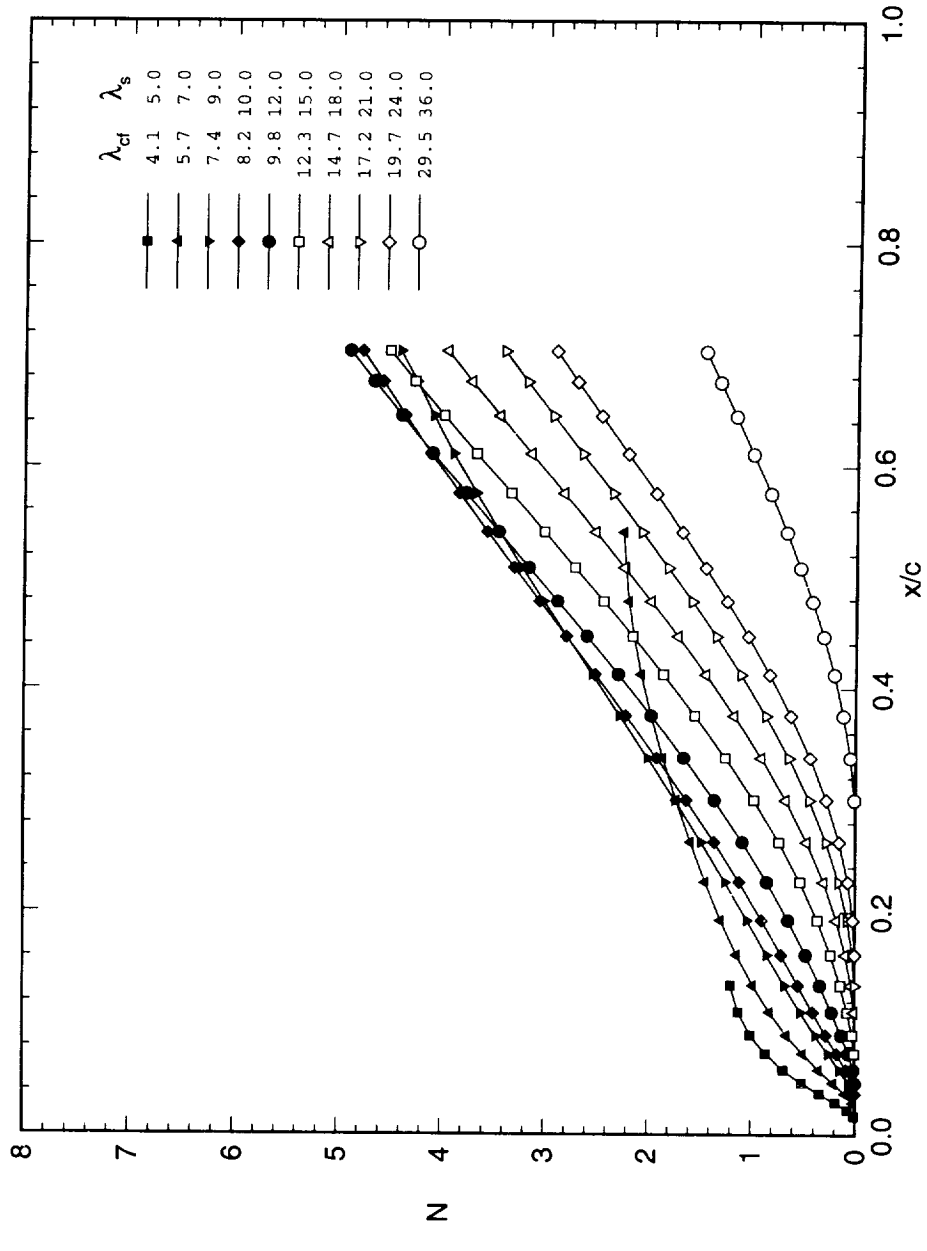

Figure 4.13. SALLY N-factors for stationary crossflow vortices at $\alpha = -1°$, $Re_c = 3.0 \times 10^6$.

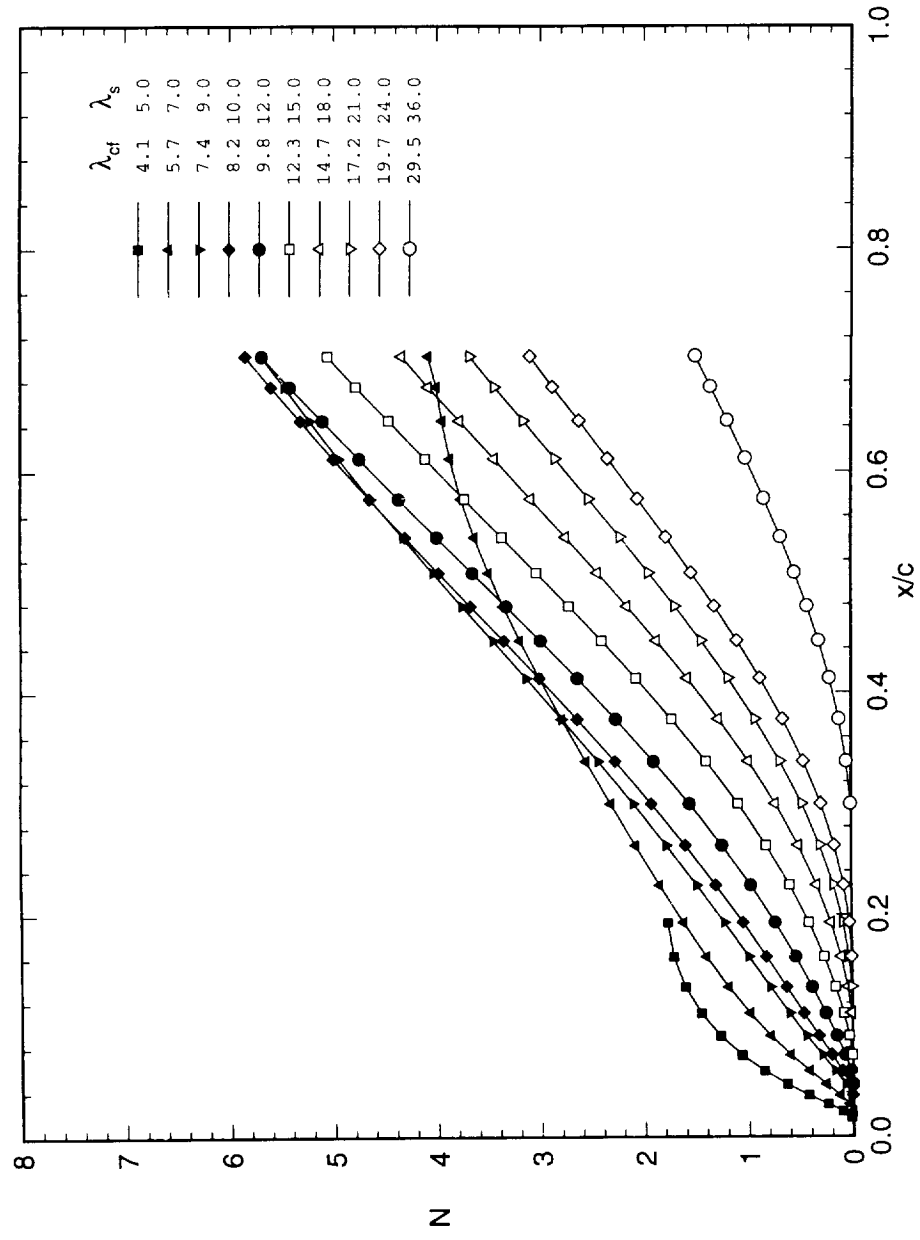

Figure 4.14. SALLY N-factors for stationary crossflow vortices at $\alpha = -1°$, $Re_c = 3.6 \times 10^6$.

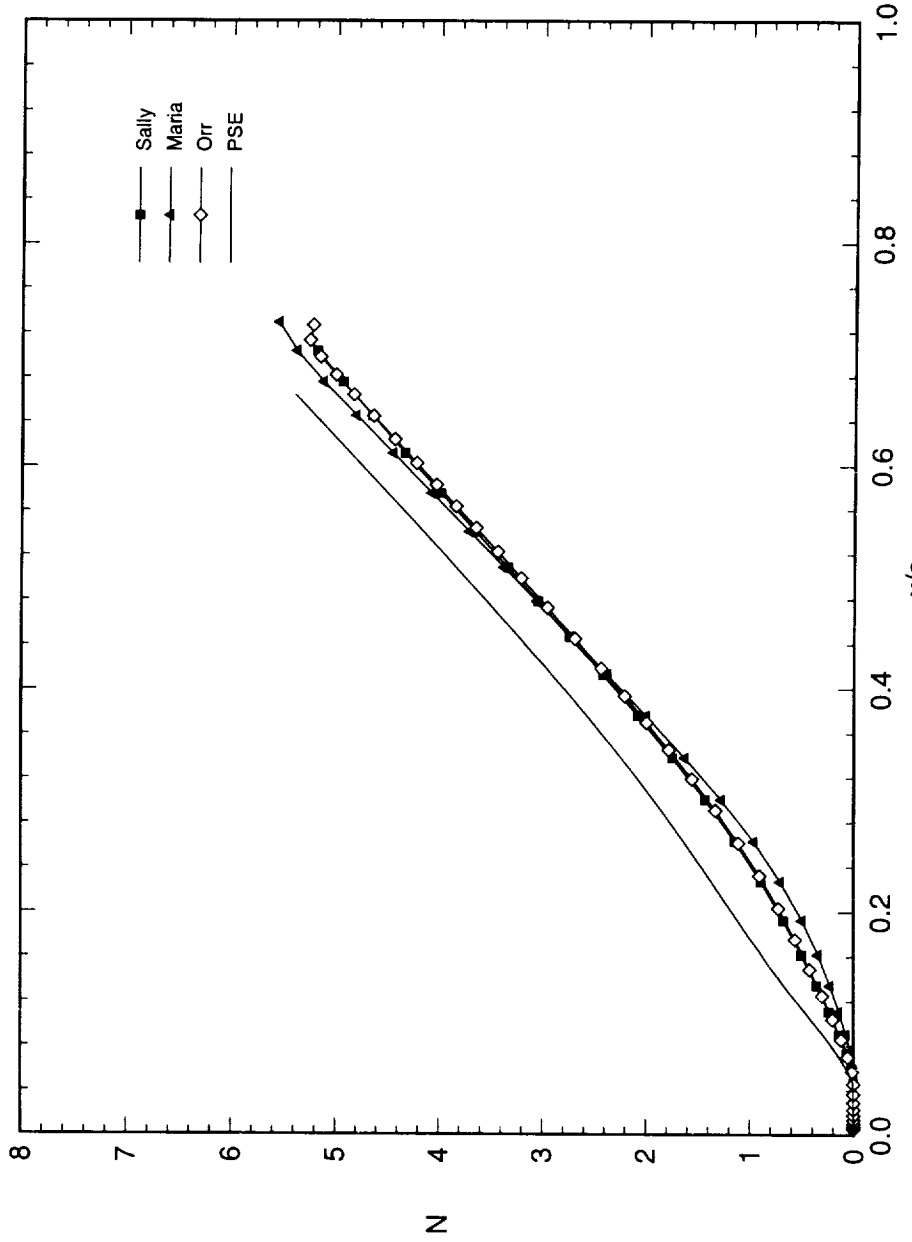

Figure 4.15. Comparison of theoretical stability predictions for $\alpha = 0°$, $\lambda_s = 12$ mm, $Re_c = 3.0 \times 10^6$.

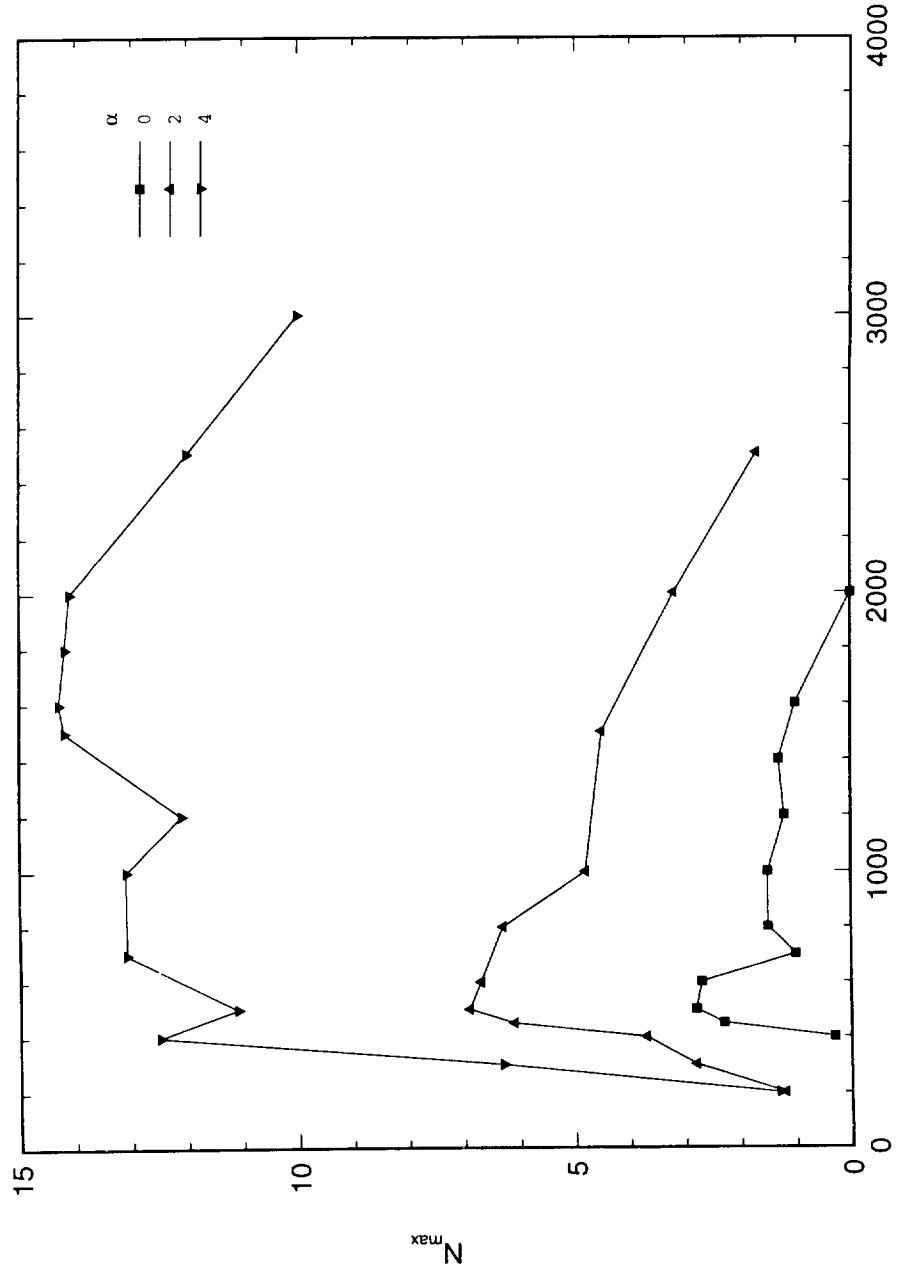

Figure 4.16. Maximum N-factors for Tollmien-Schlichting waves for $Re_c = 3.8 \times 10^6$.

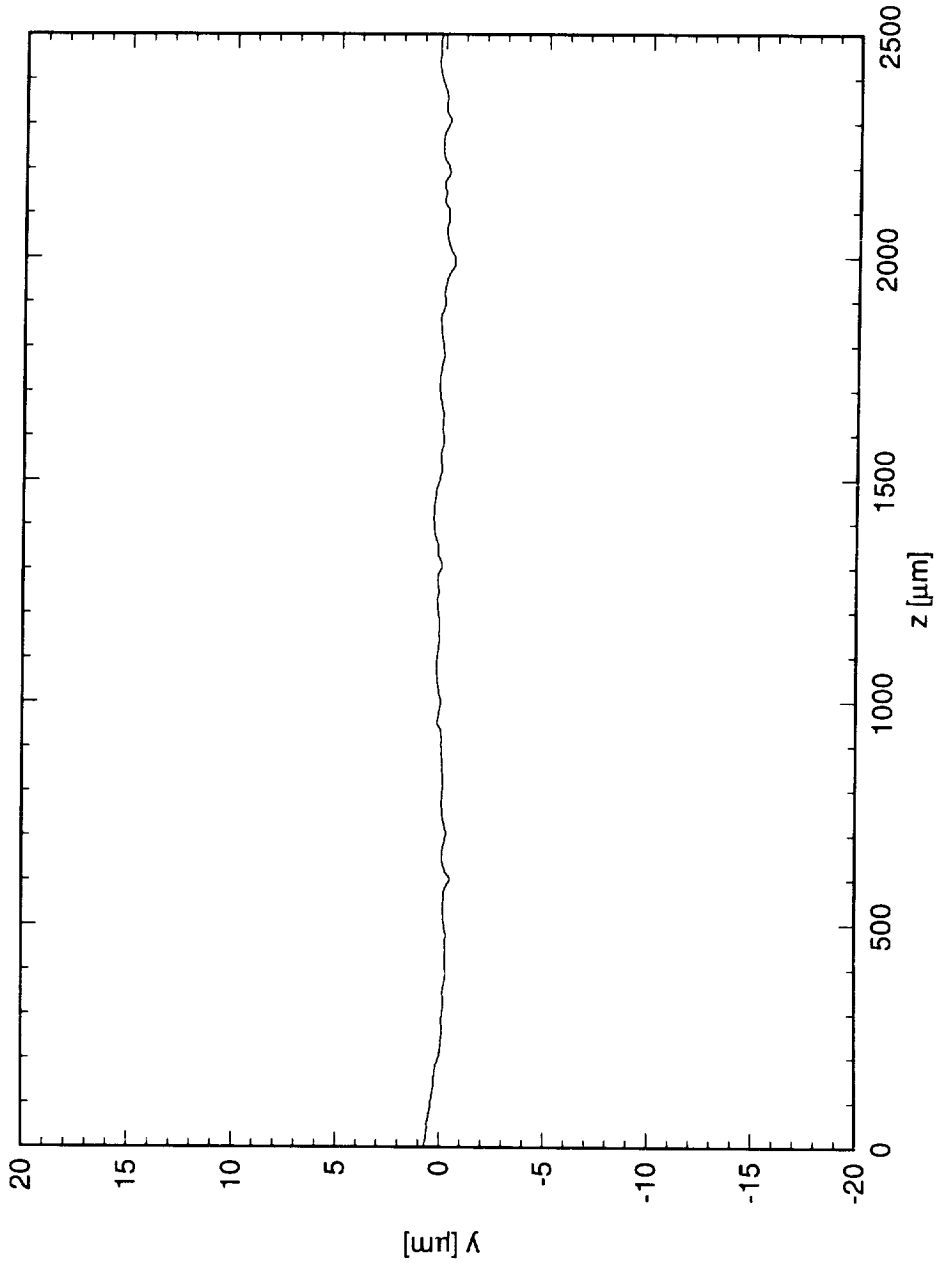

Figure 4.17. Profilometer measurement of NLF(2)-0415 surface roughness after polishing. Filtered $20\mu m$–$1500\mu m$, rms = $0.121\mu m$.

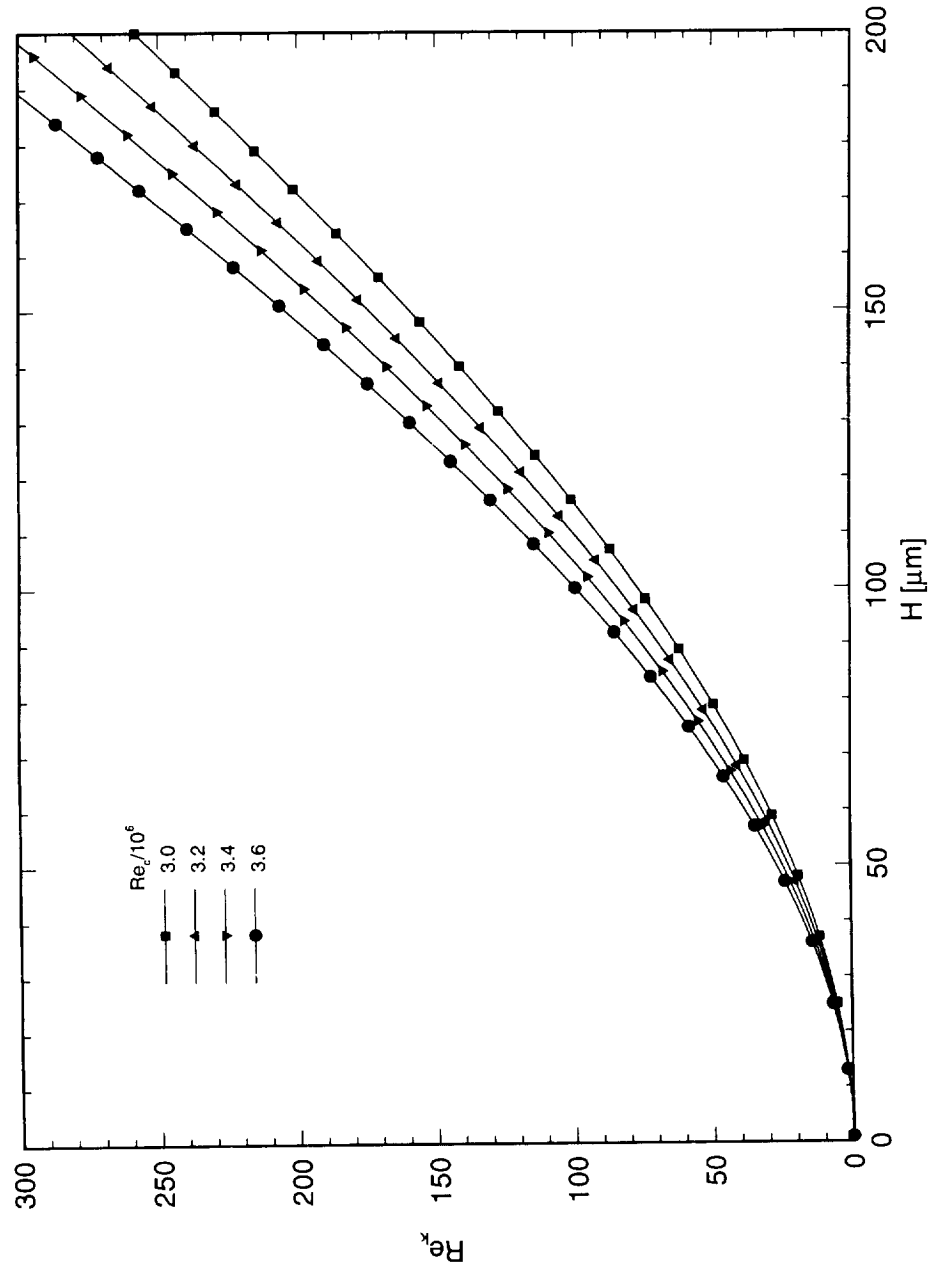

Figure 4.18. Roughness Reynolds number Re_k, based on roughness height and velocity at top of roughness. $\alpha = 0°$.

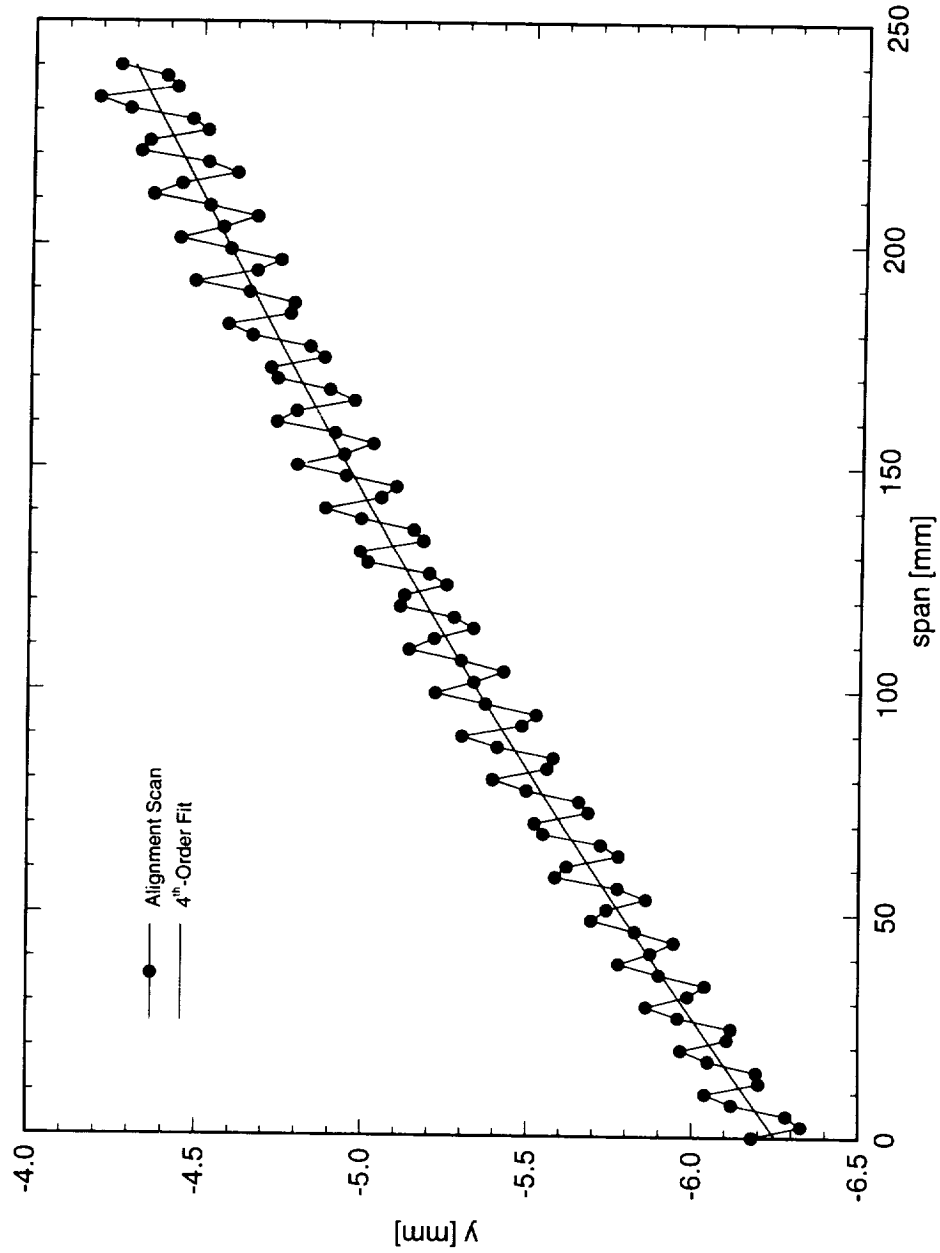

Figure 5.1. Typical traverse-alignment scan taken before spanwise hot-wire scan. 146 μm roughness with 10 mm spacing at $x/c = 0.005$. Scan at $x/c = 0.6$ with $Re_c = 3.0 \times 10^6$.

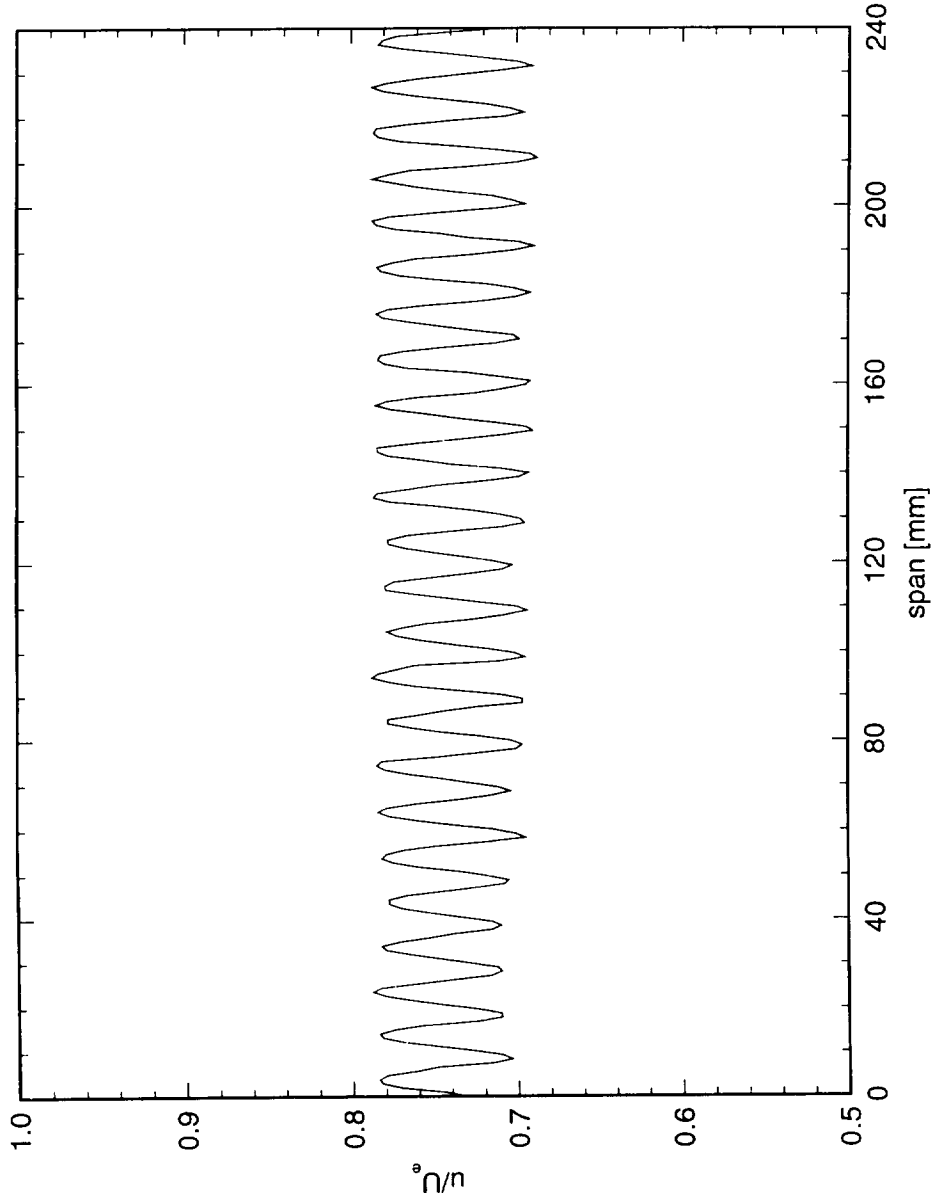

Figure 5.2. Typical spanwise hot-wire scan showing mean-flow distortion due to stationary crossflow. 146 μm roughness with 10 mm spacing at $x/c = 0.005$. Scan at $x/c = 0.6$ with $Re_c = 3.0 \times 10^6$.

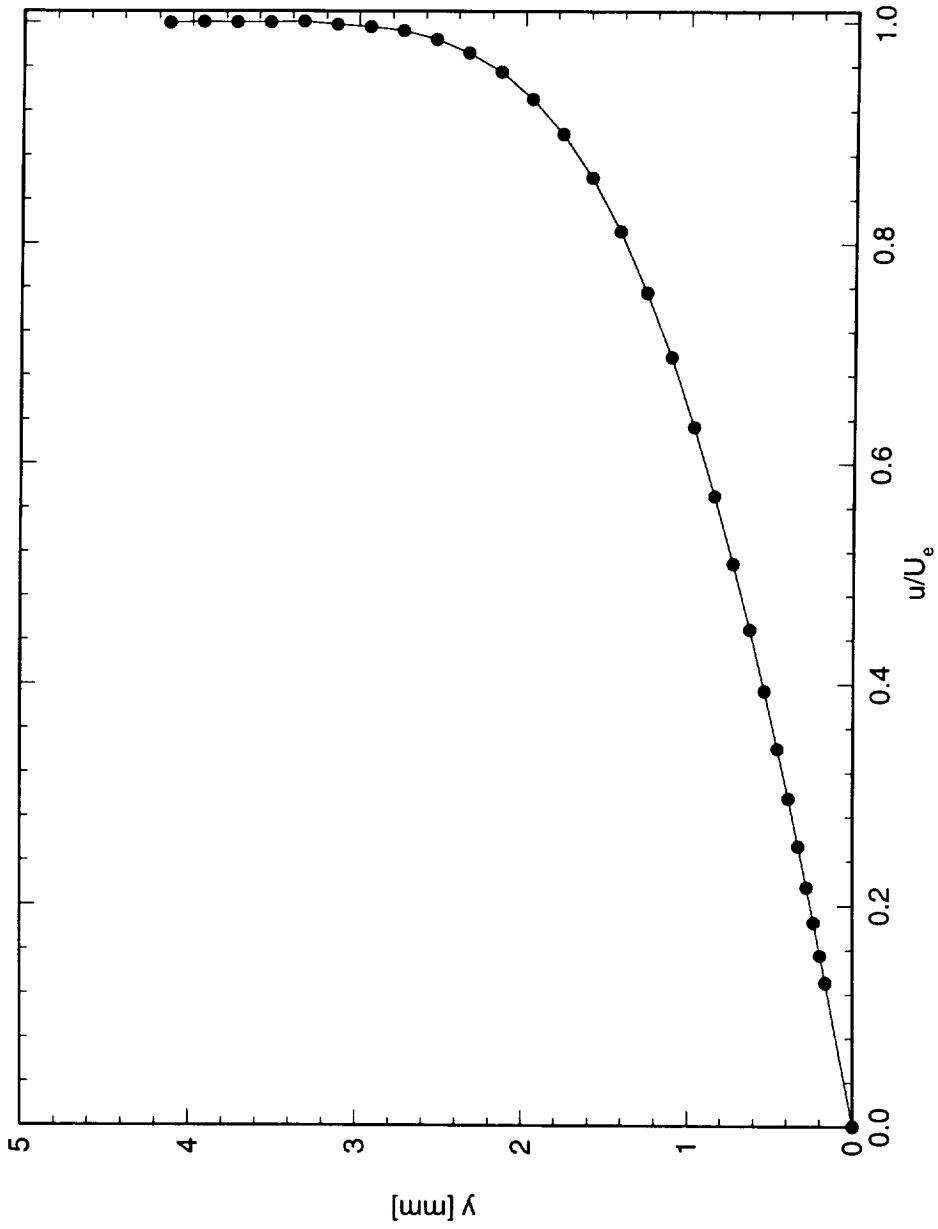

Figure 5.3. Typical high-resolution boundary-layer scan. $x/c = 0.6$, $Re_c = 3.0 \times 10^6$.

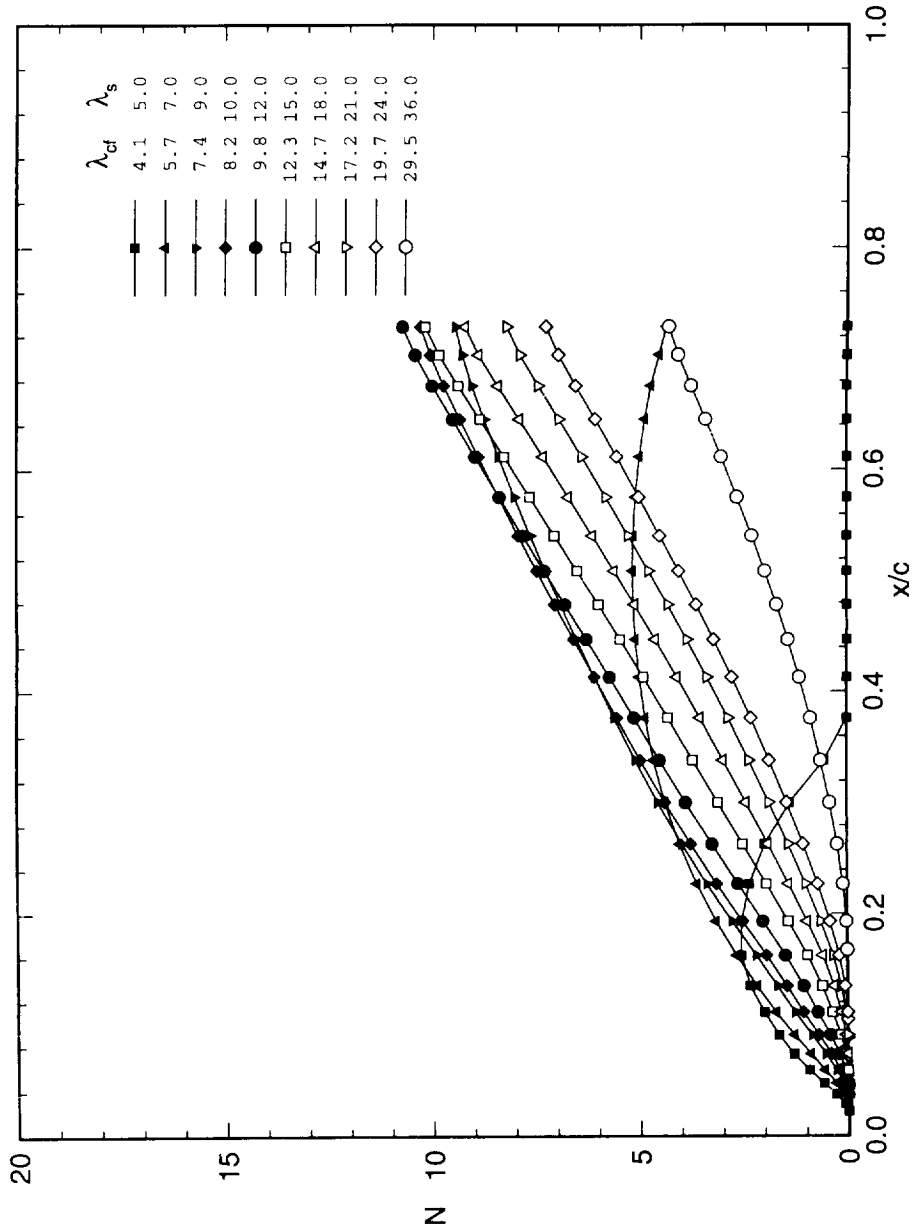

Figure 6.1. MARIA N-factors for stationary crossflow vortices at $\alpha = -4°$, $Re_c = 2.6 \times 10^6$.

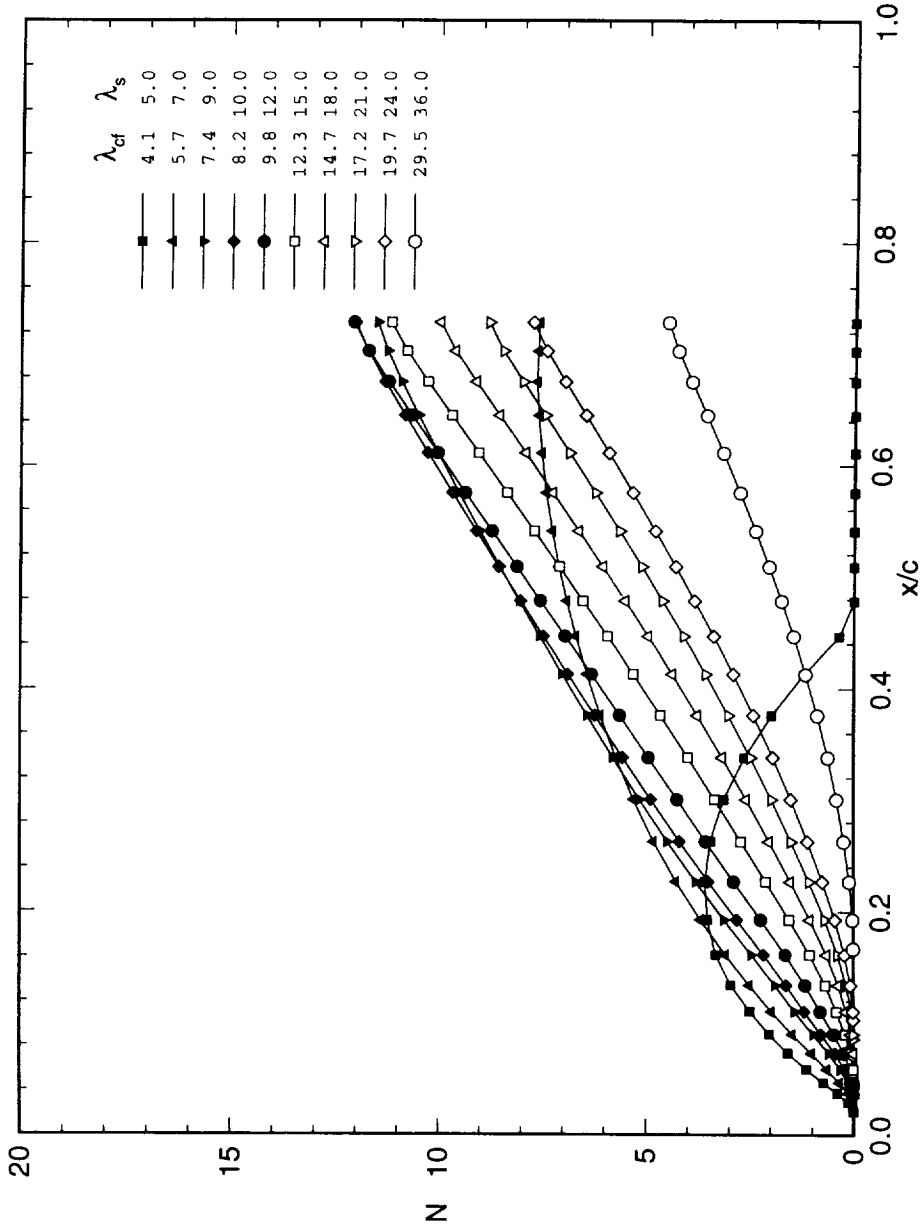

Figure 6.2. MARIA N-factors for stationary crossflow vortices at $\alpha = -4°$, $Re_c = 3.0 \times 10^6$.

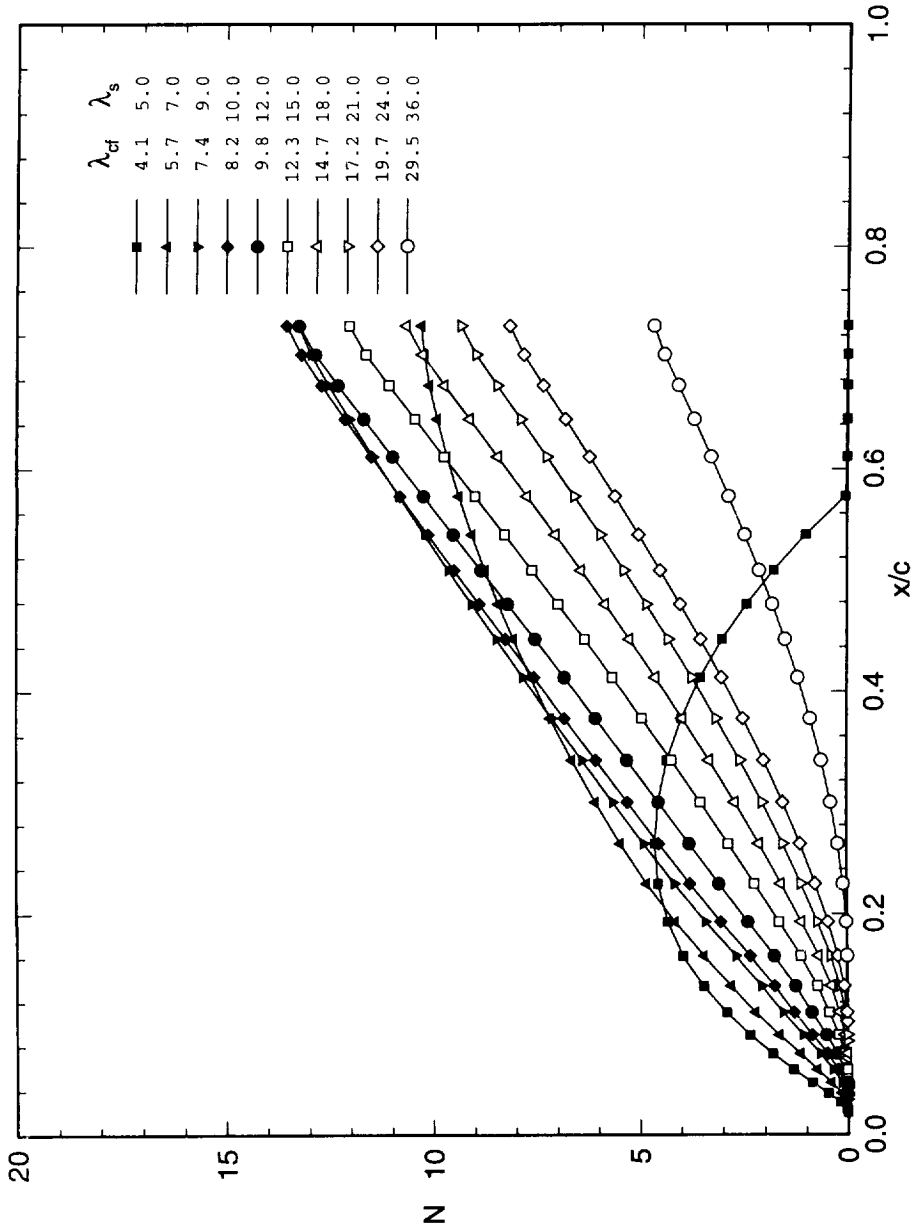

Figure 6.3. MARIA N-factors for stationary crossflow vortices at $\alpha = -4°$, $Re_c = 3.4 \times 10^6$.

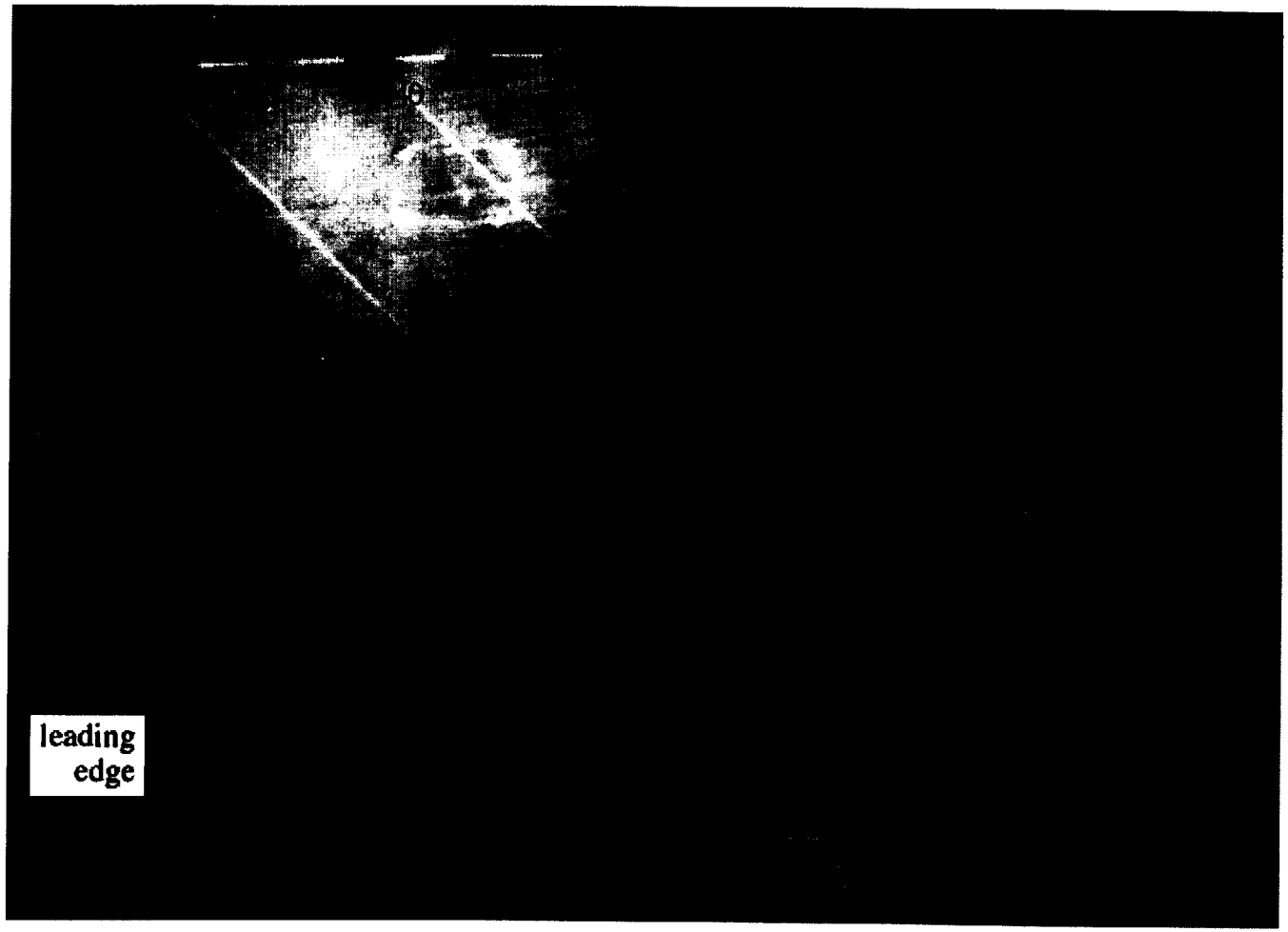

Figure 6.4. Naphthalene flow visualization at $Re_c = 2.6 \times 10^6$ showing jagged transition front near $x/c = 0.5$, and strong stationary vortex tracks. Flow is from left to right. Numbers indicate chordwise position.

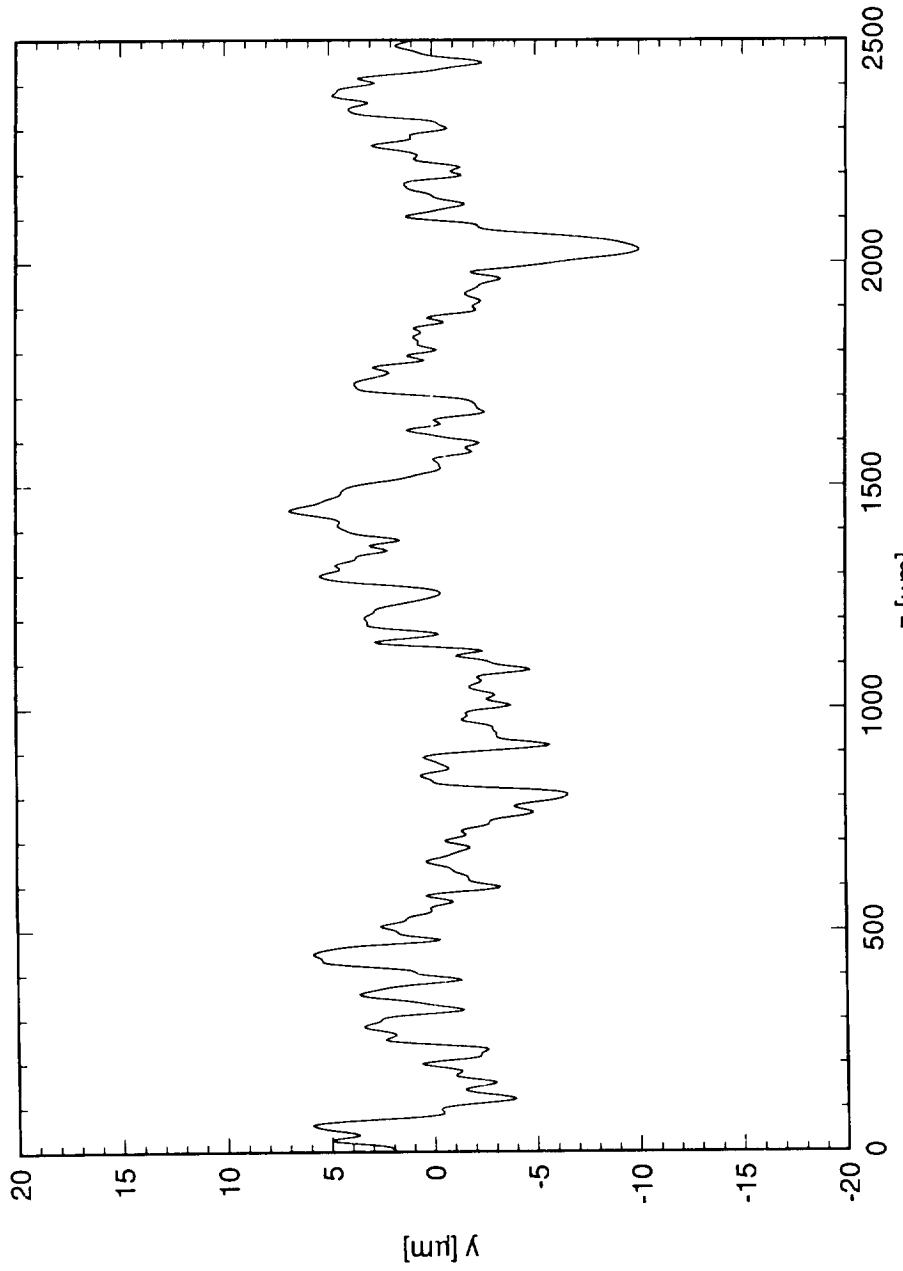

Figure 6.5. Profilometer measurement of NLF(2)-0415 painted surface. Filtered 20μm–1500μm, peak-peak =9 μm.

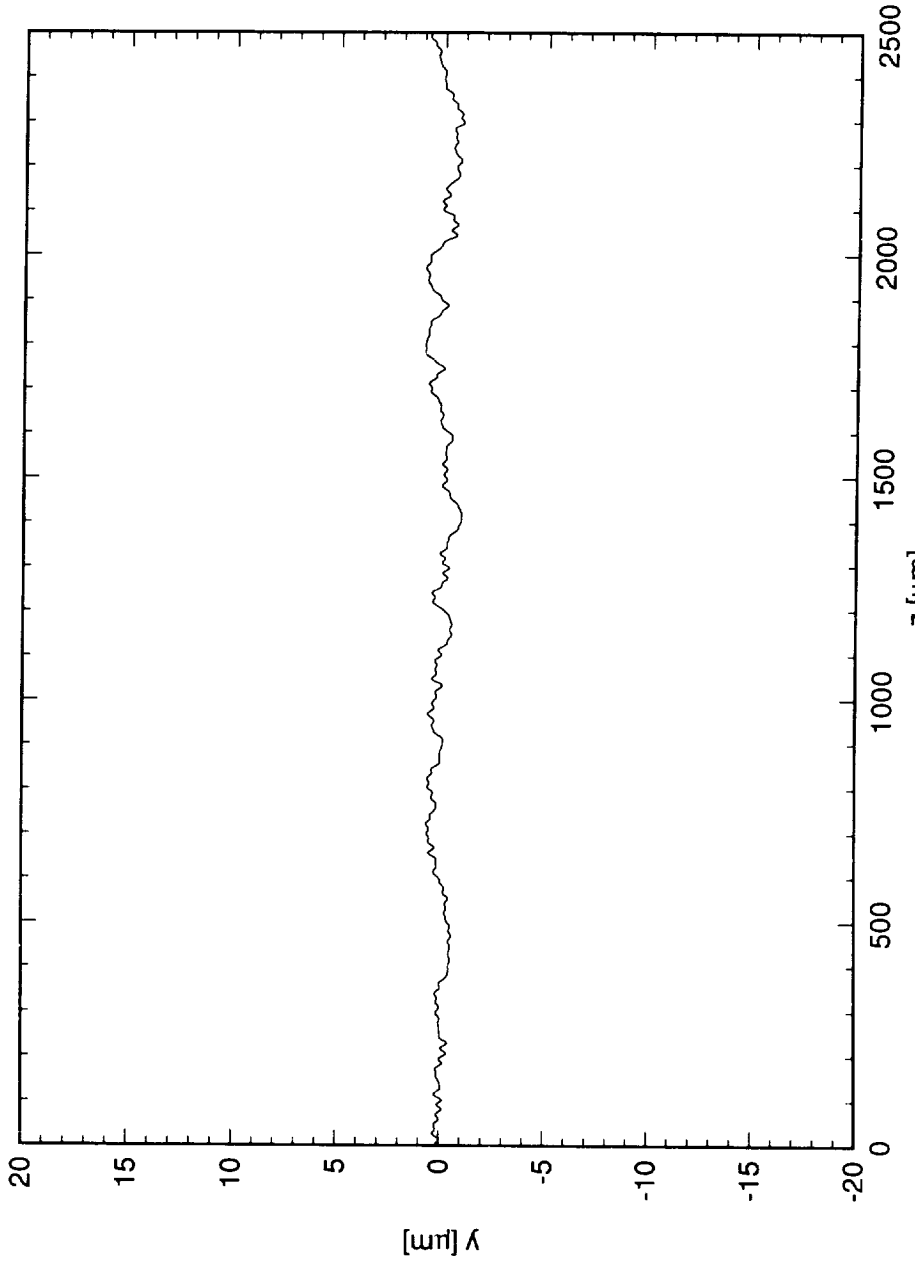

Figure 6.6. Profilometer measurement of NLF(2)-0415 surface after initial polishing stage. Filtered 20μm–1500μm, rms = 0.509 μm.

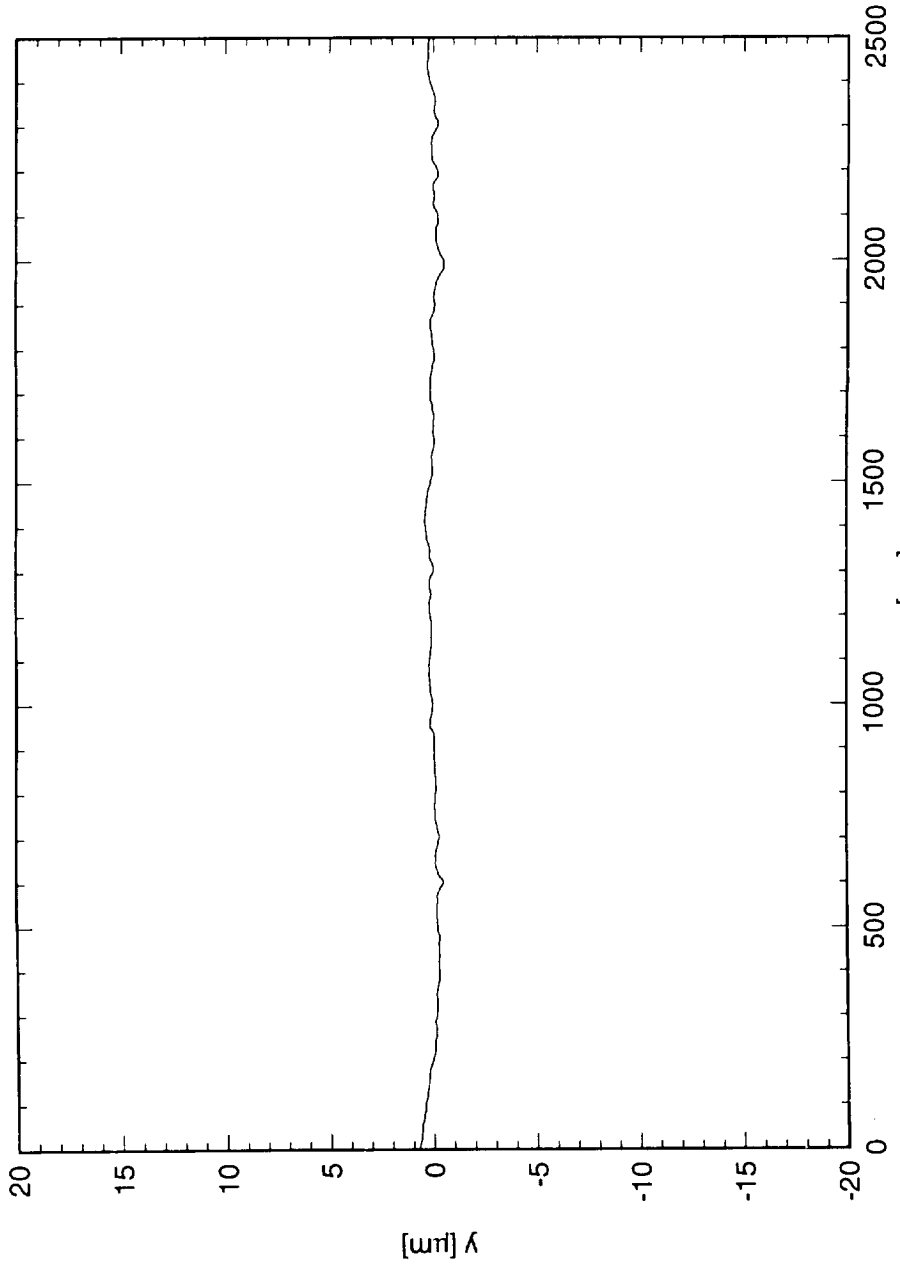

Figure 6.7. Profilometer measurement of NLF(2)-0415 surface after final polishing stage. Filtered $20\mu m$–$1500\mu m$, rms = 0.121 μm.

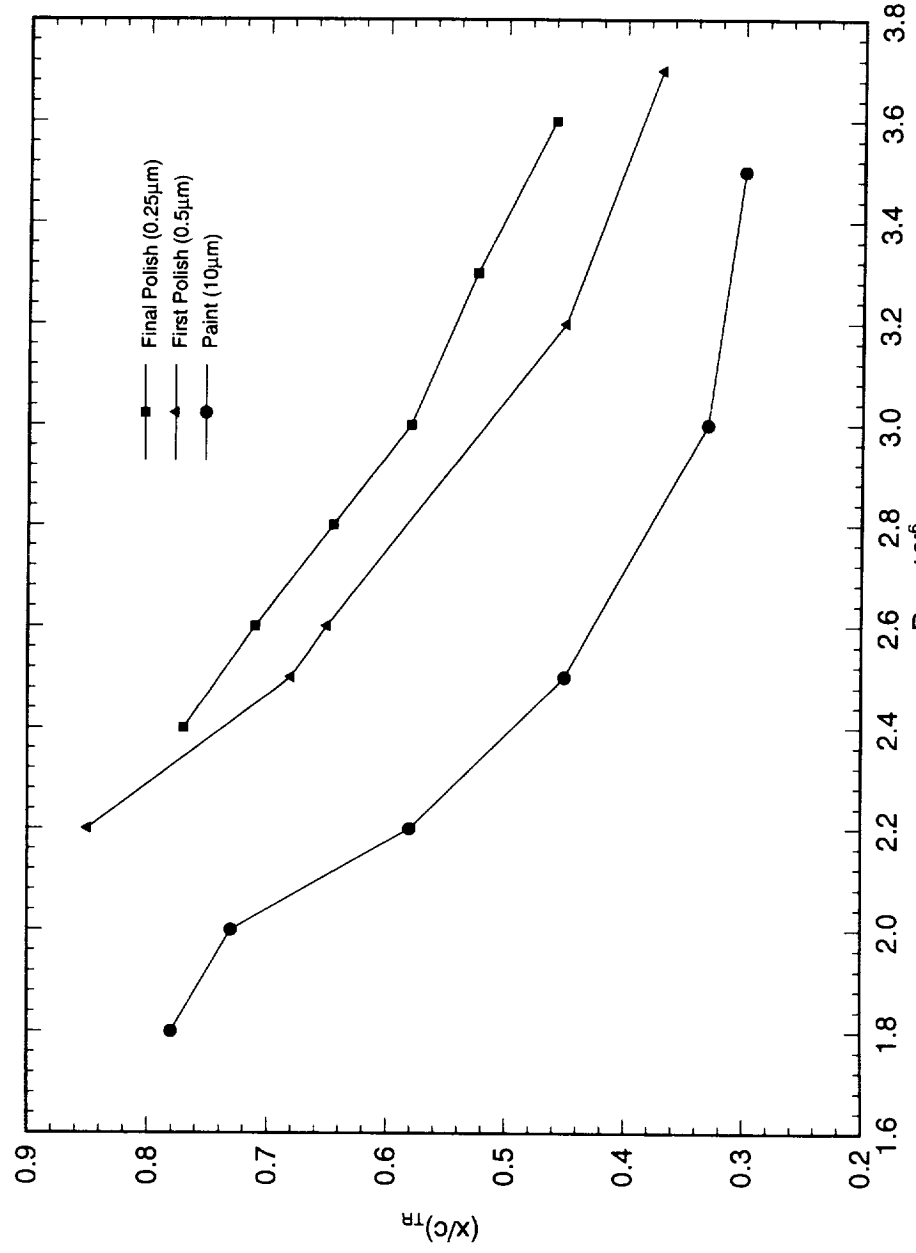

Figure 6.8. Naphthalene flow visualization measurement of average transition location with different surface finishes. $\alpha = -4°$.

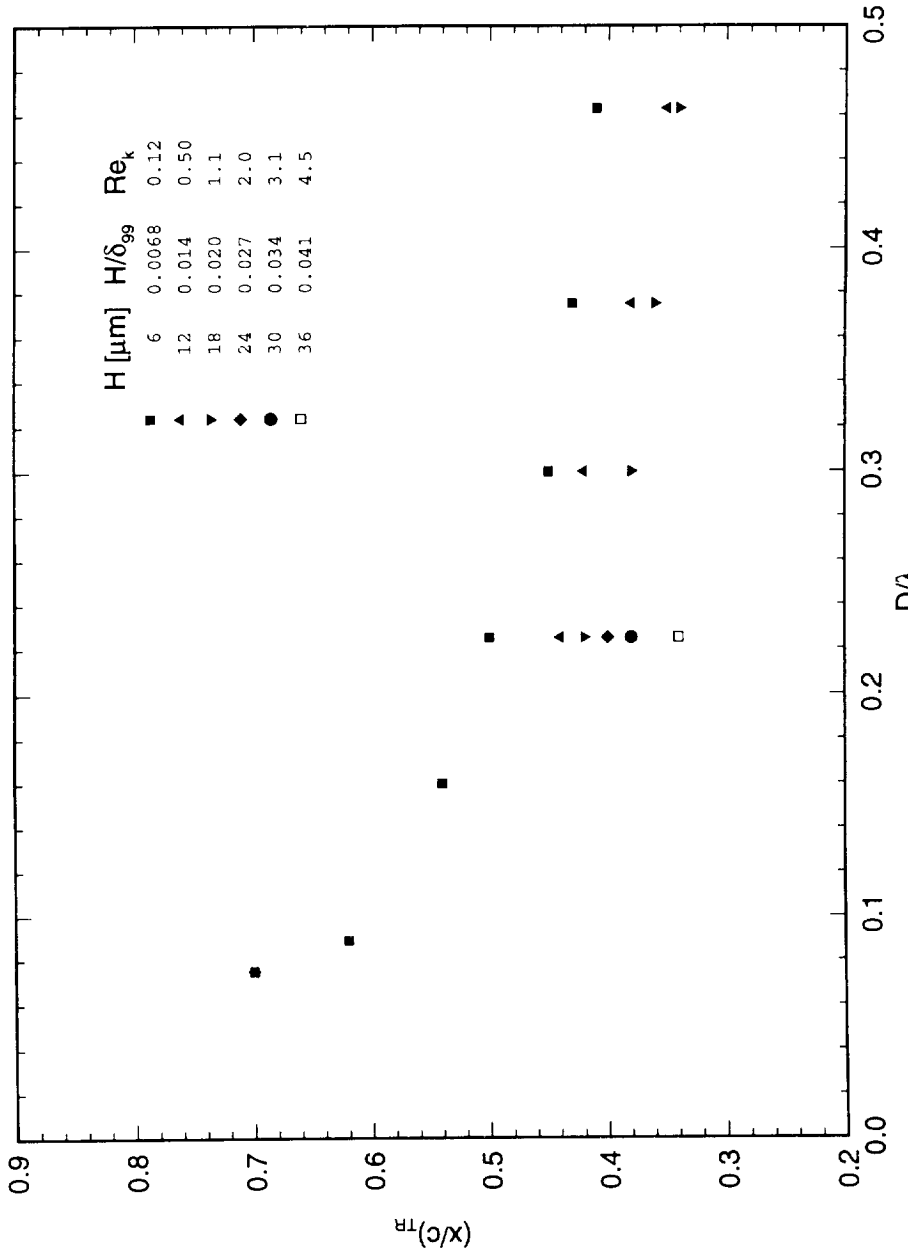

Figure 6.9. Naphthalene visualization results showing location of transition wedge behind applied roughness elements. Roughness is at $x/c = 0.023$. $Re_c = 2.6 \times 10^6$, $\alpha = -4°$.

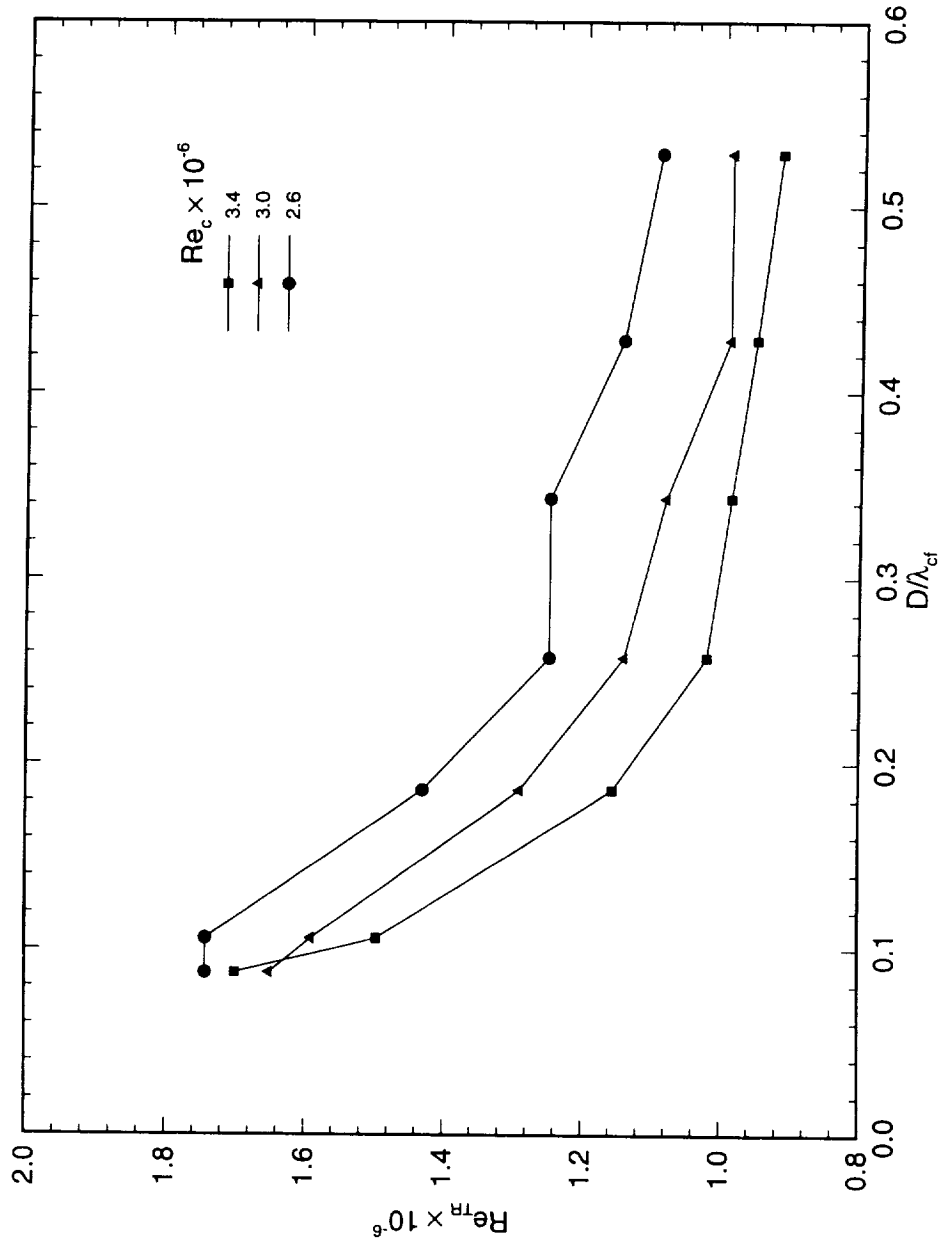

Figure 6.10. Variation of transition Reynolds number with roughness diameter. Roughness is at $x/c = 0.023$. Roughness height is 6 μm. $\alpha = -4°$.

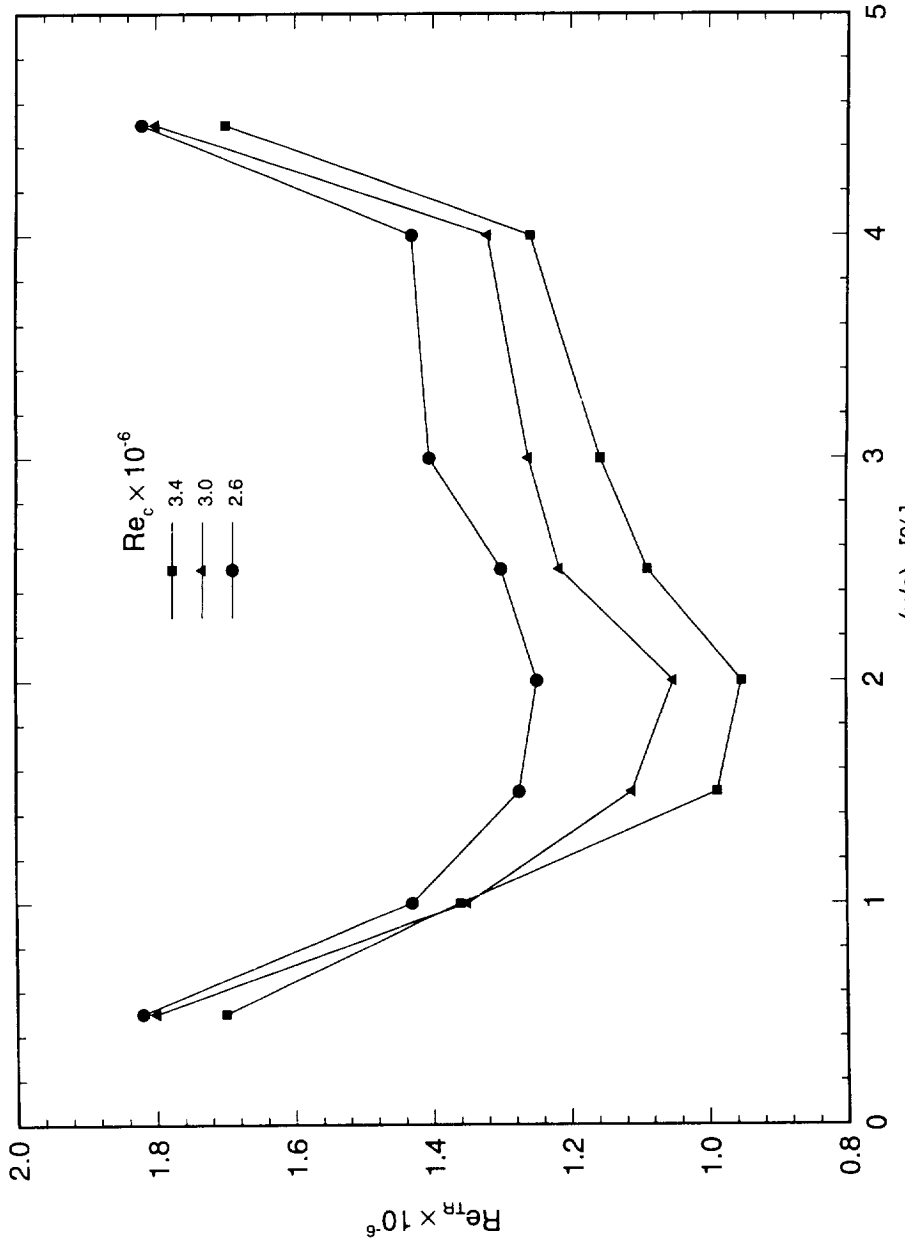

Figure 6.11. Variation of transition Reynolds number with roughness position. Roughness height is 6 μm. $\alpha = -4°$.

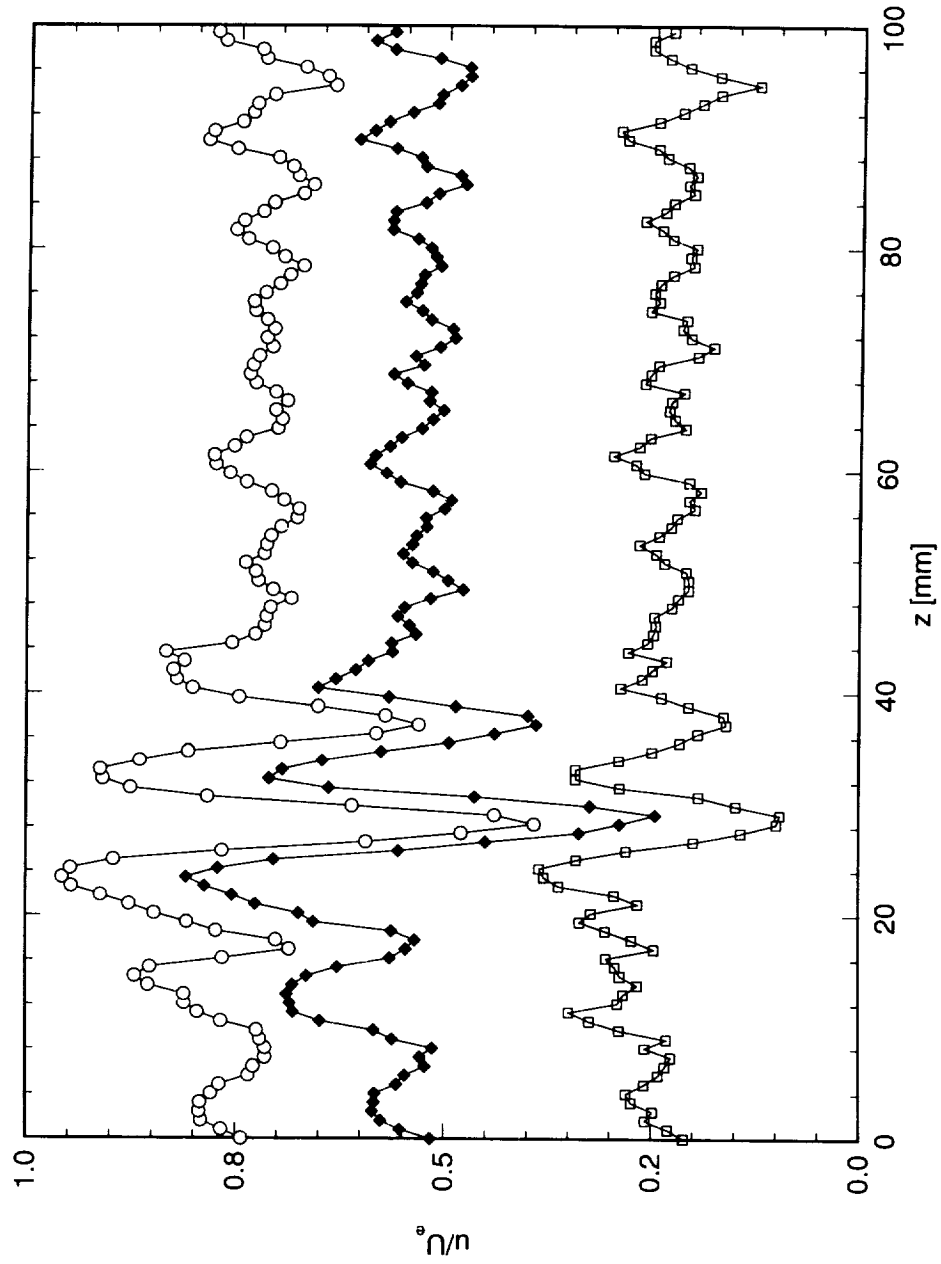

Figure 6.12. Spanwise hot-wire scans at $x/c = 0.35$. Constant-y scans at $\bar{u}/U_e$ of 0.25, 0.5, and 0.75. A single roughness element with $D = 0.37$ mm, $H = 6$ μm is at $x/c = 0.023$. $Re_c = 2.6 \times 10^6$, $\alpha = -4°$.

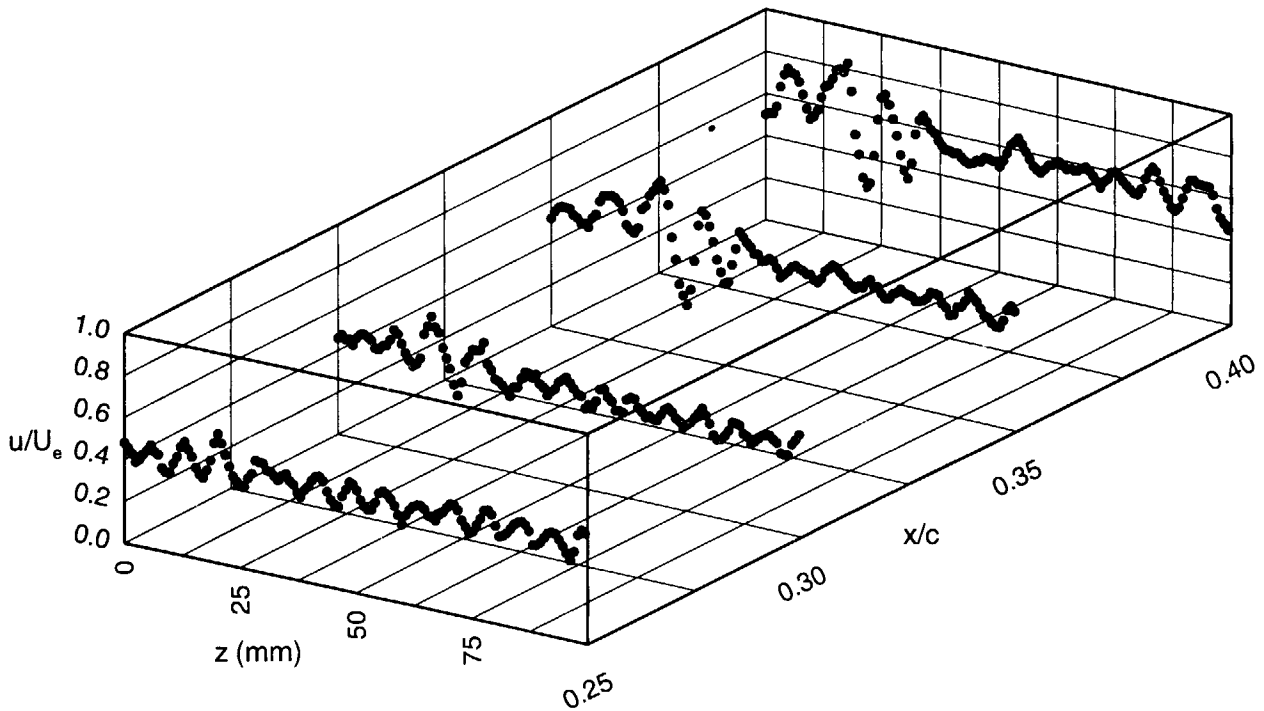

Figure 6.13. Spanwise hot-wire scans showing streamwise vortex growth. Constant-y scans at $\bar{u}/U_e = 0.5$. A single roughness element with $D = 0.37$ mm, $H = 6$ μm is at $x/c = 0.023$. $Re_c = 2.6 \times 10^6$, $\alpha = -4°$.

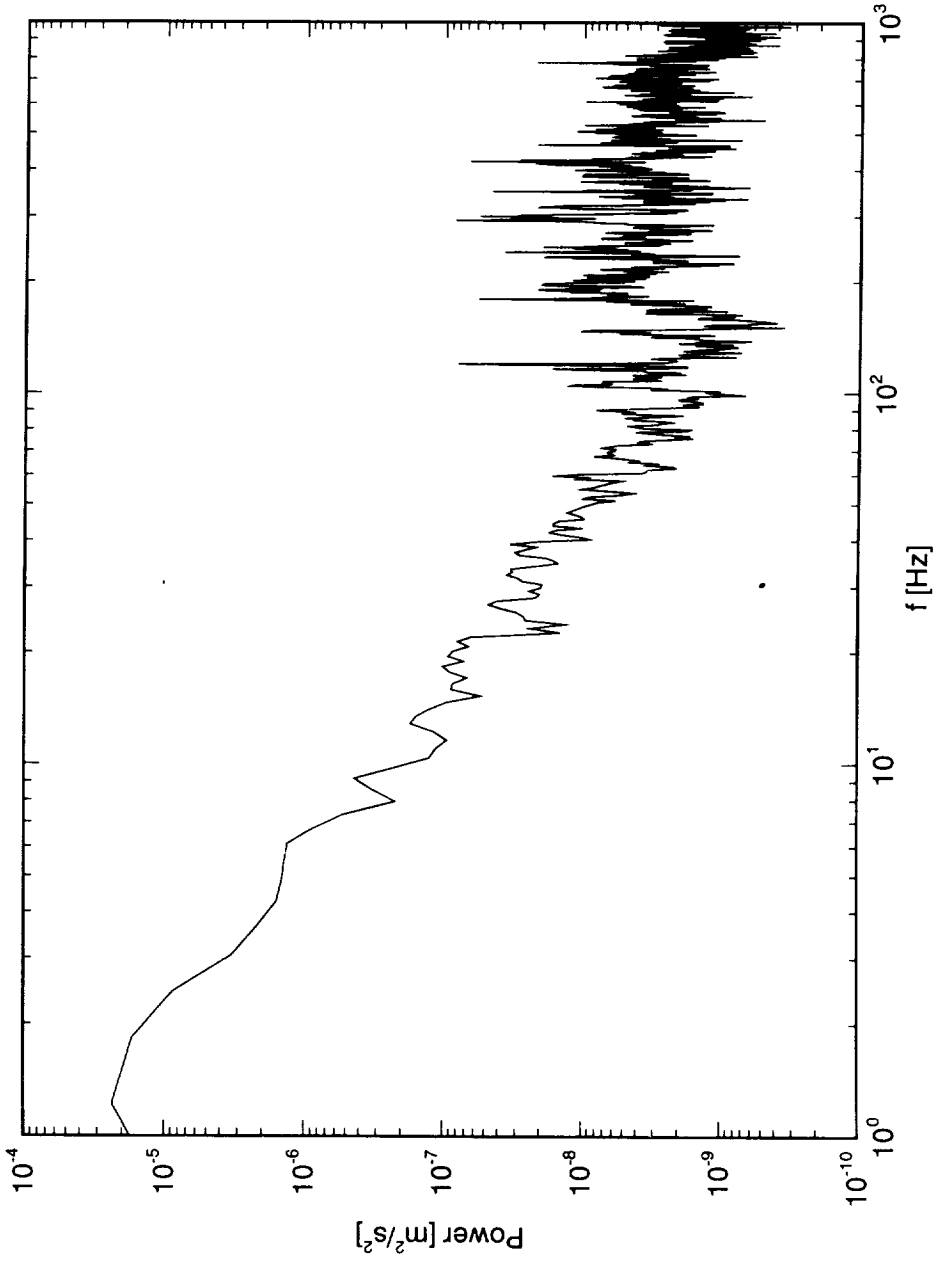

Figure 7.1. Freestream turbulence measurement (U' component). Filter pass band is 1–1000 Hz. $U_\infty = 18$ m/s.

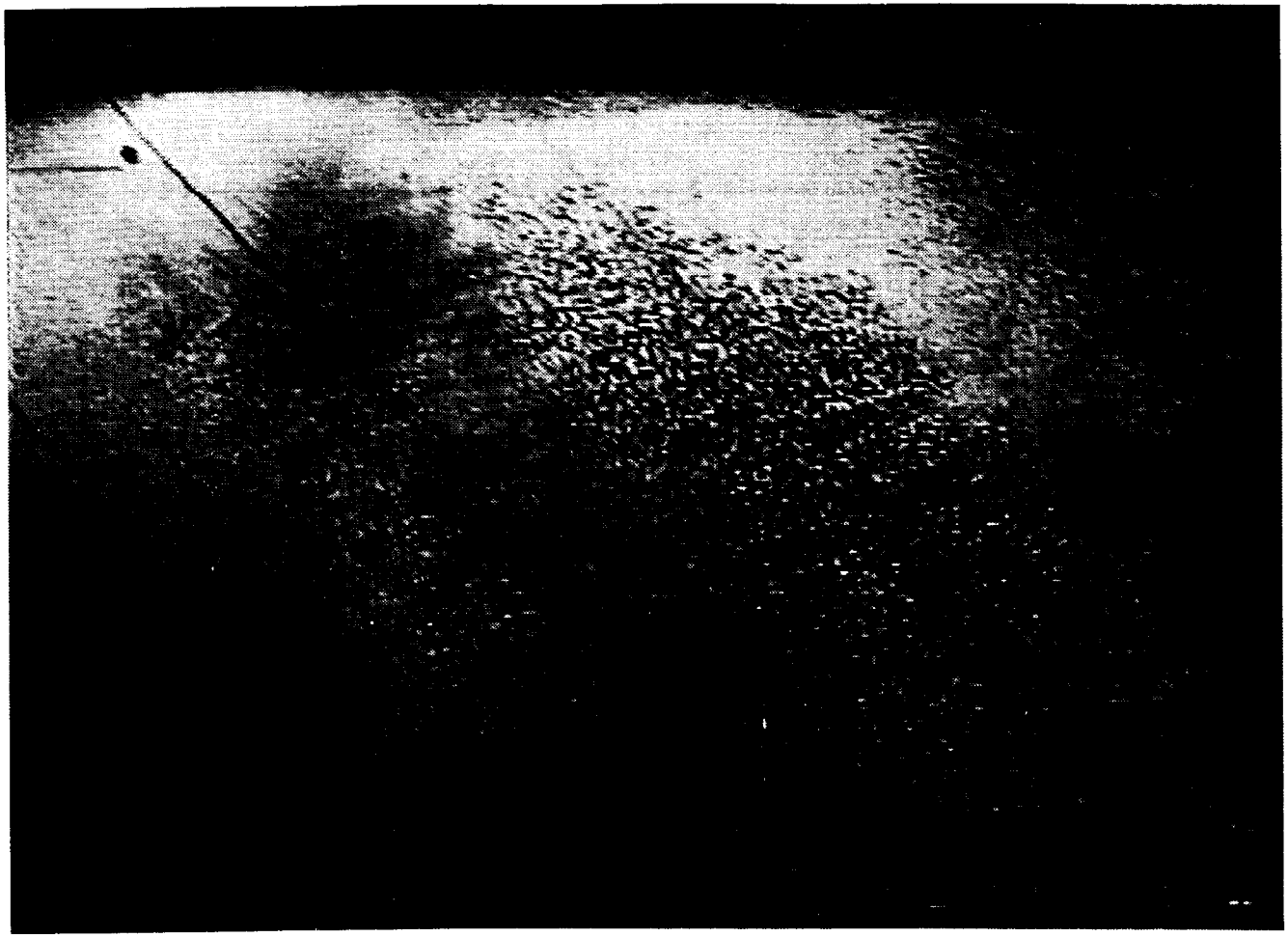

Figure 7.2. Naphthalene flow-visualization photograph showing very weak stationary vortex tracks. $Re_c = 3.6 \times 10^6$. 146 μm roughness with 10 mm spacing at $x/c = 0.005$.

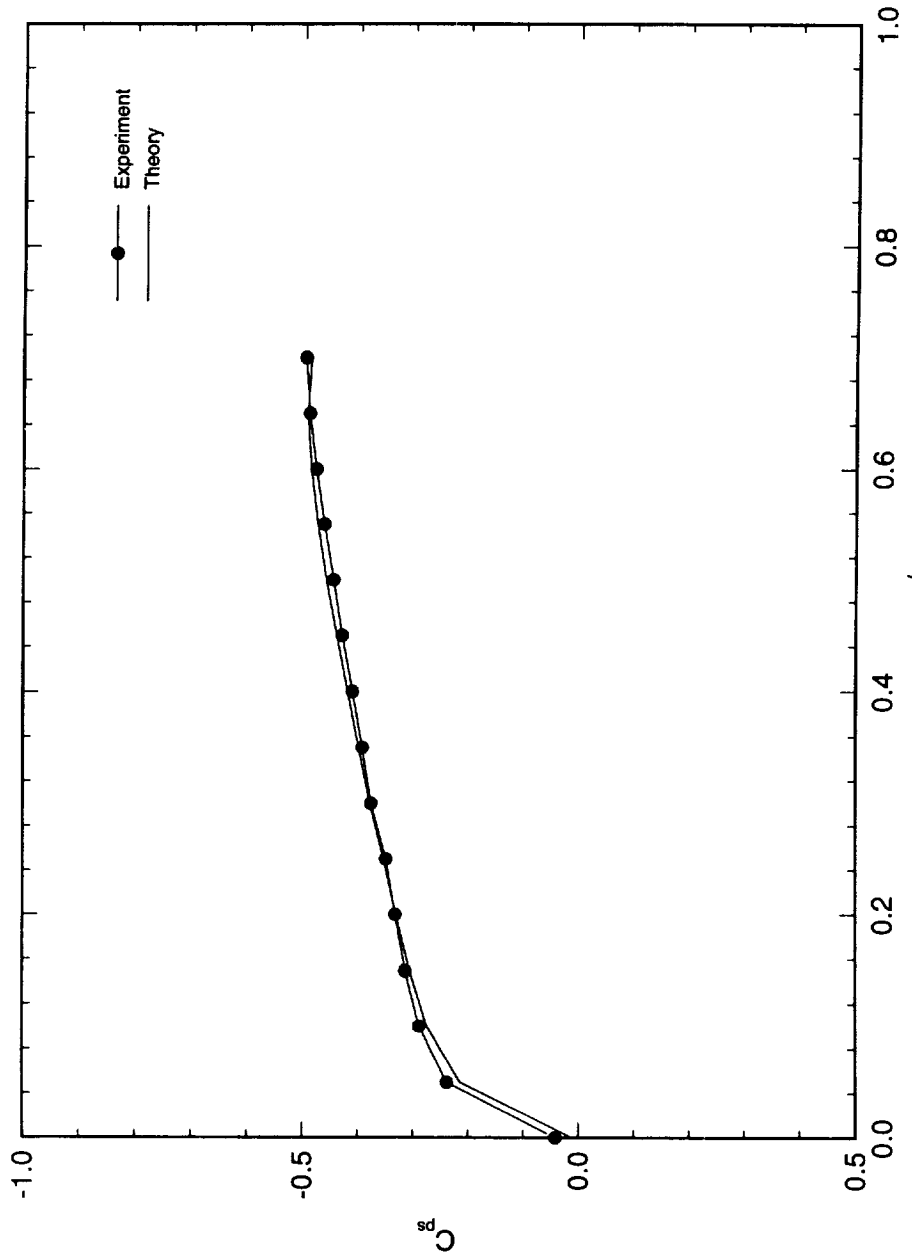

Figure 7.3. Comparison of experimental and theoretical pressure coefficients. Data from near-wing hot-wire scan with $U_\infty = 30$ m/s.

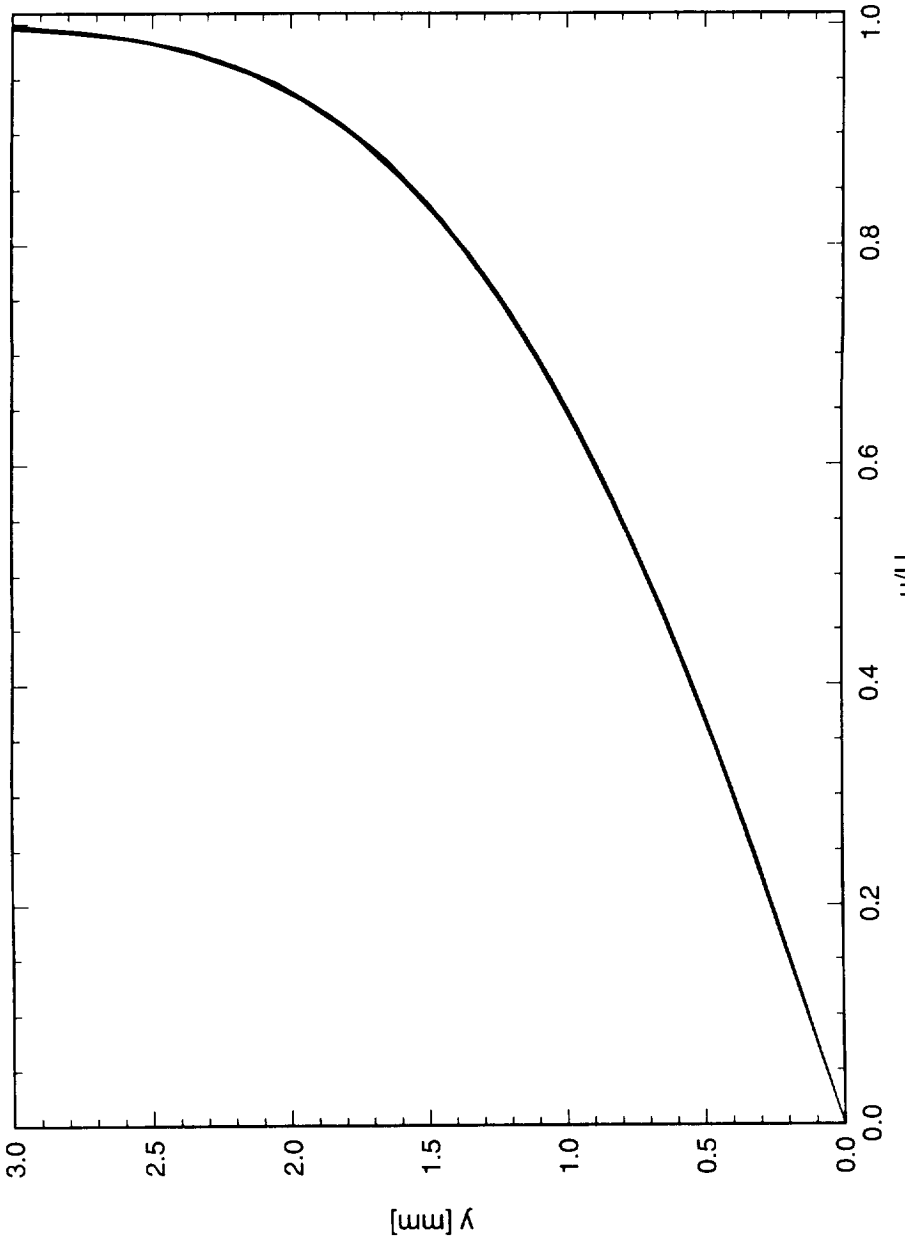

Figure 7.4. Spanwise array of boundary-layer scans at $x/c = 0.6$. No roughness on airfoil. $Re_c = 3.2 \times 10^6$.

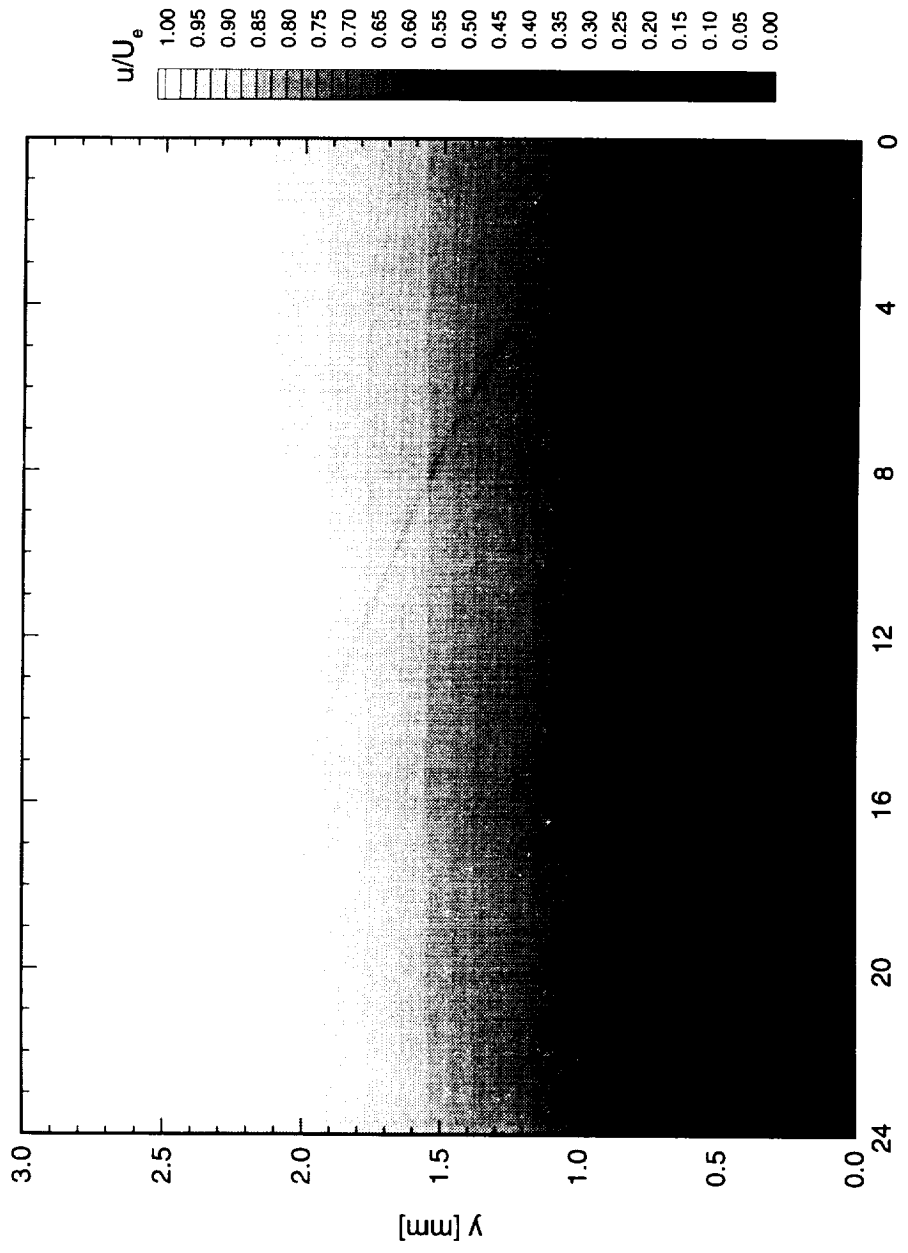

Figure 7.5. Velocity contours for boundary-layer scans at $x/c = 0.6$. No roughness on airfoil. $Re_c = 3.2 \times 10^6$.

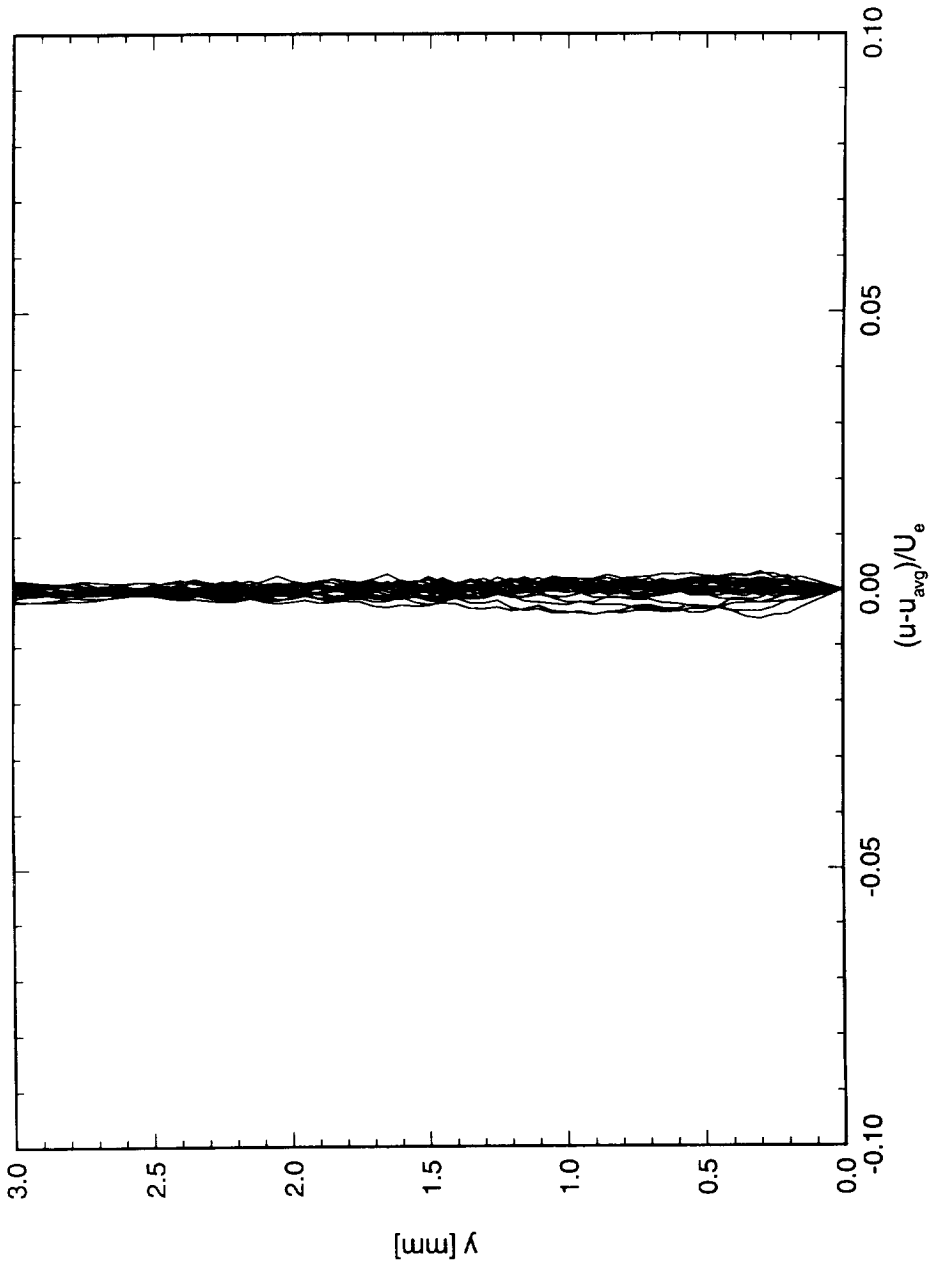

Figure 7.6. Disturbance profiles for boundary-layer scans at $x/c = 0.6$. No roughness on airfoil. $Re_c = 3.2 \times 10^6$.

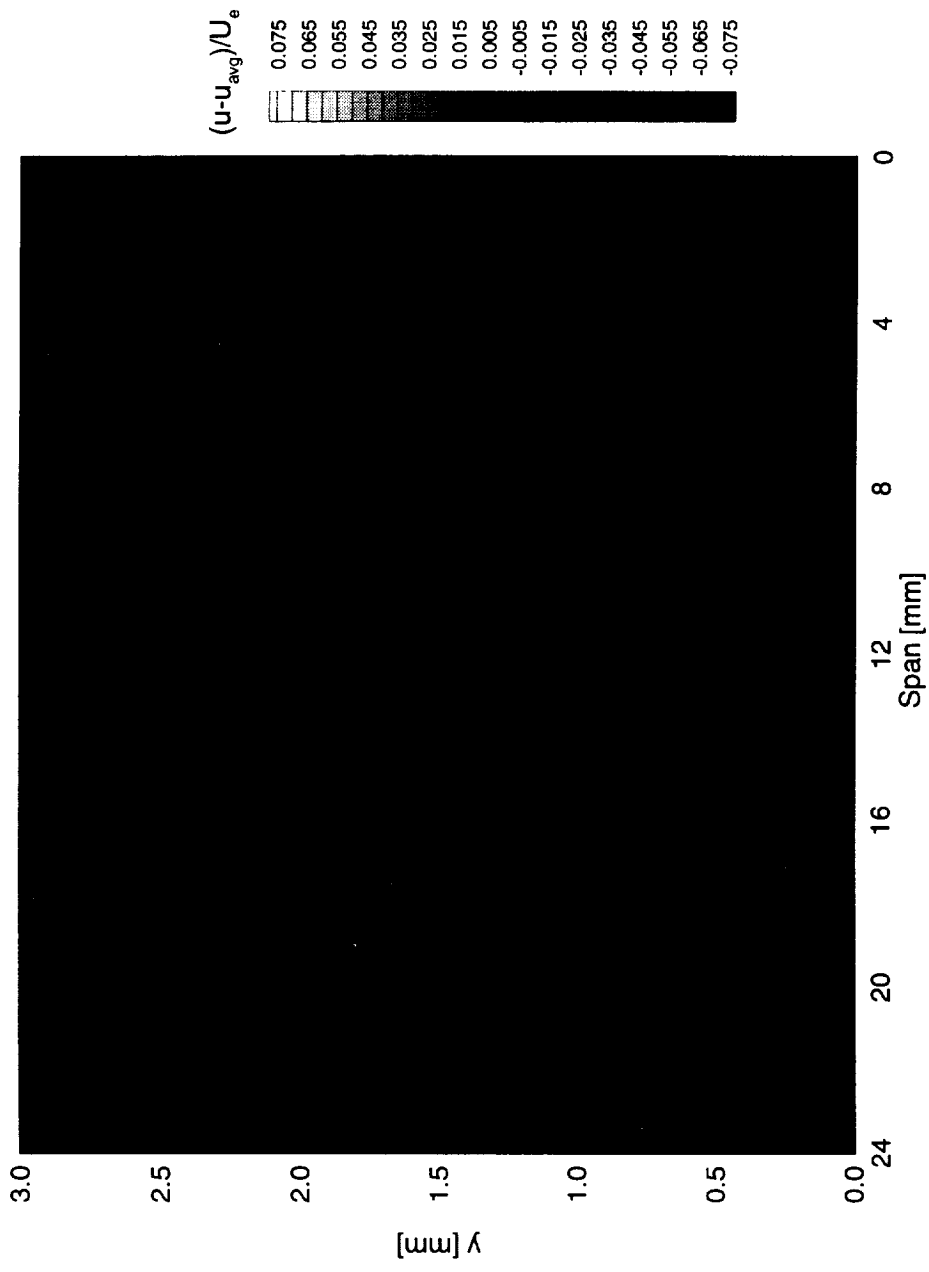

Figure 7.7. Disturbance contours for boundary-layer scans at $x/c = 0.6$. No roughness on airfoil. $Re_c = 3.2 \times 10^6$.

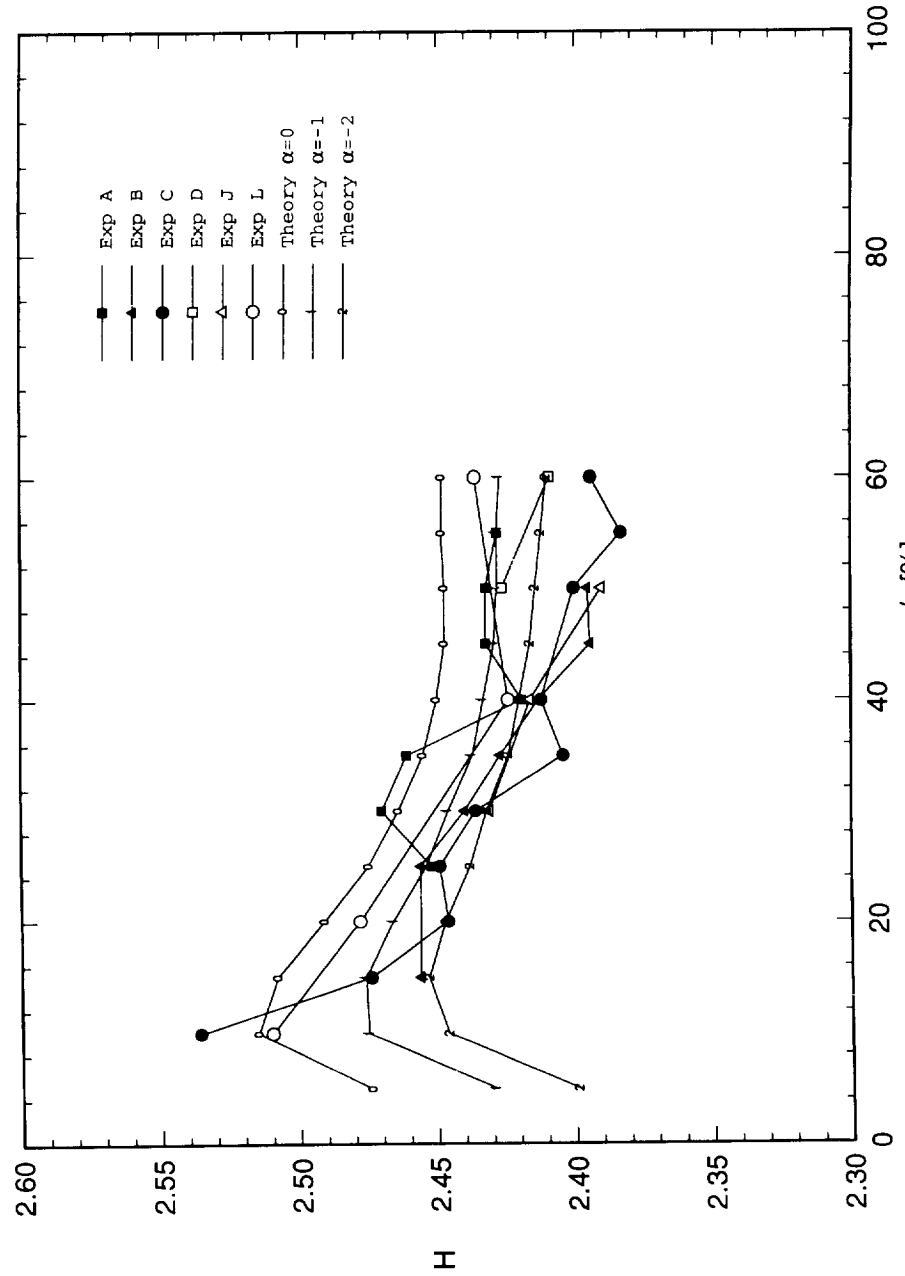

Figure 7.8. Shape factor comparison showing slight flow misalignment. Experimental data are spanwise-averaged.

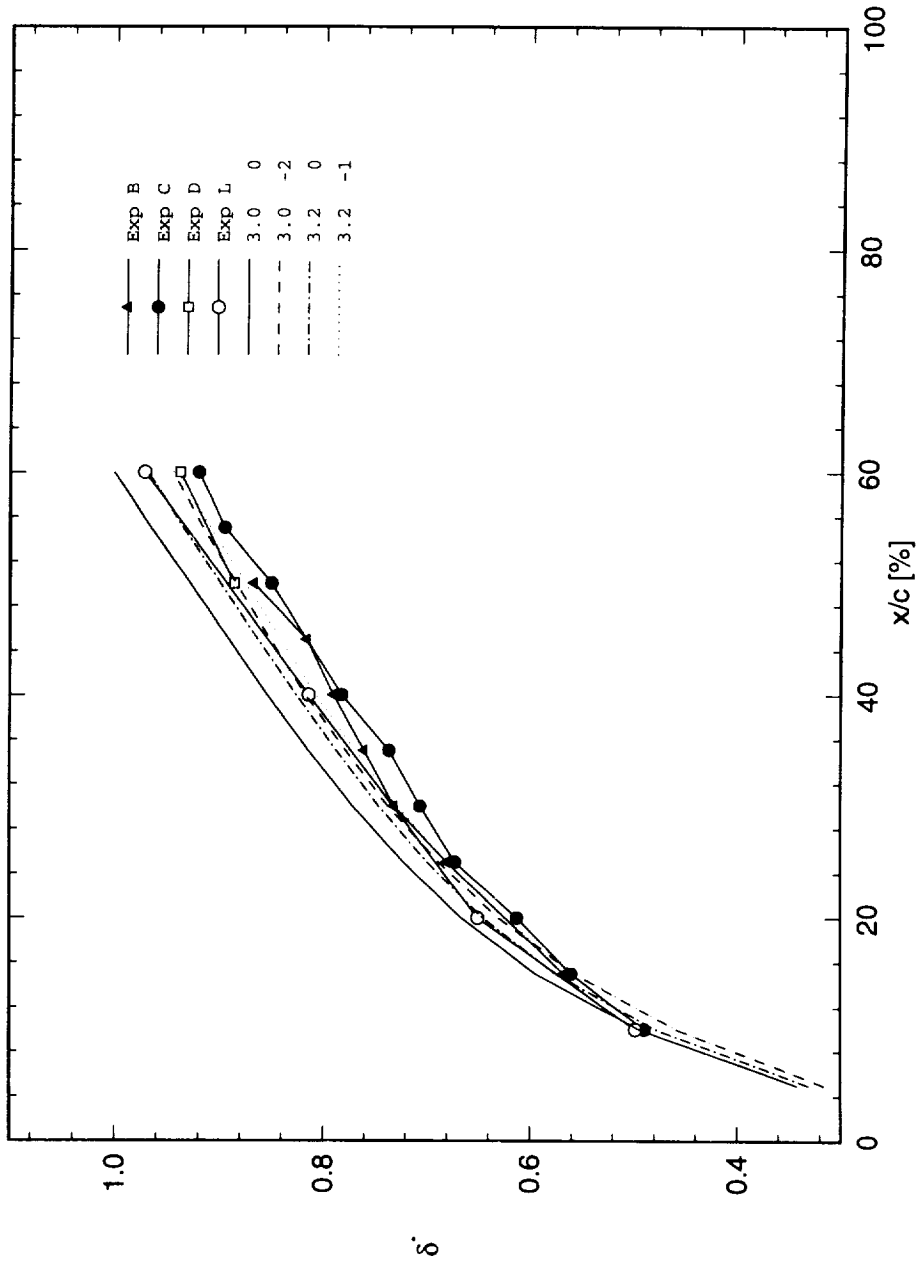

Figure 7.9. Displacement thickness comparison between experimental boundary-layer measurements and theoretical basic state. Experimental data are spanwise-averaged. Numbers in key denote Re_c in millions and α.

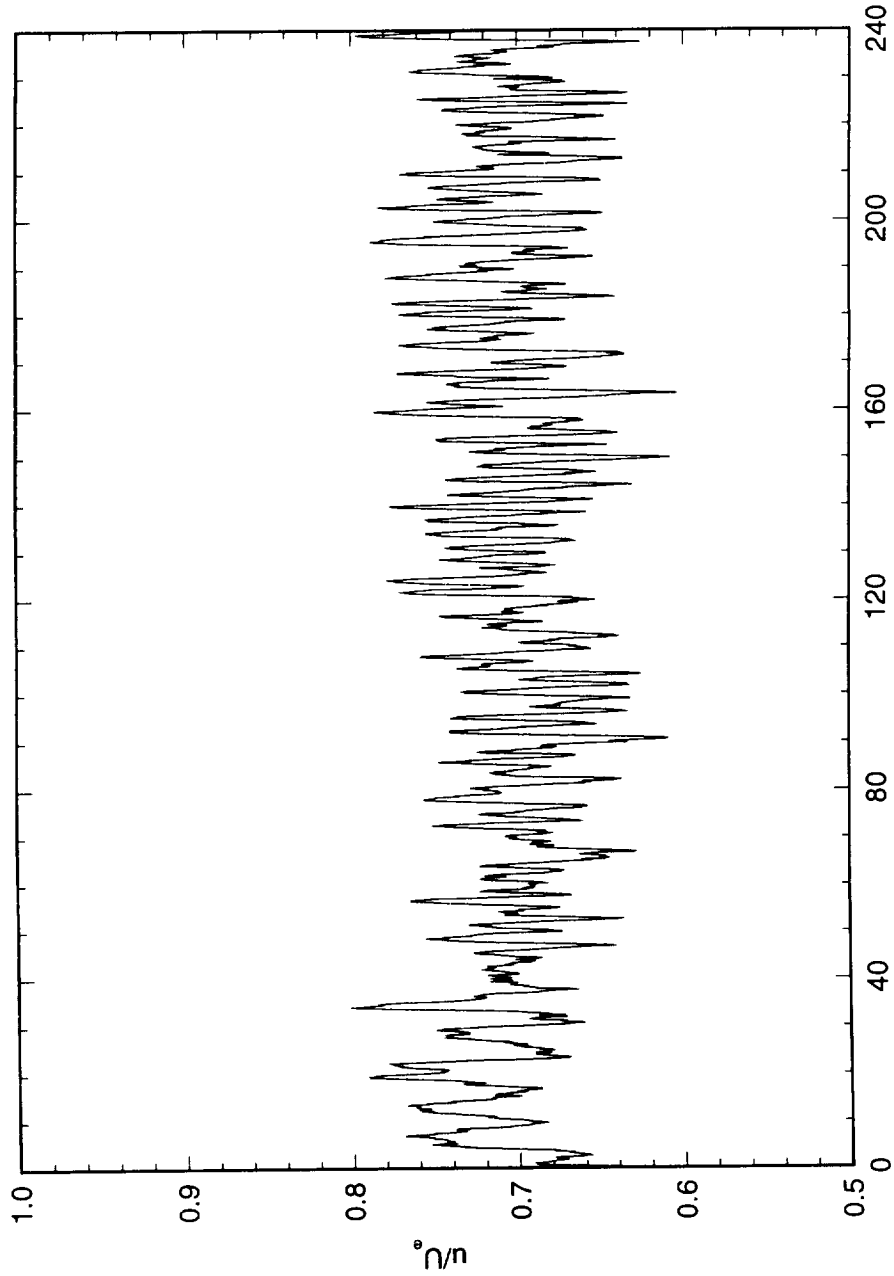

Figure 7.10. Spanwise hot-wire scan at $x/c = 0.05$. No roughness on airfoil. $Re_c = 3.0 \times 10^6$.

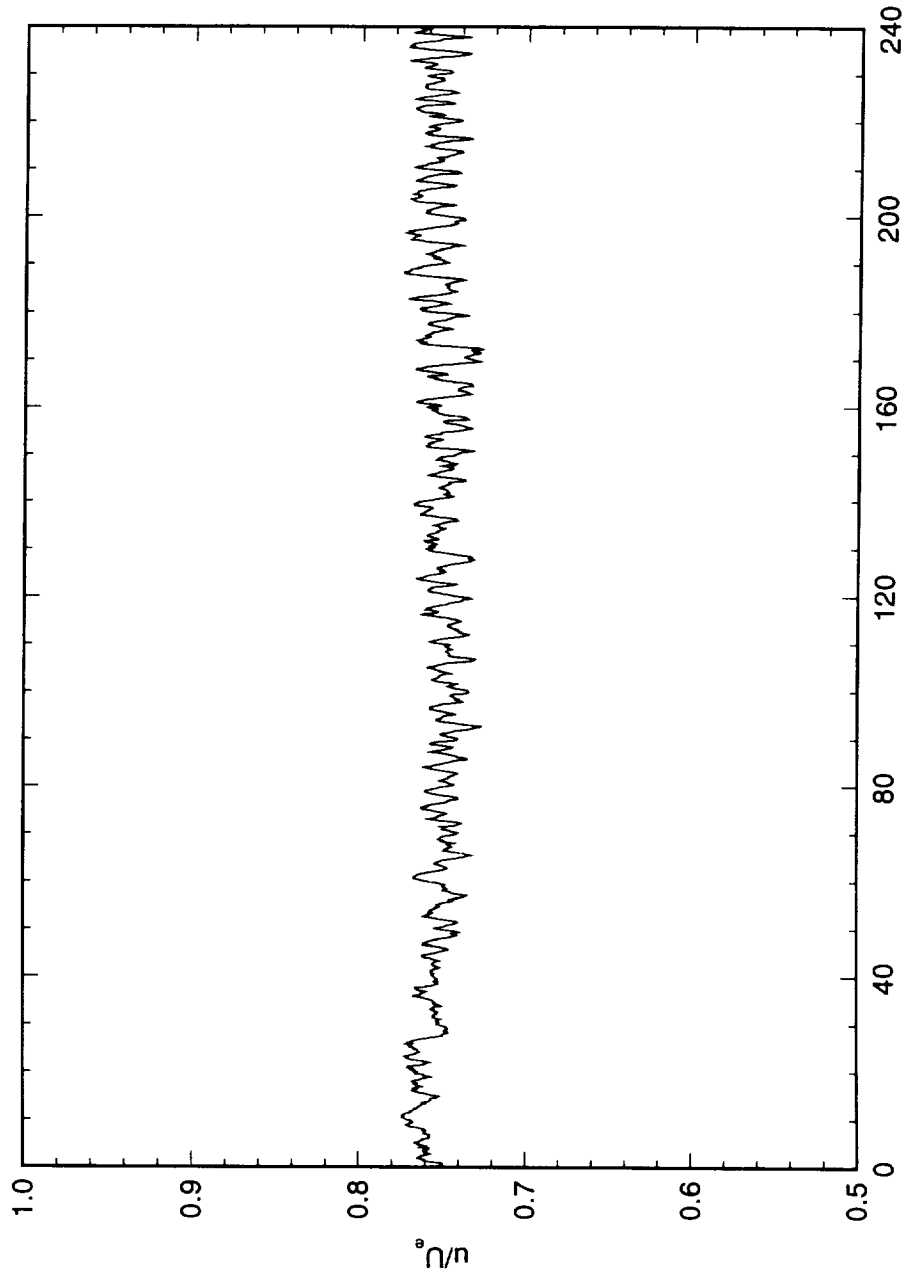

Figure 7.11. Spanwise hot-wire scan at $x/c = 0.20$. No roughness on airfoil. $Re_c = 3.0 \times 10^6$.

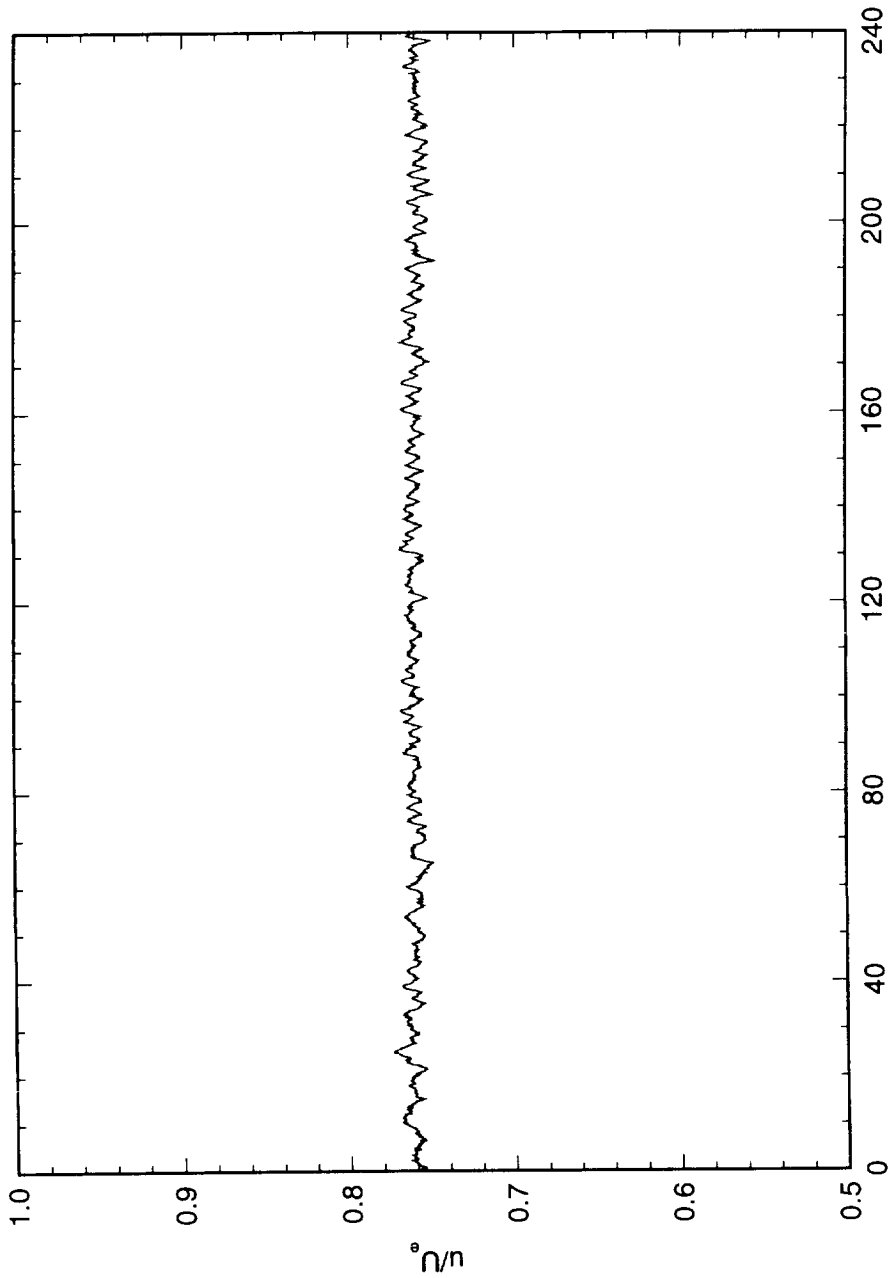

Figure 7.12. Spanwise hot-wire scan at $x/c = 0.40$. No roughness on airfoil. $Re_c = 3.0 \times 10^6$.

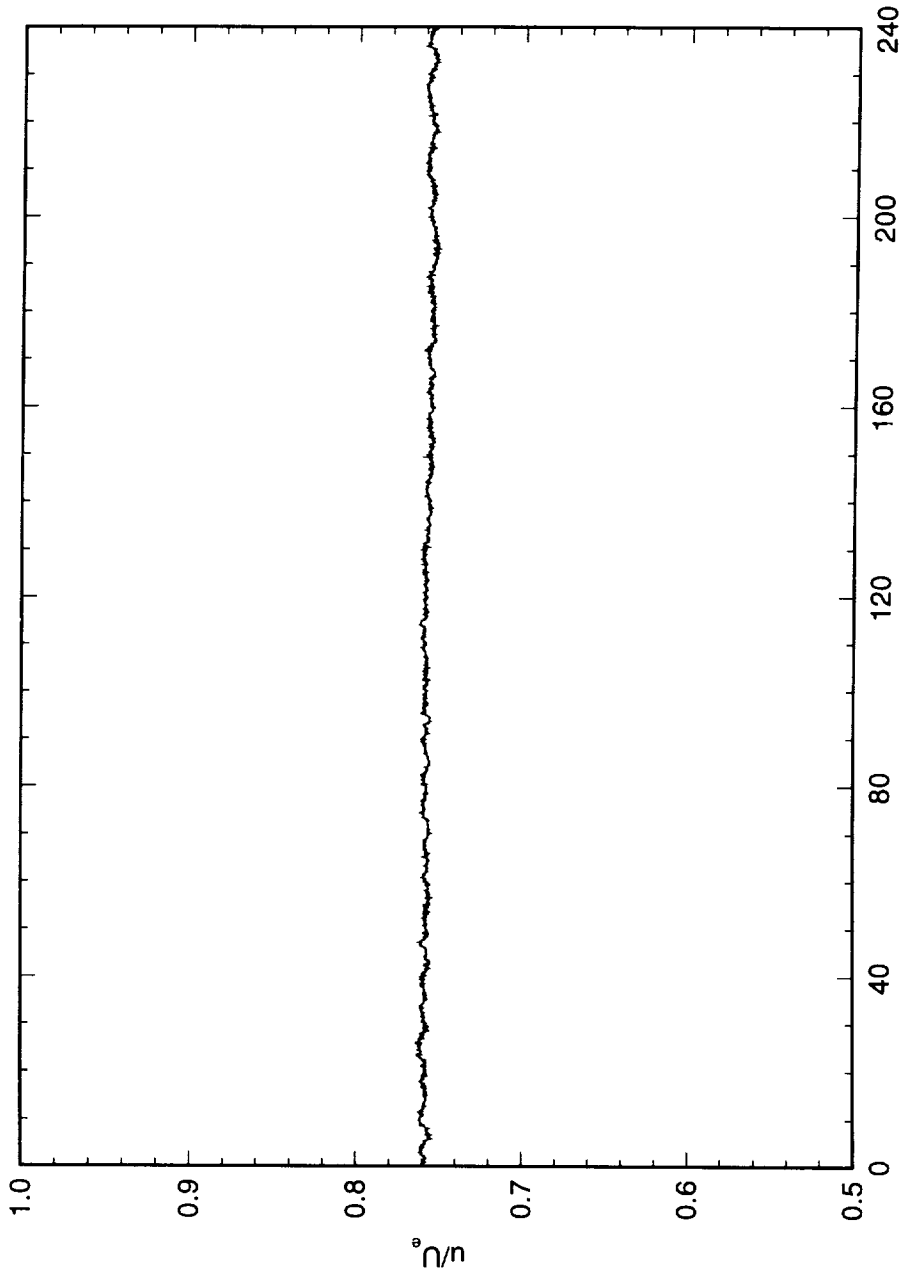

Figure 7.13. Spanwise hot-wire scan at $x/c = 0.60$. No roughness on airfoil. $Re_c = 3.0 \times 10^6$.

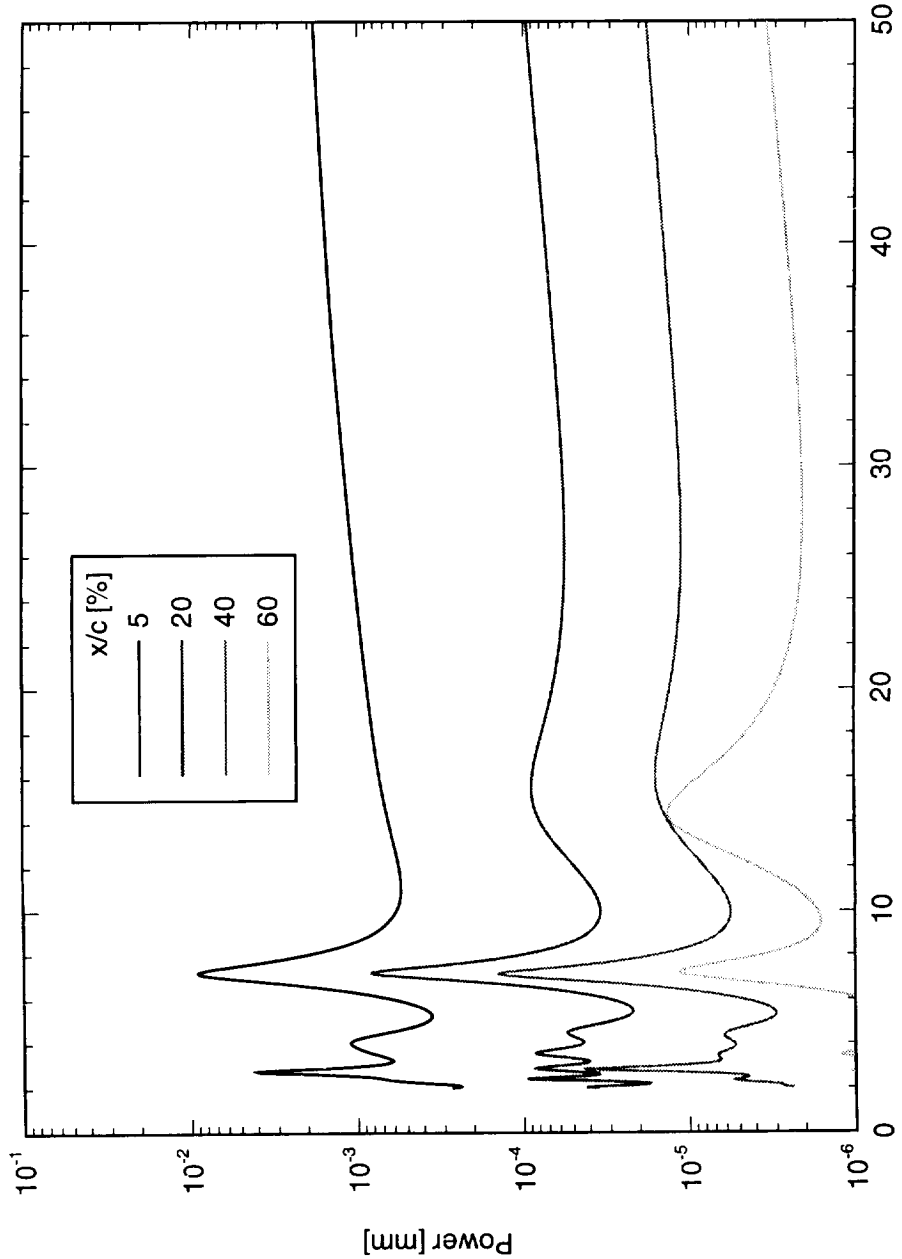

Figure 7.14. Maximum-entropy power spectra of spanwise scans with no roughness. Traverse contamination peak is near 7.2 mm.

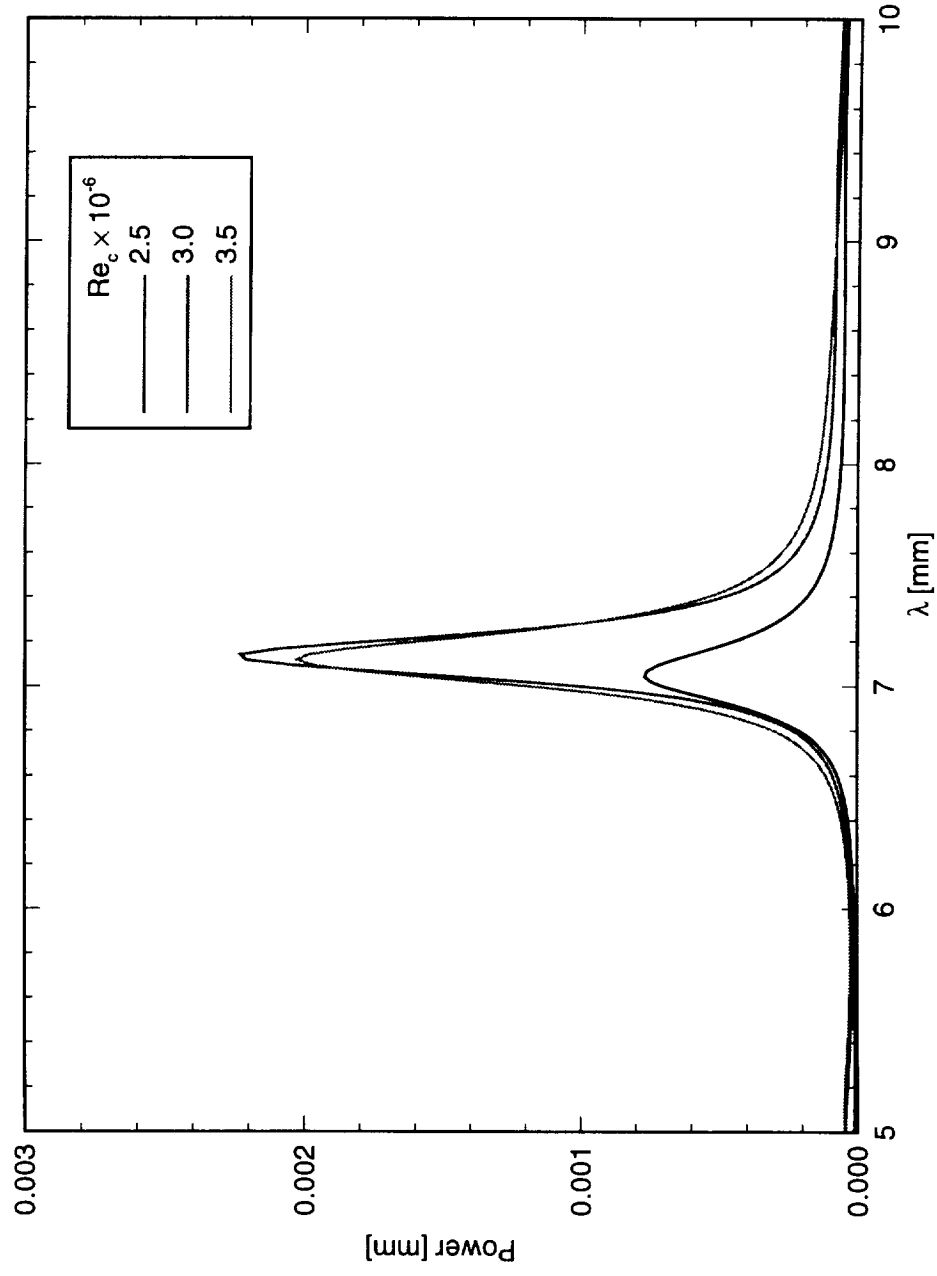

Figure 7.15. Maximum-entropy power spectra of spanwise scans with no roughness. $x/c = 0.2$.

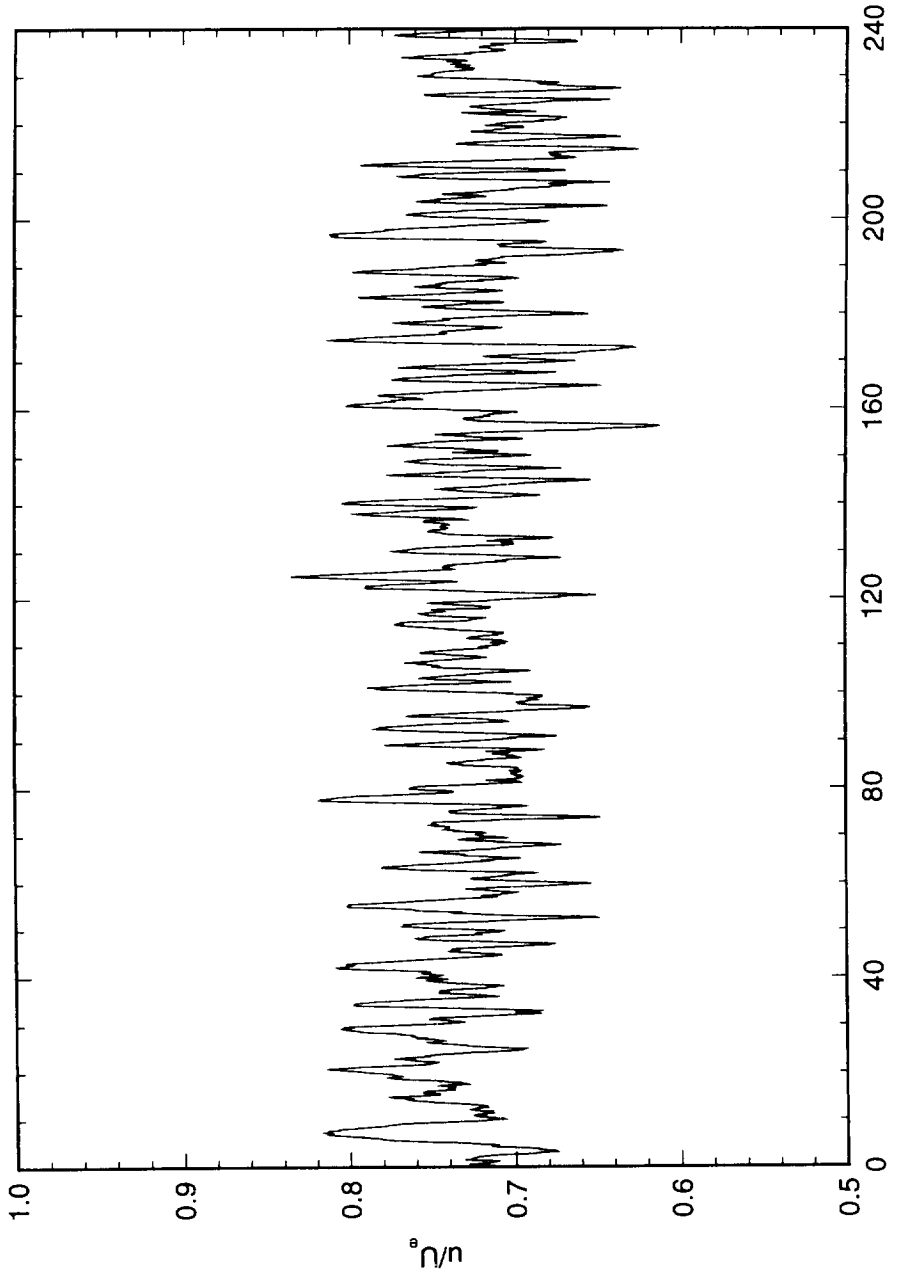

Figure 7.16. Spanwise hot-wire scan at $x/c = 0.05$. $Re_c = 3.0 \times 10^6$. Full array of 73 μm roughness with 12 mm spacing. Data set E.

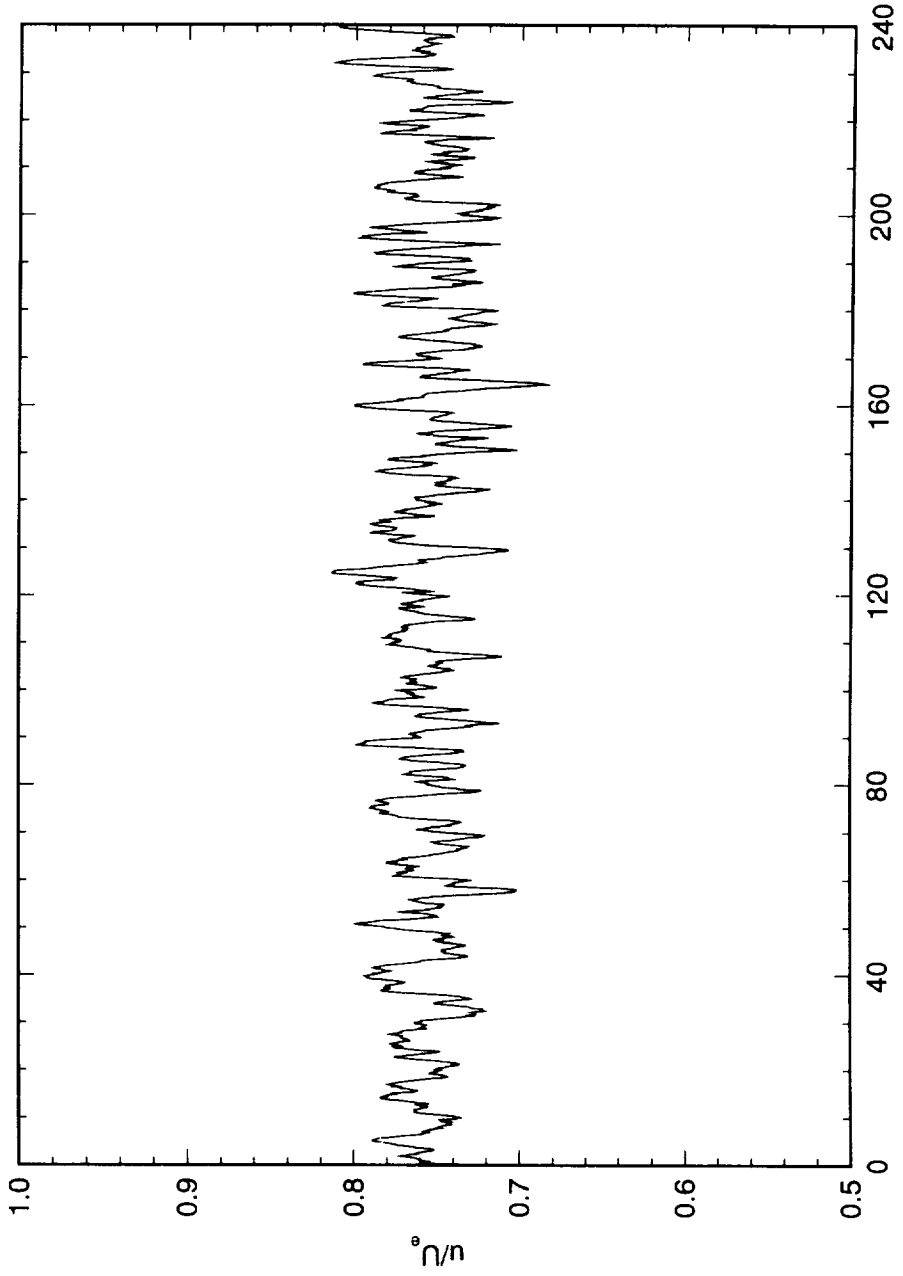

Figure 7.17. Spanwise hot-wire scan at $x/c = 0.10$. $Re_c = 3.0 \times 10^6$. Full array of 73 μm roughness with 12 mm spacing. Data set E.

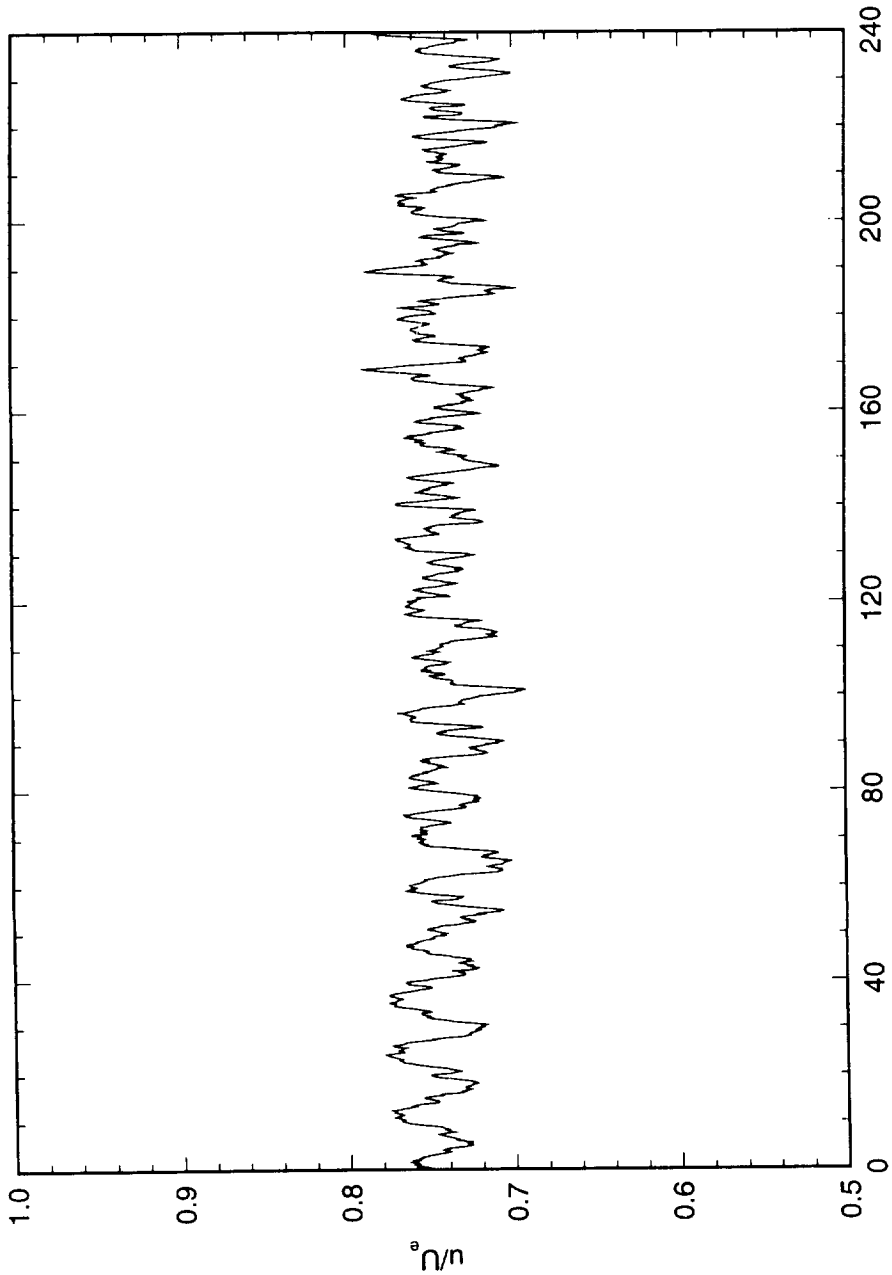

Figure 7.18. Spanwise hot-wire scan at $x/c = 0.15$. $Re_c = 3.0 \times 10^6$. Full array of 73 μm roughness with 12 mm spacing. Data set E.

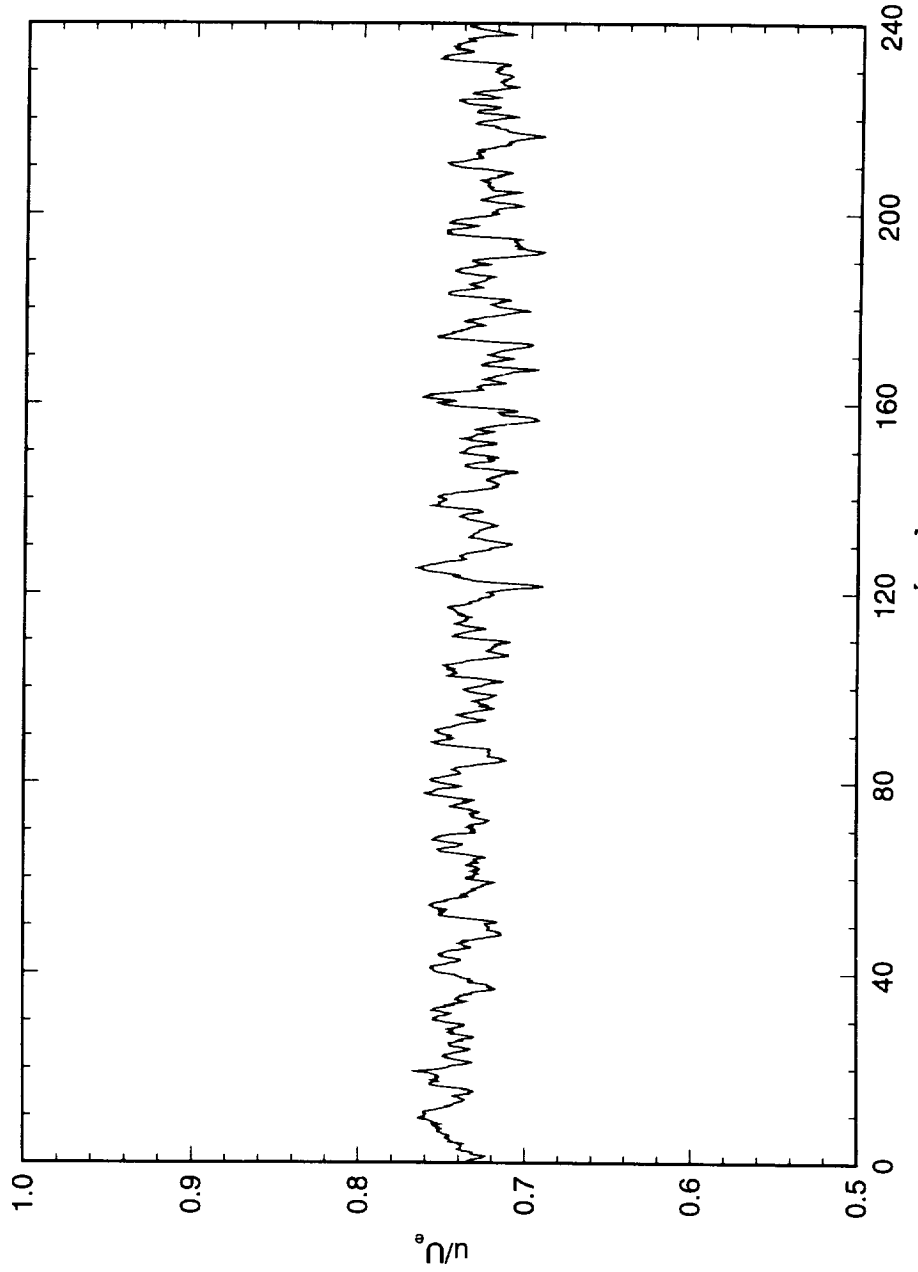

Figure 7.19. Spanwise hot-wire scan at $x/c = 0.20$. $Re_c = 3.0 \times 10^6$. Full array of 73 μm roughness with 12 mm spacing. Data set E.

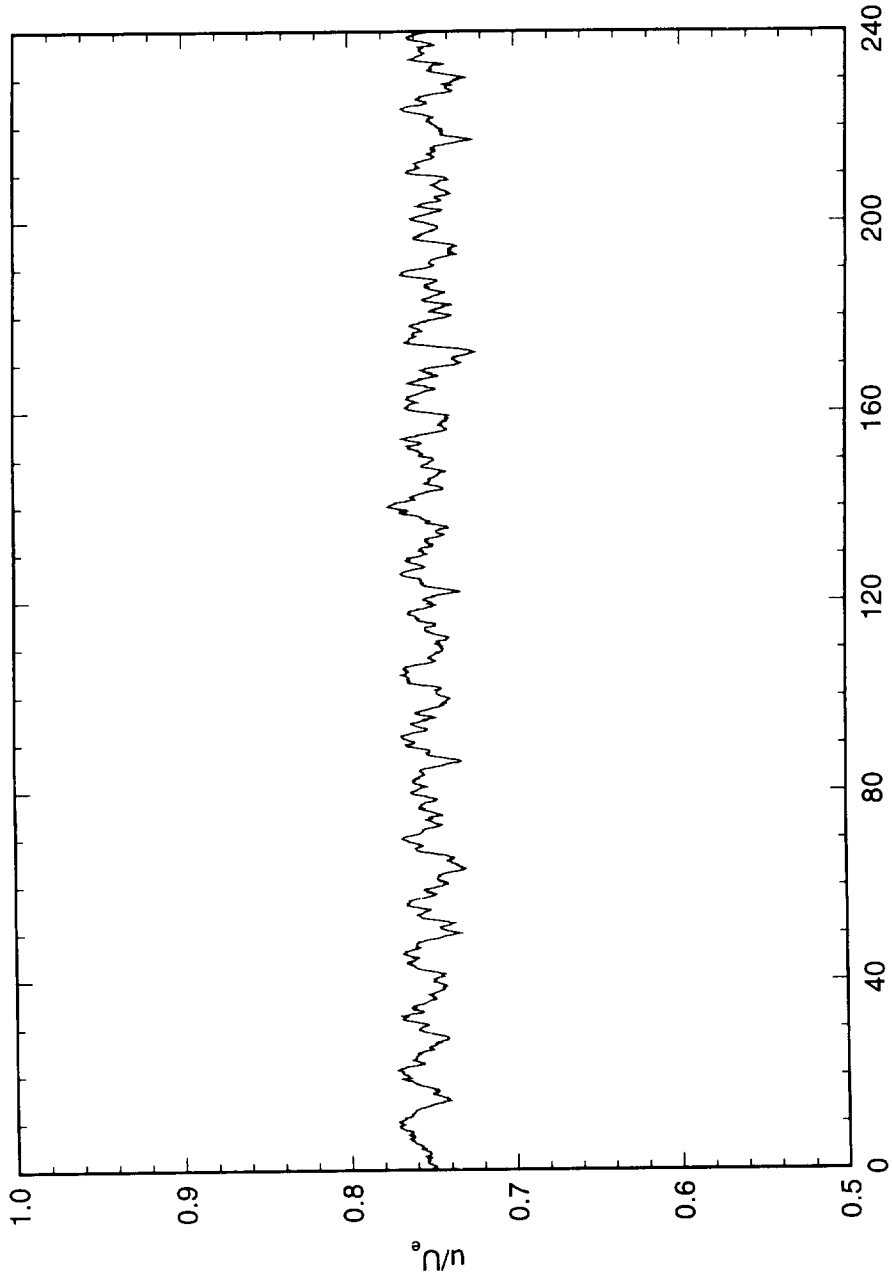

Figure 7.20. Spanwise hot-wire scan at $x/c = 0.30$. $Re_c = 3.0 \times 10^6$. Full array of 73 μm roughness with 12 mm spacing. Data set E.

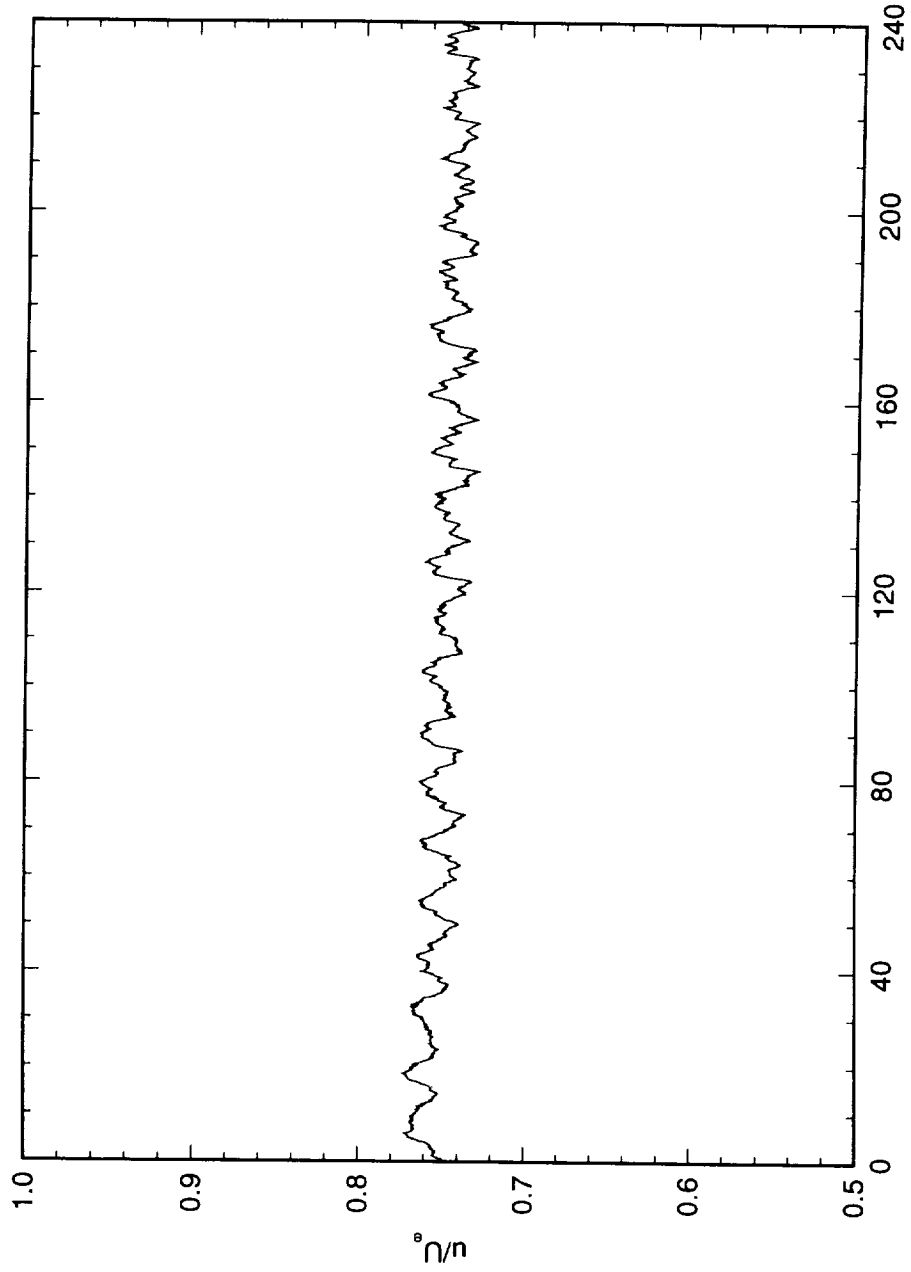

Figure 7.21. Spanwise hot-wire scan at $x/c = 0.40$. $Re_c = 3.0 \times 10^6$. Full array of 73 μm roughness with 12 mm spacing. Data set E.

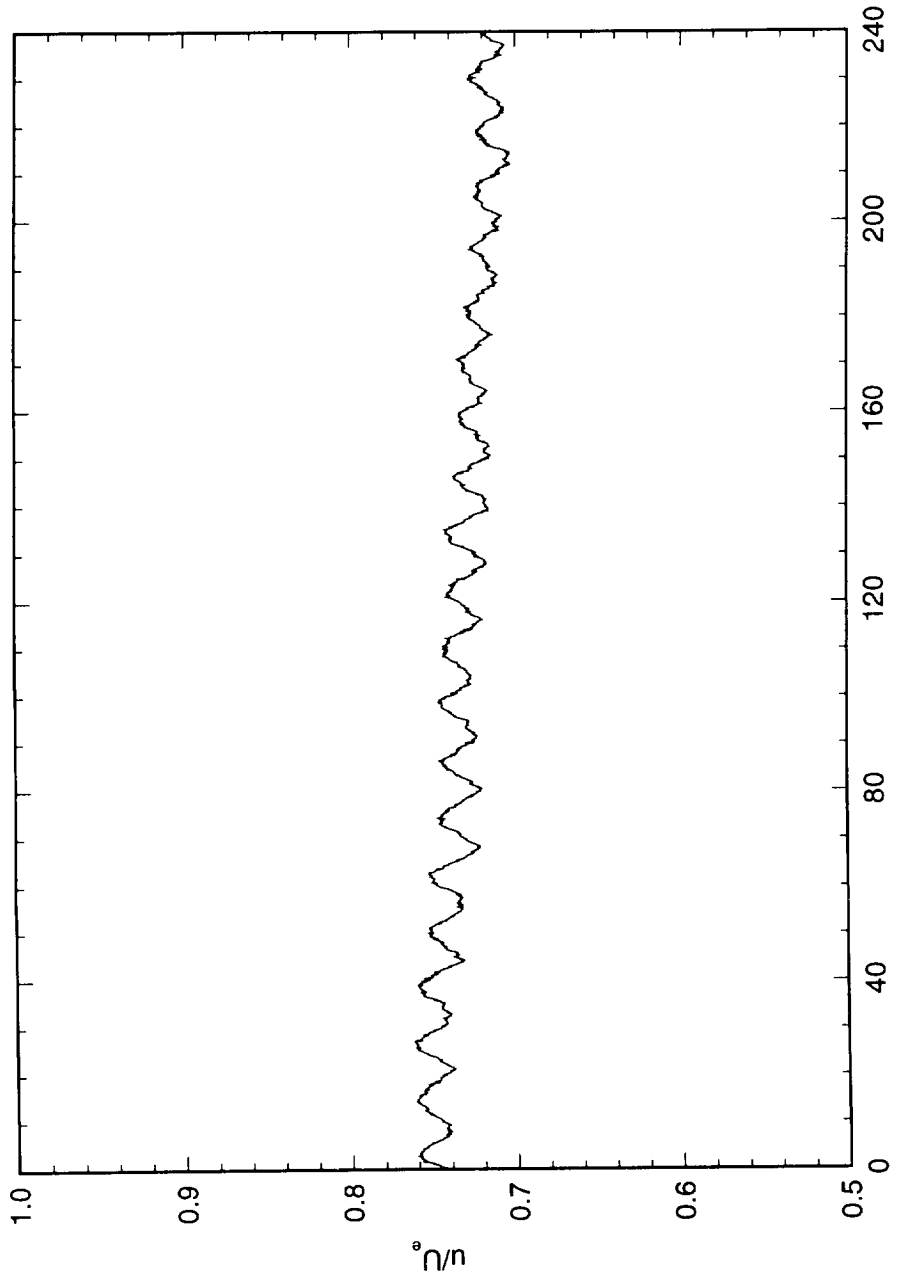

Figure 7.22. Spanwise hot-wire scan at $x/c = 0.50$. $Re_c = 3.0 \times 10^6$. Full array of 73 μm roughness with 12 mm spacing. Data set E.

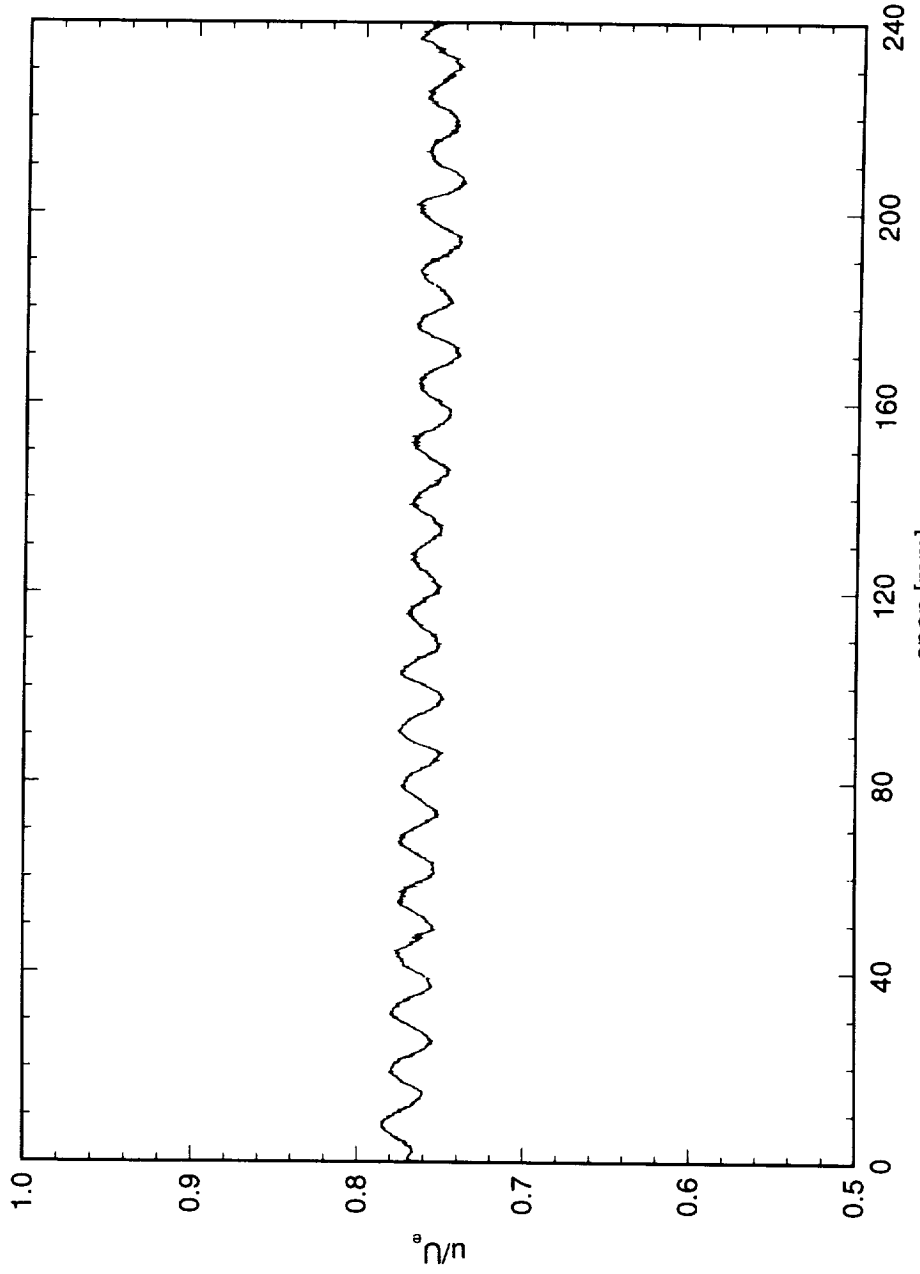

Figure 7.23. Spanwise hot-wire scan at $x/c = 0.60$. $Re_c = 3.0 \times 10^6$. Full array of 73 μm roughness with 12 mm spacing. Data set E.

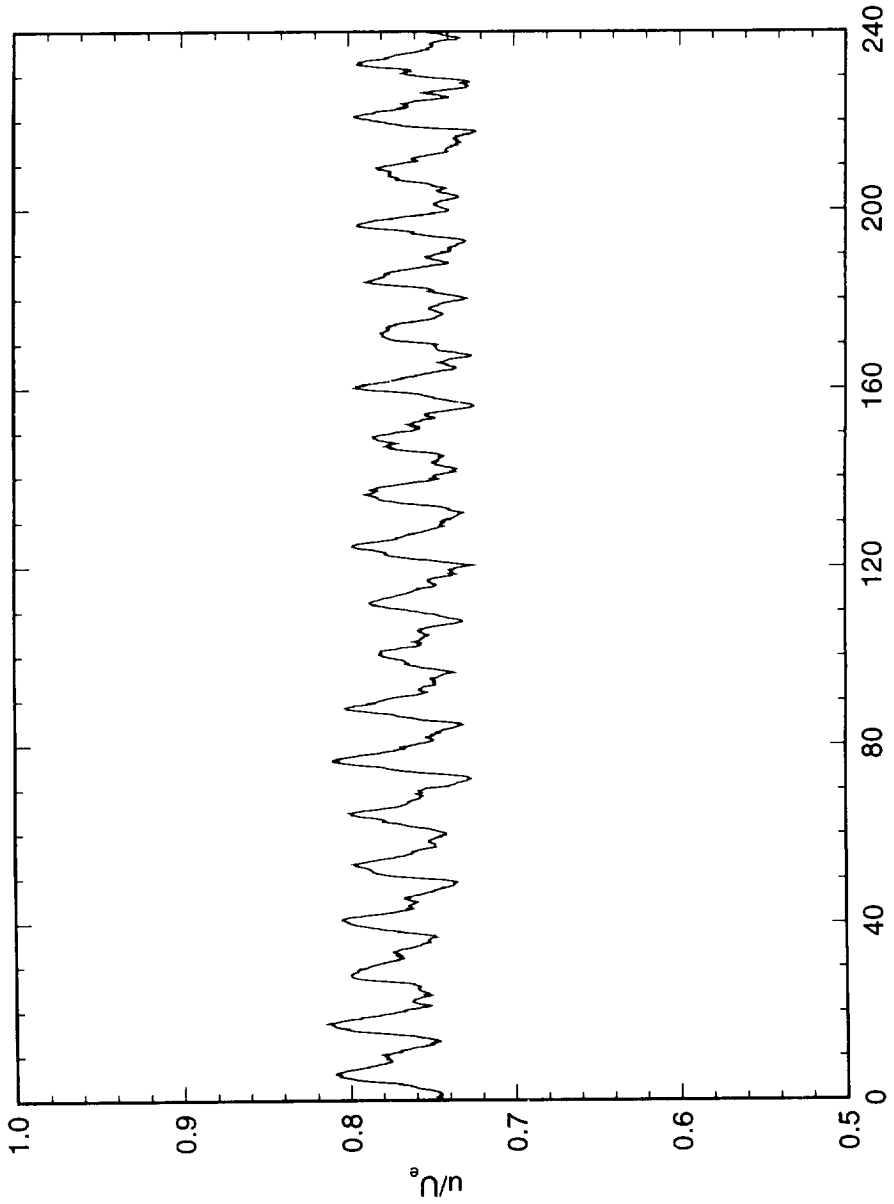

Figure 7.24. Spanwise hot-wire scan at $x/c = 0.30$. $Re_c = 3.0 \times 10^6$. Full array of 146 μm roughness with 12 mm spacing. Data set F.

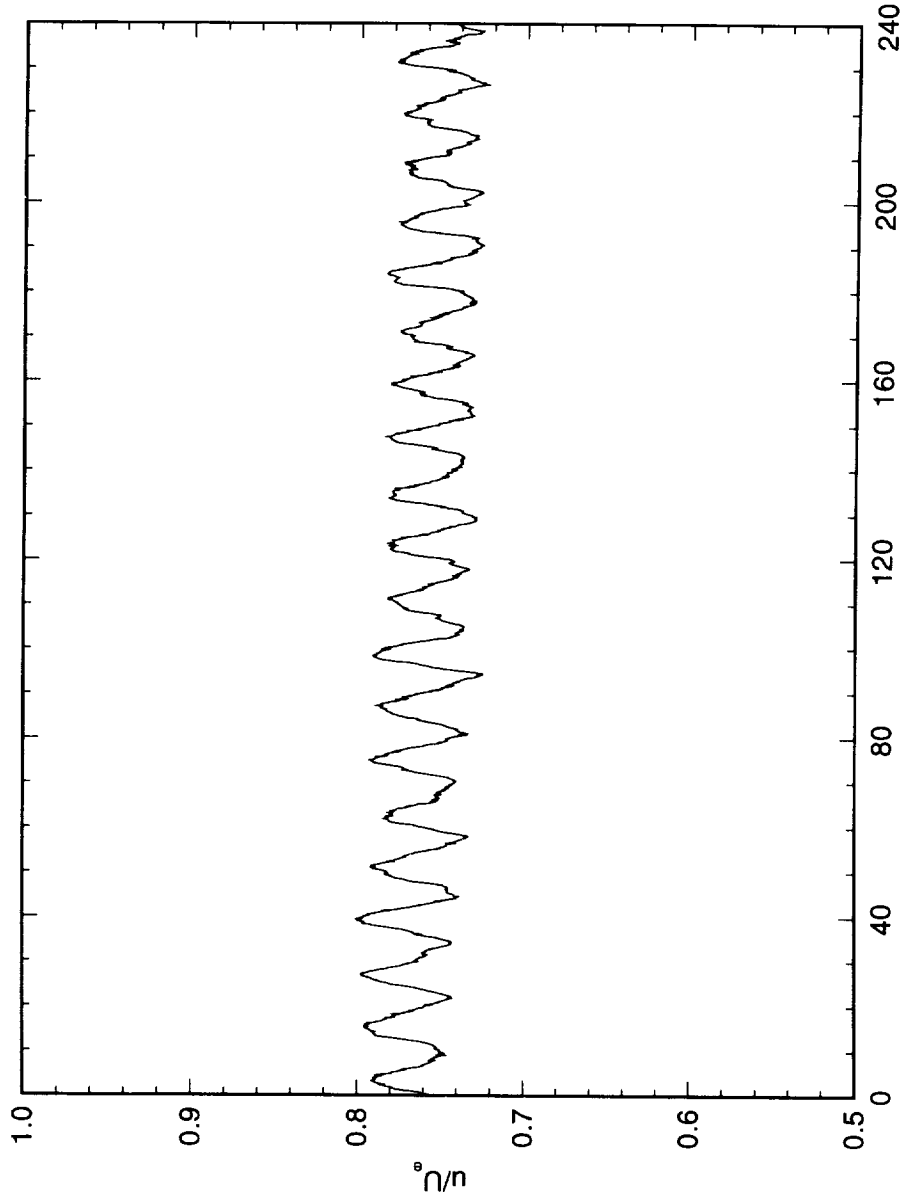

Figure 7.25. Spanwise hot-wire scan at $x/c = 0.40$. $Re_c = 3.0 \times 10^6$. Full array of 146 μm roughness with 12 mm spacing. Data set F.

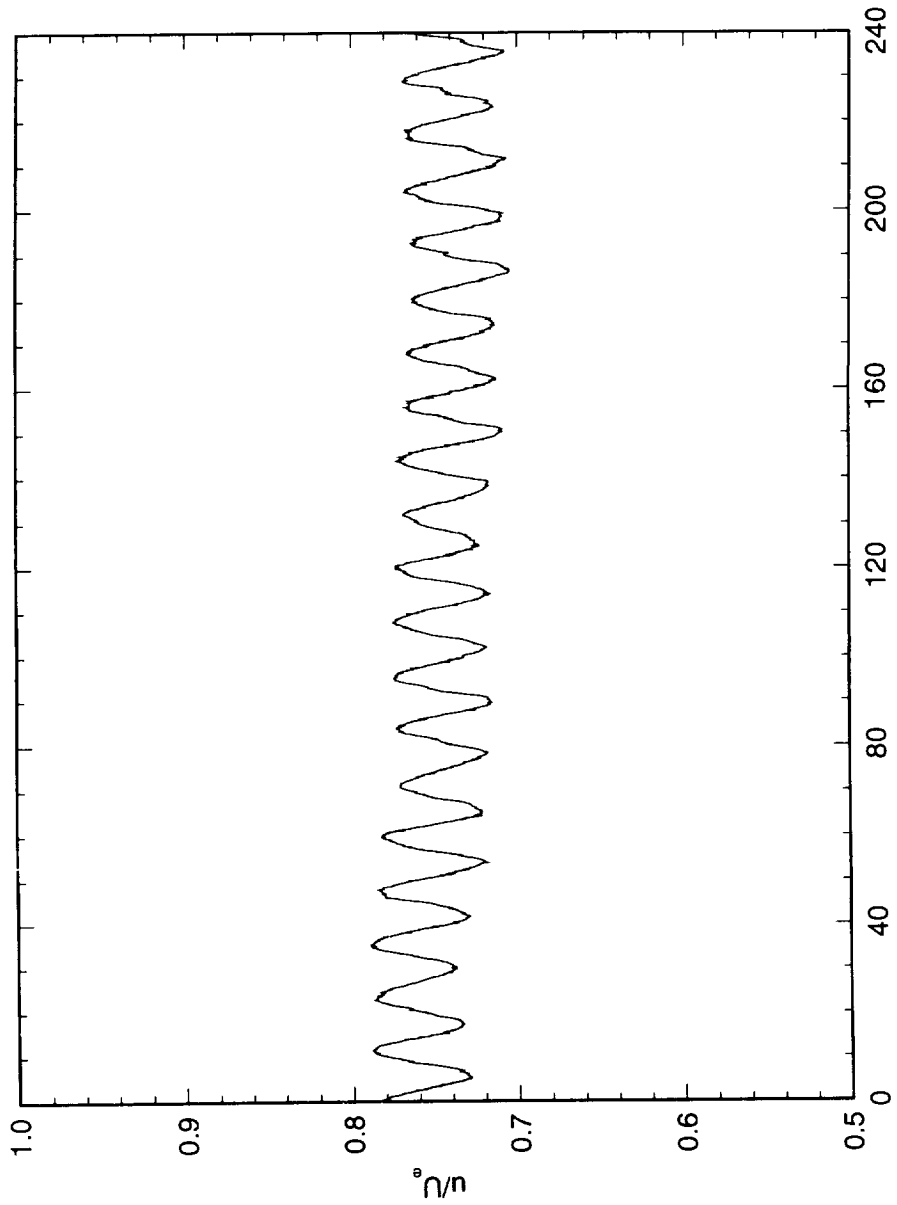

Figure 7.26. Spanwise hot-wire scan at $x/c = 0.50$. $Re_c = 3.0 \times 10^6$. Full array of 146 μm roughness with 12 mm spacing. Data set F.

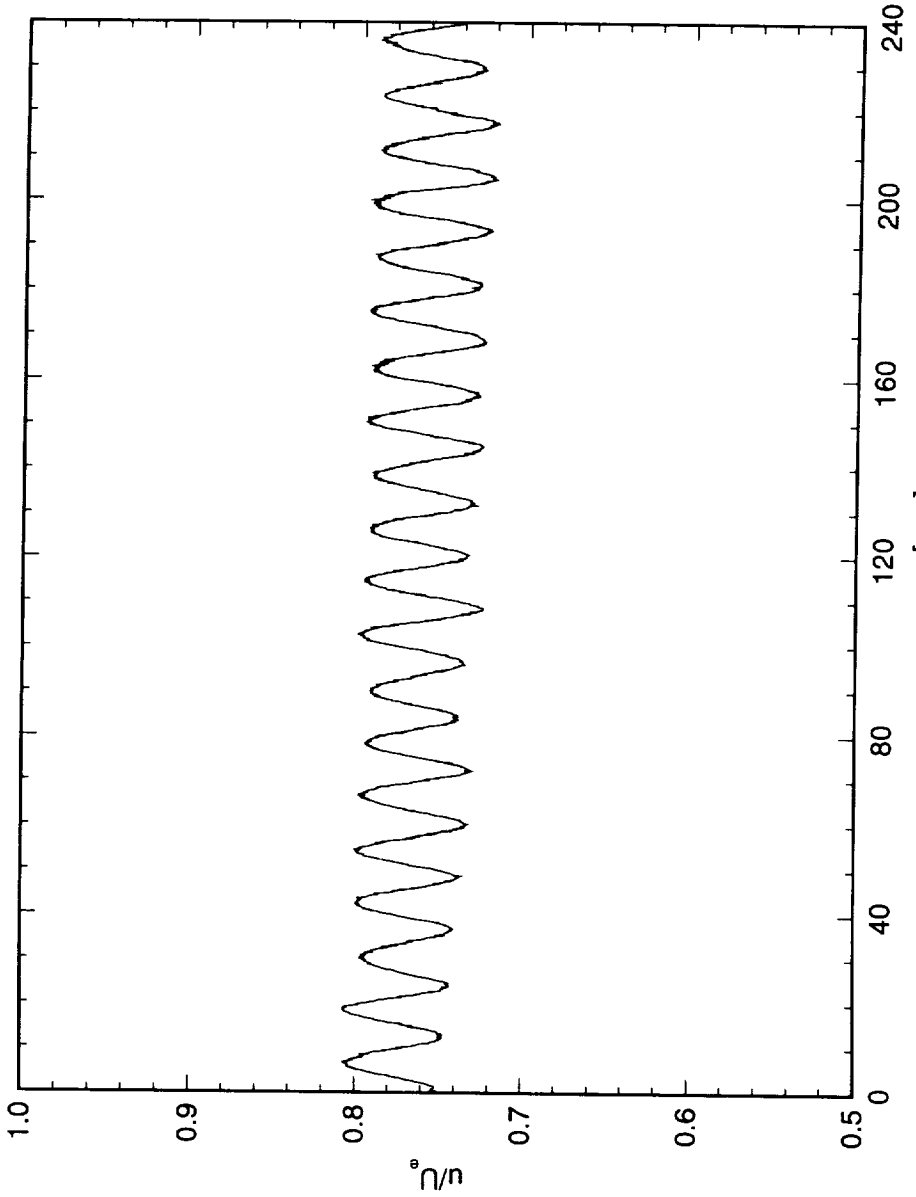

Figure 7.27. Spanwise hot-wire scan at $x/c = 0.60$. $Re_c = 3.0 \times 10^6$. Full array of 146 μm roughness with 12 mm spacing. Data set F.

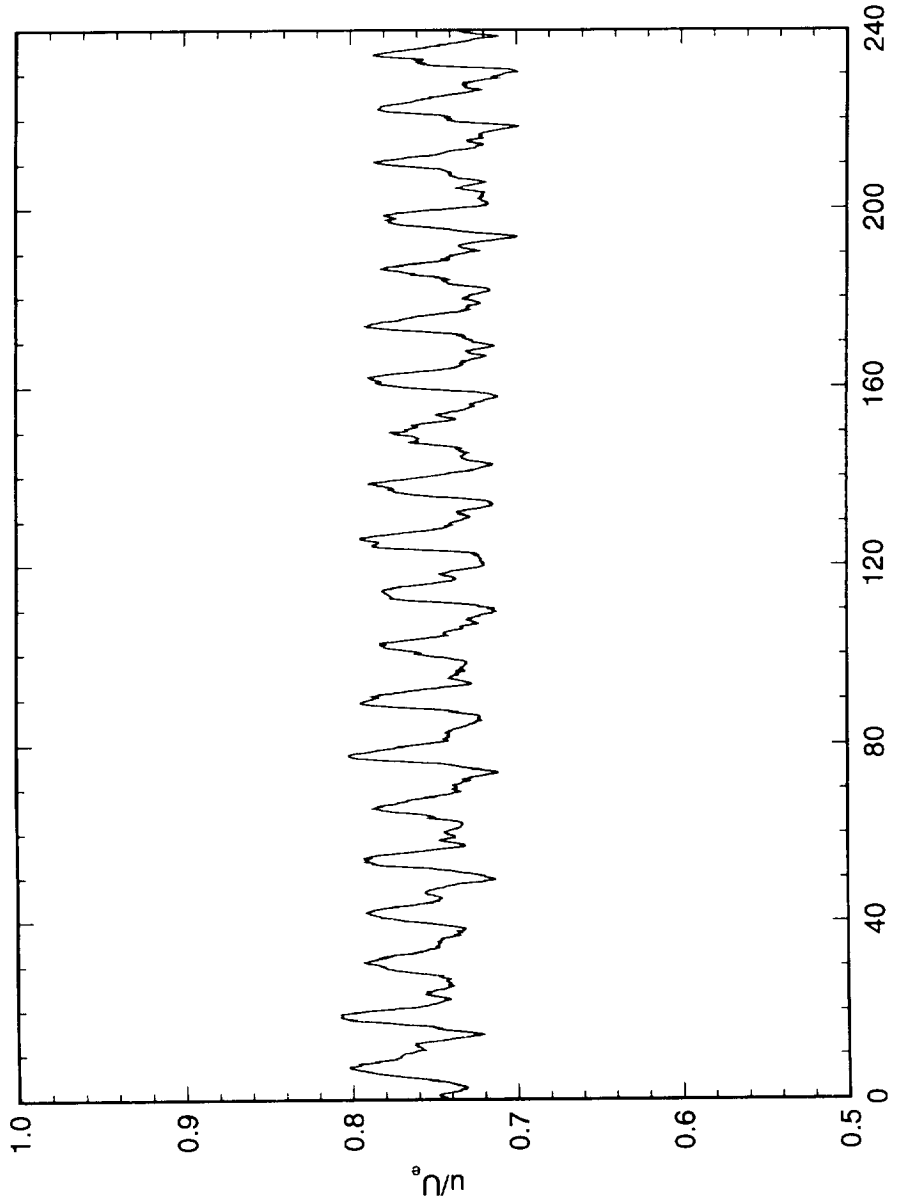

Figure 7.28. Spanwise hot-wire scan at $x/c = 0.30$. $Re_c = 3.2 \times 10^6$. Full array of 146 μm roughness with 12 mm spacing. Data set G.

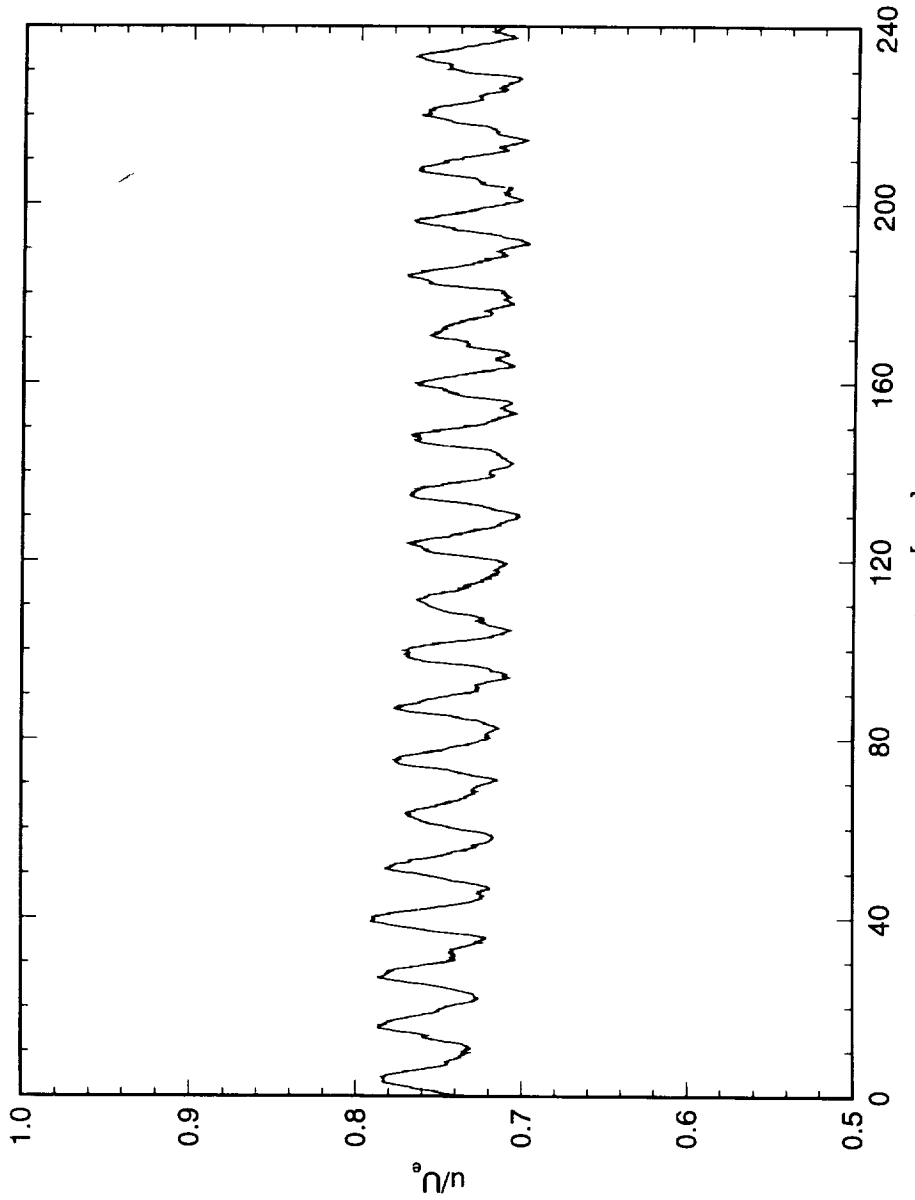

Figure 7.29. Spanwise hot-wire scan at $x/c = 0.40$. $Re_c = 3.2 \times 10^6$. Full array of 146 μm roughness with 12 mm spacing. Data set G.

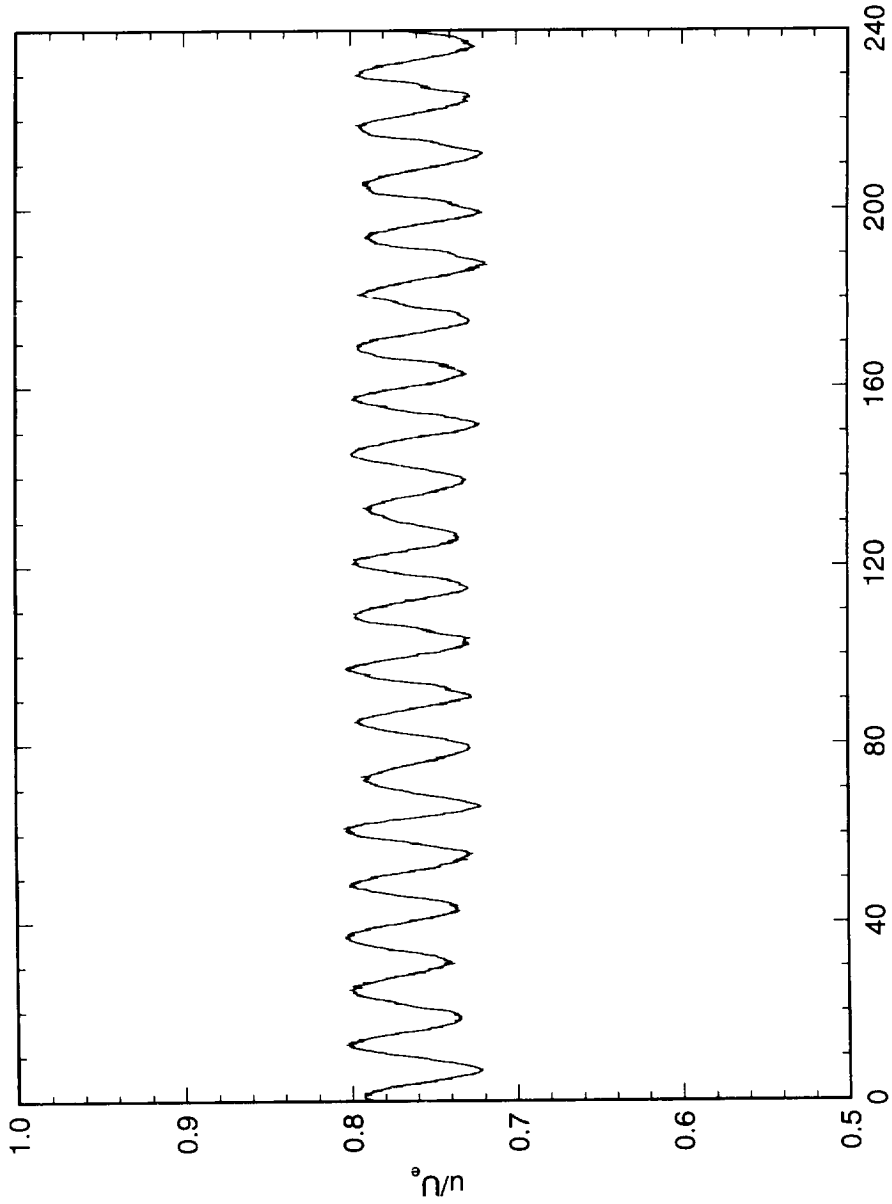

Figure 7.30. Spanwise hot-wire scan at $x/c = 0.50$. $Re_c = 3.2 \times 10^6$. Full array of 146 μm roughness with 12 mm spacing. Data set G.

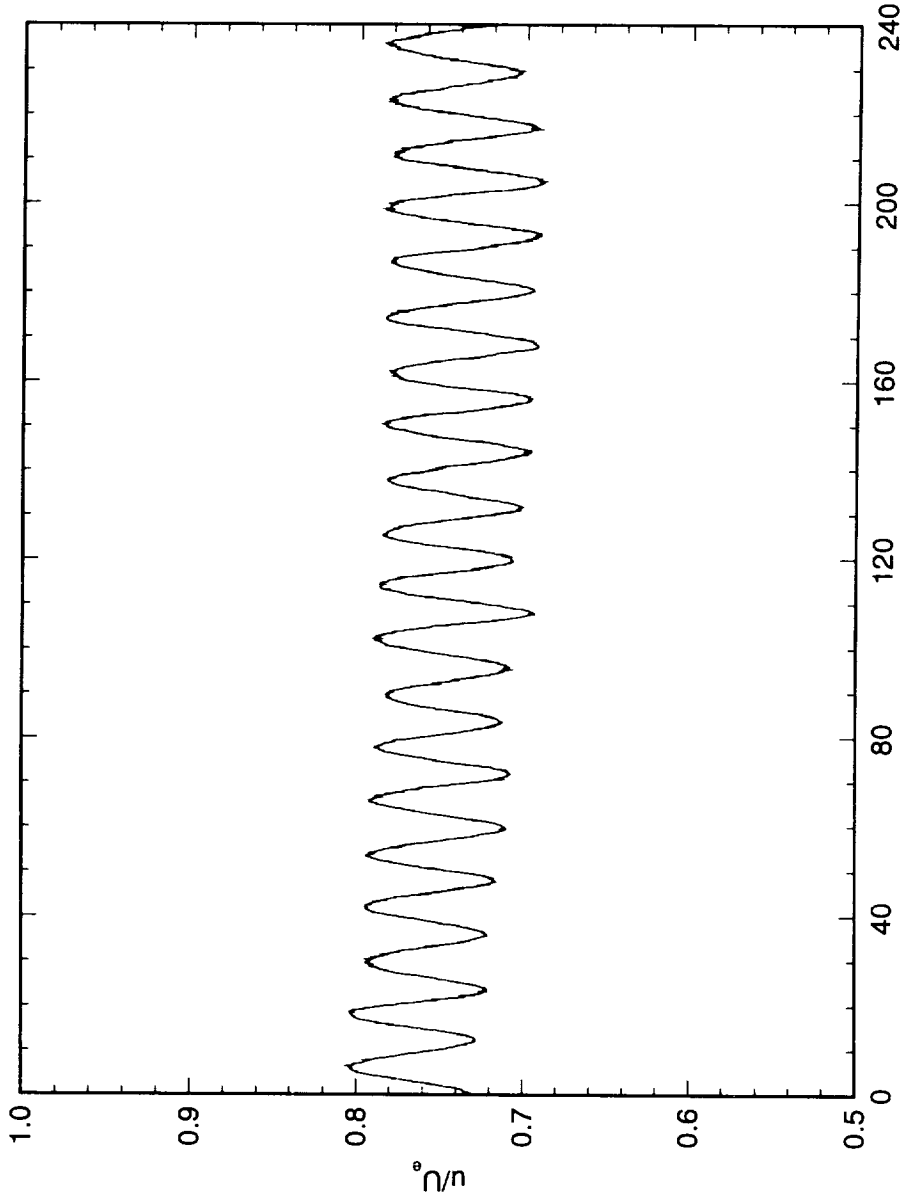

Figure 7.31. Spanwise hot-wire scan at $x/c = 0.60$. $Re_c = 3.2 \times 10^6$. Full array of 146 μm roughness with 12 mm spacing. Data set G.

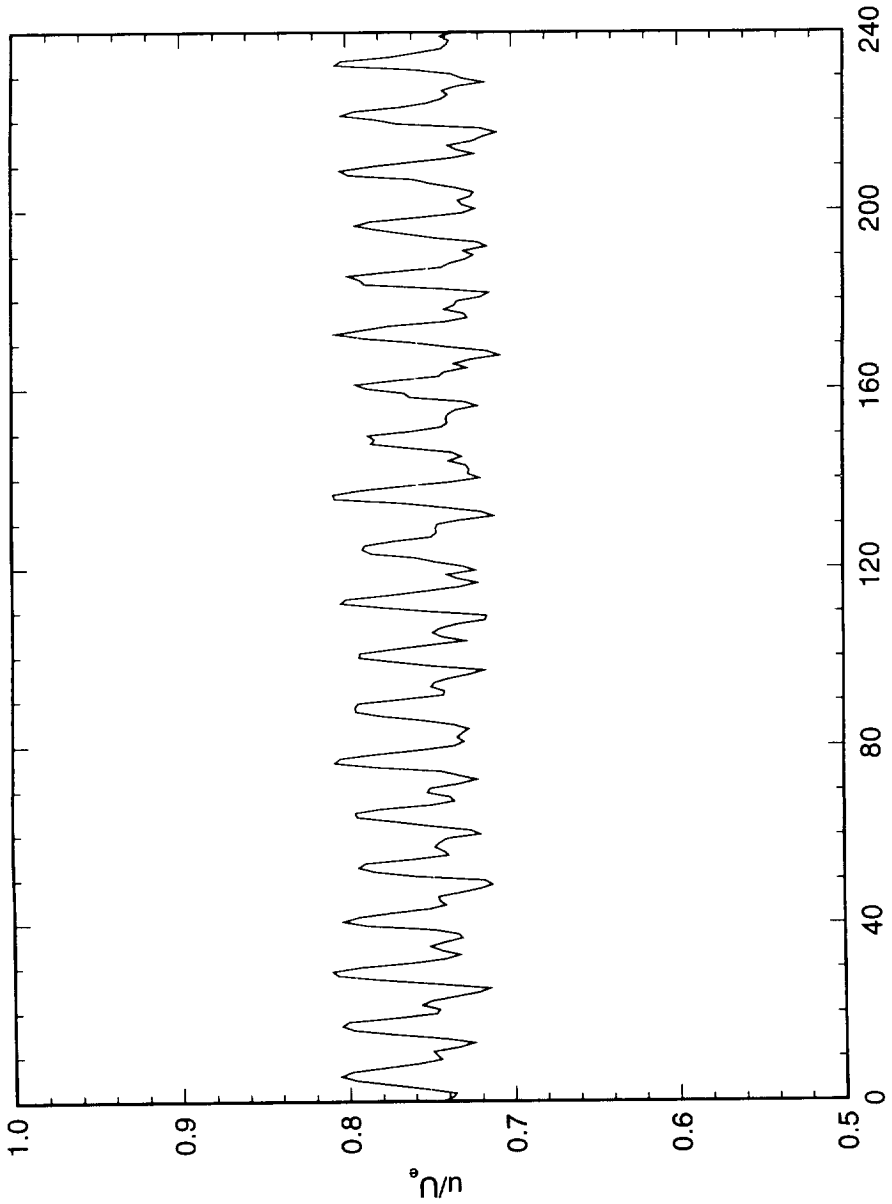

Figure 7.32. Spanwise hot-wire scan at $x/c = 0.30$. $Re_c = 3.4 \times 10^6$. Full array of 146 μm roughness with 12 mm spacing. Data set *H*.

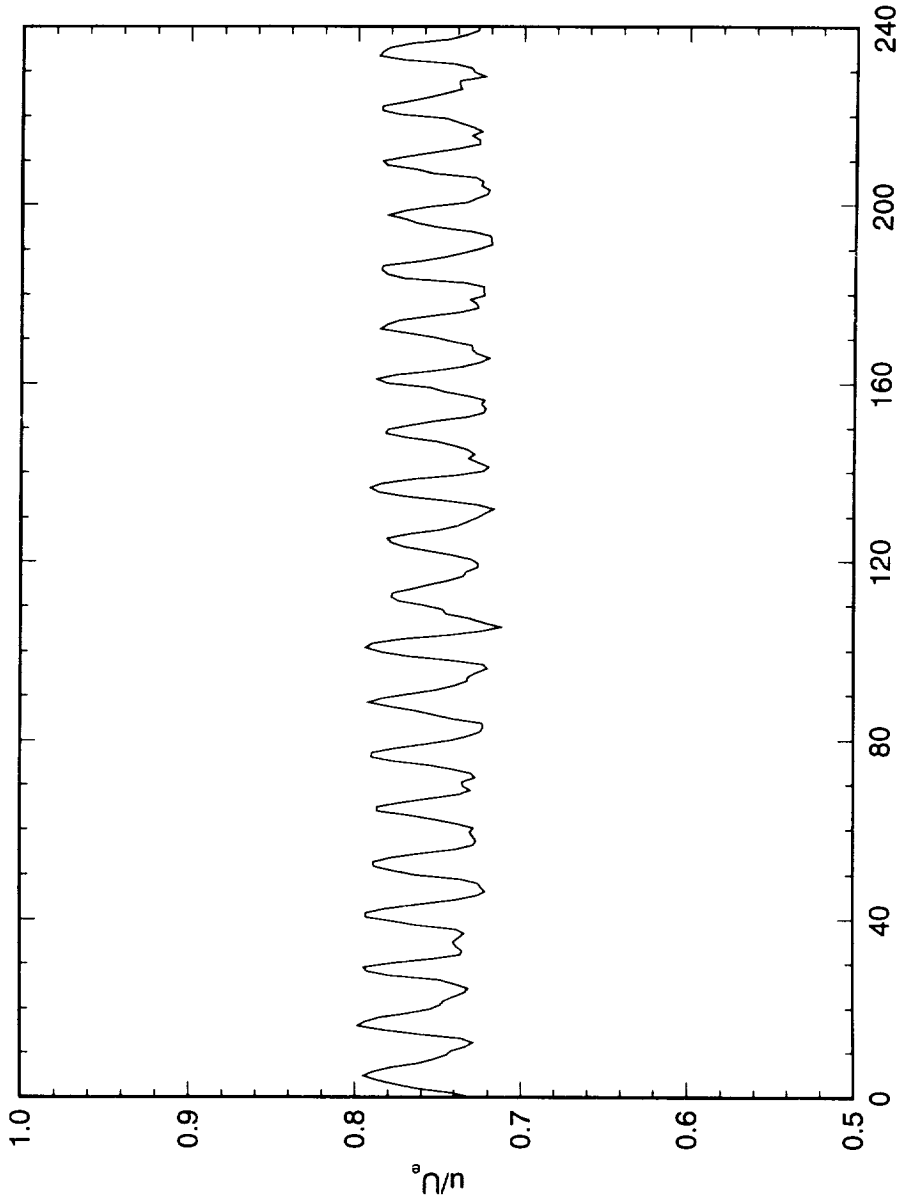

Figure 7.33. Spanwise hot-wire scan at $x/c = 0.40$. $Re_c = 3.4 \times 10^6$. Full array of 146 μm roughness with 12 mm spacing. Data set *H*.

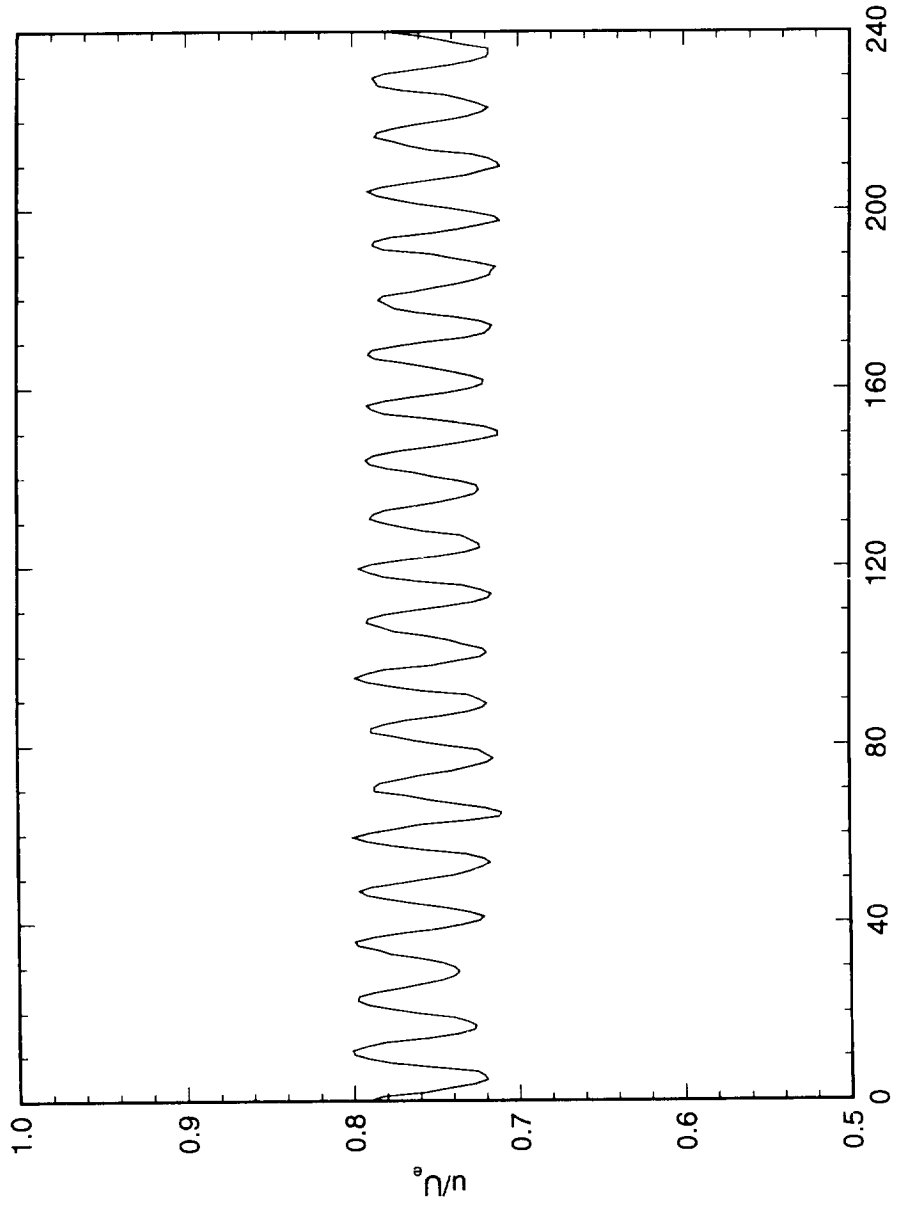

Figure 7.34. Spanwise hot-wire scan at $x/c = 0.50$. $Re_c = 3.4 \times 10^6$. Full array of 146 μm roughness with 12 mm spacing. Data set *H*.

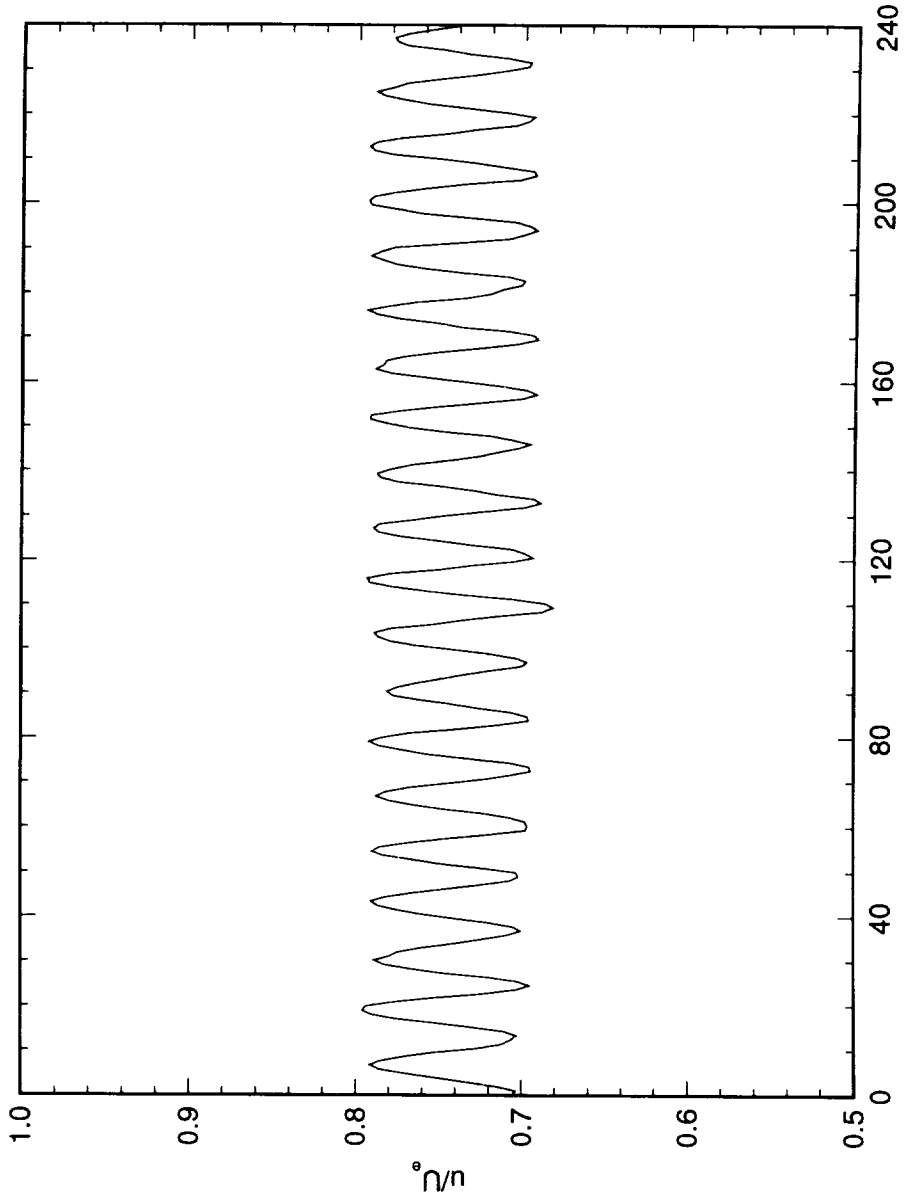

Figure 7.35. Spanwise hot-wire scan at $x/c = 0.60$. $Re_c = 3.4 \times 10^6$. Full array of 146 μm roughness with 12 mm spacing. Data set *H*.

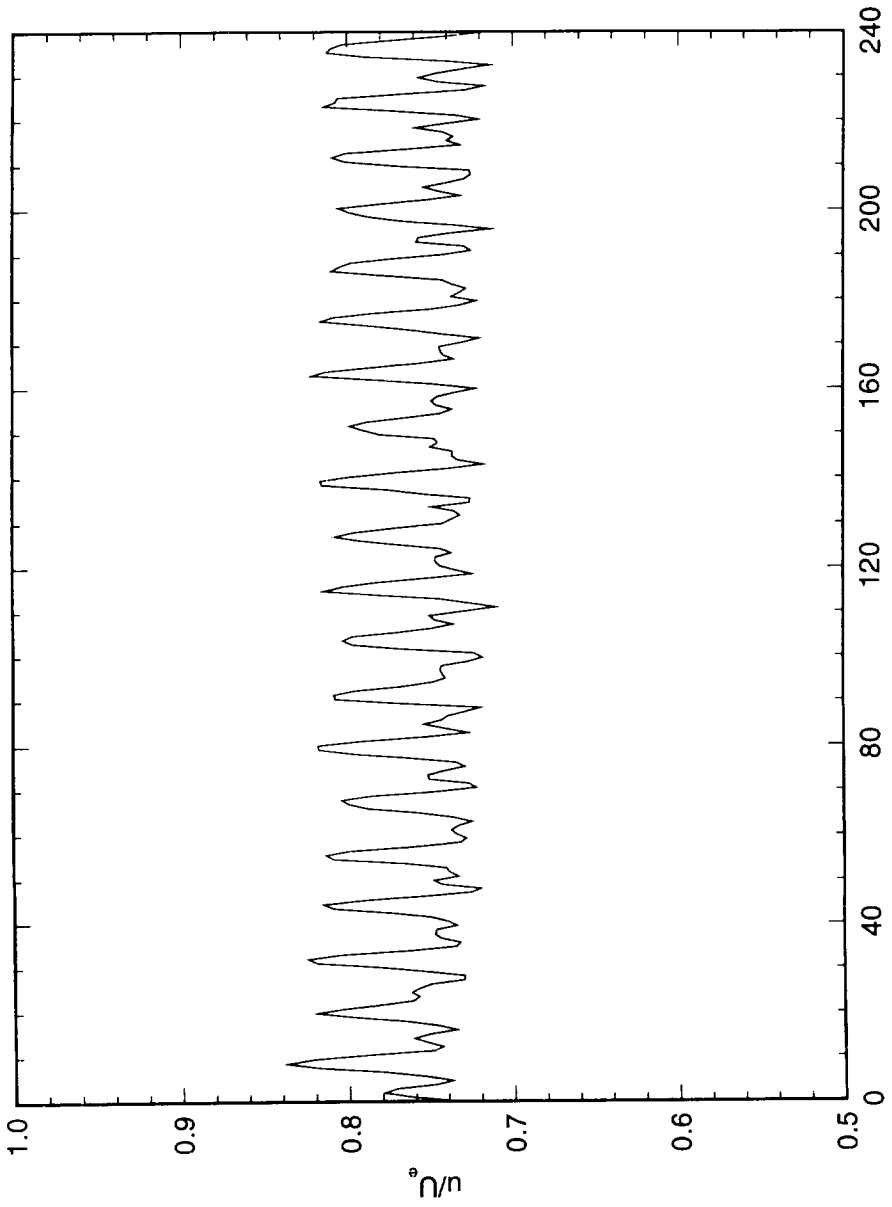

Figure 7.36. Spanwise hot-wire scan at $x/c = 0.30$. $Re_c = 3.6 \times 10^6$. Full array of 146 μm roughness with 12 mm spacing. Data set *I*.

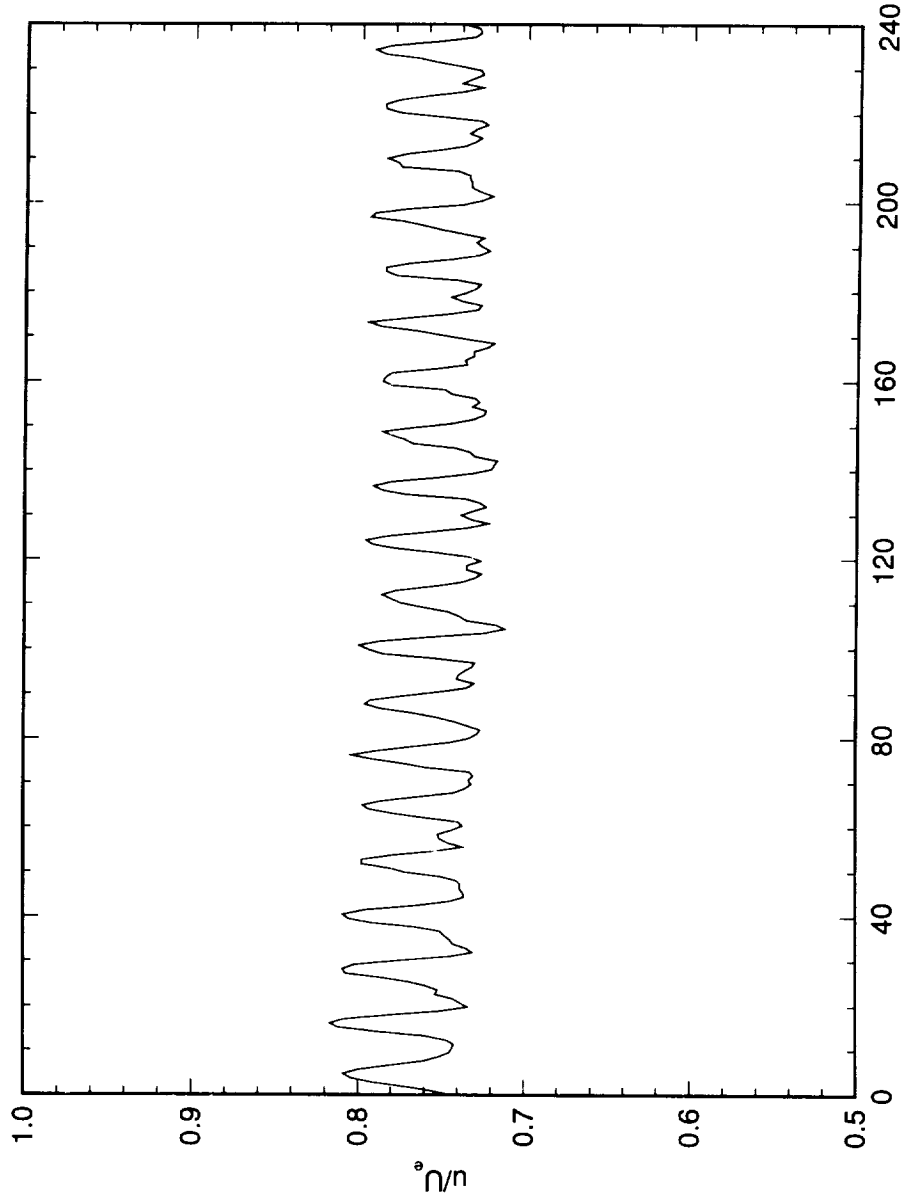

Figure 7.37. Spanwise hot-wire scan at $x/c = 0.40$. $Re_c = 3.6 \times 10^6$. Full array of 146 μm roughness with 12 mm spacing. Data set *I*.

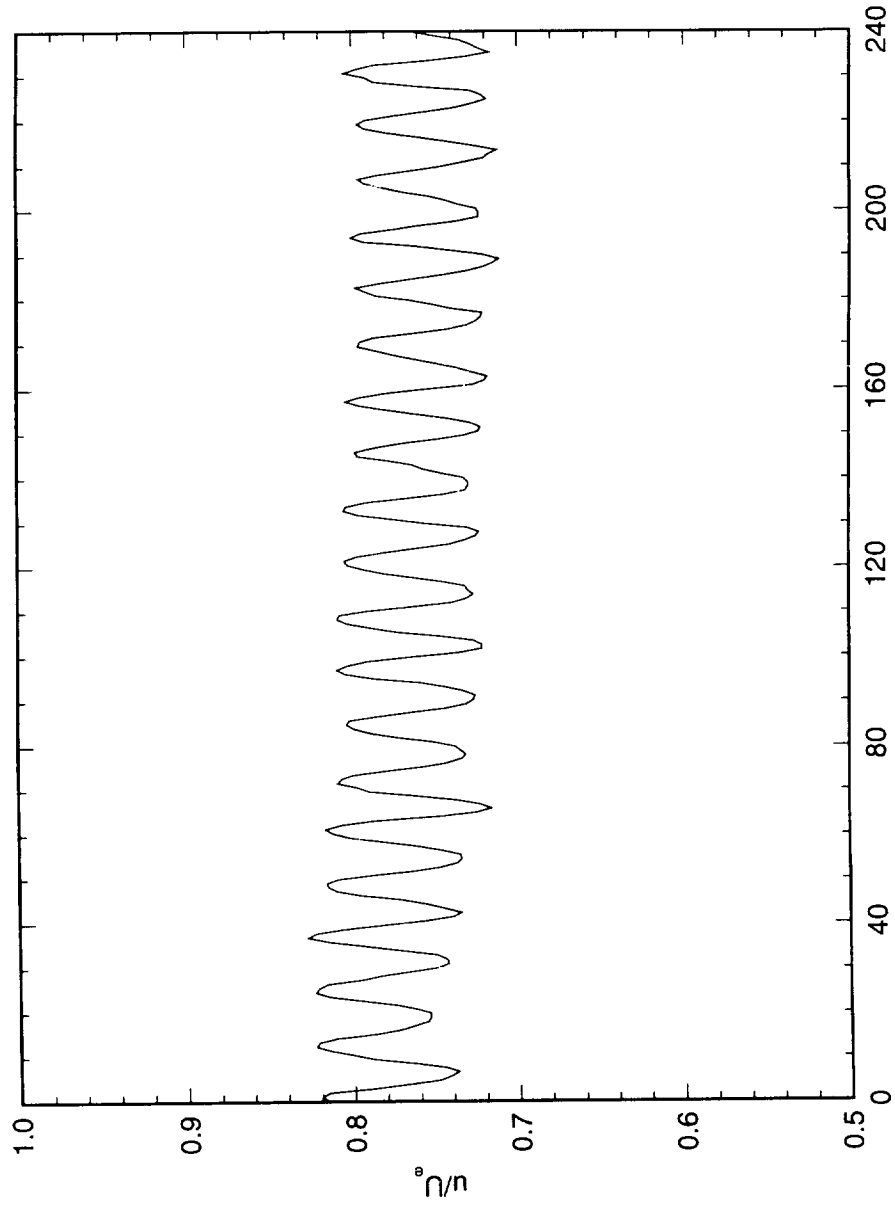

Figure 7.38. Spanwise hot-wire scan at $x/c = 0.50$. $Re_c = 3.6 \times 10^6$. Full array of 146 μm roughness with 12 mm spacing. Data set *I*.

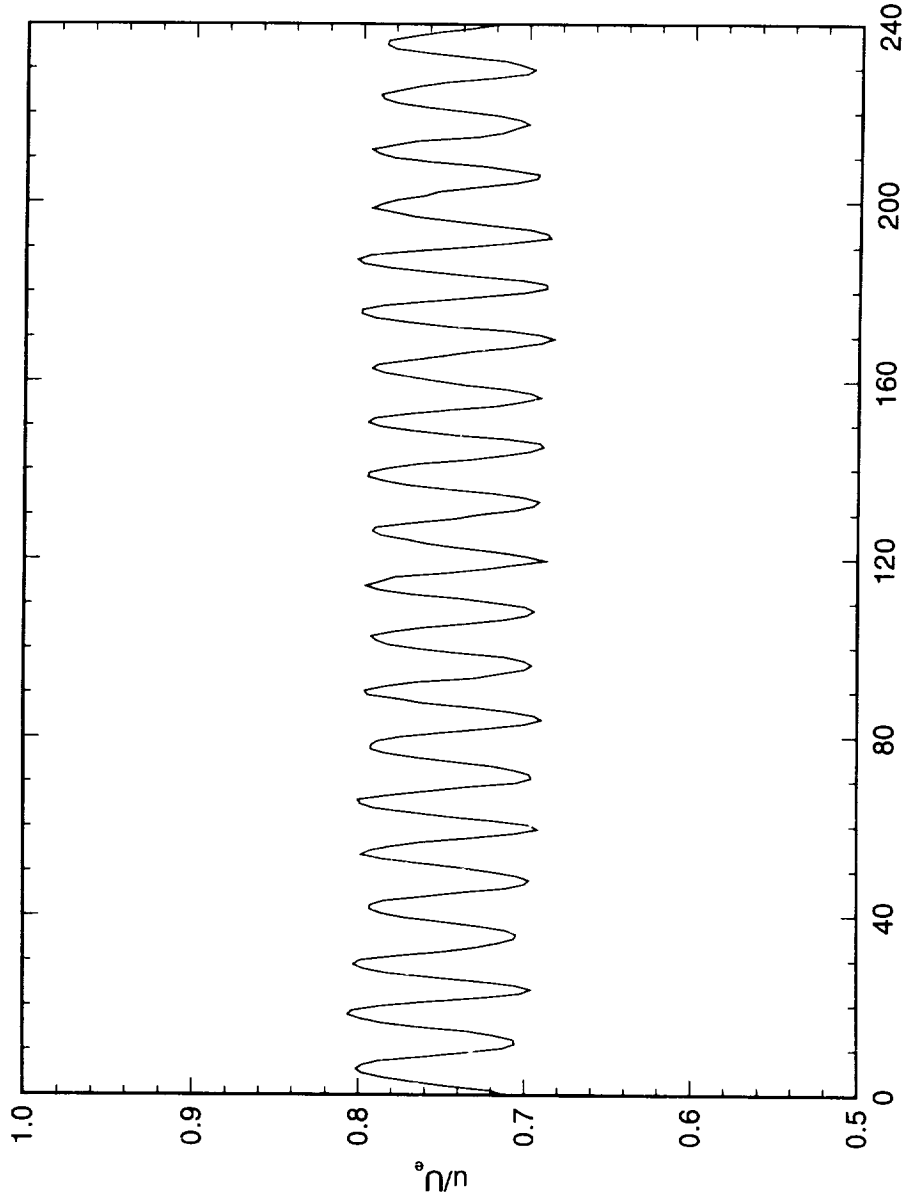

Figure 7.39. Spanwise hot-wire scan at $x/c = 0.60$. $Re_c = 3.6 \times 10^6$. Full array of 146 μm roughness with 12 mm spacing. Data set *I*.

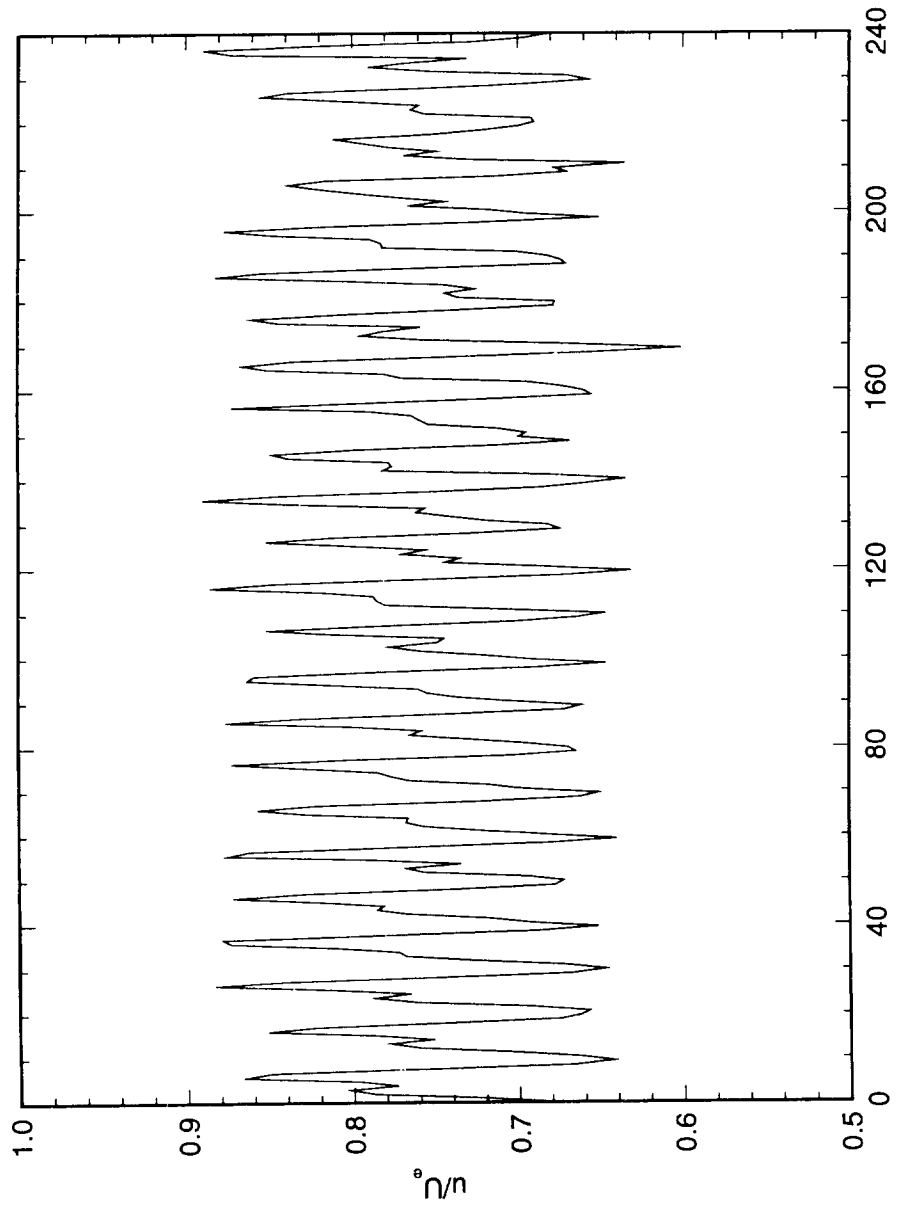

Figure 7.40. Spanwise hot-wire scan at $x/c = 0.10$. $Re_c = 3.0 \times 10^6$. Full array of 146 μm roughness with 10 mm spacing. Data set K.

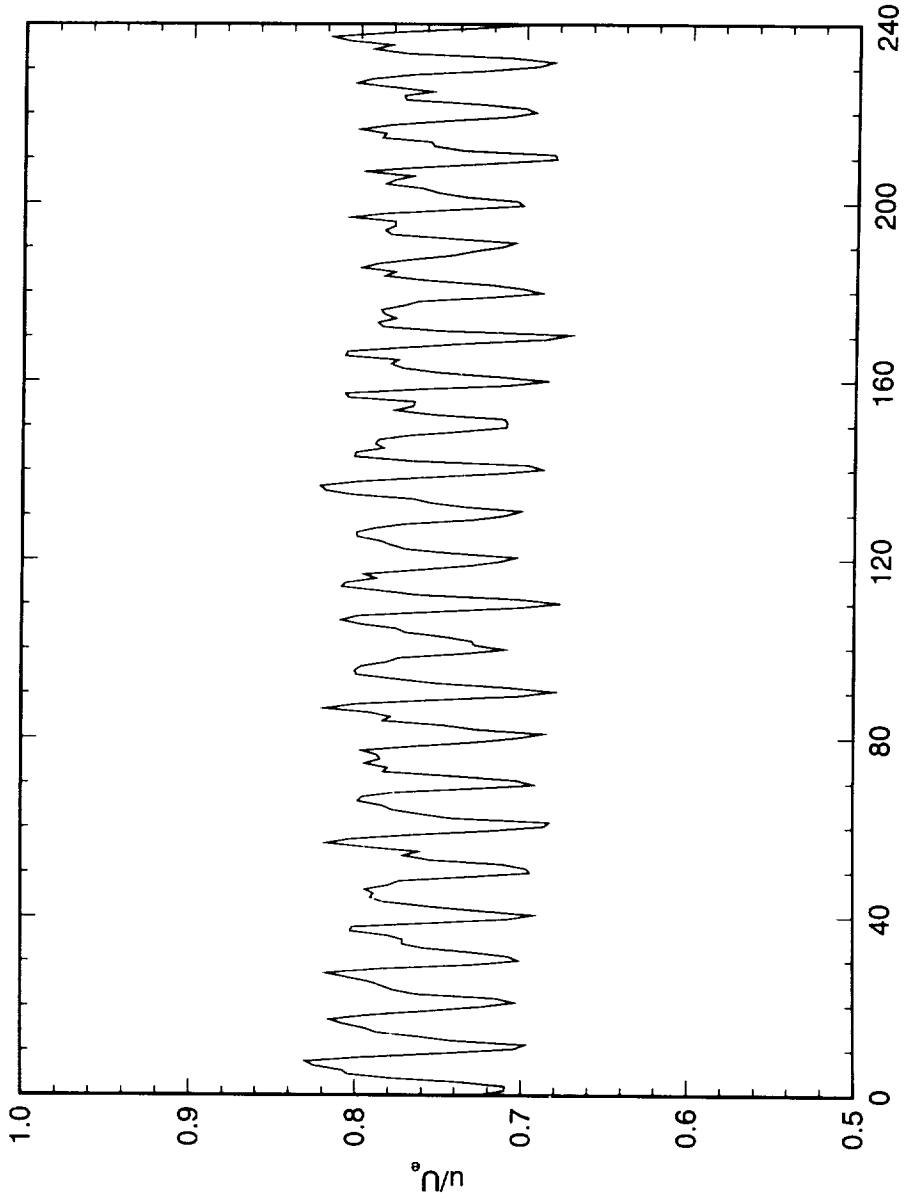

Figure 7.41. Spanwise hot-wire scan at $x/c = 0.20$. $Re_c = 3.0 \times 10^6$. Full array of 146 μm roughness with 10 mm spacing. Data set K.

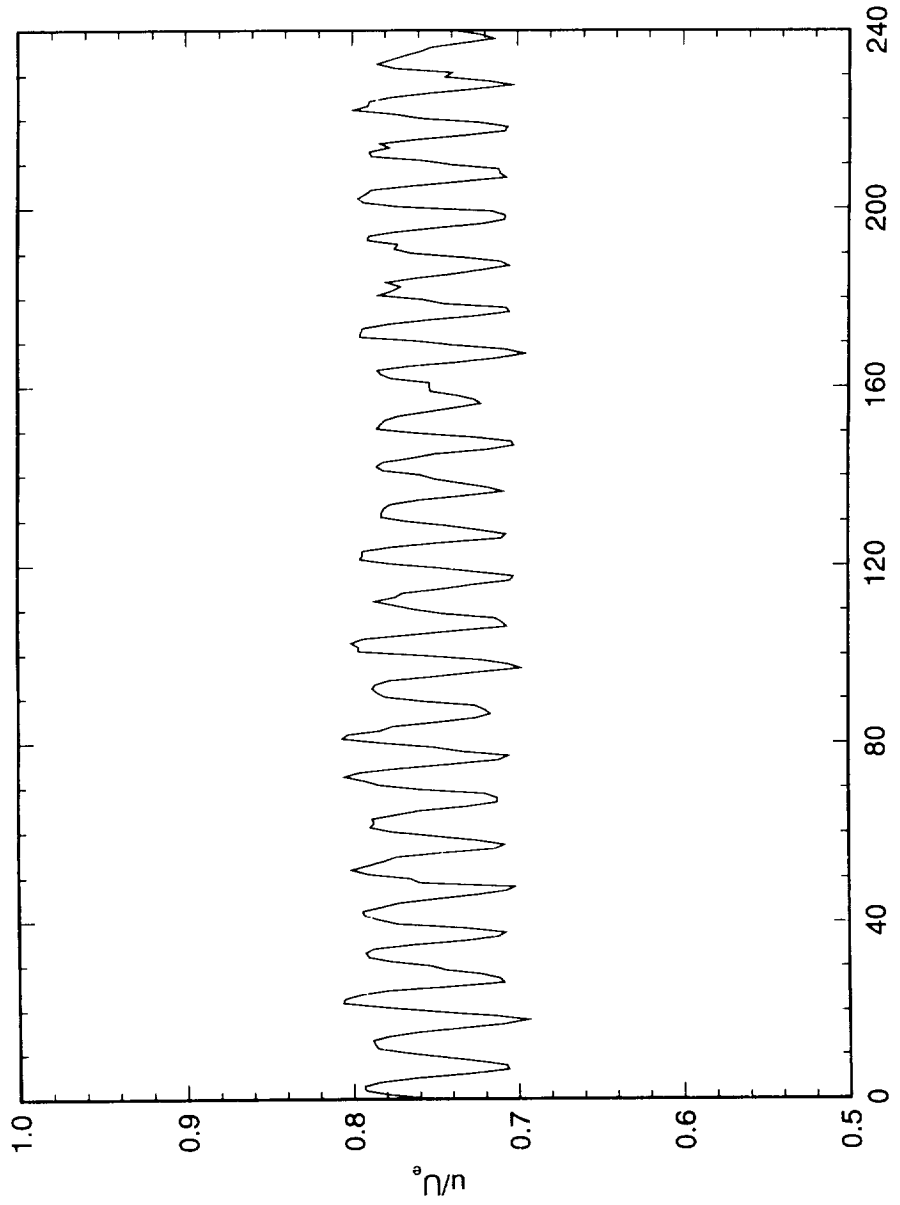

Figure 7.42. Spanwise hot-wire scan at $x/c = 0.30$. $Re_c = 3.0 \times 10^6$. Full array of 146 μm roughness with 10 mm spacing. Data set K.

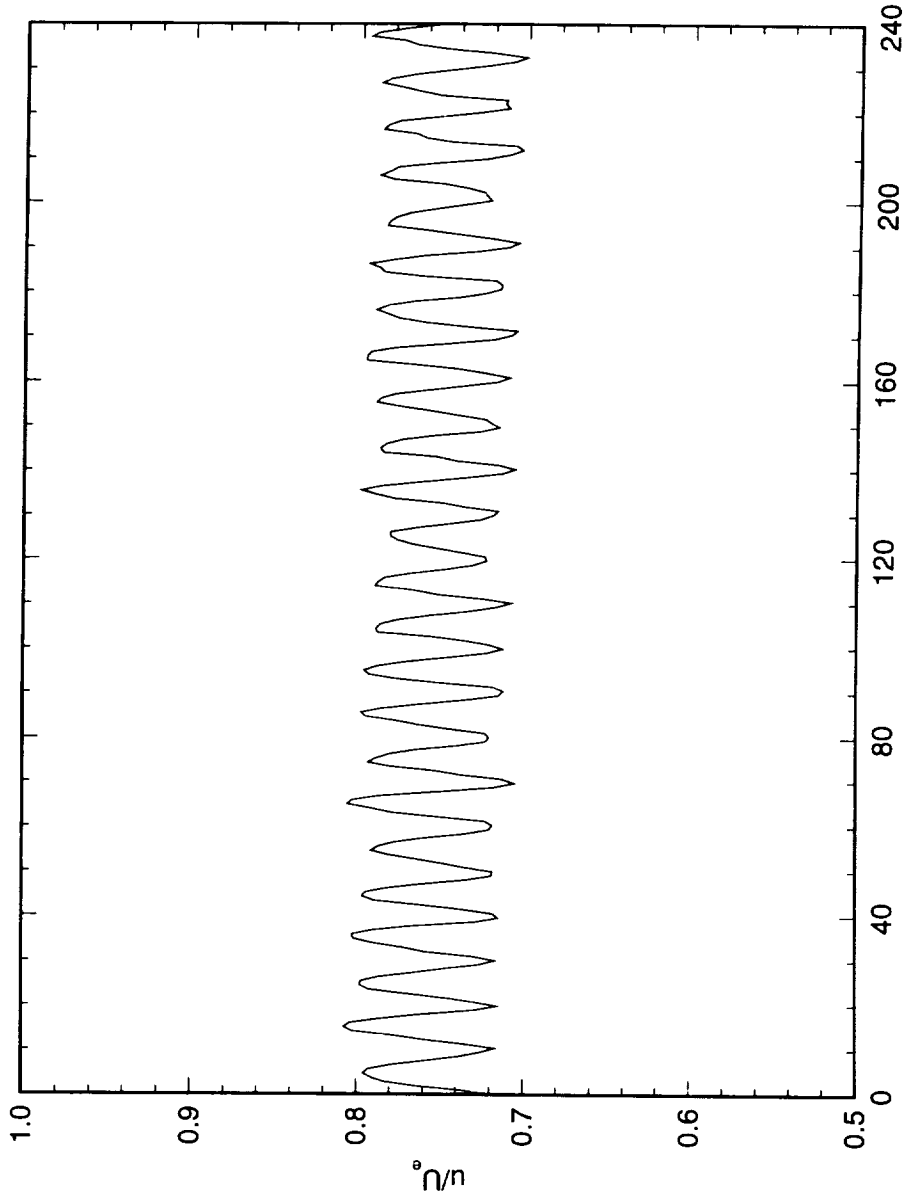

Figure 7.43. Spanwise hot-wire scan at $x/c = 0.40$. $Re_c = 3.0 \times 10^6$. Full array of 146 μm roughness with 10 mm spacing. Data set K.

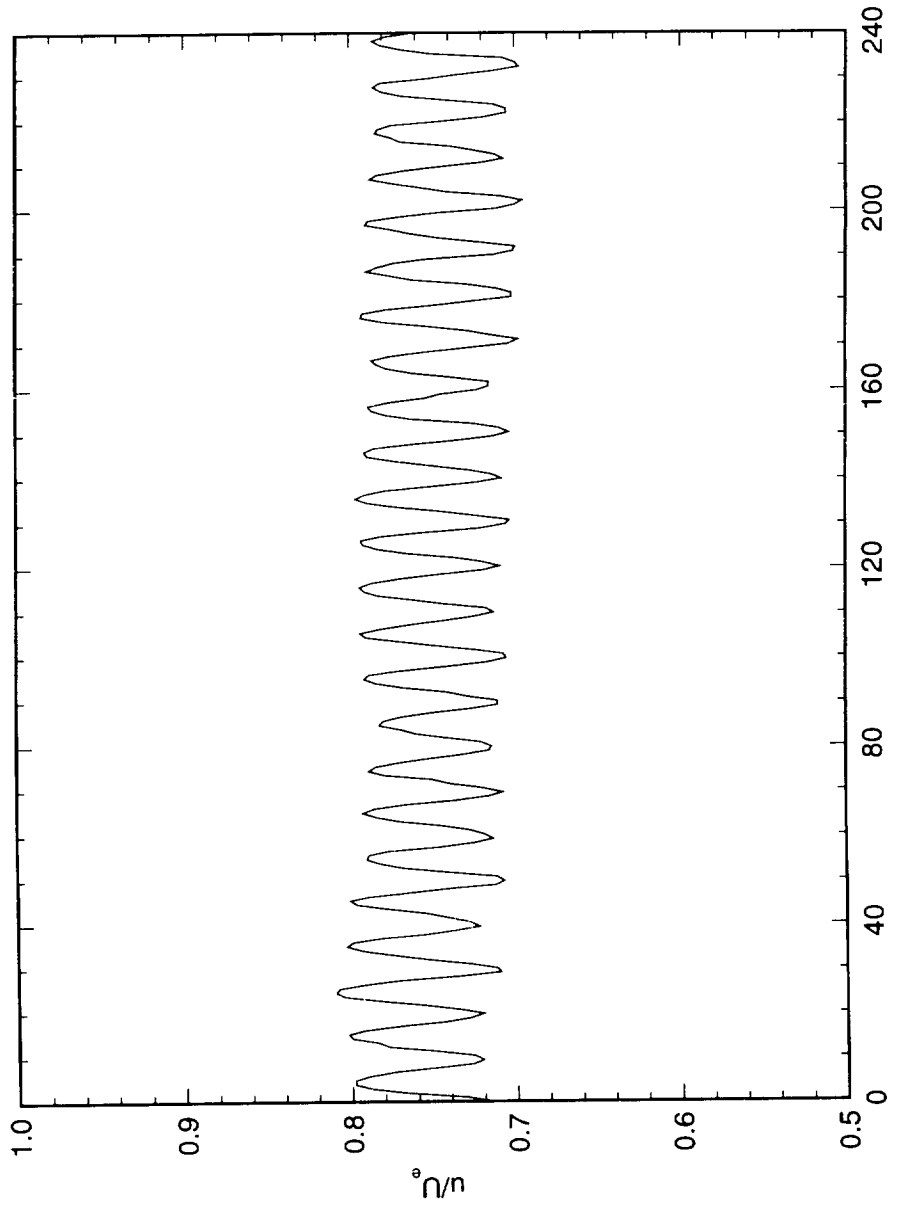

Figure 7.44. Spanwise hot-wire scan at $x/c = 0.50$. $Re_c = 3.0 \times 10^6$. Full array of 146 μm roughness with 10 mm spacing. Data set K.

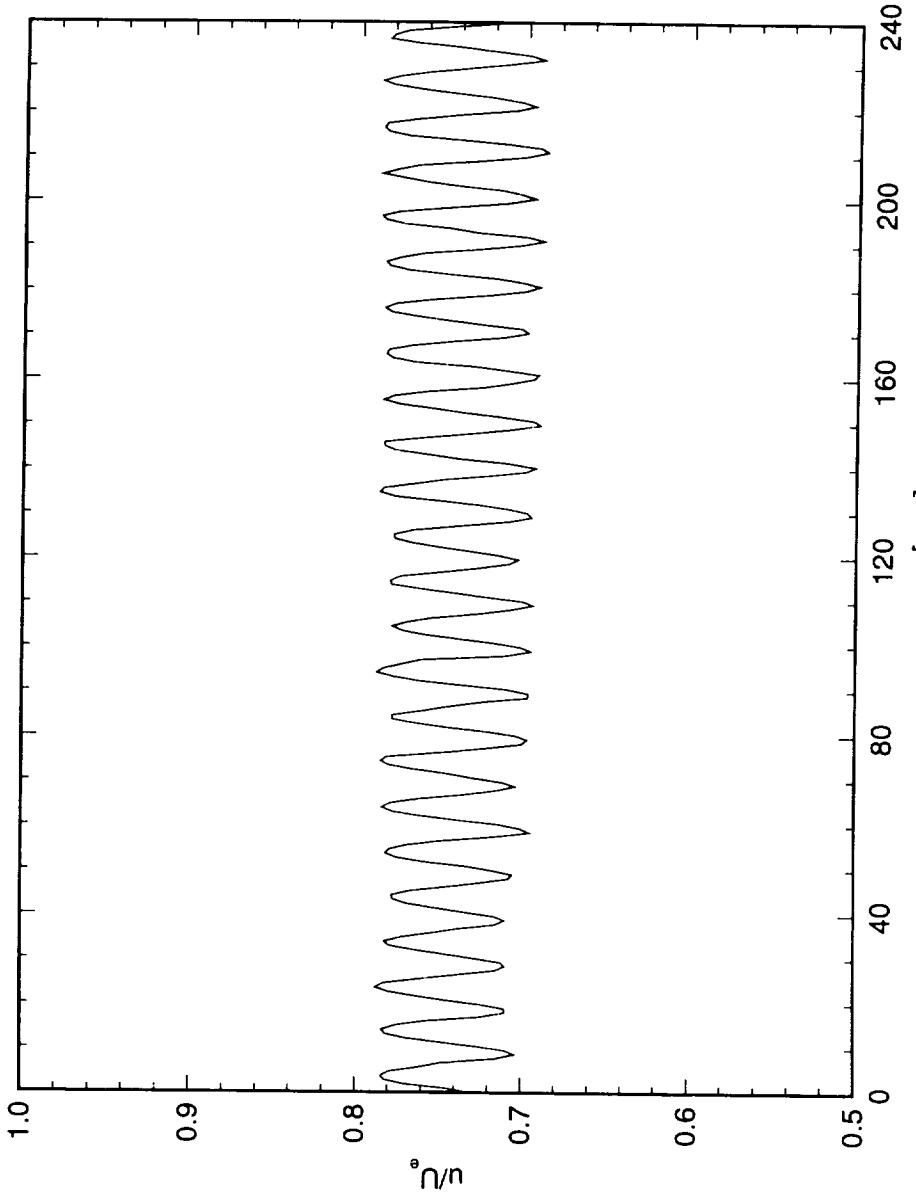

Figure 7.45. Spanwise hot-wire scan at $x/c = 0.60$. $Re_c = 3.0 \times 10^6$. Full array of 146 μm roughness with 10 mm spacing. Data set K.

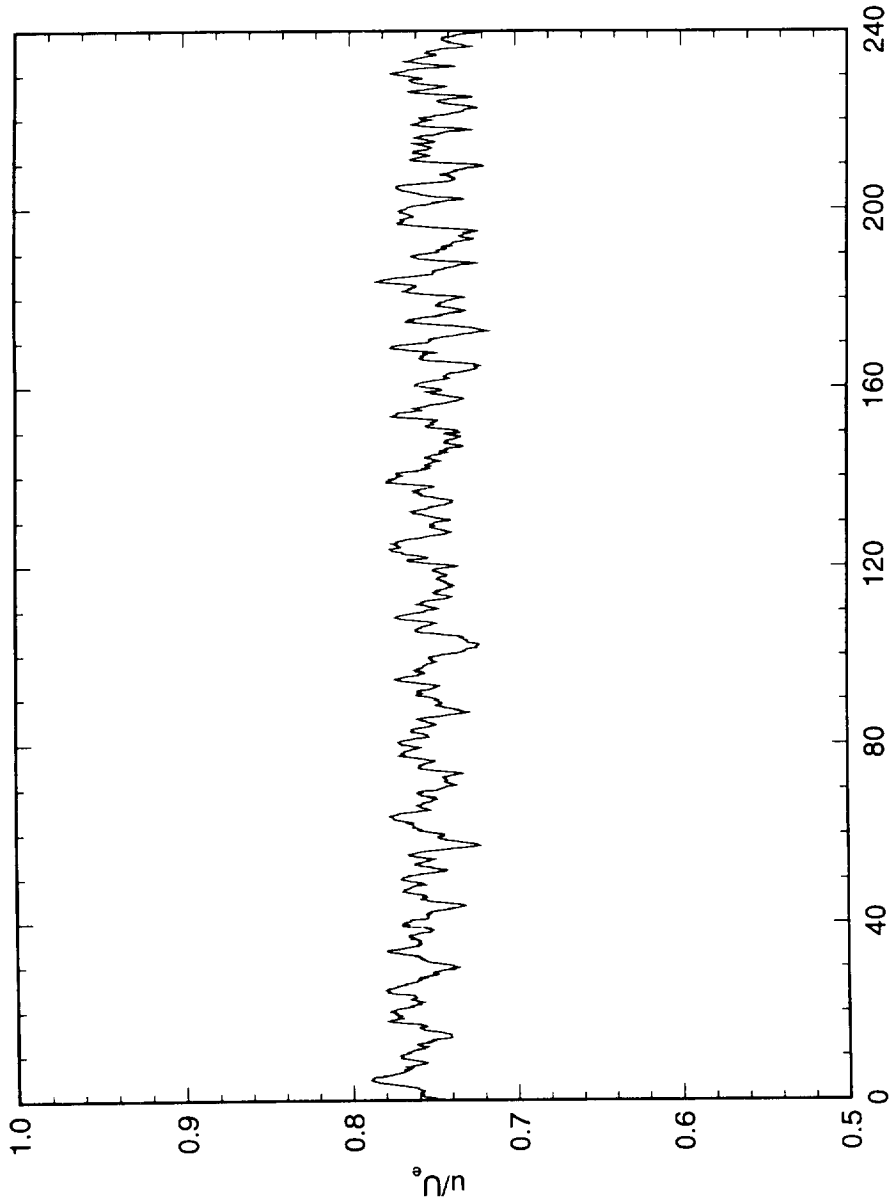

Figure 7.46. Spanwise hot-wire scan at $x/c = 0.20$. $Re_c = 3.0 \times 10^6$. Full array of 73 μm roughness with 15 mm spacing. Data set M.

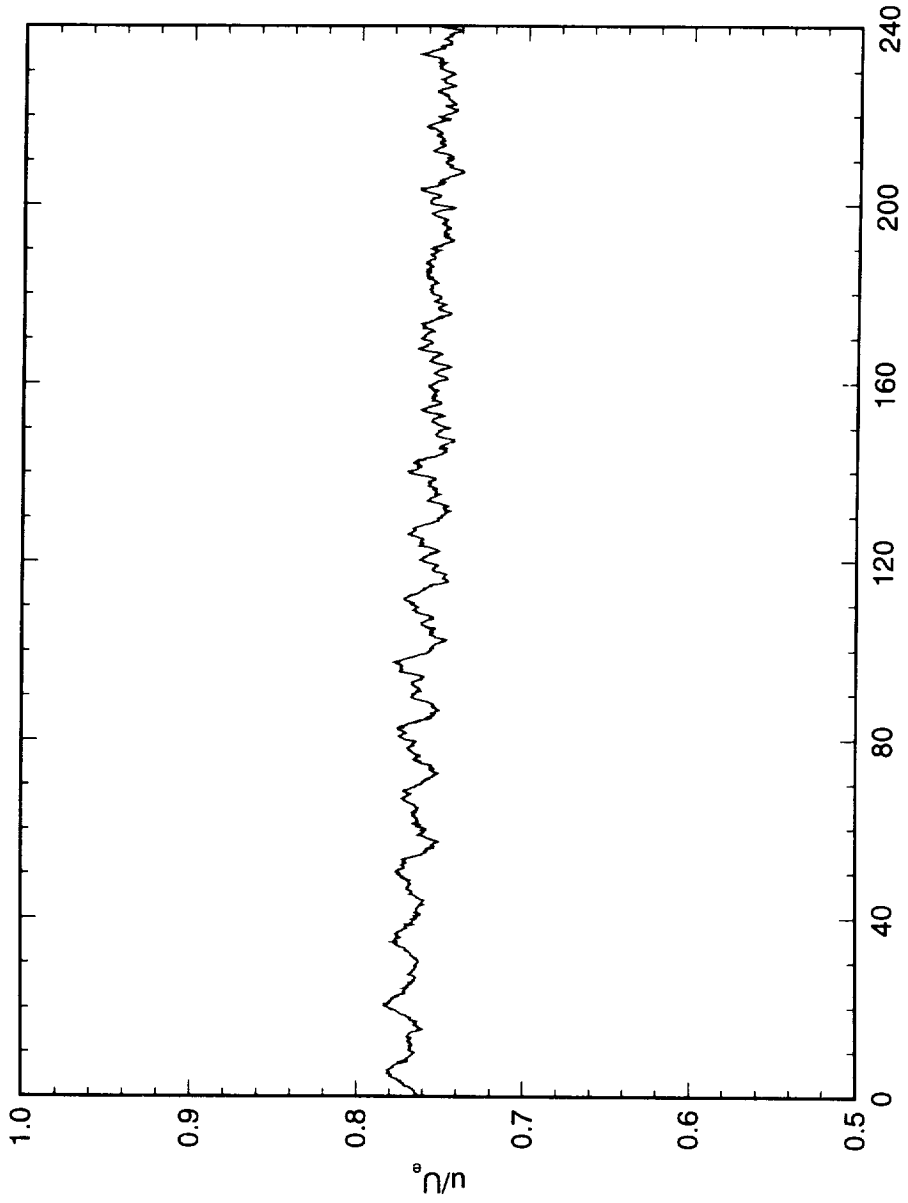

Figure 7.47. Spanwise hot-wire scan at $x/c = 0.40$. $Re_c = 3.0 \times 10^6$. Full array of 73 μm roughness with 15 mm spacing. Data set *M*.

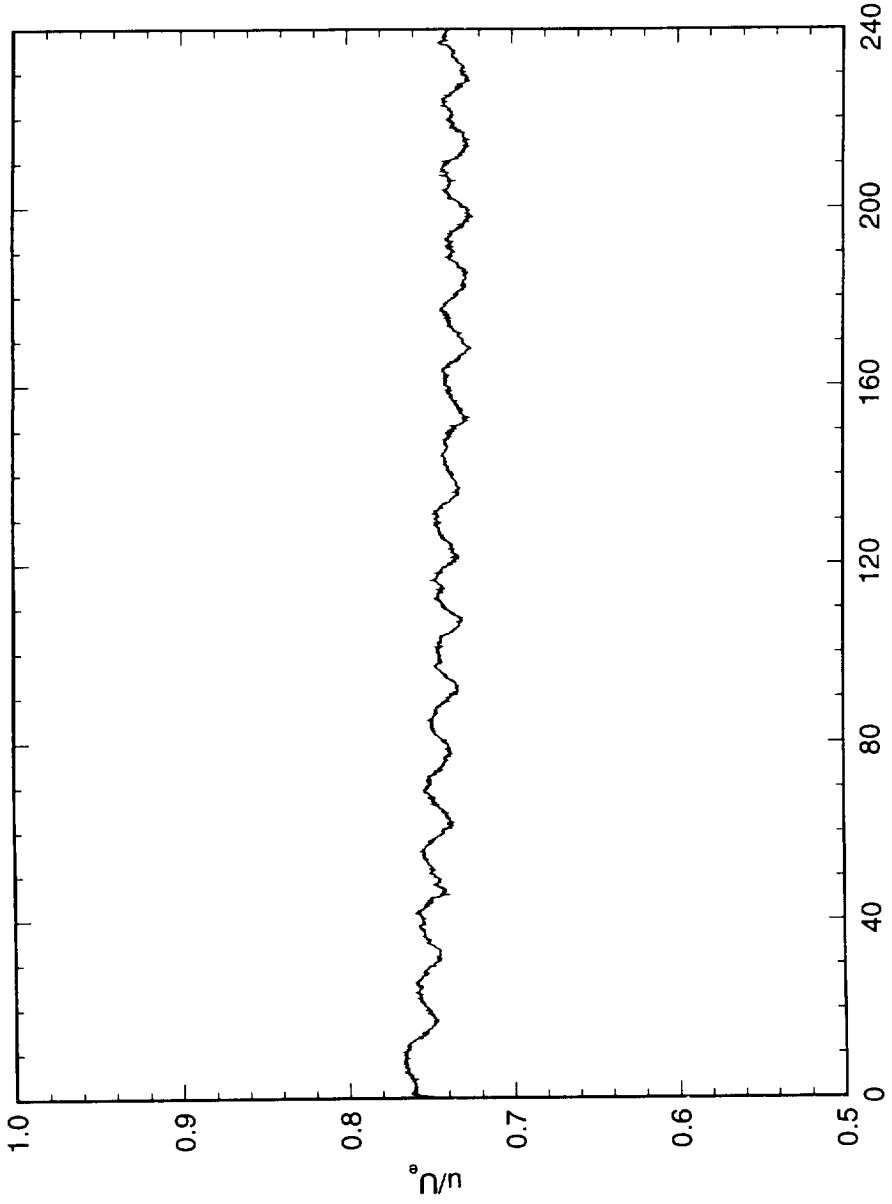

Figure 7.48. Spanwise hot-wire scan at $x/c = 0.60$. $Re_c = 3.0 \times 10^6$. Full array of 73 μm roughness with 15 mm spacing. Data set M.

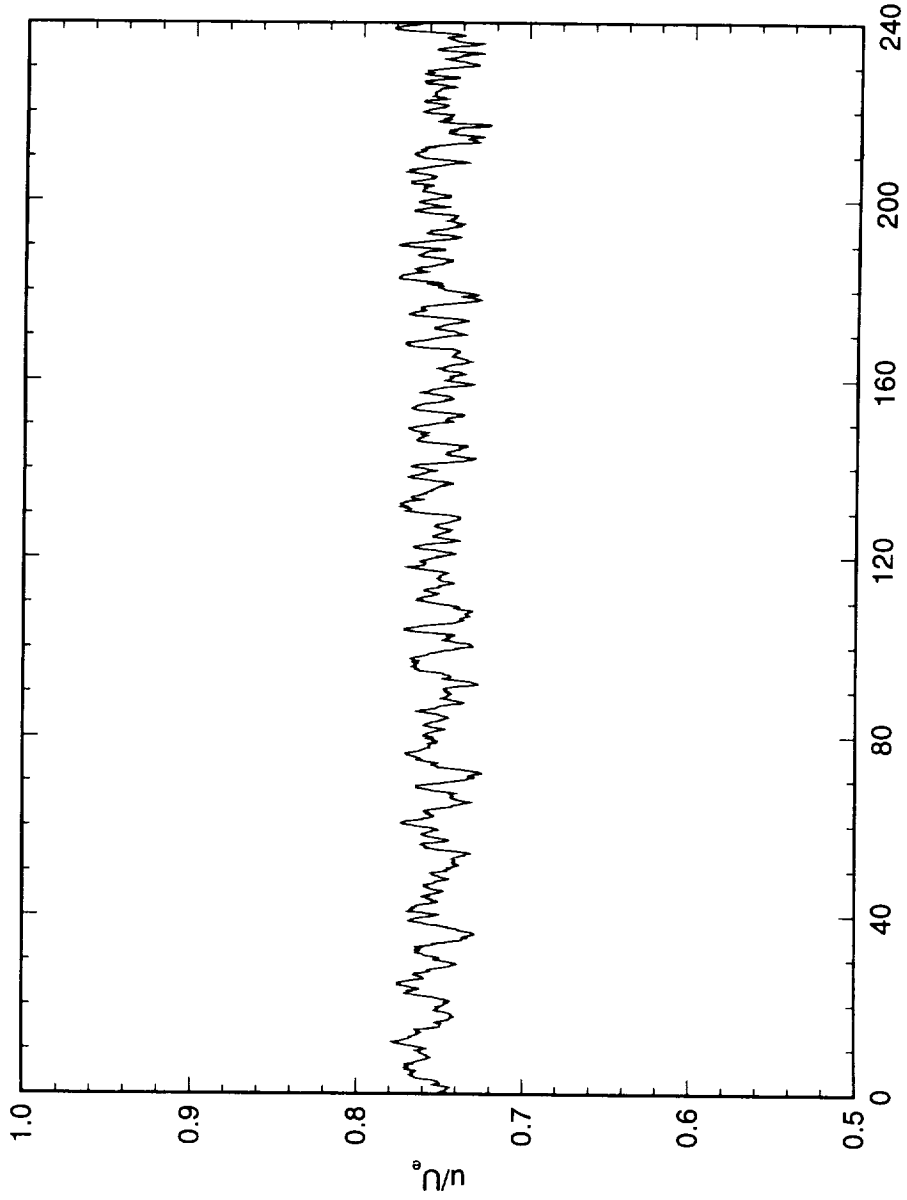

Figure 7.49. Spanwise hot-wire scan at $x/c = 0.20$. $Re_c = 3.0 \times 10^6$. Full array of 73 μm roughness with 18 mm spacing. Data set *N*.

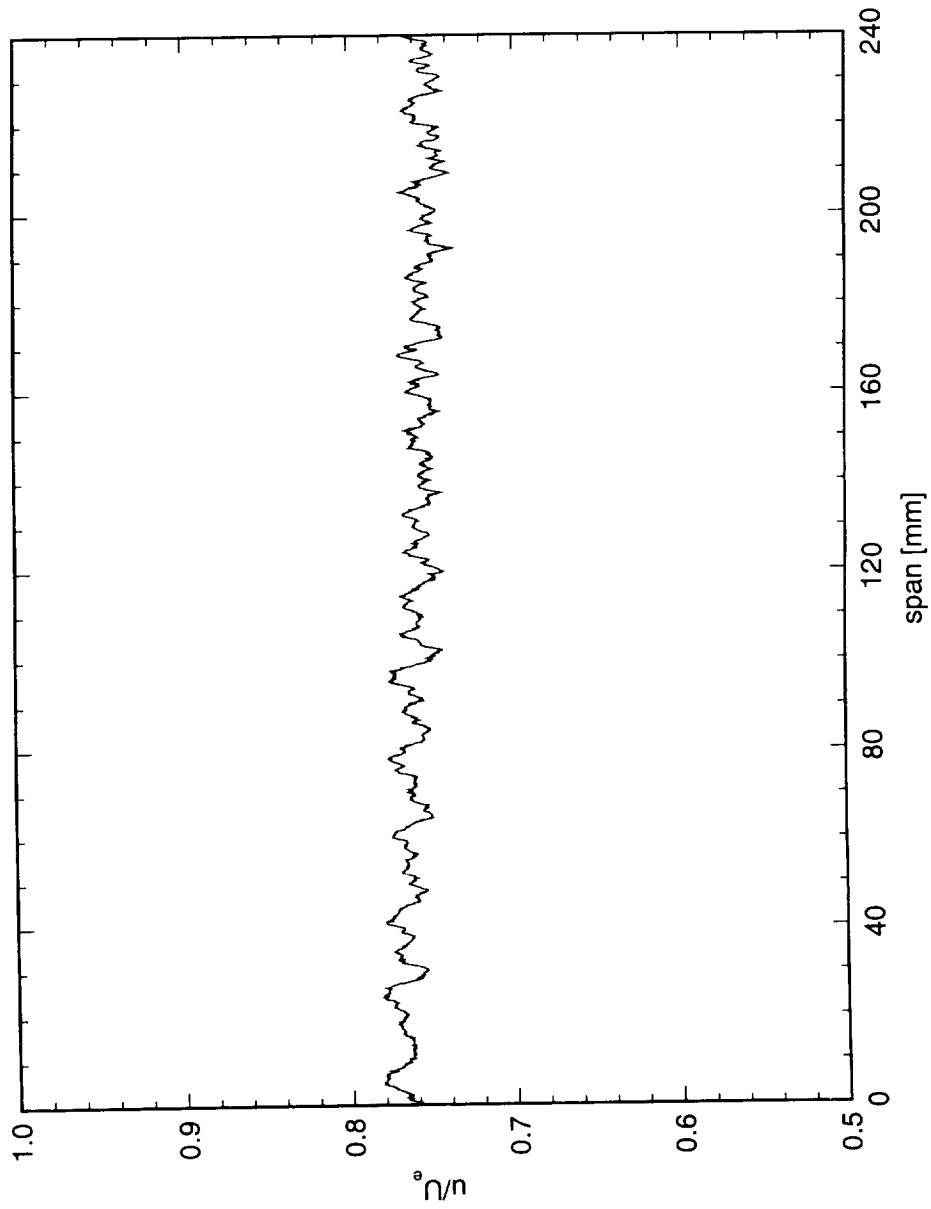

Figure 7.50. Spanwise hot-wire scan at $x/c = 0.40$. $Re_c = 3.0 \times 10^6$. Full array of 73 μm roughness with 18 mm spacing. Data set *N*.

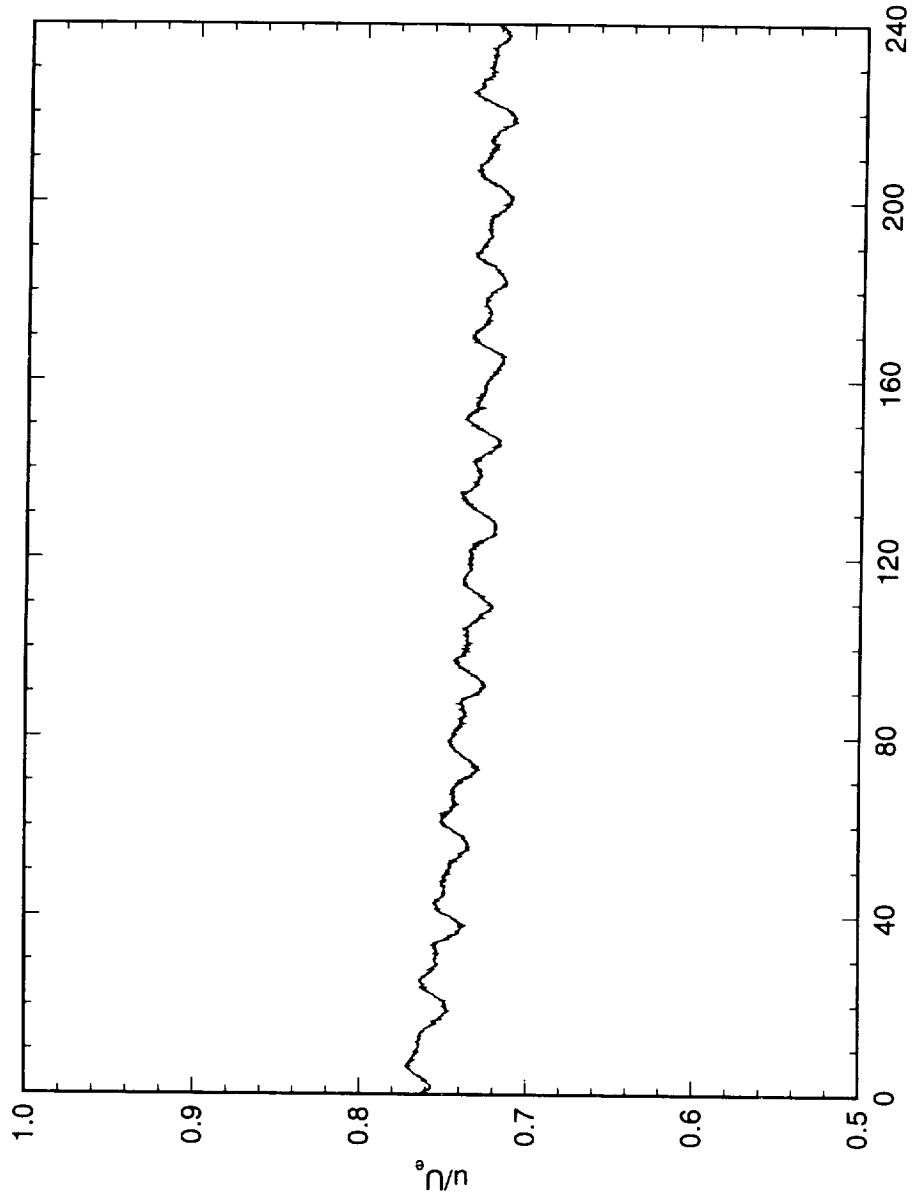

Figure 7.51. Spanwise hot-wire scan at $x/c = 0.60$. $Re_c = 3.0 \times 10^6$. Full array of 73 μm roughness with 18 mm spacing. Data set N.

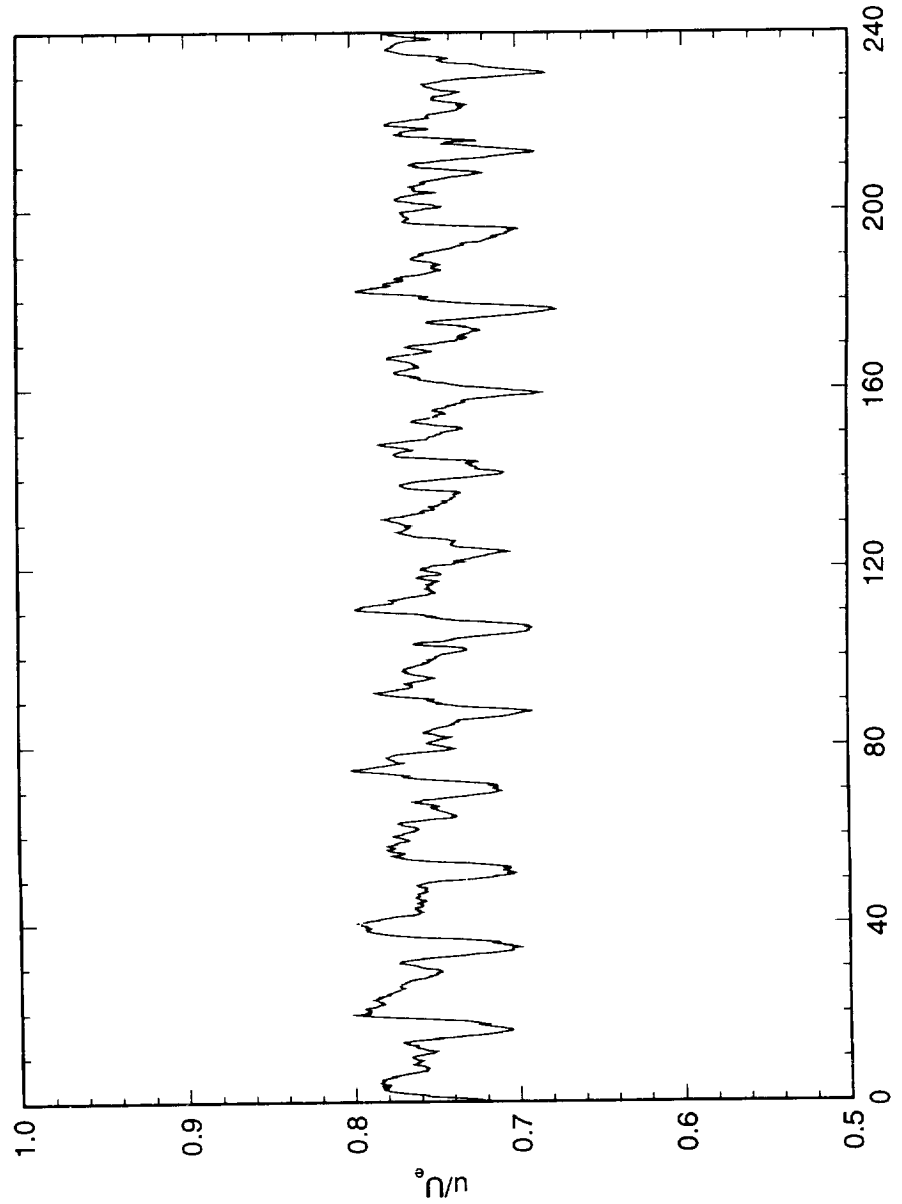

Figure 7.52. Spanwise hot-wire scan at $x/c = 0.20$. $Re_c = 3.0 \times 10^6$. Full array of 146 μm roughness with 18 mm spacing. Data set Q.

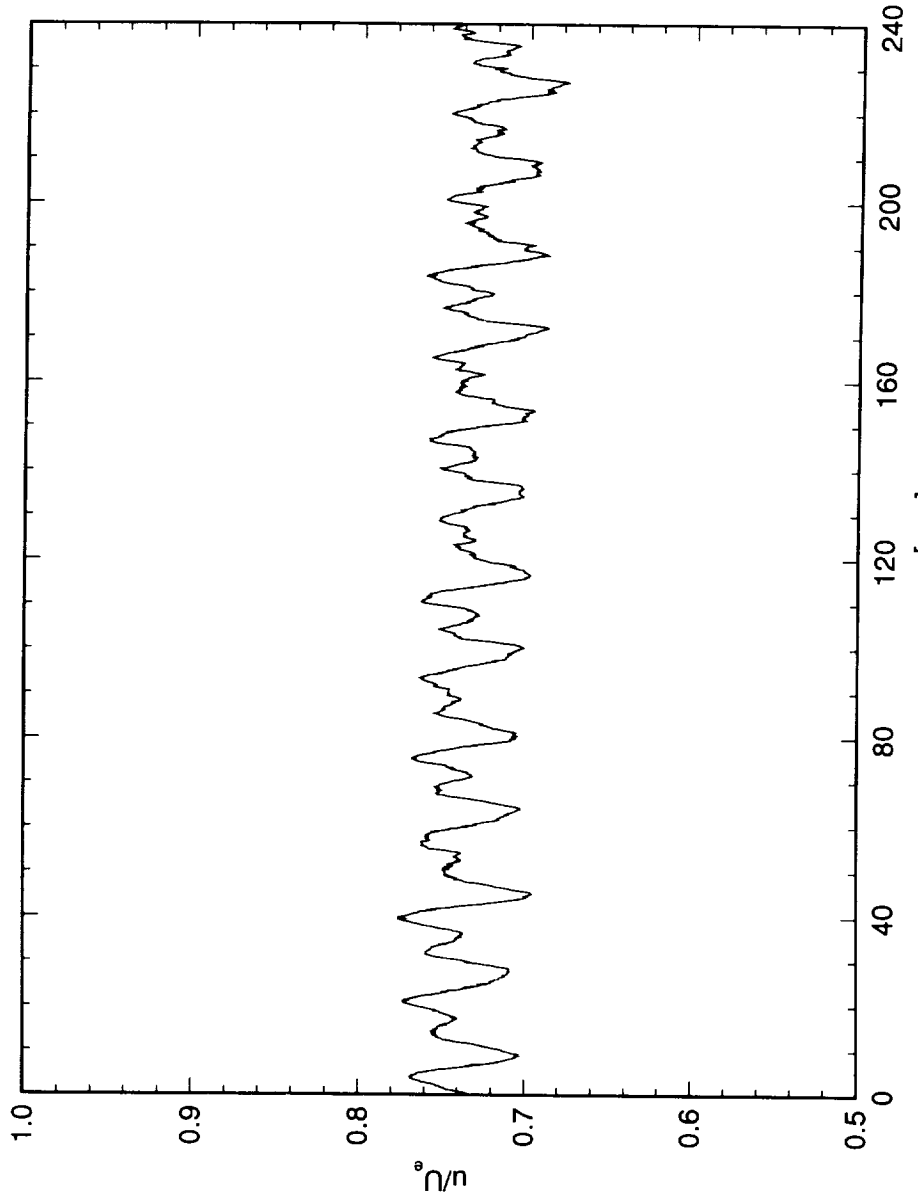

Figure 7.53. Spanwise hot-wire scan at $x/c = 0.40$. $Re_c = 3.0 \times 10^6$. Full array of 146 μm roughness with 18 mm spacing. Data set Q.

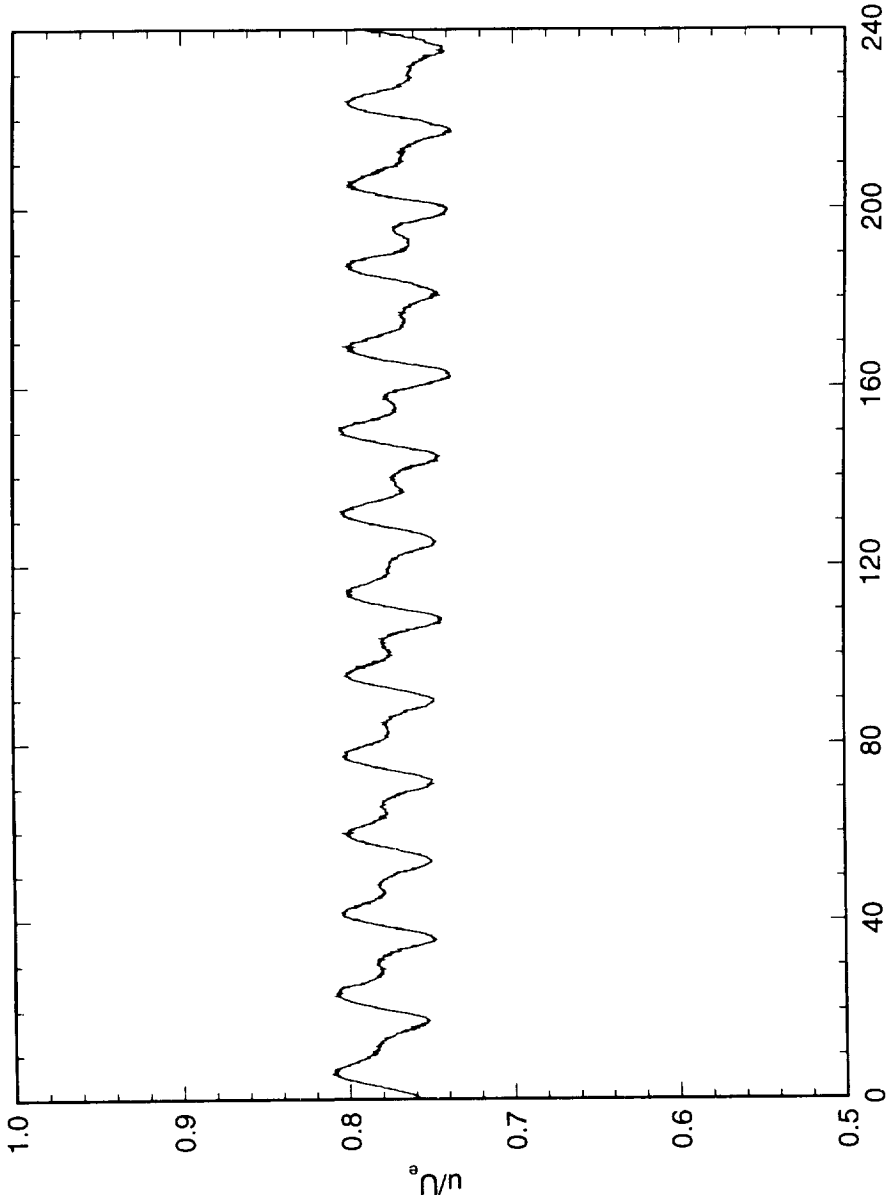

Figure 7.54. Spanwise hot-wire scan at $x/c = 0.60$. $Re_c = 3.0 \times 10^6$. Full array of 146 μm roughness with 18 mm spacing. Data set Q.

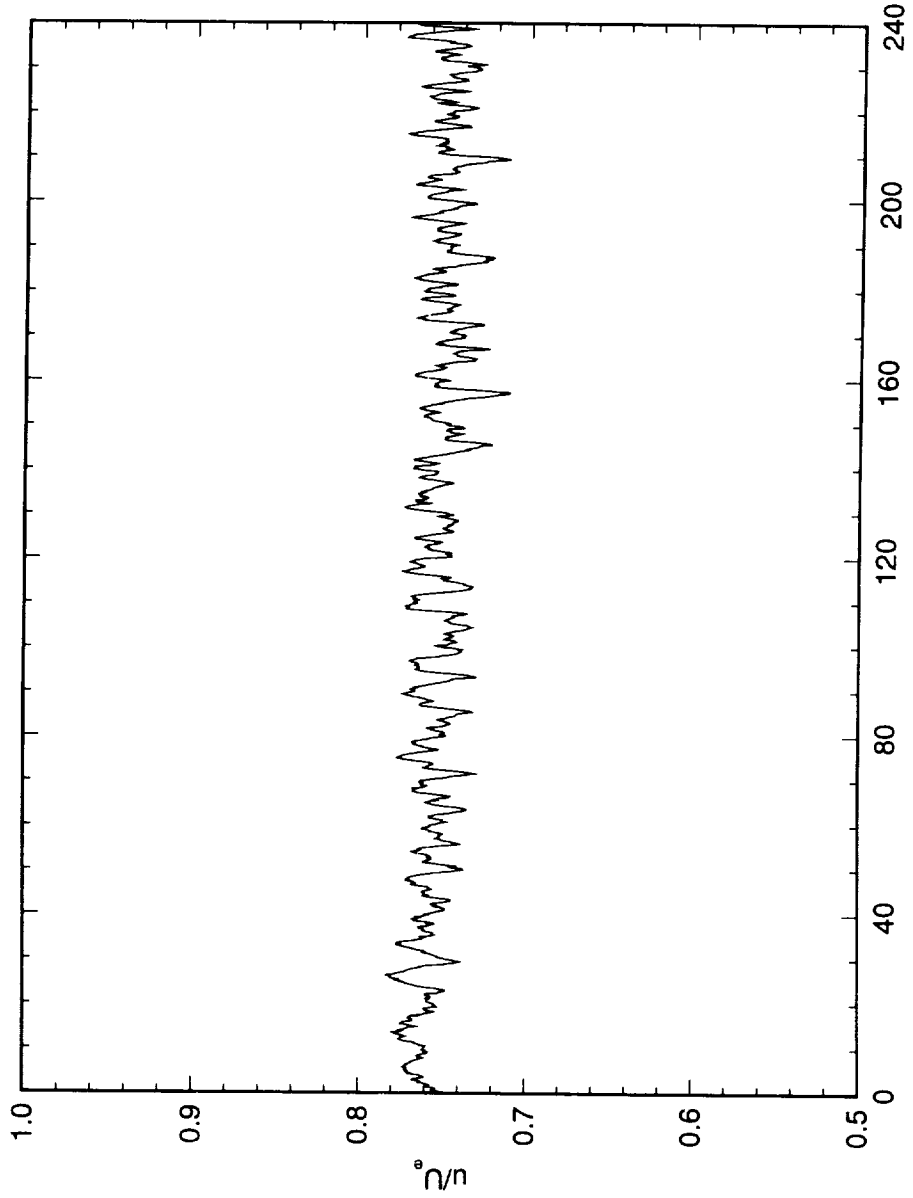

Figure 7.55. Spanwise hot-wire scan at $x/c = 0.20$. $Re_c = 3.0 \times 10^6$. Full array of 73 μm roughness with 21 mm spacing. Data set *R*.

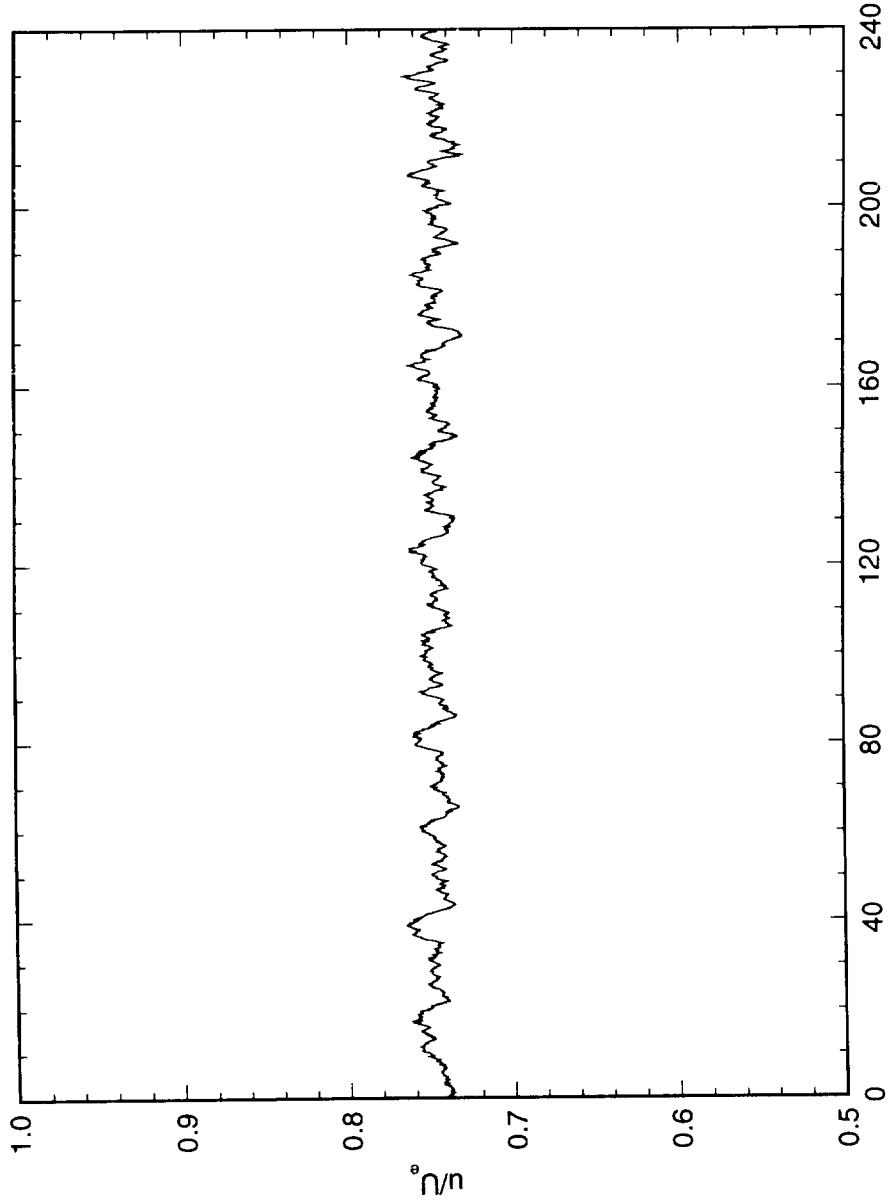

Figure 7.56. Spanwise hot-wire scan at $x/c = 0.40$. $Re_c = 3.0 \times 10^6$. Full array of 73 μm roughness with 21 mm spacing. Data set R.

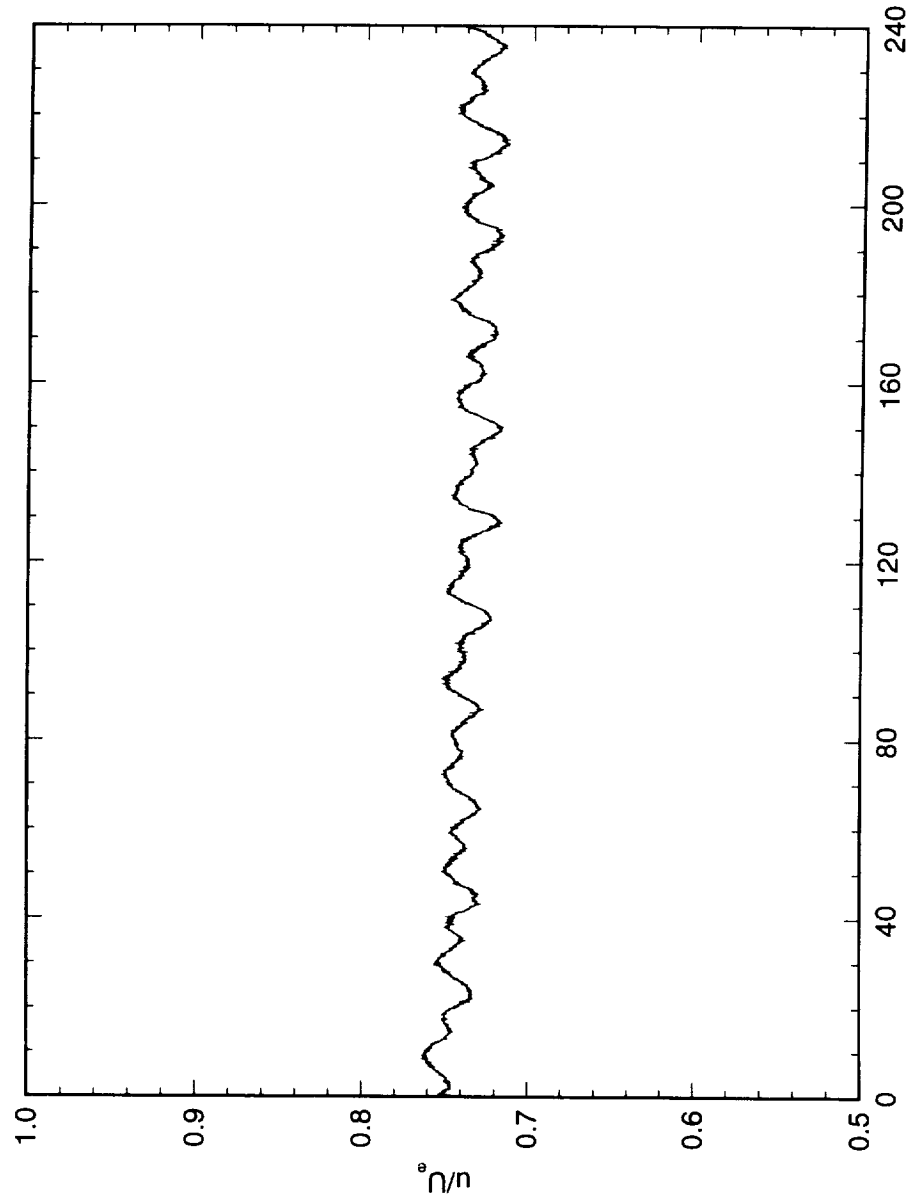

Figure 7.57. Spanwise hot-wire scan at $x/c = 0.60$. $Re_c = 3.0 \times 10^6$. Full array of 73 μm roughness with 21 mm spacing. Data set R.

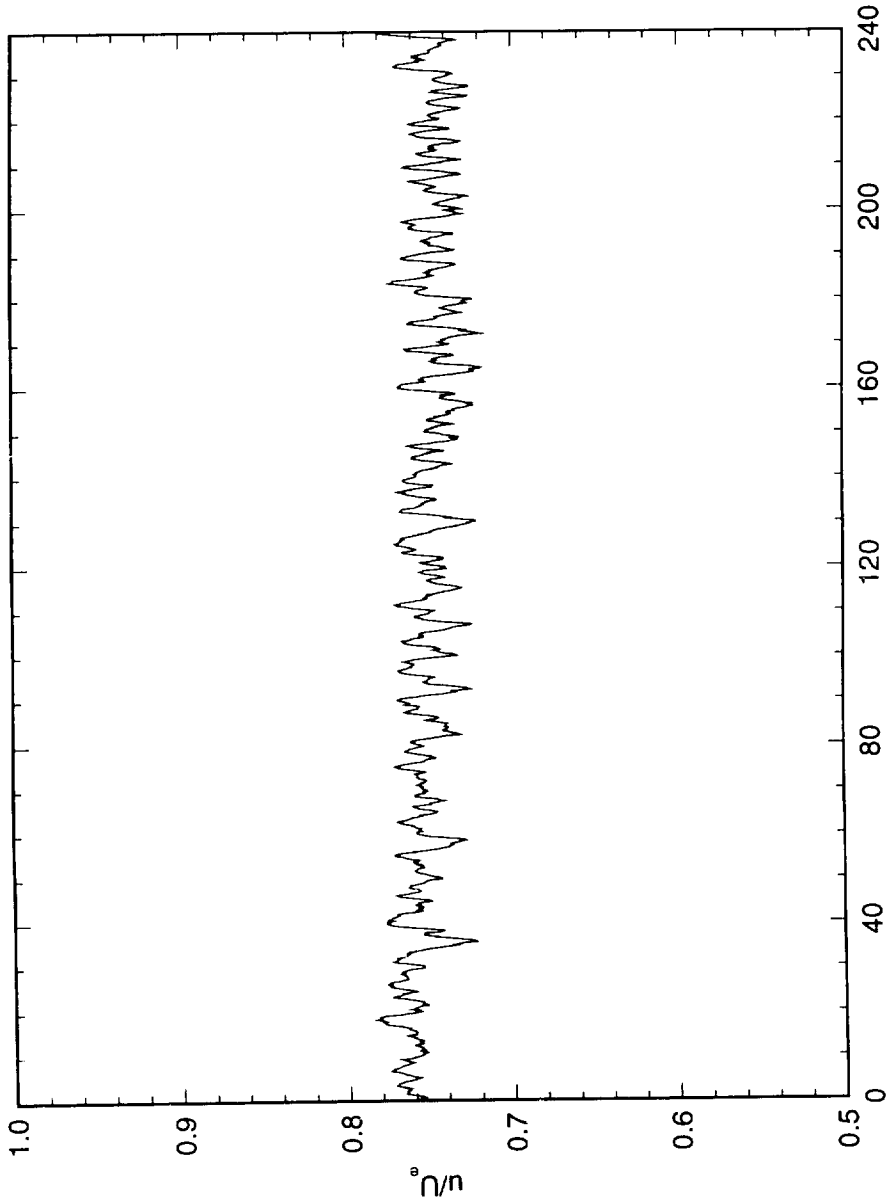

Figure 7.58. Spanwise hot-wire scan at $x/c = 0.20$. $Re_c = 3.0 \times 10^6$. Full array of 73 μm roughness with 24 mm spacing. Data set S.

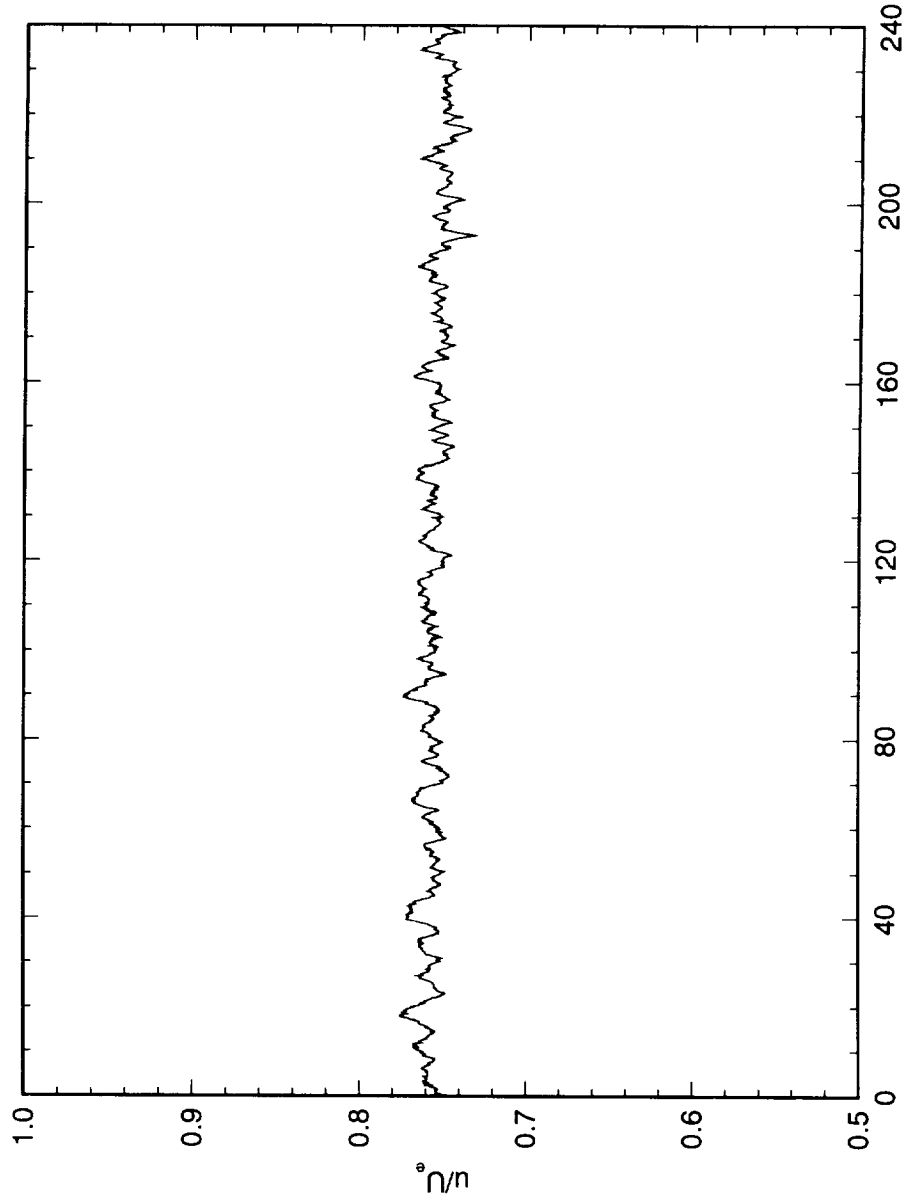

Figure 7.59. Spanwise hot-wire scan at $x/c = 0.40$. $Re_c = 3.0 \times 10^6$. Full array of 73 μm roughness with 24 mm spacing. Data set S.

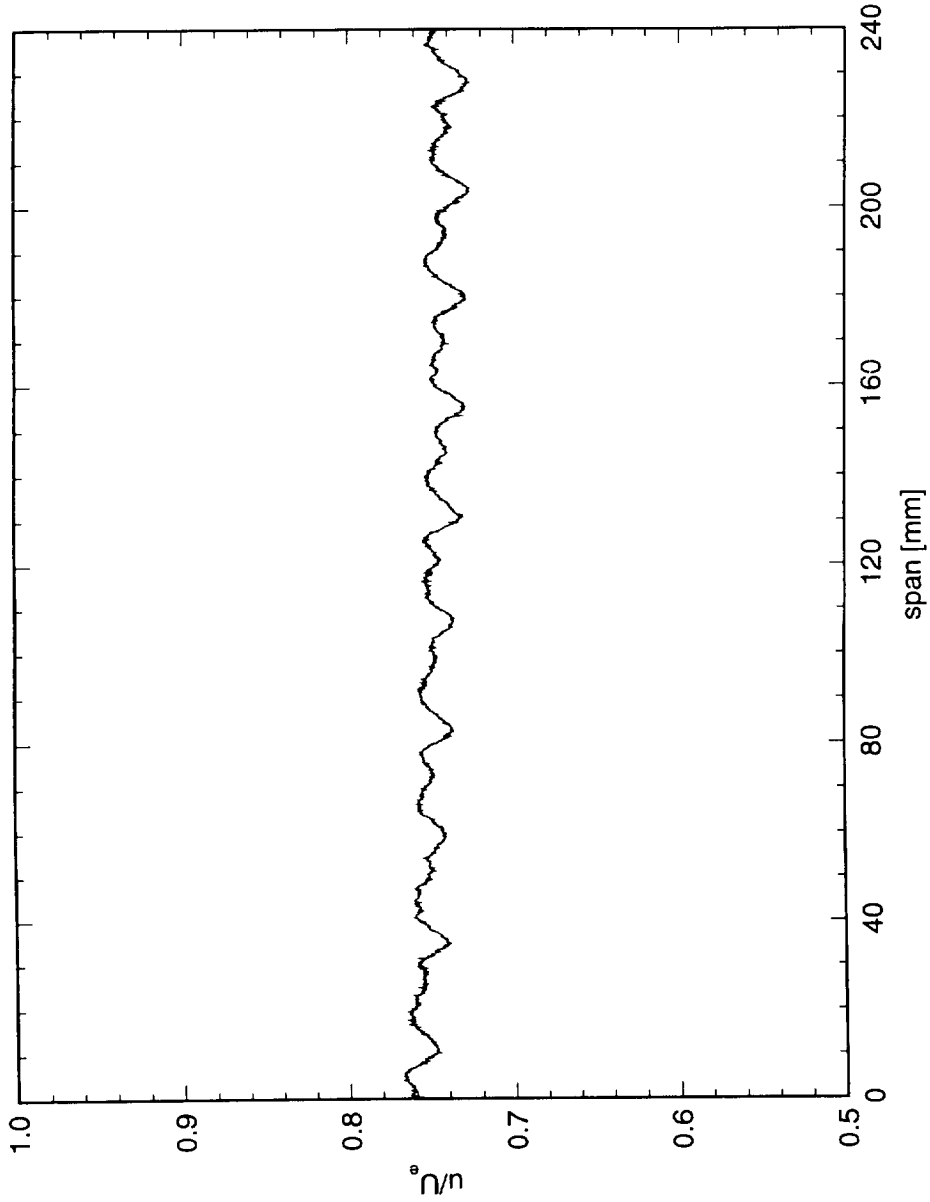

Figure 7.60. Spanwise hot-wire scan at $x/c = 0.60$. $Re_c = 3.0 \times 10^6$. Full array of 73 μm roughness with 24 mm spacing. Data set S.

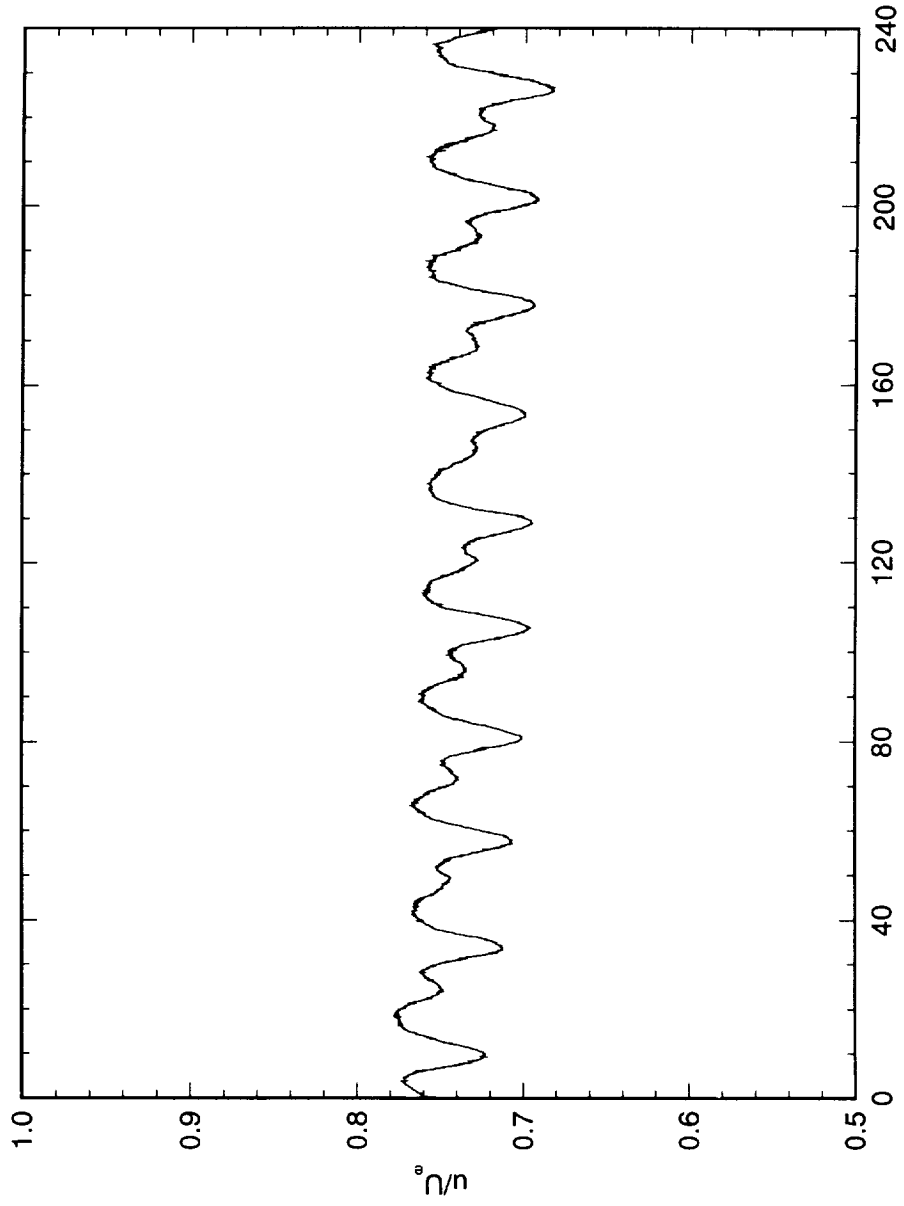

Figure 7.61. Spanwise hot-wire scan at $x/c = 0.60$. $Re_c = 3.0 \times 10^6$. Full array of 146 μm roughness with 24 mm spacing. Data set T.

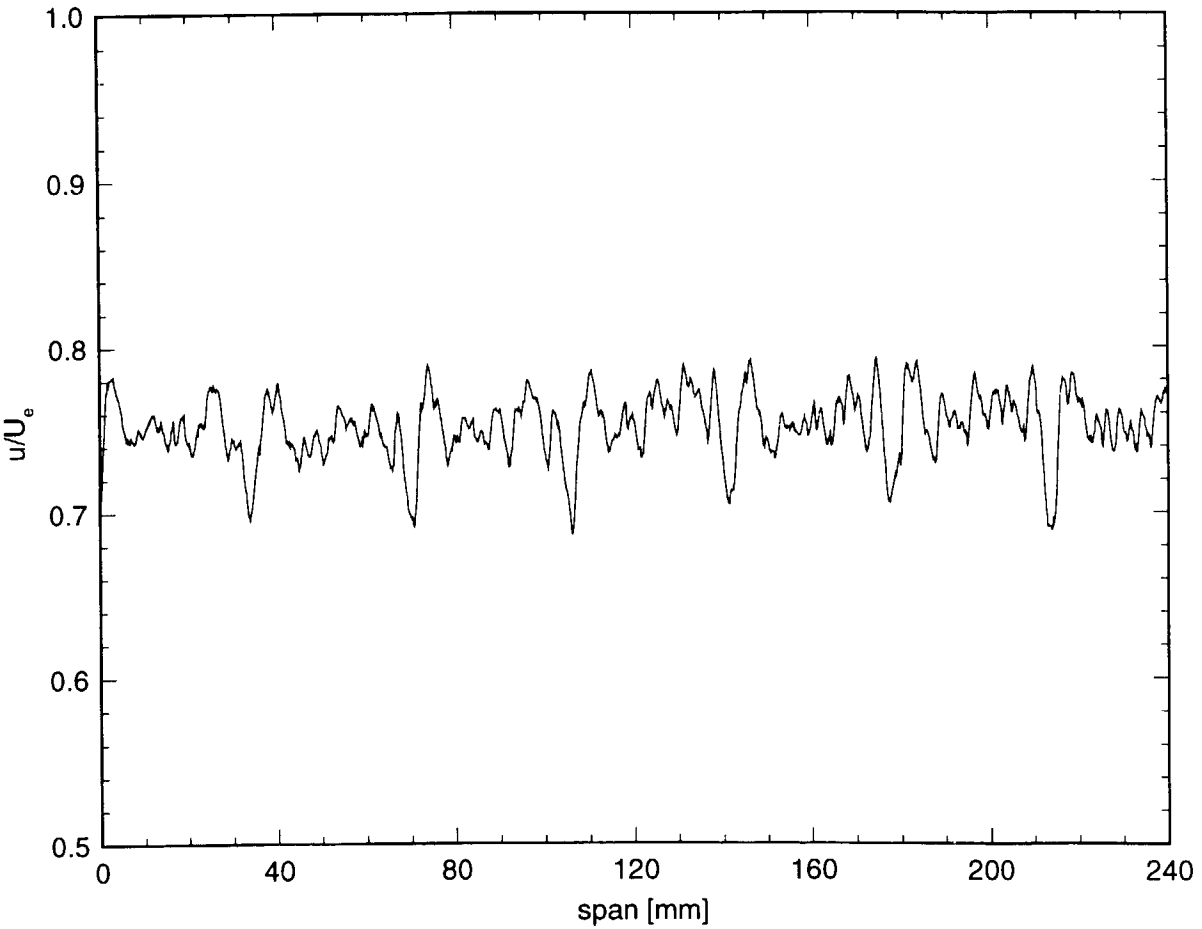

Figure 7.62. Spanwise hot-wire scan at $x/c = 0.20$. $Re_c = 3.0 \times 10^6$. Full array of 146 μm roughness with 36 mm spacing. Data set U.

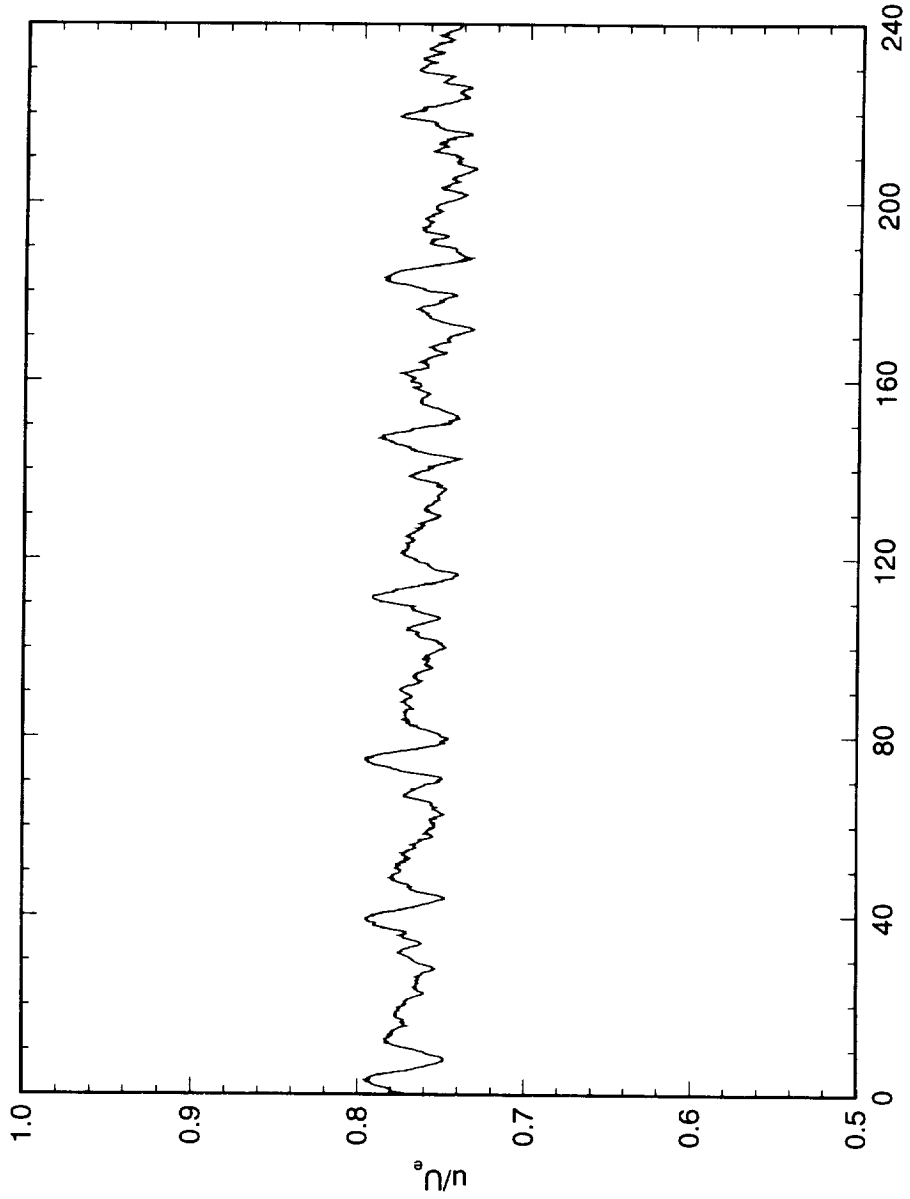

Figure 7.63. Spanwise hot-wire scan at $x/c = 0.40$. $Re_c = 3.0 \times 10^6$. Full array of 146 μm roughness with 36 mm spacing. Data set U.

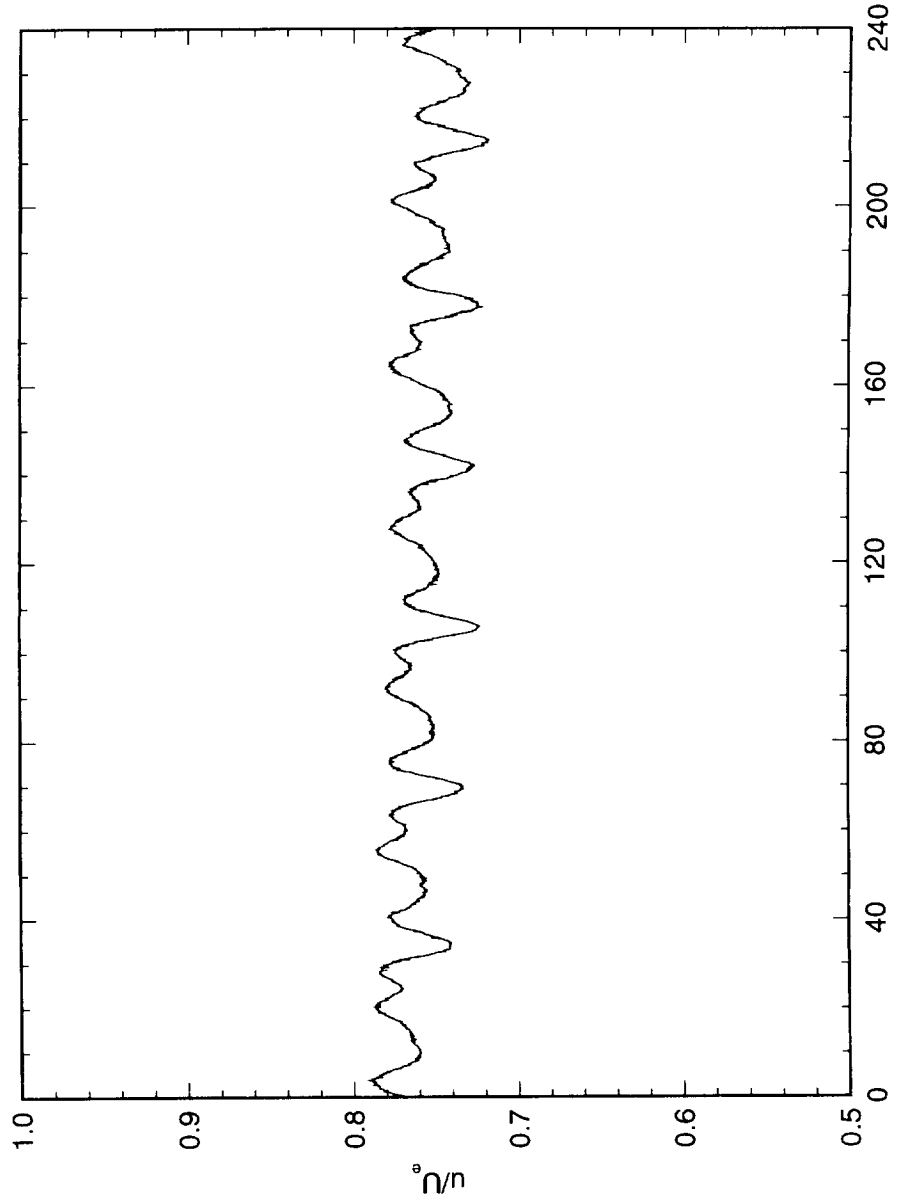

Figure 7.64. Spanwise hot-wire scan at $x/c = 0.60$. $Re_c = 3.0 \times 10^6$. Full array of 146 μm roughness with 36 mm spacing. Data set U.

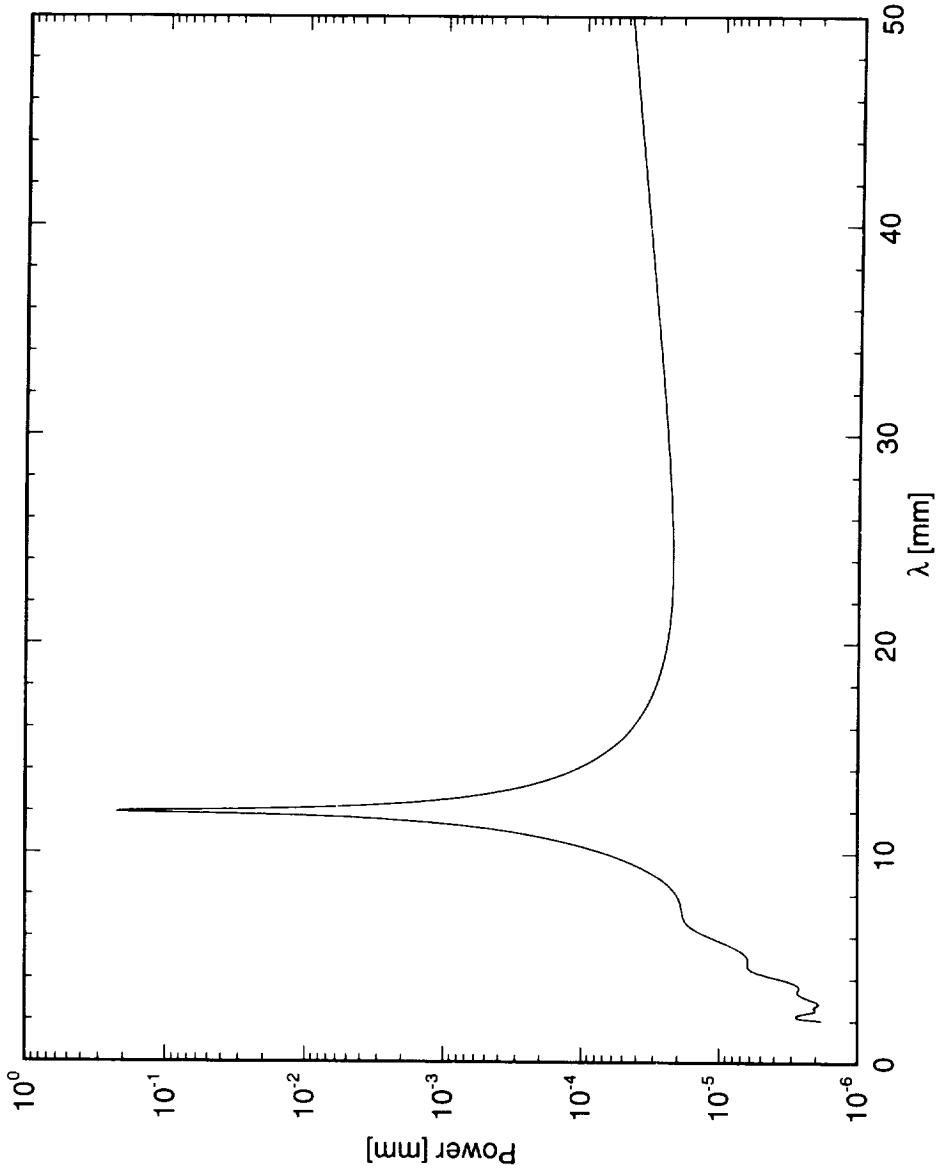

Figure 7.65. Maximum-entropy power spectrum of spanwise hot-wire scan. $Re_c = 3.0 \times 10^6$. Full array of 146 μm roughness with 12 mm spacing. Data set *F*.

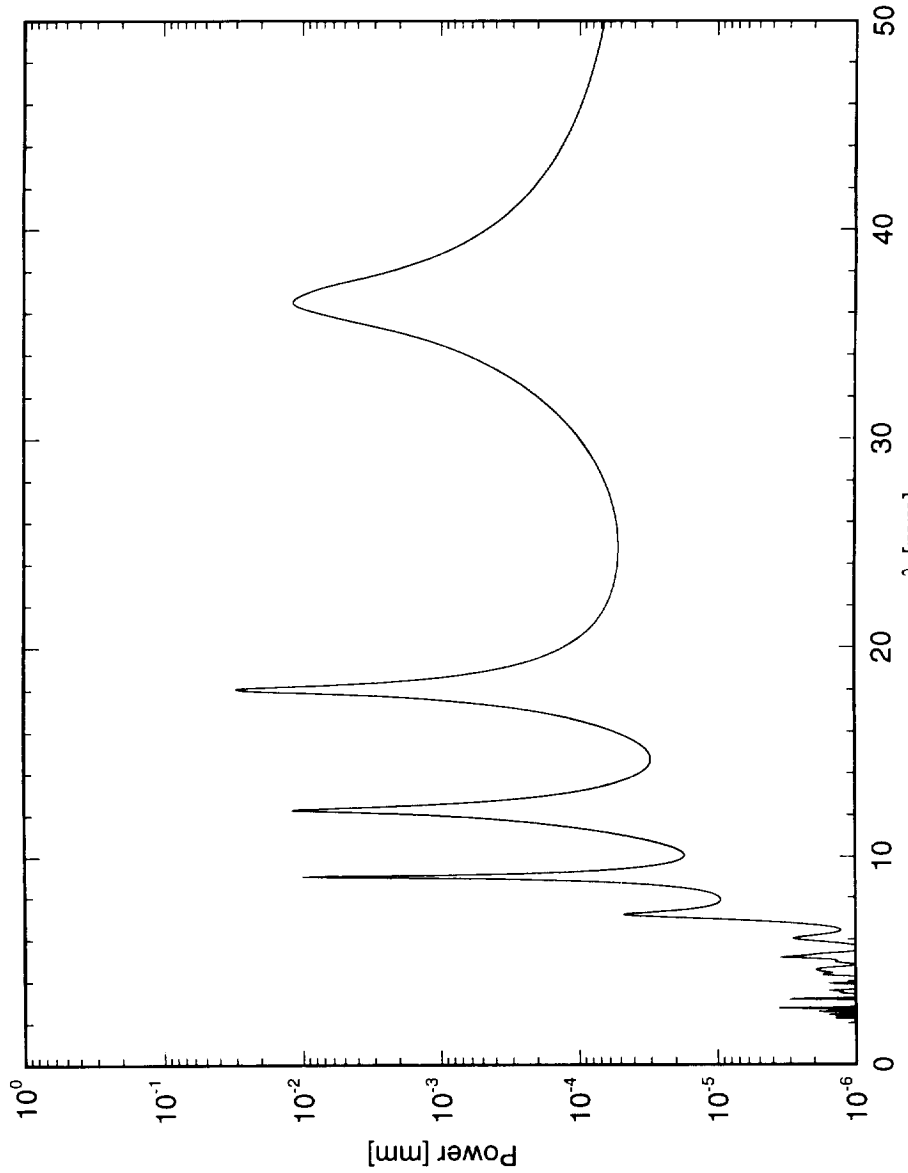

Figure 7.66. Maximum-entropy power spectrum of spanwise hot-wire scan. $Re_c = 3.0 \times 10^6$. Full array of 146 μm roughness with 36 mm spacing. Data set U.

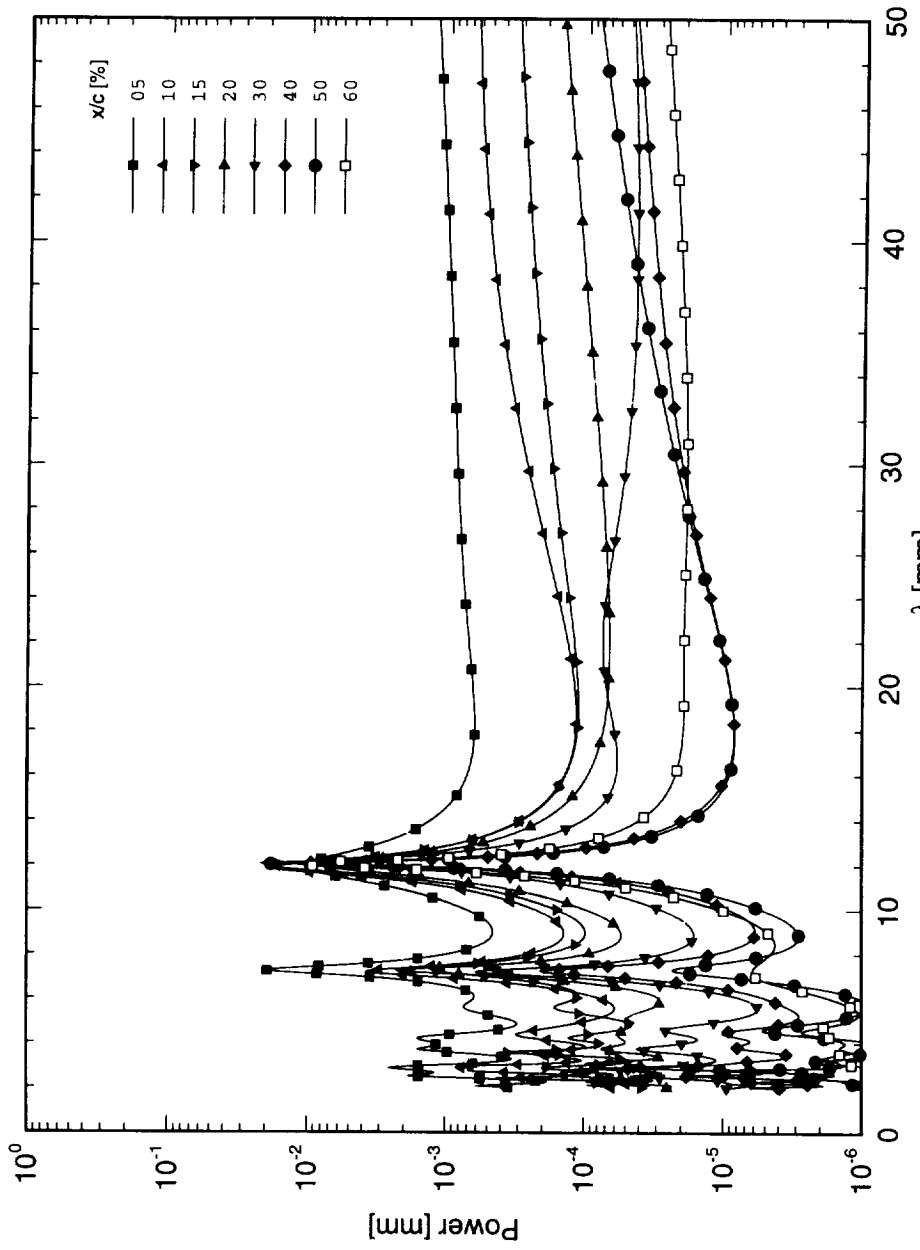

Figure 7.67. Maximum-entropy power spectra of spanwise hot-wire scans. $Re_c = 3.0 \times 10^6$. Full array of 73 μm roughness with 12 mm spacing. Data set *E*.

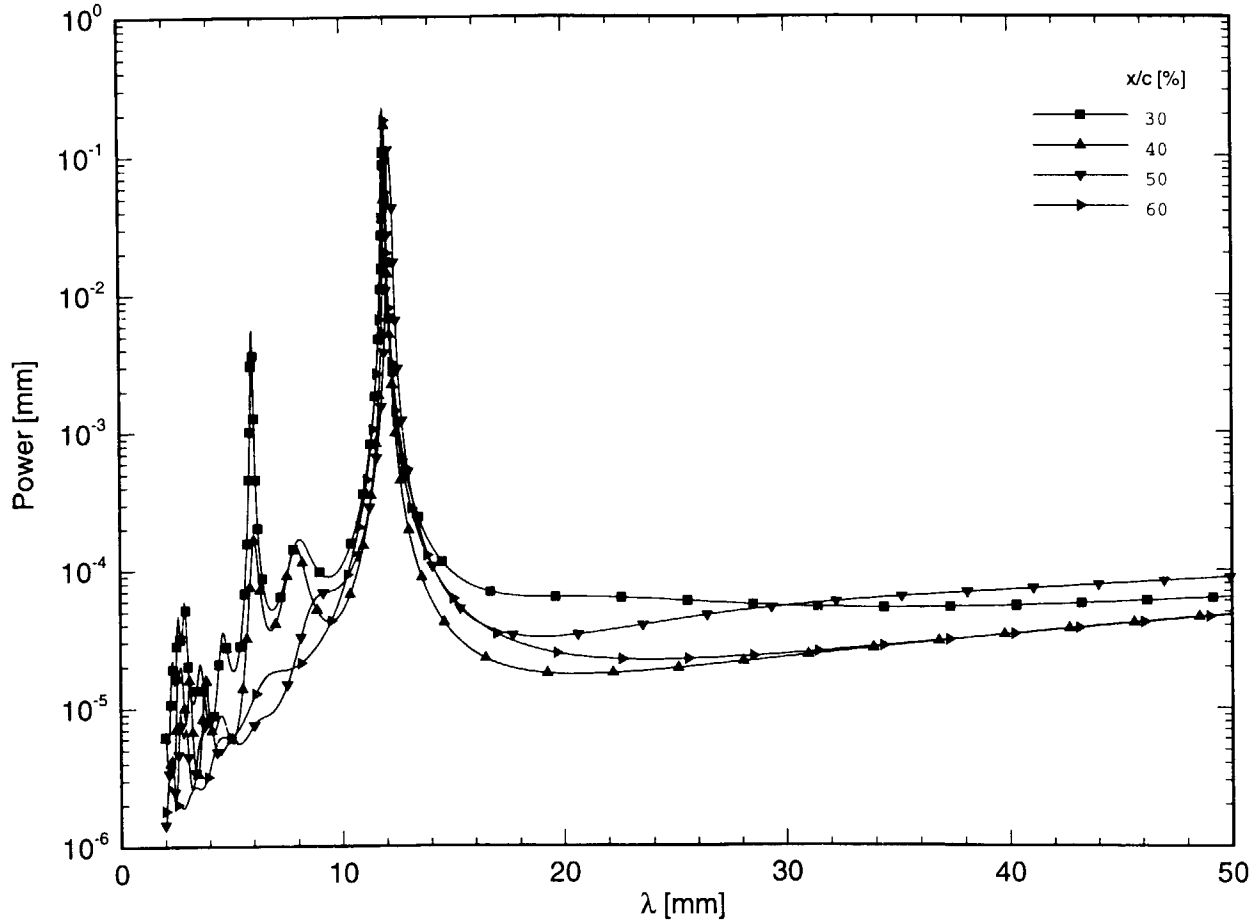

Figure 7.68. Maximum-entropy power spectra of spanwise hot-wire scans. $Re_c = 3.0 \times 10^6$. Full array of 146 μm roughness with 12 mm spacing. Data set *F*.

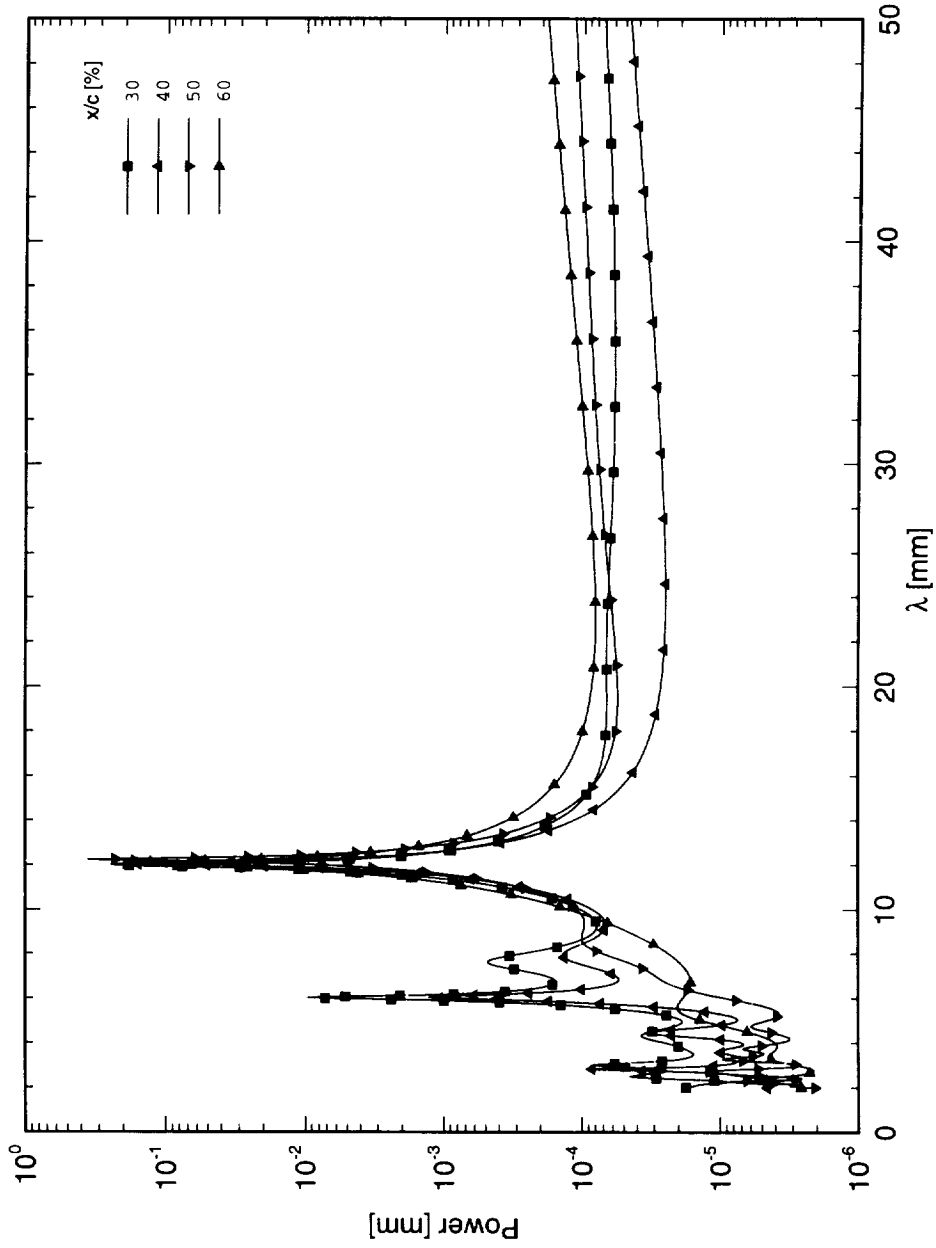

Figure 7.69. Maximum-entropy power spectra of spanwise hot-wire scans. $Re_c = 3.2 \times 10^6$. Full array of 146 μm roughness with 12 mm spacing. Data set G.

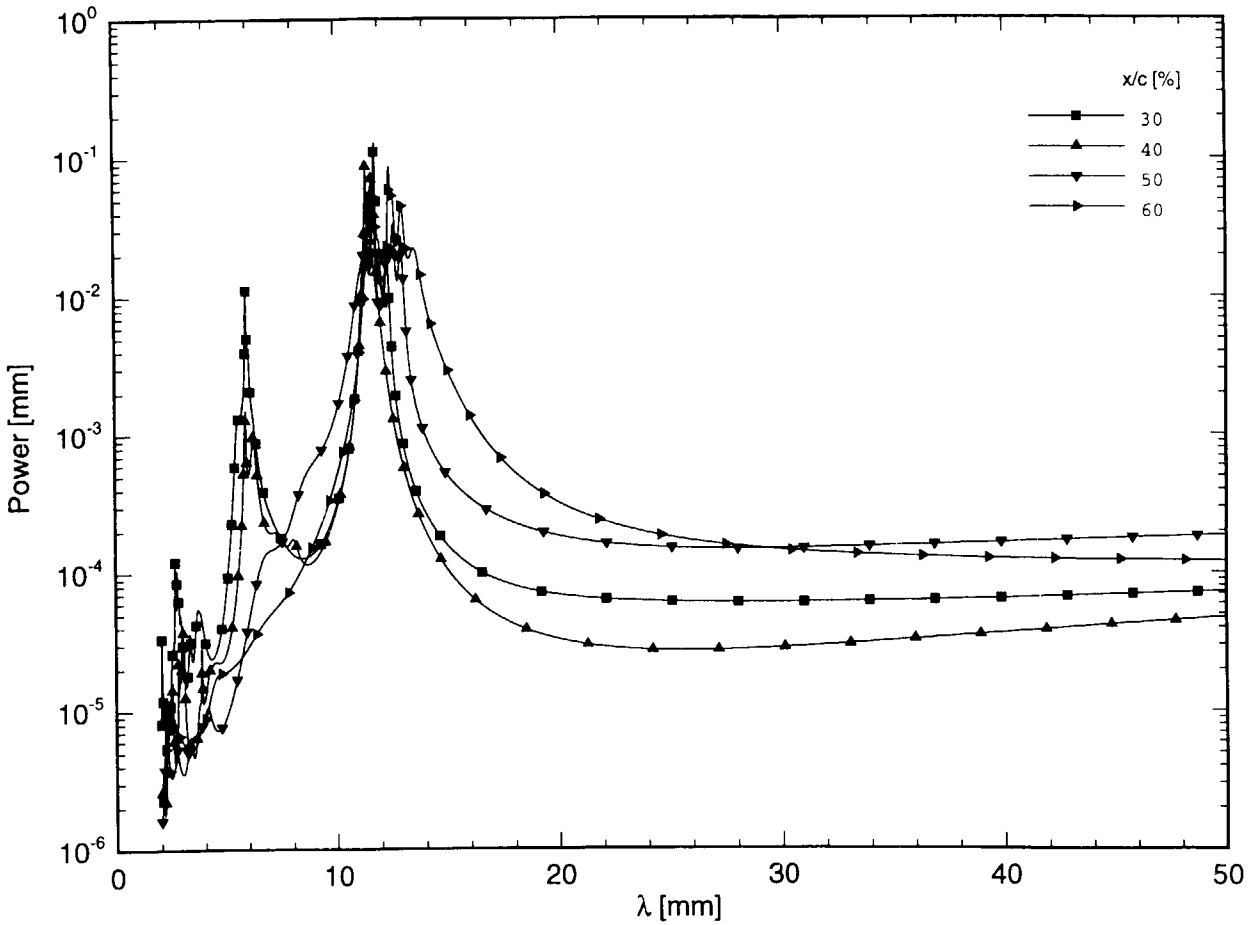

Figure 7.70. Maximum-entropy power spectra of spanwise hot-wire scans. $Re_c = 3.4 \times 10^6$. Full array of 146 μm roughness with 12 mm spacing. Data set *H*.

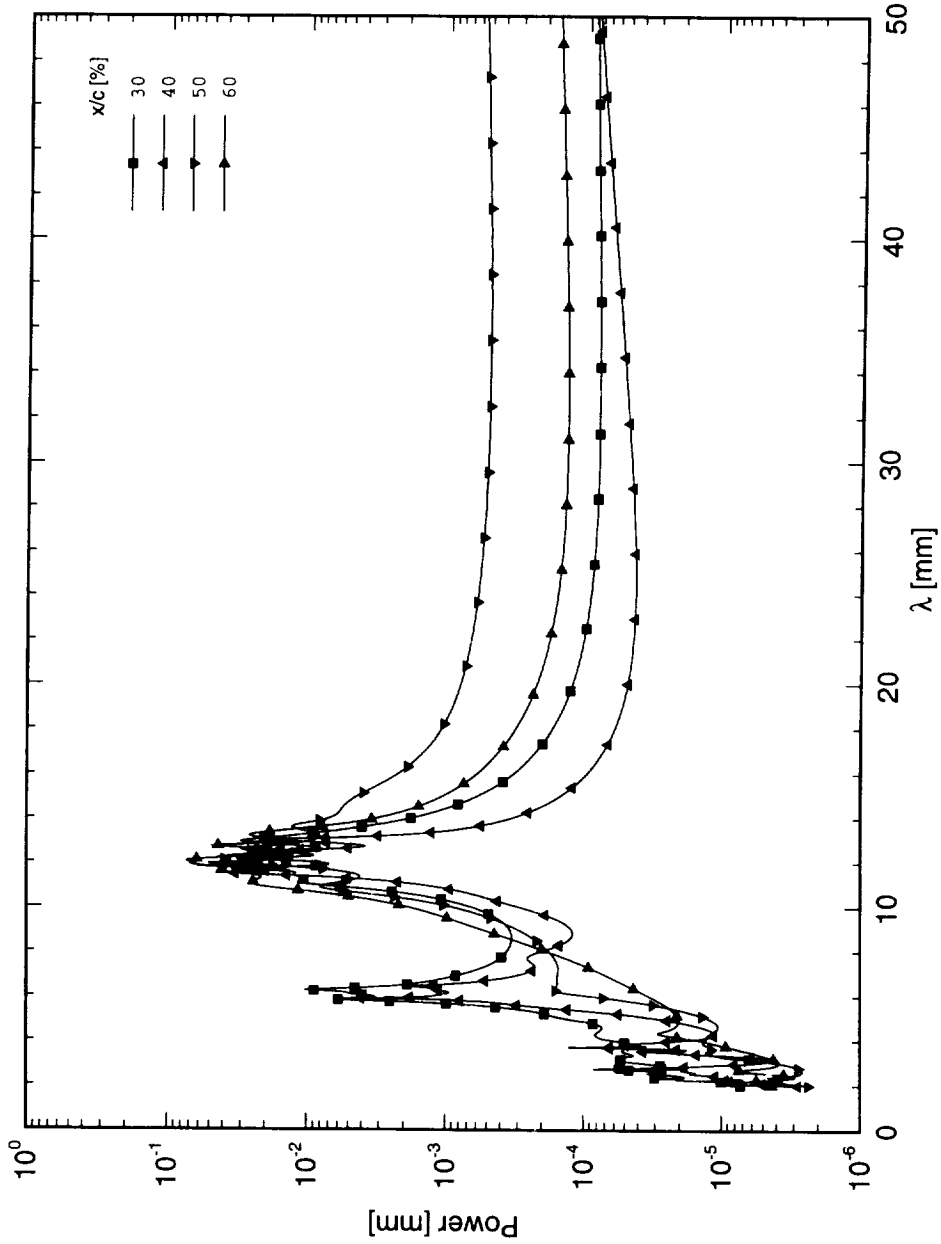

Figure 7.71. Maximum-entropy power spectra of spanwise hot-wire scans. $Re_c = 3.6 \times 10^6$. Full array of 146 μm roughness with 12 mm spacing. Data set *I*.

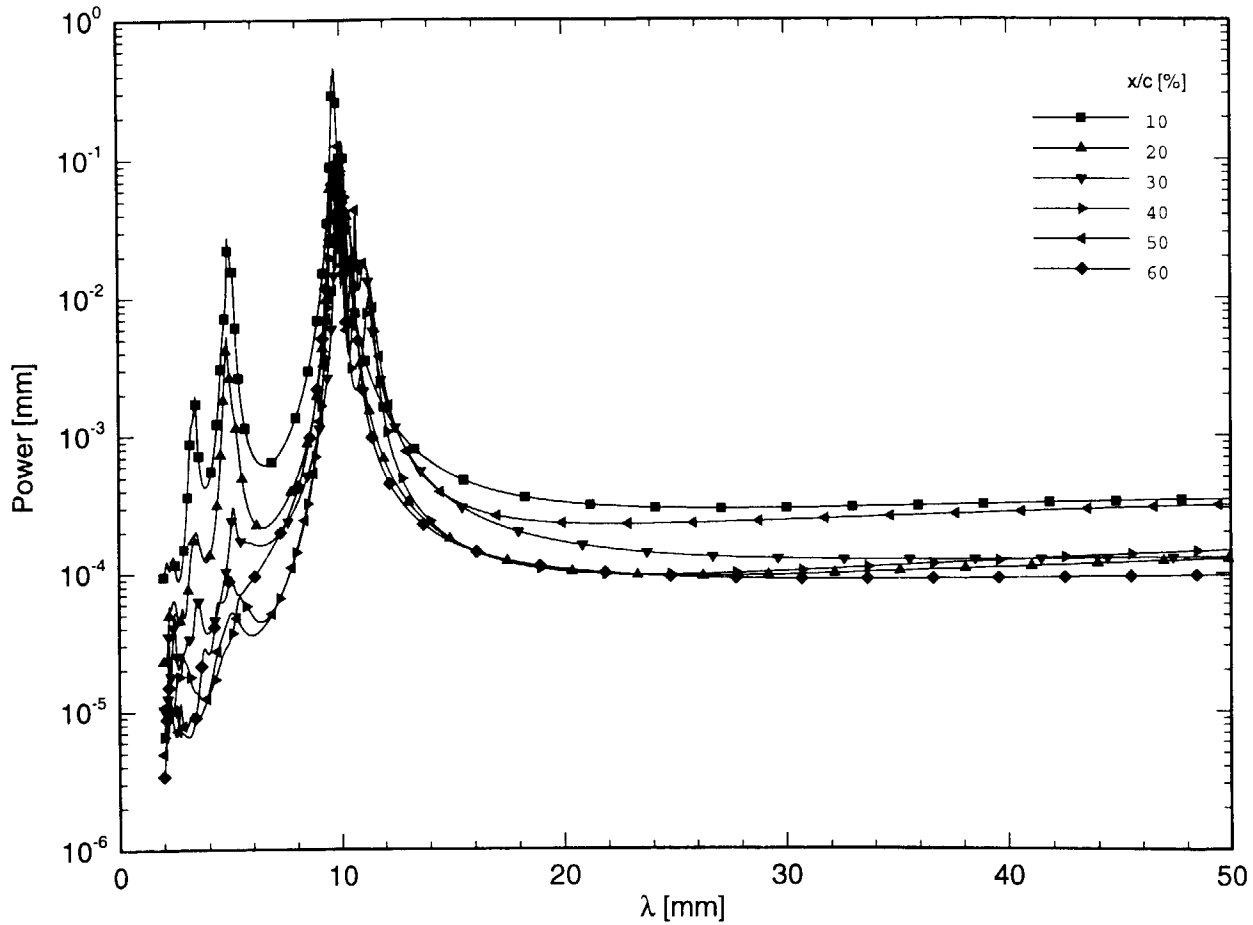

Figure 7.72. Maximum-entropy power spectra of spanwise hot-wire scans. $Re_c = 3.0 \times 10^6$. Full array of 146 μm roughness with 10 mm spacing. Data set K.

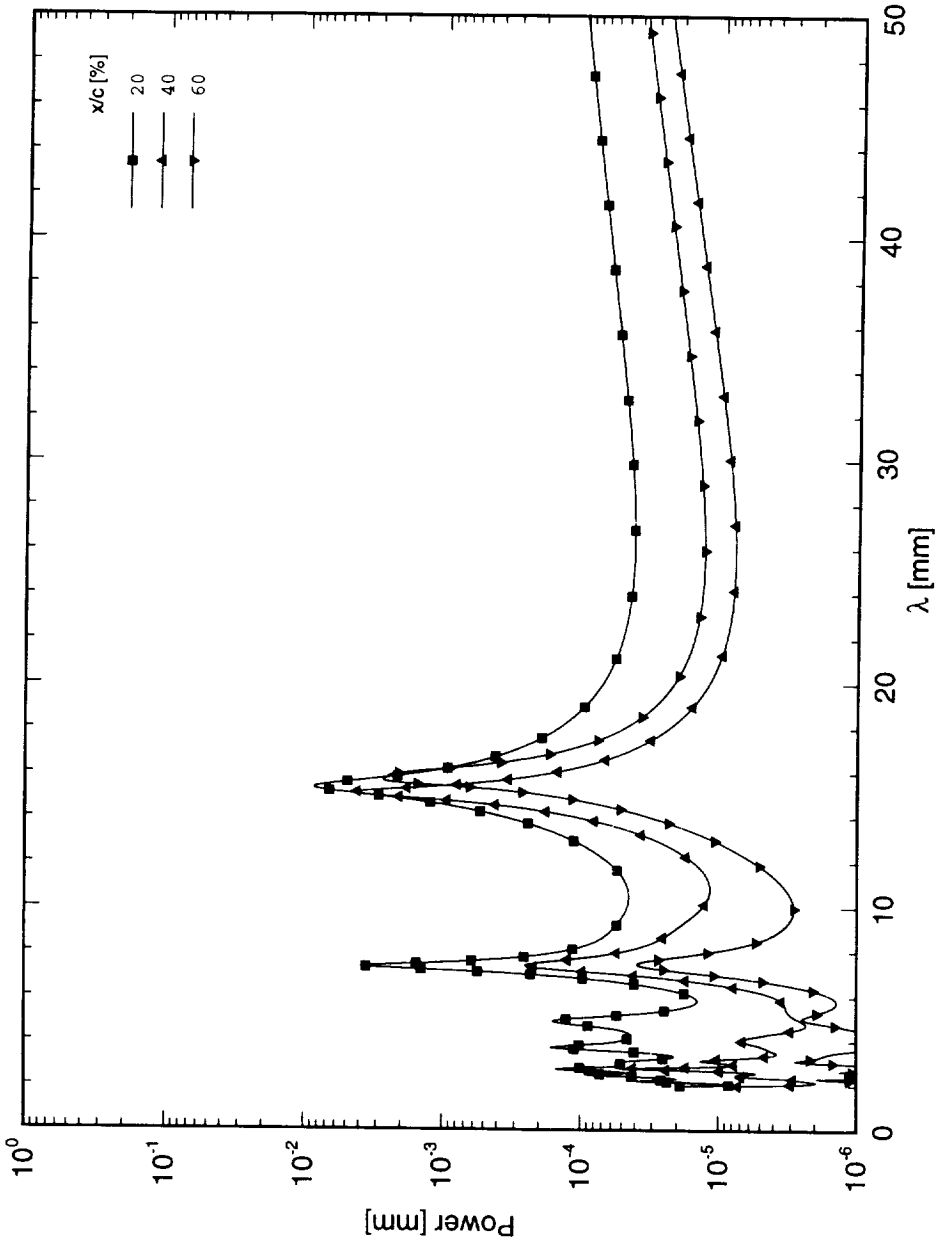

Figure 7.73. Maximum-entropy power spectra of spanwise hot-wire scans. $Re_c = 3.0 \times 10^6$. Full array of 73 μm roughness with 15 mm spacing. Data set *M*.

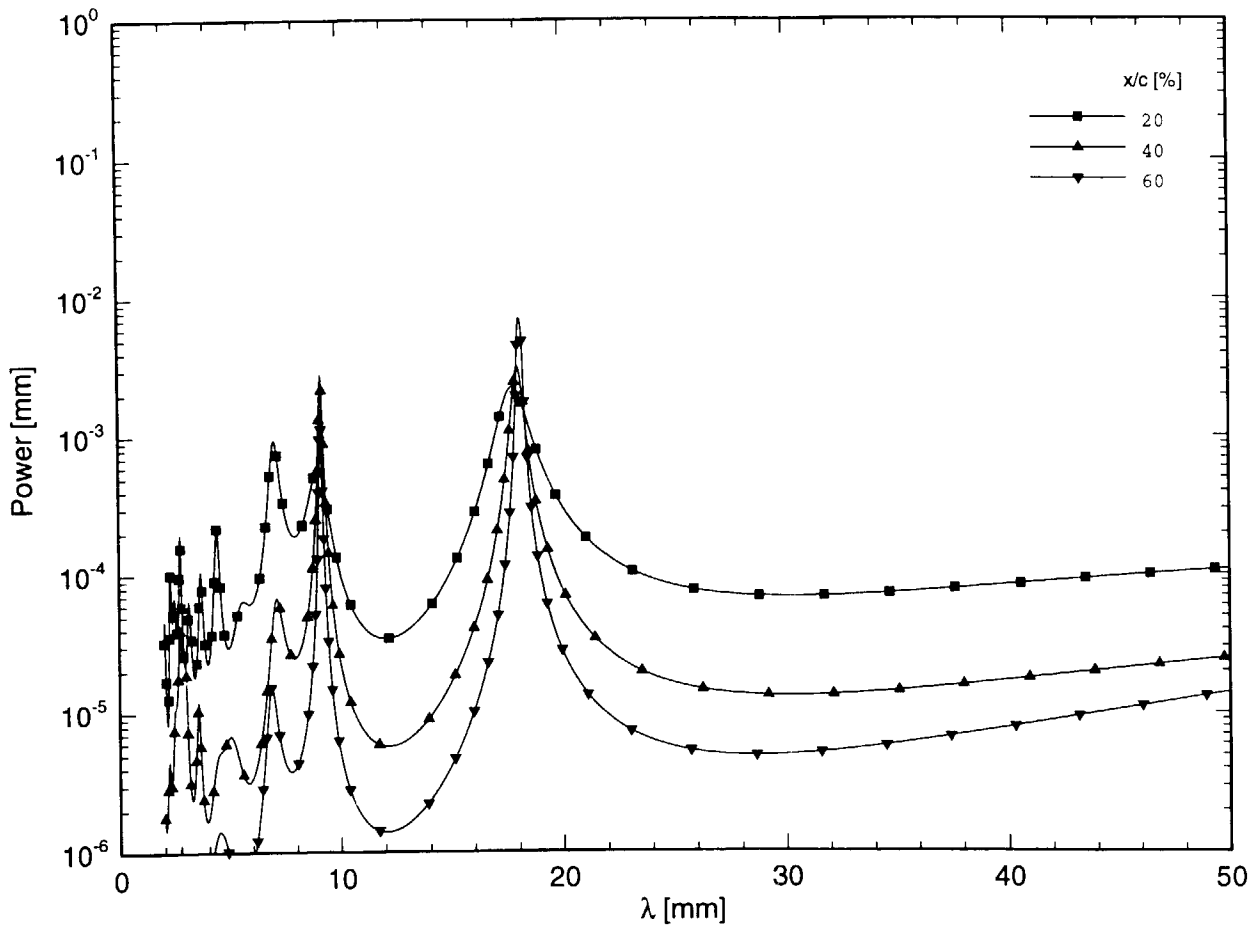

Figure 7.74. Maximum-entropy power spectra of spanwise hot-wire scans. $Re_c = 3.0 \times 10^6$. Full array of 73 μm roughness with 18 mm spacing. Data set *N*.

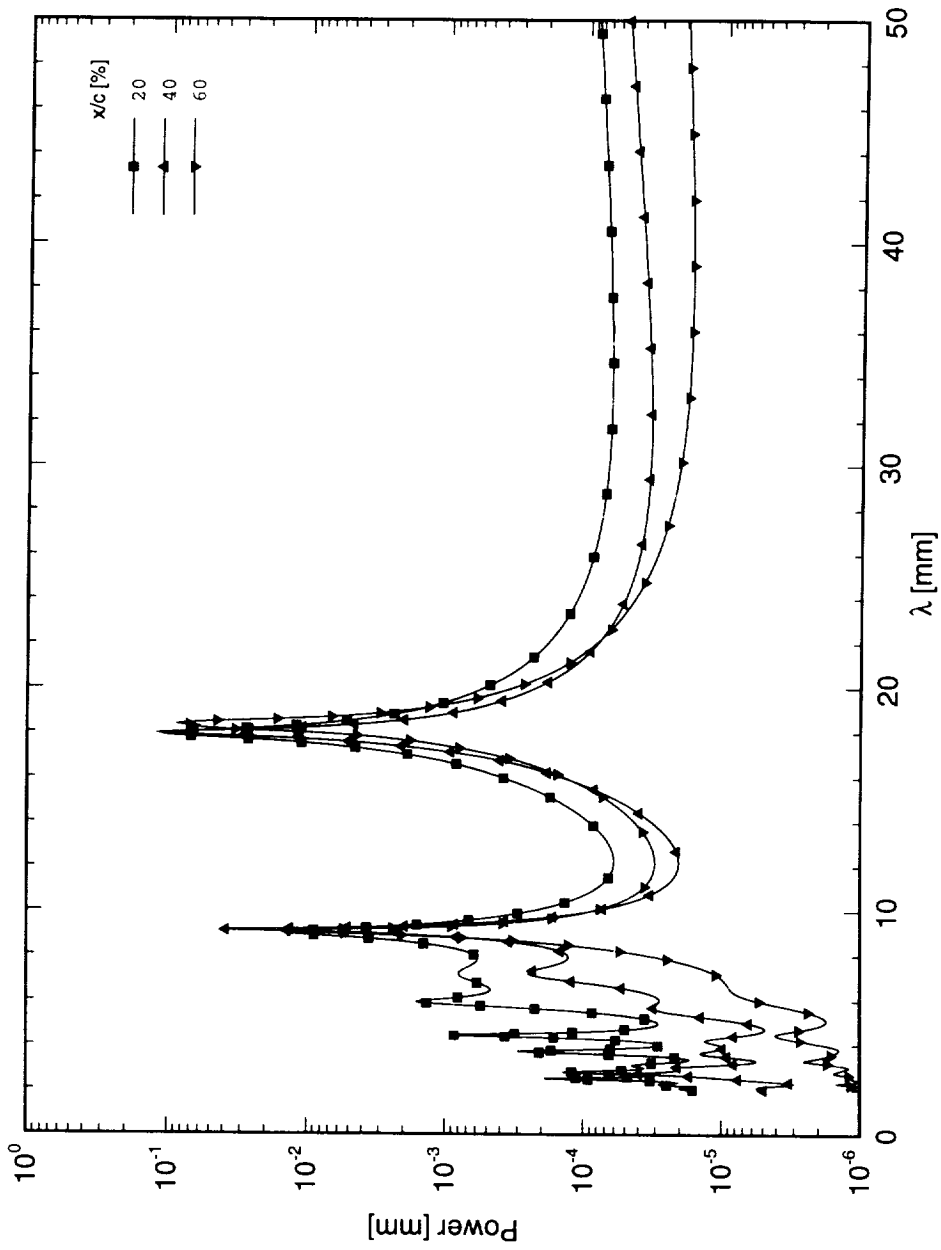

Figure 7.75. Maximum-entropy power spectra of spanwise hot-wire scans. $Re_c = 3.0 \times 10^6$. Full array of 146 μm roughness with 18 mm spacing. Data set Q.

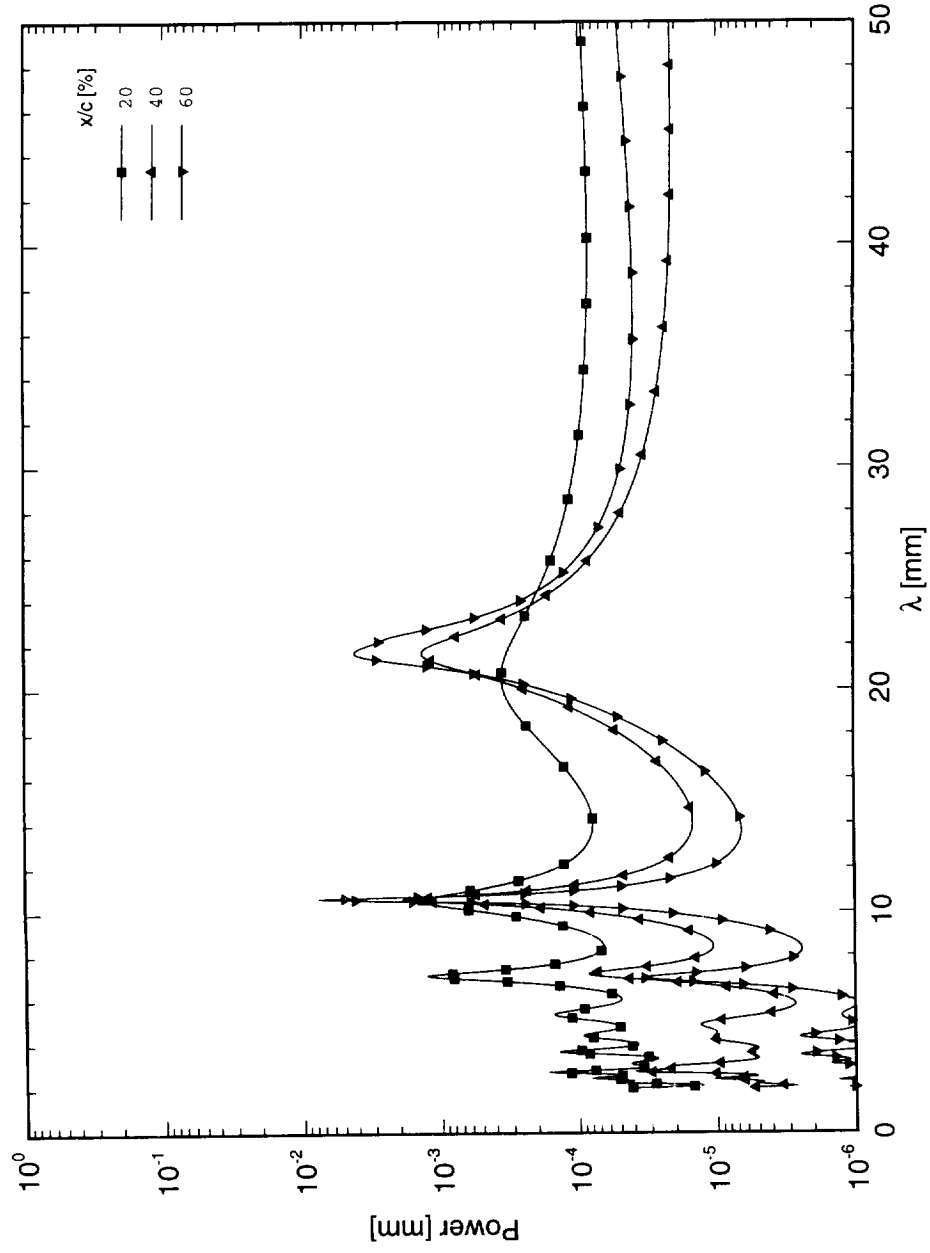

Figure 7.76. Maximum-entropy power spectra of spanwise hot-wire scans. $Re_c = 3.0 \times 10^6$. Full array of 73 μm roughness with 21 mm spacing. Data set R.

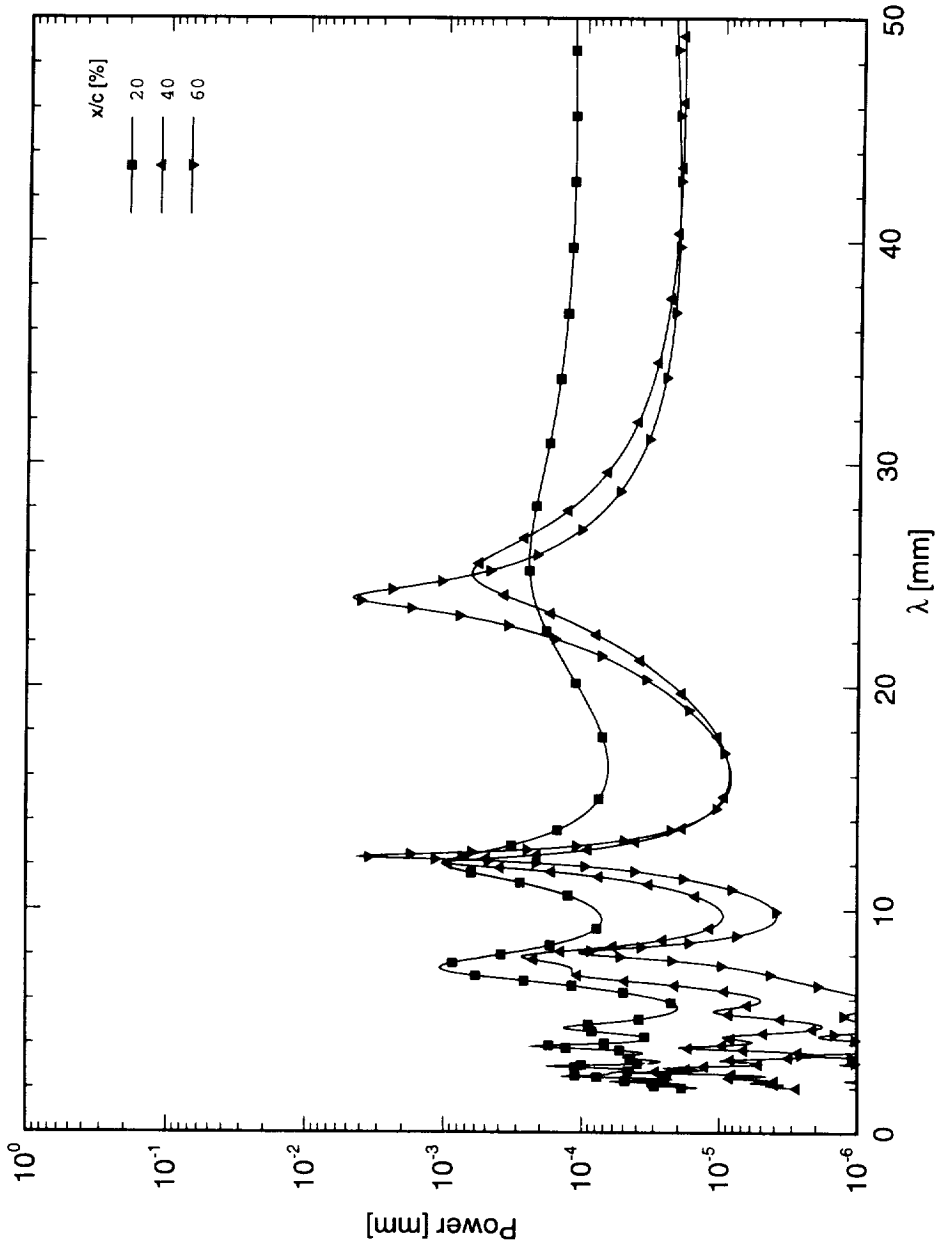

Figure 7.77. Maximum-entropy power spectra of spanwise hot-wire scans. $Re_c = 3.0 \times 10^6$. Full array of 73 μm roughness with 24 mm spacing. Data set S.

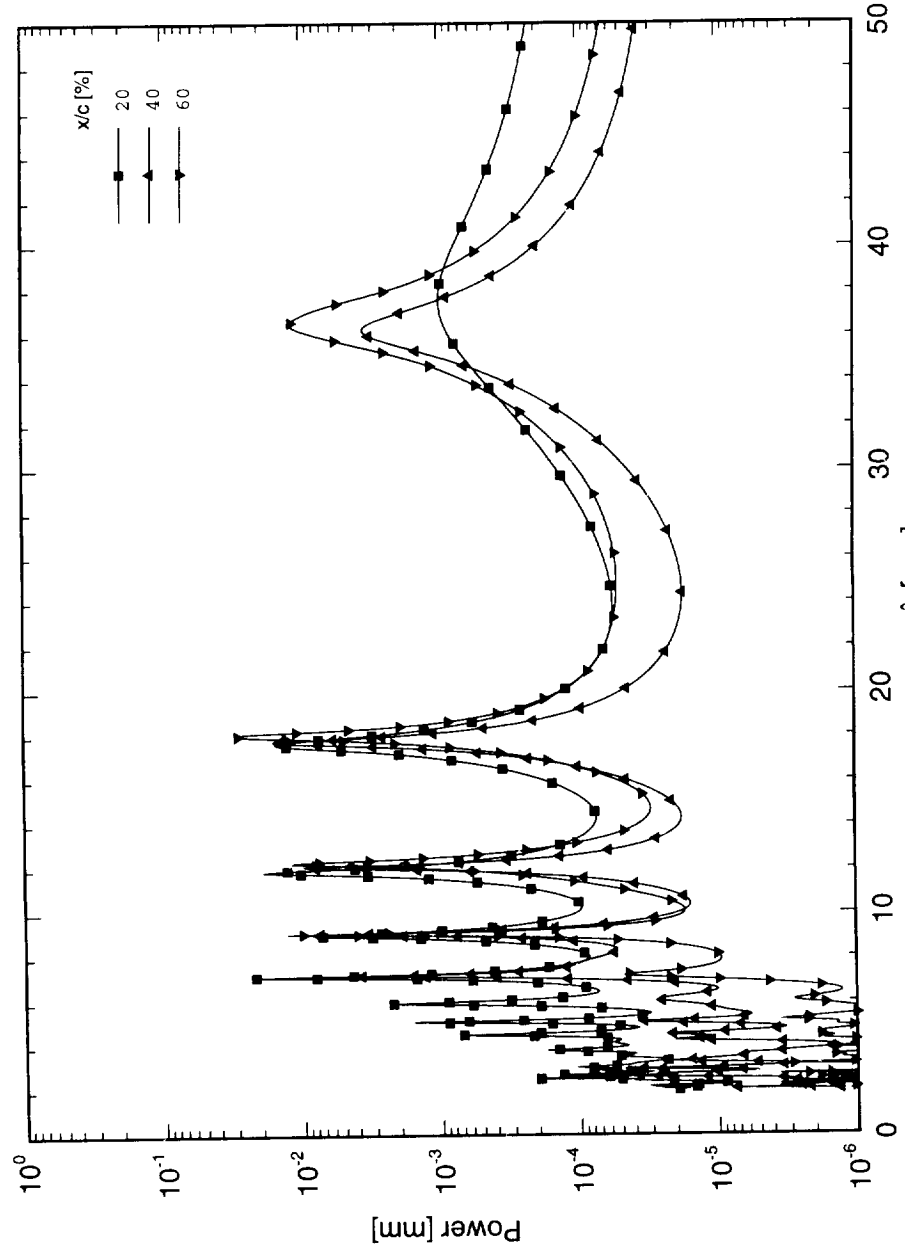

Figure 7.78. Maximum-entropy power spectra of spanwise hot-wire scans. $Re_c = 3.0 \times 10^6$. Full array of 146 μm roughness with 36 mm spacing. Data set U.

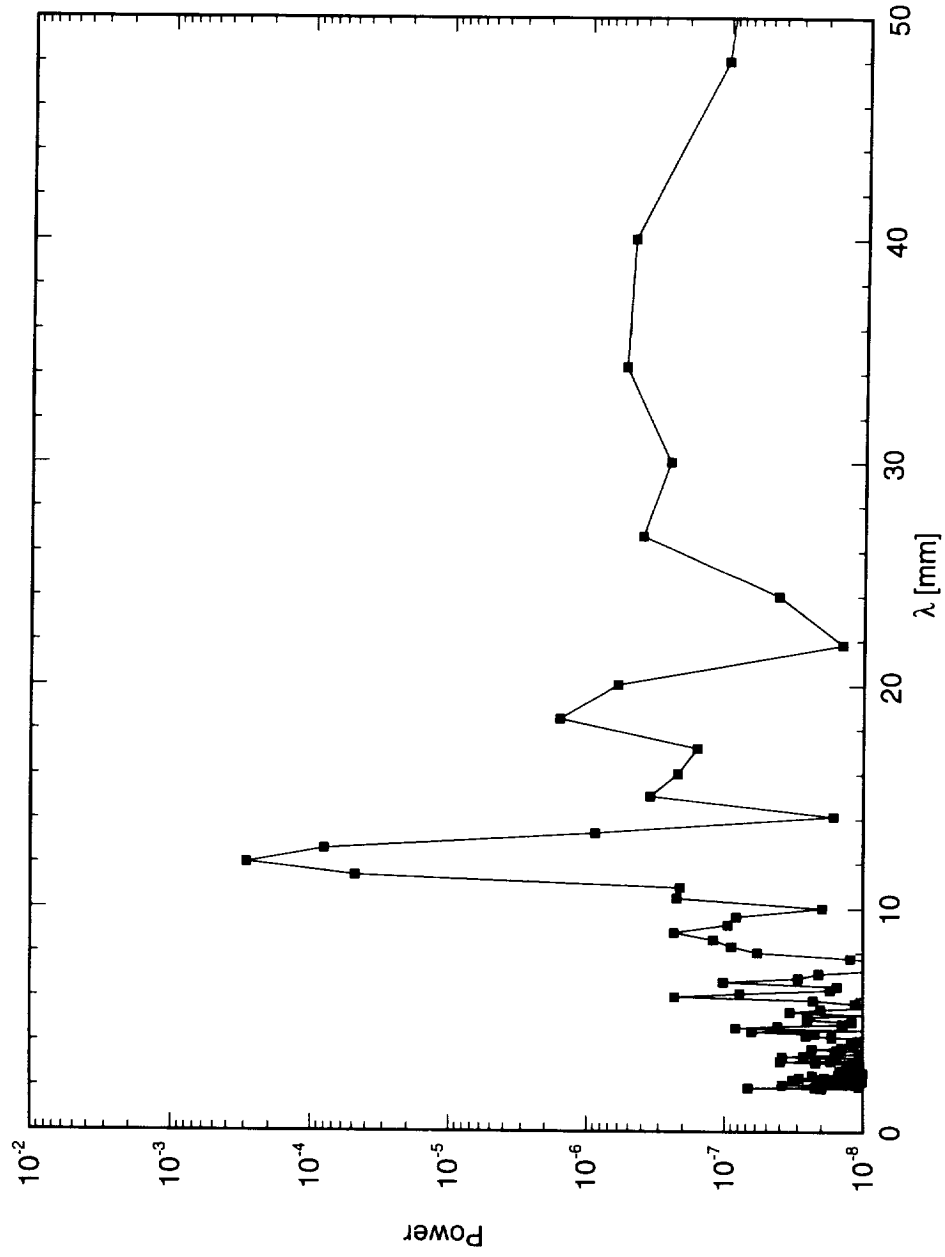

Figure 7.79. FFT power spectrum of spanwise hot-wire scan. $Re_c = 3.0 \times 10^6$. Full array of 146 μm roughness with 12 mm spacing. Data set *F*.

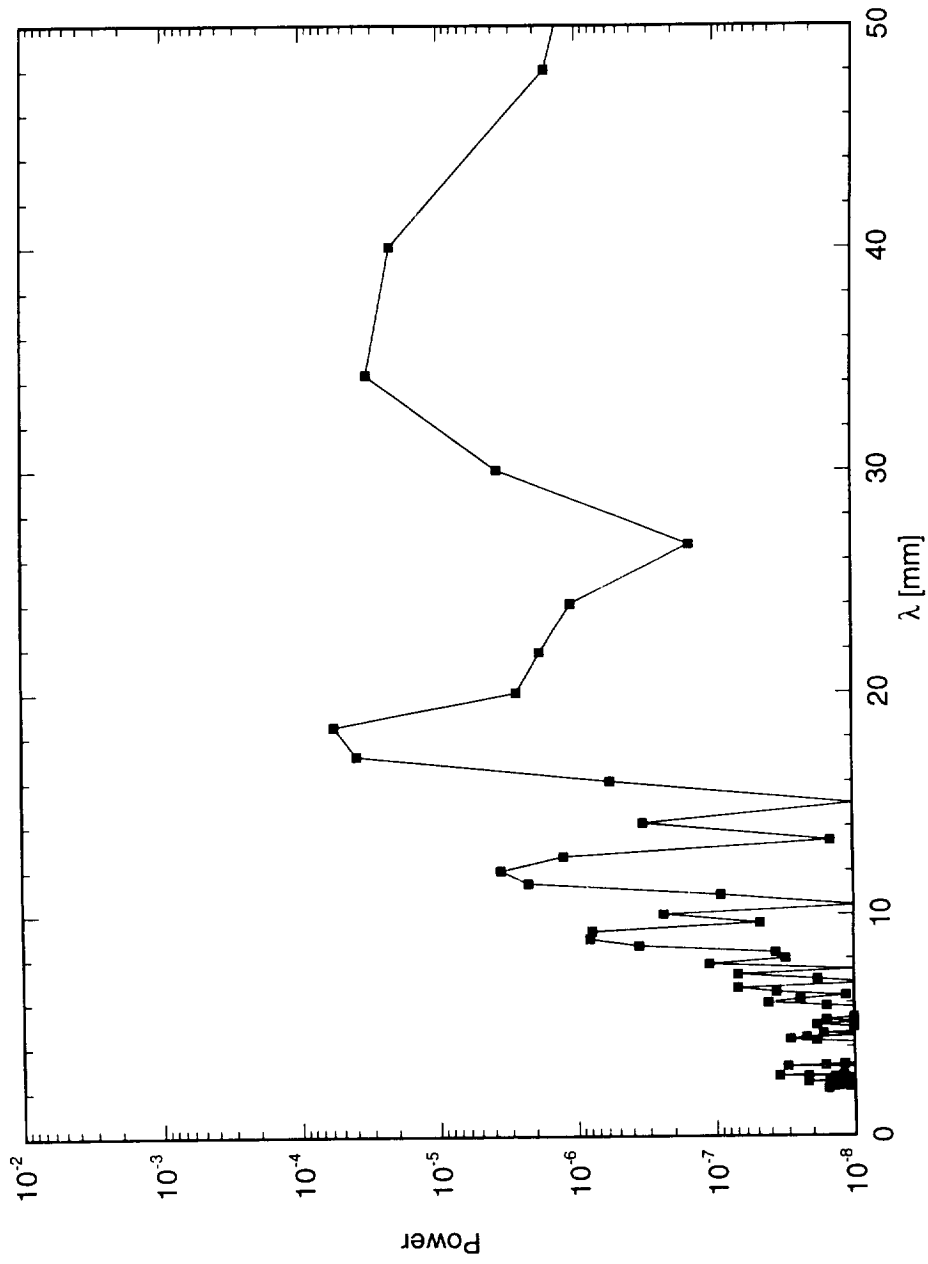

Figure 7.80. FFT power spectrum of spanwise hot-wire scan. $Re_c = 3.0 \times 10^6$. Full array of 146 μm roughness with 36 mm spacing. Data set U.

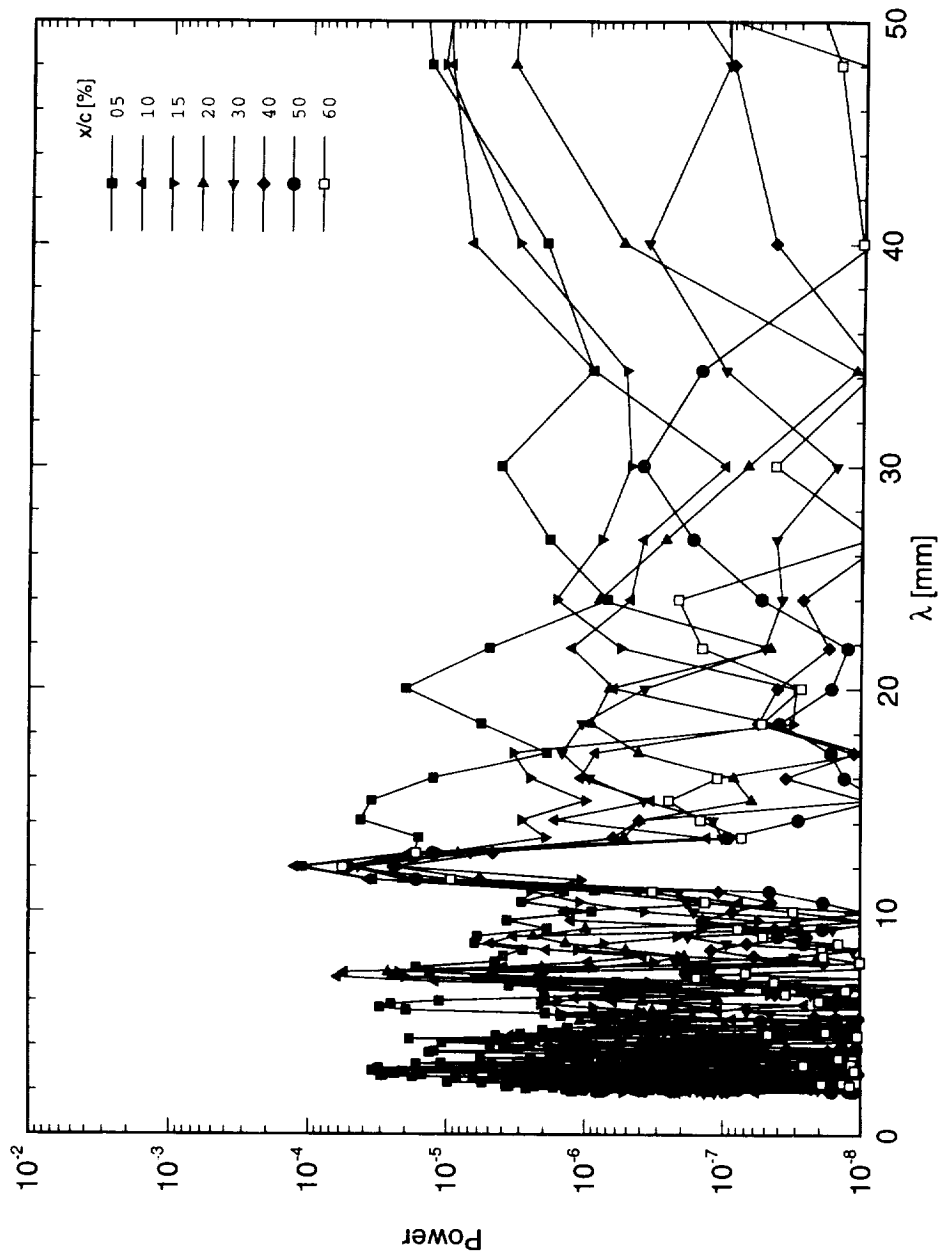

Figure 7.81. FFT power spectra of spanwise hot-wire scans. $Re_c = 3.0 \times 10^6$. Full array of 73 μm roughness with 12 mm spacing. Data set *E*.

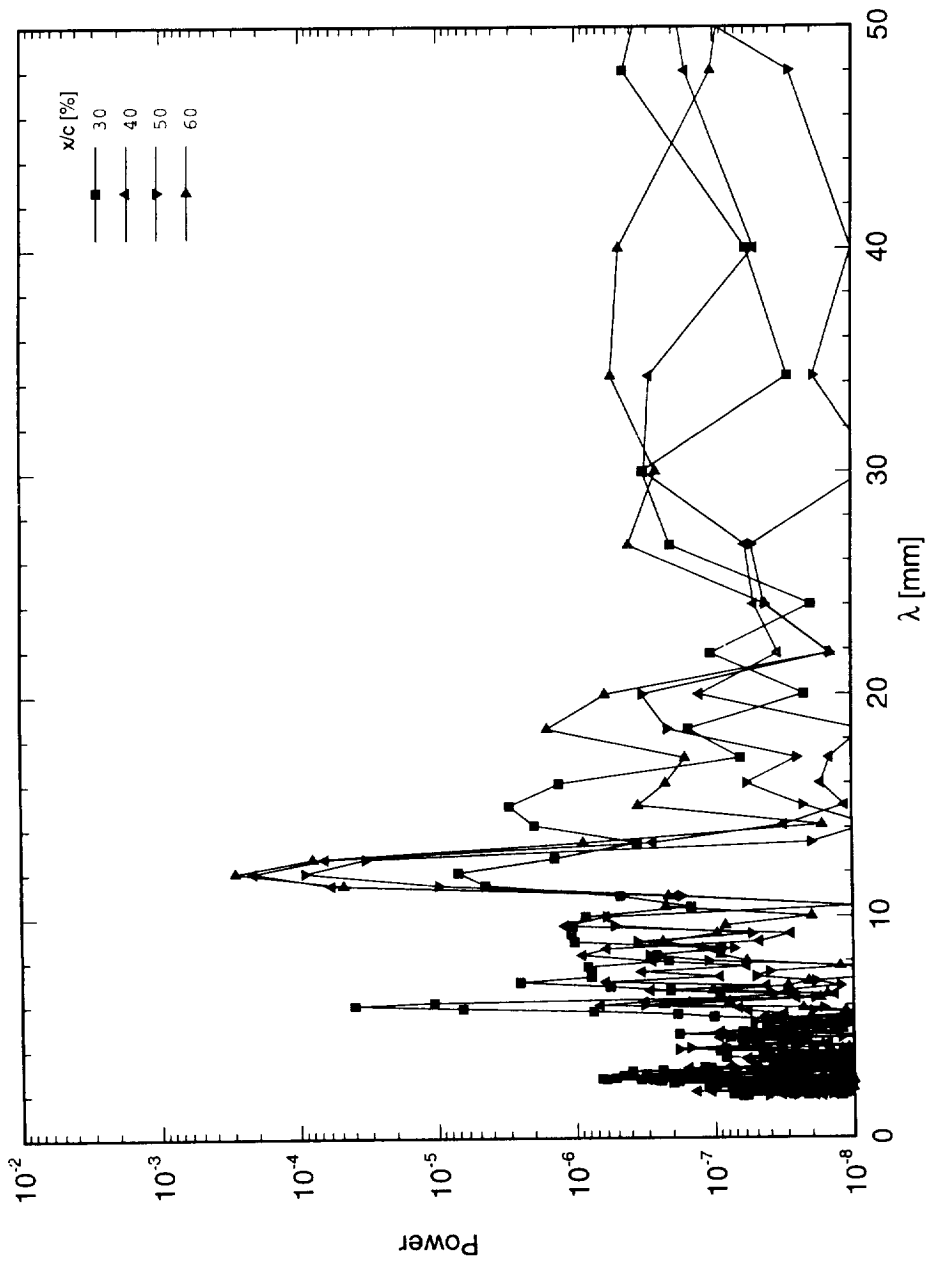

Figure 7.82. FFT power spectra of spanwise hot-wire scans. $Re_c = 3.0 \times 10^6$. Full array of 146 μm roughness with 12 mm spacing. Data set F.

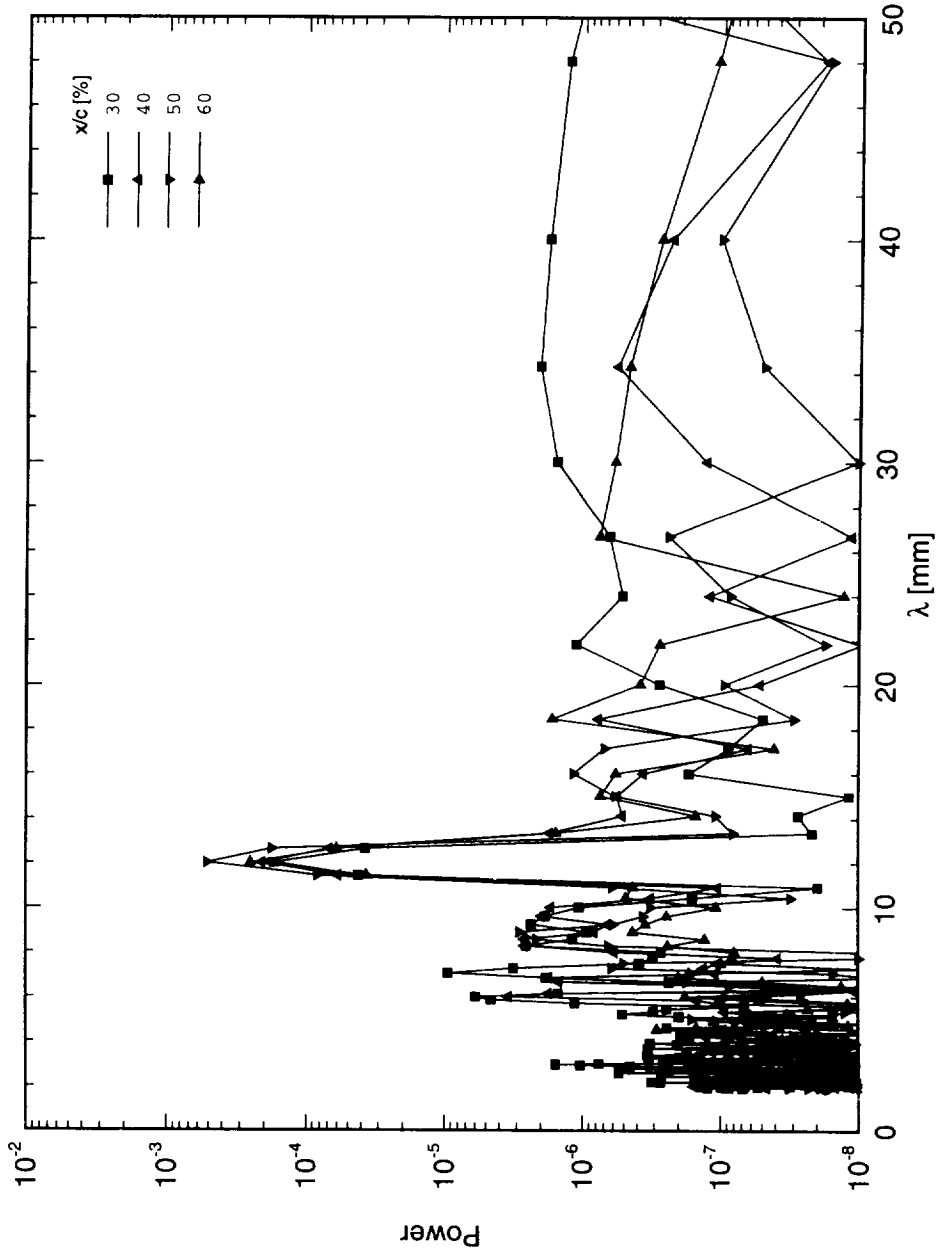

Figure 7.83. FFT power spectra of spanwise hot-wire scans. $Re_c = 3.2 \times 10^6$. Full array of 146 μm roughness with 12 mm spacing. Data set G.

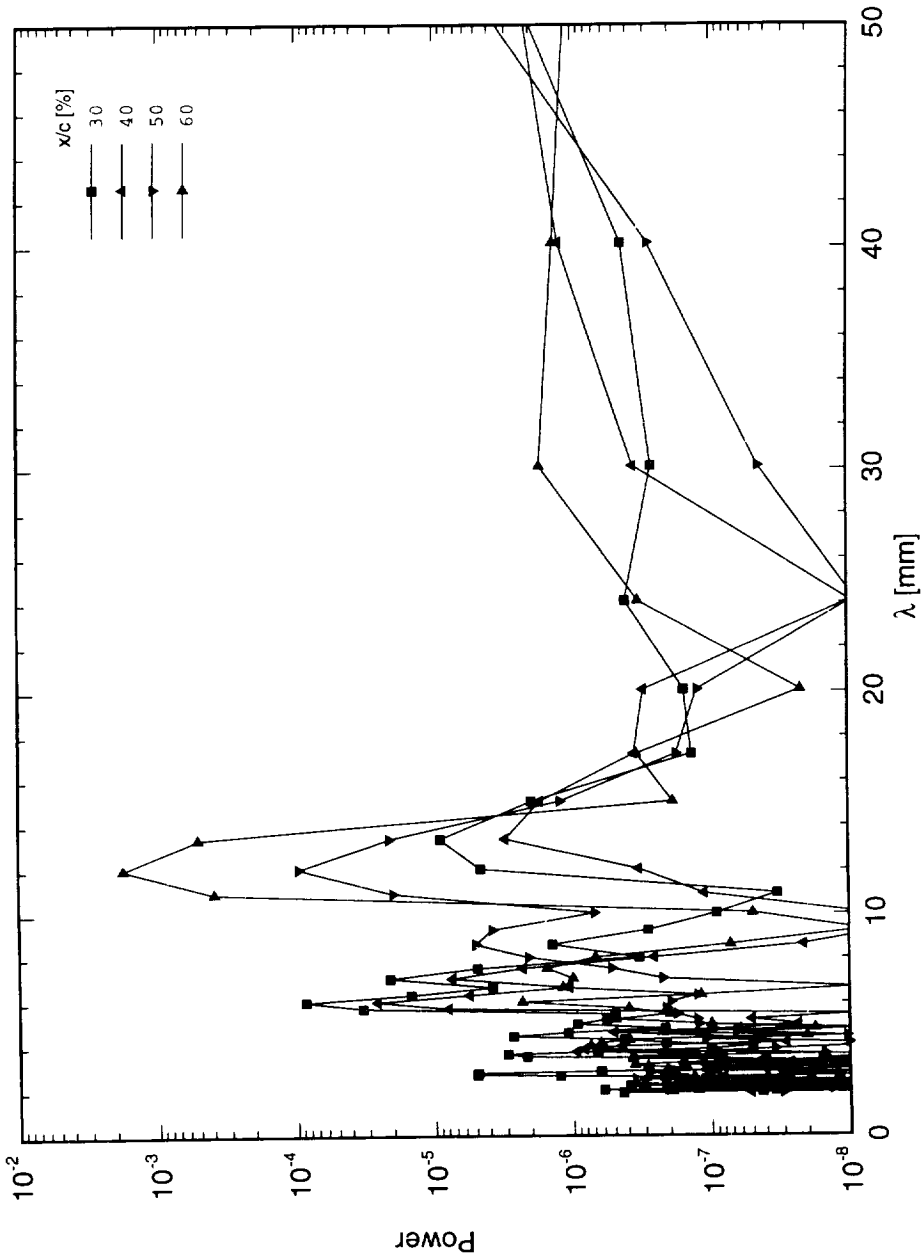

Figure 7.84. FFT power spectra of spanwise hot-wire scans. $Re_c = 3.4 \times 10^6$. Full array of 146 μm roughness with 12 mm spacing. Data set *H*.

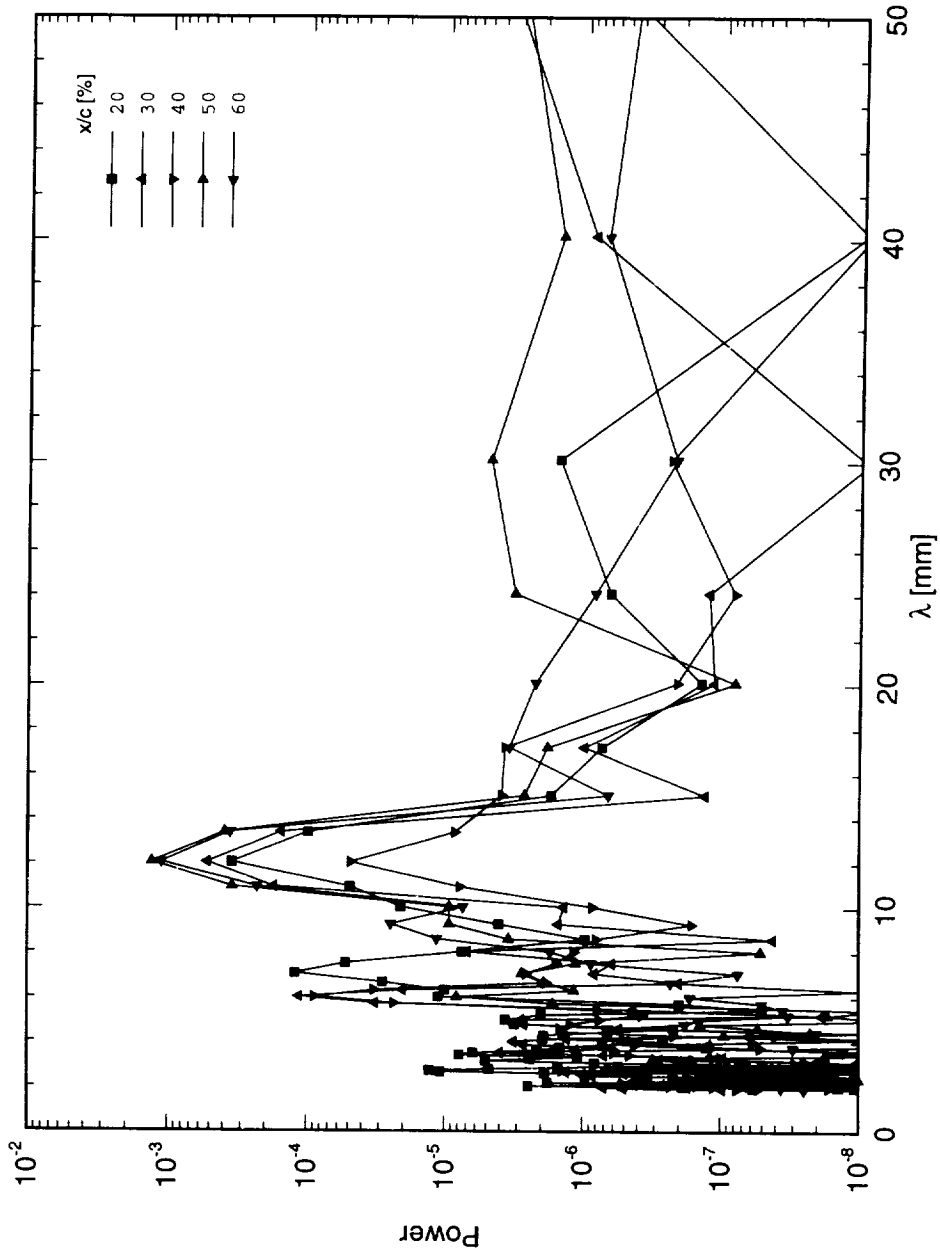

Figure 7.85. FFT power spectra of spanwise hot-wire scans. $Re_c = 3.6 \times 10^6$. Full array of 146 μm roughness with 12 mm spacing. Data set *I*.

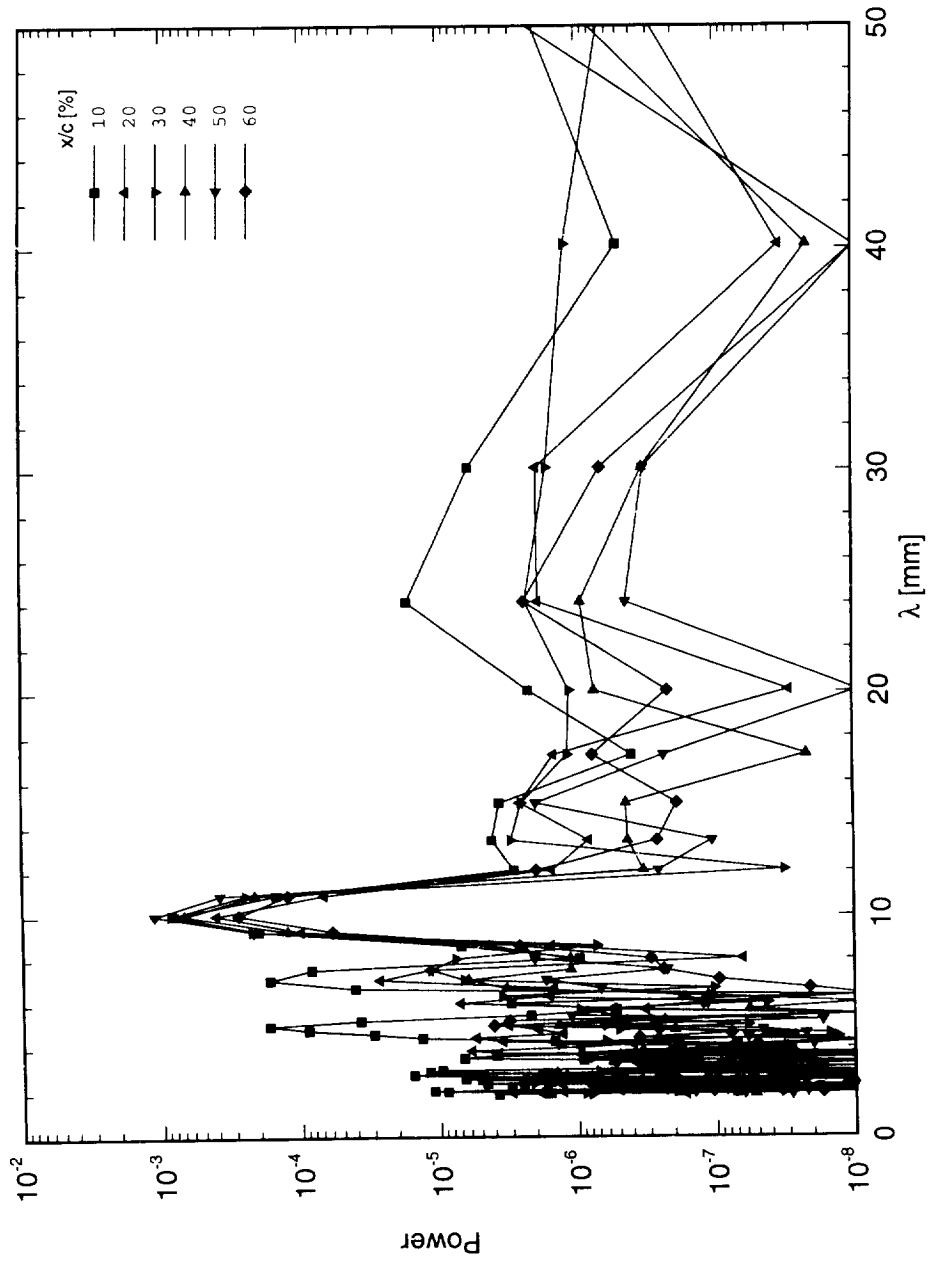

Figure 7.86. FFT power spectra of spanwise hot-wire scans. $Re_c = 3.0 \times 10^6$. Full array of 146 μm roughness with 10 mm spacing. Data set K.

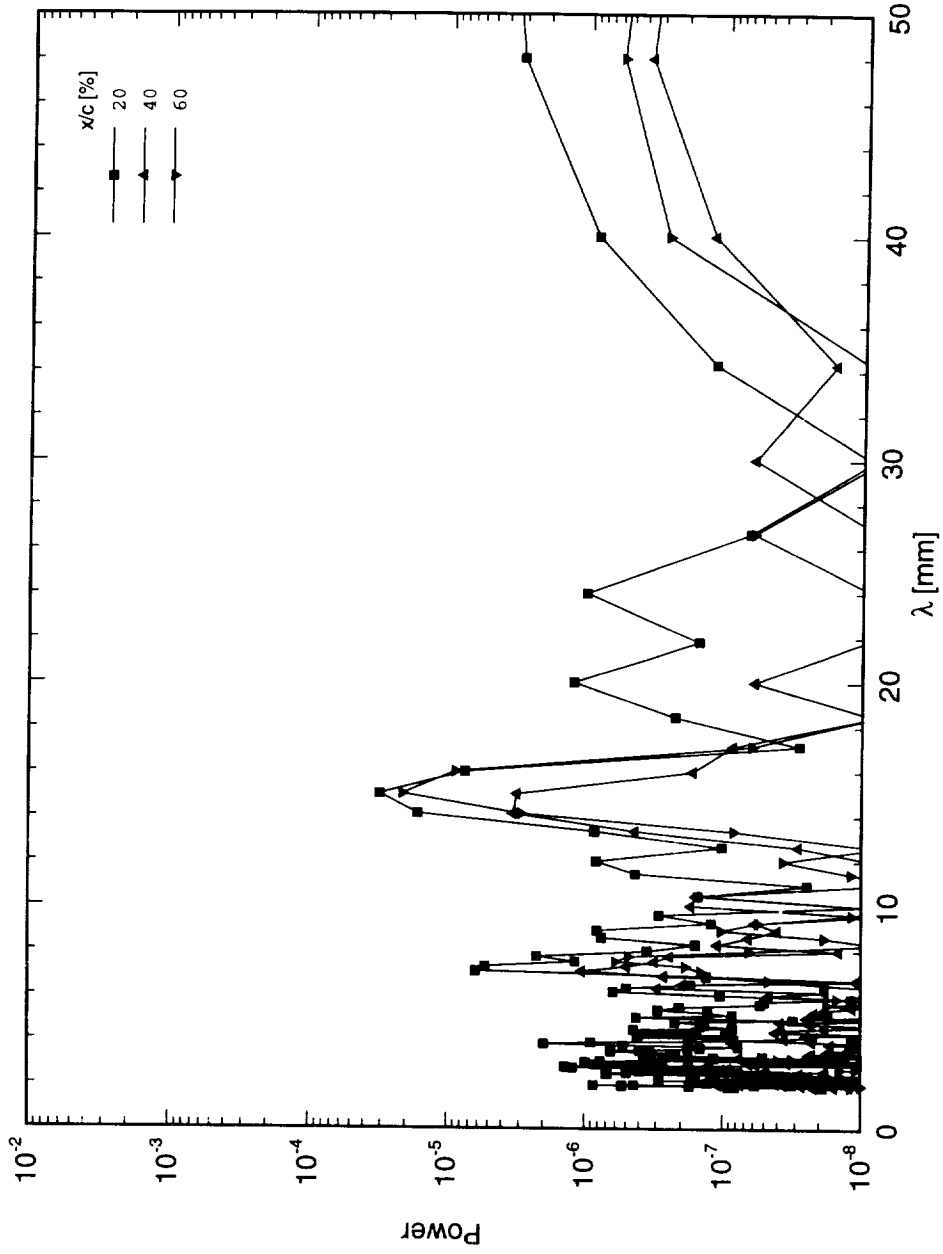

Figure 7.87. FFT power spectra of spanwise hot-wire scans. $Re_c = 3.0 \times 10^6$. Full array of 73 μm roughness with 15 mm spacing. Data set M.

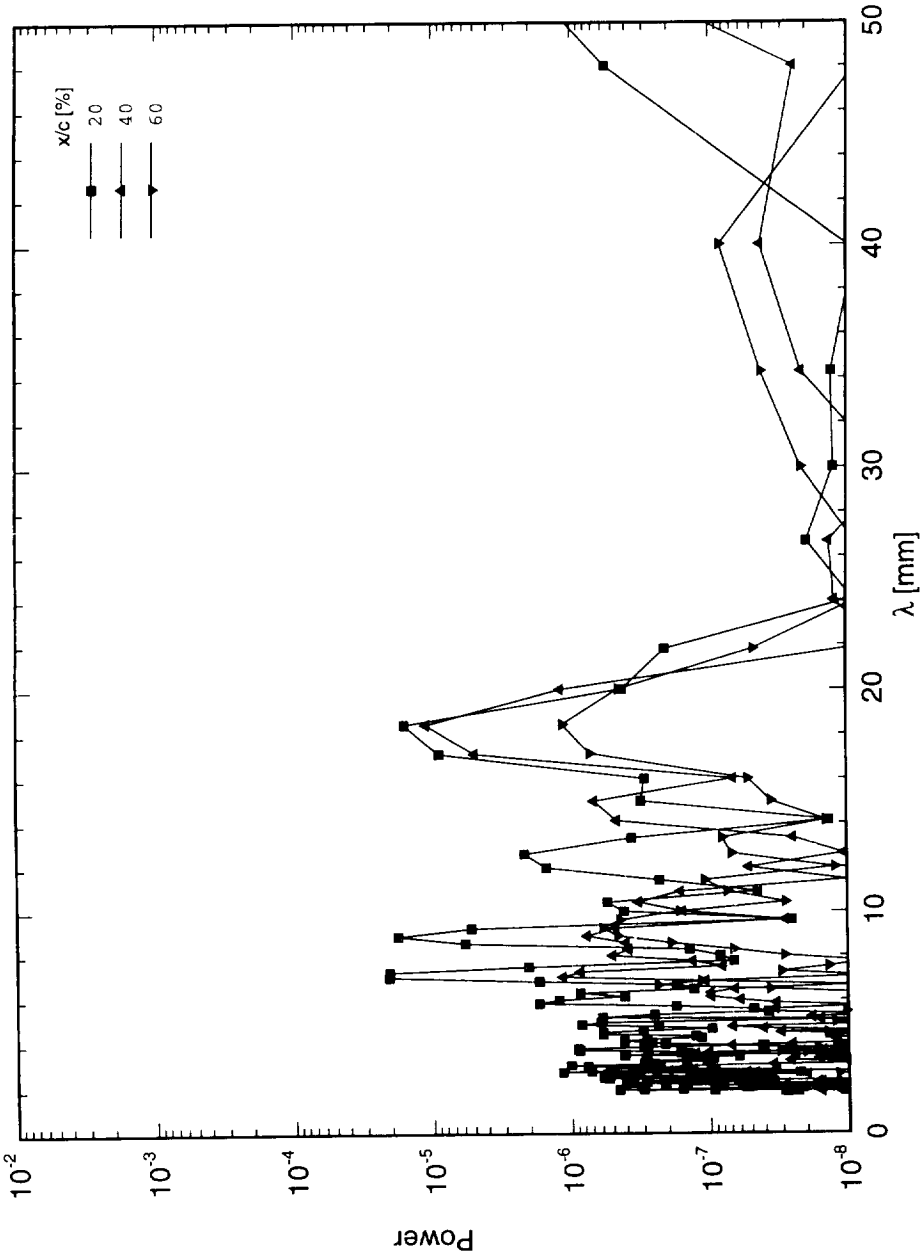

Figure 7.88. FFT power spectra of spanwise hot-wire scans. $Re_c = 3.0 \times 10^6$. Full array of 73 μm roughness with 18 mm spacing. Data set N.

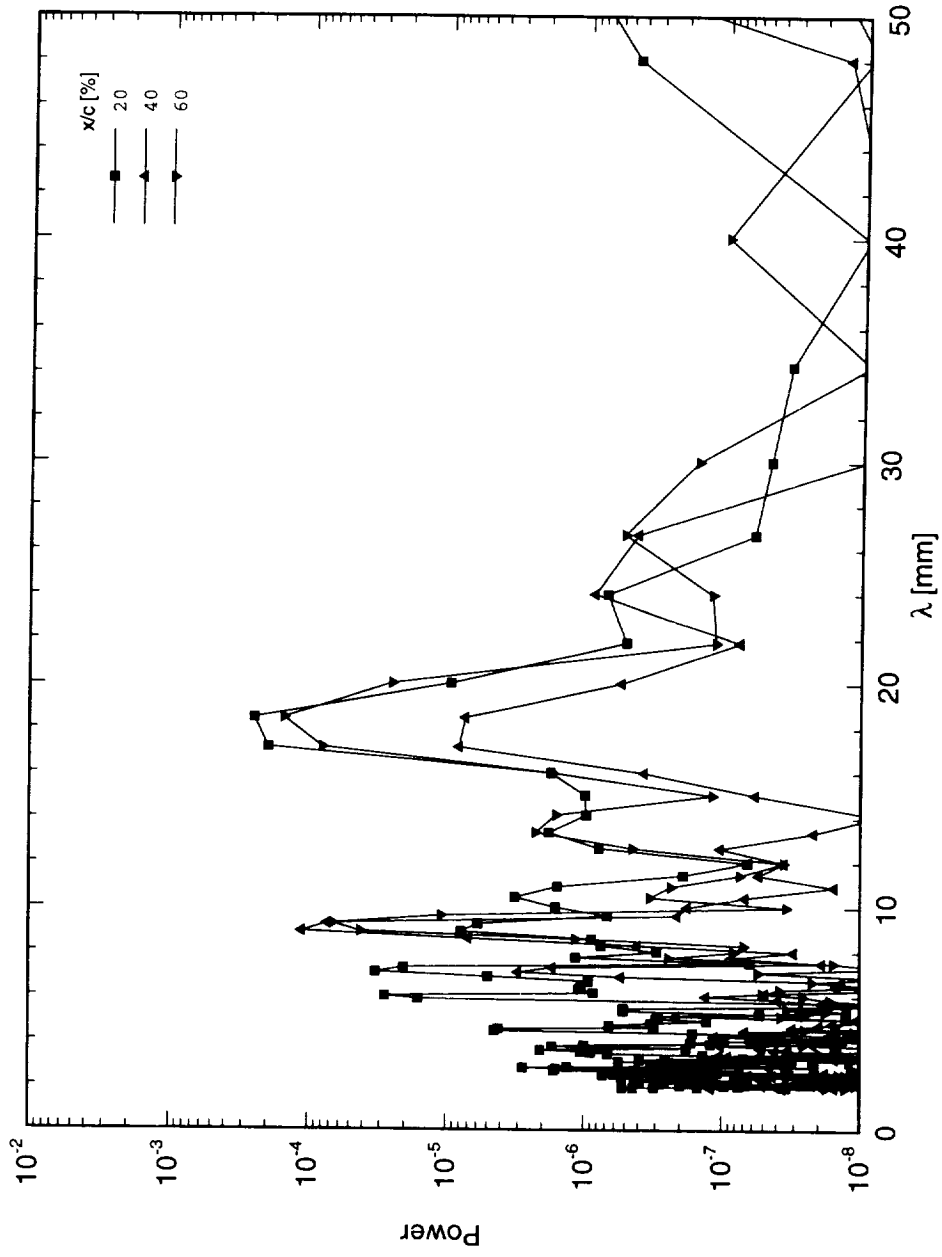

Figure 7.89. FFT power spectra of spanwise hot-wire scans. $Re_c = 3.0 \times 10^6$. Full array of 146 μm roughness with 18 mm spacing. Data set Q.

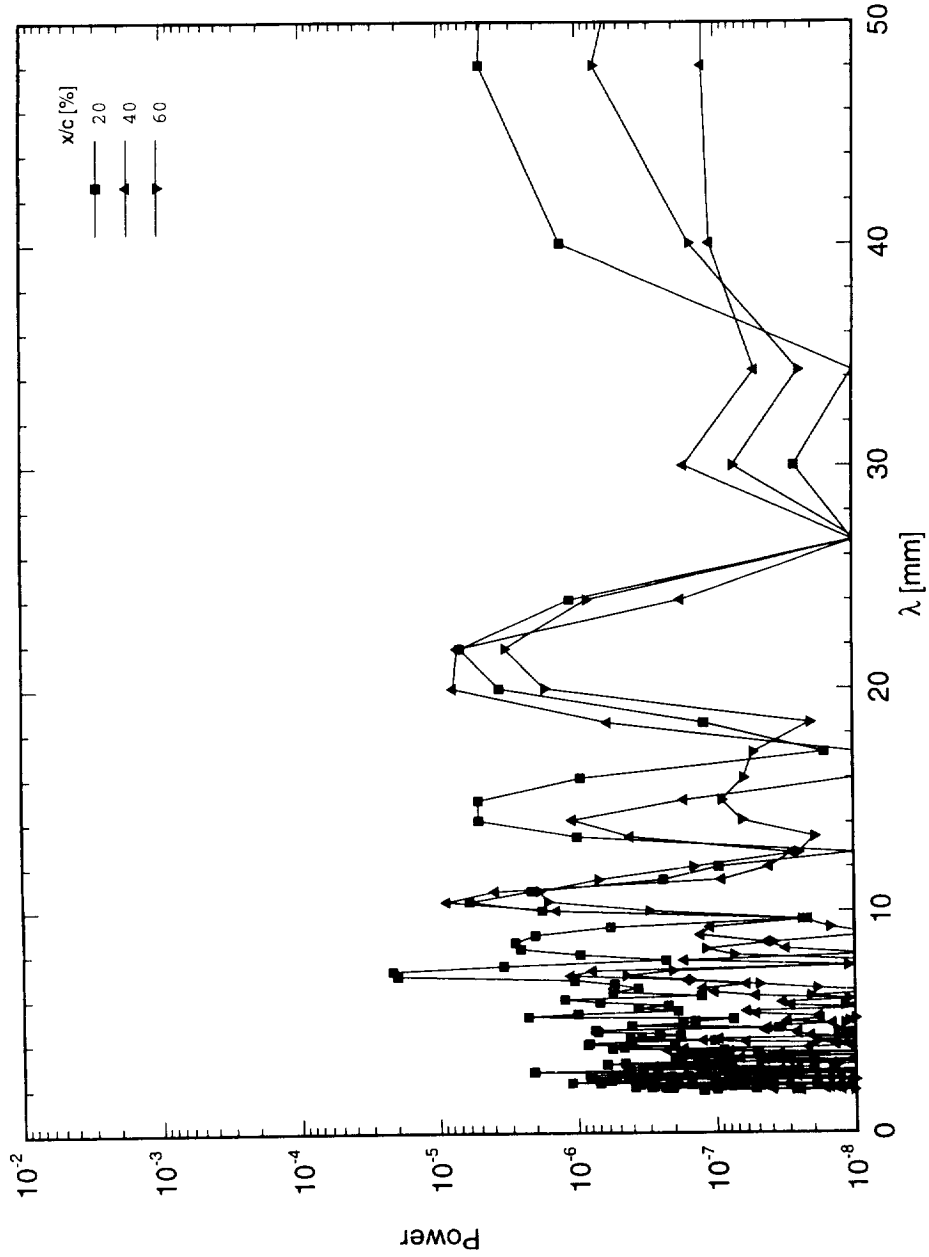

Figure 7.90. FFT power spectra of spanwise hot-wire scans. $Re_c = 3.0 \times 10^6$. Full array of 73 μm roughness with 21 mm spacing. Data set R.

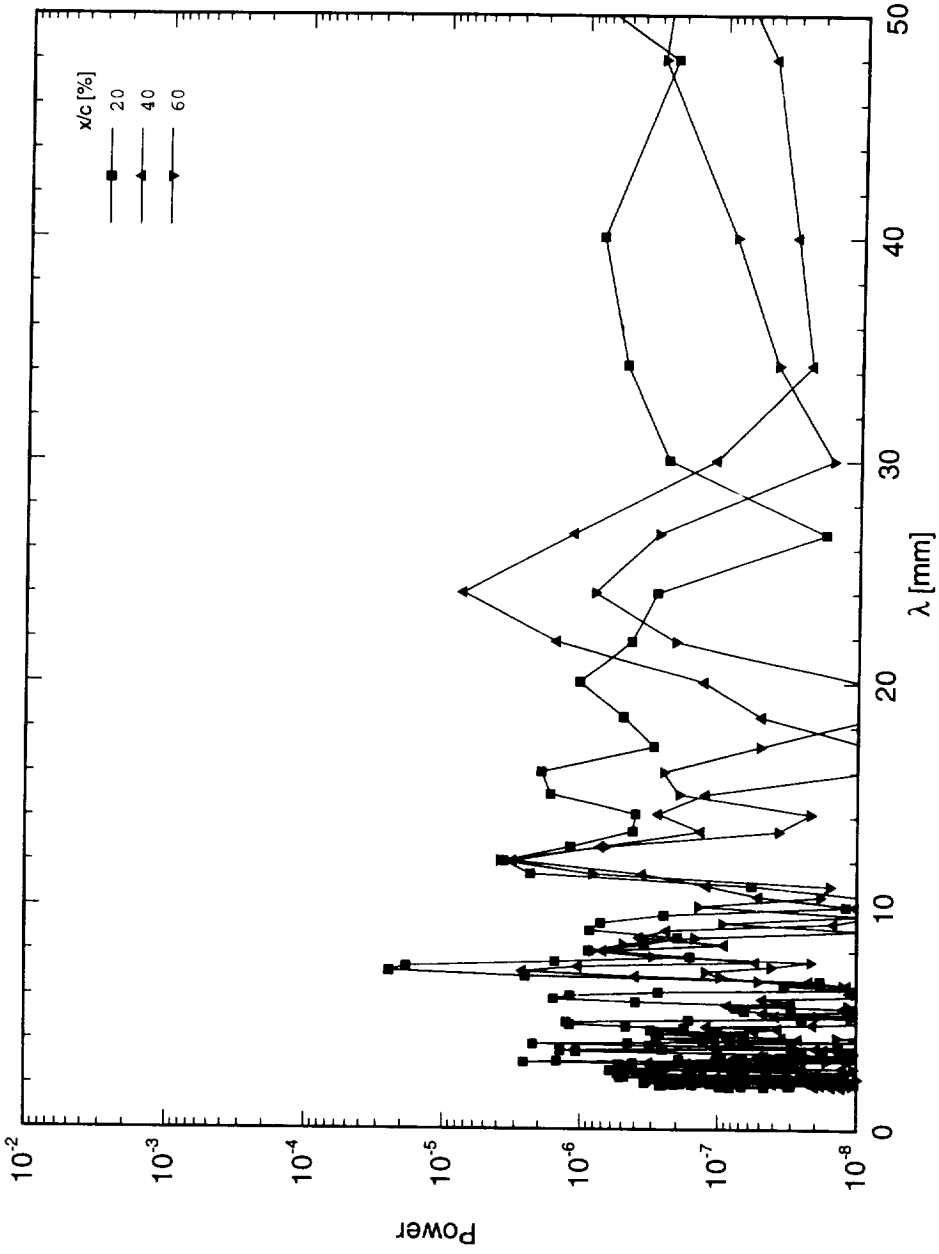

Figure 7.91. FFT power spectra of spanwise hot-wire scans. $Re_c = 3.0 \times 10^6$. Full array of 73 μm roughness with 24 mm spacing. Data set S.

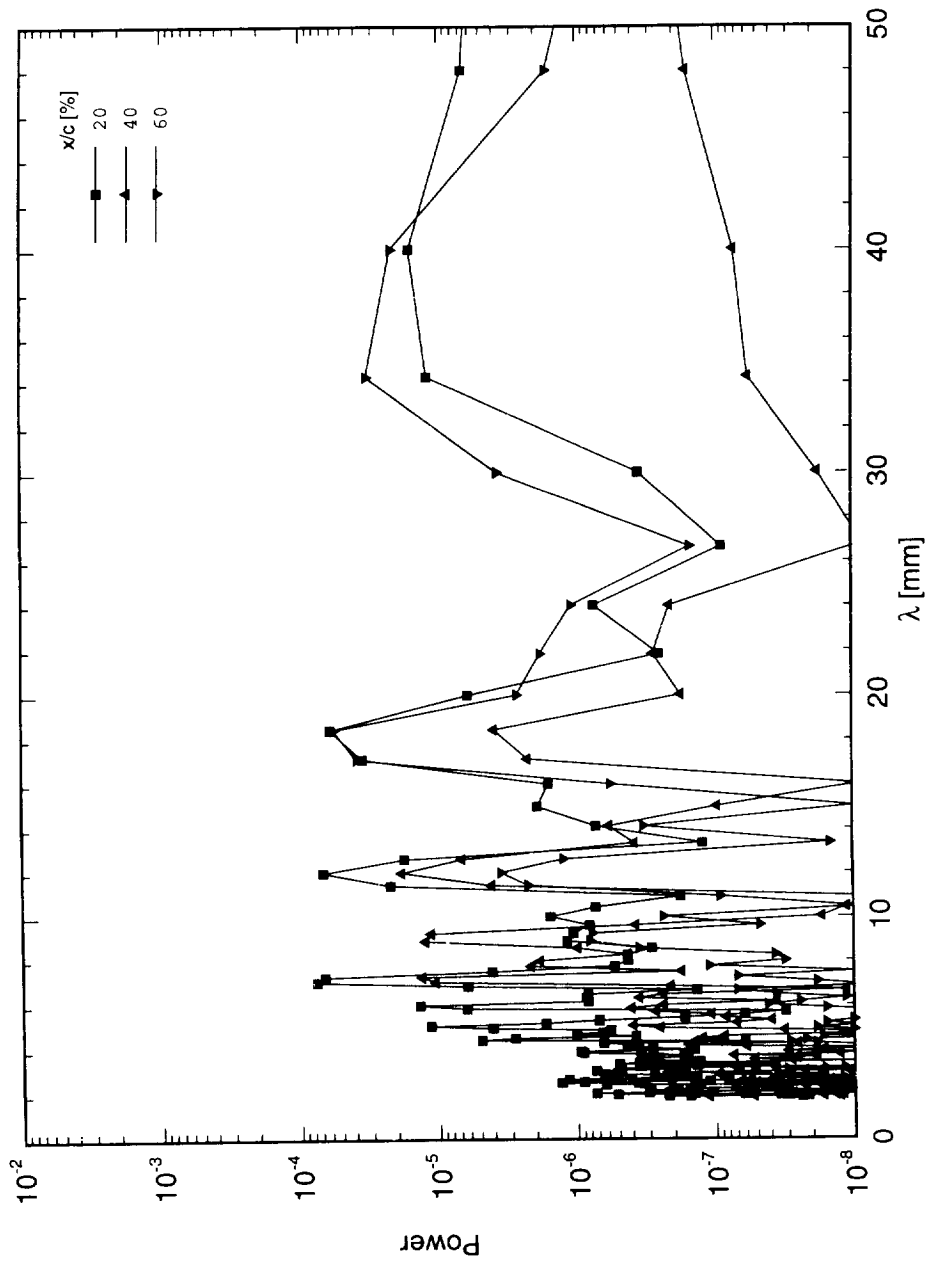

Figure 7.92. FFT power spectra of spanwise hot-wire scans. $Re_c = 3.0 \times 10^6$. Full array of 146 μm roughness with 36 mm spacing. Data set U.

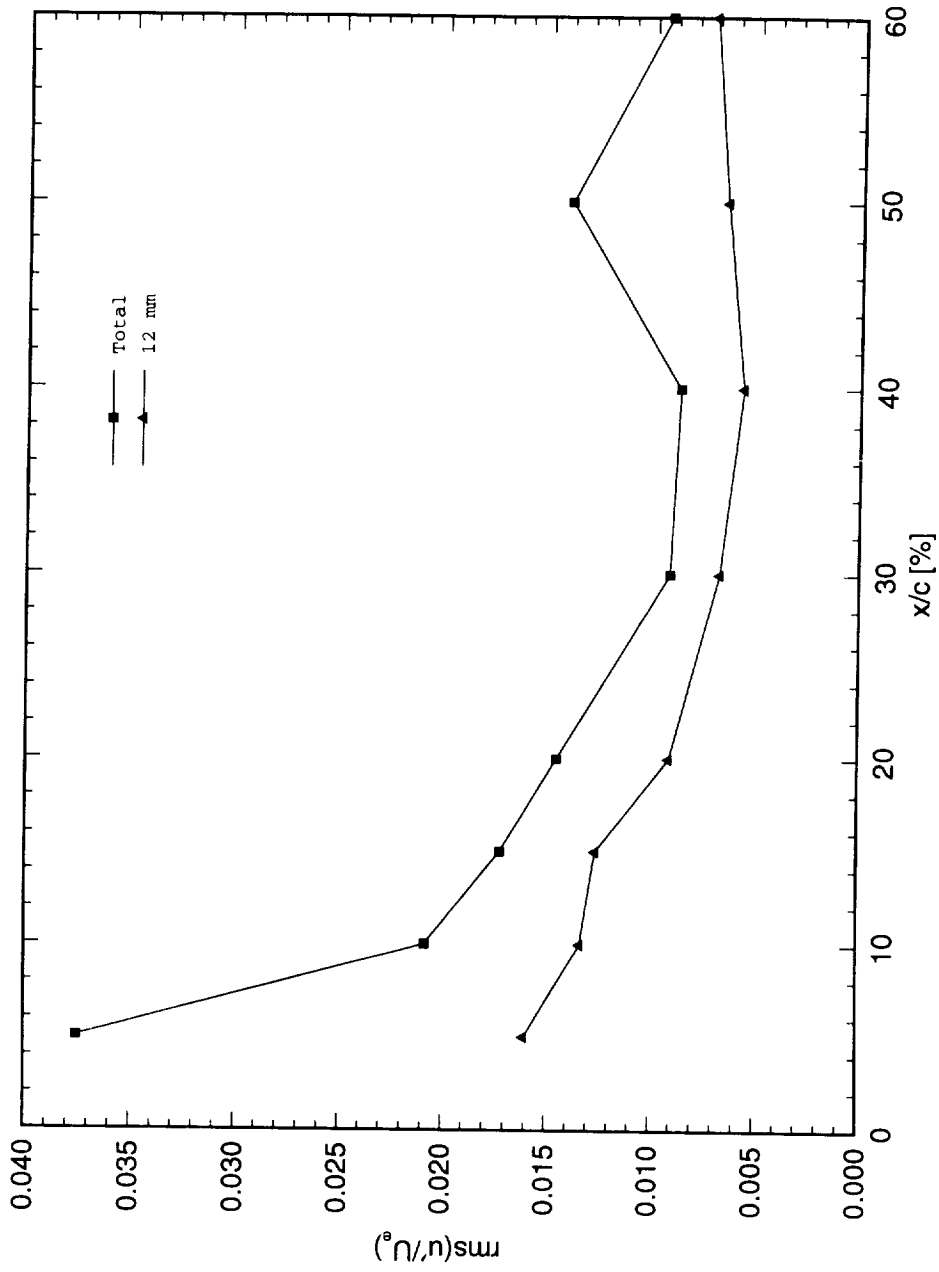

Figure 7.93. Total and discrete-wavelength stationary crossflow rms amplitudes. $Re_c = 3.0 \times 10^6$. Full array of 73 μm roughness with 12 mm spacing. Data set E.

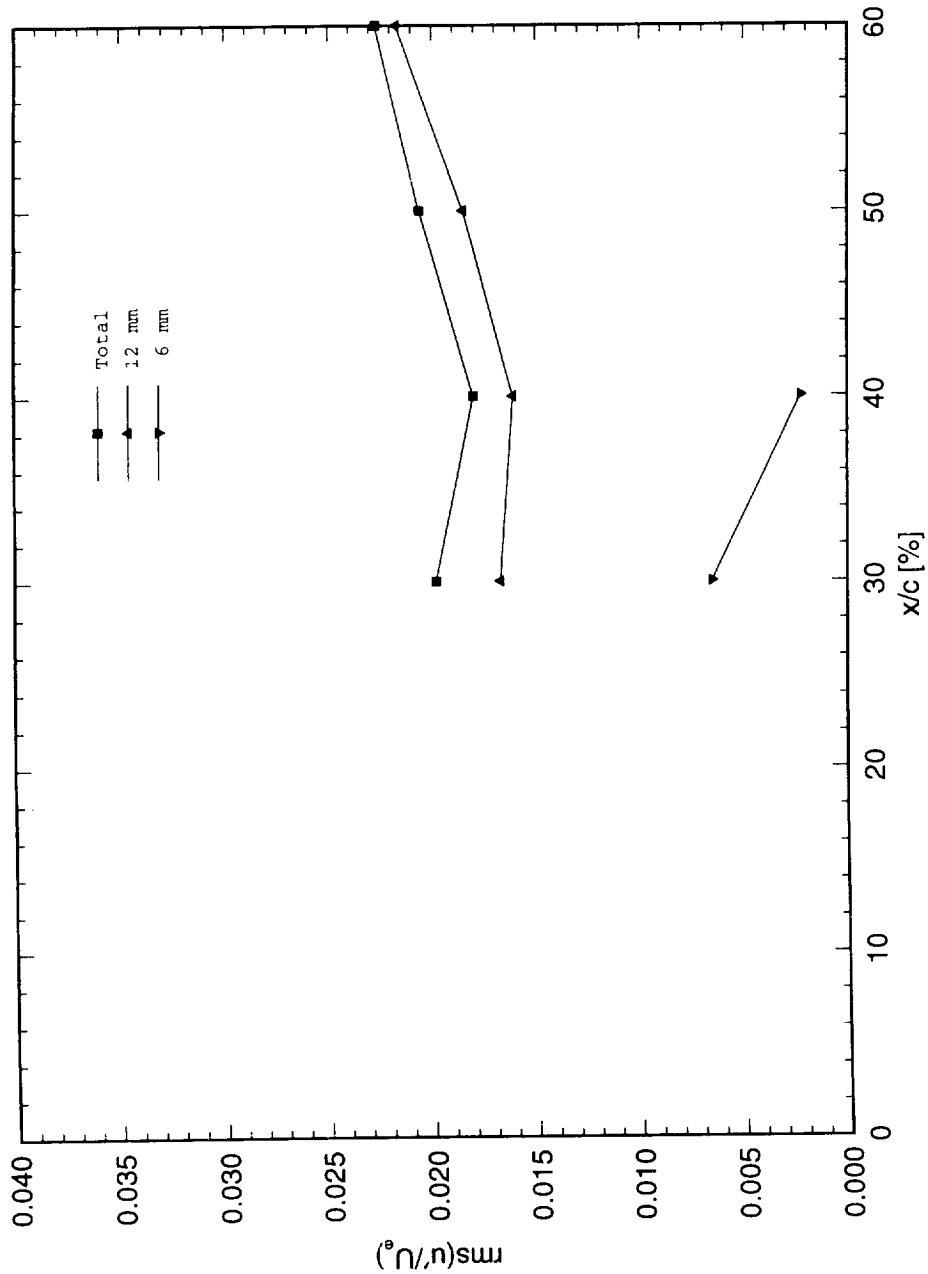

Figure 7.94. Total and discrete-wavelength stationary crossflow rms amplitudes. $Re_c = 3.0 \times 10^6$. Full array of 146 μm roughness with 12 mm spacing. Data set F.

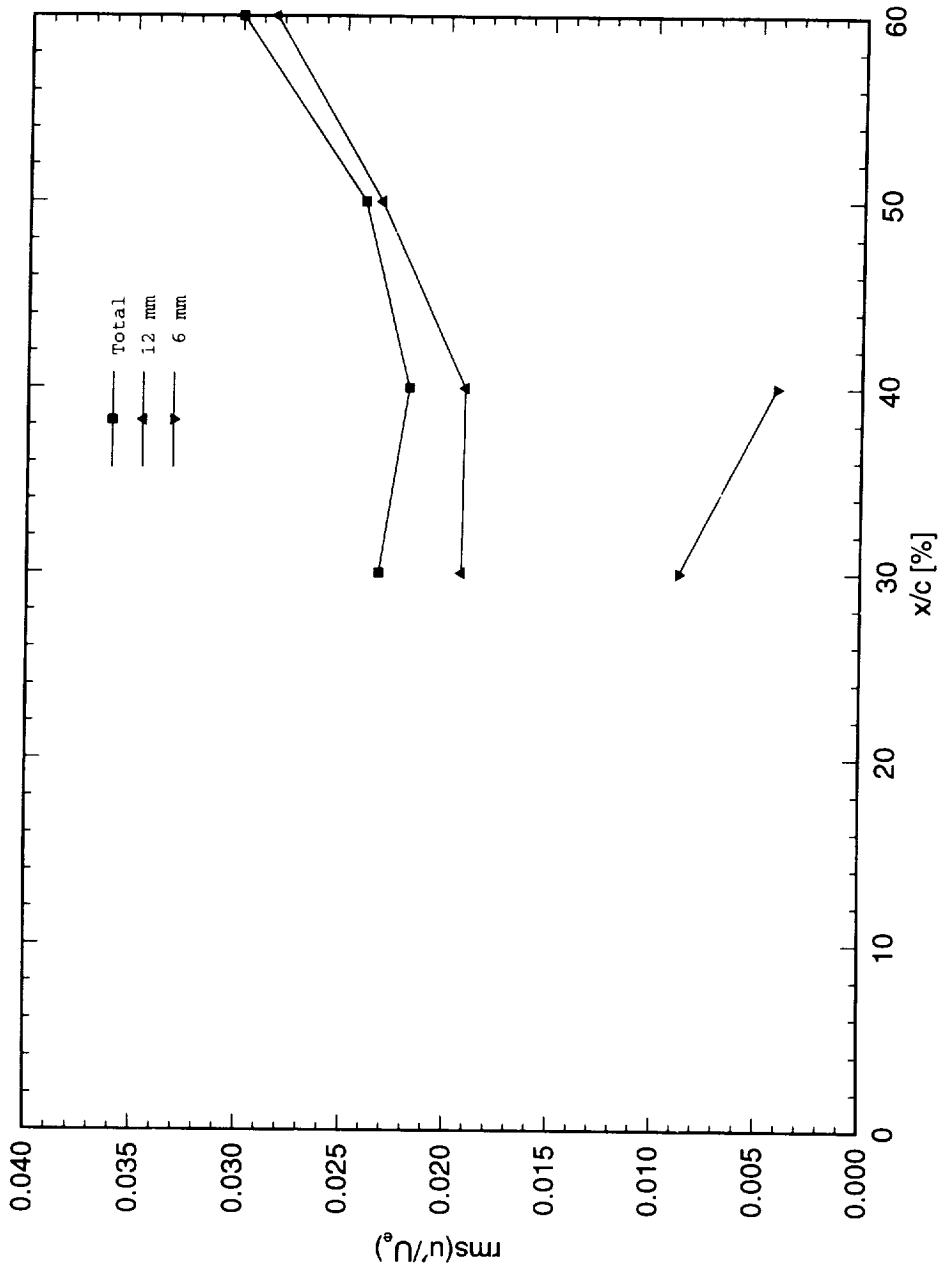

Figure 7.95. Total and discrete-wavelength stationary crossflow rms amplitudes. $Re_c = 3.2 \times 10^6$. Full array of 146 μm roughness with 12 mm spacing. Data set G.

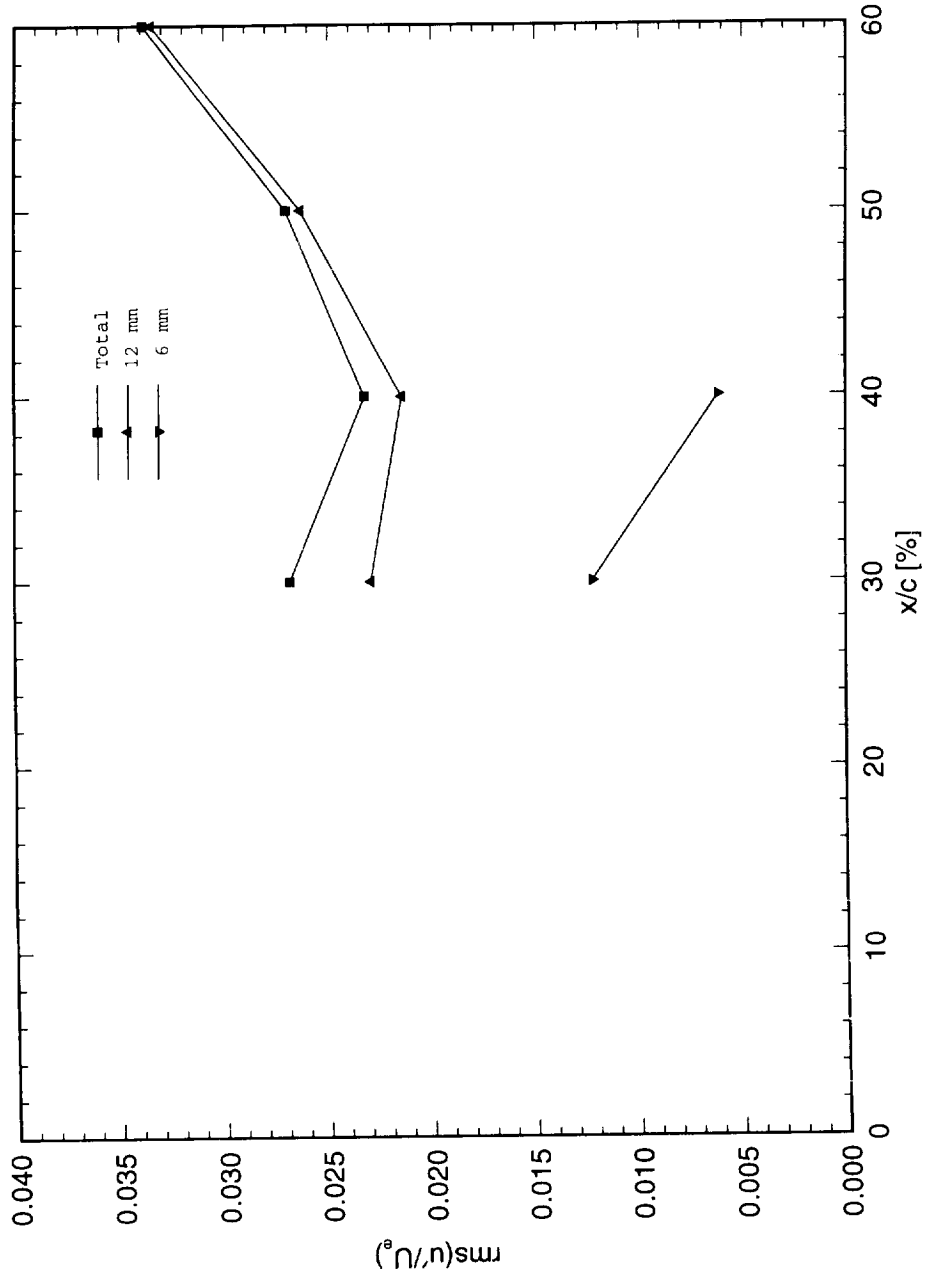

Figure 7.96. Total and discrete-wavelength stationary crossflow rms amplitudes. $Re_c = 3.4 \times 10^6$. Full array of 146 μm roughness with 12 mm spacing. Data set H.

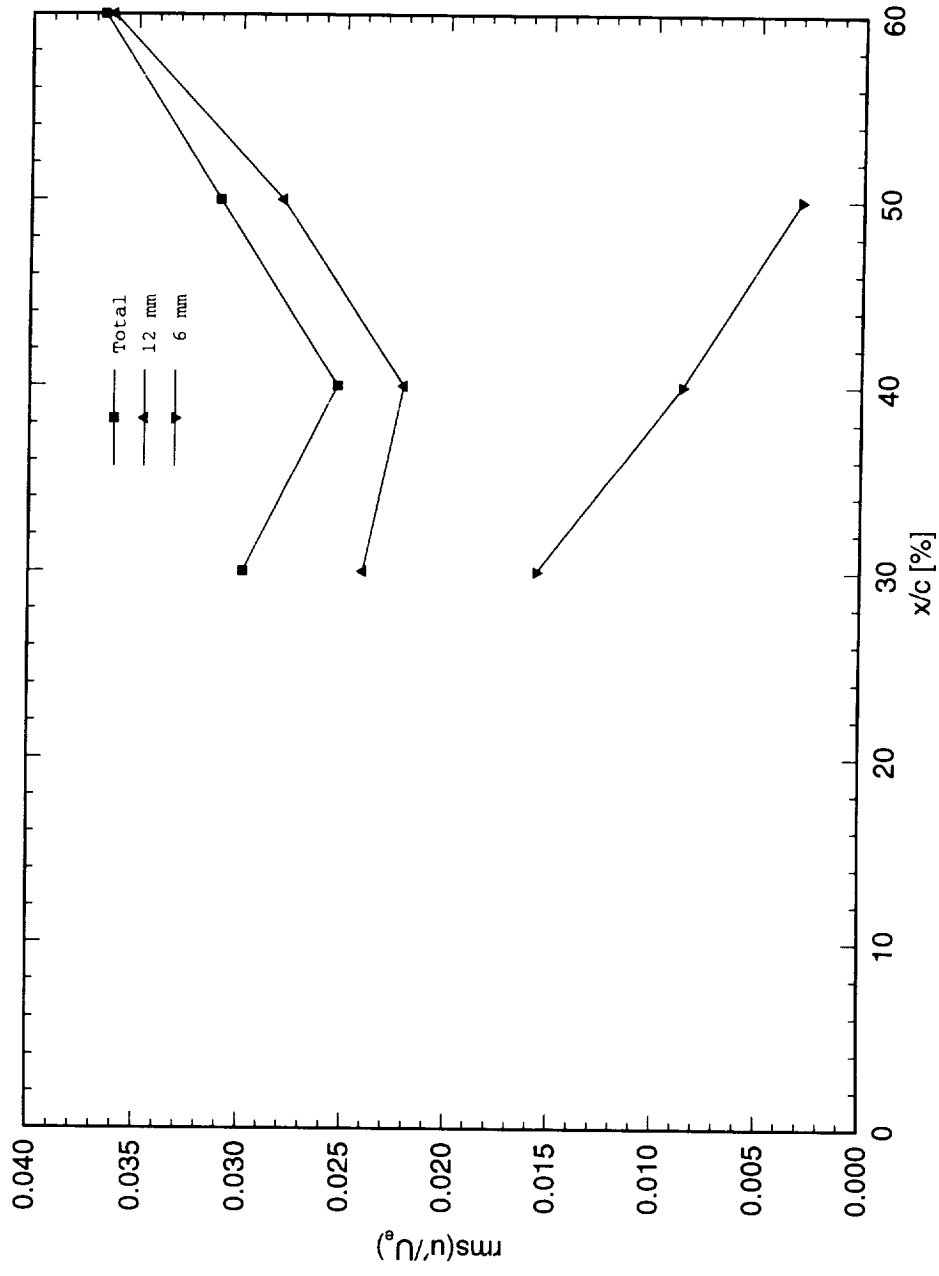

Figure 7.97. Total and discrete-wavelength stationary crossflow rms amplitudes. $Re_c = 3.6 \times 10^6$. Full array of 146 μm roughness with 12 mm spacing. Data set *I*.

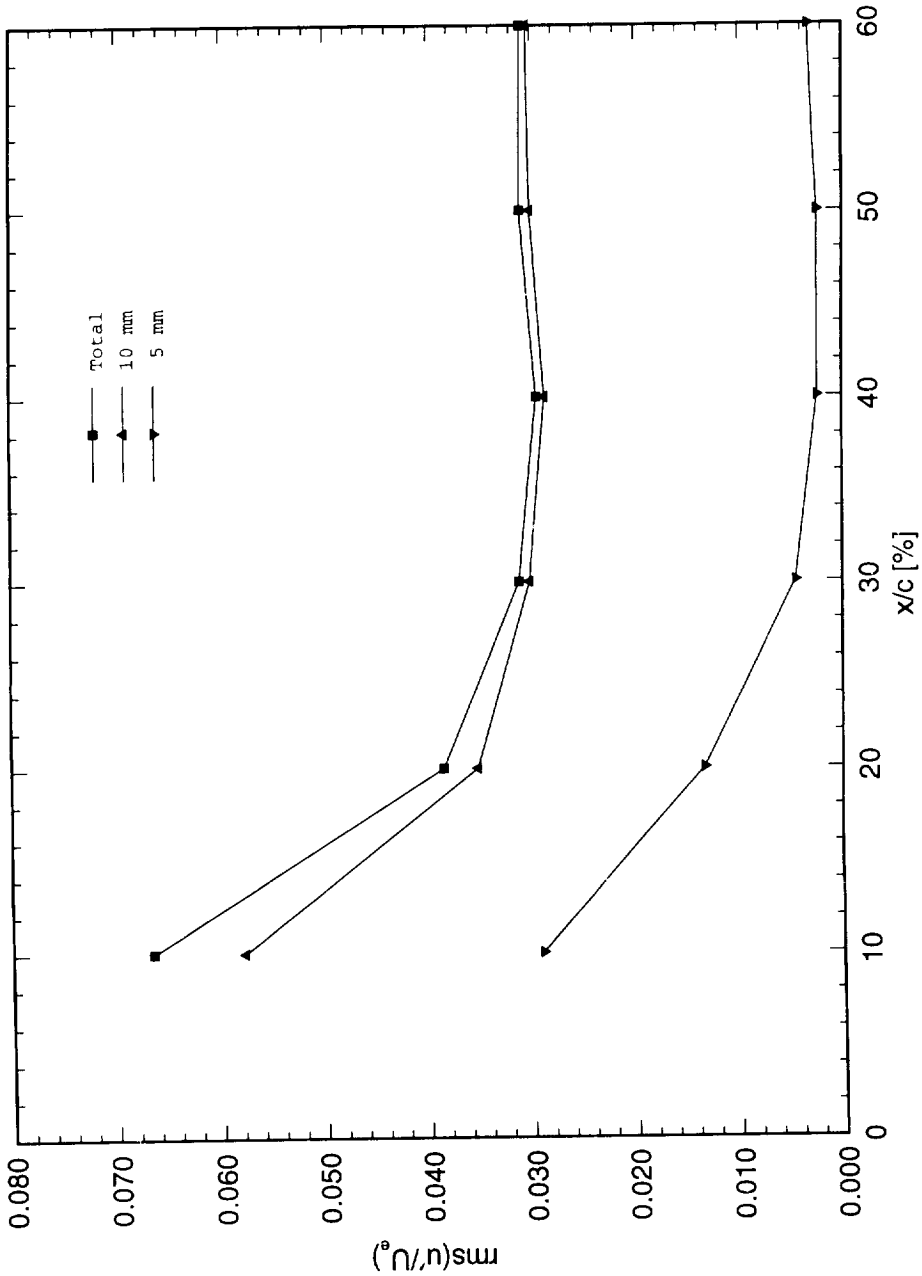

Figure 7.98. Total and discrete-wavelength stationary crossflow rms amplitudes. $Re_c = 3.0 \times 10^6$. Full array of 146 μm roughness with 10 mm spacing. Data set K.

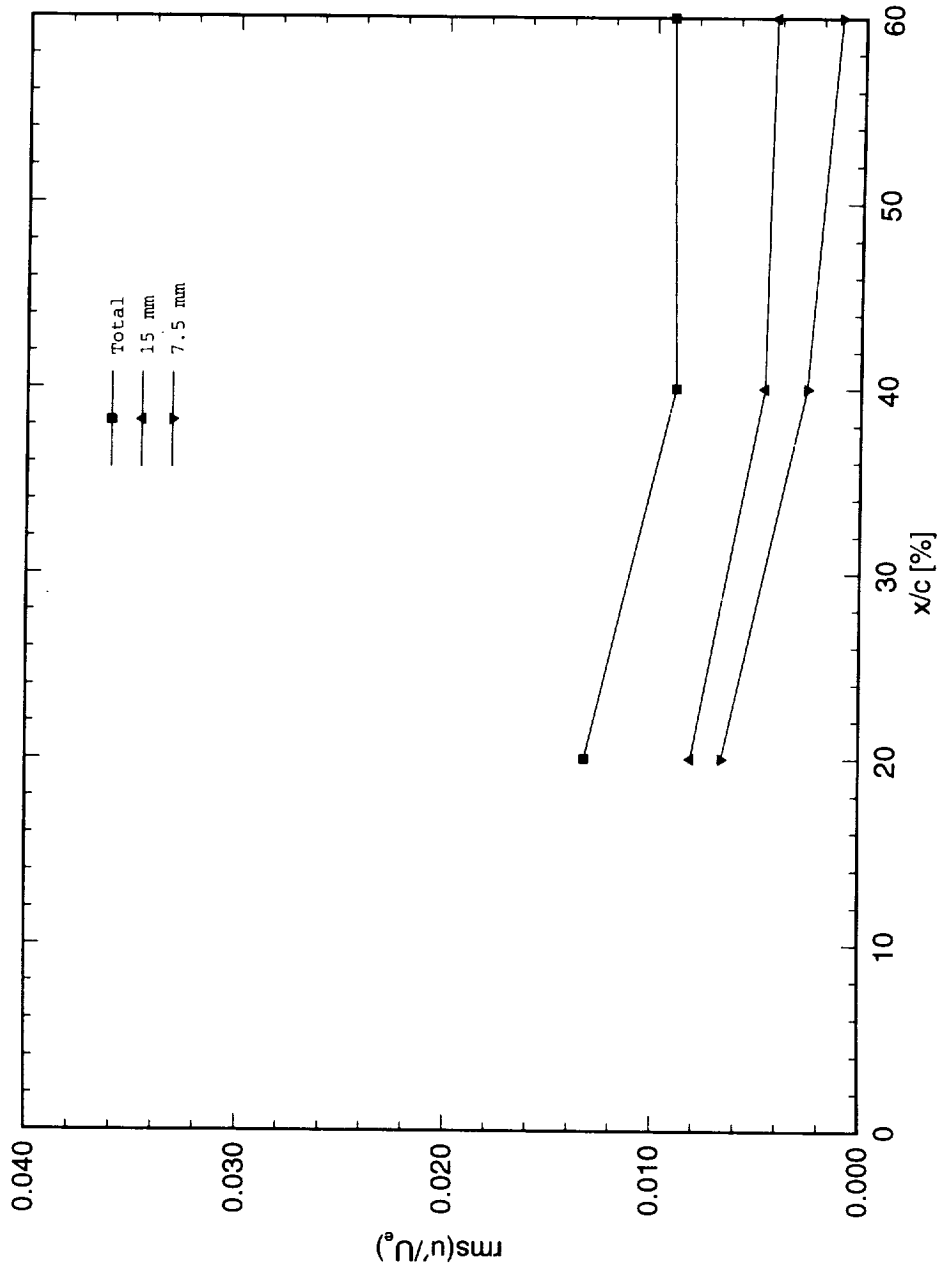

Figure 7.99. Total and discrete-wavelength stationary crossflow rms amplitudes. $Re_c = 3.0 \times 10^6$. Full array of 73 μm roughness with 15 mm spacing. Data set M.

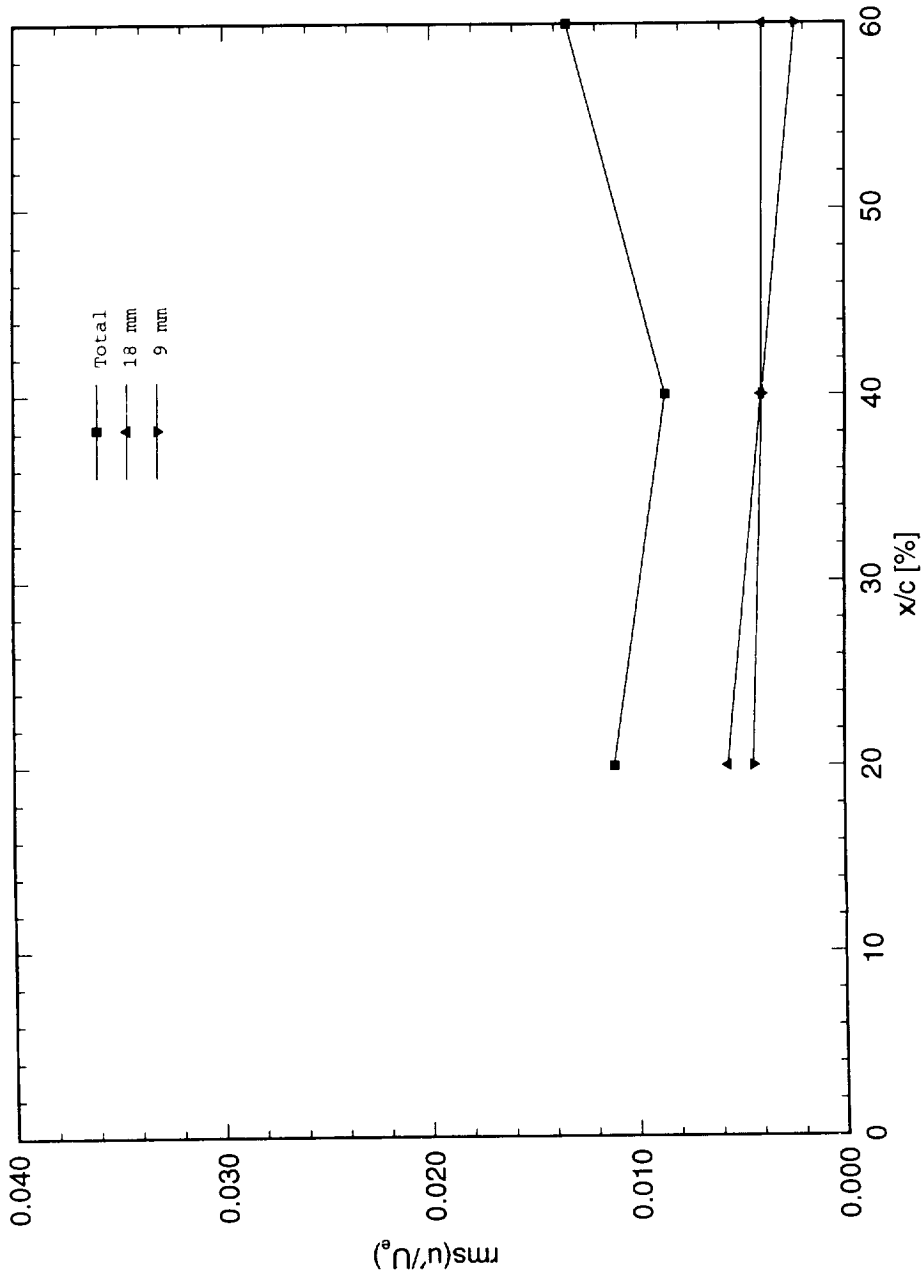

Figure 7.100. Total and discrete-wavelength stationary crossflow rms amplitudes. $Re_c = 3.0 \times 10^6$. Full array of 73 μm roughness with 18 mm spacing. Data set N.

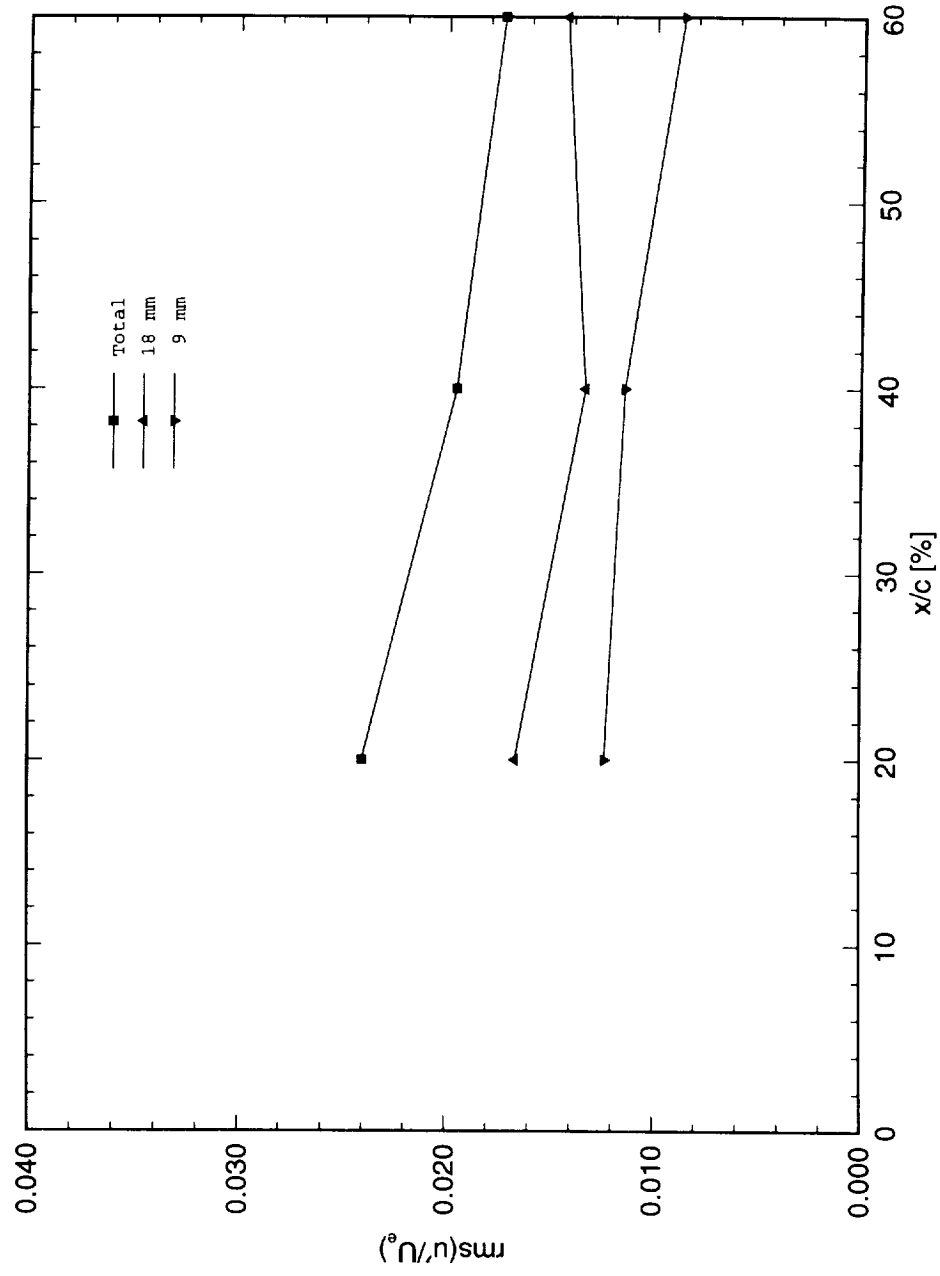

Figure 7.101. Total and discrete-wavelength stationary crossflow rms amplitudes. $Re_c = 3.0 \times 10^6$. Full array of 146 μm roughness with 18 mm spacing. Data set Q.

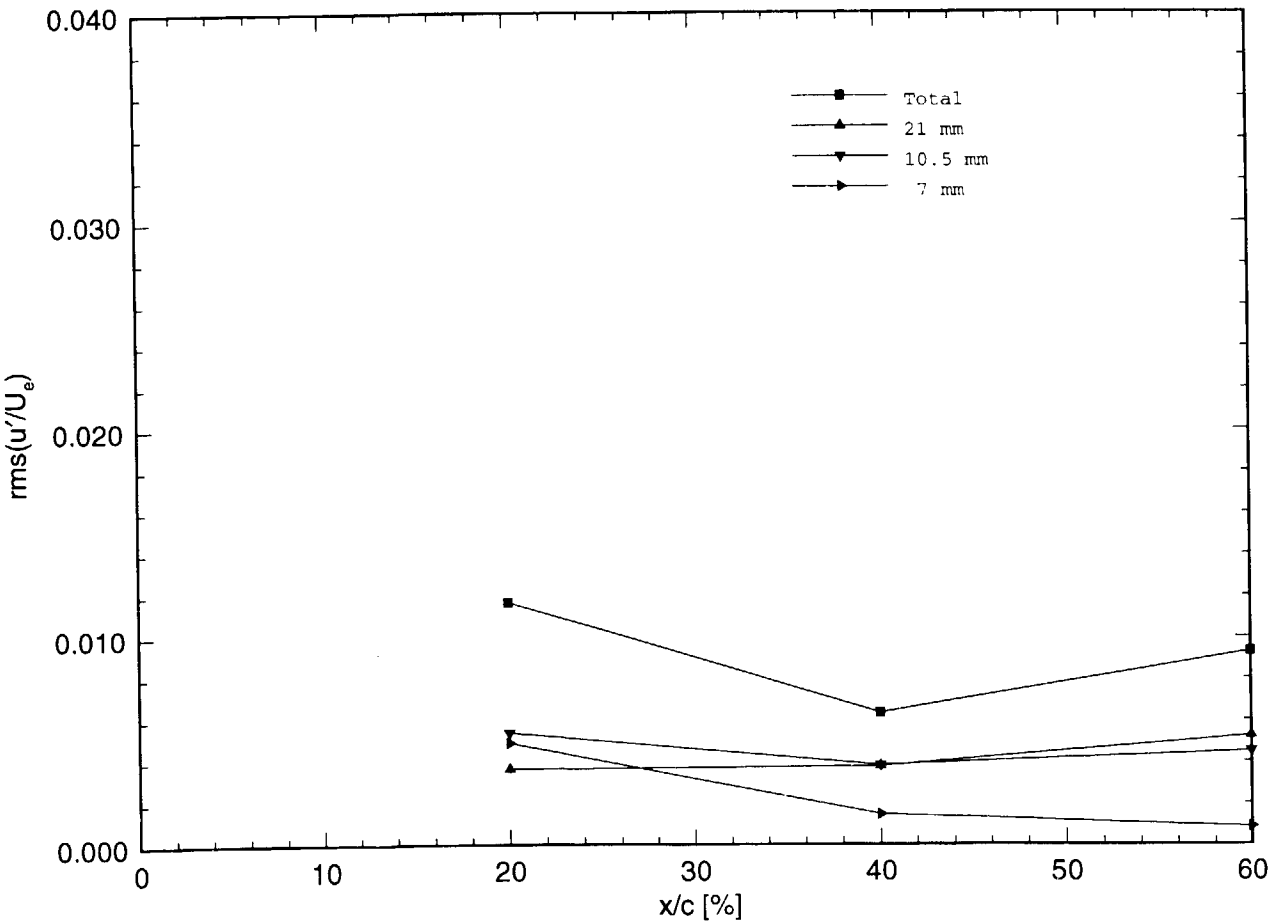

Figure 7.102. Total and discrete-wavelength stationary crossflow rms amplitudes. $Re_c = 3.0 \times 10^6$. Full array of 73 μm roughness with 21 mm spacing. Data set R.

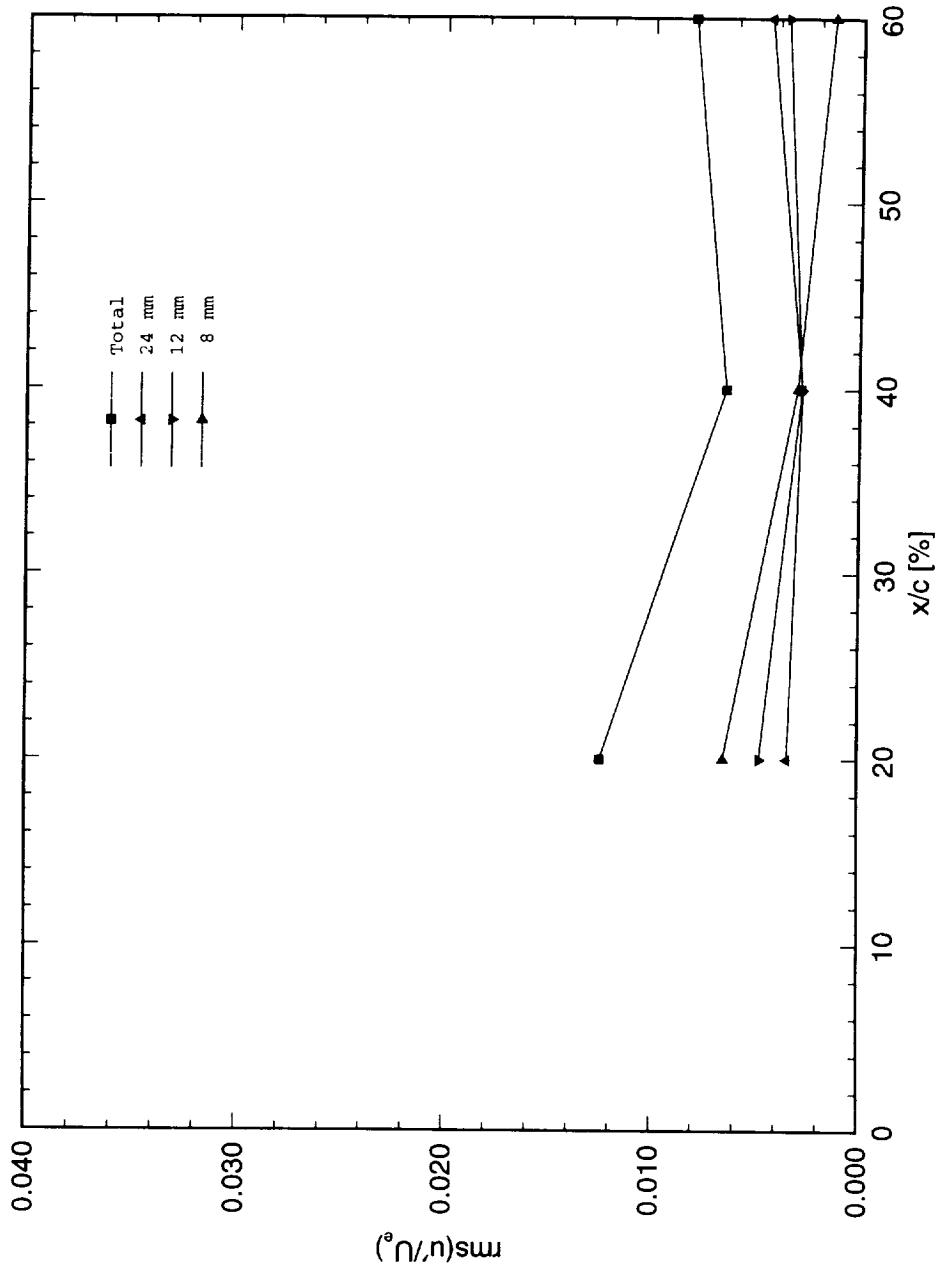

Figure 7.103. Total and discrete-wavelength stationary crossflow rms amplitudes. $Re_c = 3.0 \times 10^6$. Full array of 73 μm roughness with 24 mm spacing. Data set *S*.

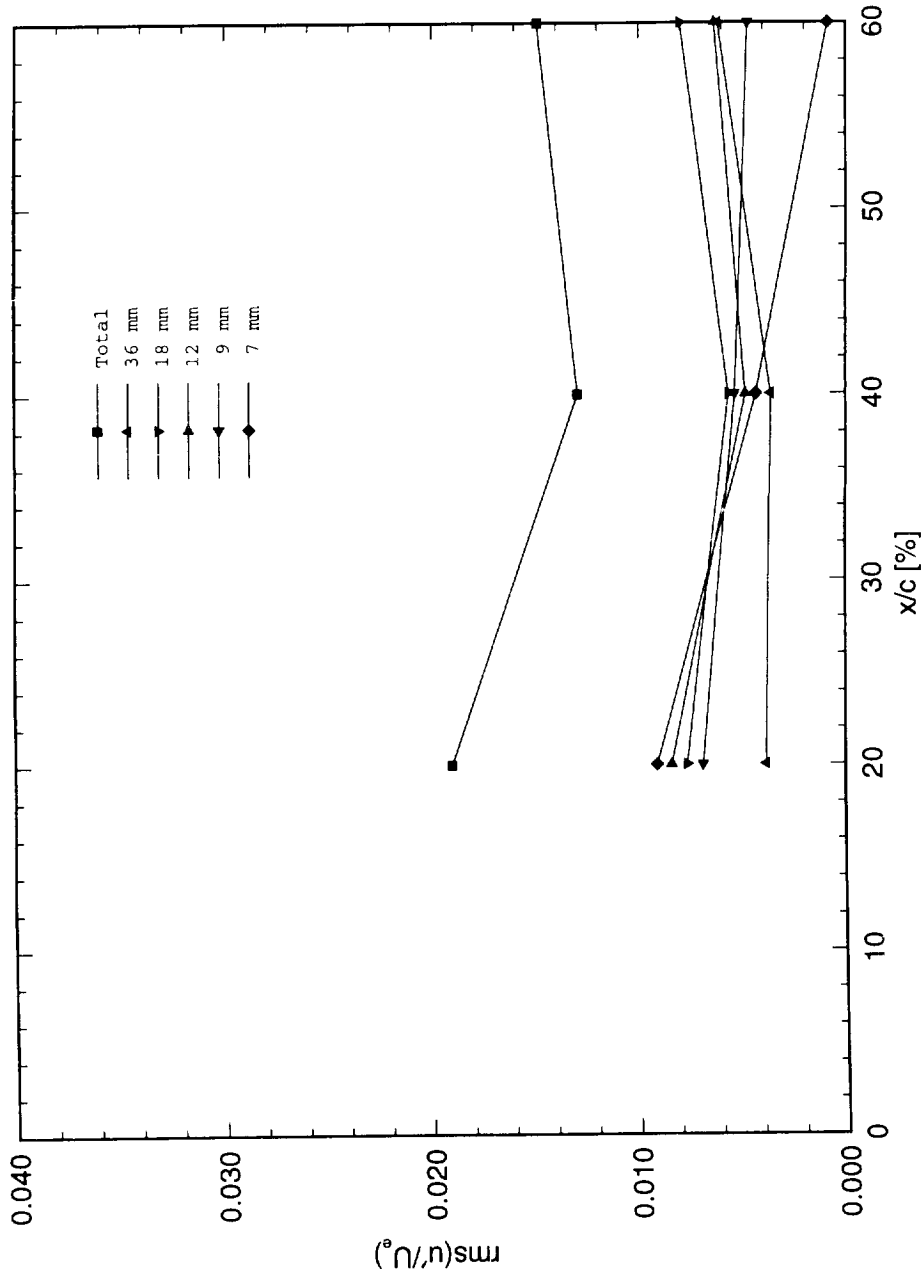

Figure 7.104. Total and discrete-wavelength stationary crossflow rms amplitudes. $Re_c = 3.0 \times 10^6$. Full array of 146 μm roughness with 36 mm spacing. Data set U.

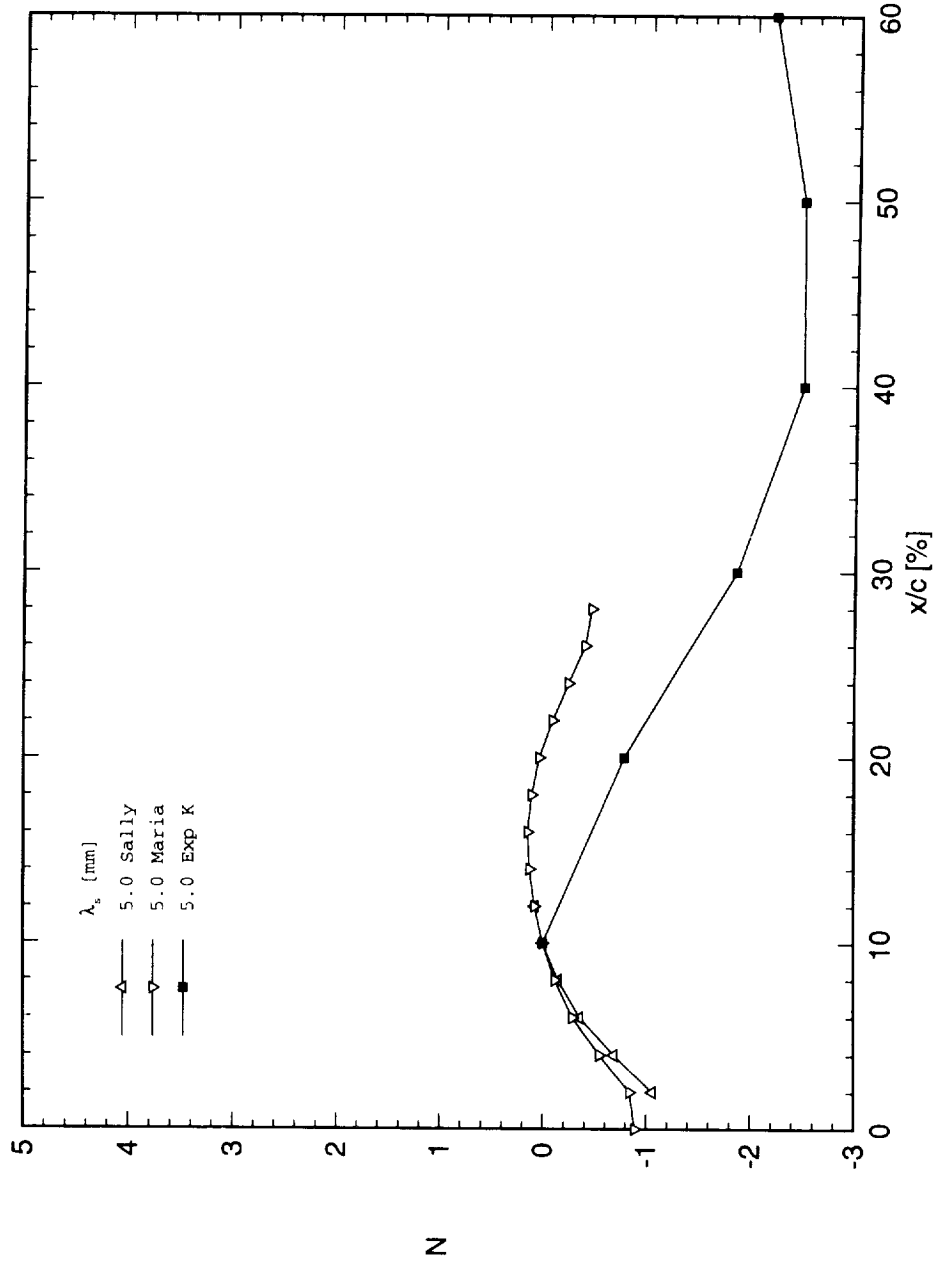

Figure 7.105. Measured and theoretical relative N-factors for $\lambda_s = 5$ mm. Reference point is $x/c = 0.1$. $Re_c = 3.0 \times 10^6$.

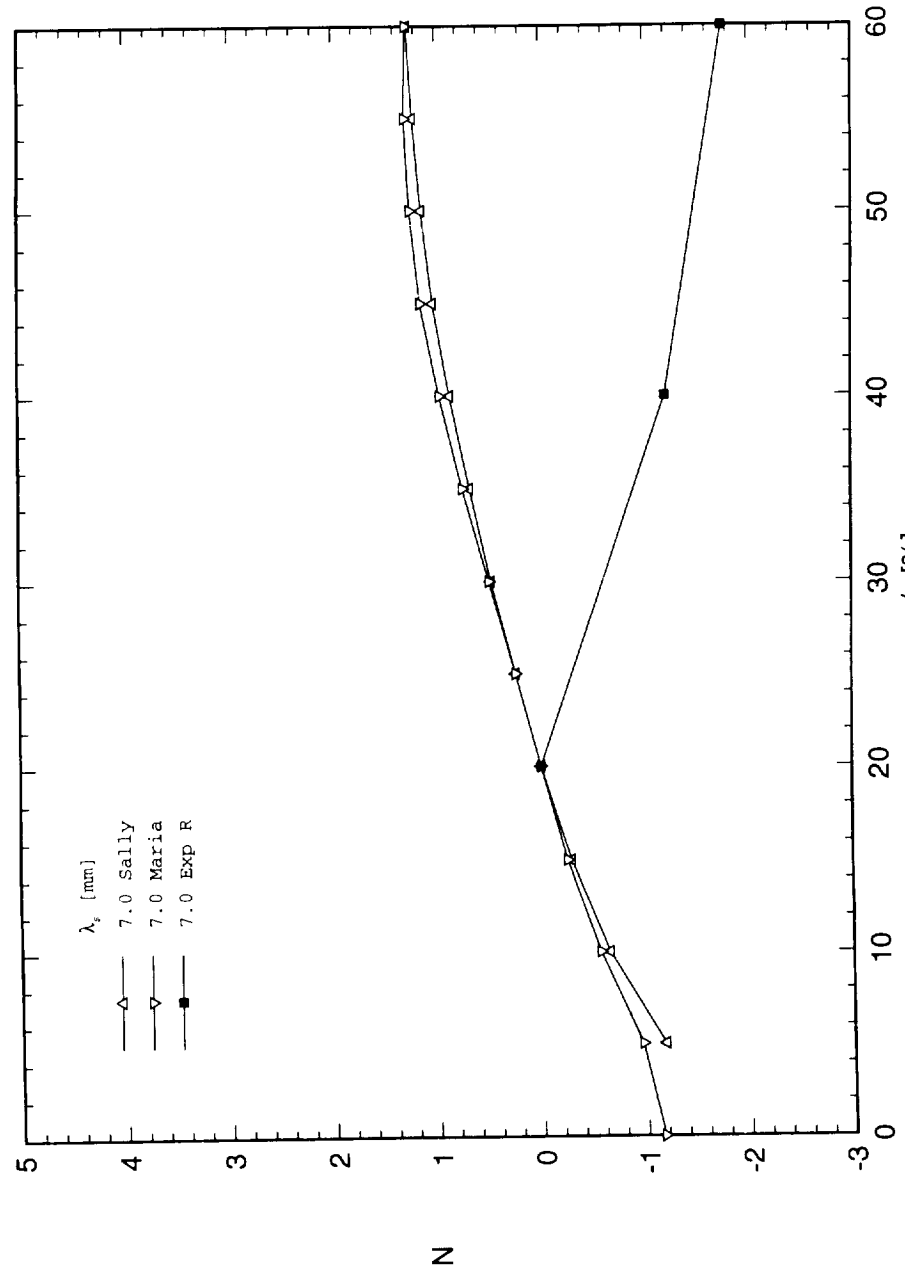

Figure 7.106. Measured and theoretical relative N-factors for $\lambda_s = 7$ mm. Reference point is $x/c = 0.2$. $Re_c = 3.0 \times 10^6$.

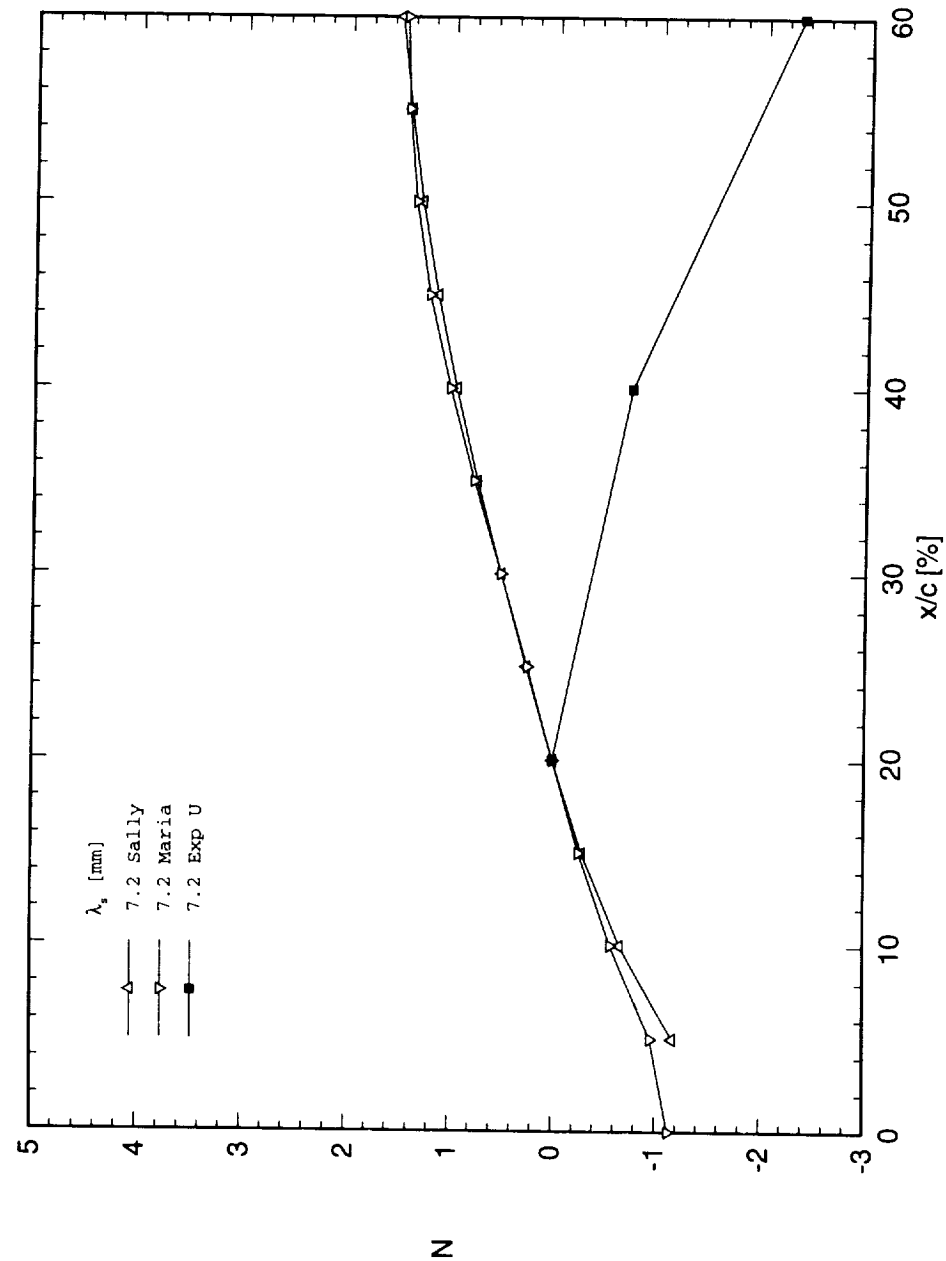

Figure 7.107. Measured and theoretical relative N-factors for $\lambda_s = 7.2$ mm. Reference point is $x/c = 0.2$. $Re_c = 3.0 \times 10^6$.

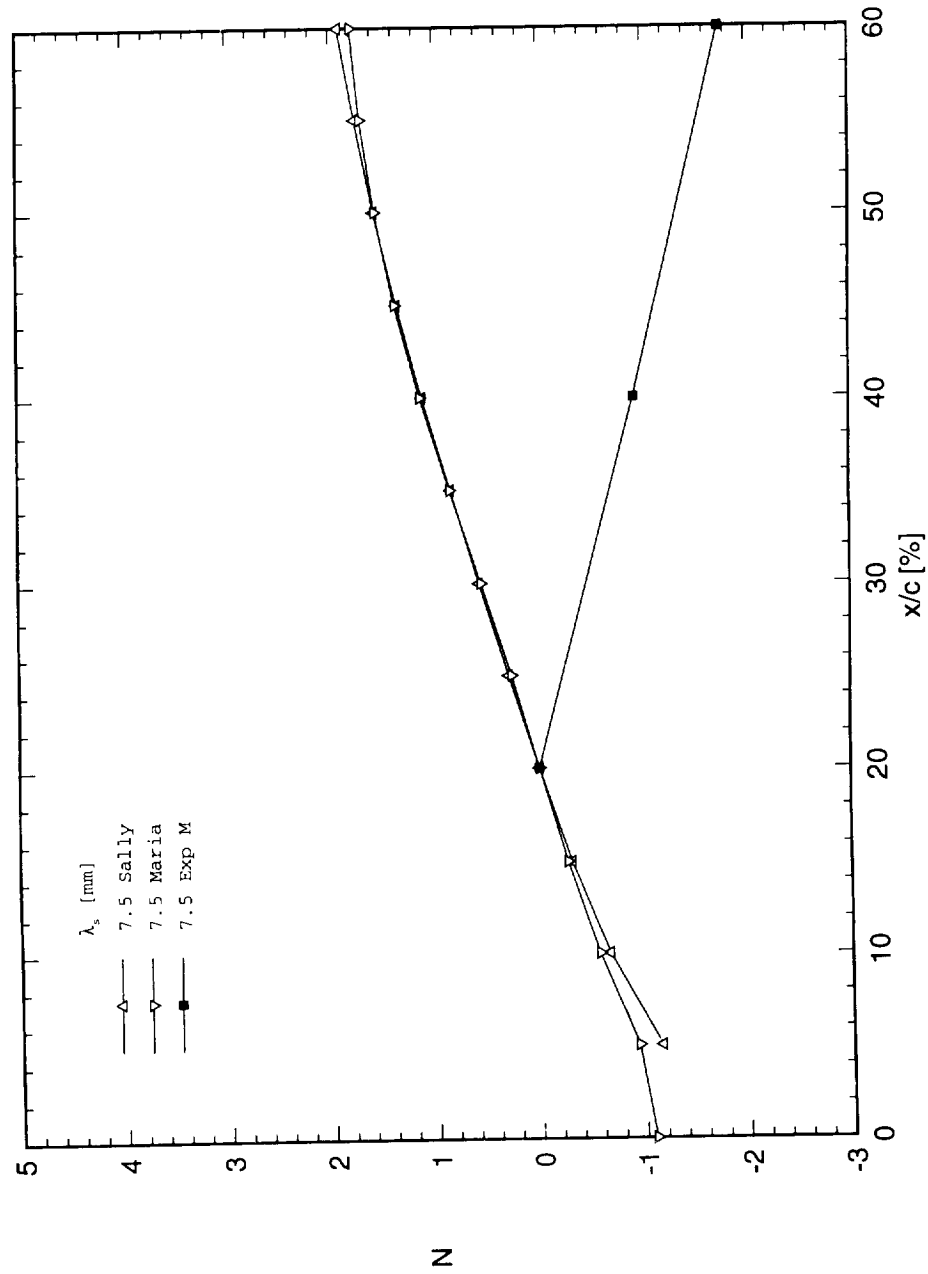

Figure 7.108. Measured and theoretical relative N-factors for $\lambda_s = 7.5$ mm. Reference point is $x/c = 0.2$. $Re_c = 3.0 \times 10^6$.

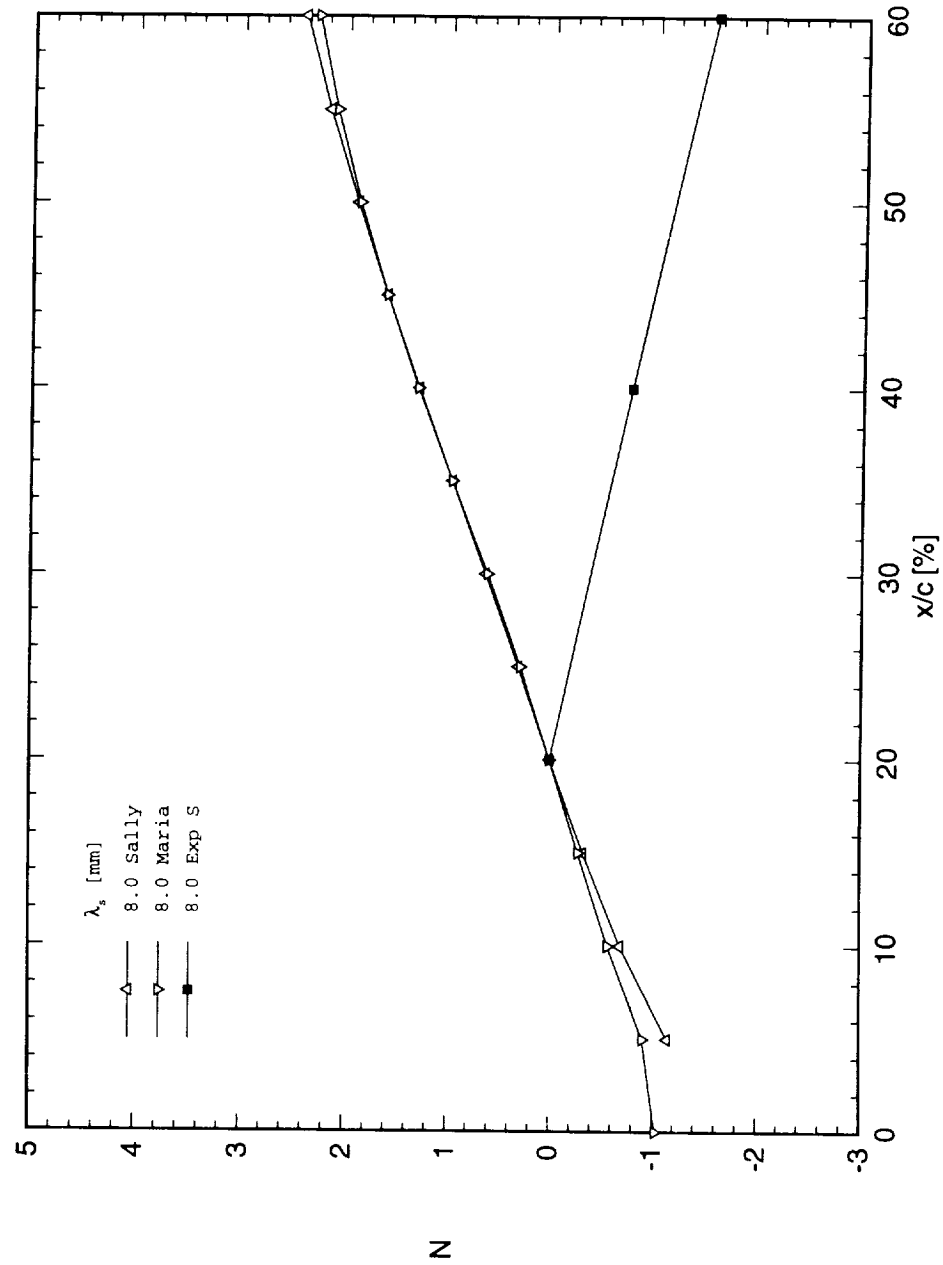

Figure 7.109. Measured and theoretical relative N-factors for $\lambda_s = 8$ mm. Reference point is $x/c = 0.2$. $Re_c = 3.0 \times 10^6$.

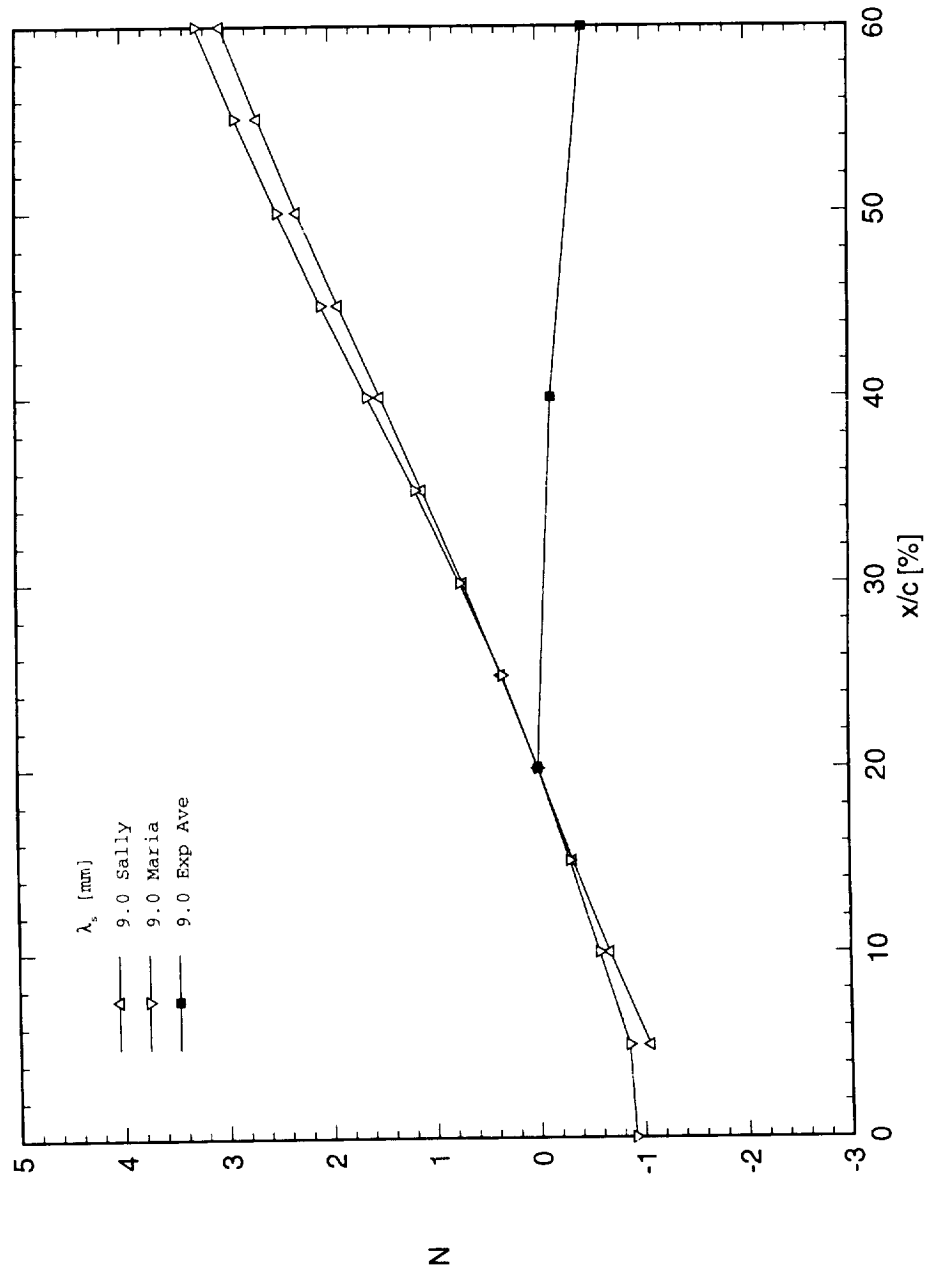

Figure 7.110. Measured and theoretical relative N-factors for $\lambda_s = 9$ mm. Reference point is $x/c = 0.2$. $Re_c = 3.0 \times 10^6$.

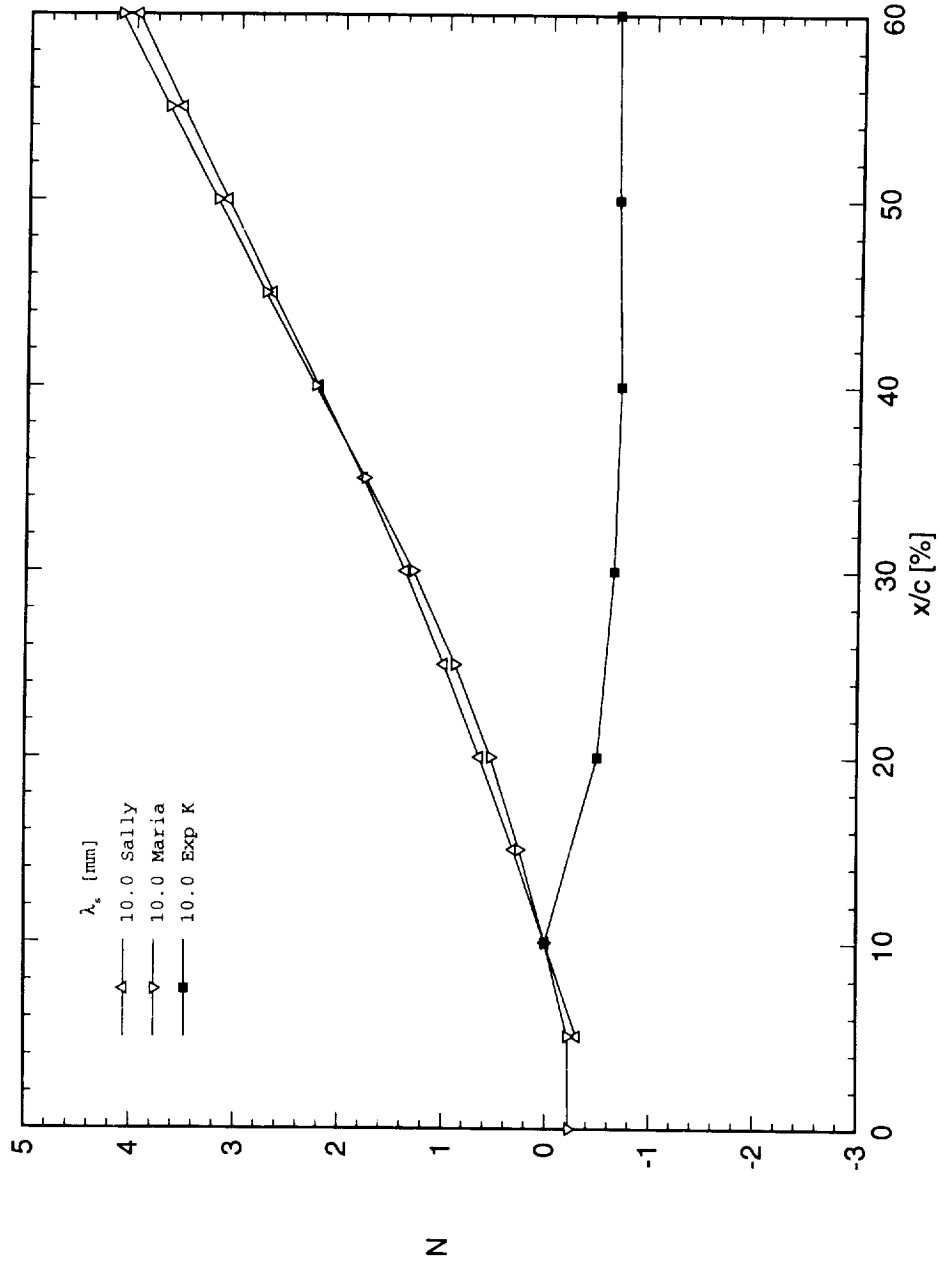

Figure 7.111. Measured and theoretical relative N-factors for $\lambda_s = 10$ mm. Reference point is $x/c = 0.1$. $Re_c = 3.0 \times 10^6$.

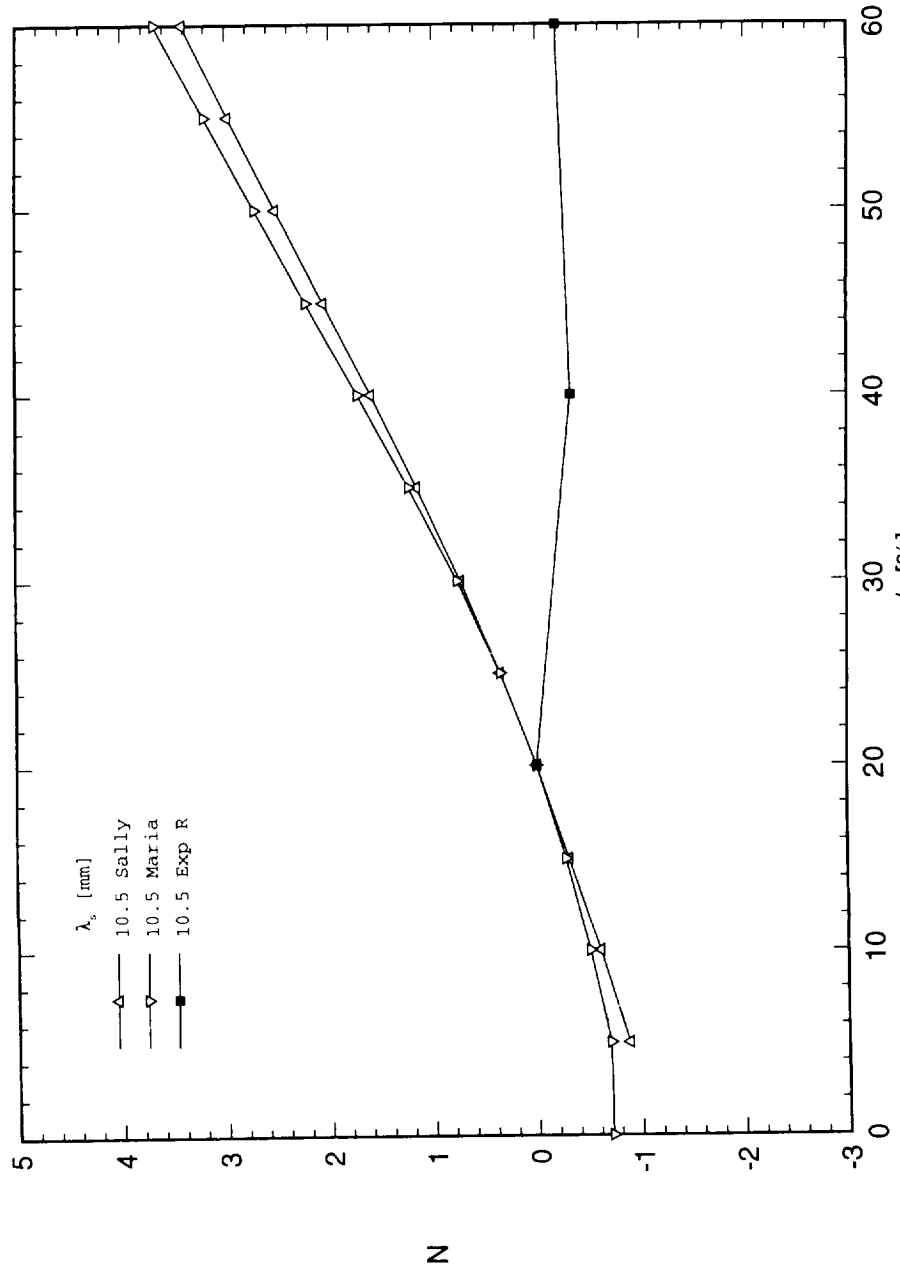

Figure 7.112. Measured and theoretical relative N-factors for $\lambda_s = 10.5$ mm. Reference point is $x/c = 0.2$. $Re_c = 3.0 \times 10^6$.

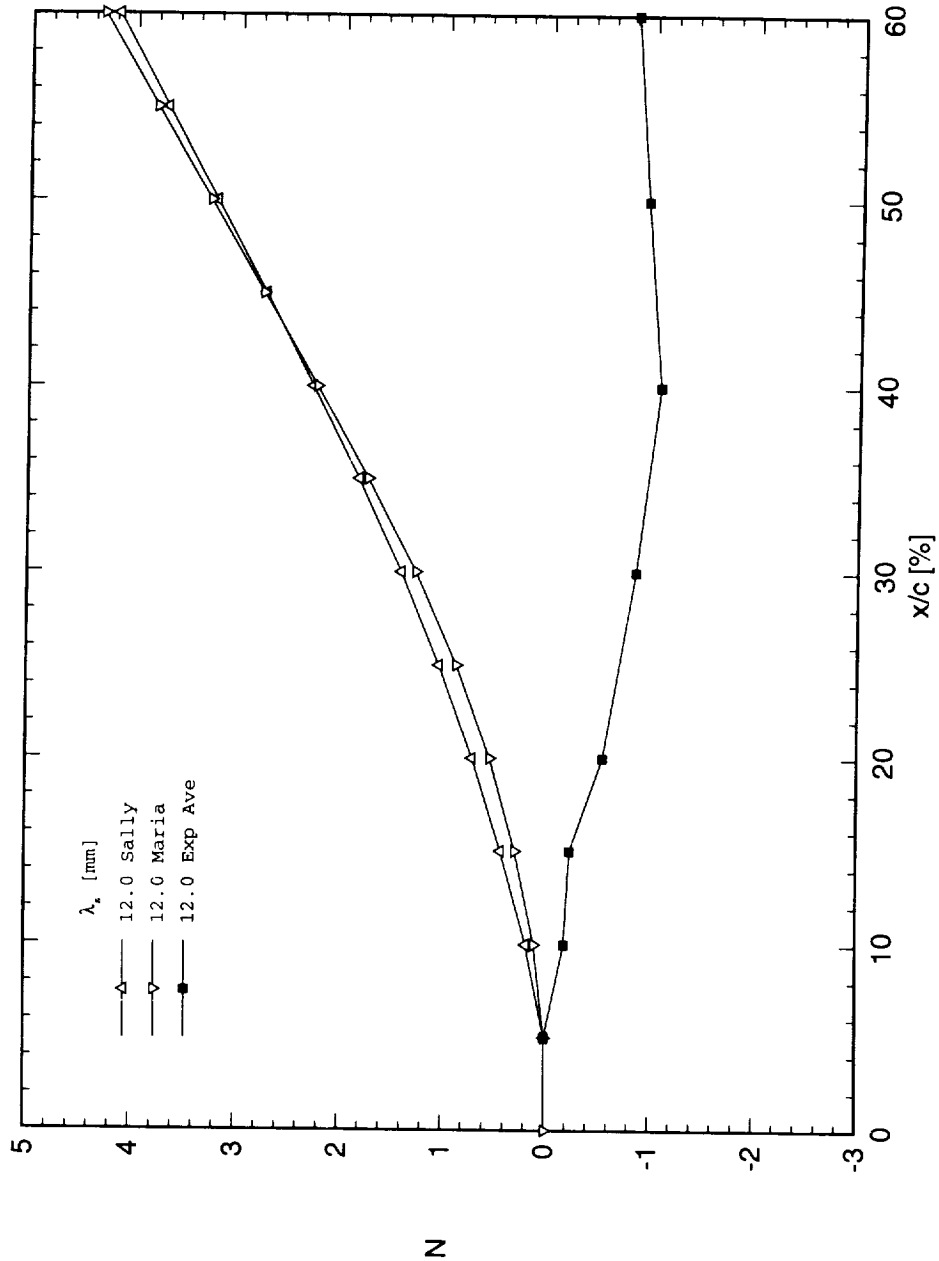

Figure 7.113. Measured and theoretical relative N-factors for $\lambda_s = 12$ mm. Reference point is $x/c = 0.05$. $Re_c = 3.0 \times 10^6$.

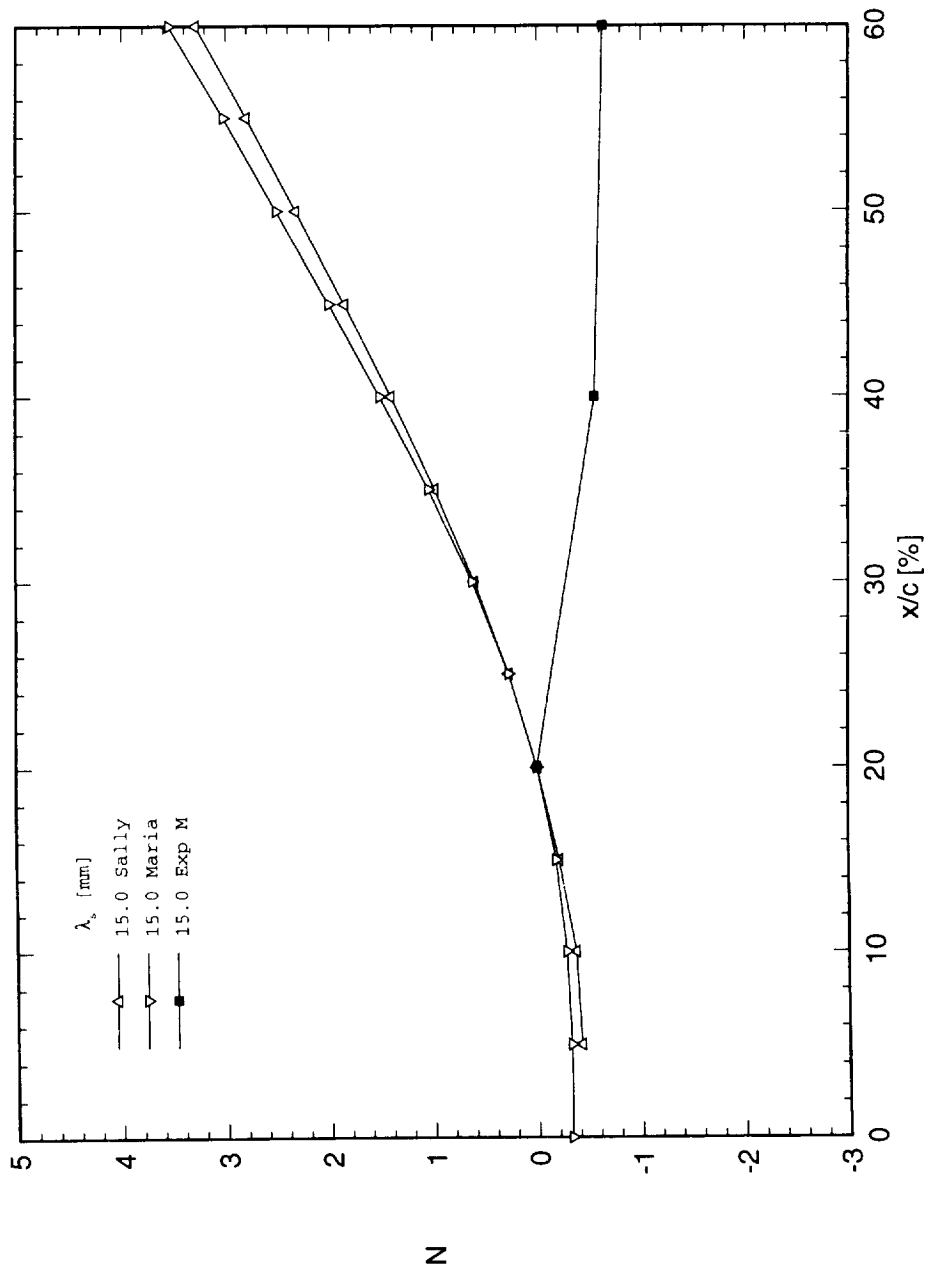

Figure 7.114. Measured and theoretical relative N-factors for $\lambda_s = 15$ mm. Reference point is $x/c = 0.2$. $Re_c = 3.0 \times 10^6$.

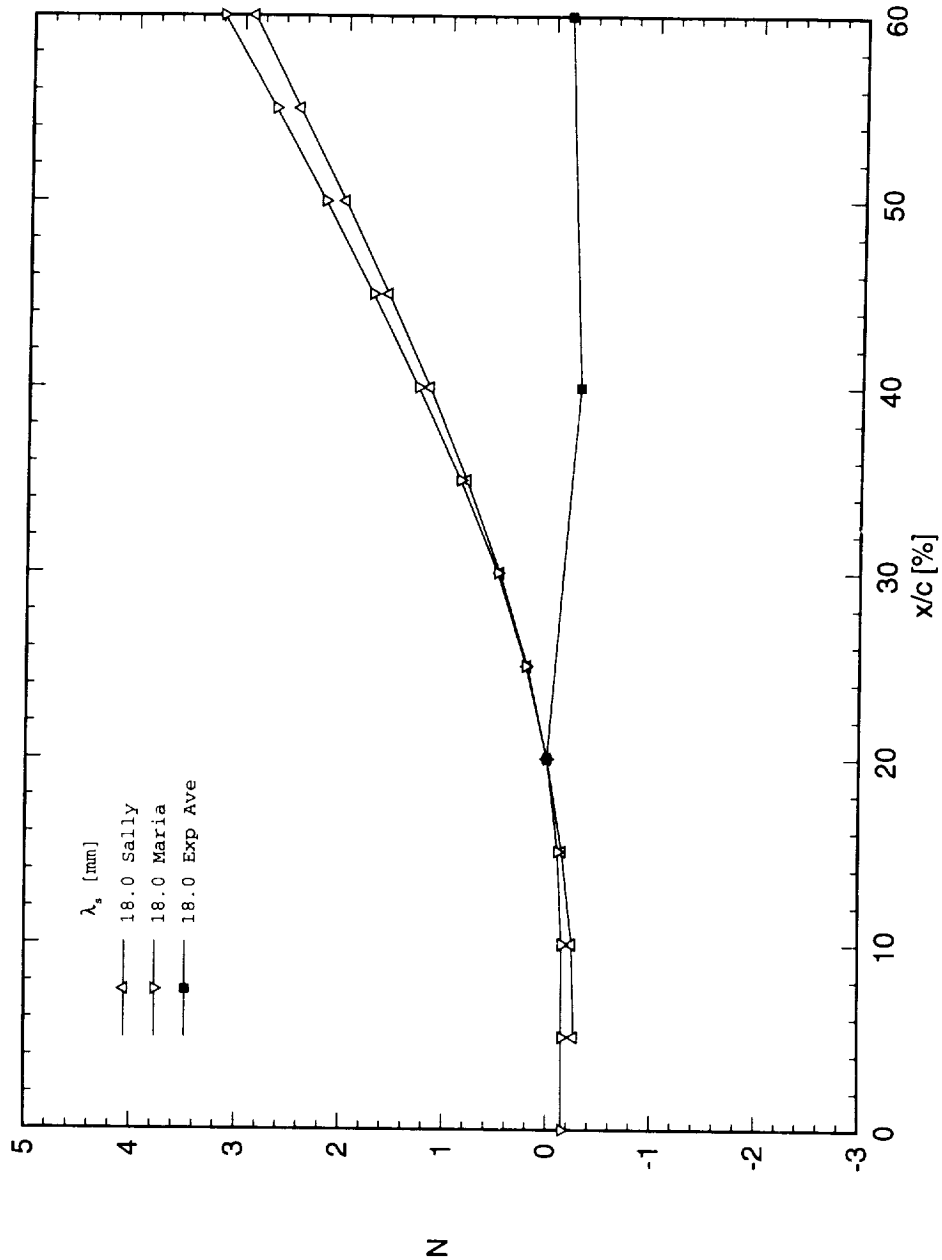

Figure 7.115. Measured and theoretical relative N-factors for $\lambda_s = 18$ mm. Reference point is $x/c = 0.2$. $Re_c = 3.0 \times 10^6$.

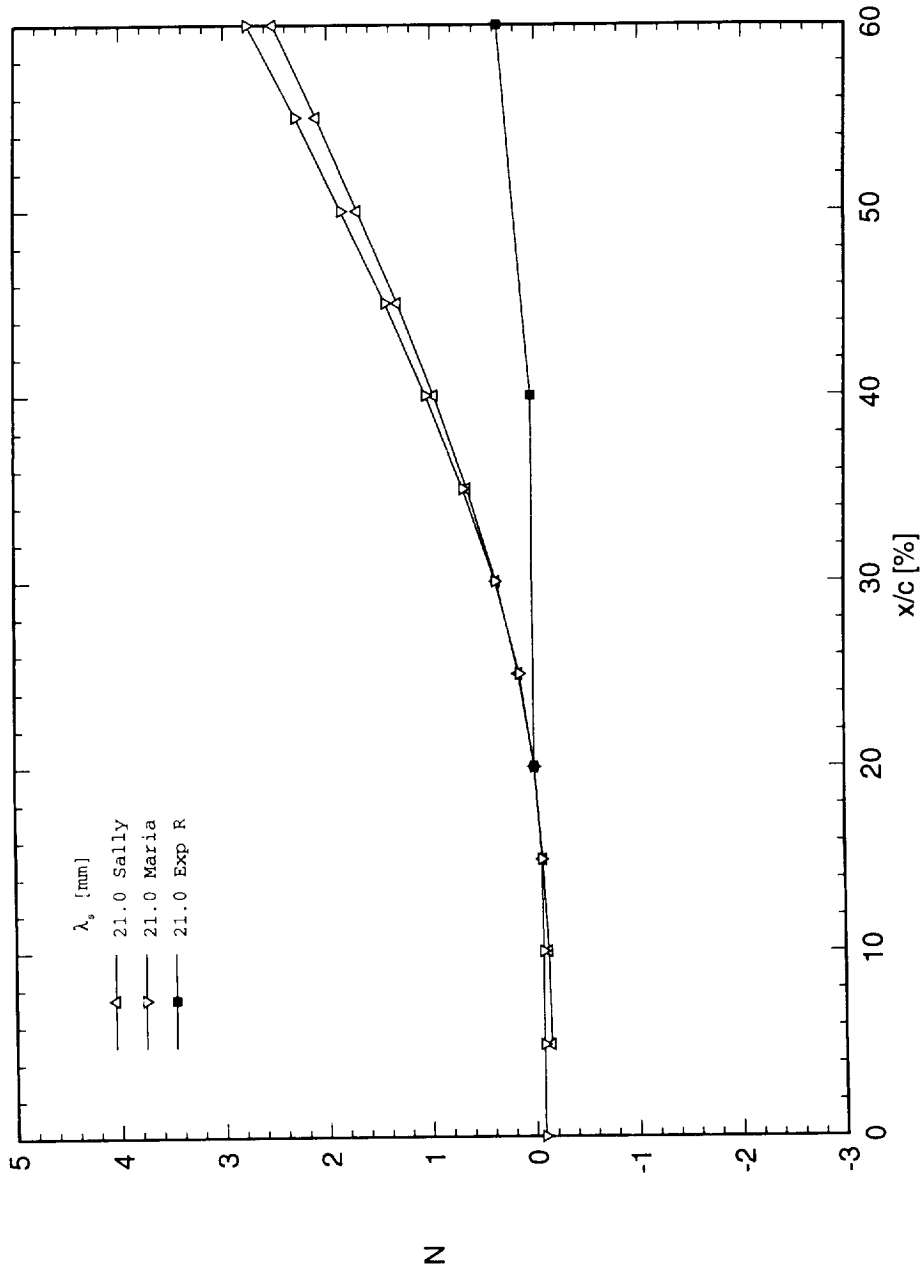

Figure 7.116. Measured and theoretical relative N-factors for $\lambda_s = 21$ mm. Reference point is $x/c = 0.2$. $Re_c = 3.0 \times 10^6$.

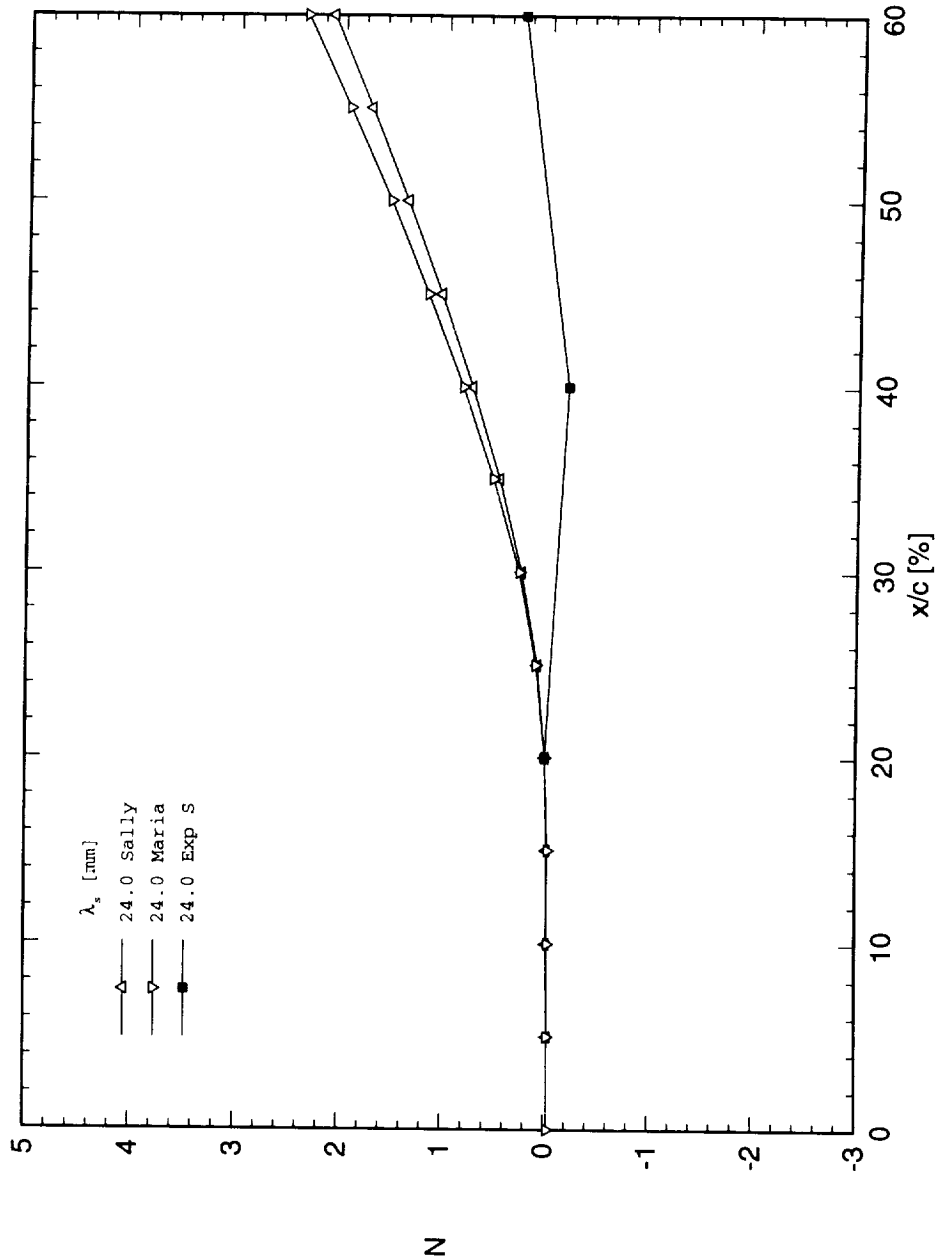

Figure 7.117. Measured and theoretical relative N-factors for $\lambda_s = 24$ mm. Reference point is $x/c = 0.2$. $Re_c = 3.0 \times 10^6$.

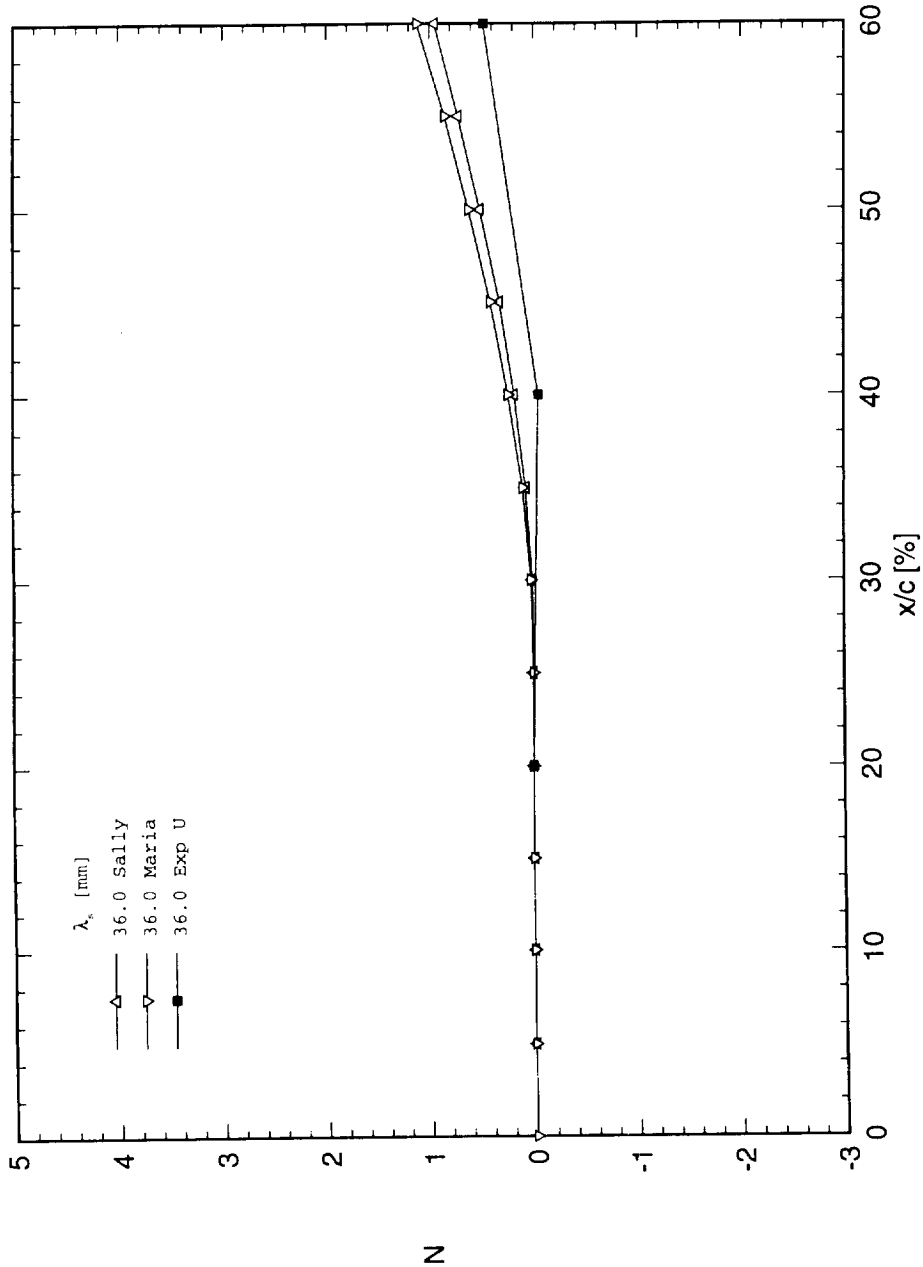

Figure 7.118. Measured and theoretical relative N-factors for $\lambda_s = 36$ mm. Reference point is $x/c = 0.2$. $Re_c = 3.0 \times 10^6$.

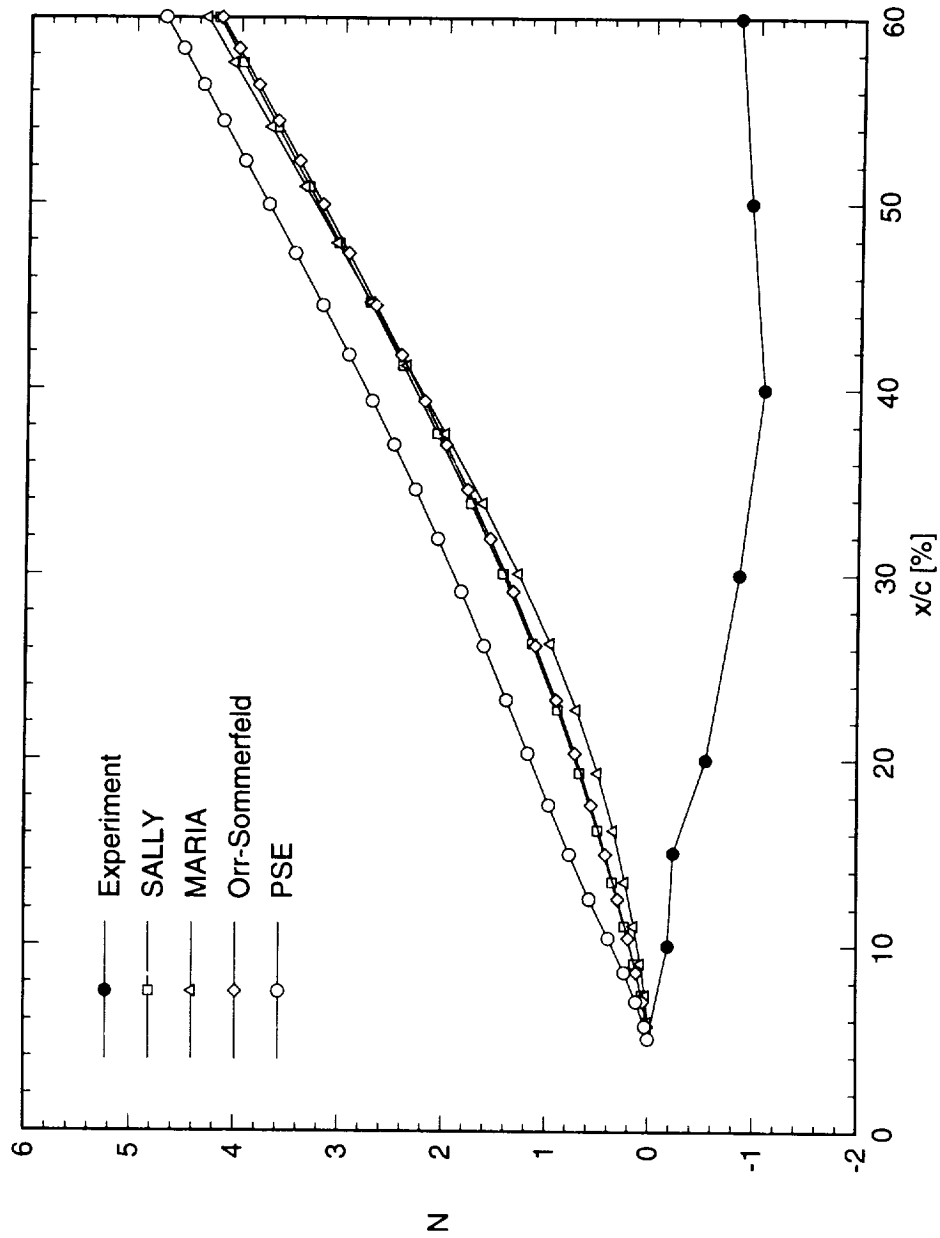

Figure 7.119. Measured and theoretical N-factors for $\lambda_s = 12$ mm. Reference point is $x/c = 0.05$. $Re_c = 3.0 \times 10^6$.

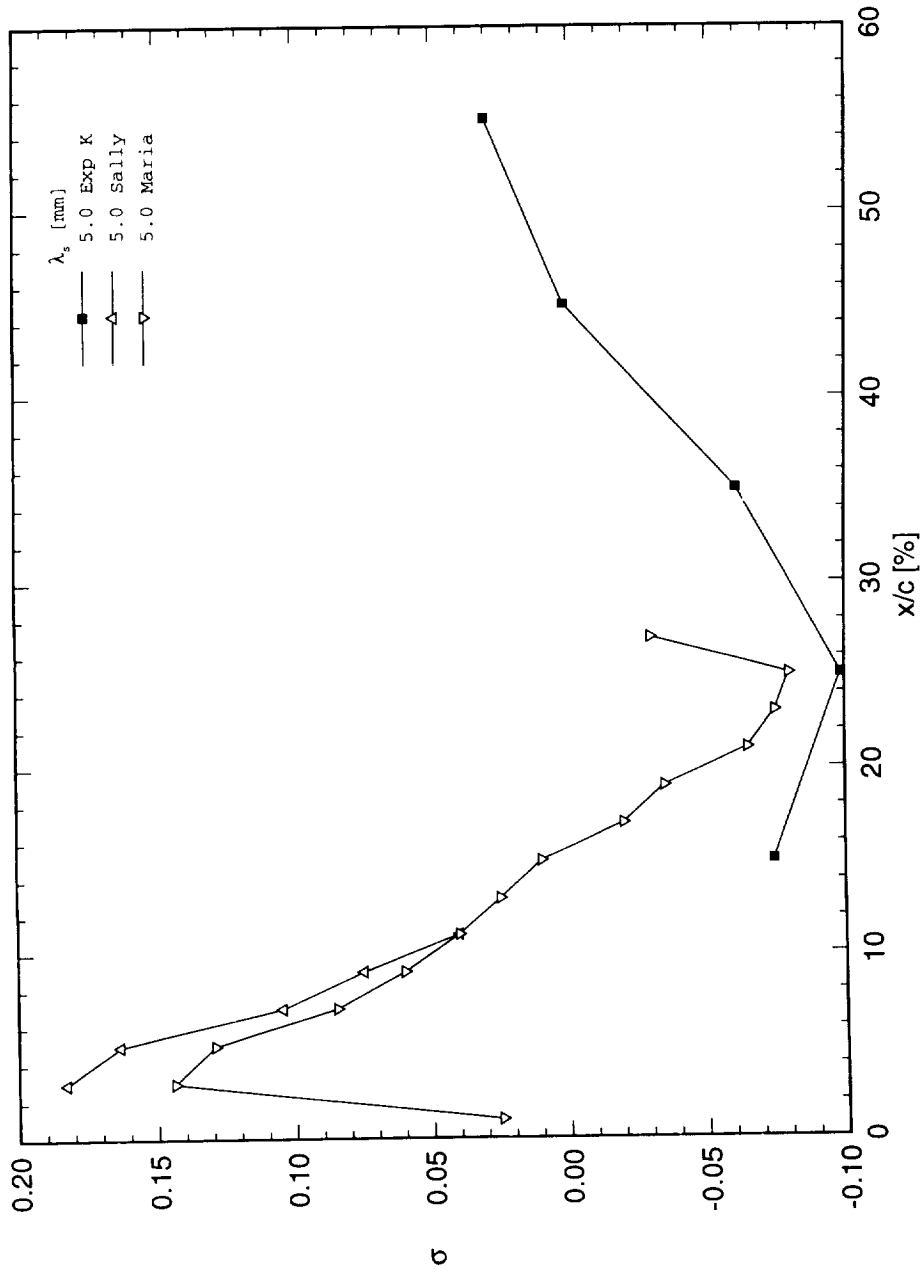

Figure 7.120. Measured and theoretical dimensionless growth rates for $\lambda_s = 5$ mm. $Re_c = 3.0 \times 10^6$.

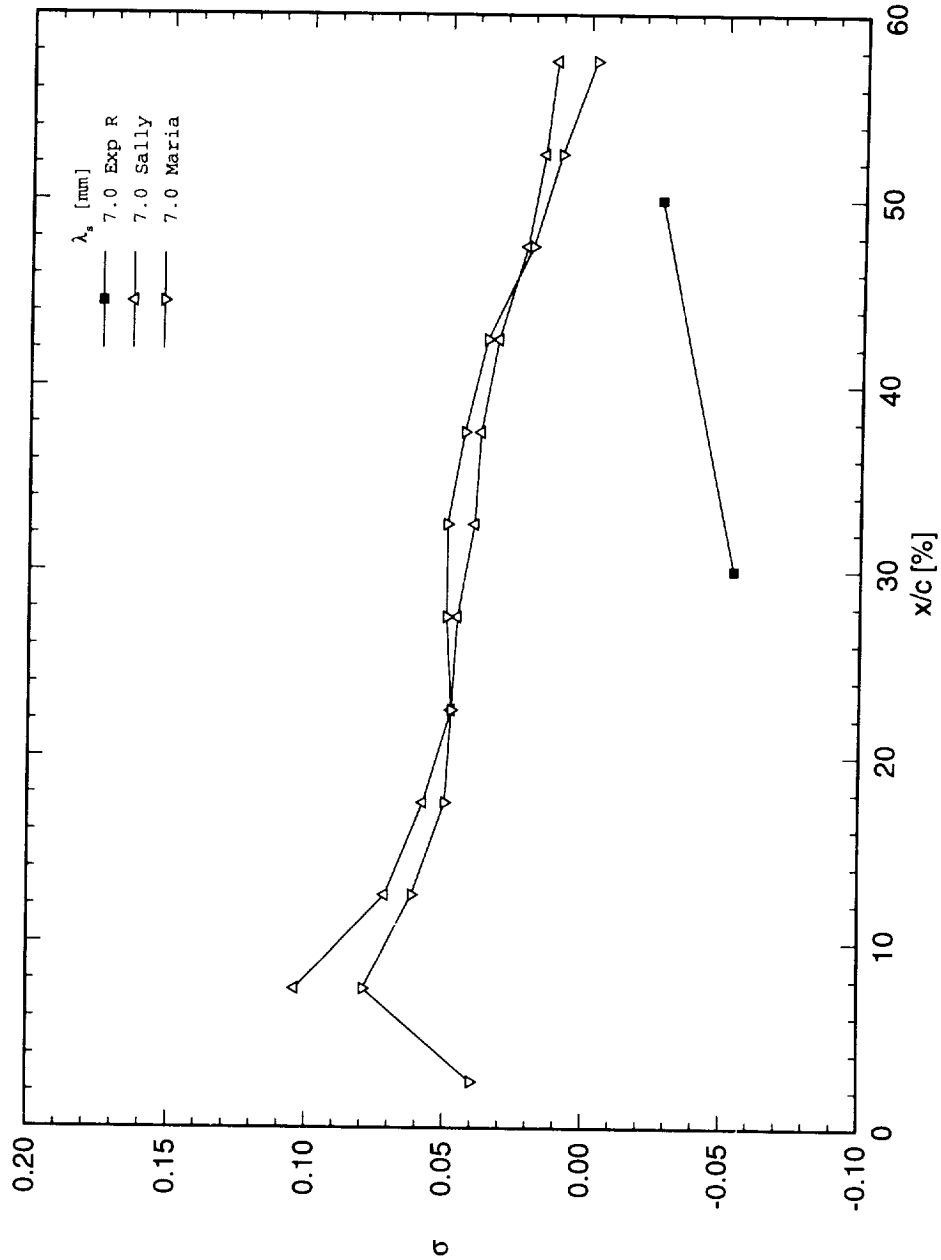

Figure 7.121. Measured and theoretical dimensionless growth rates for $\lambda_s = 7$ mm. $Re_c = 3.0 \times 10^6$.

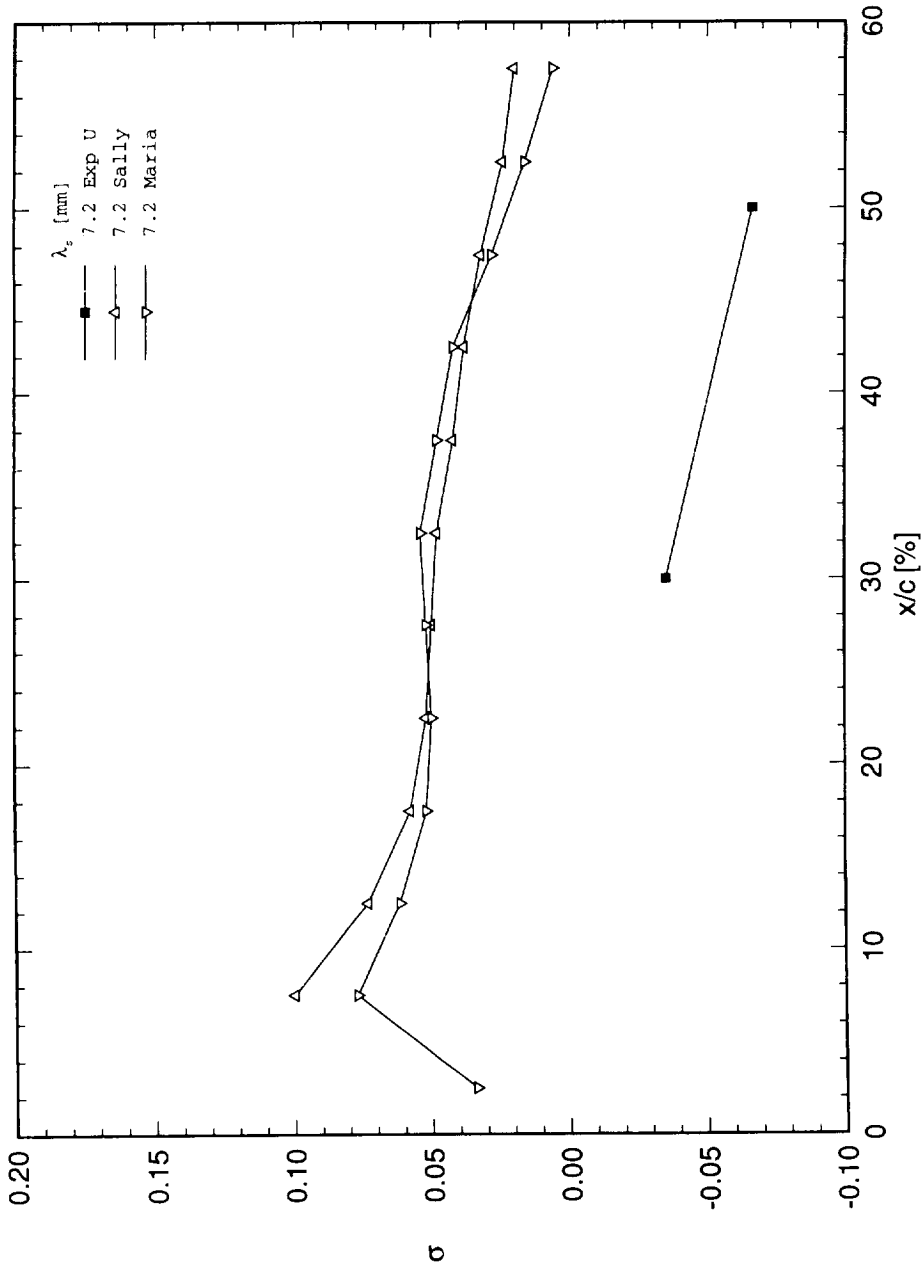

Figure 7.122. Measured and theoretical dimensionless growth rates for $\lambda_s = 7.2$ mm. $Re_c = 3.0 \times 10^6$.

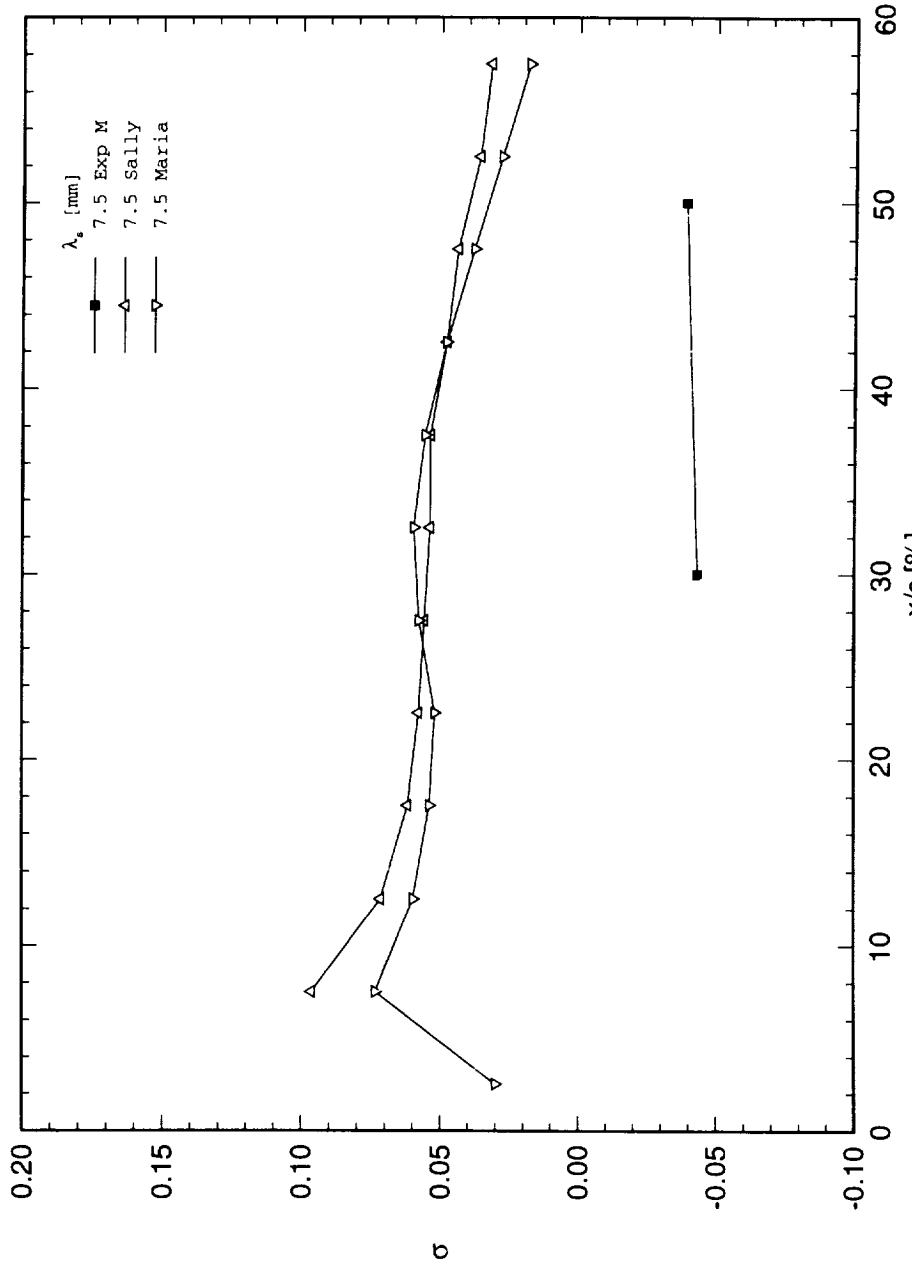

Figure 7.123. Measured and theoretical dimensionless growth rates for $\lambda_s = 7.5$ mm. $Re_c = 3.0 \times 10^6$.

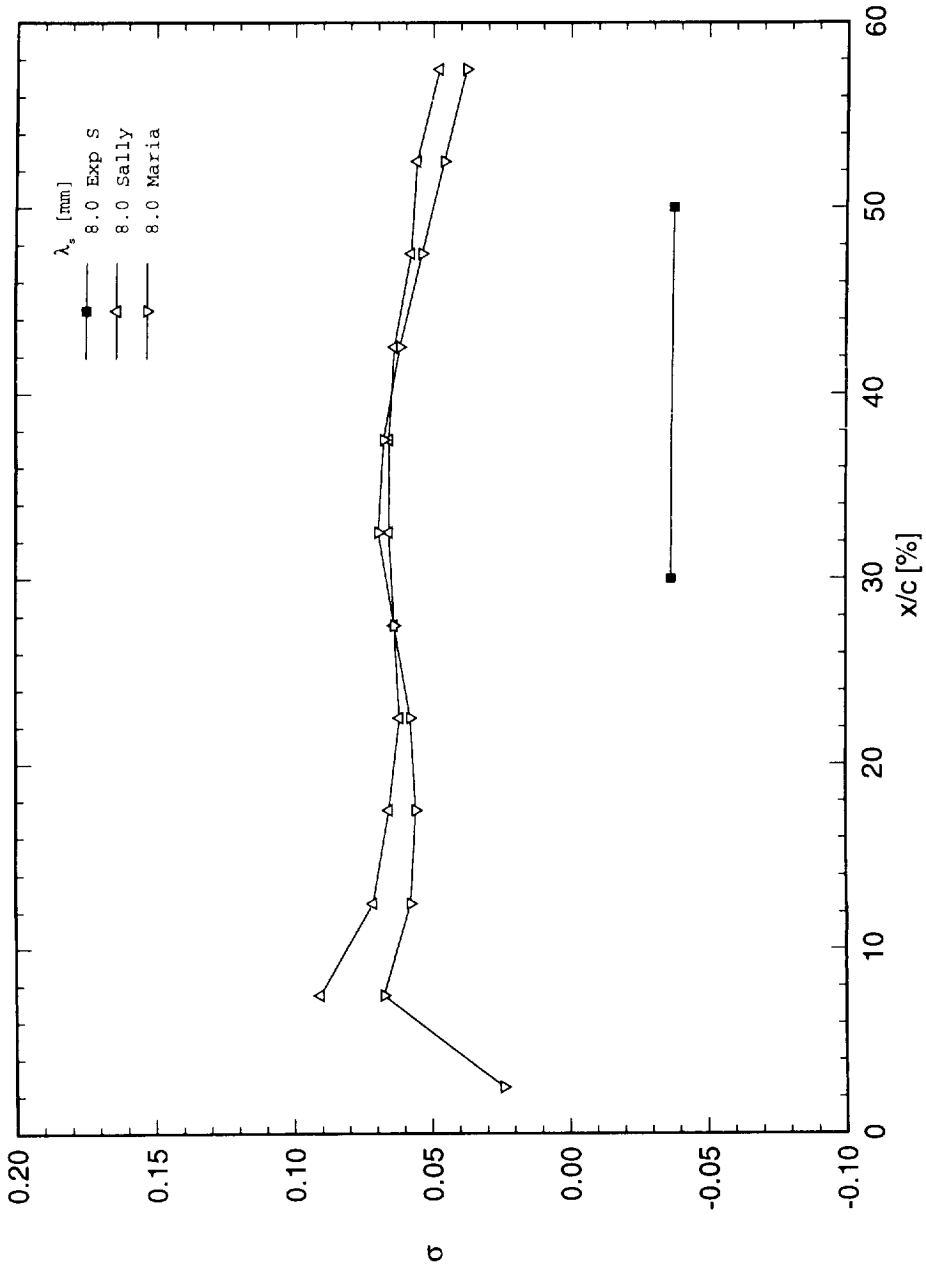

Figure 7.124. Measured and theoretical dimensionless growth rates for $\lambda_s = 8$ mm. $Re_c = 3.0 \times 10^6$.

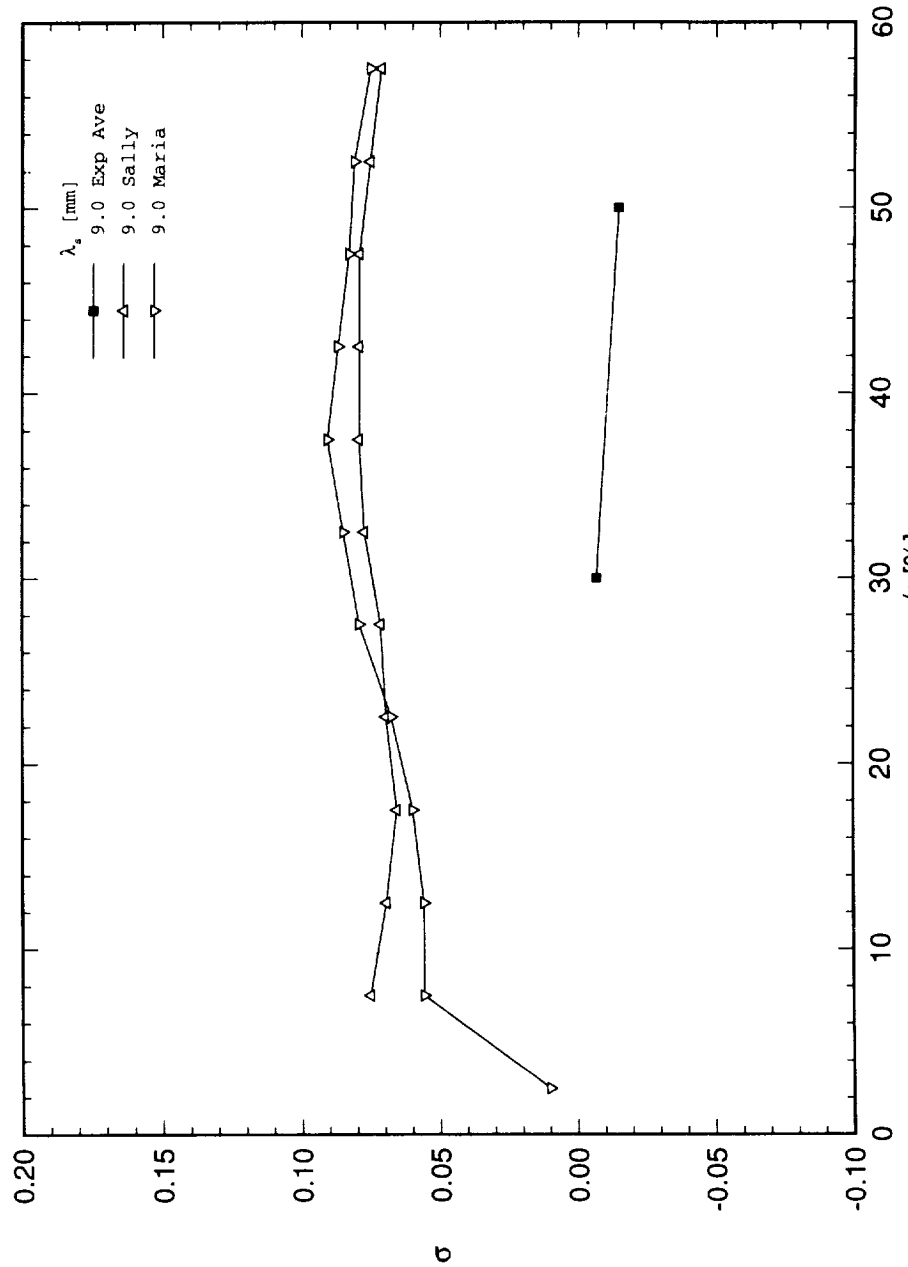

Figure 7.125. Measured and theoretical dimensionless growth rates for $\lambda_s = 9$ mm. $Re_c = 3.0 \times 10^6$.

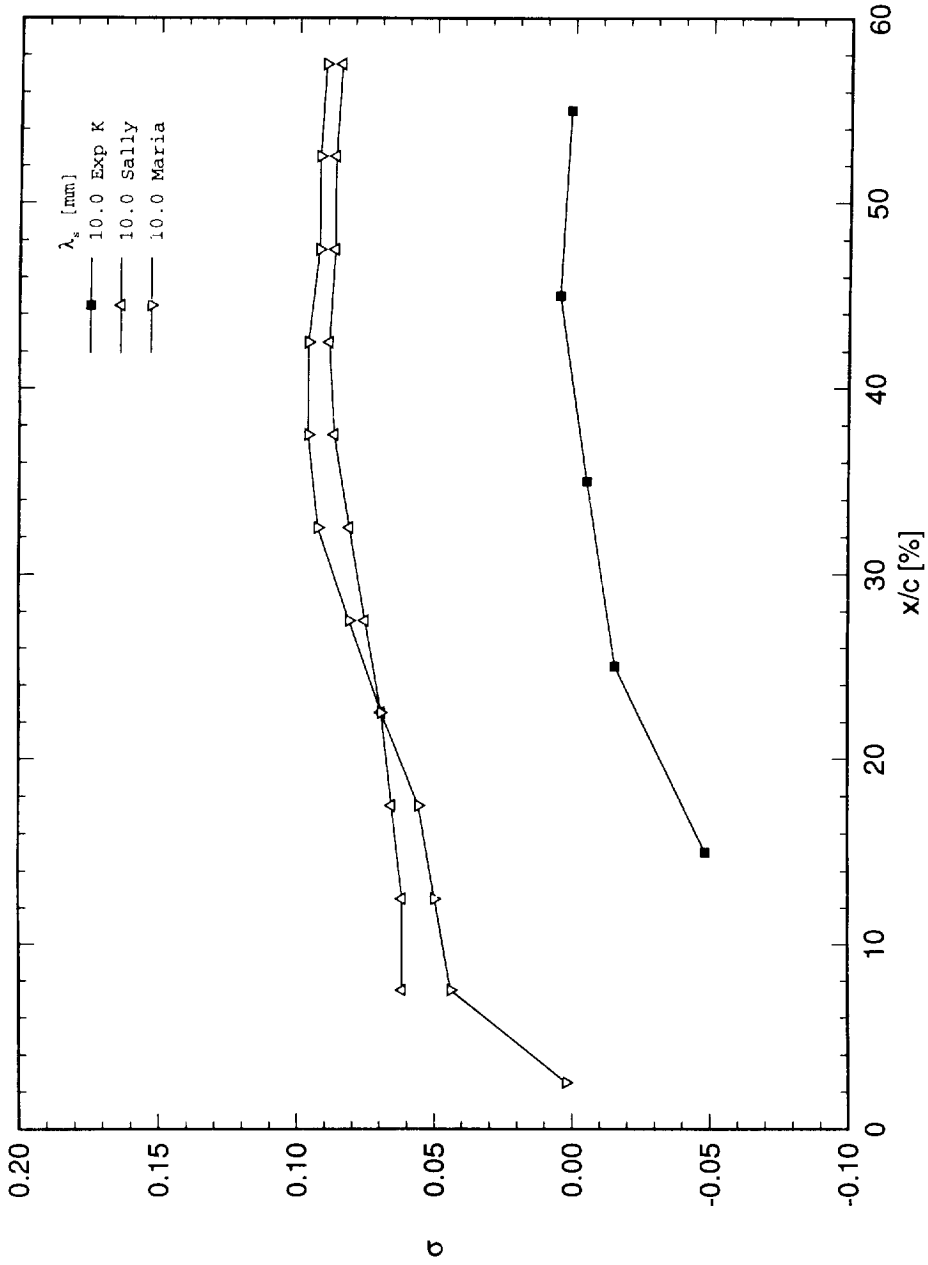

Figure 7.126. Measured and theoretical dimensionless growth rates for $\lambda_s = 10$ mm. $Re_c = 3.0 \times 10^6$.

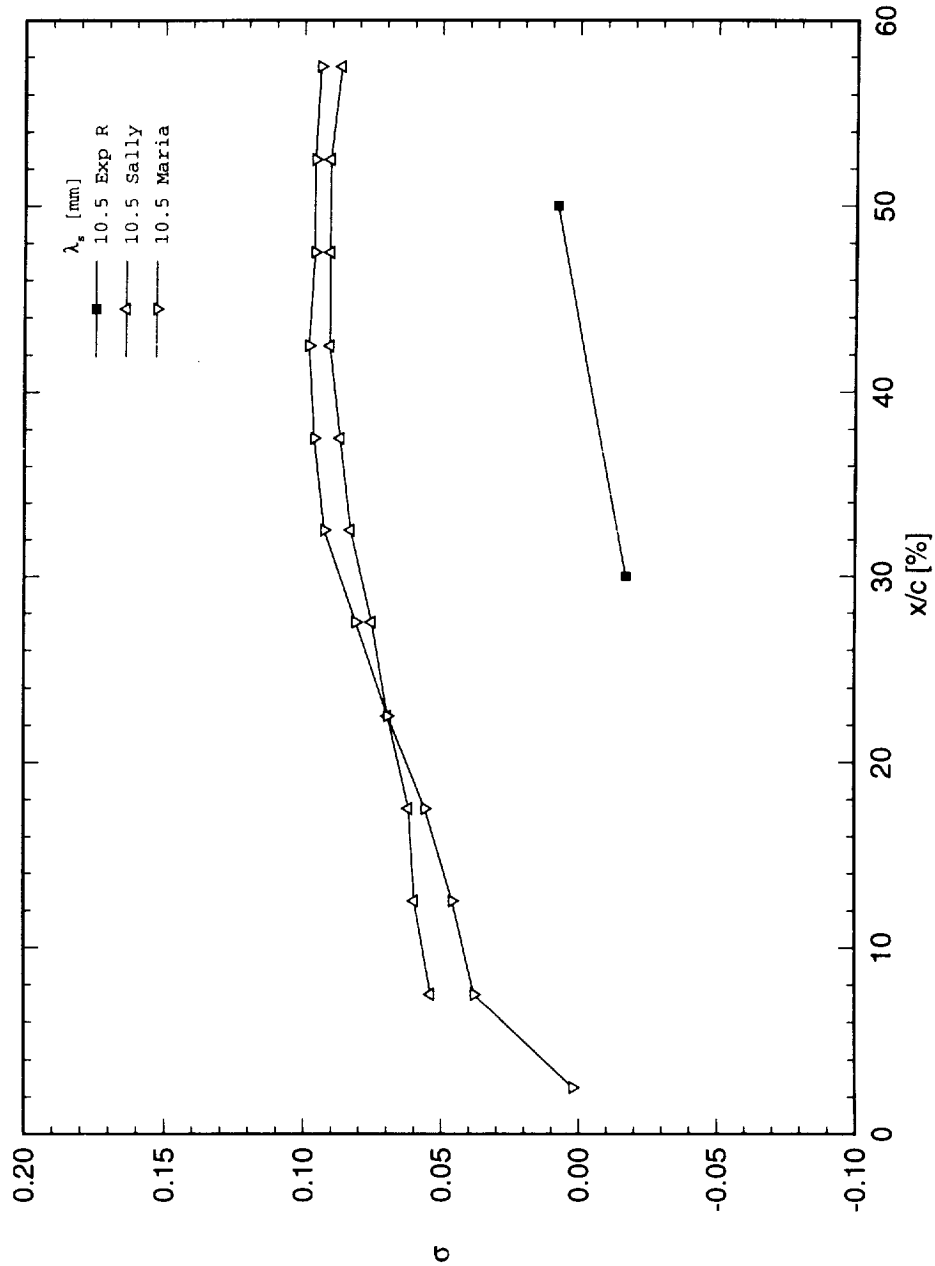

Figure 7.127. Measured and theoretical dimensionless growth rates for $\lambda_s = 10.5$ mm. $Re_c = 3.0 \times 10^6$.

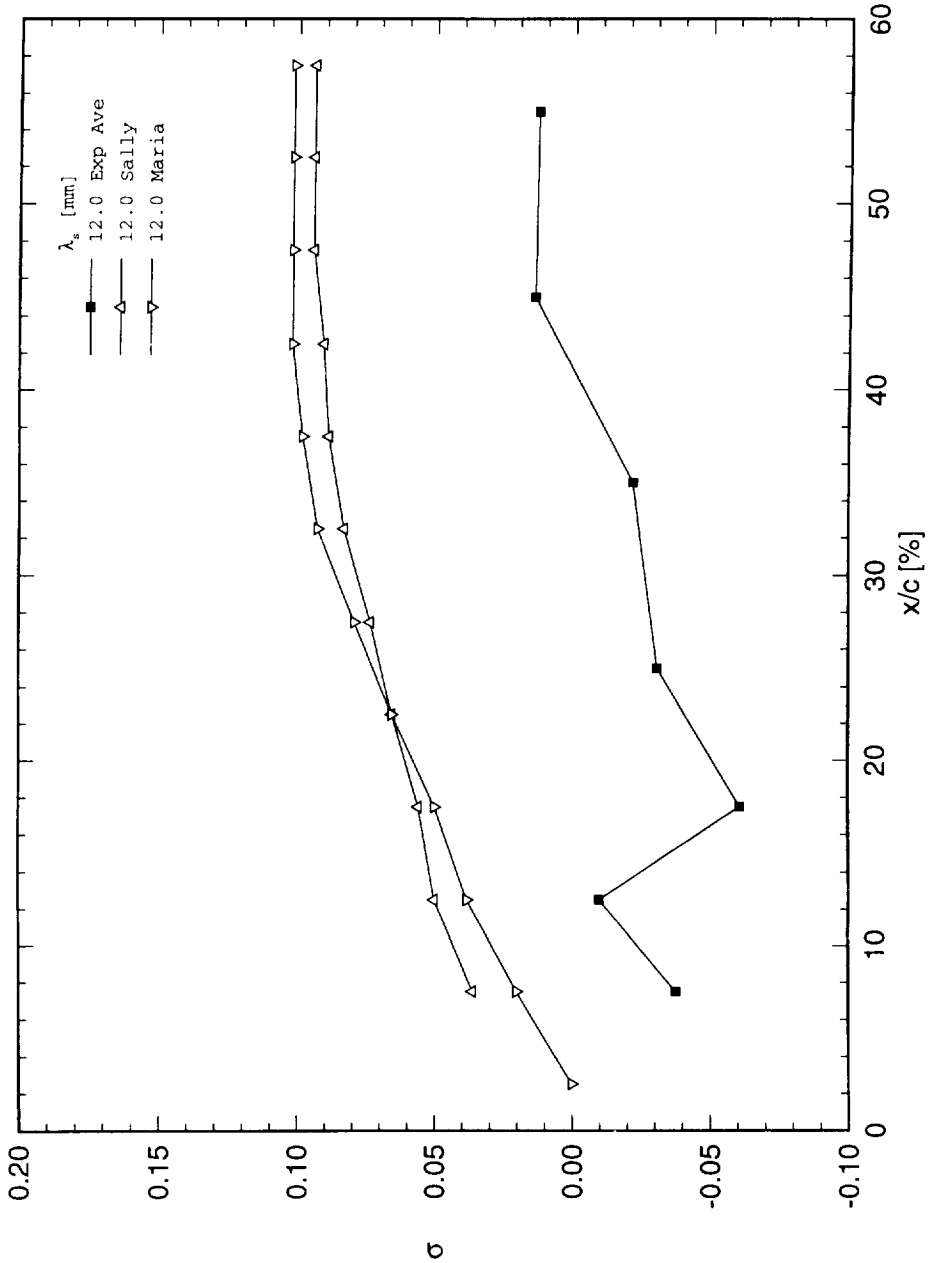

Figure 7.128. Measured and theoretical dimensionless growth rates for $\lambda_s = 12$ mm. $Re_c = 3.0 \times 10^6$.

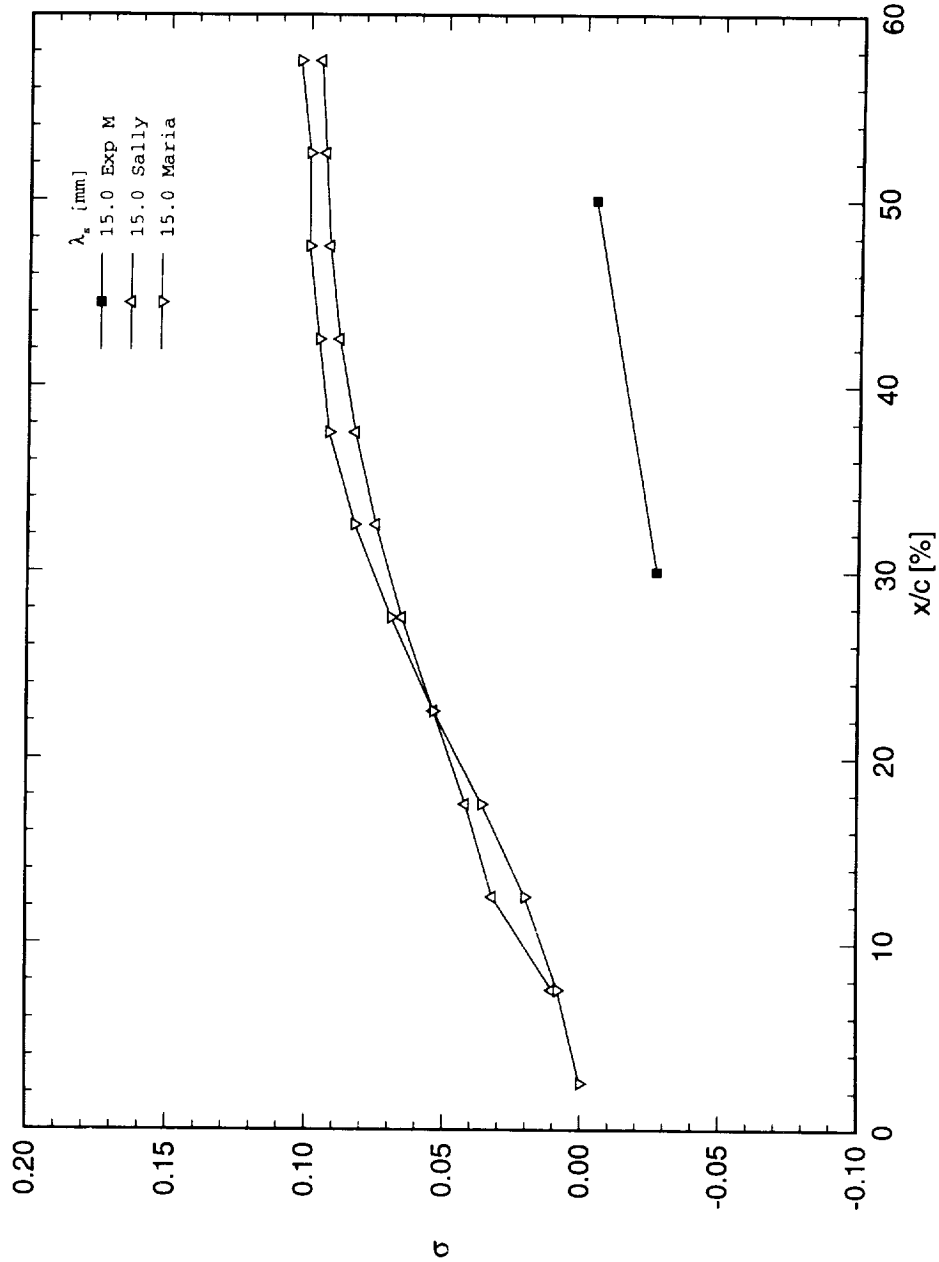

Figure 7.129. Measured and theoretical dimensionless growth rates for $\lambda_s = 15$ mm. $Re_c = 3.0 \times 10^6$.

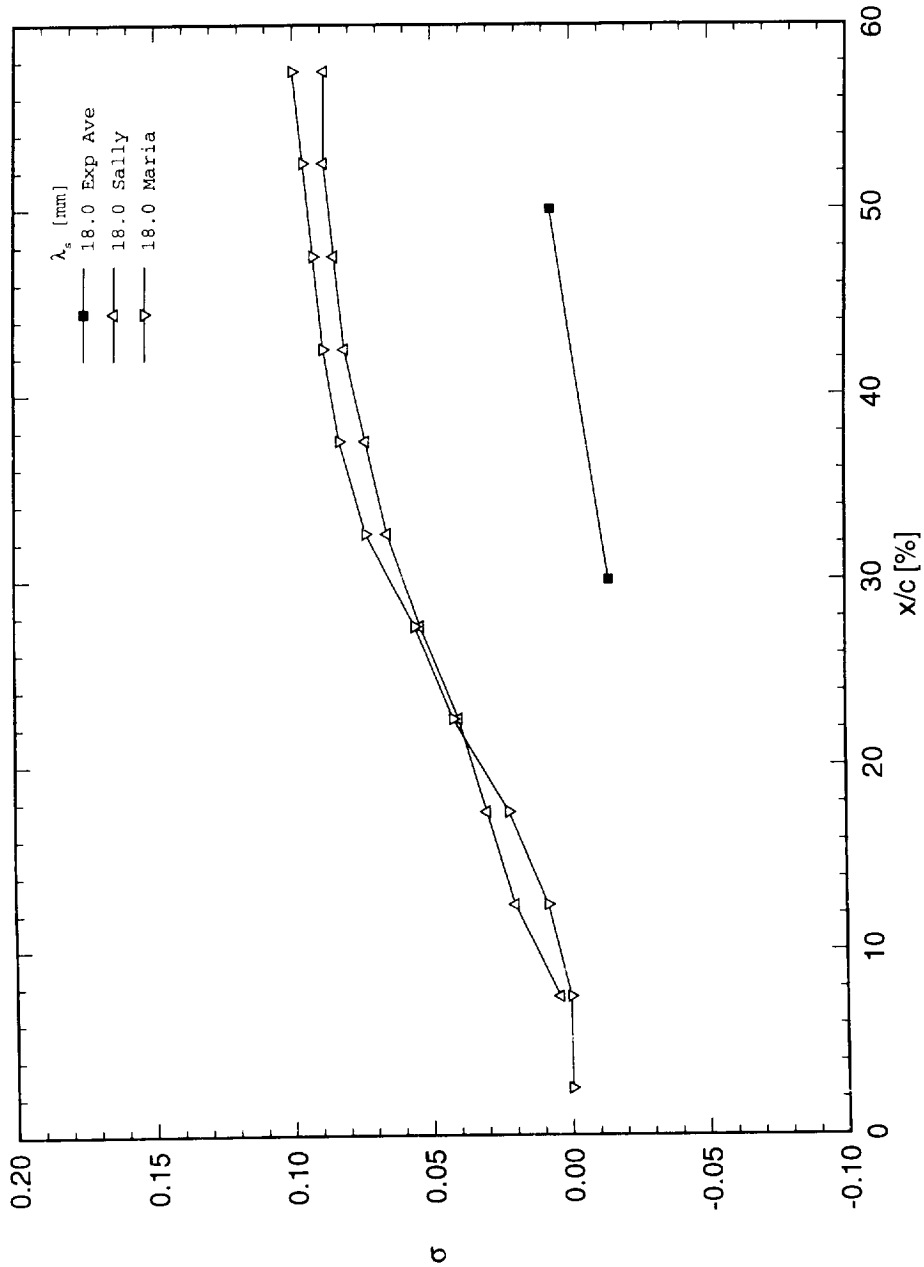

Figure 7.130. Measured and theoretical dimensionless growth rates for $\lambda_s = 18$ mm. $Re_c = 3.0 \times 10^6$.

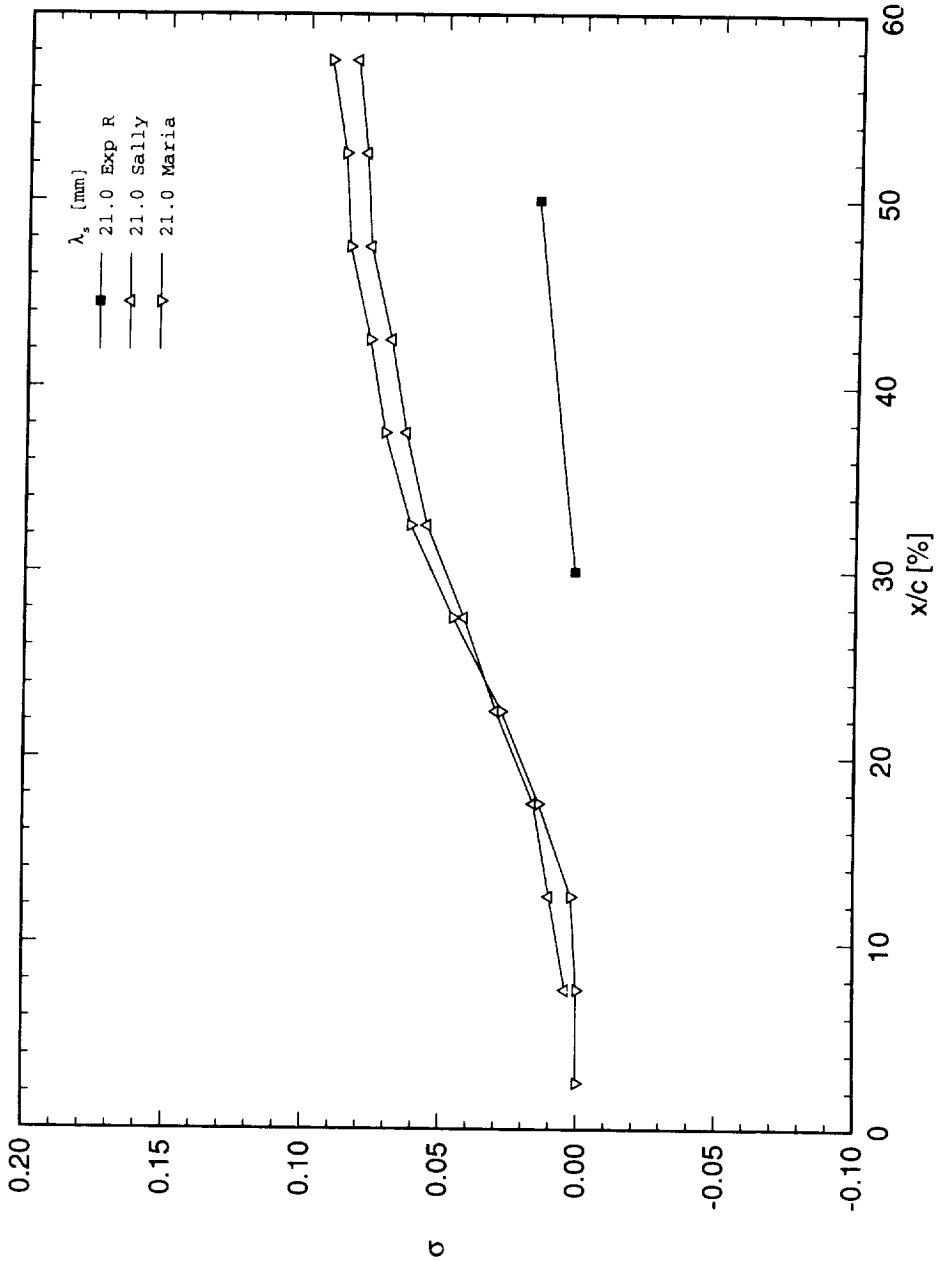

Figure 7.131. Measured and theoretical dimensionless growth rates for $\lambda_s = 21$ mm. $Re_c = 3.0 \times 10^6$.

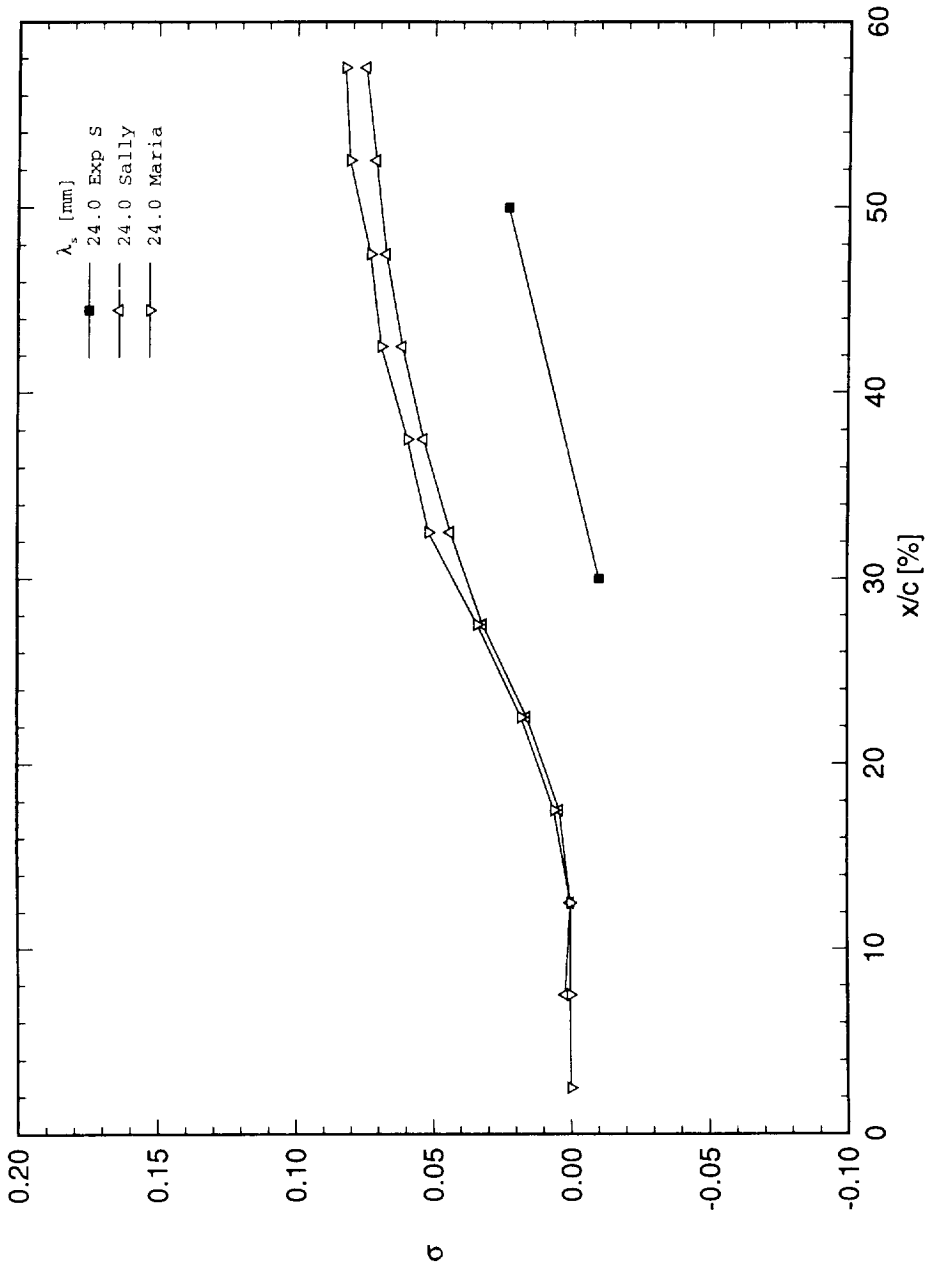

Figure 7.132. Measured and theoretical dimensionless growth rates for $\lambda_s = 24$ mm. $Re_c = 3.0 \times 10^6$.

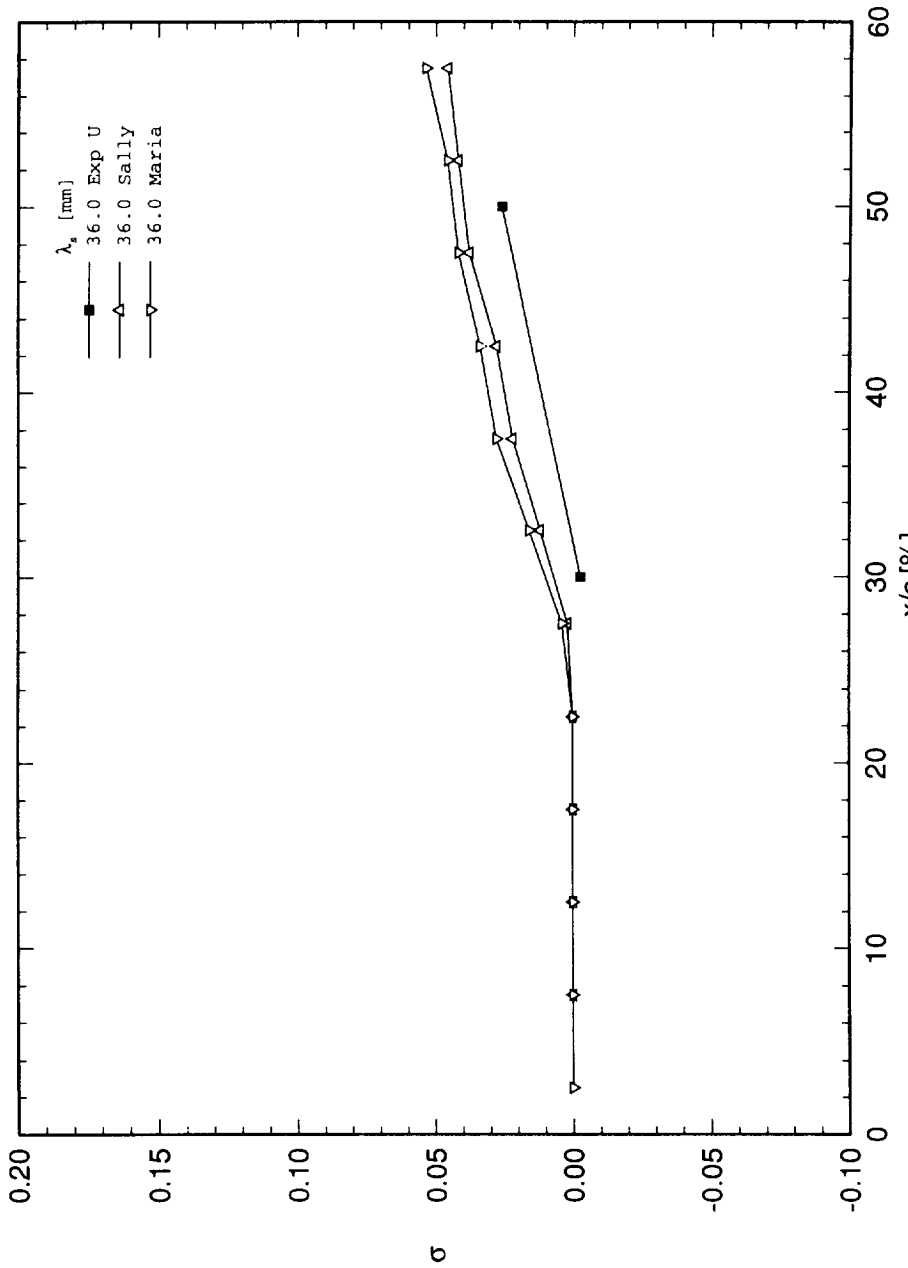

Figure 7.133. Measured and theoretical dimensionless growth rates for $\lambda_s = 36$ mm. $Re_c = 3.0 \times 10^6$.

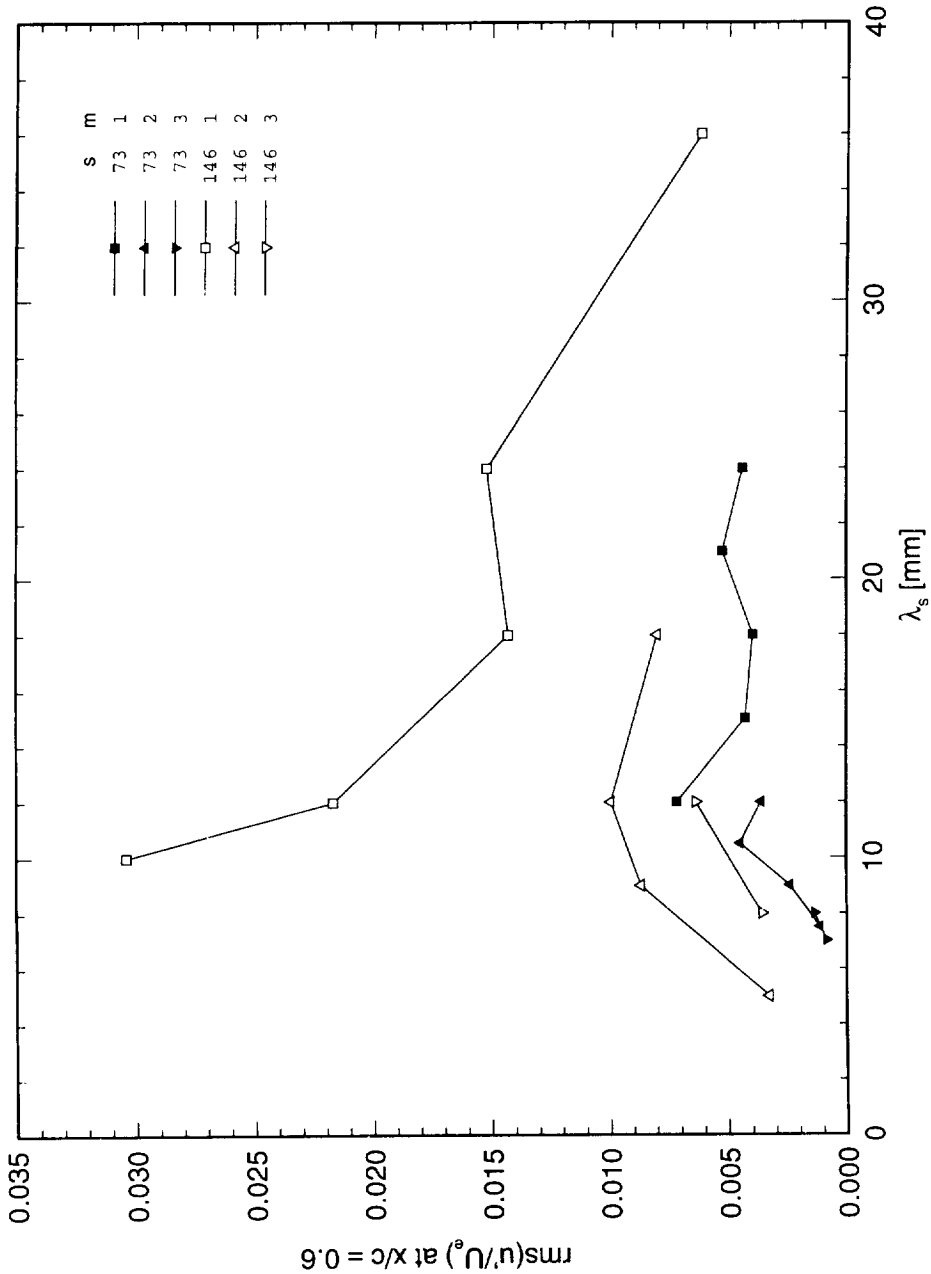

Figure 7.134. Measured stationary crossflow amplitude at $x/c = 0.6$. s is the roughness height, and m is the mode number. $Re_c = 3.0 \times 10^6$.

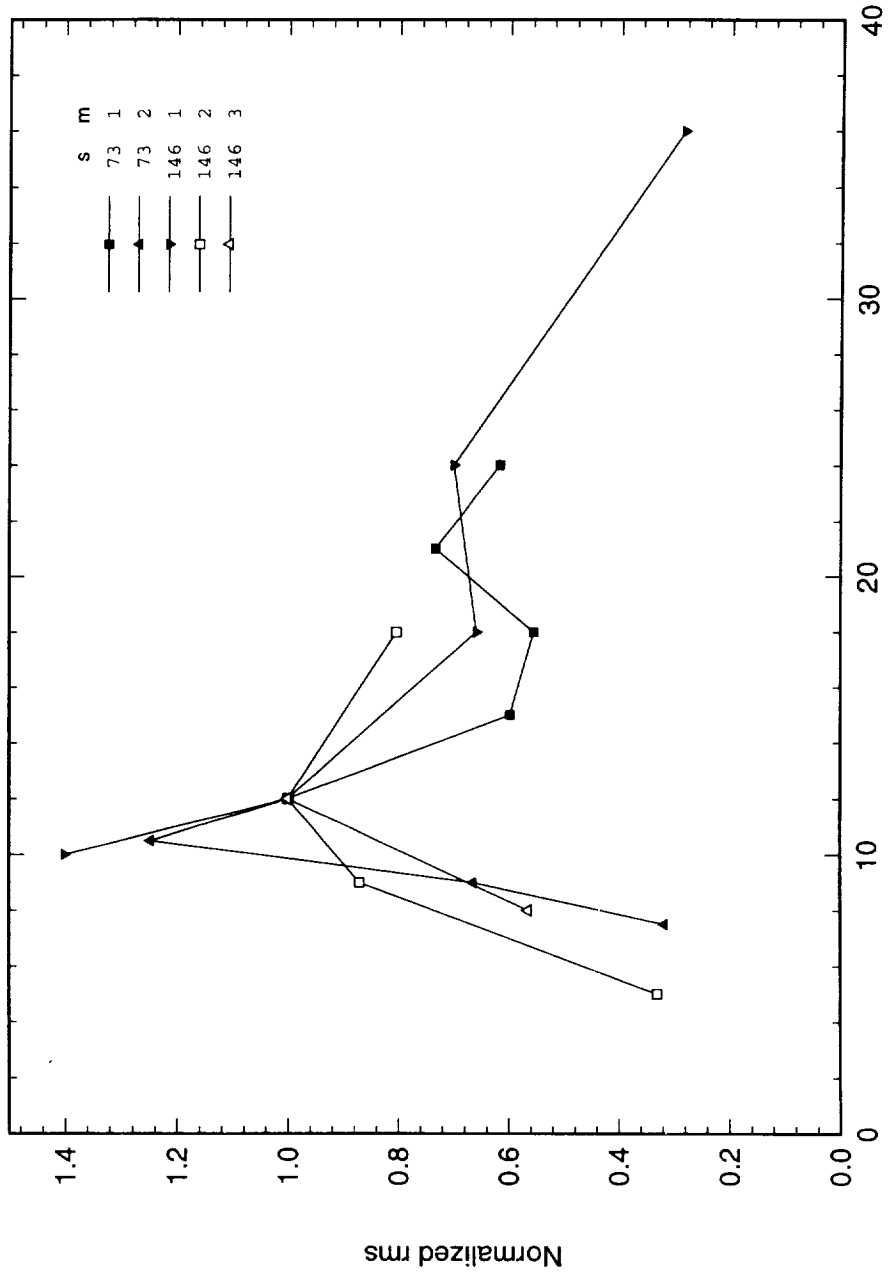

Figure 7.135. Measured stationary crossflow amplitude at $x/c = 0.6$, normalized by value for $\lambda_s = 12$ mm within each group.

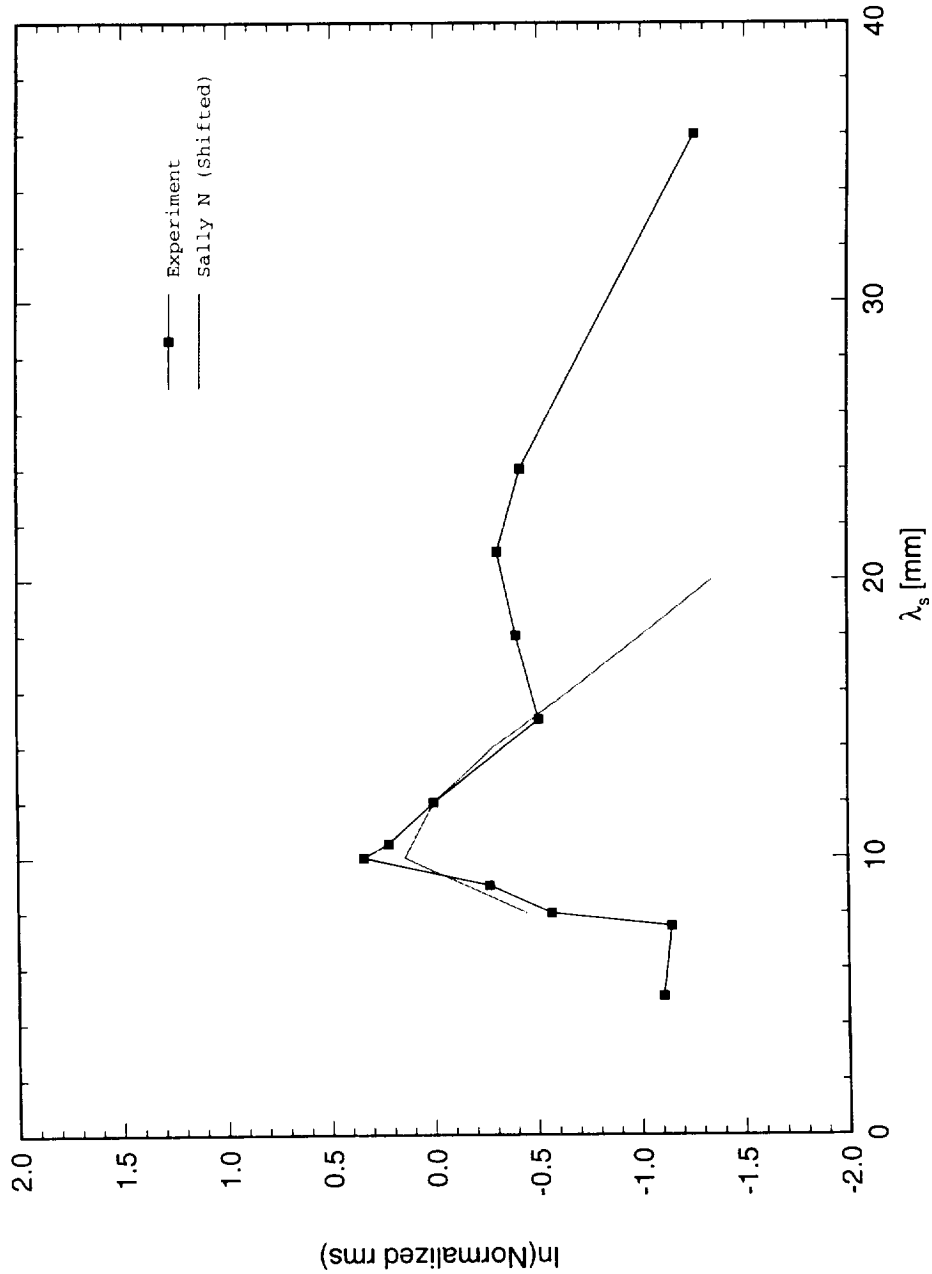

Figure 7.136. Comparison of measured roughness sensitivity and SALLY N-factors. $Re_c = 3.0 \times 10^6$, $\alpha = 0°$.

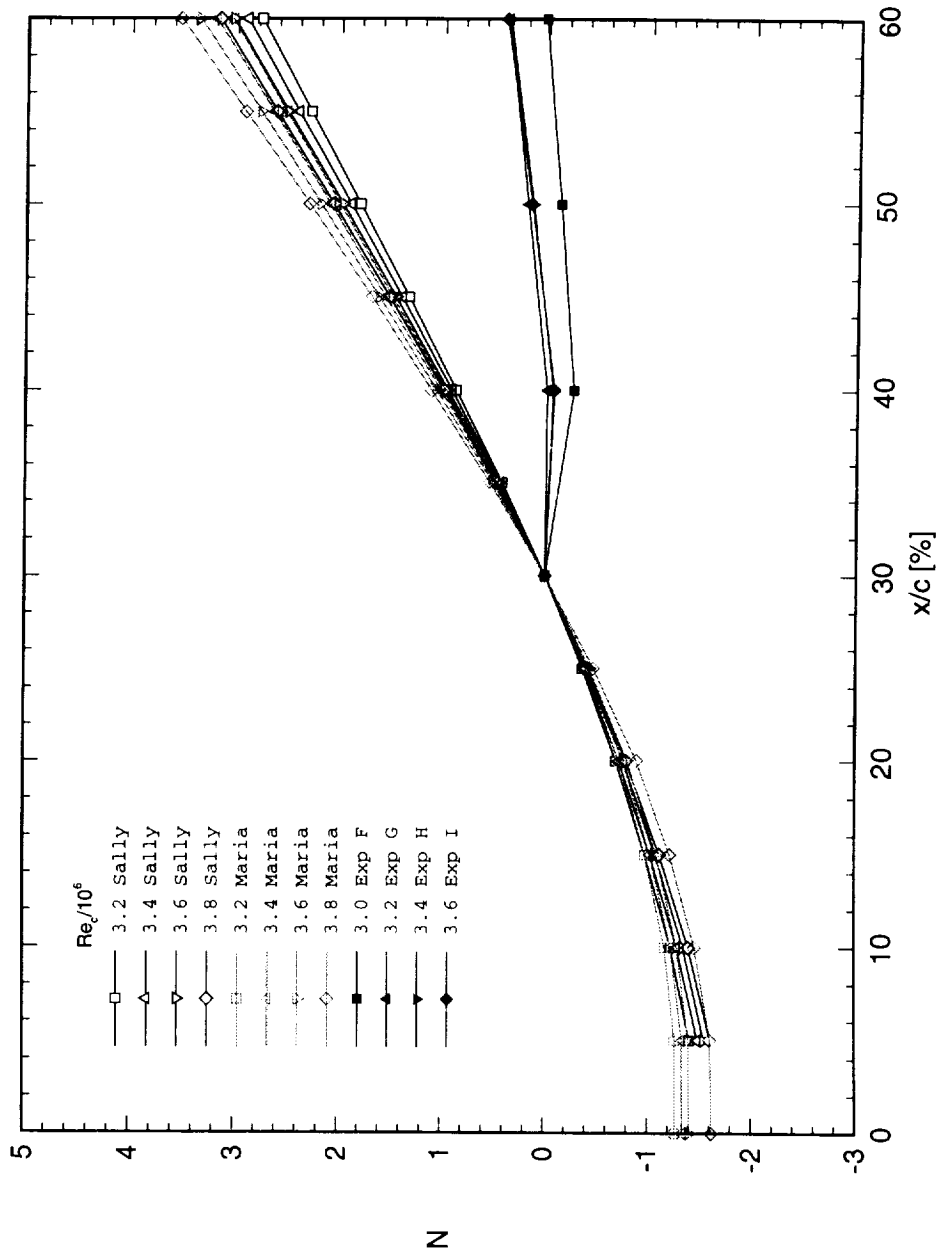

Figure 7.137. Measured and theoretical relative N-factors for $\lambda_s = 12$ mm with varying Reynolds number. Reference point is $x/c = 0.3$.

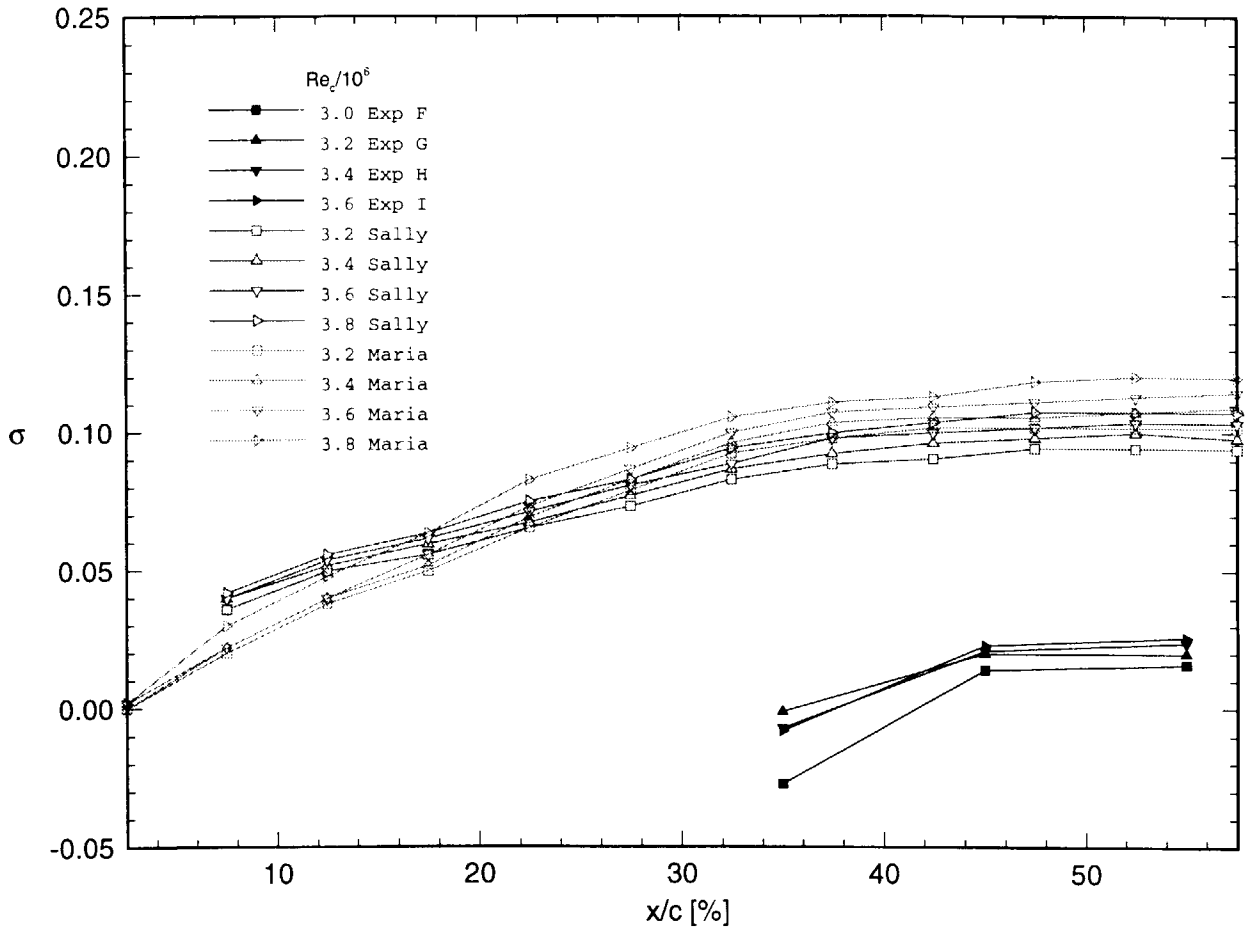

Figure 7.138. Measured and theoretical relative growth rates for $\lambda_s = 12$ mm with varying Reynolds number.

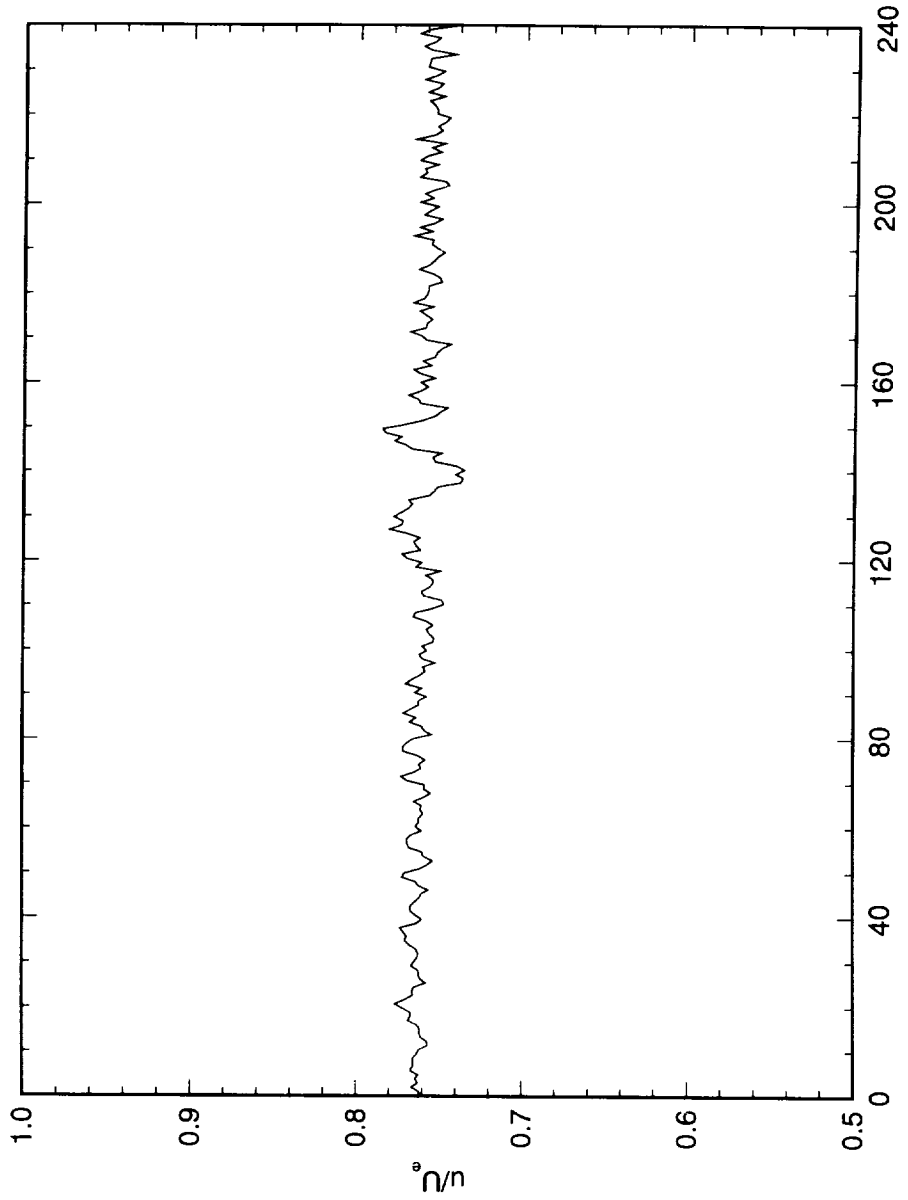

Figure 7.139. Spanwise hot-wire scan at $x/c = 0.3$ with single 146 μm roughness element at $x/c = 0.005$. Rougness diameter is 6.2 mm, $Re_c = 3.0 \times 10^6$.

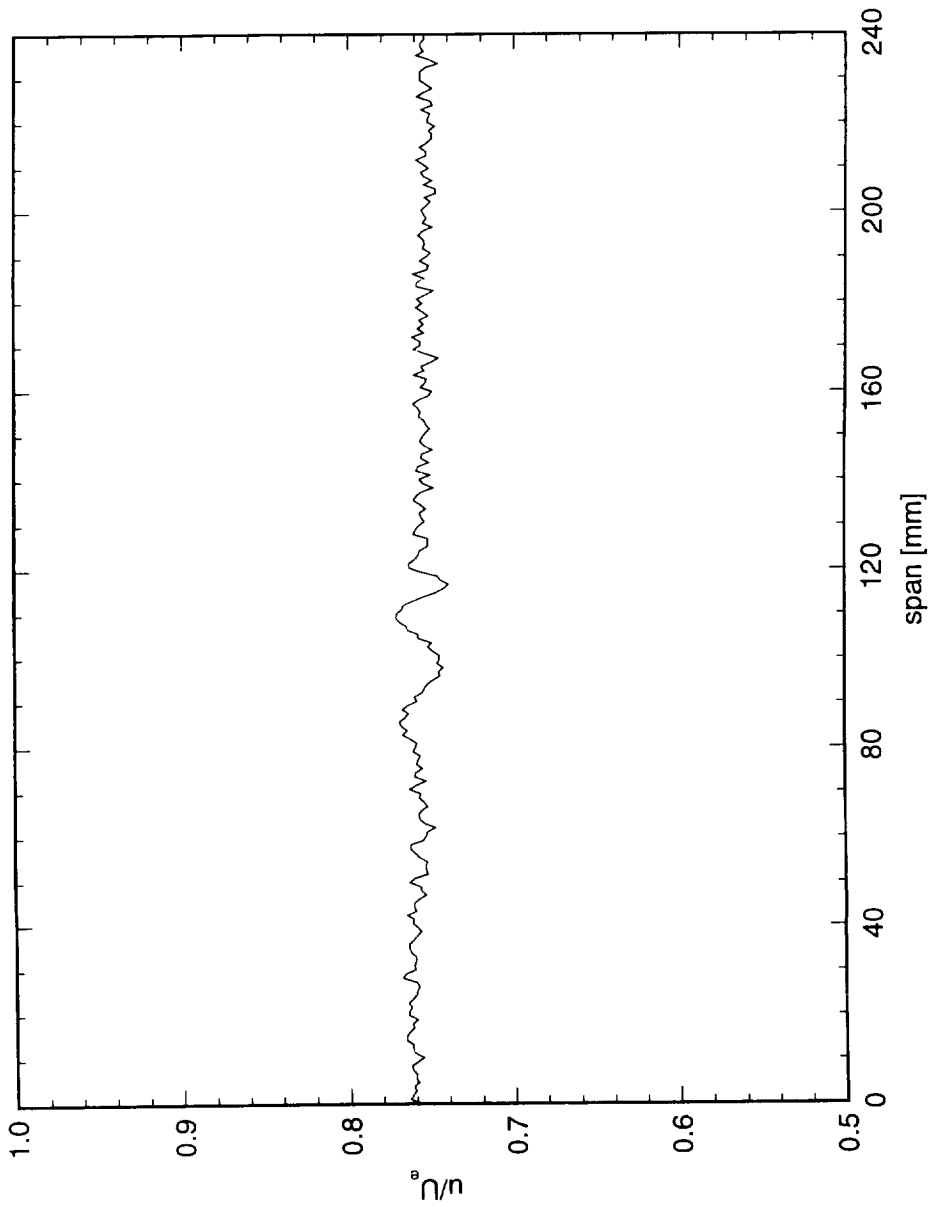

Figure 7.140. Spanwise hot-wire scan at $x/c = 0.4$ with single 146 μm roughness element at $x/c = 0.005$. Rougness diameter is 6.2 mm, $Re_c = 3.0 \times 10^6$.

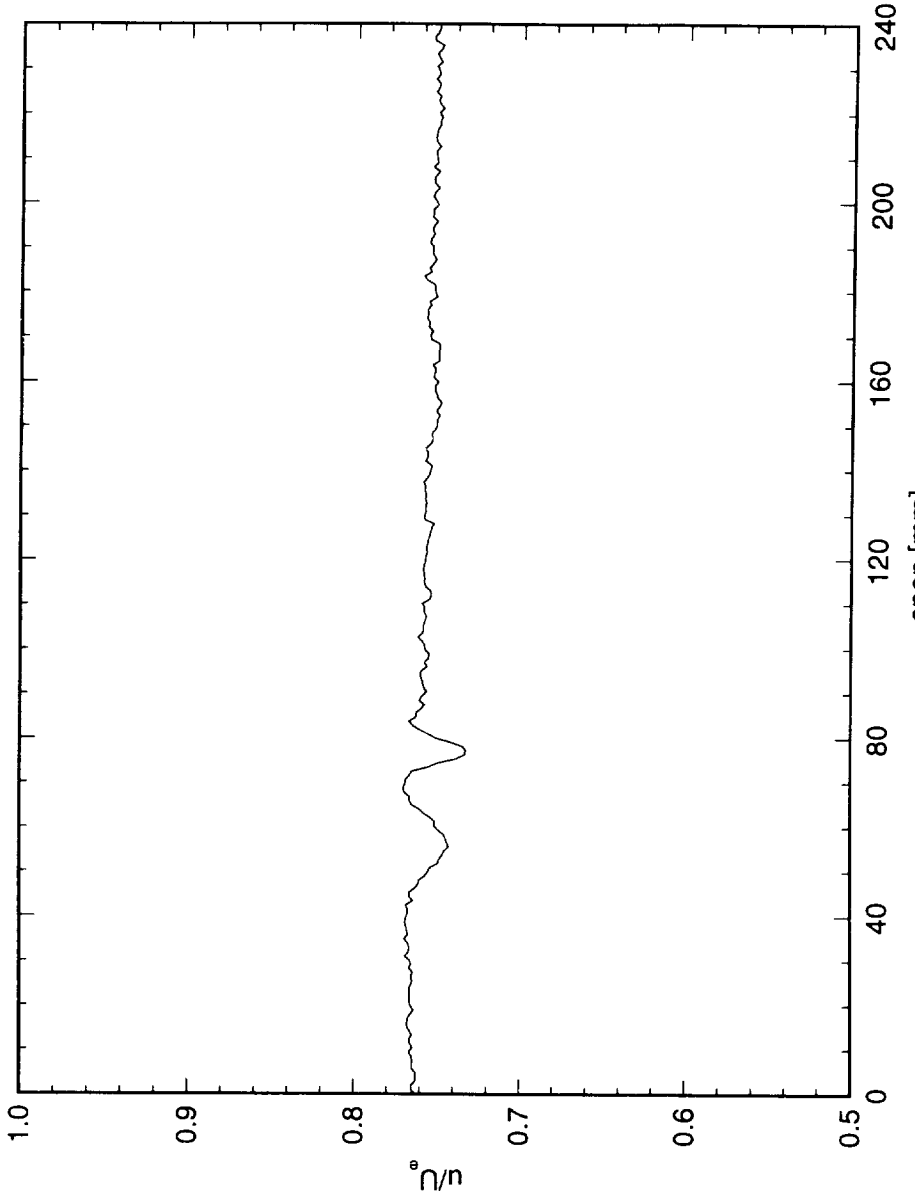

Figure 7.141. Spanwise hot-wire scan at $x/c = 0.5$ with single 146 μm roughness element at $x/c = 0.005$. Rougness diameter is 6.2 mm, $Re_c = 3.0 \times 10^6$.

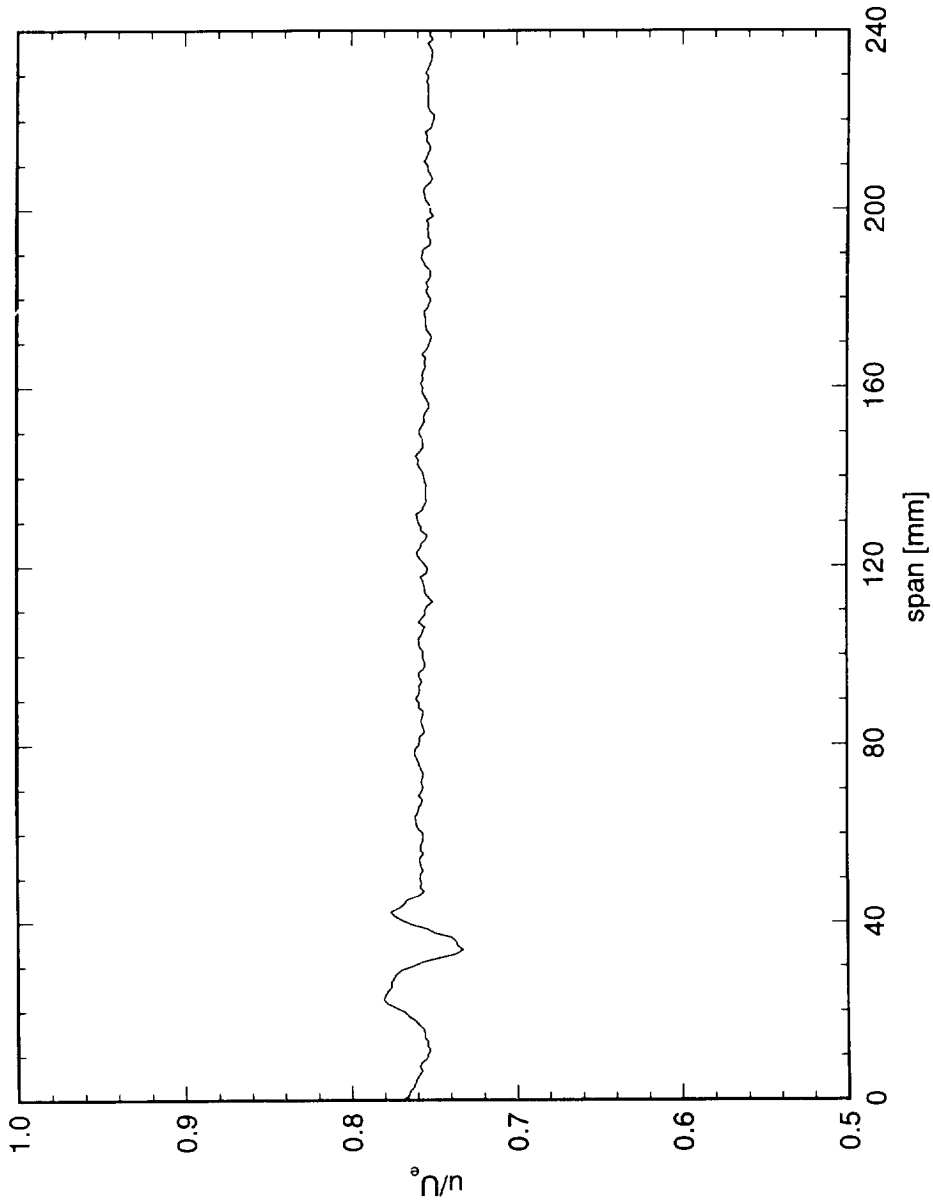

Figure 7.142. Spanwise hot-wire scan at $x/c = 0.6$ with single 146 μm roughness element at $x/c = 0.005$. Rougness diameter is 6.2 mm, $Re_c = 3.0 \times 10^6$.

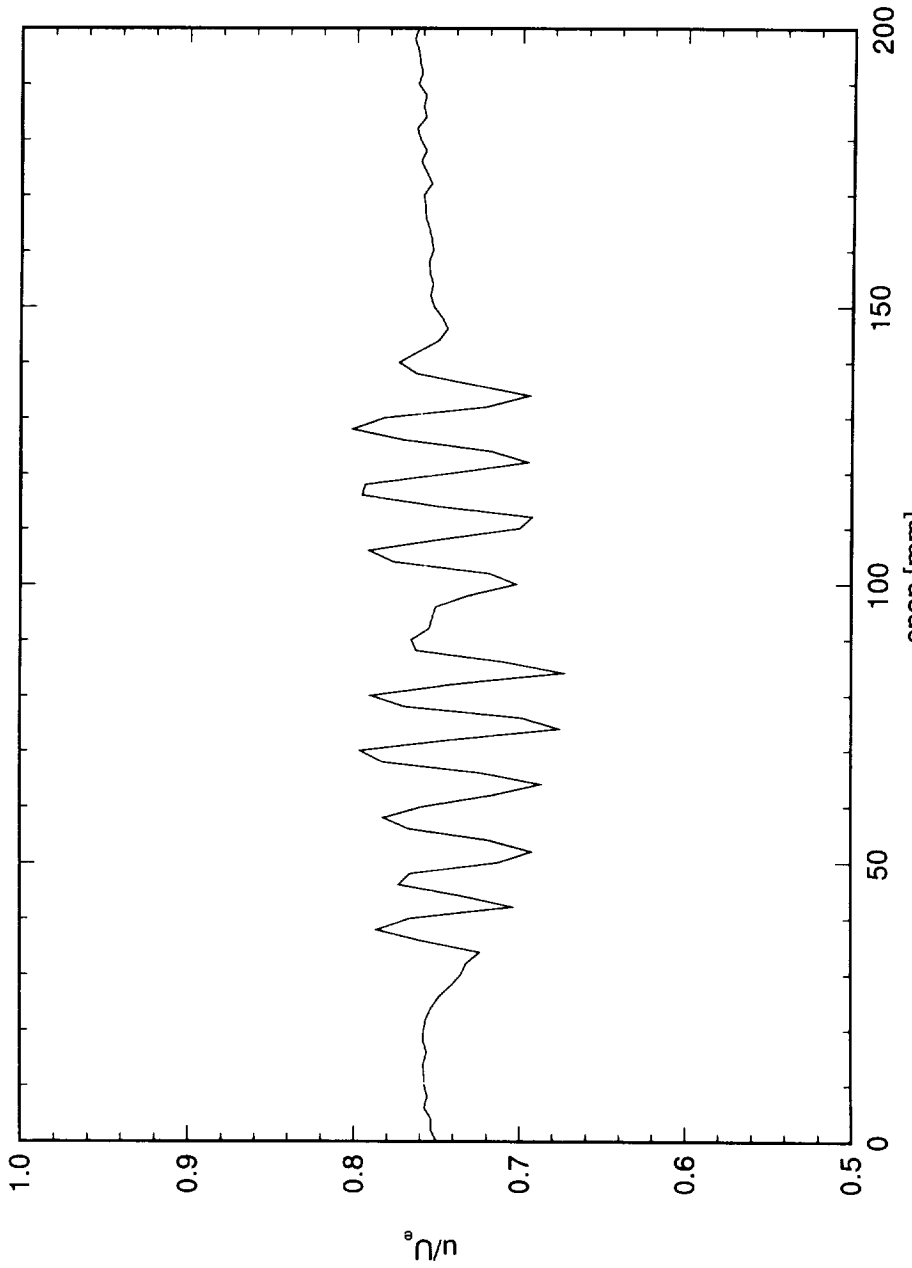

Figure 7.143. Spanwise scan at $x/c = 0.5$ with 10-element roughness array at $x/c = 0.005$. $Re_c = 3.2 \times 10^6$, roughness spacing is 12 mm, roughness height is 117 μm.

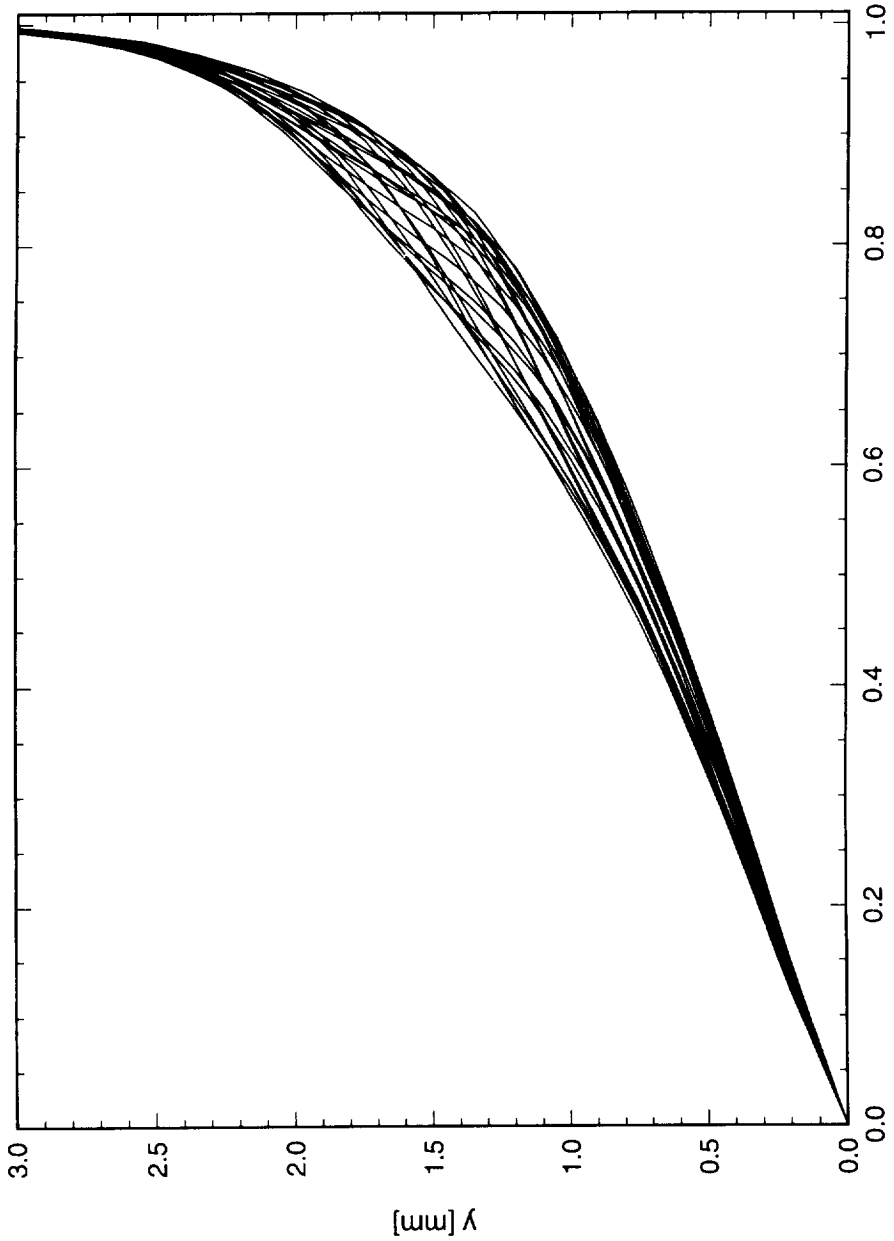

Figure 7.144. Spanwise array of boundary-layer scans at $x/c = 0.6$. A 10-element array of 117 μm roughness with a spacing of 12 mm is at $x/c = 0.005$. $Re_c = 3.2 \times 10^6$. Data set A.

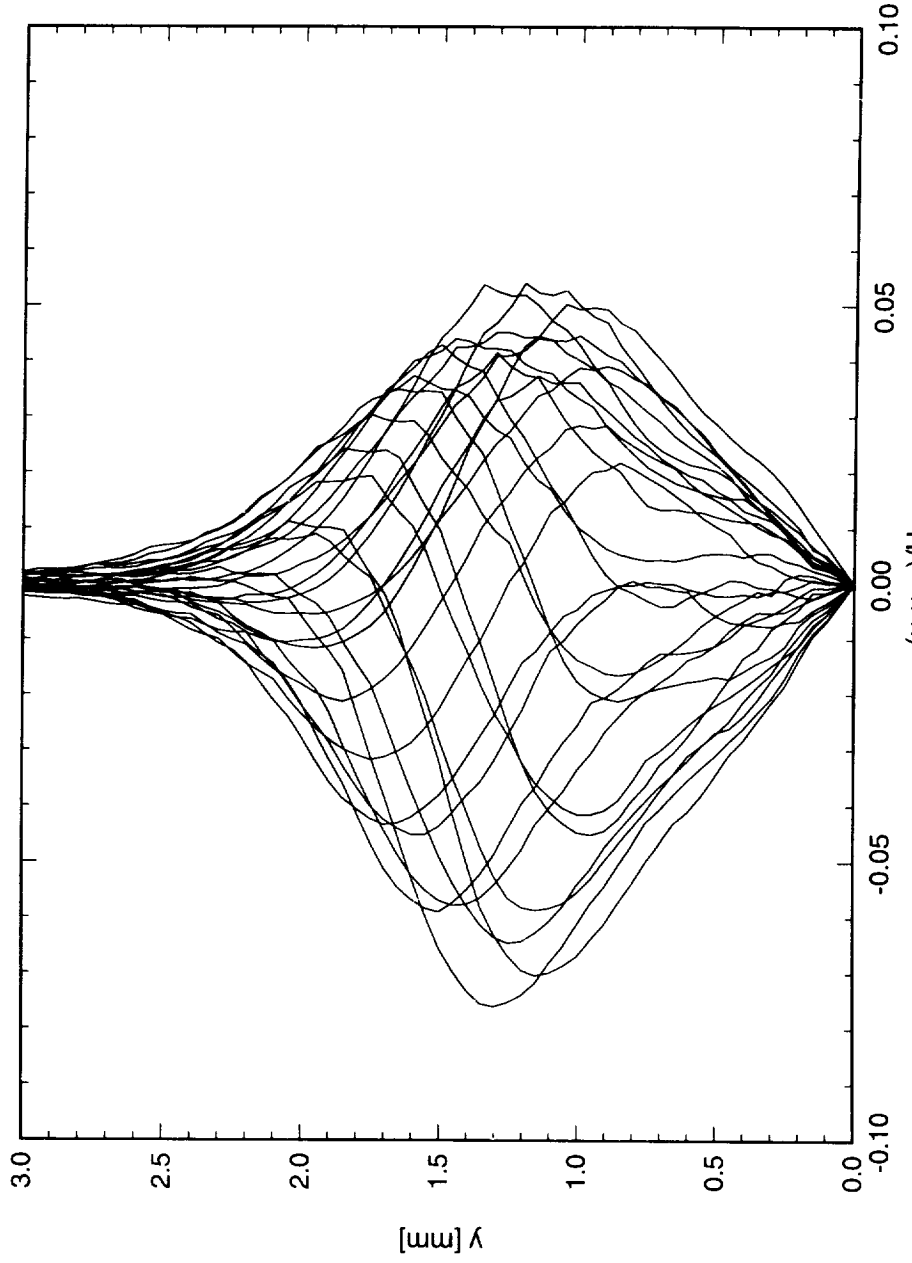

Figure 7.145. Disturbance profiles for boundary-layer scans at $x/c = 0.6$. A 10-element array of 117 μm roughness with a spacing of 12 mm is at $x/c = 0.005$. $Re_c = 3.2 \times 10^6$. Data set A.

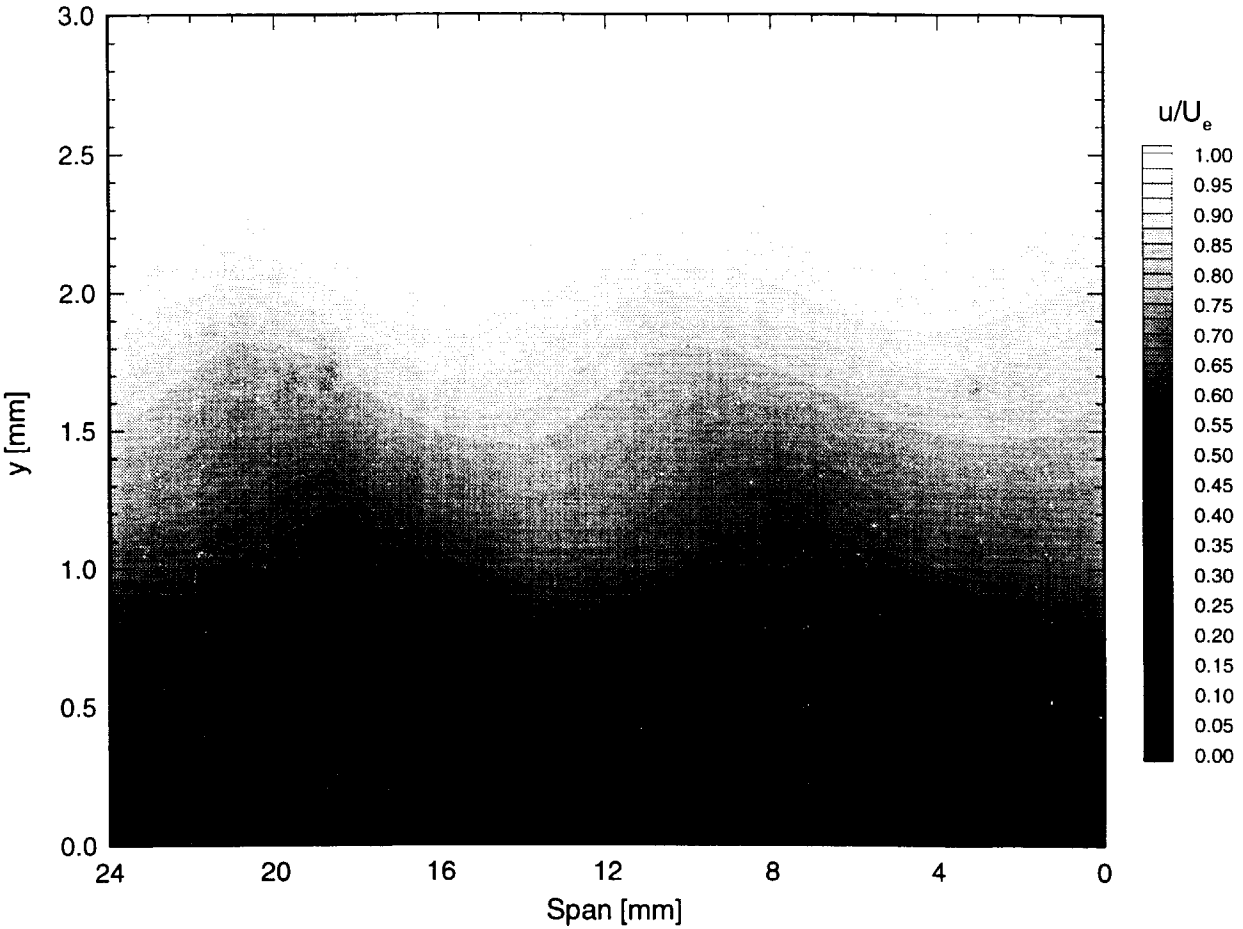

Figure 7.146. Velocity contours at $x/c = 0.6$, showing total u component. A 10-element array of 117 μm roughness with a spacing of 12 mm is at $x/c = 0.005$. $Re_c = 3.2 \times 10^6$. Data set A.

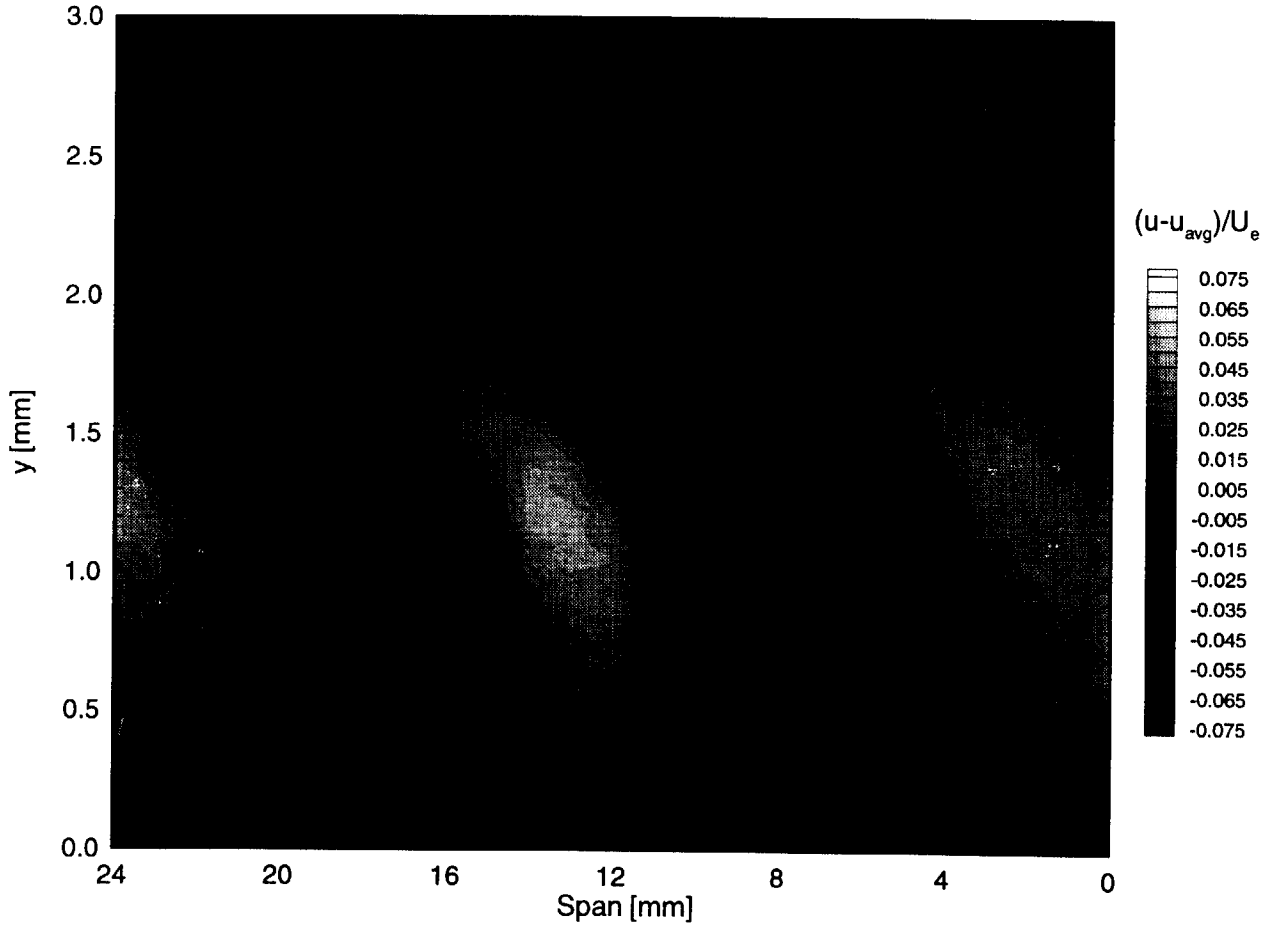

Figure 7.147. Disturbance contours for boundary-layer scans at $x/c = 0.6$. A 10-element array of 117 μm roughness with a spacing of 12 mm is at $x/c = 0.005$. $Re_c = 3.2 \times 10^6$. Data set A.

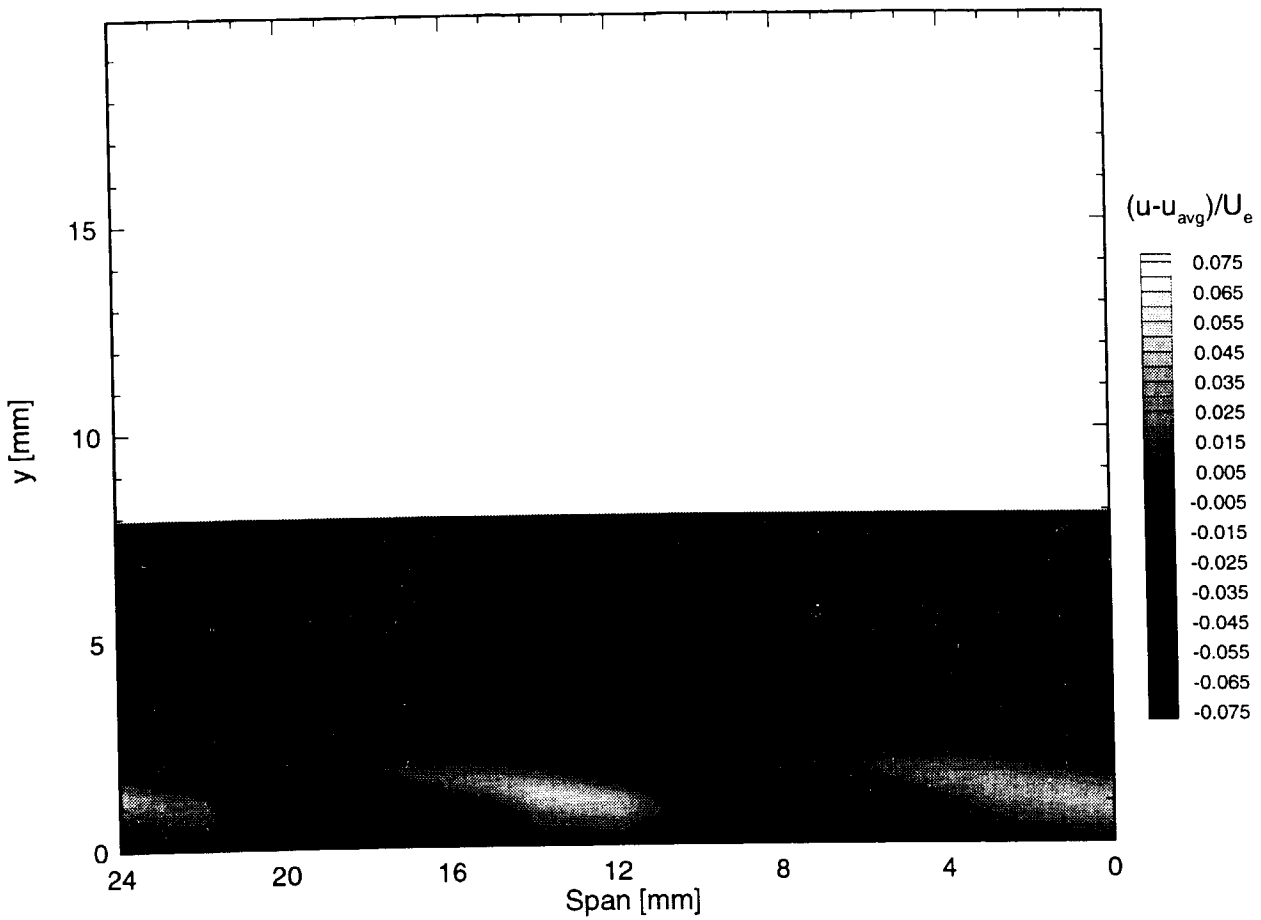

Figure 7.148. Disturbance contours for boundary-layer scans at $x/c = 0.6$. Aspect ratio is 1:1. A 10-element array of 117 μm roughness with a spacing of 12 mm is at $x/c = 0.005$. $Re_c = 3.2 \times 10^6$. Data set A.

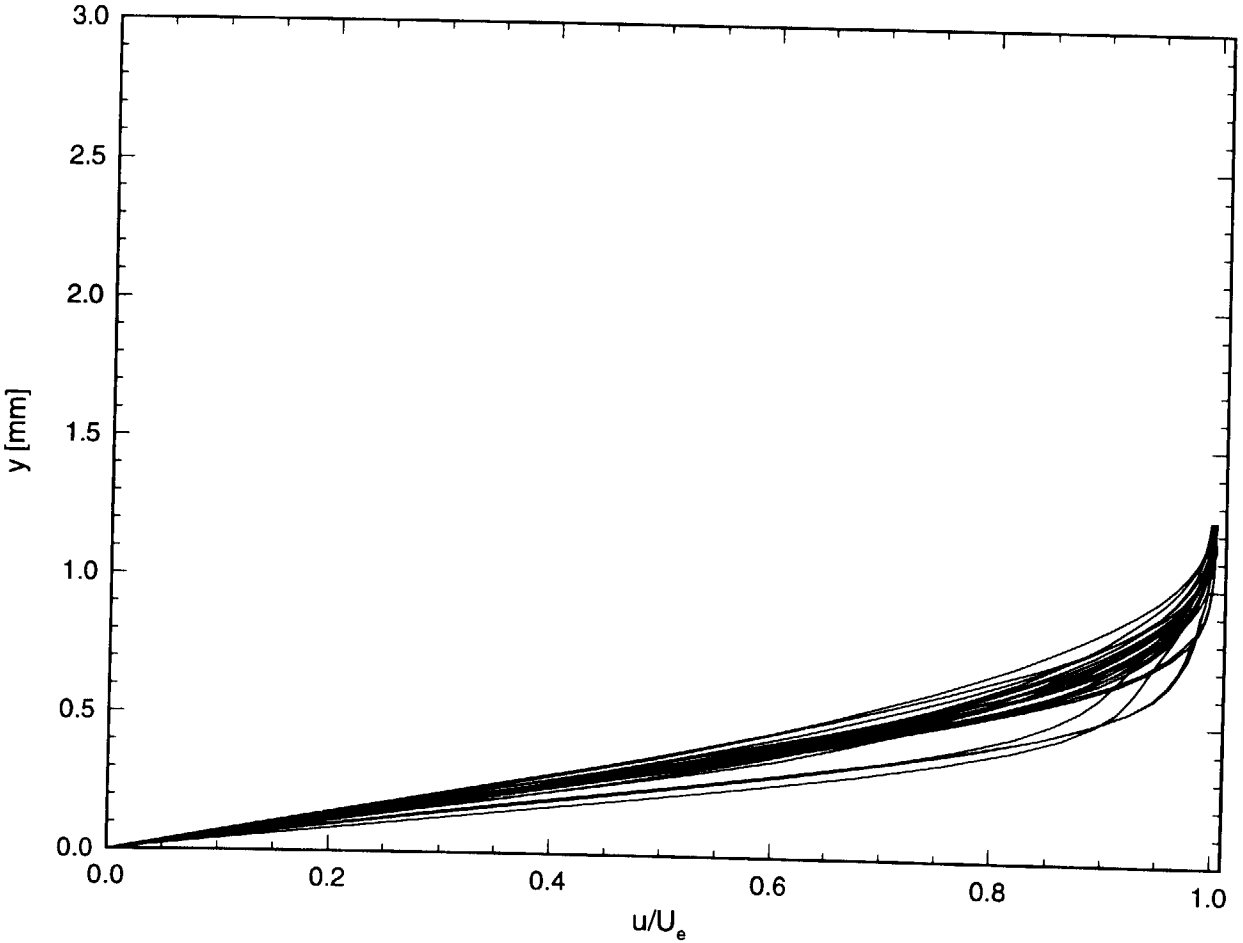

Figure 7.149. Spanwise array of boundary-layer scans at $x/c = 0.05$. A 10-element array of 117 μm roughness with a spacing of 12 mm is at $x/c = 0.005$. $Re_c = 3.2 \times 10^6$. Data set A.

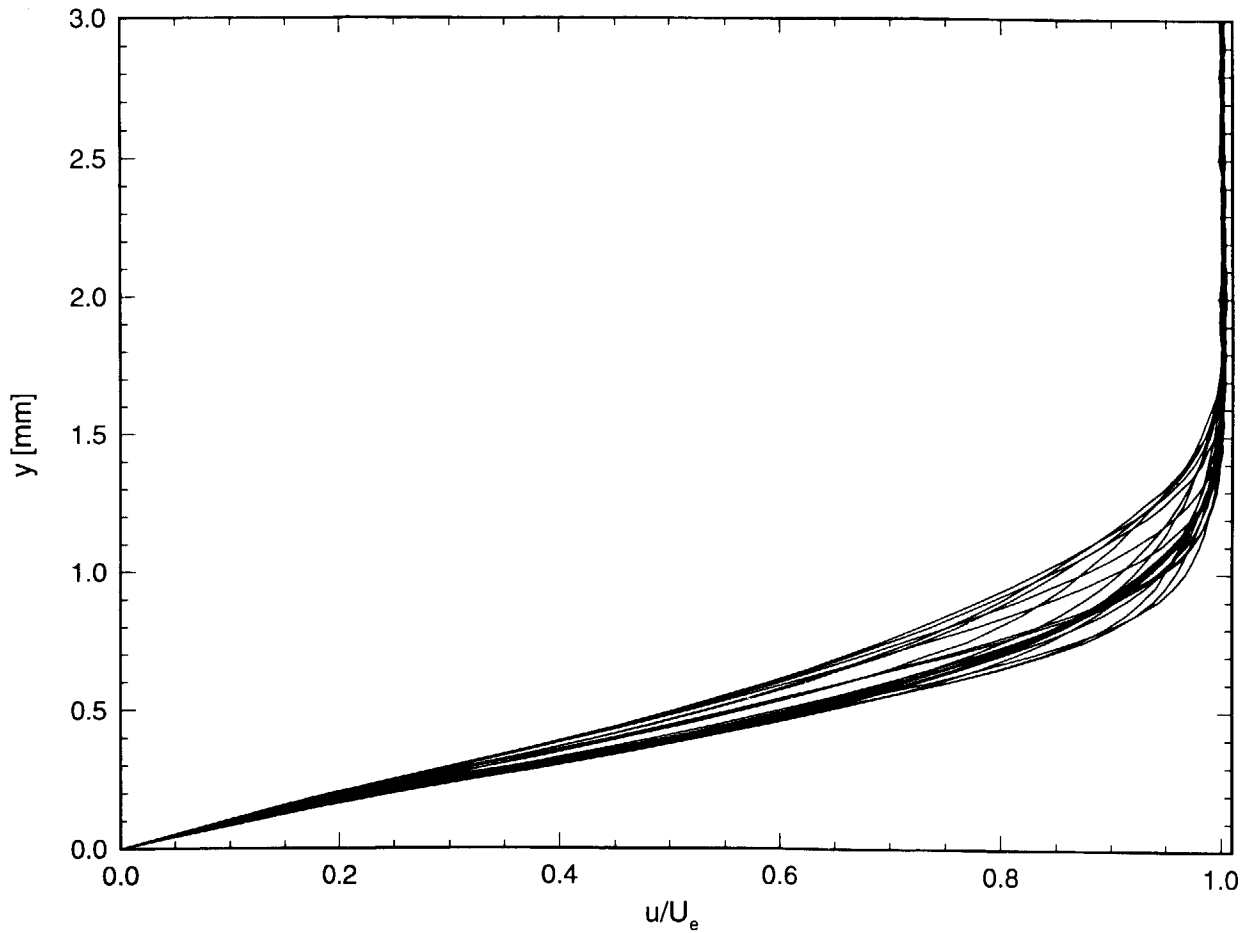

Figure 7.150. Spanwise array of boundary-layer scans at $x/c = 0.10$. A 10-element array of 117 μm roughness with a spacing of 12 mm is at $x/c = 0.005$. $Re_c = 3.2 \times 10^6$. Data set A.

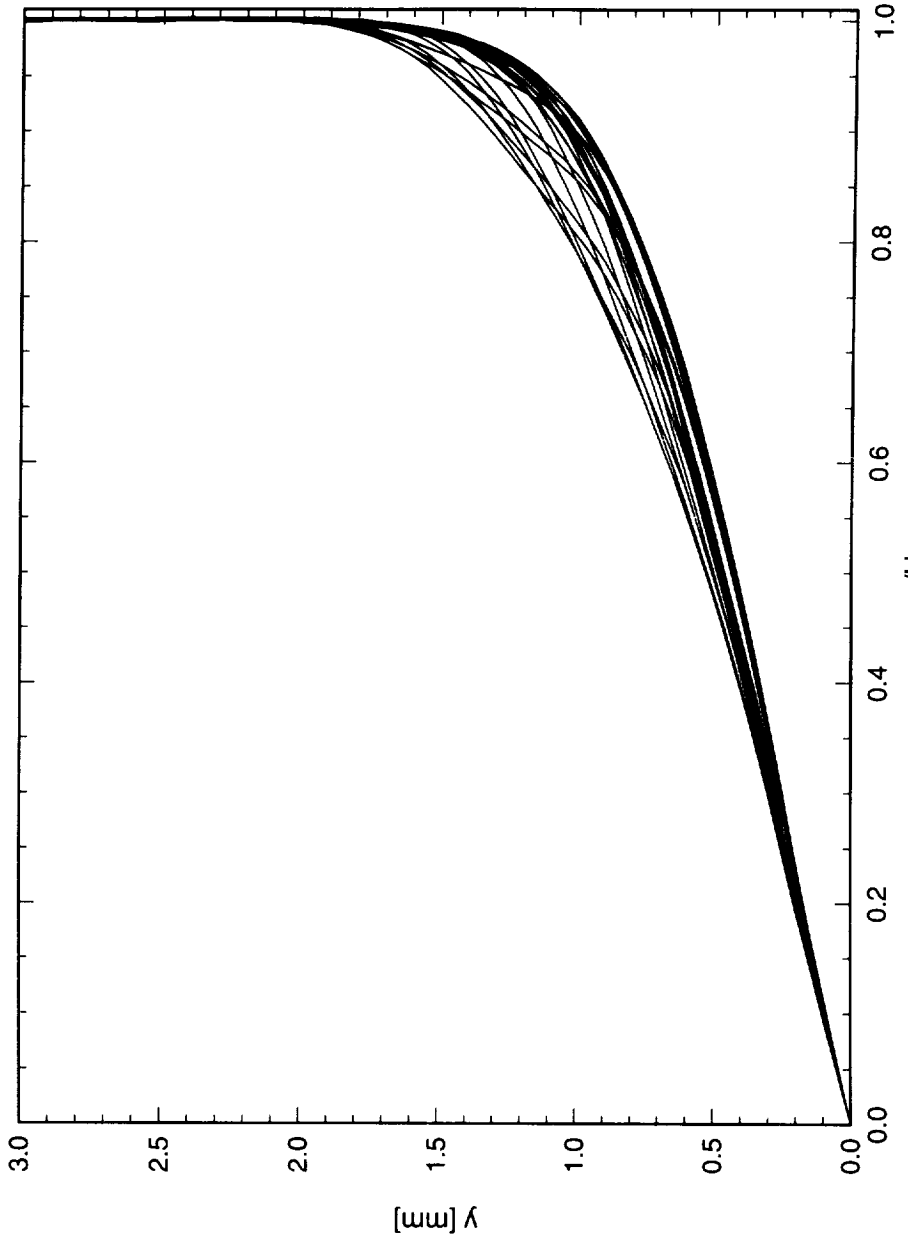

Figure 7.151. Spanwise array of boundary-layer scans at $x/c = 0.15$. A 10-element array of 117 μm roughness with a spacing of 12 mm is at $x/c = 0.005$. $Re_c = 3.2 \times 10^6$. Data set A.

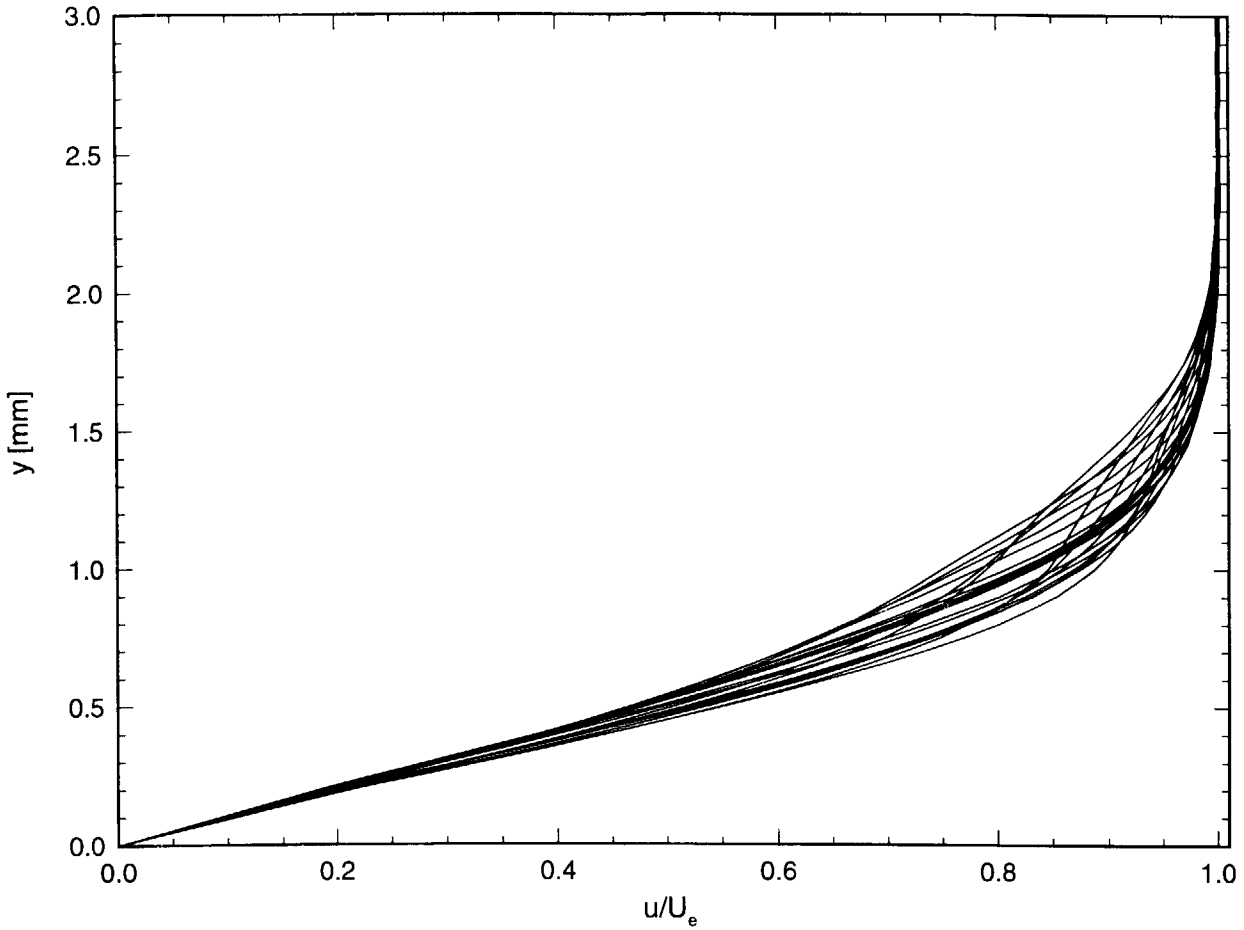

Figure 7.152. Spanwise array of boundary-layer scans at $x/c = 0.20$. A 10-element array of 117 μm roughness with a spacing of 12 mm is at $x/c = 0.005$. $Re_c = 3.2 \times 10^6$. Data set A.

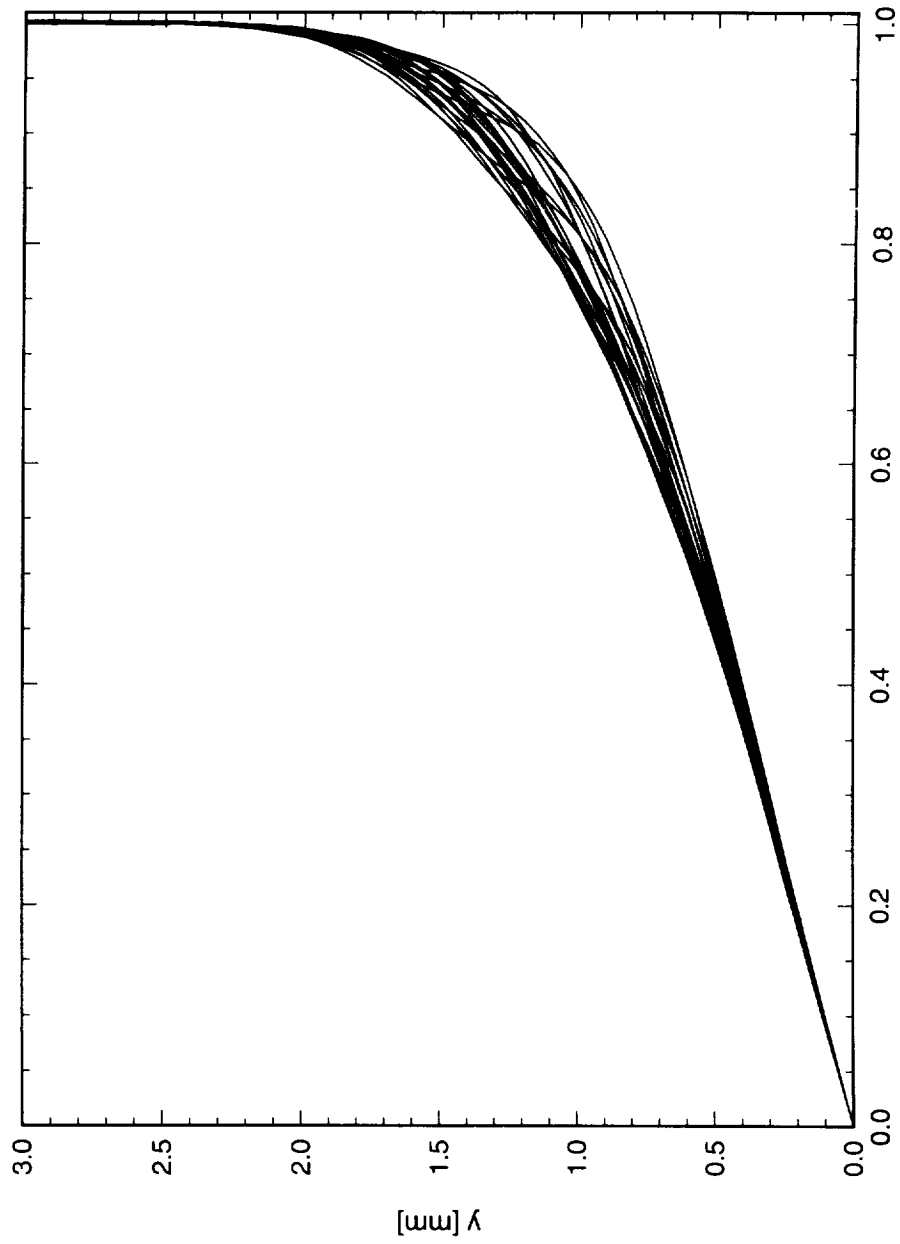

Figure 7.153. Spanwise array of boundary-layer scans at $x/c = 0.25$. A 10-element array of 117 μm roughness with a spacing of 12 mm is at $x/c = 0.005$. $Re_c = 3.2 \times 10^6$. Data set A.

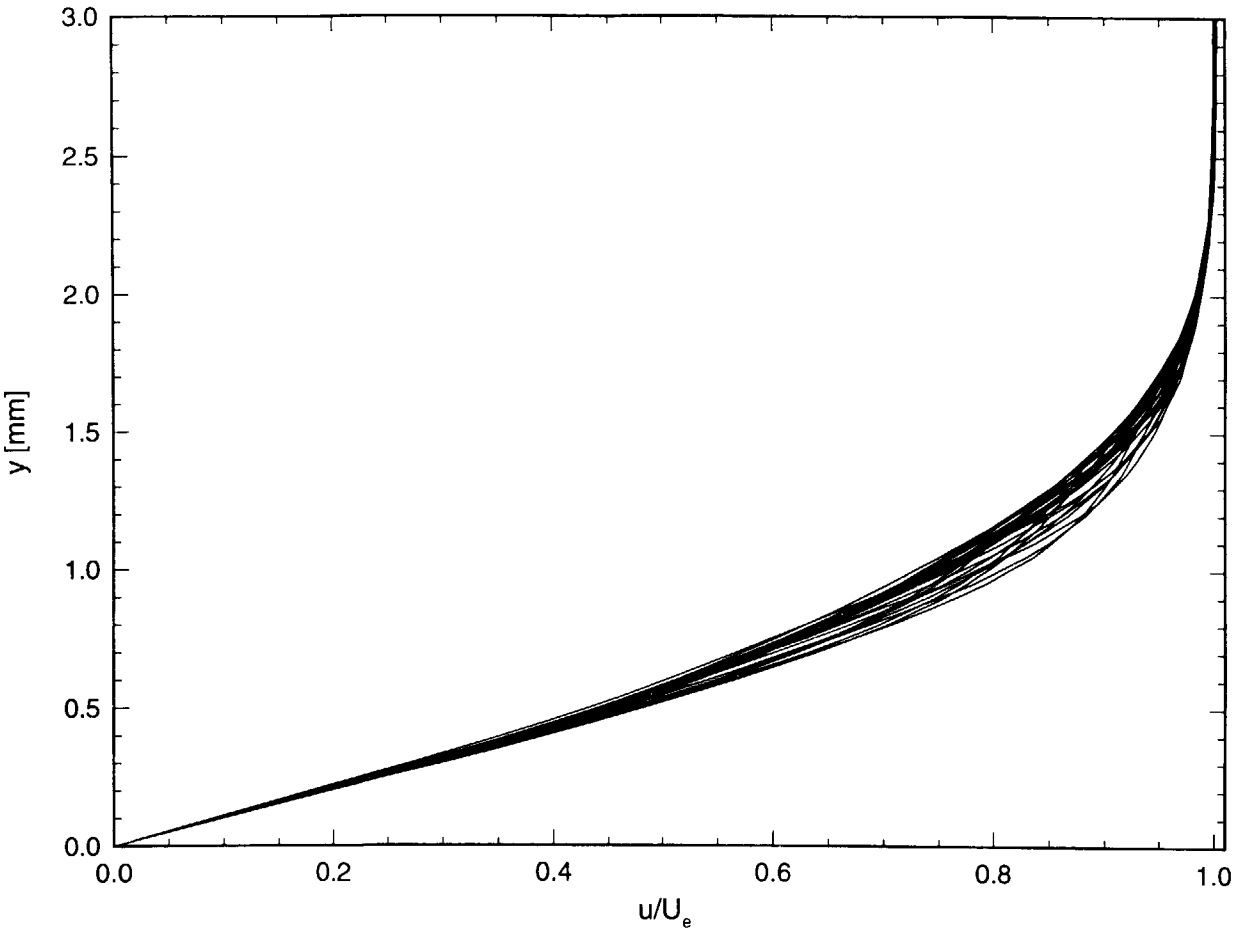

Figure 7.154. Spanwise array of boundary-layer scans at $x/c = 0.30$. A 10-element array of 117 μm roughness with a spacing of 12 mm is at $x/c = 0.005$. $Re_c = 3.2 \times 10^6$. Data set A.

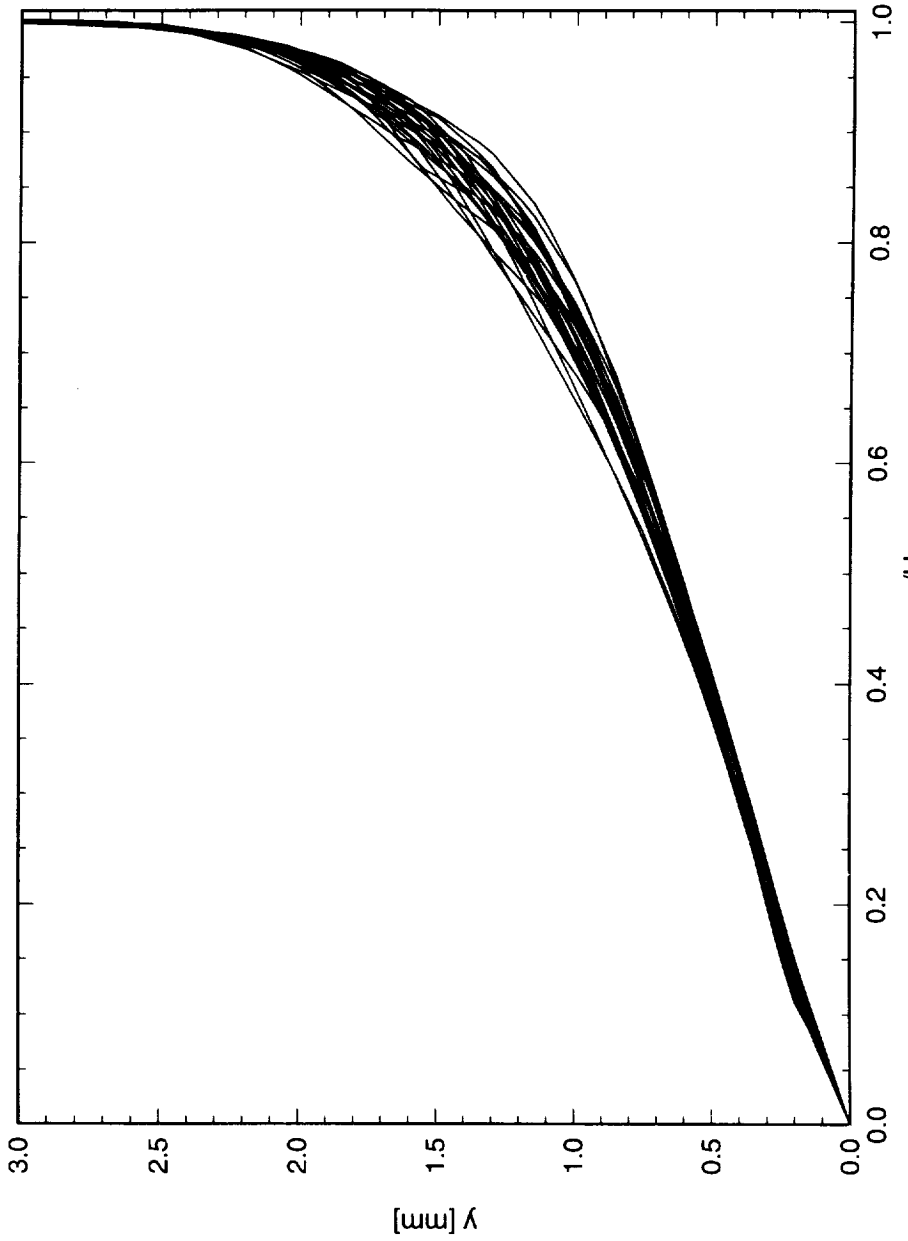

Figure 7.155. Spanwise array of boundary-layer scans at $x/c = 0.35$. A 10-element array of 117 μm roughness with a spacing of 12 mm is at $x/c = 0.005$. $Re_c = 3.2 \times 10^6$. Data set A.

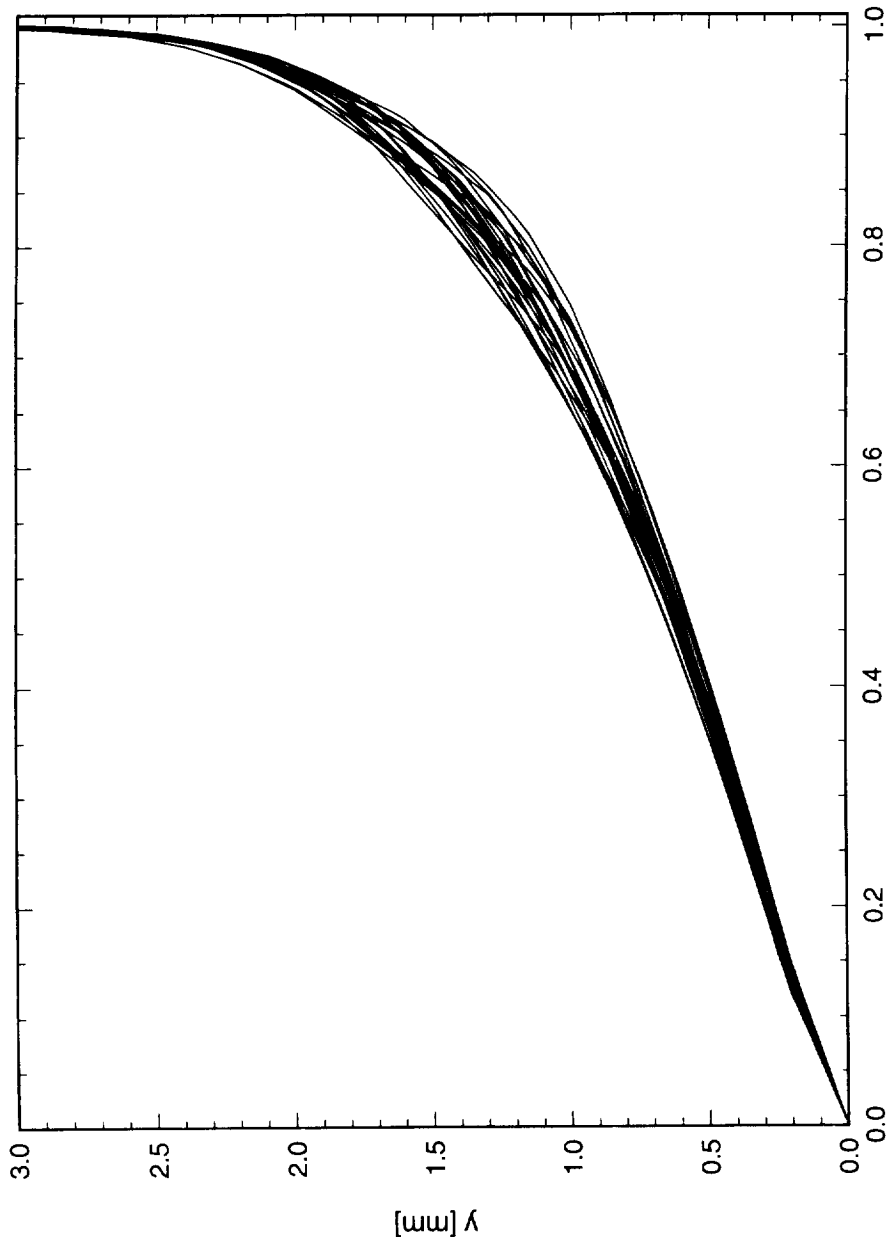

Figure 7.156. Spanwise array of boundary-layer scans at $x/c = 0.40$. A 10-element array of 117 μm roughness with a spacing of 12 mm is at $x/c = 0.005$. $Re_c = 3.2 \times 10^6$. Data set A.

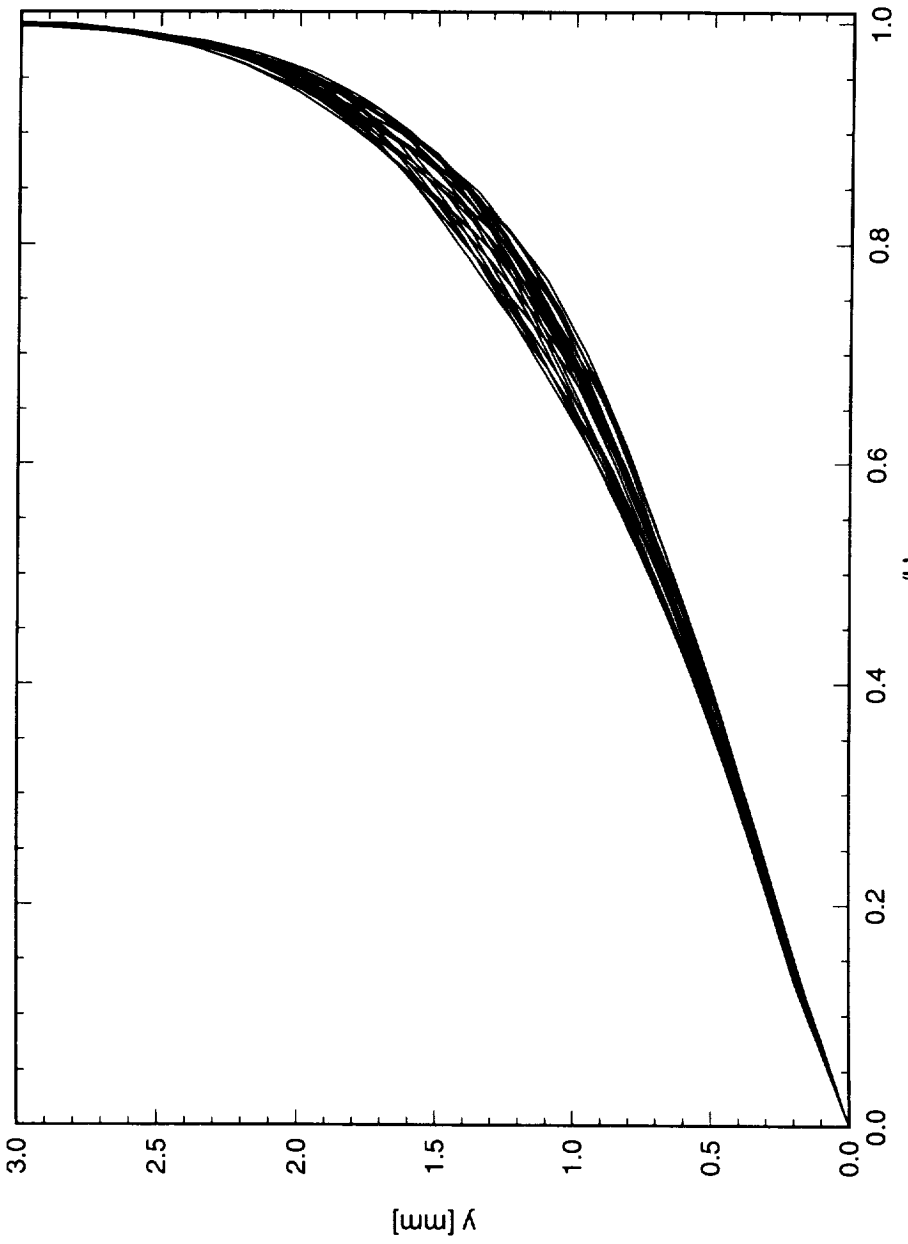

Figure 7.157. Spanwise array of boundary-layer scans at $x/c = 0.45$. A 10-element array of 117 μm roughness with a spacing of 12 mm is at $x/c = 0.005$. $Re_c = 3.2 \times 10^6$. Data set A.

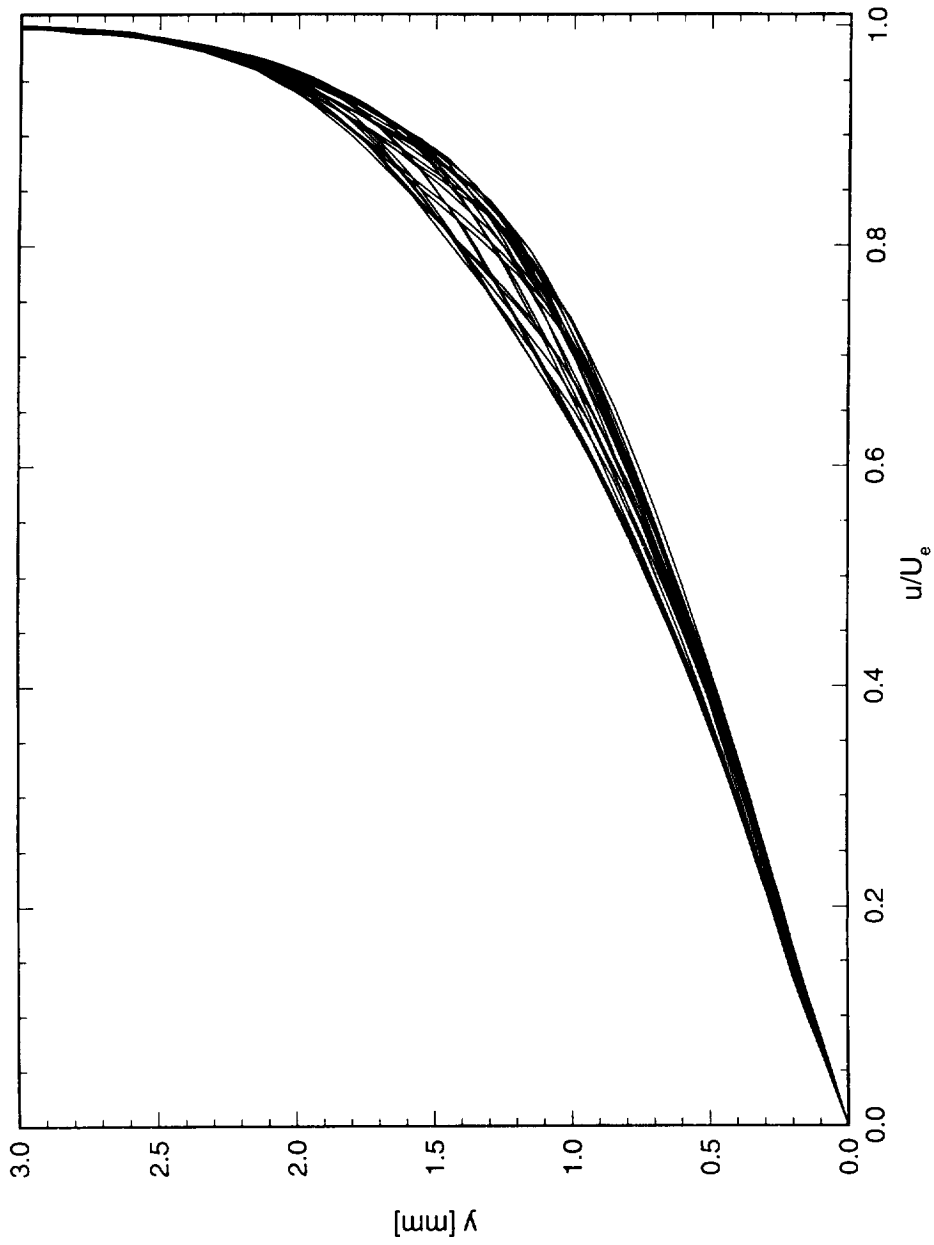

Figure 7.158. Spanwise array of boundary-layer scans at $x/c = 0.50$. A 10-element array of 117 μm roughness with a spacing of 12 mm is at $x/c = 0.005$. $Re_c = 3.2 \times 10^6$. Data set A.

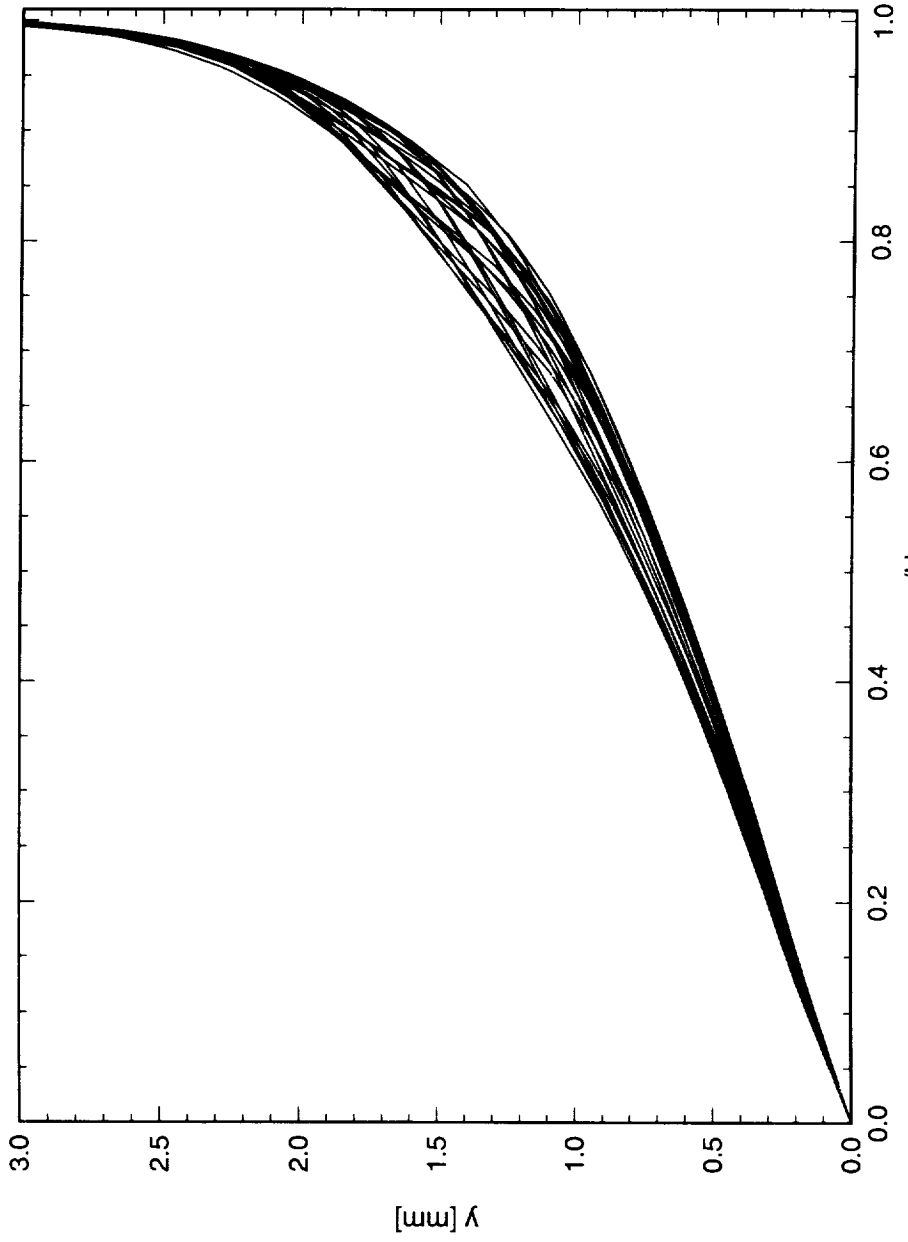

Figure 7.159. Spanwise array of boundary-layer scans at $x/c = 0.55$. A 10-element array of 117 μm roughness with a spacing of 12 mm is at $x/c = 0.005$. $Re_c = 3.2 \times 10^6$. Data set A.

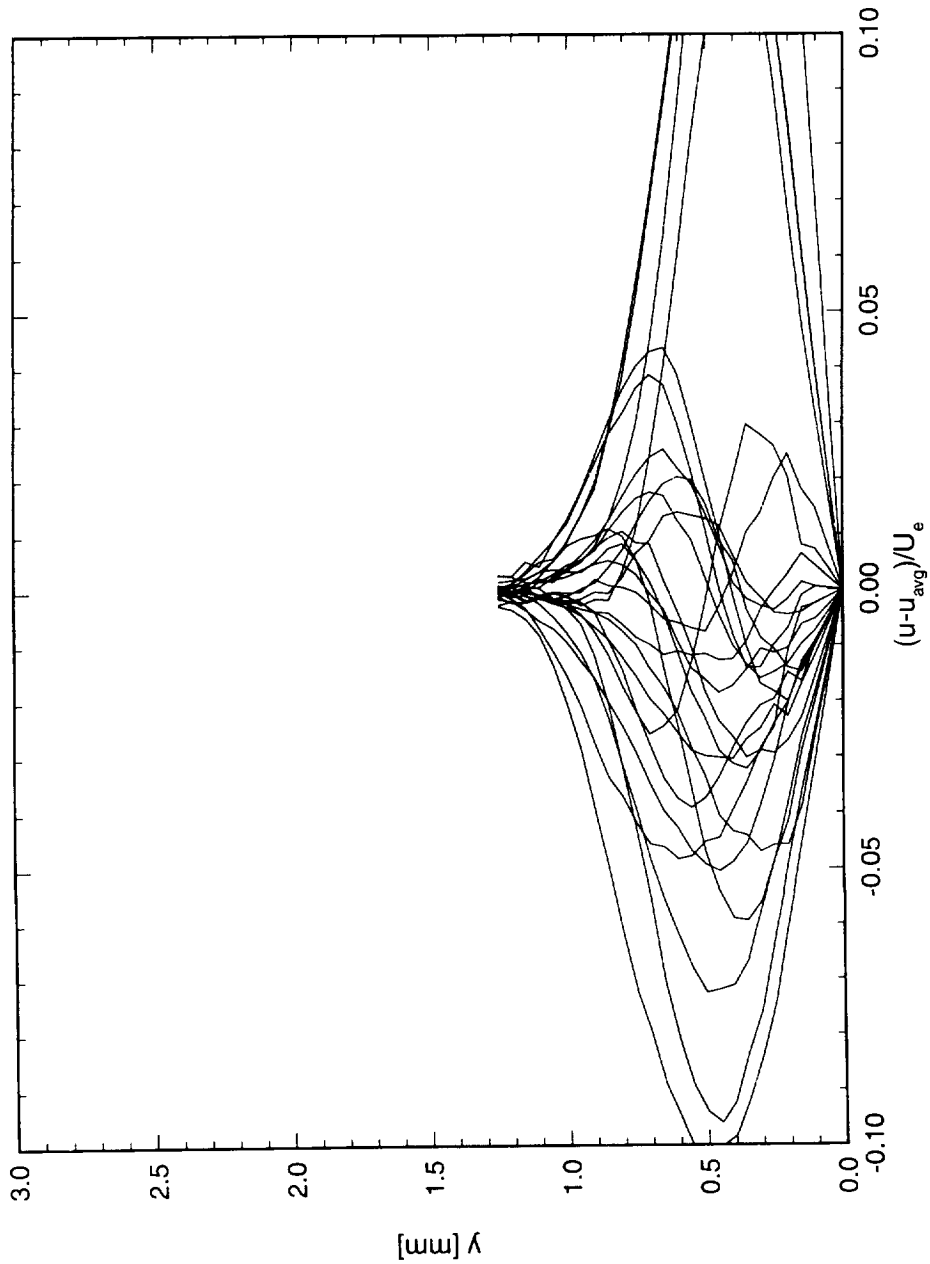

Figure 7.160. Disturbance profiles for boundary-layer scans at $x/c = 0.05$. A 10-element array of 117 μm roughness with a spacing of 12 mm is at $x/c = 0.005$. $Re_c = 3.2 \times 10^6$. Data set A.

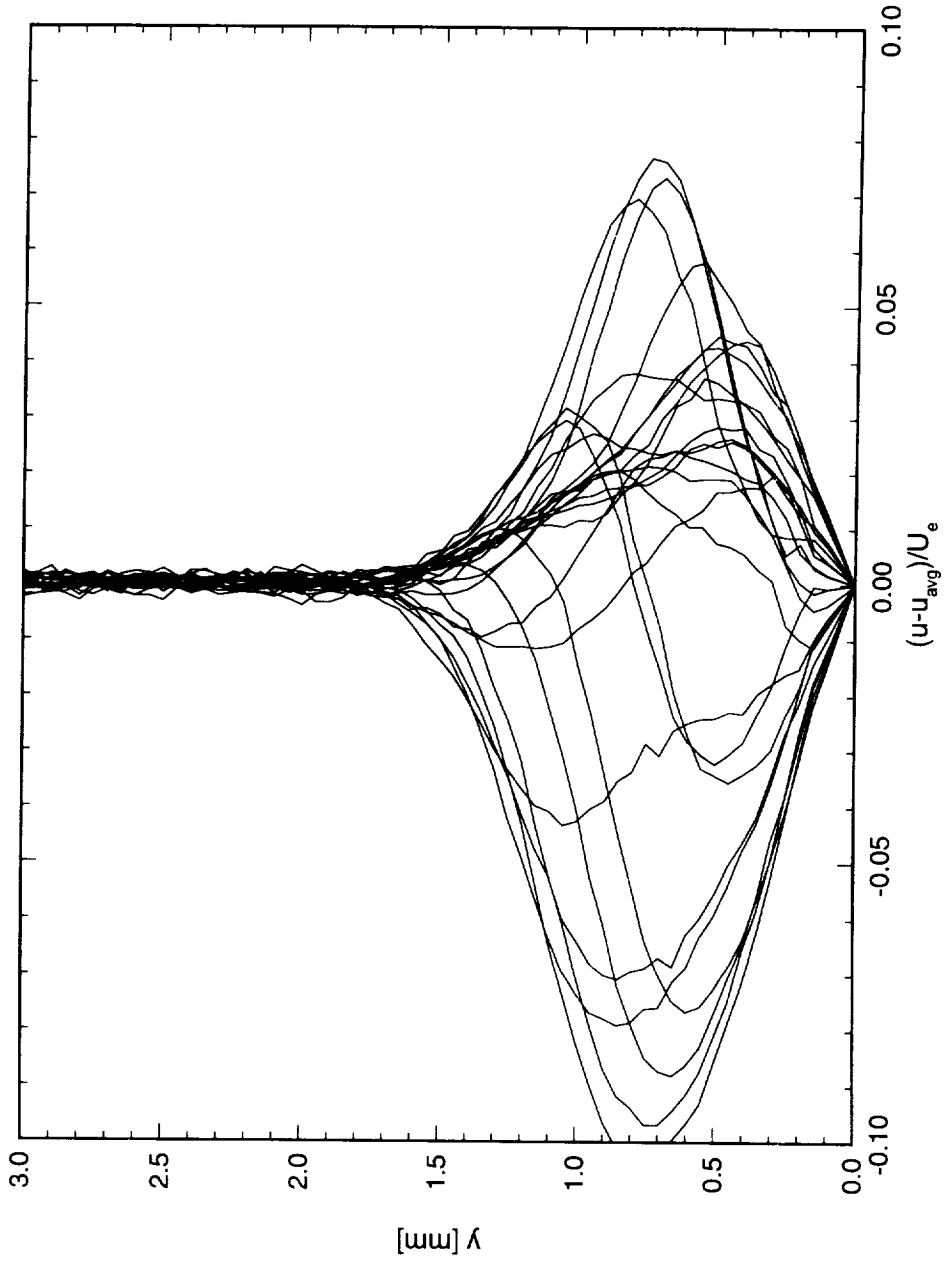

Figure 7.161. Disturbance profiles for boundary-layer scans at $x/c = 0.10$. A 10-element array of 117 μm roughness with a spacing of 12 mm is at $x/c = 0.005$. $Re_c = 3.2 \times 10^6$. Data set A.

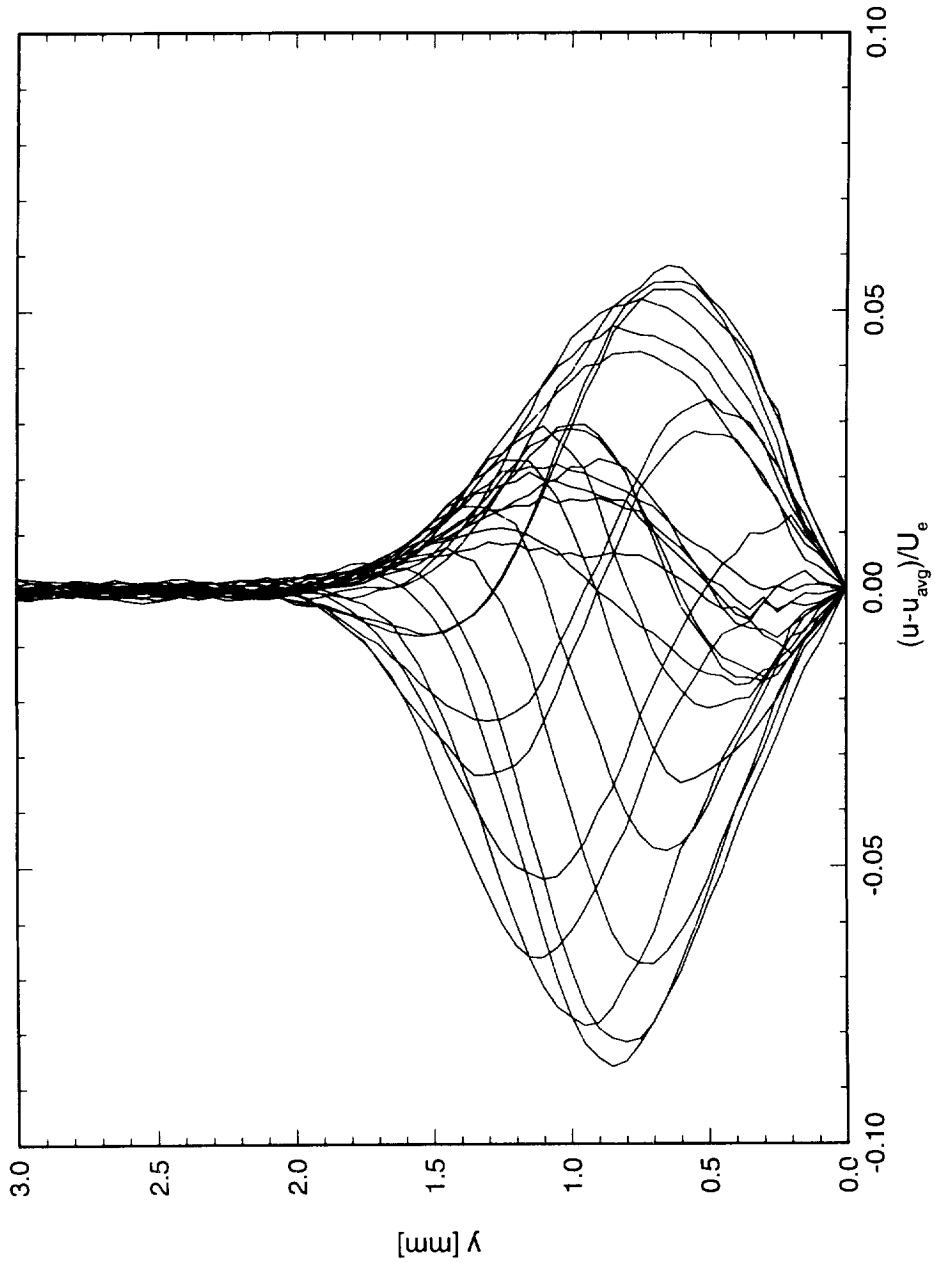

Figure 7.162. Disturbance profiles for boundary-layer scans at $x/c = 0.15$. A 10-element array of 117 μm roughness with a spacing of 12 mm is at $x/c = 0.005$. $Re_c = 3.2 \times 10^6$. Data set A.

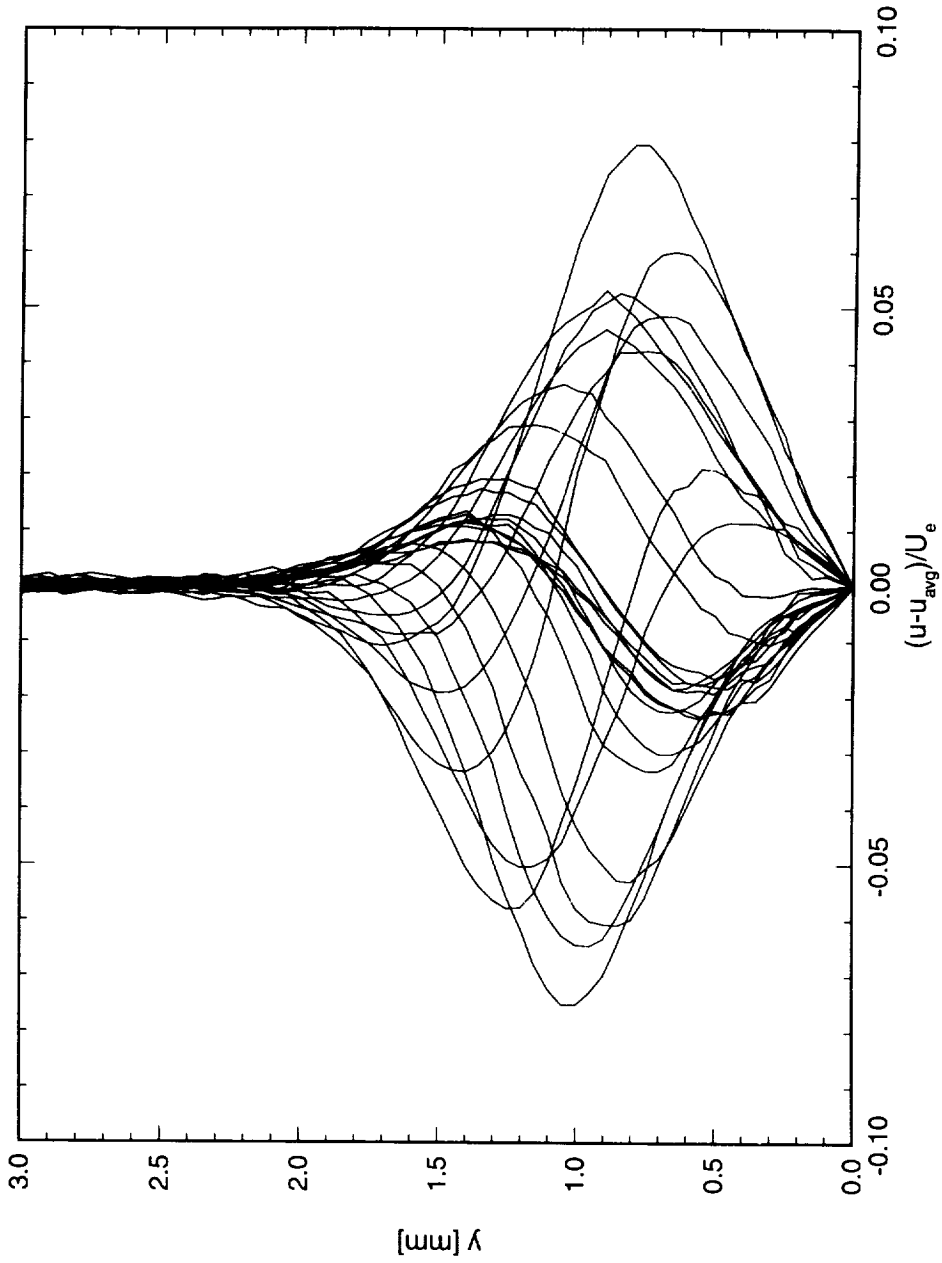

Figure 7.163. Disturbance profiles for boundary-layer scans at $x/c = 0.20$. A 10-element array of 117 μm roughness with a spacing of 12 mm is at $x/c = 0.005$. $Re_c = 3.2 \times 10^6$. Data set A.

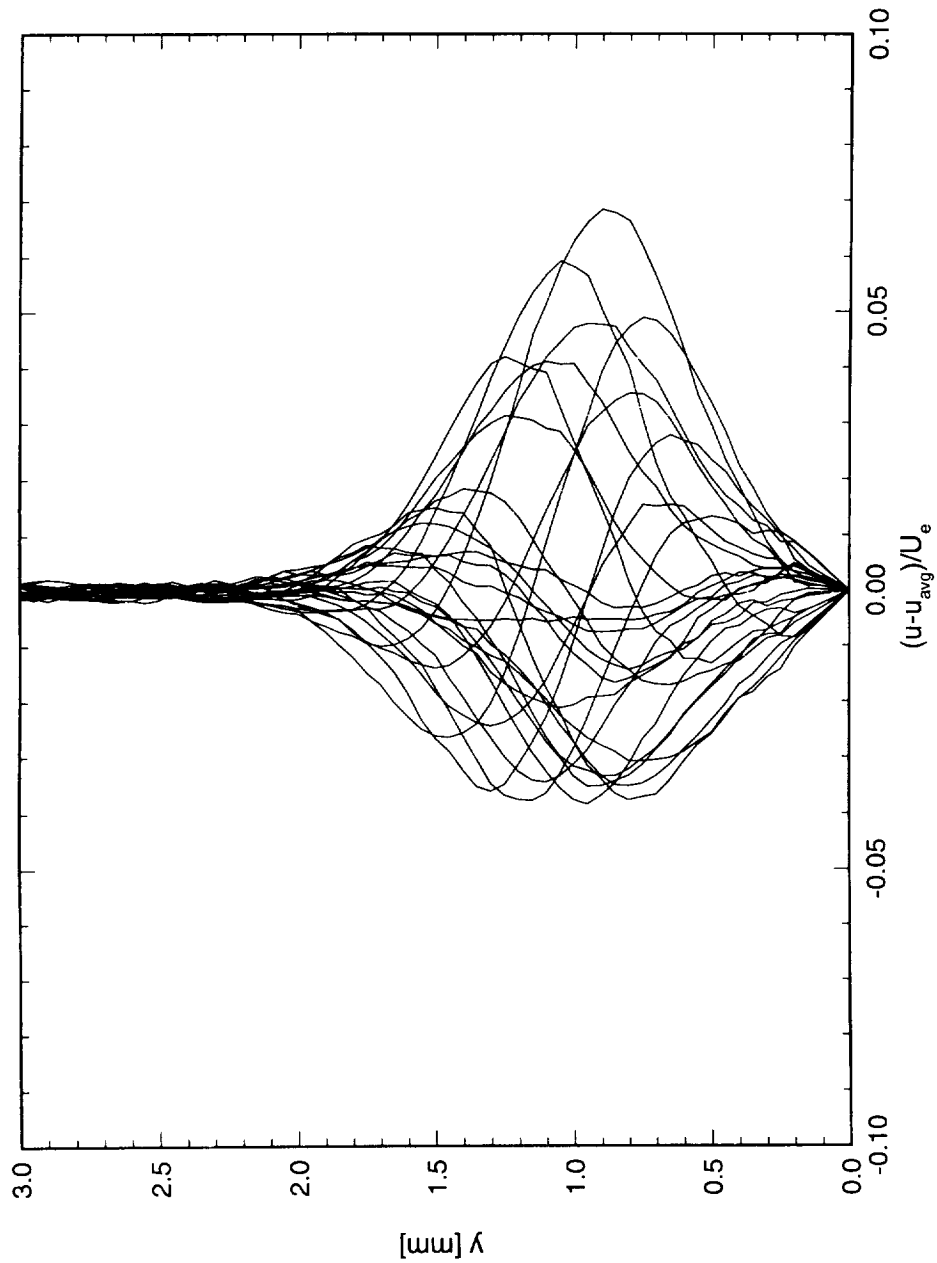

Figure 7.164. Disturbance profiles for boundary-layer scans at $x/c = 0.25$. A 10-element array of 117 μm roughness with a spacing of 12 mm is at $x/c = 0.005$. $Re_c = 3.2 \times 10^6$. Data set A.

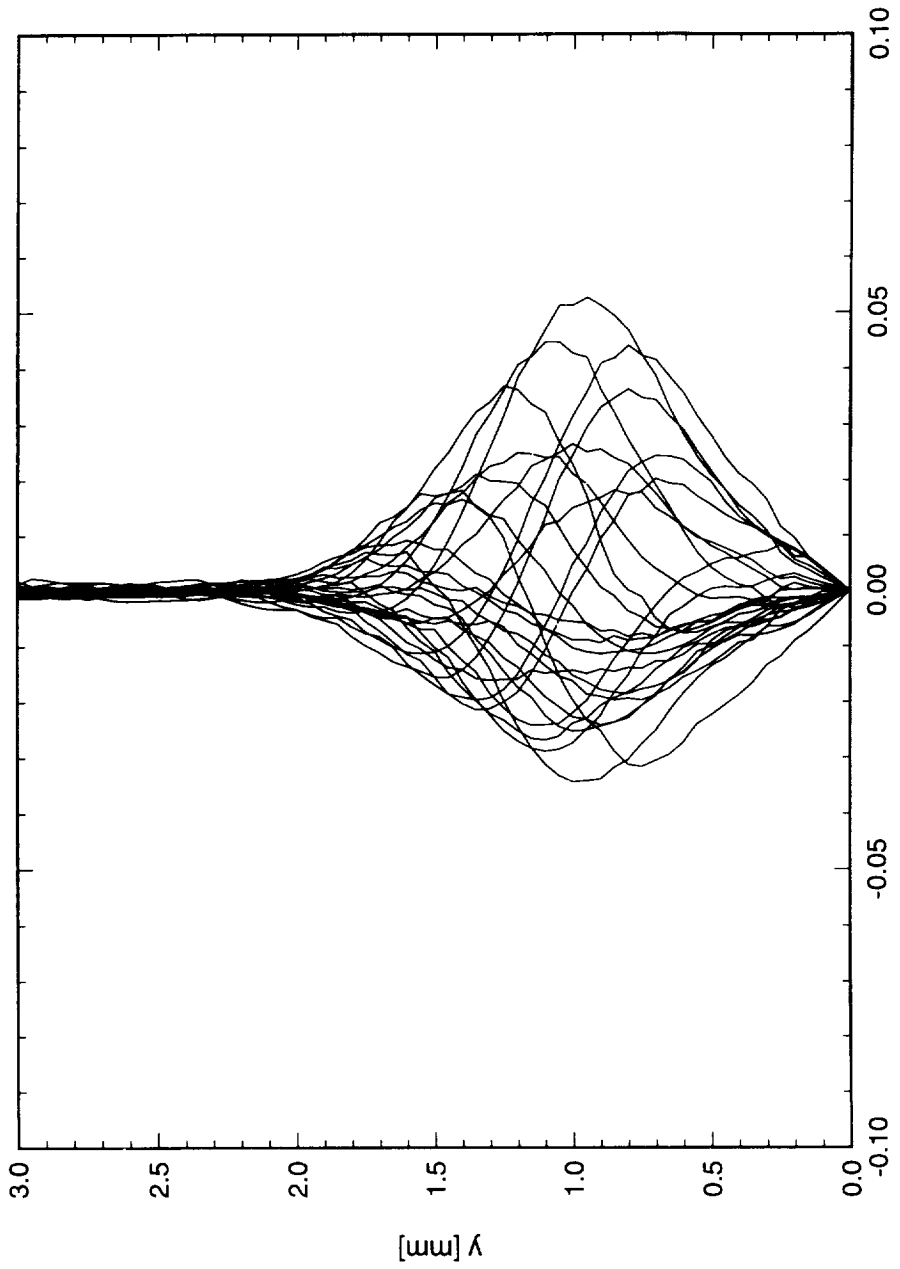

Figure 7.165. Disturbance profiles for boundary-layer scans at $x/c = 0.30$. A 10-element array of 117 μm roughness with a spacing of 12 mm is at $x/c = 0.005$. $Re_c = 3.2 \times 10^6$. Data set A.

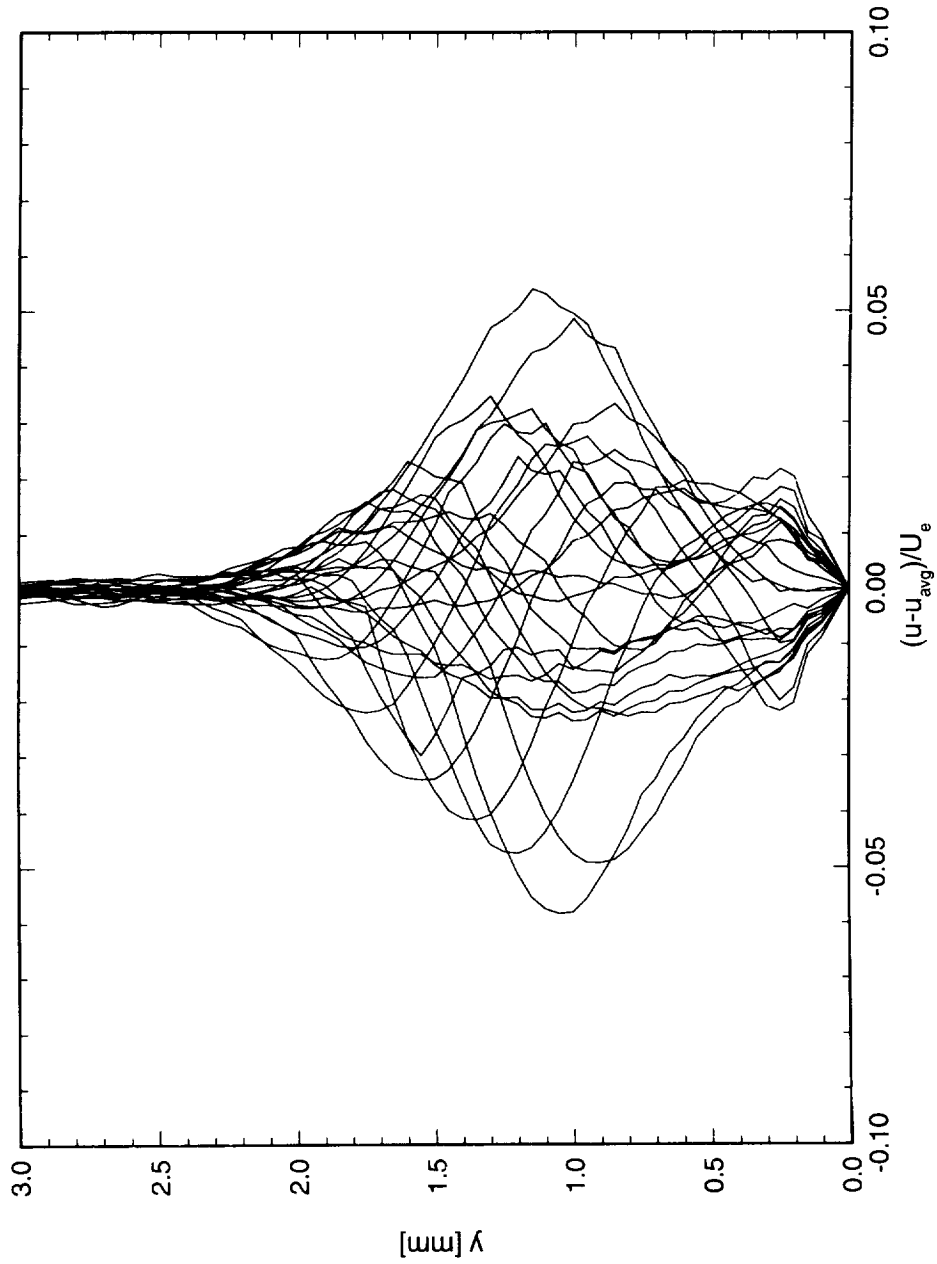

Figure 7.166. Disturbance profiles for boundary-layer scans at $x/c = 0.35$. A 10-element array of 117 μm roughness with a spacing of 12 mm is at $x/c = 0.005$. $Re_c = 3.2 \times 10^6$. Data set A.

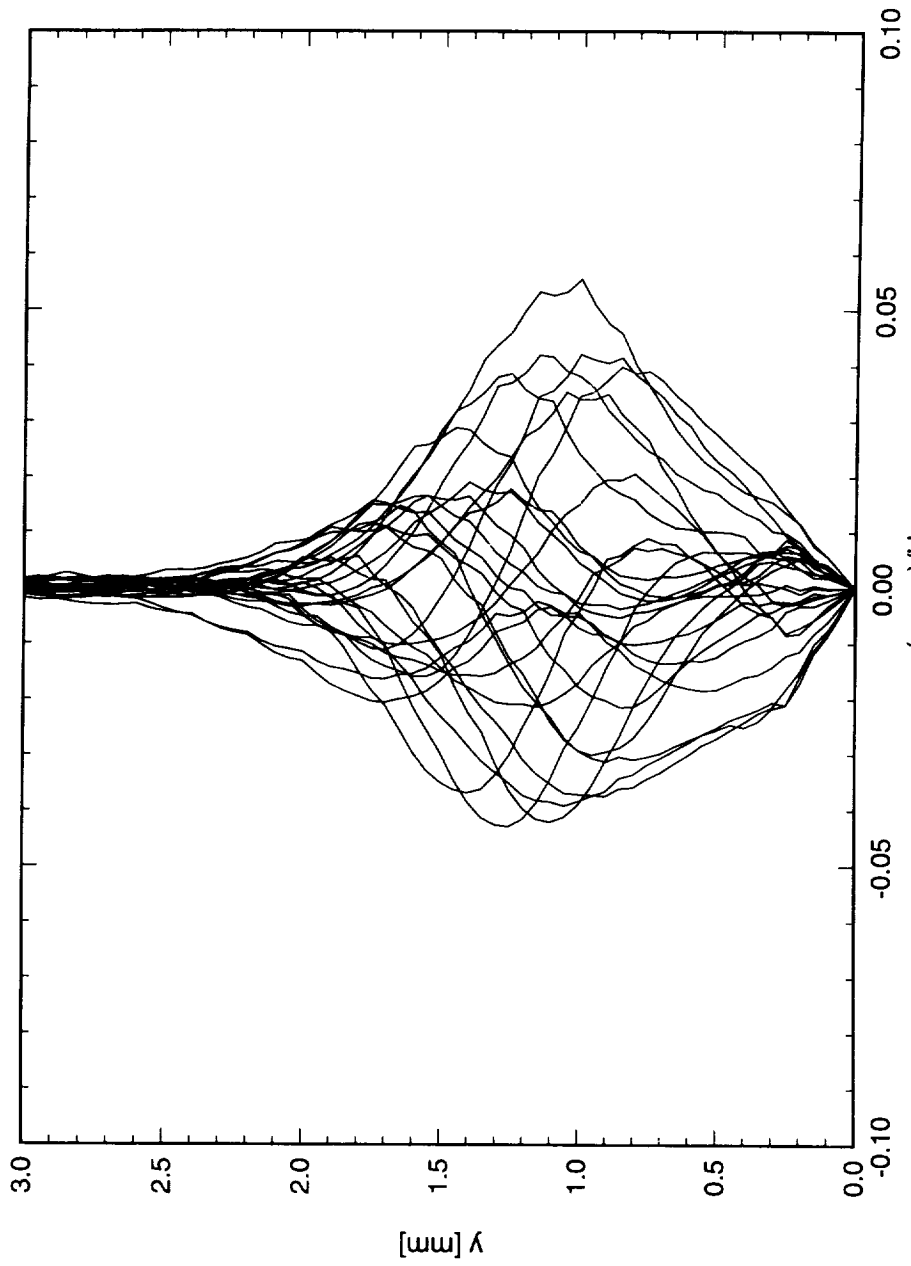

Figure 7.167. Disturbance profiles for boundary-layer scans at $x/c = 0.40$. A 10-element array of 117 μm roughness with a spacing of 12 mm is at $x/c = 0.005$. $Re_c = 3.2 \times 10^6$. Data set A.

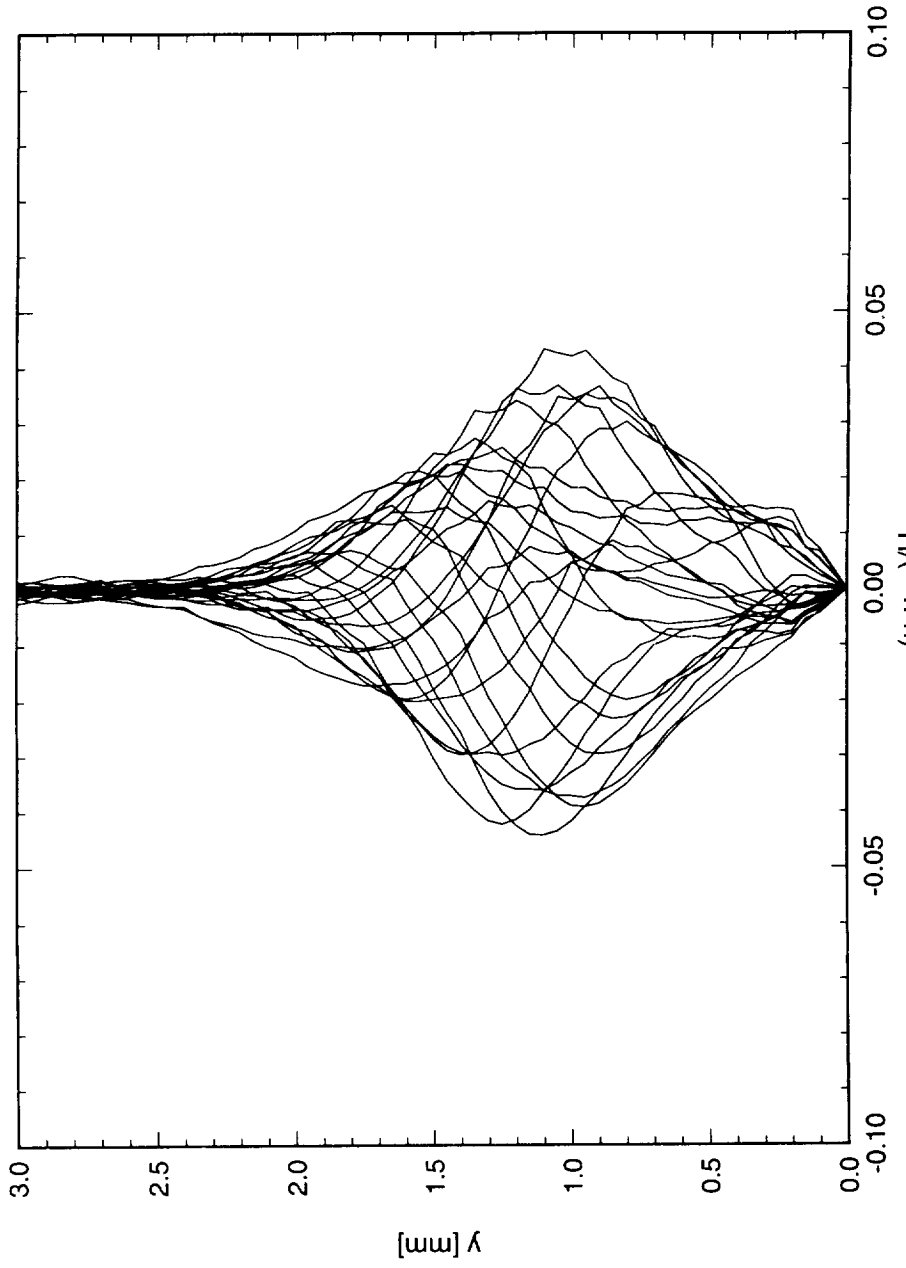

Figure 7.168. Disturbance profiles for boundary-layer scans at $x/c = 0.45$. A 10-element array of 117 μm roughness with a spacing of 12 mm is at $x/c = 0.005$. $Re_c = 3.2 \times 10^6$. Data set A.

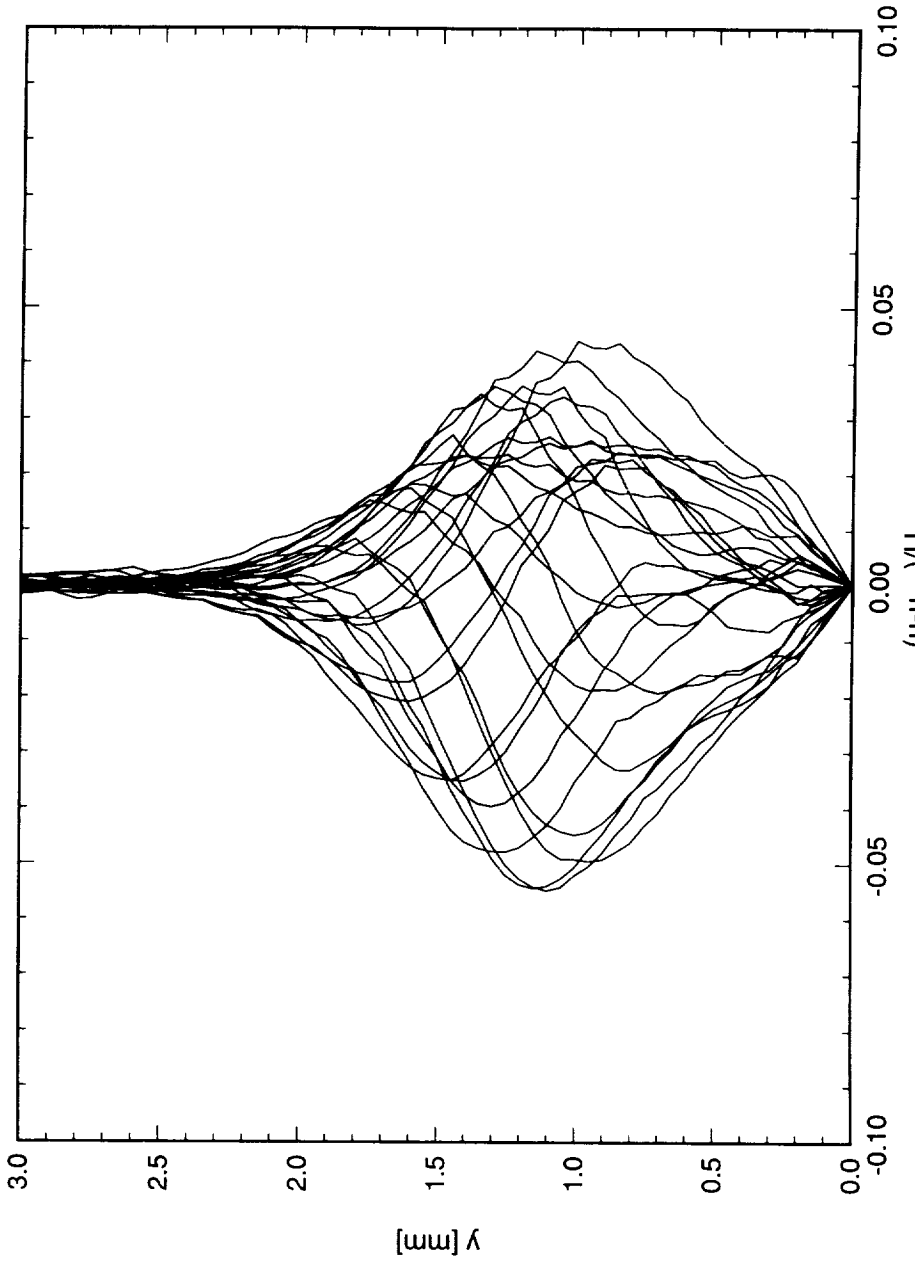

Figure 7.169. Disturbance profiles for boundary-layer scans at $x/c = 0.50$. A 10-element array of 117 μm roughness with a spacing of 12 mm is at $x/c = 0.005$. $Re_c = 3.2 \times 10^6$. Data set A.

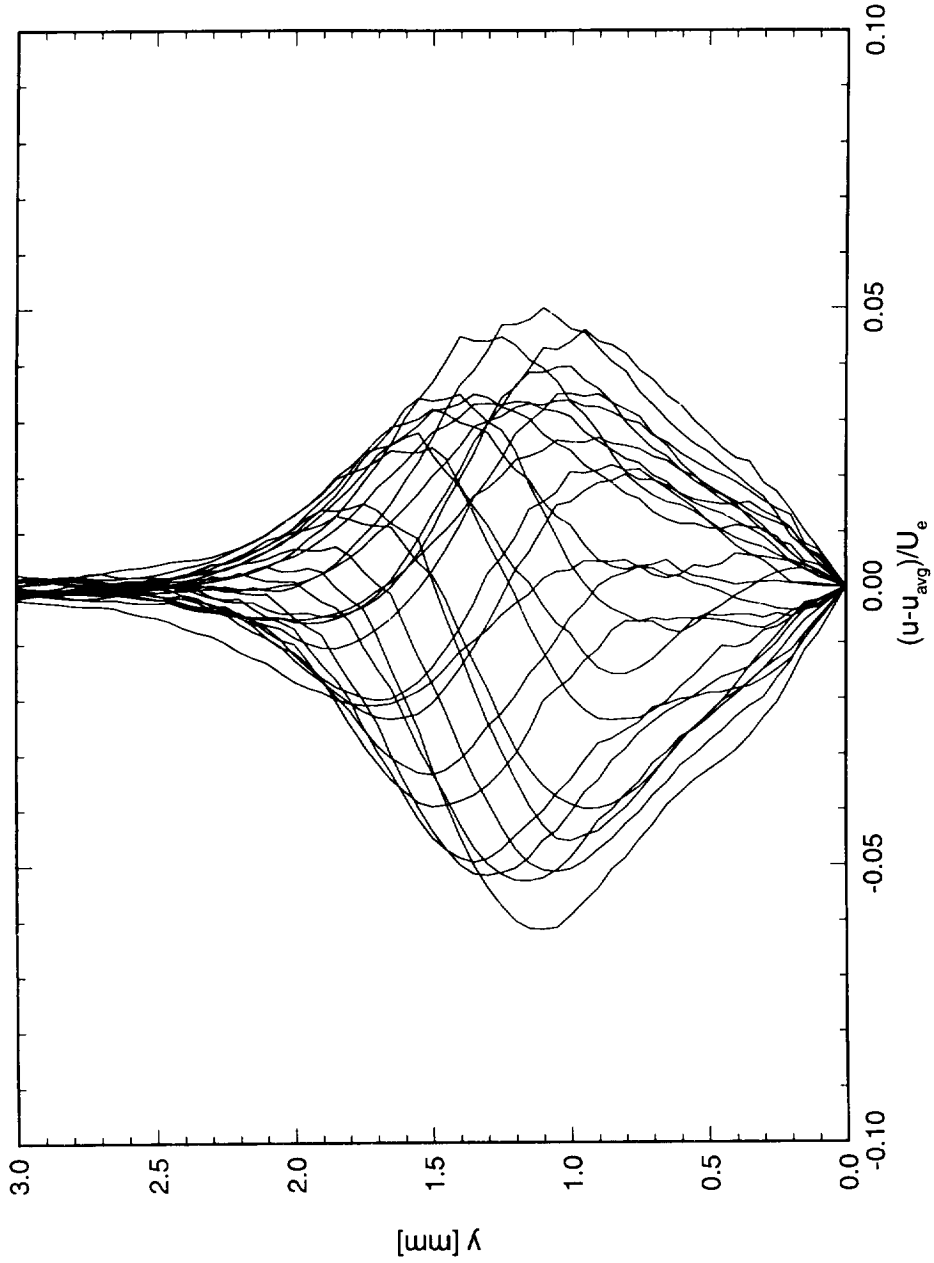

Figure 7.170. Disturbance profiles for boundary-layer scans at $x/c = 0.55$. A 10-element array of 117 μm roughness with a spacing of 12 mm is at $x/c = 0.005$. $Re_c = 3.2 \times 10^6$. Data set A.

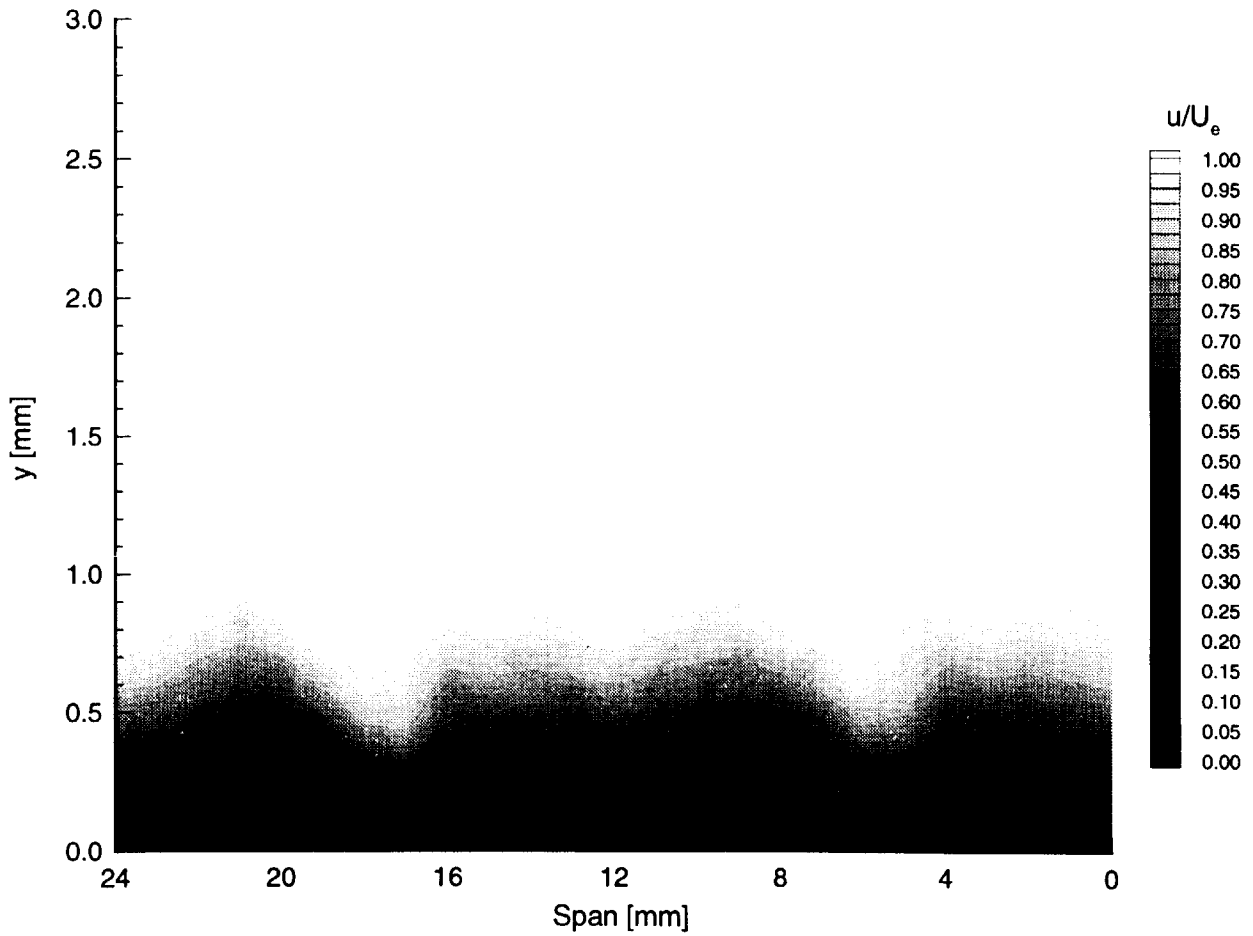

Figure 7.171. Velocity contours for boundary-layer scans at $x/c = 0.05$. A 10-element array of 117 μm roughness with a spacing of 12 mm is at $x/c = 0.005$. $Re_c = 3.2 \times 10^6$. Data set A.

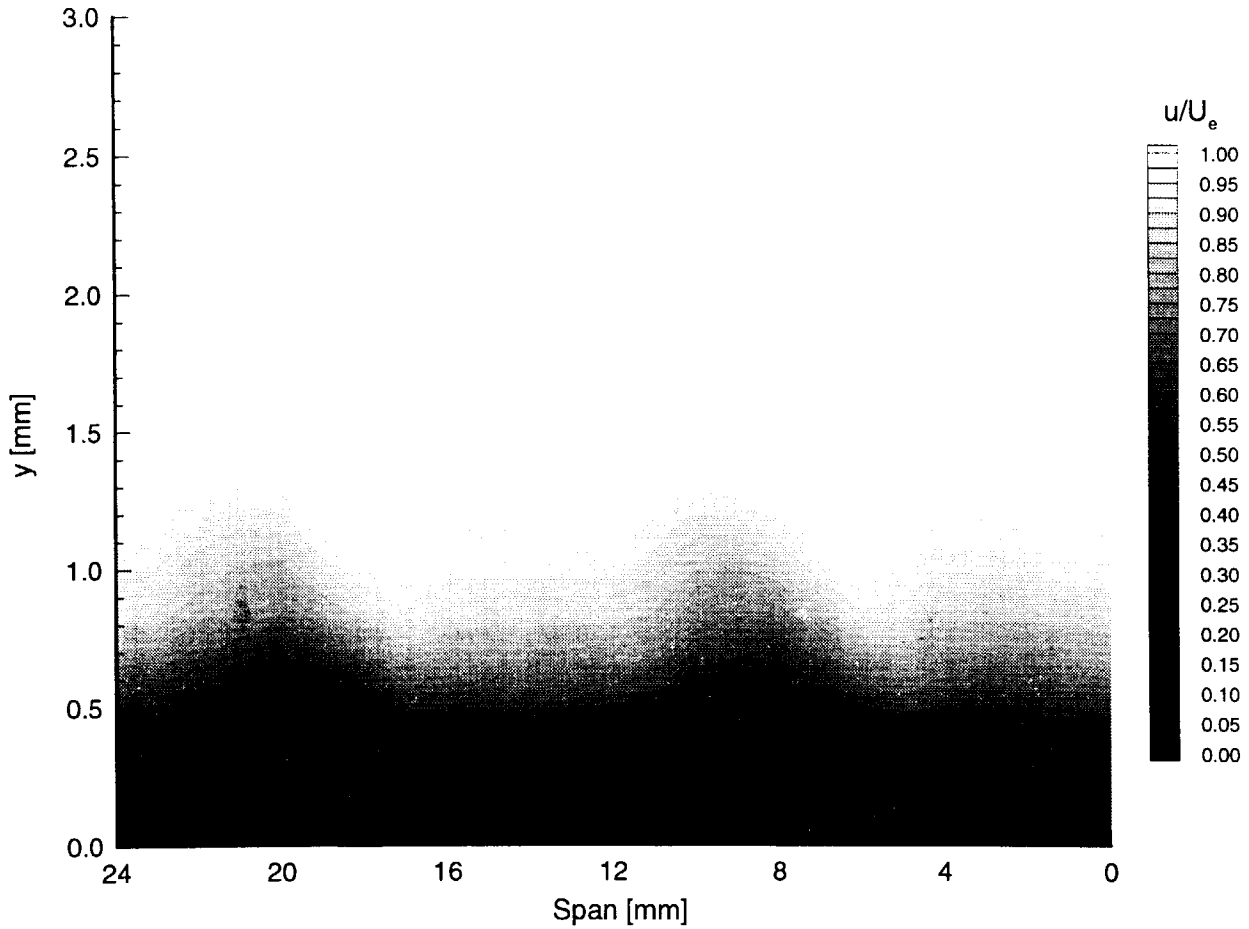

Figure 7.172. Velocity contours for boundary-layer scans at $x/c = 0.10$. A 10-element array of 117 μm roughness with a spacing of 12 mm is at $x/c = 0.005$. $Re_c = 3.2 \times 10^6$. Data set A.

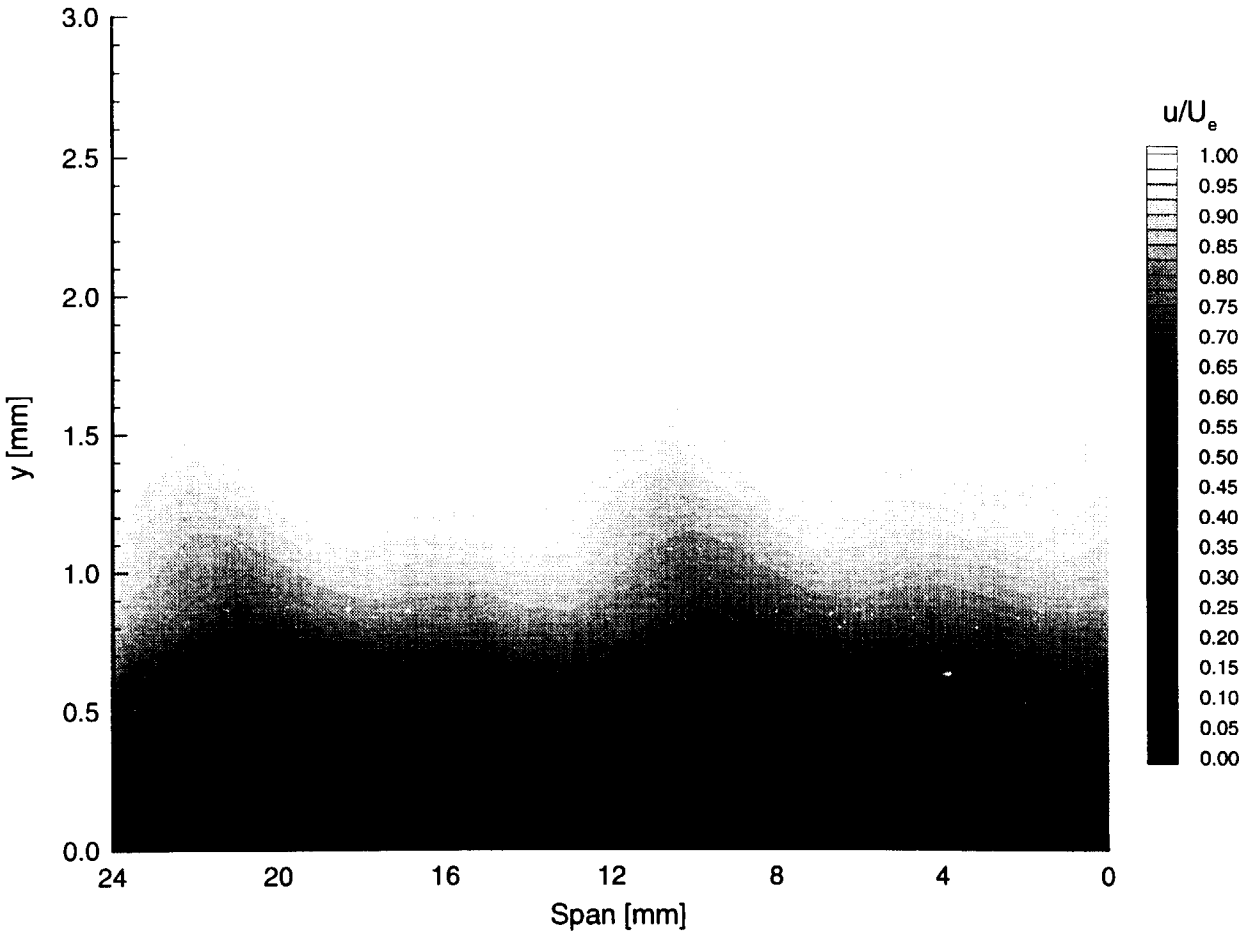

Figure 7.173. Velocity contours for boundary-layer scans at $x/c = 0.15$. A 10-element array of 117 μm roughness with a spacing of 12 mm is at $x/c = 0.005$. $Re_c = 3.2 \times 10^6$. Data set A.

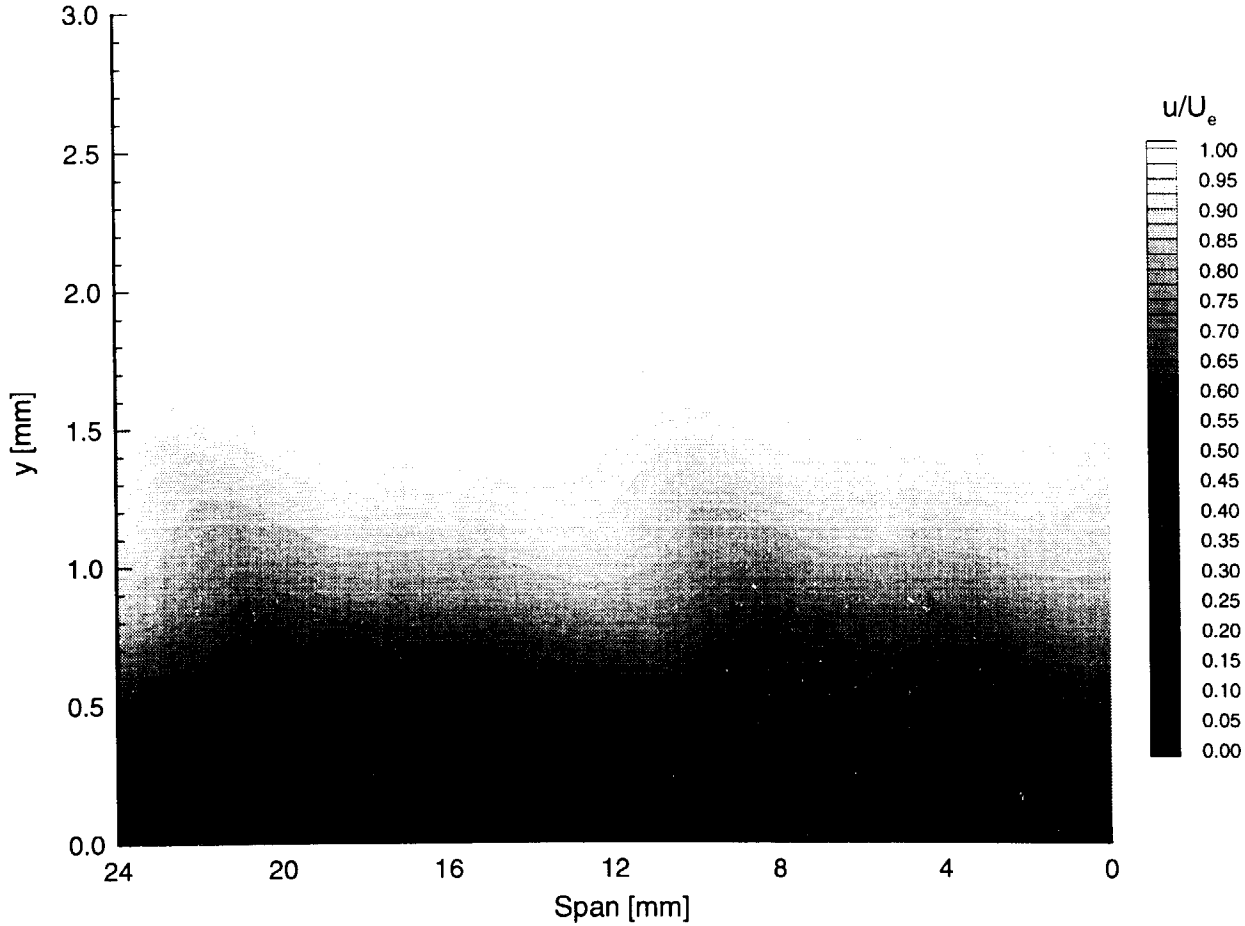

Figure 7.174. Velocity contours for boundary-layer scans at $x/c = 0.20$. A 10-element array of 117 μm roughness with a spacing of 12 mm is at $x/c = 0.005$. $Re_c = 3.2 \times 10^6$. Data set A.

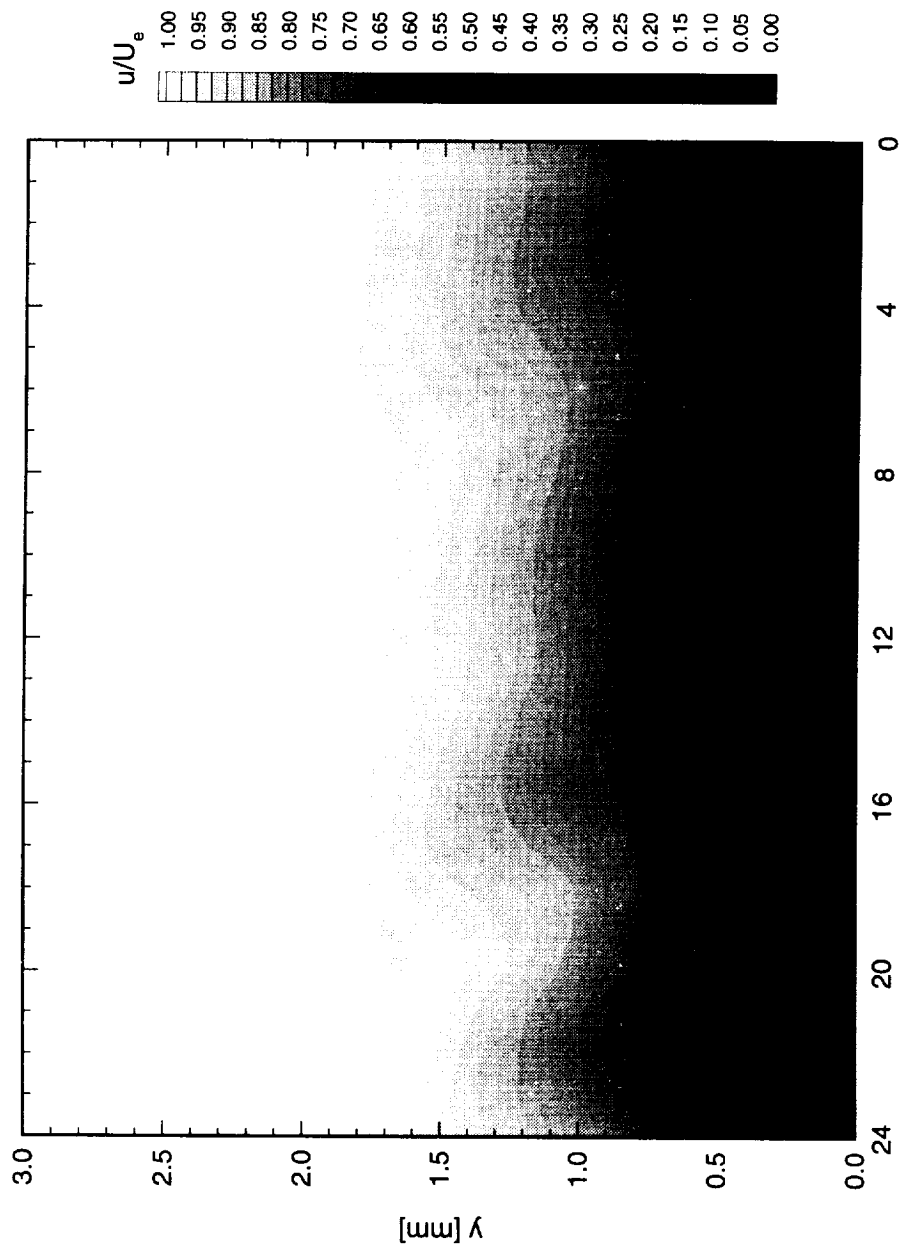

Figure 7.175. Velocity contours for boundary-layer scans at $x/c = 0.25$. A 10-element array of 117 μm roughness with a spacing of 12 mm is at $x/c = 0.005$. $Re_c = 3.2 \times 10^6$. Data set A.

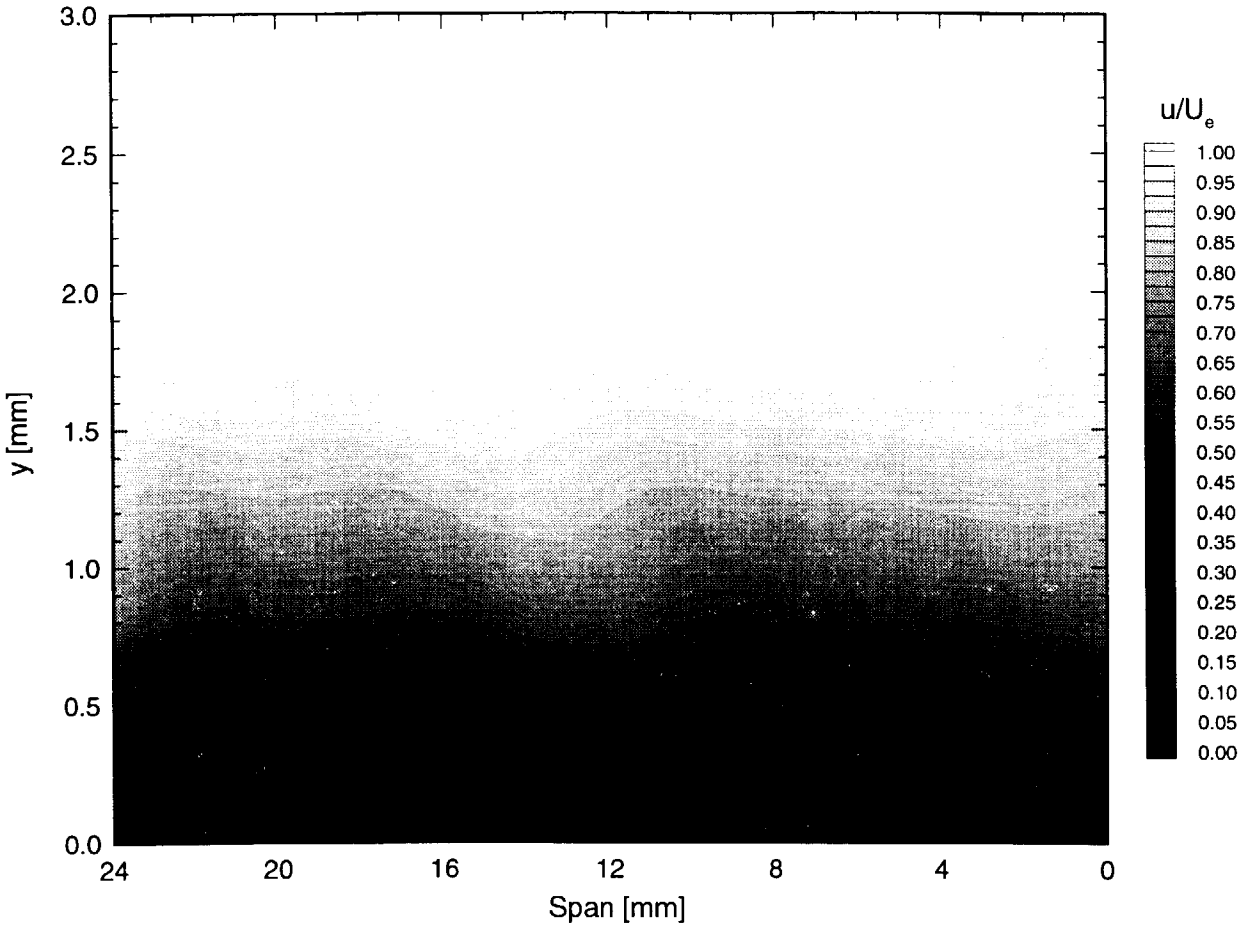

Figure 7.176. Velocity contours for boundary-layer scans at $x/c = 0.30$. A 10-element array of 117 μm roughness with a spacing of 12 mm is at $x/c = 0.005$. $Re_c = 3.2 \times 10^6$. Data set A.

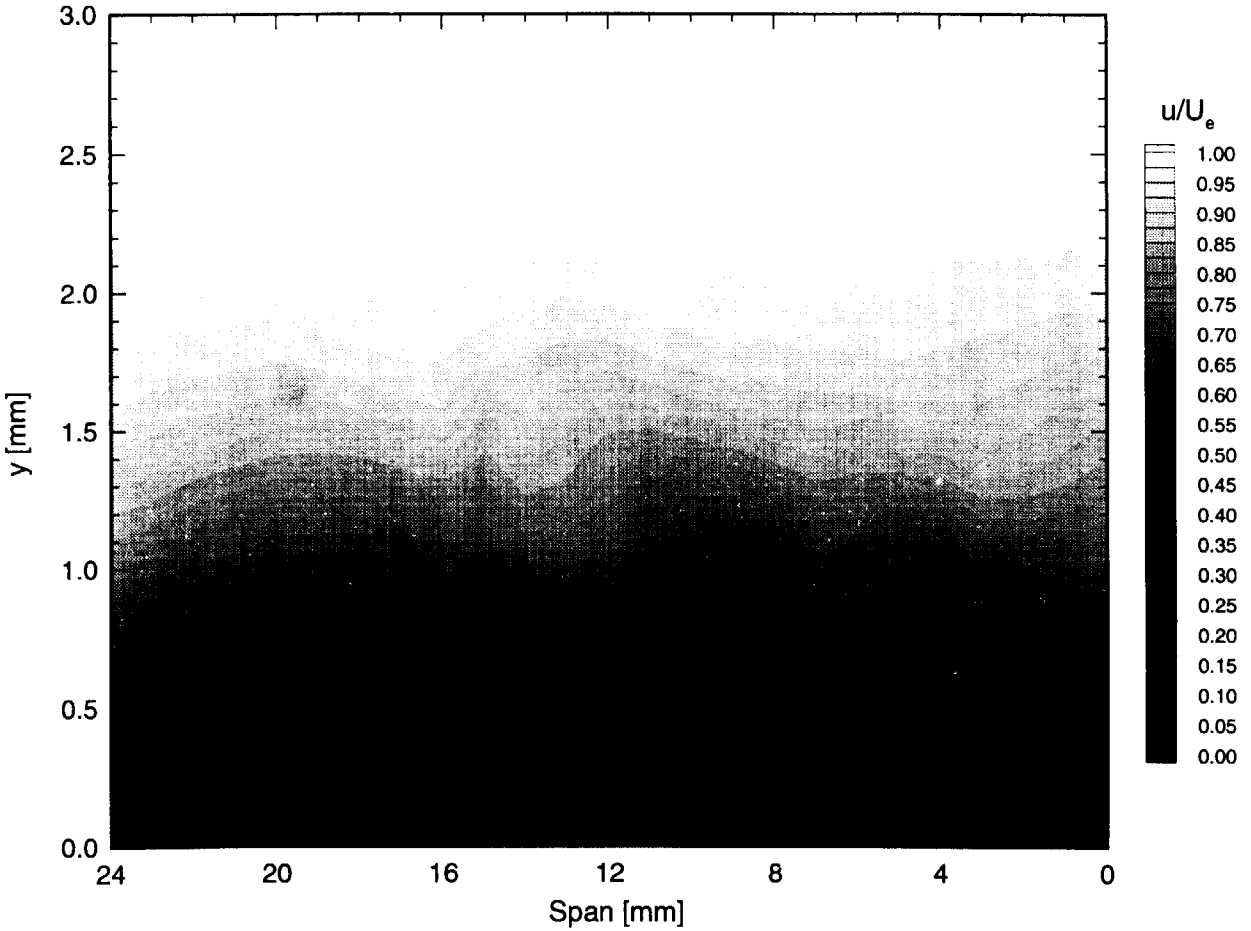

Figure 7.177. Velocity contours for boundary-layer scans at $x/c = 0.35$. A 10-element array of 117 μm roughness with a spacing of 12 mm is at $x/c = 0.005$. $Re_c = 3.2 \times 10^6$. Data set A.

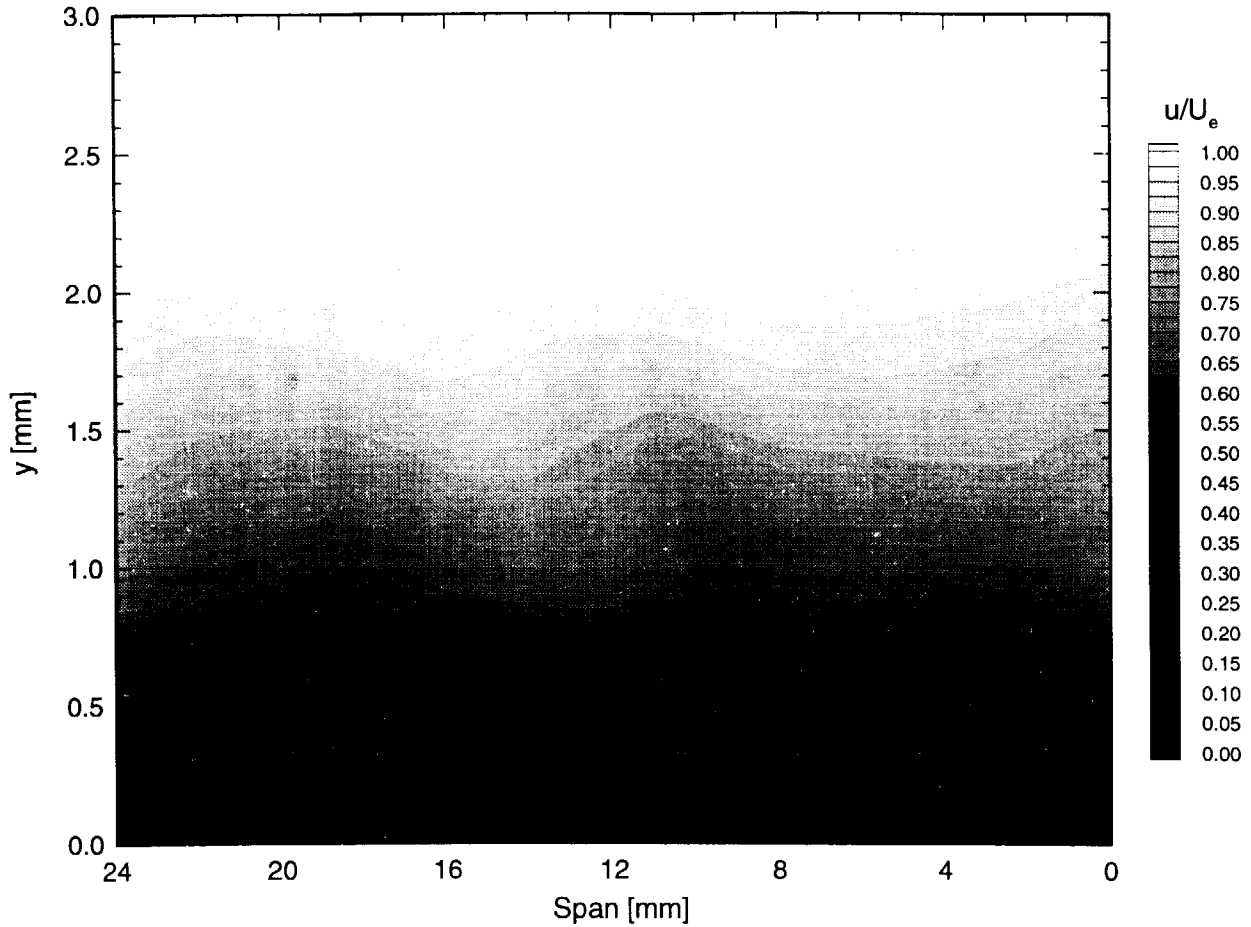

Figure 7.178. Velocity contours for boundary-layer scans at $x/c = 0.40$. A 10-element array of 117 μm roughness with a spacing of 12 mm is at $x/c = 0.005$. $Re_c = 3.2 \times 10^6$. Data set A.

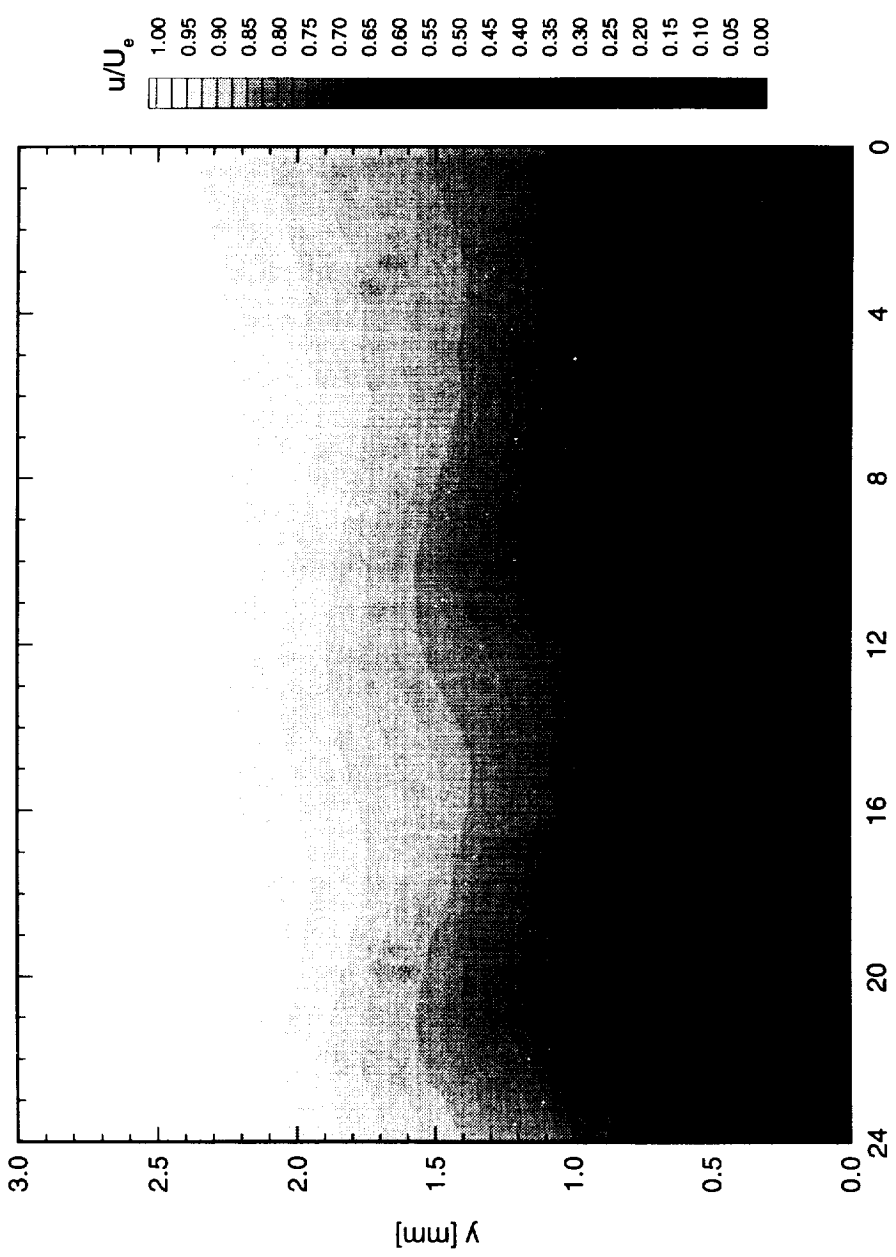

Figure 7.179. Velocity contours for boundary-layer scans at $x/c = 0.45$. A 10-element array of 117 μm roughness with a spacing of 12 mm is at $x/c = 0.005$. $Re_c = 3.2 \times 10^6$. Data set A.

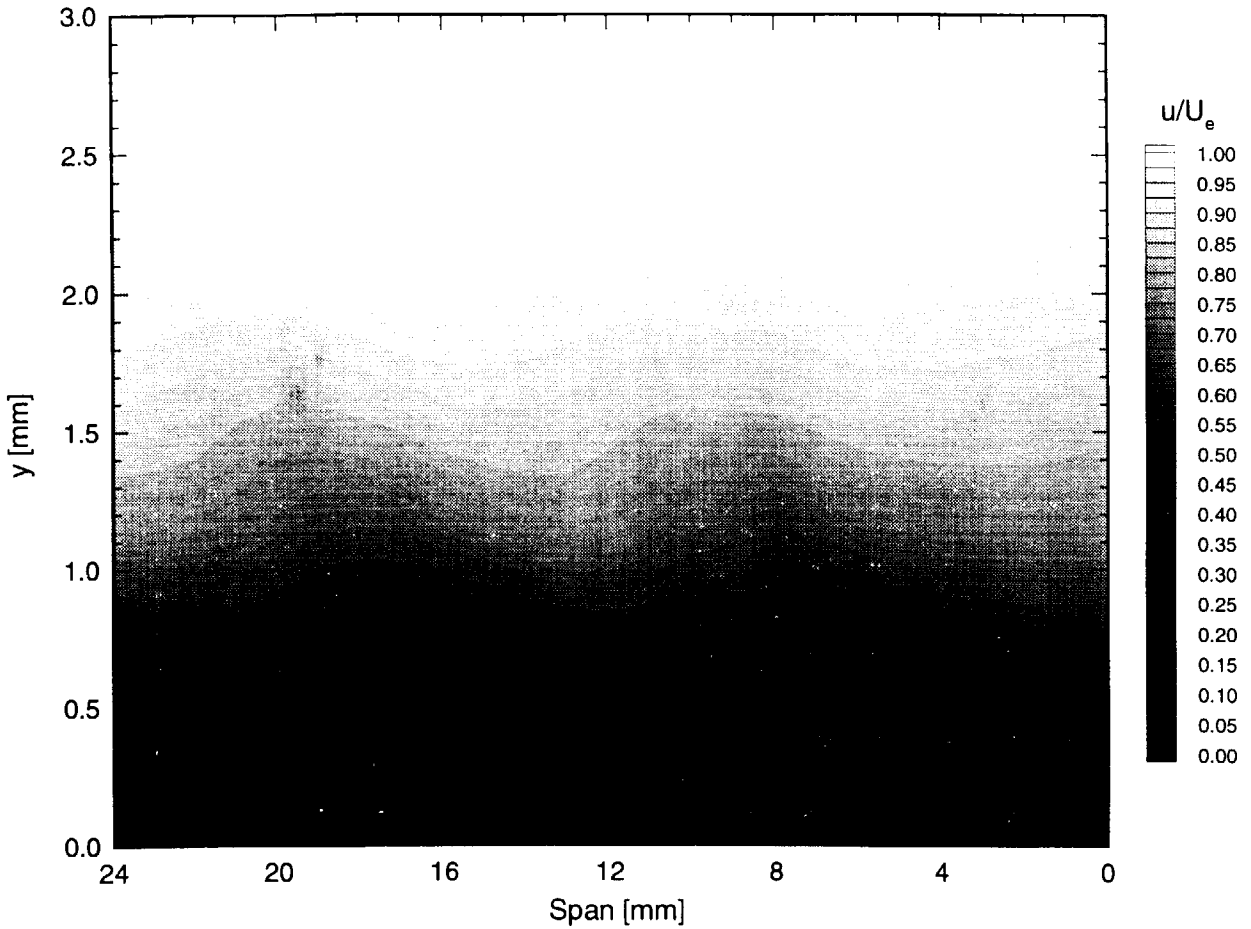

Figure 7.180. Velocity contours for boundary-layer scans at $x/c = 0.50$. A 10-element array of 117 μm roughness with a spacing of 12 mm is at $x/c = 0.005$. $Re_c = 3.2 \times 10^6$. Data set A.

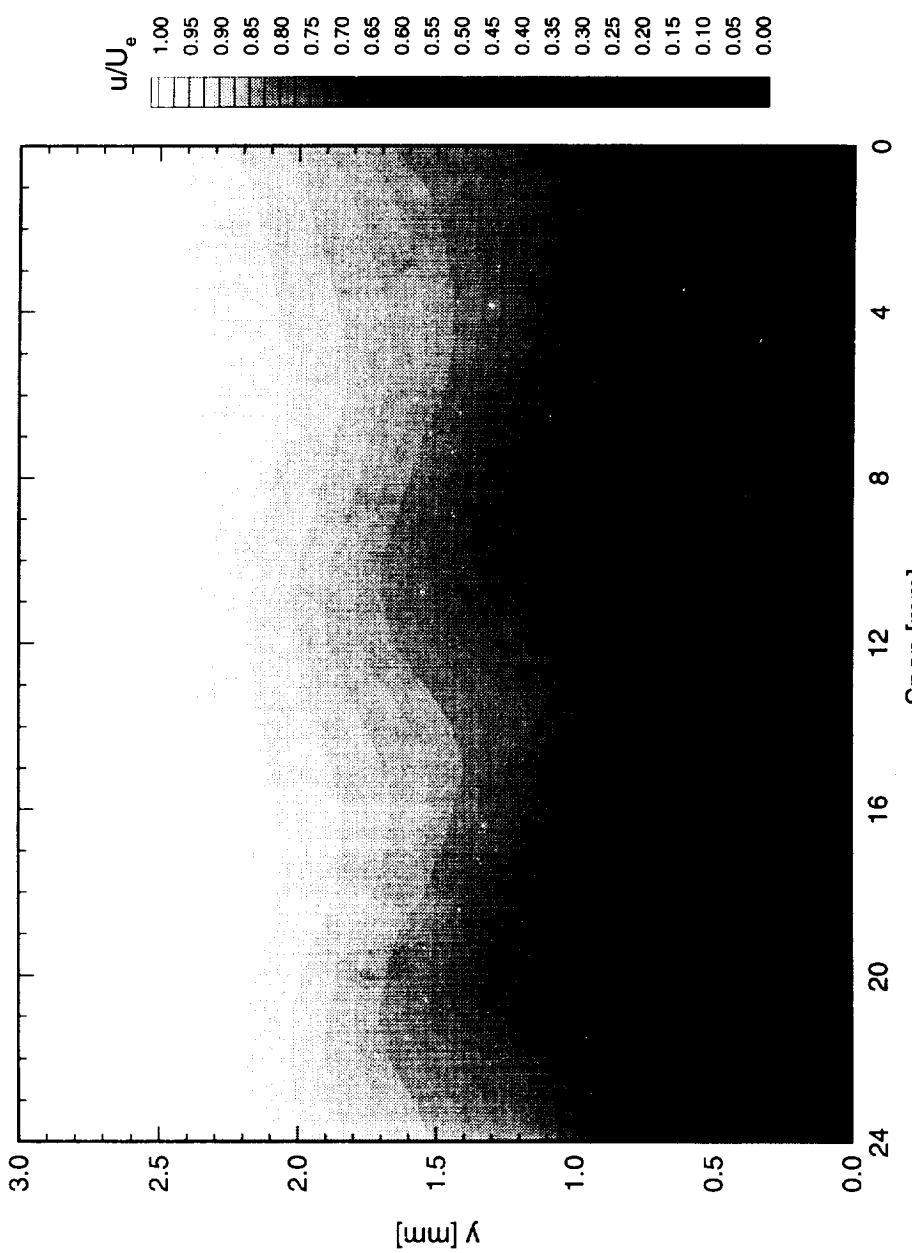

Figure 7.181. Velocity contours for boundary-layer scans at $x/c = 0.55$. A 10-element array of 117 μm roughness with a spacing of 12 mm is at $x/c = 0.005$. $Re_c = 3.2 \times 10^6$. Data set A.

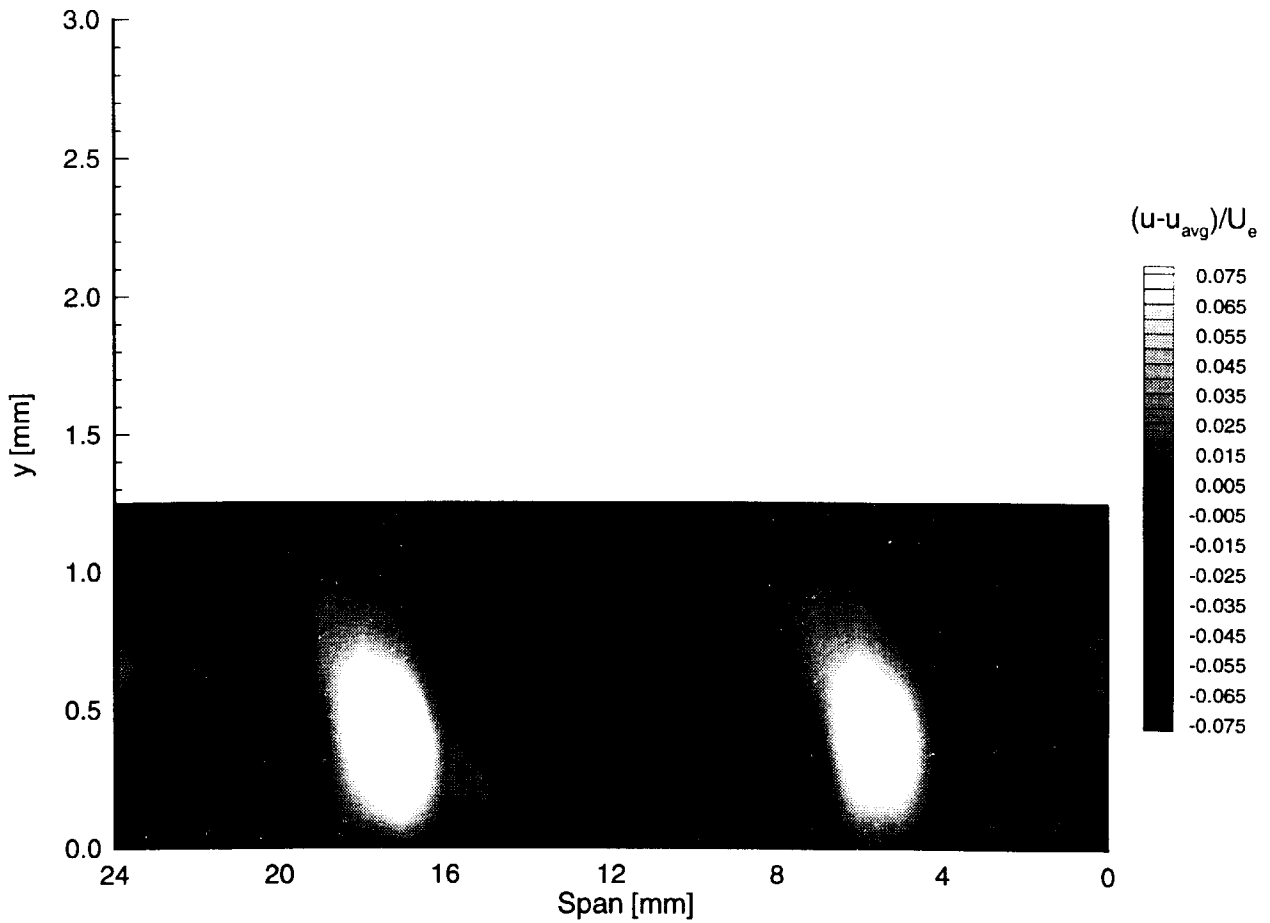

Figure 7.182. Disturbance contours for boundary-layer scans at $x/c = 0.05$. A 10-element array of 117 μm roughness with a spacing of 12 mm is at $x/c = 0.005$. $Re_c = 3.2 \times 10^6$. Data set A.

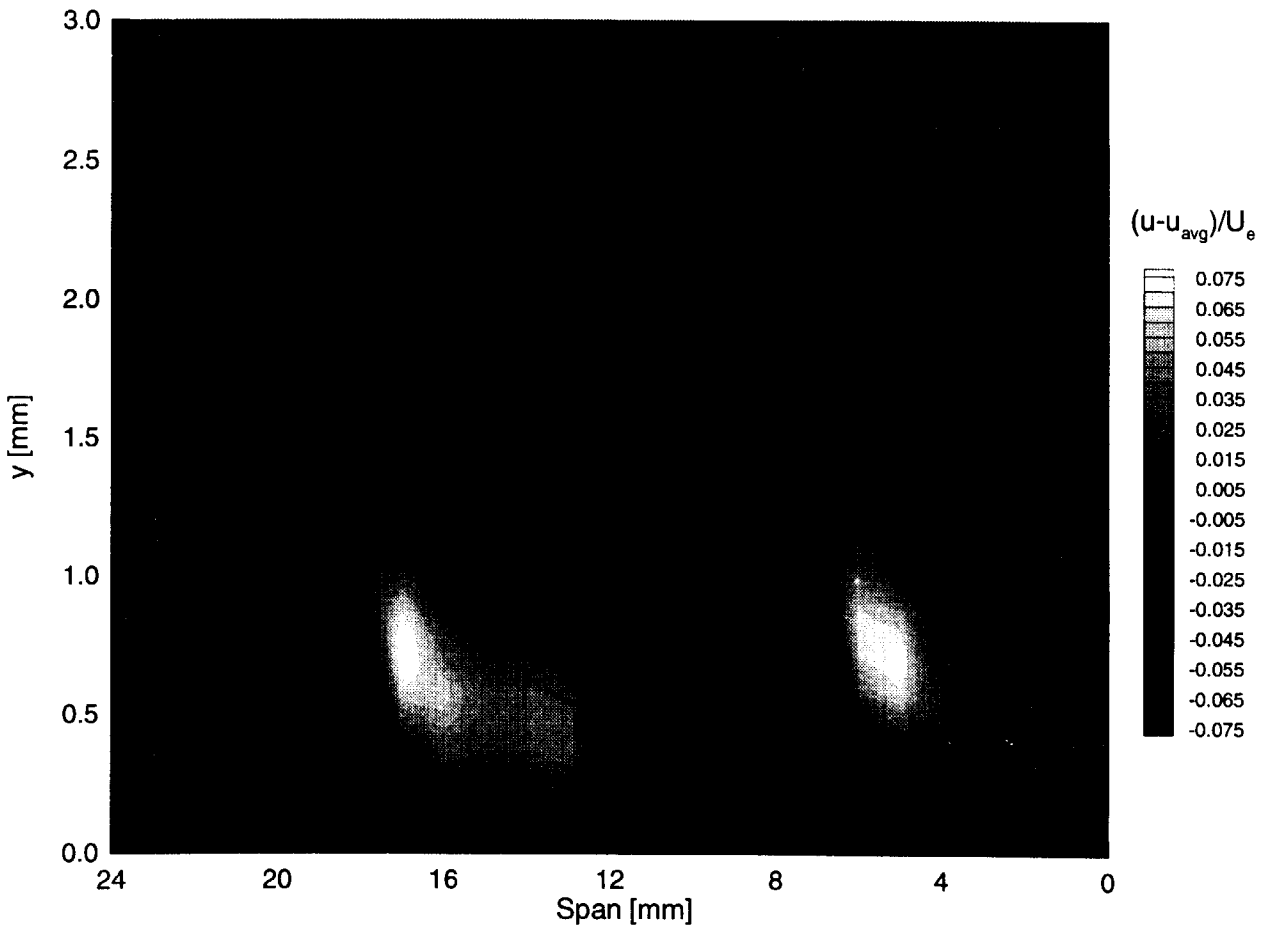

Figure 7.183. Disturbance contours for boundary-layer scans at $x/c = 0.10$. A 10-element array of 117 μm roughness with a spacing of 12 mm is at $x/c = 0.005$. $Re_c = 3.2 \times 10^6$. Data set A.

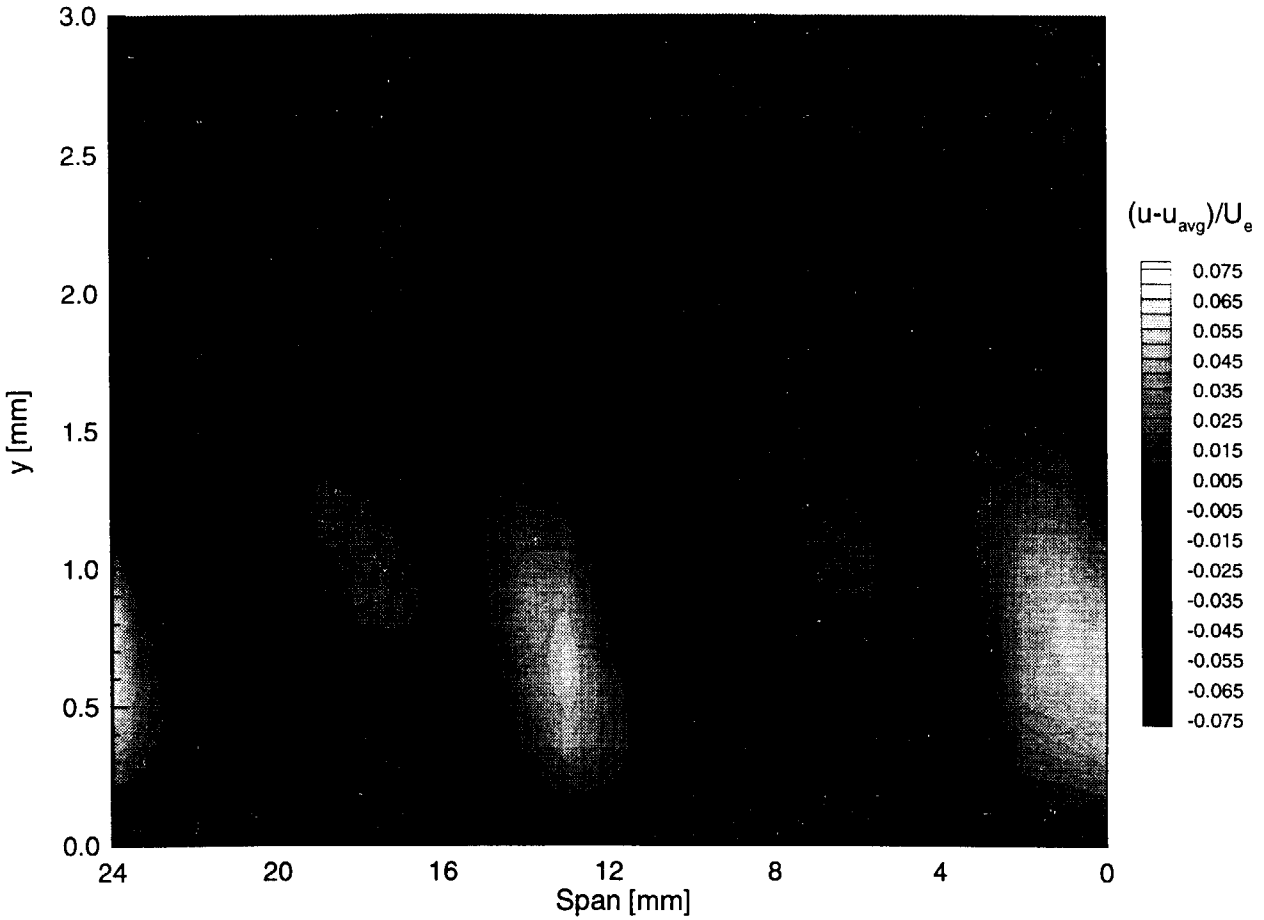

Figure 7.184. Disturbance contours for boundary-layer scans at $x/c = 0.15$. A 10-element array of 117 μm roughness with a spacing of 12 mm is at $x/c = 0.005$. $Re_c = 3.2 \times 10^6$. Data set A.

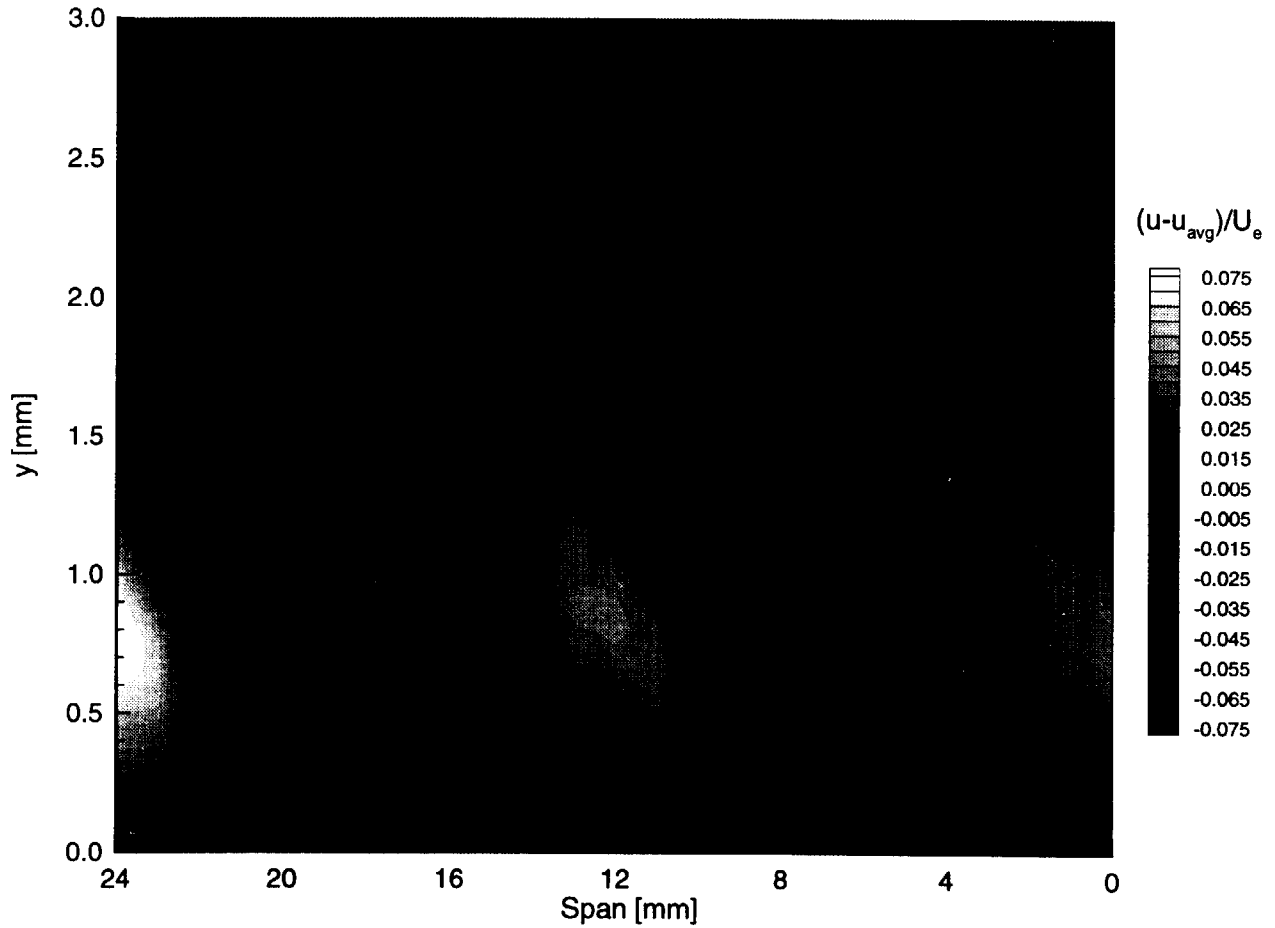

Figure 7.185. Disturbance contours for boundary-layer scans at $x/c = 0.20$. A 10-element array of 117 μm roughness with a spacing of 12 mm is at $x/c = 0.005$. $Re_c = 3.2 \times 10^6$. Data set A.

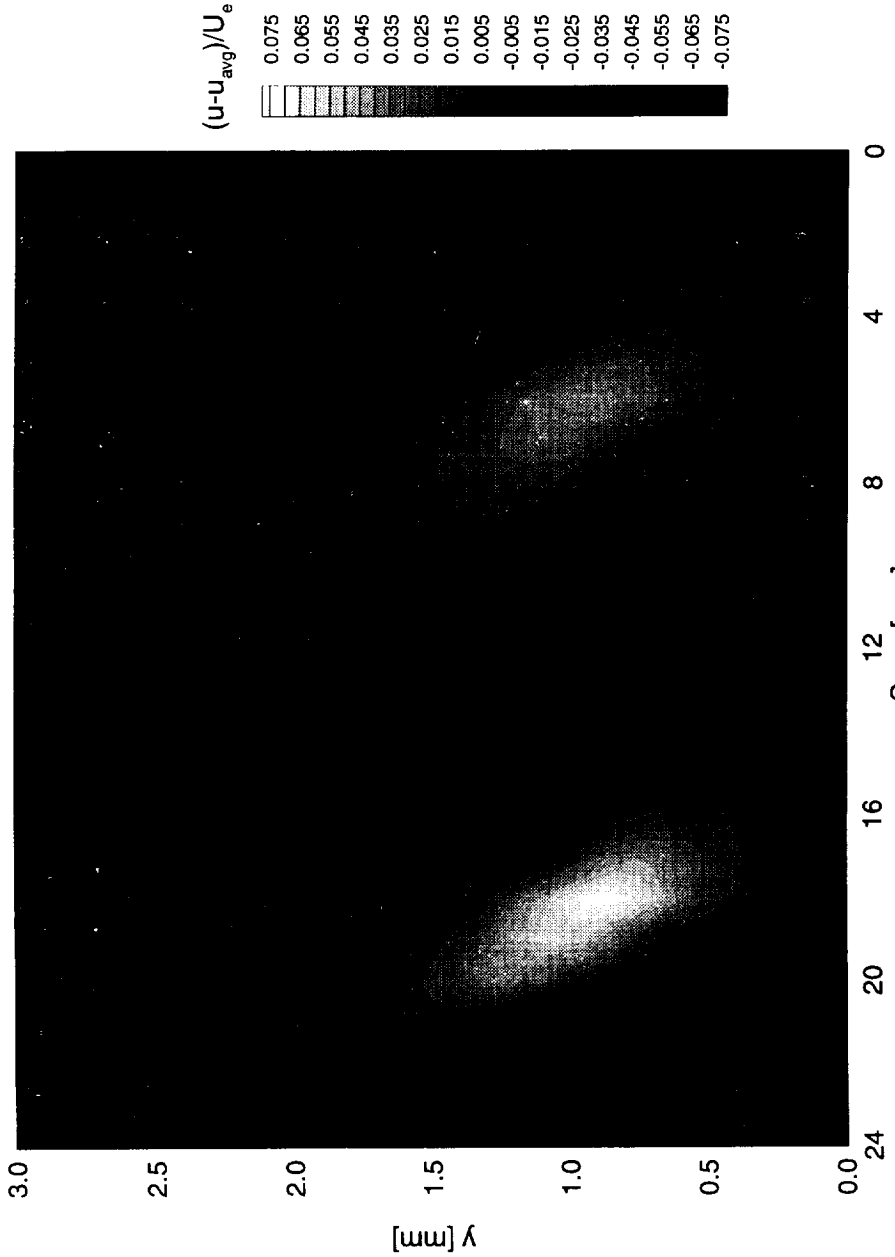

Figure 7.186. Disturbance contours for boundary-layer scans at $x/c = 0.25$. A 10-element array of 117 μm roughness with a spacing of 12 mm is at $x/c = 0.005$. $Re_c = 3.2 \times 10^6$. Data set A.

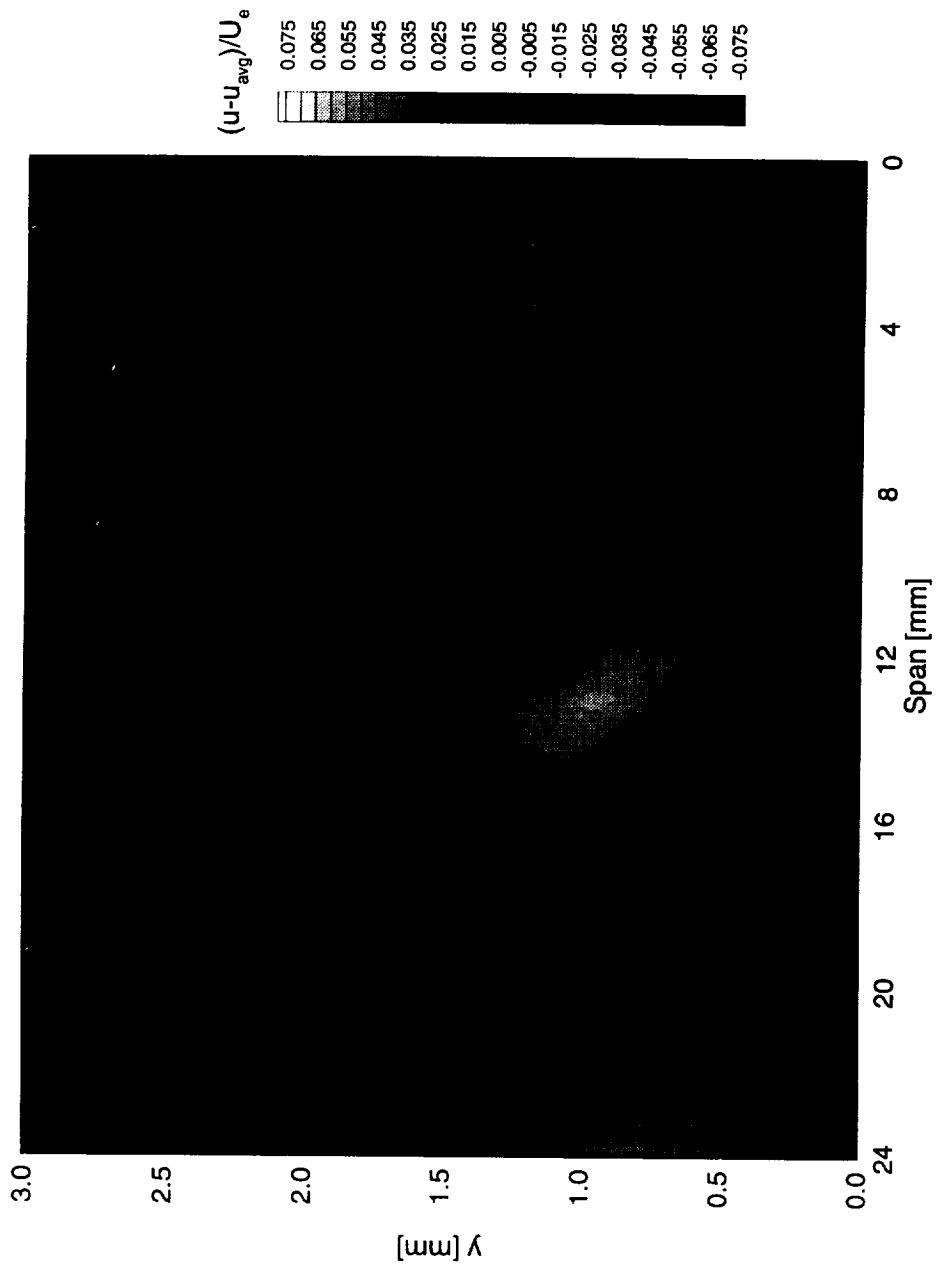

Figure 7.187. Disturbance contours for boundary-layer scans at $x/c = 0.30$. A 10-element array of 117 μm roughness with a spacing of 12 mm is at $x/c = 0.005$. $Re_c = 3.2 \times 10^6$. Data set A.

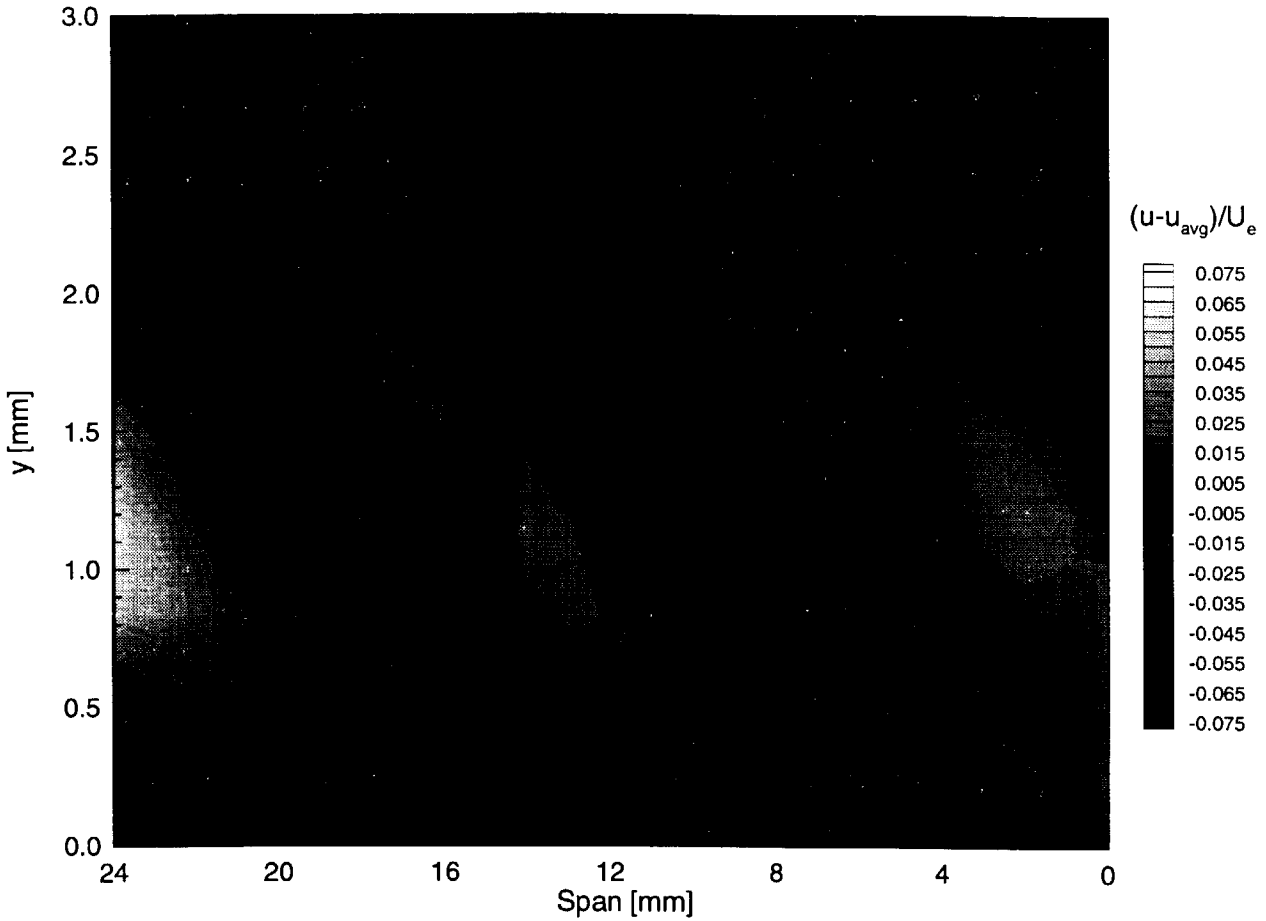

Figure 7.188. Disturbance contours for boundary-layer scans at $x/c = 0.35$. A 10-element array of 117 μm roughness with a spacing of 12 mm is at $x/c = 0.005$. $Re_c = 3.2 \times 10^6$. Data set A.

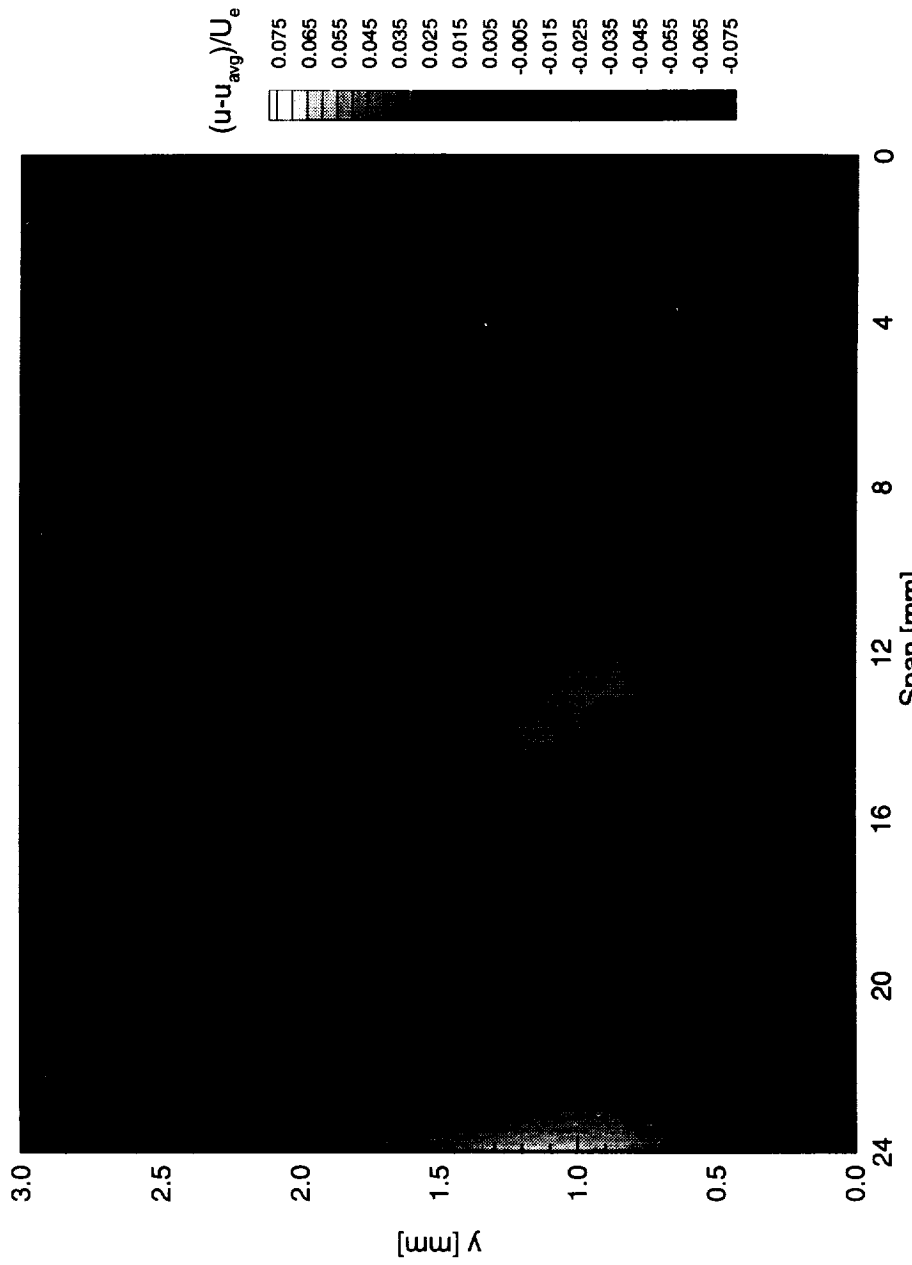

Figure 7.189. Disturbance contours for boundary-layer scans at $x/c = 0.40$. A 10-element array of 117 μm roughness with a spacing of 12 mm is at $x/c = 0.005$. $Re_c = 3.2 \times 10^6$. Data set A.

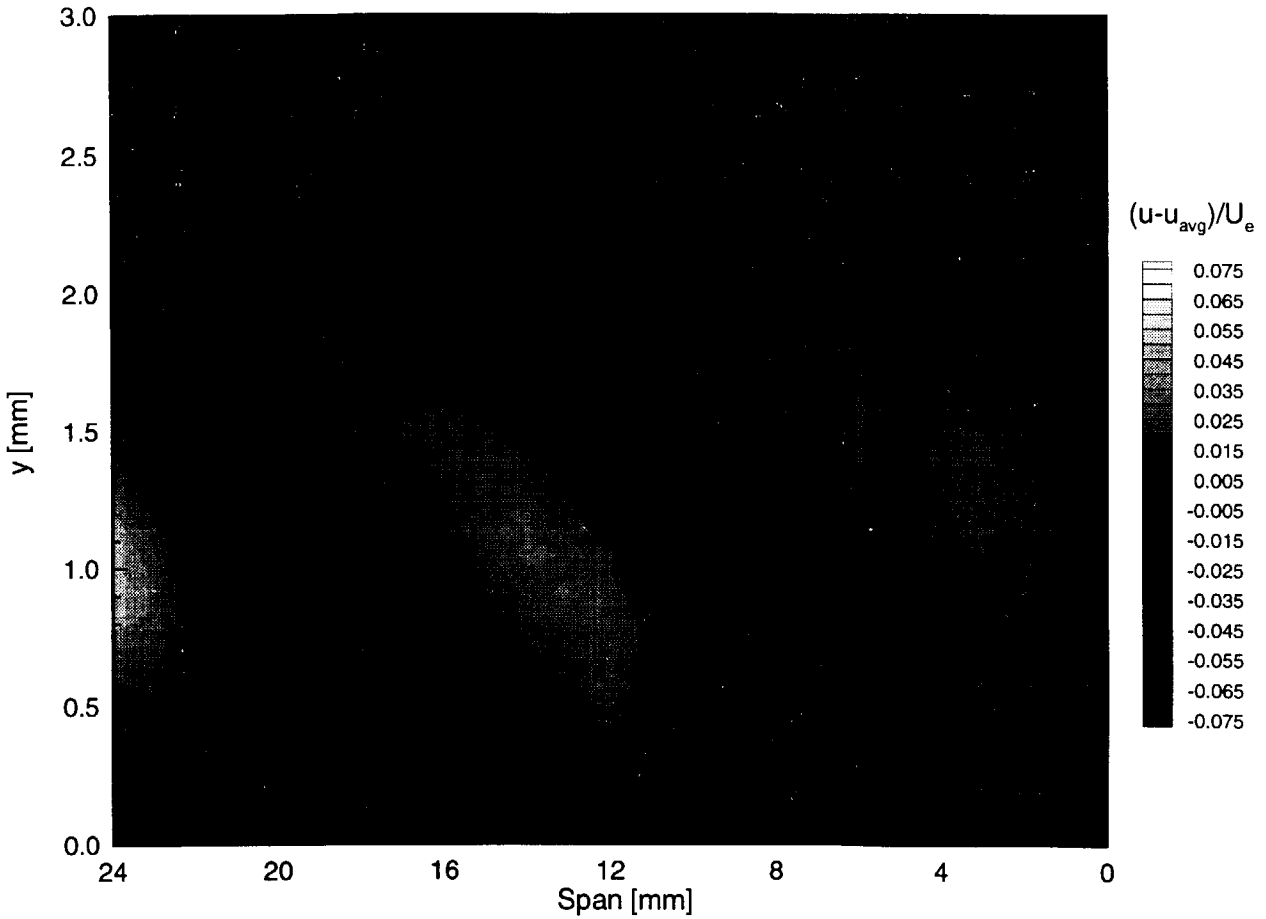

Figure 7.190. Disturbance contours for boundary-layer scans at $x/c = 0.45$. A 10-element array of 117 μm roughness with a spacing of 12 mm is at $x/c = 0.005$. $Re_c = 3.2 \times 10^6$. Data set A.

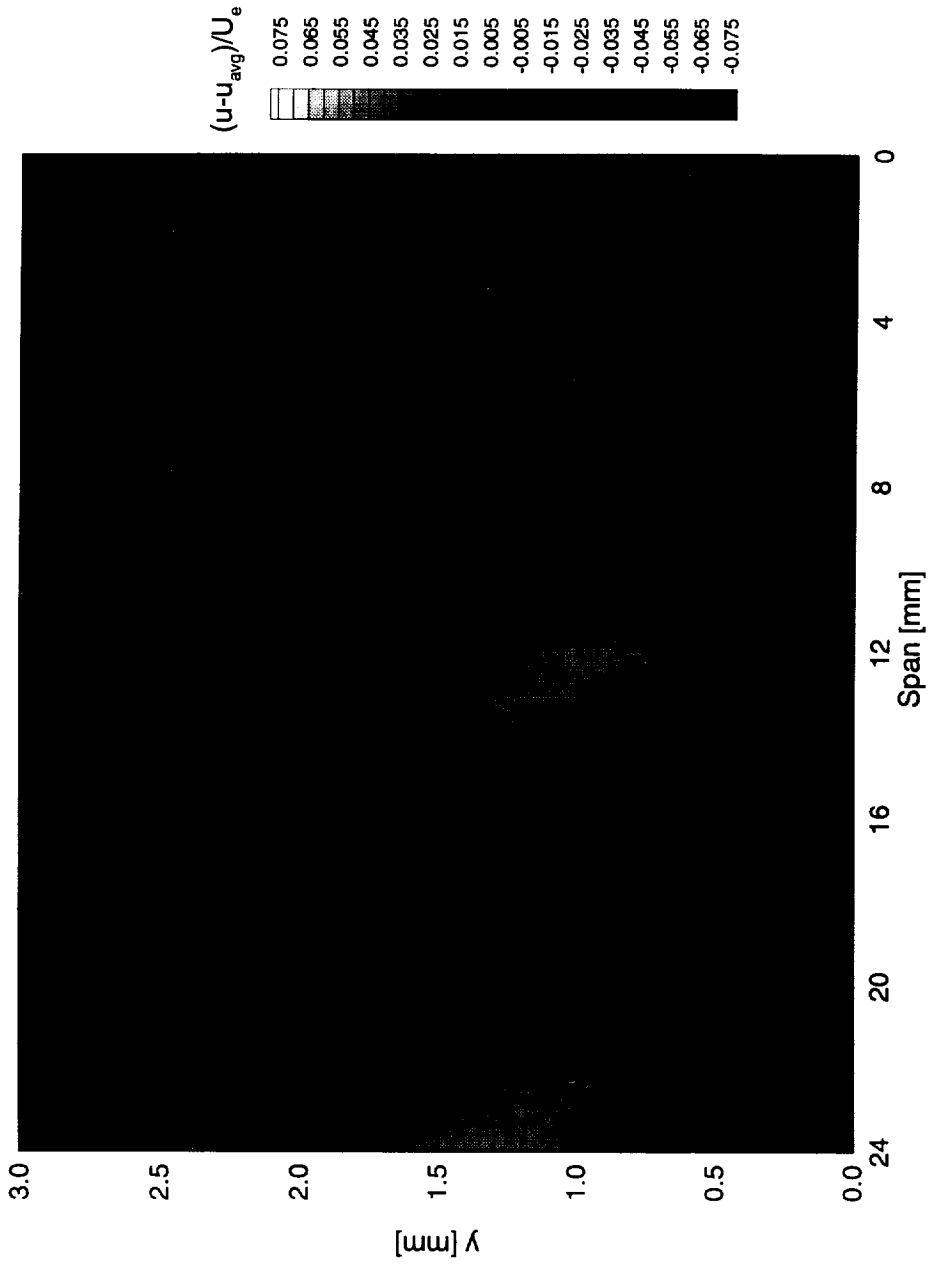

Figure 7.191. Disturbance contours for boundary-layer scans at $x/c = 0.50$. A 10-element array of 117 μm roughness with a spacing of 12 mm is at $x/c = 0.005$. $Re_c = 3.2 \times 10^6$. Data set A.

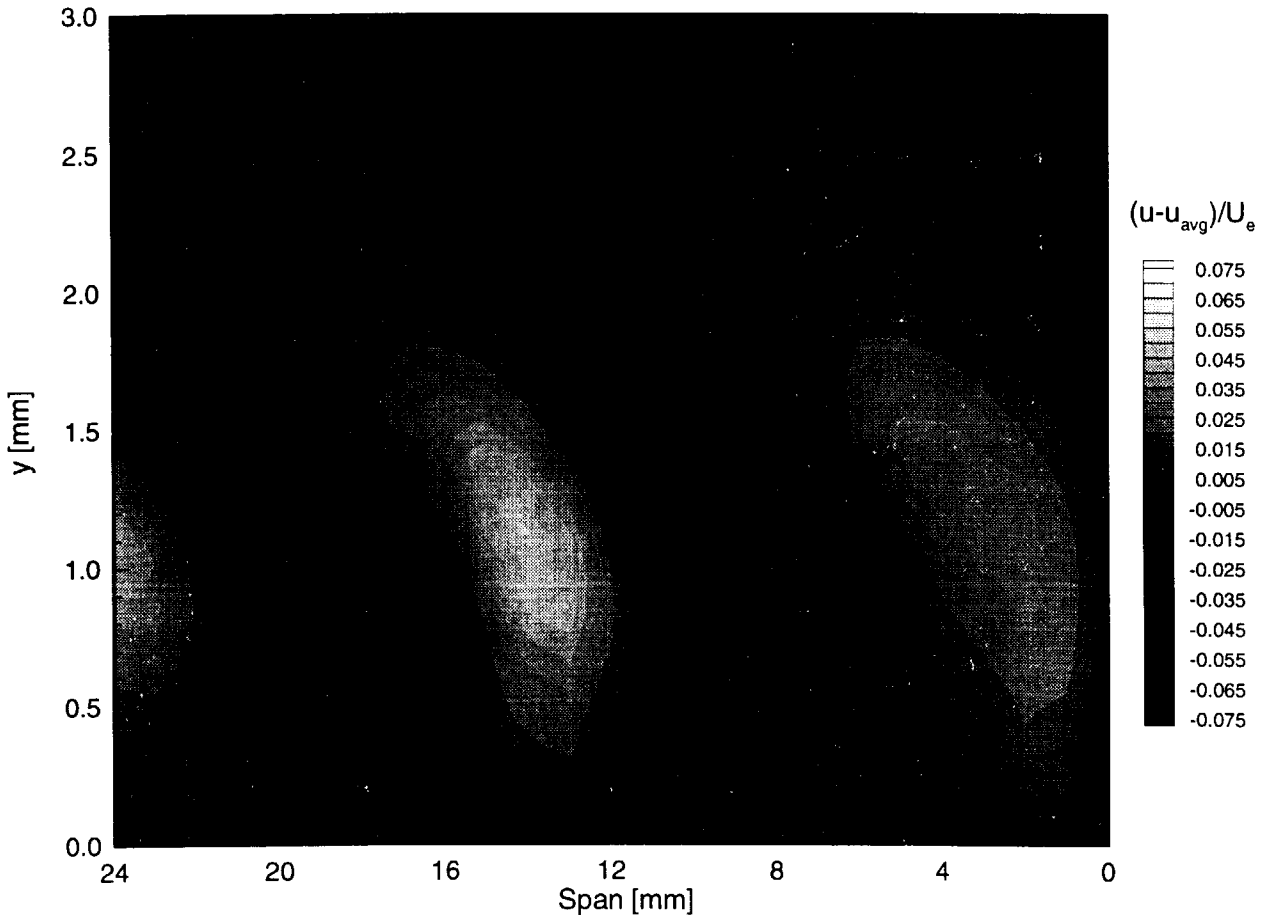

Figure 7.192. Disturbance contours for boundary-layer scans at $x/c = 0.55$. A 10-element array of 117 μm roughness with a spacing of 12 mm is at $x/c = 0.005$. $Re_c = 3.2 \times 10^6$. Data set A.

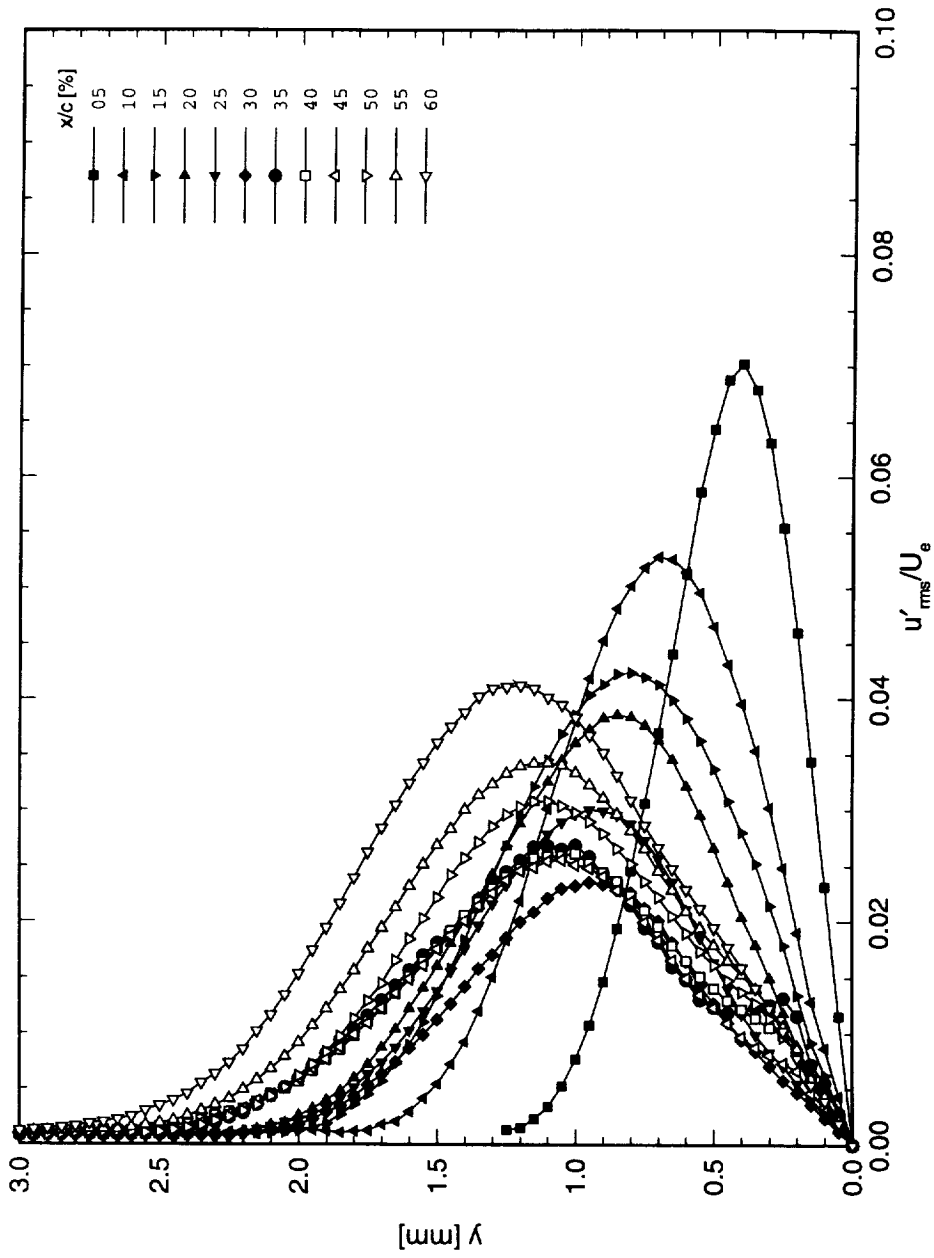

Figure 7.193. Stationary crossflow mode shapes for data set A, using rms method. $Re_c = 3.2 \times 10^6$, $\alpha = 0°$.

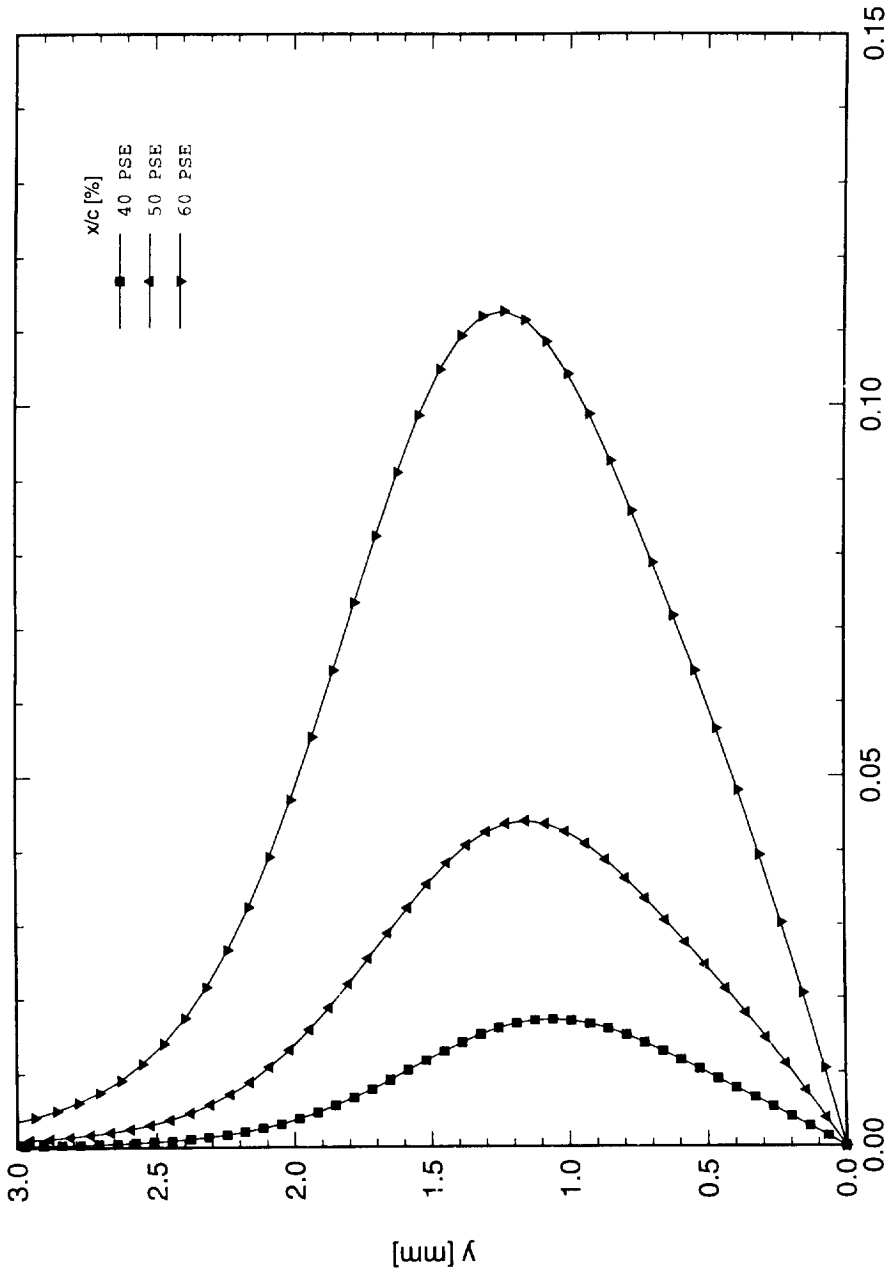

Figure 7.194. Theoretical stationary crossflow mode shapes computed with linear PSE (Arnal, et al., 1994).
$Re_c = 3.2 \times 10^6, \alpha = -1^\circ$.

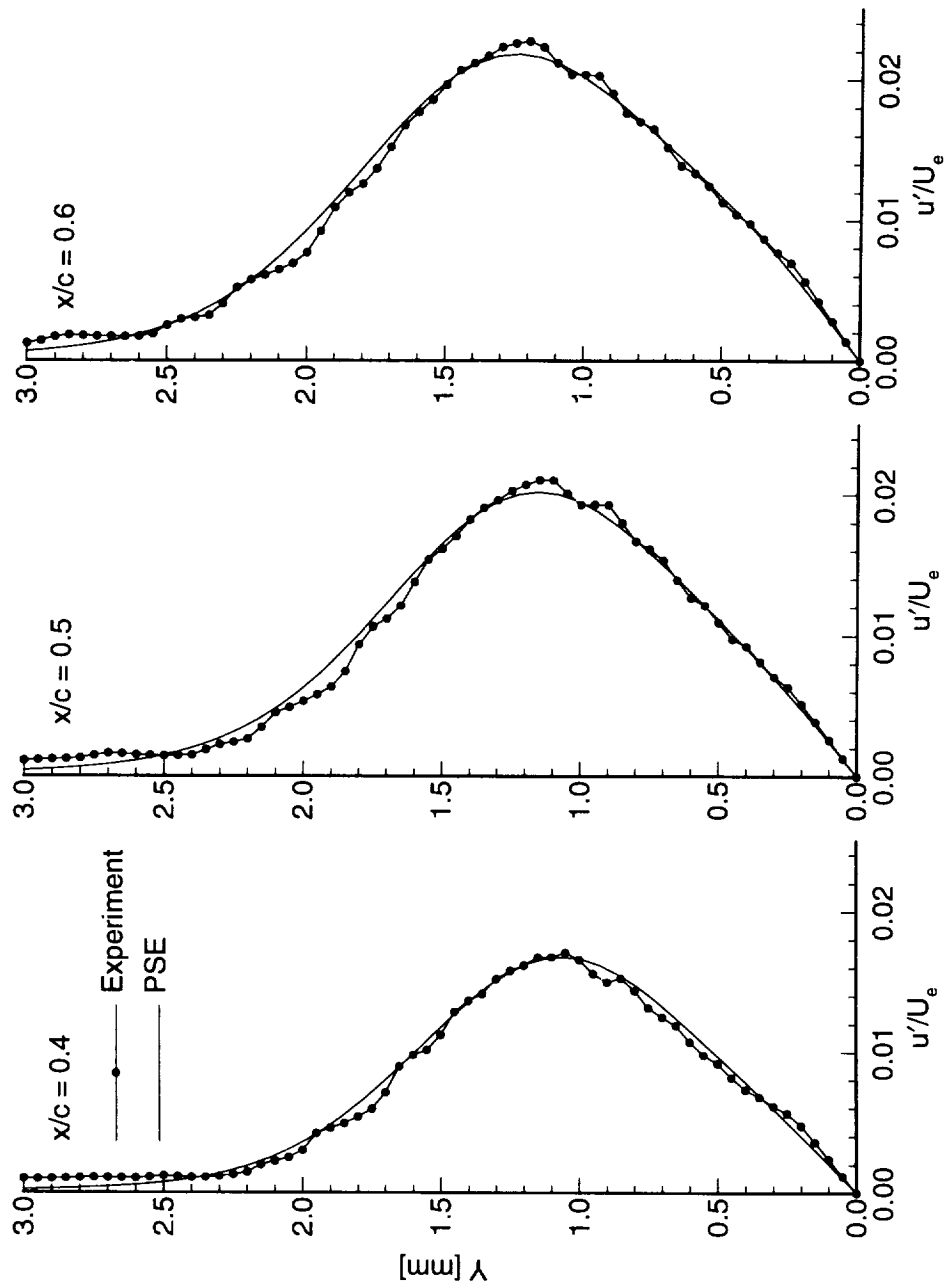

Figure 7.195. Comparison of measured and theoretical stationary-crossflow mode shapes. $Re_c = 3.0 \times 10^6$. Spanwise array of 146 μm roughnes at $x/c = 0.005$, 12 mm spacing. Data set D.

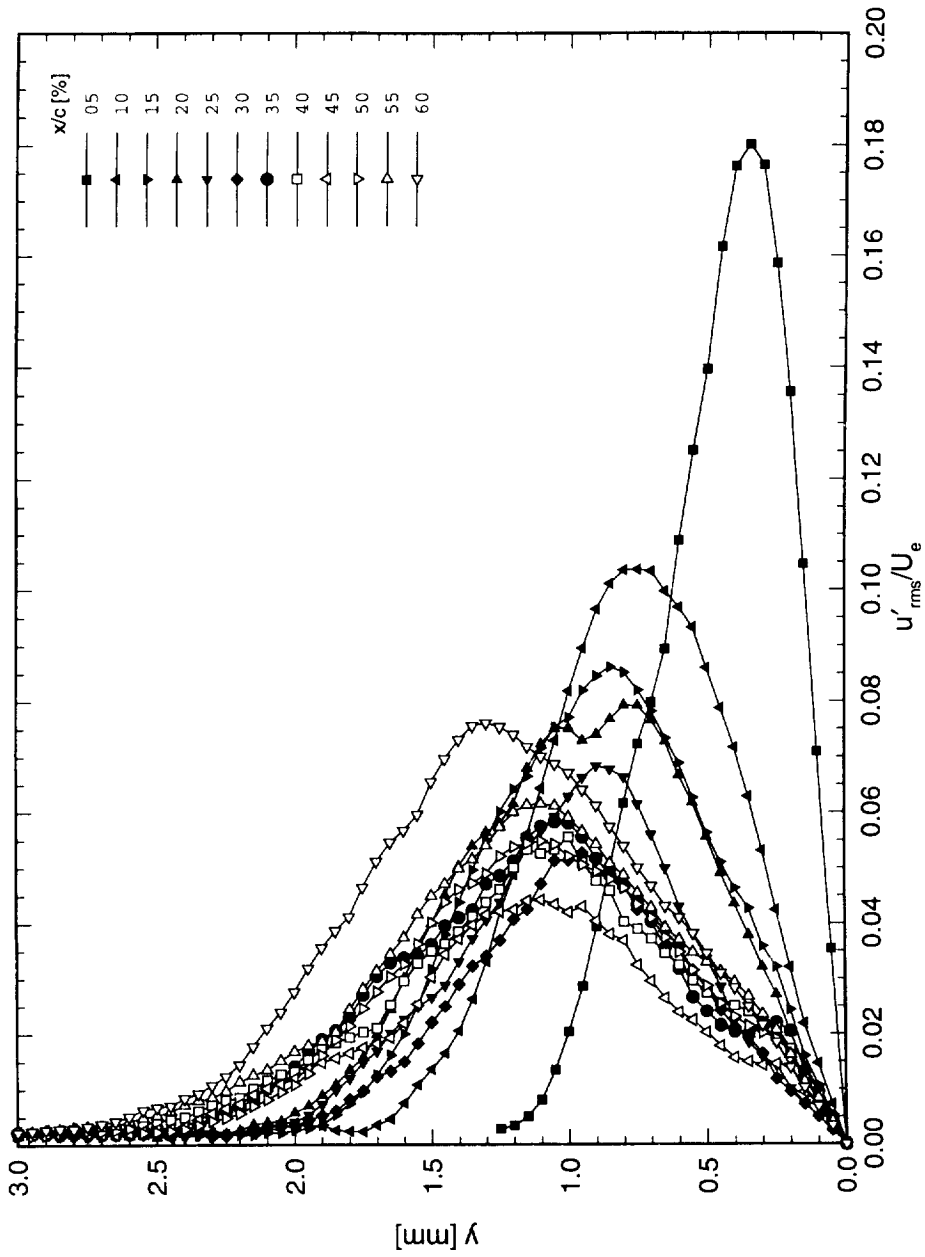

Figure 7.196. Stationary crossflow mode shapes for data set A, using max method. $Re_c = 3.2 \times 10^6$, $\alpha = 0°$.

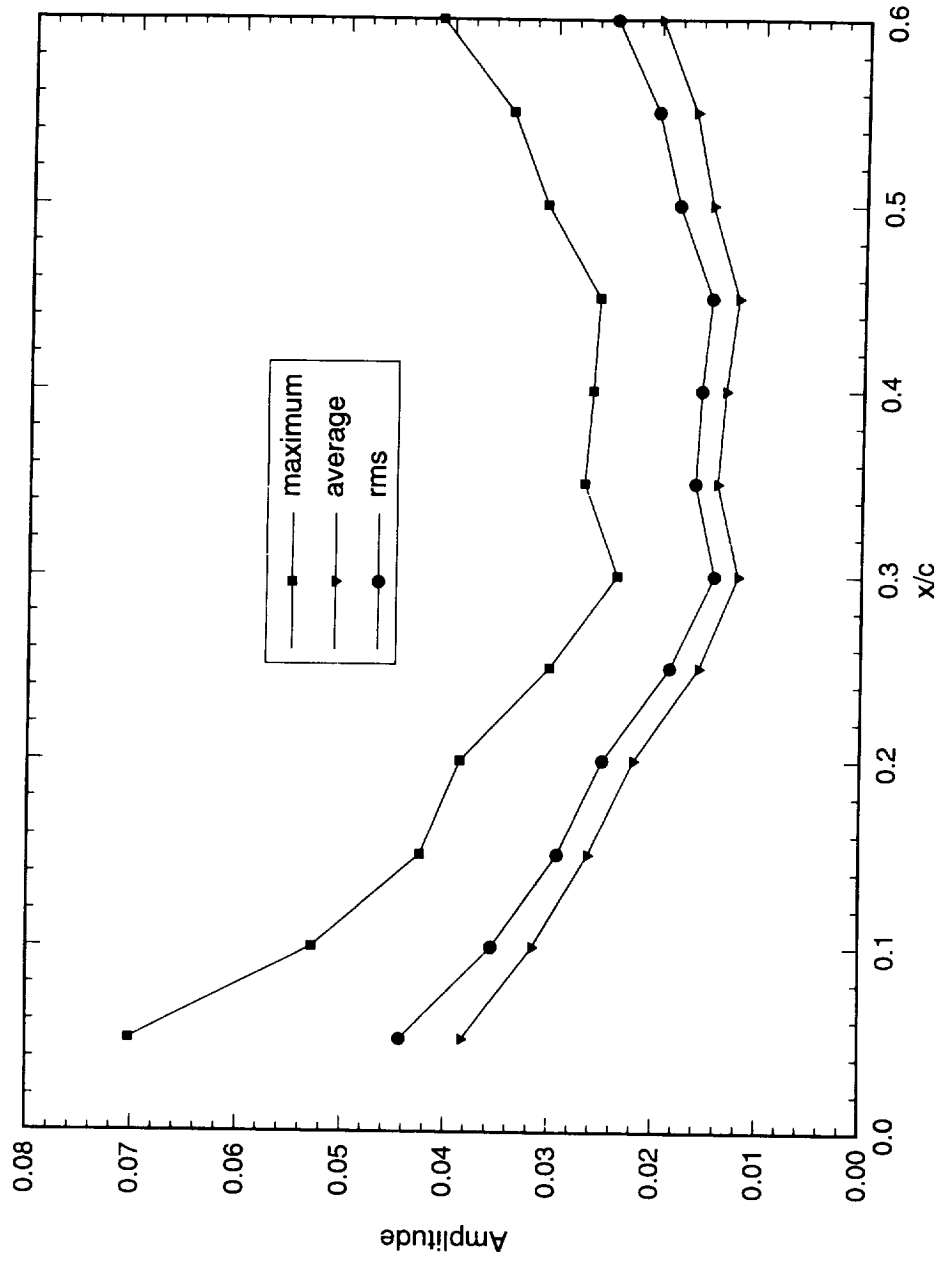

Figure 7.197. Stationary crossflow amplitudes for data set A.

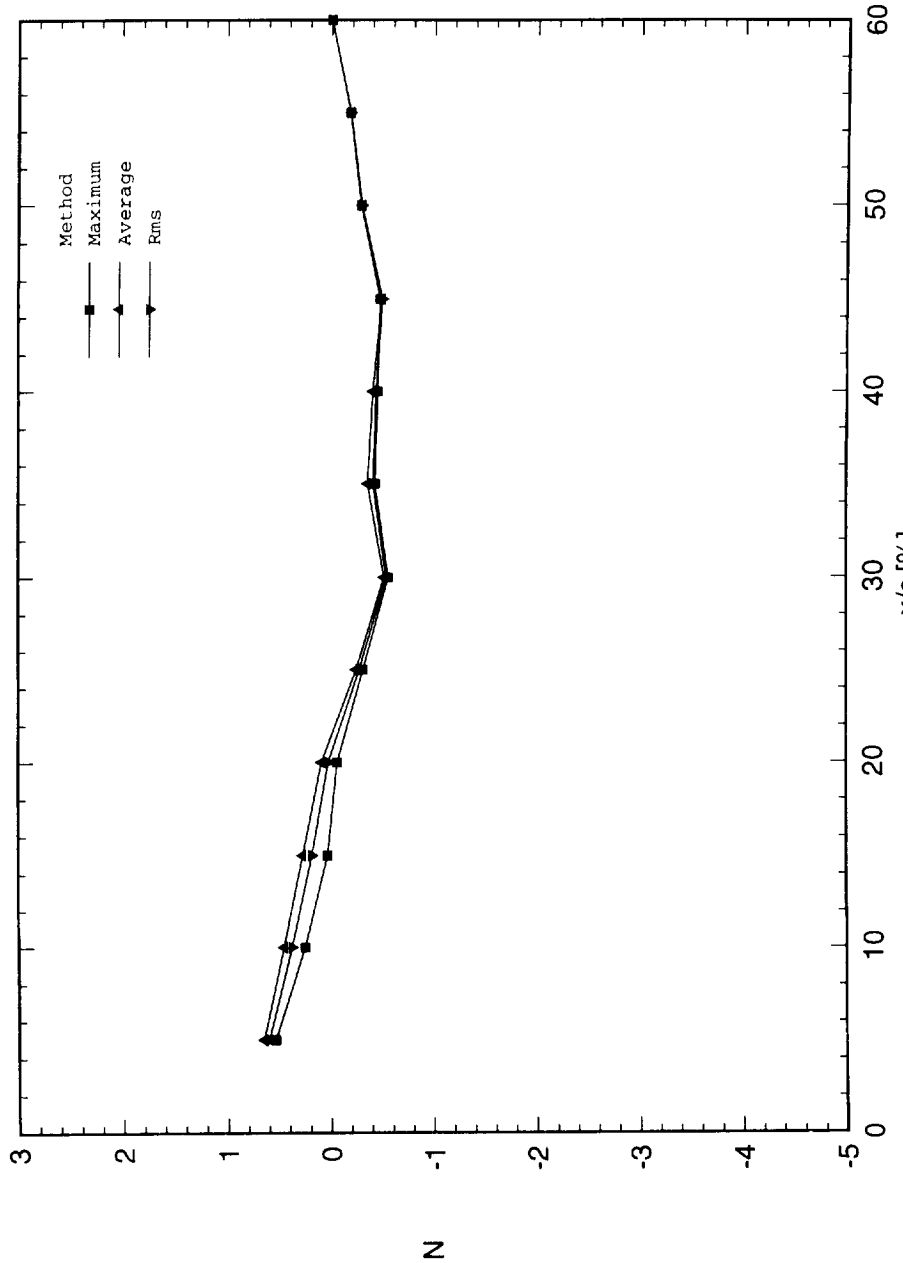

Figure 7.198. Stationary crossflow relative N-factors for data set A.

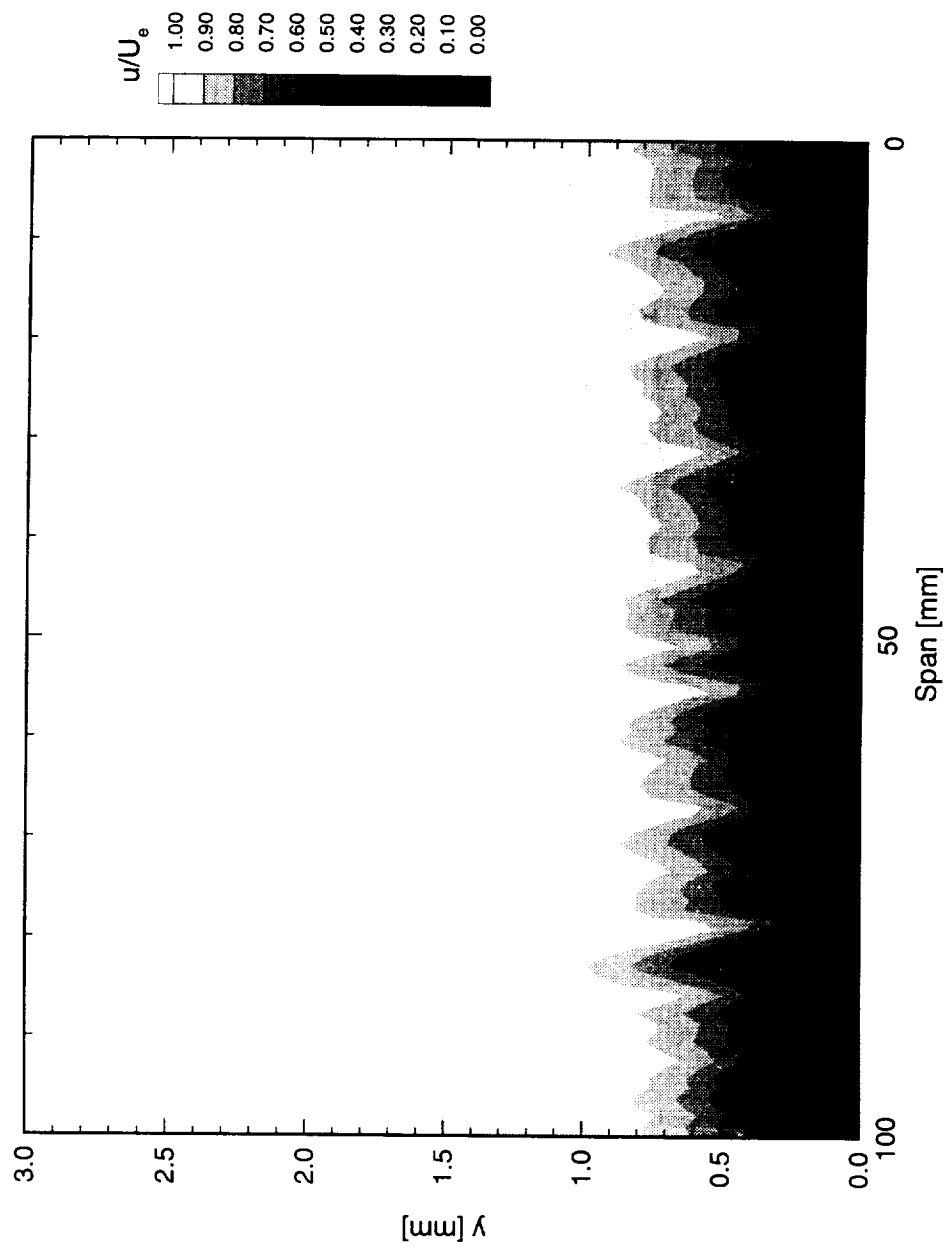

Figure 7.199. Velocity contours for boundary-layer scans at $x/c = 0.05$. A full array of 117 μm roughness with a spacing of 12 mm is at $x/c = 0.005$. $Re_c = 3.0 \times 10^6$. Data set B.

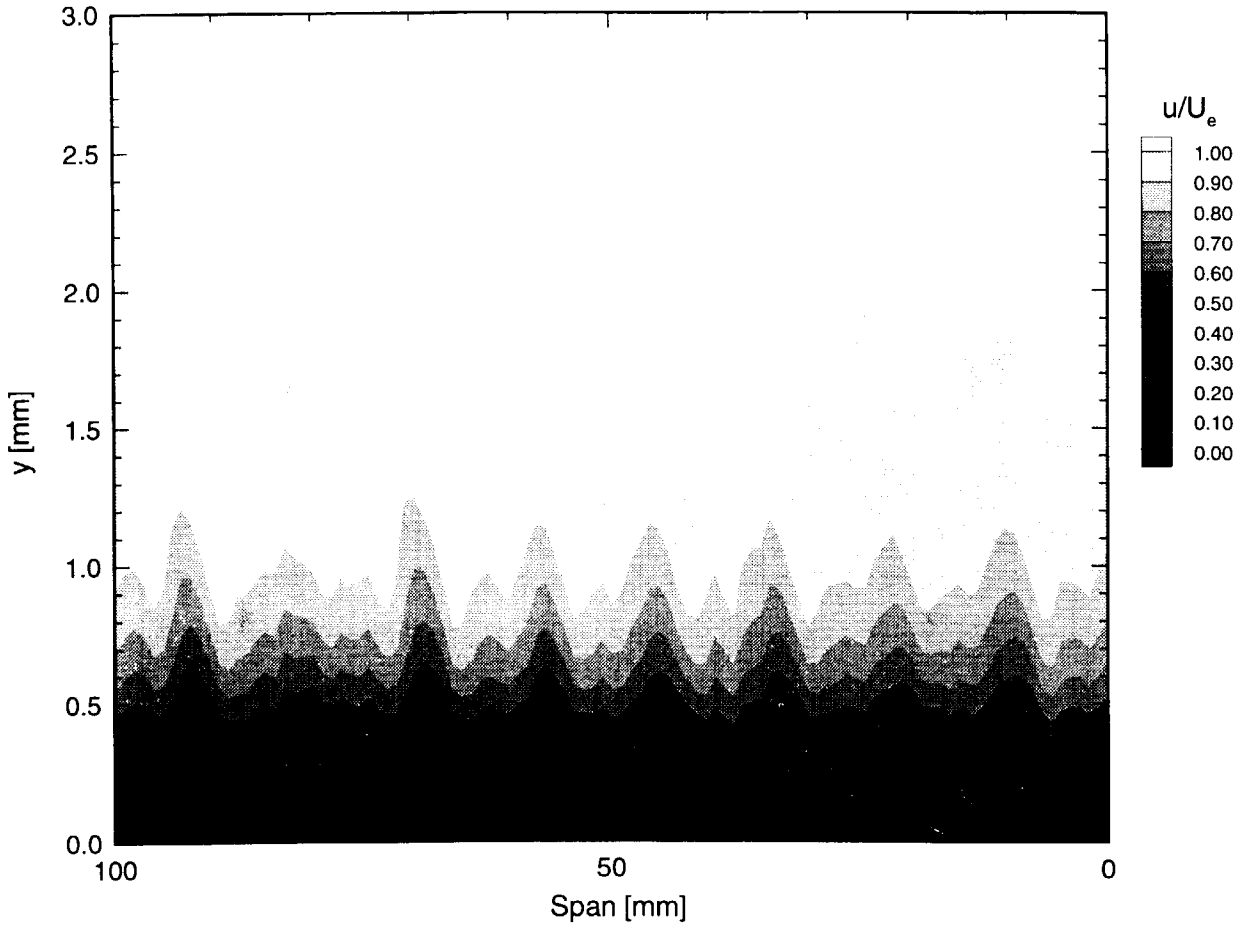

Figure 7.200. Velocity contours for boundary-layer scans at $x/c = 0.10$. A full array of 117 μm roughness with a spacing of 12 mm is at $x/c = 0.005$. $Re_c = 3.0 \times 10^6$. Data set B.

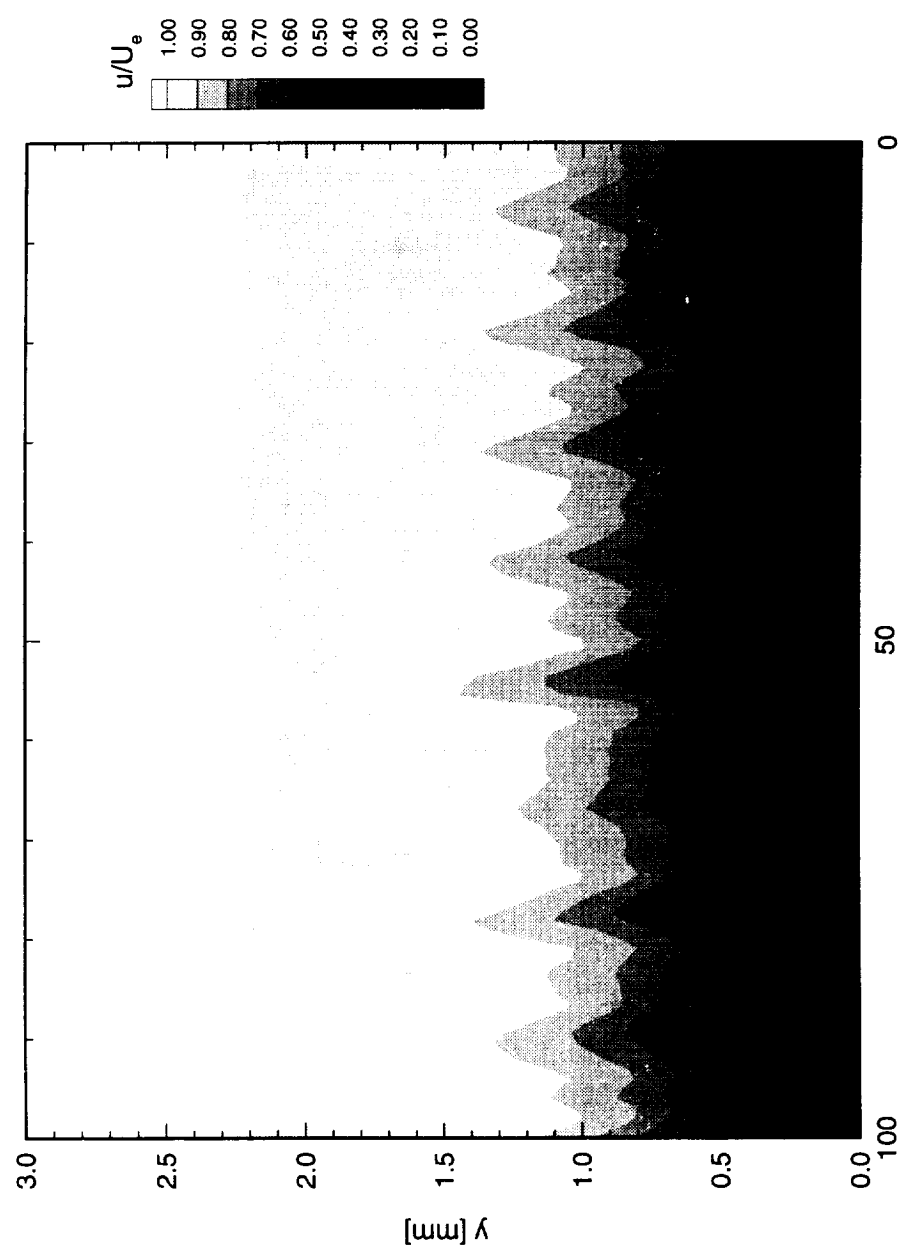

Figure 7.201. Velocity contours for boundary-layer scans at $x/c = 0.15$. A full array of 117 μm roughness with a spacing of 12 mm is at $x/c = 0.005$. $Re_c = 3.0 \times 10^6$. Data set B.

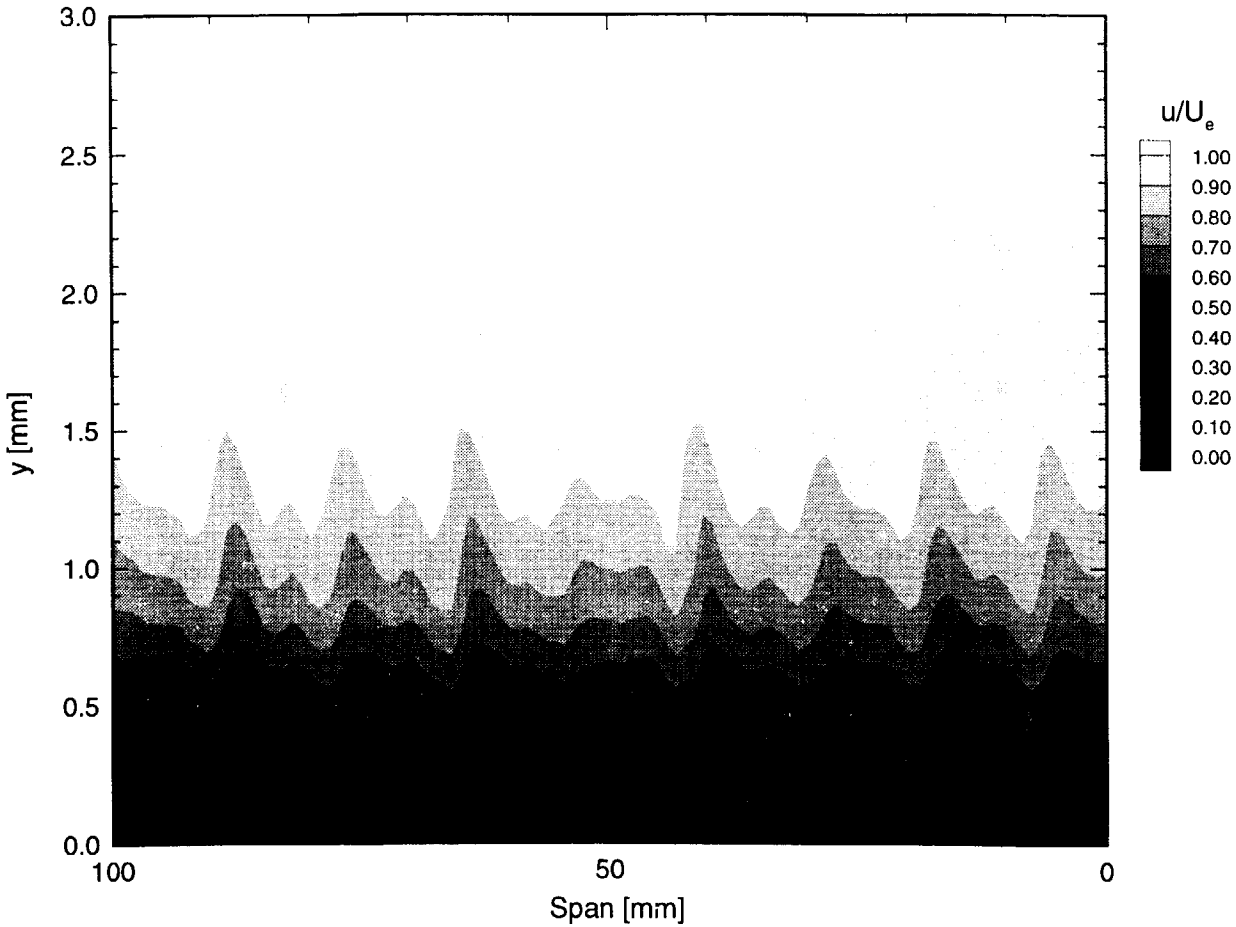

Figure 7.202. Velocity contours for boundary-layer scans at $x/c = 0.20$. A full array of 117 μm roughness with a spacing of 12 mm is at $x/c = 0.005$. $Re_c = 3.0 \times 10^6$. Data set B.

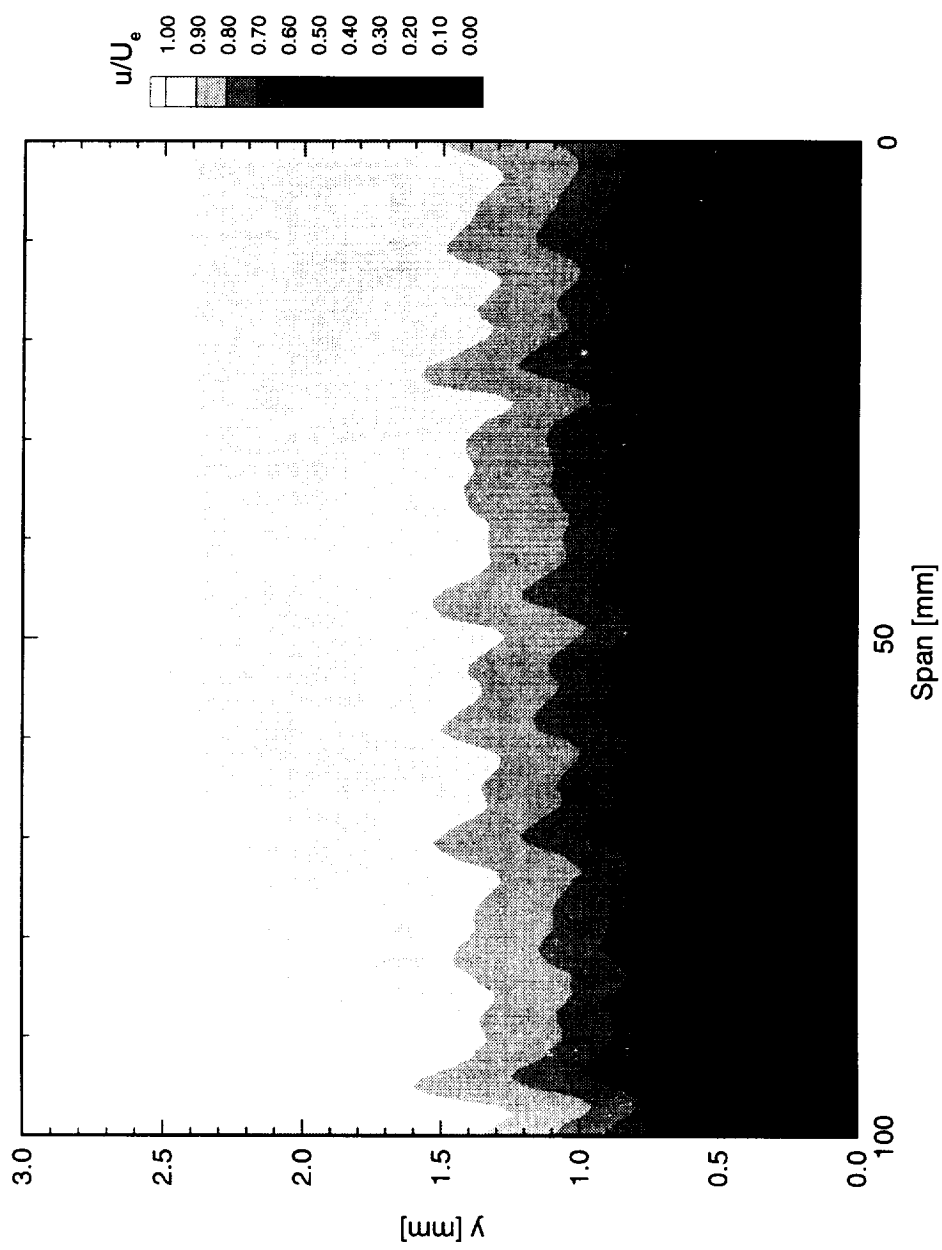

Figure 7.203. Velocity contours for boundary-layer scans at $x/c = 0.25$. A full array of 117 μm roughness with a spacing of 12 mm is at $x/c = 0.005$. $Re_c = 3.0 \times 10^6$. Data set B.

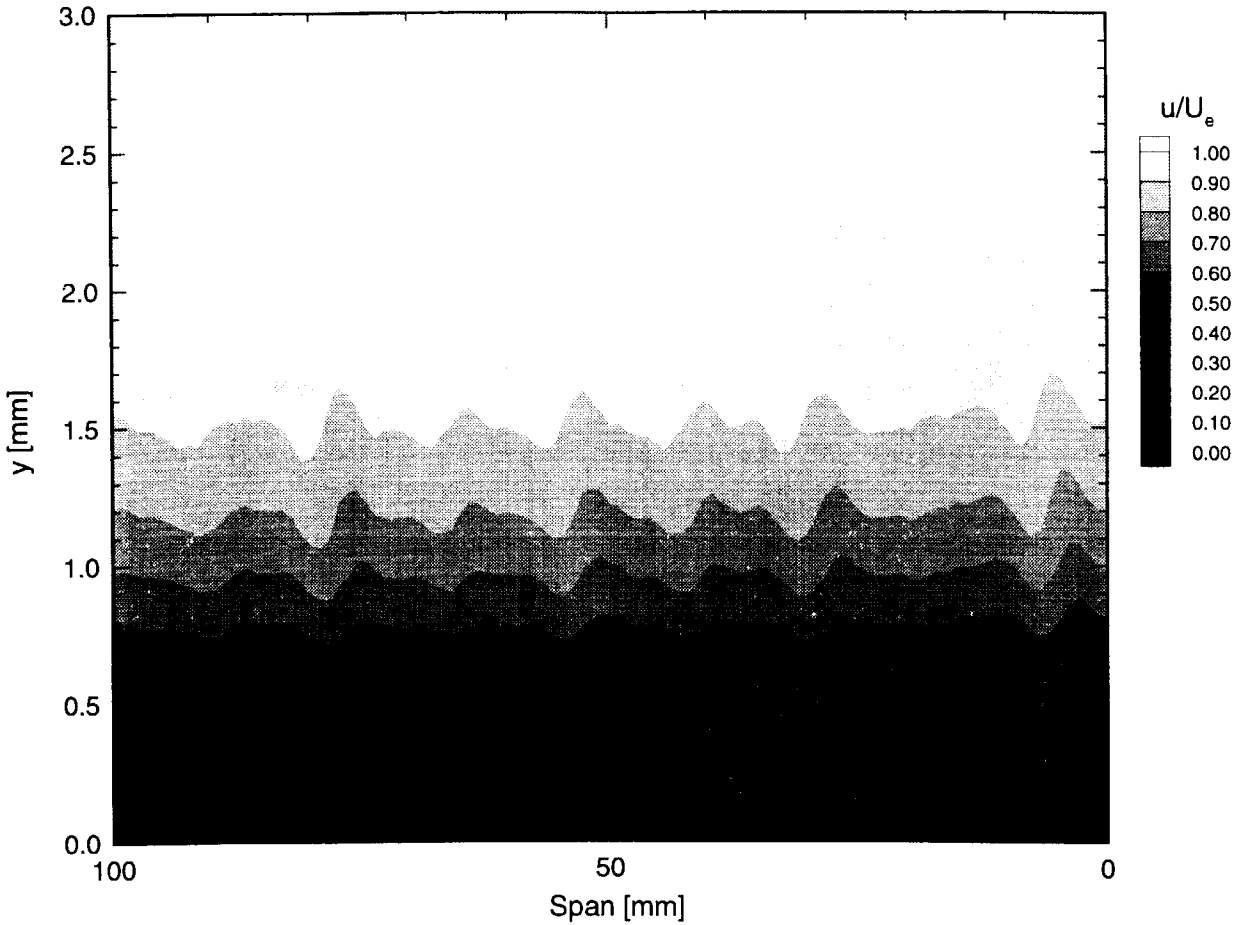

Figure 7.204. Velocity contours for boundary-layer scans at $x/c = 0.30$. A full array of 117 μm roughness with a spacing of 12 mm is at $x/c = 0.005$. $Re_c = 3.0 \times 10^6$. Data set B.

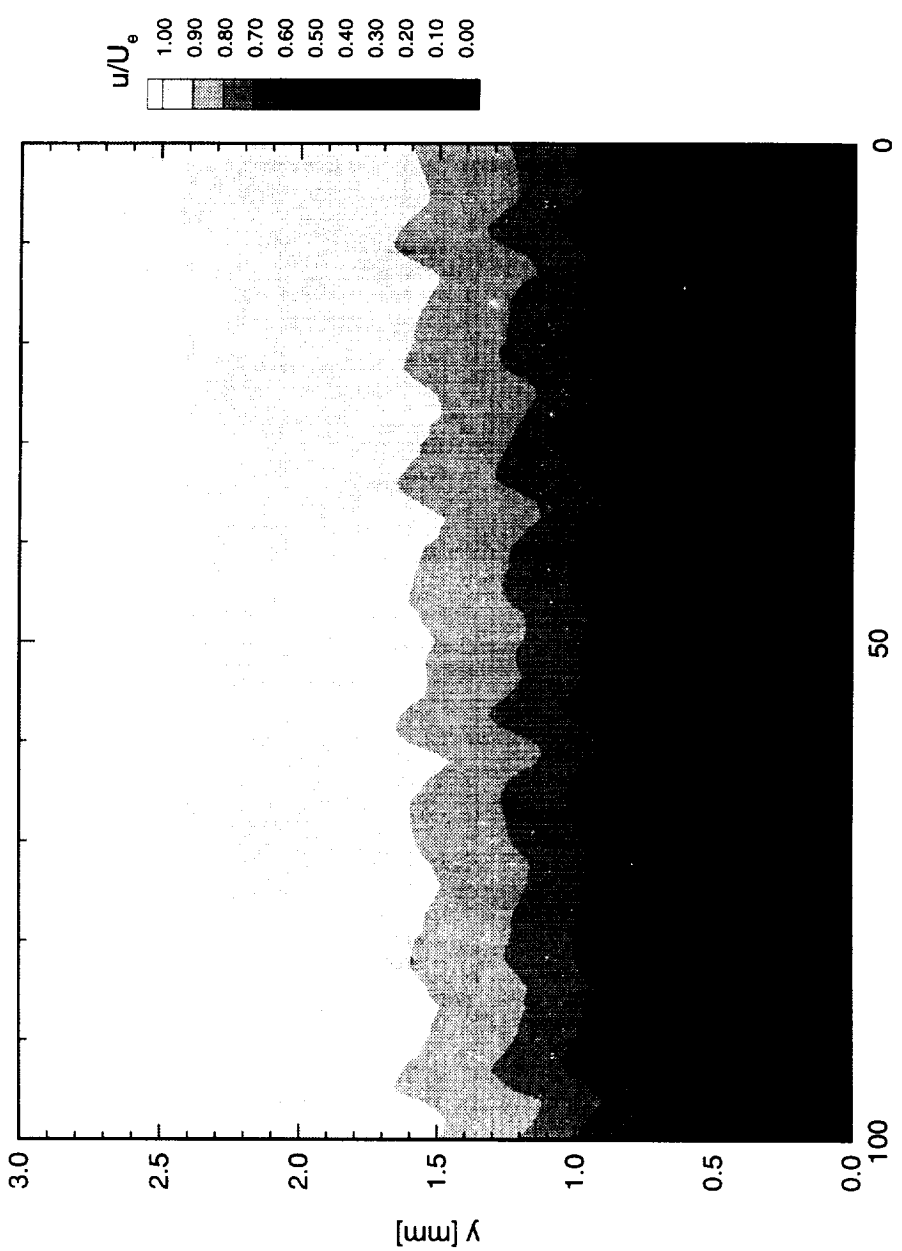

Figure 7.205. Velocity contours for boundary-layer scans at $x/c = 0.35$. A full array of 117 μm roughness with a spacing of 12 mm is at $x/c = 0.005$. $Re_c = 3.0 \times 10^6$. Data set B.

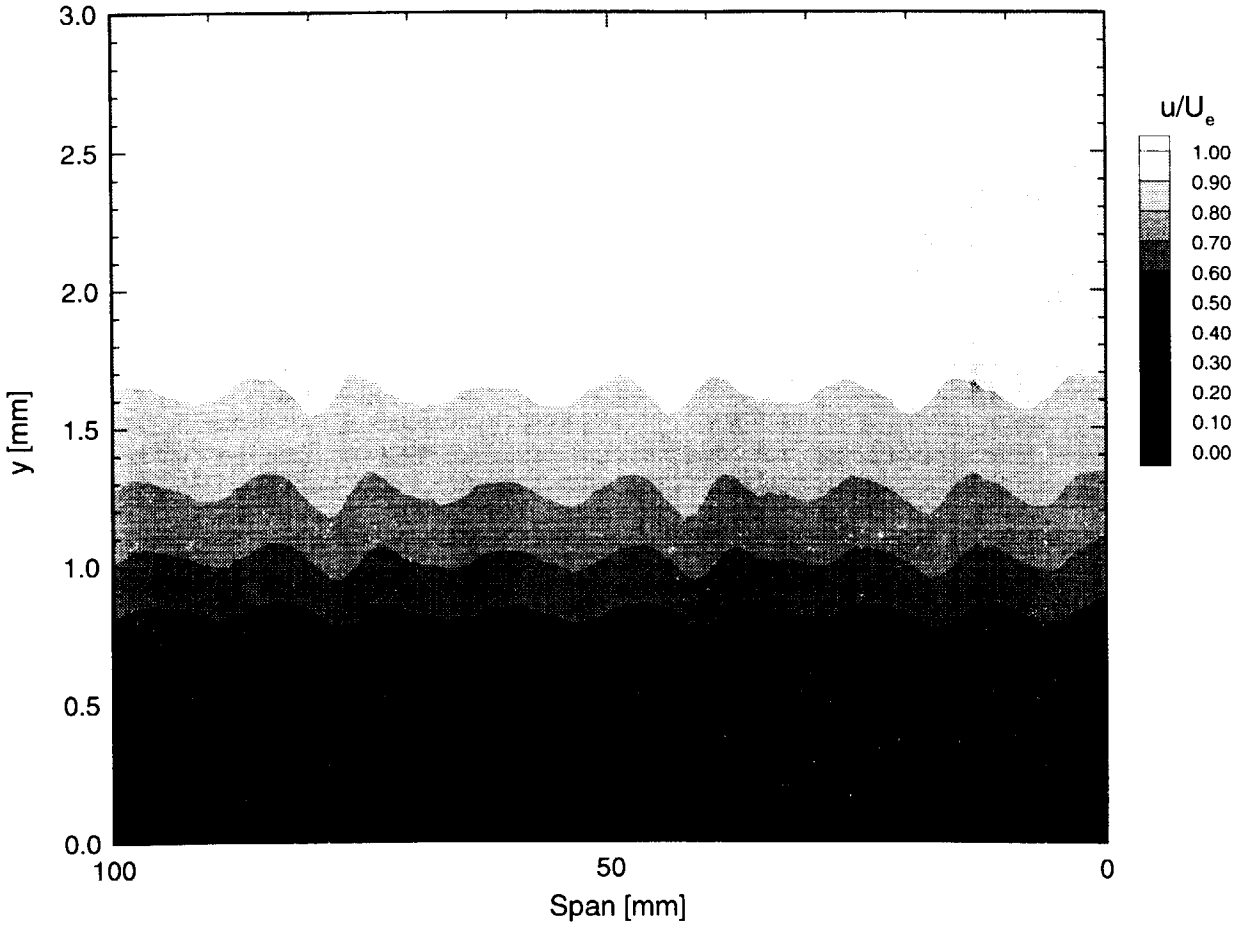

Figure 7.206. Velocity contours for boundary-layer scans at $x/c = 0.40$. A full array of 117 μm roughness with a spacing of 12 mm is at $x/c = 0.005$. $Re_c = 3.0 \times 10^6$. Data set B.

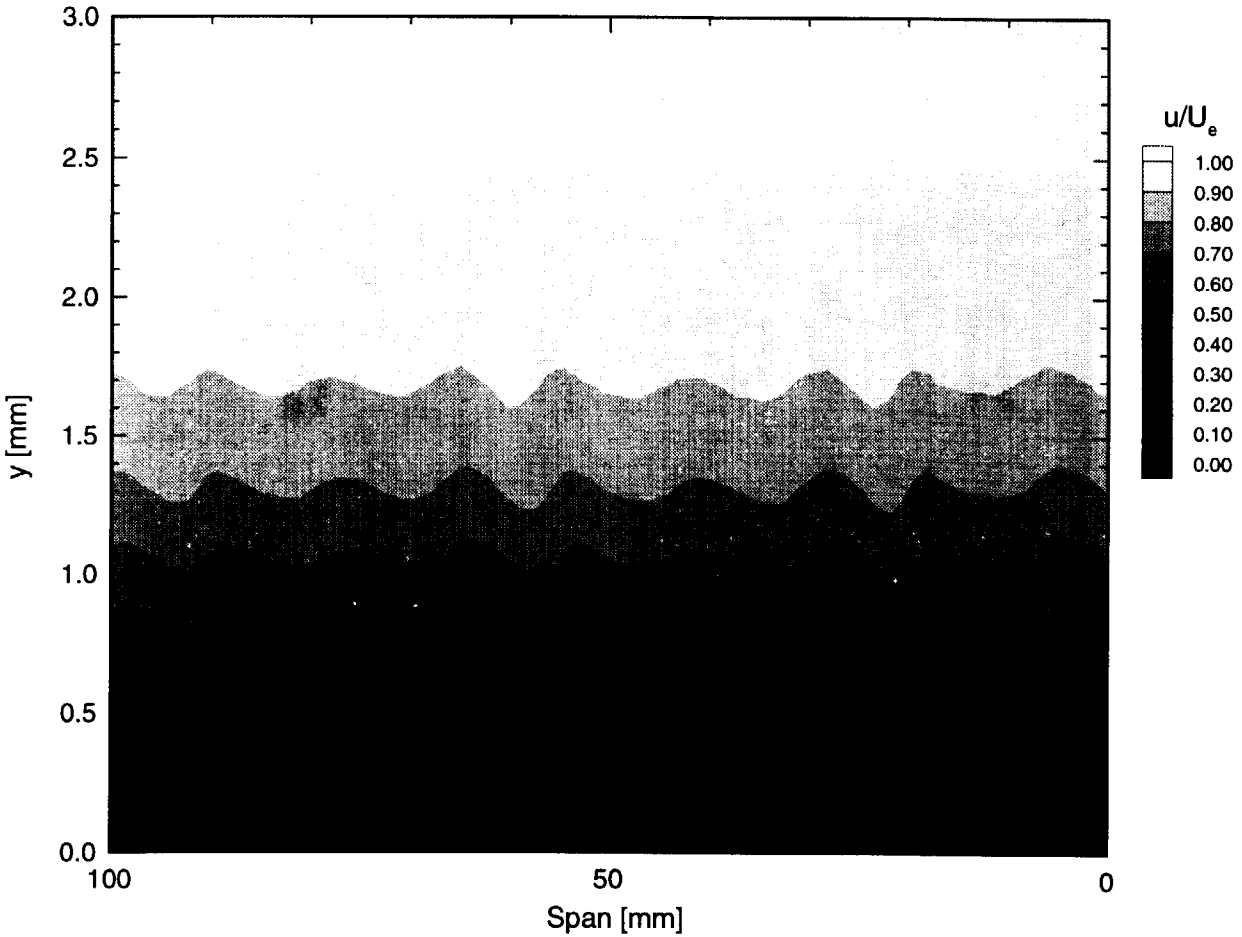

Figure 7.207. Velocity contours for boundary-layer scans at $x/c = 0.45$. A full array of 117 μm roughness with a spacing of 12 mm is at $x/c = 0.005$. $Re_c = 3.0 \times 10^6$. Data set B.

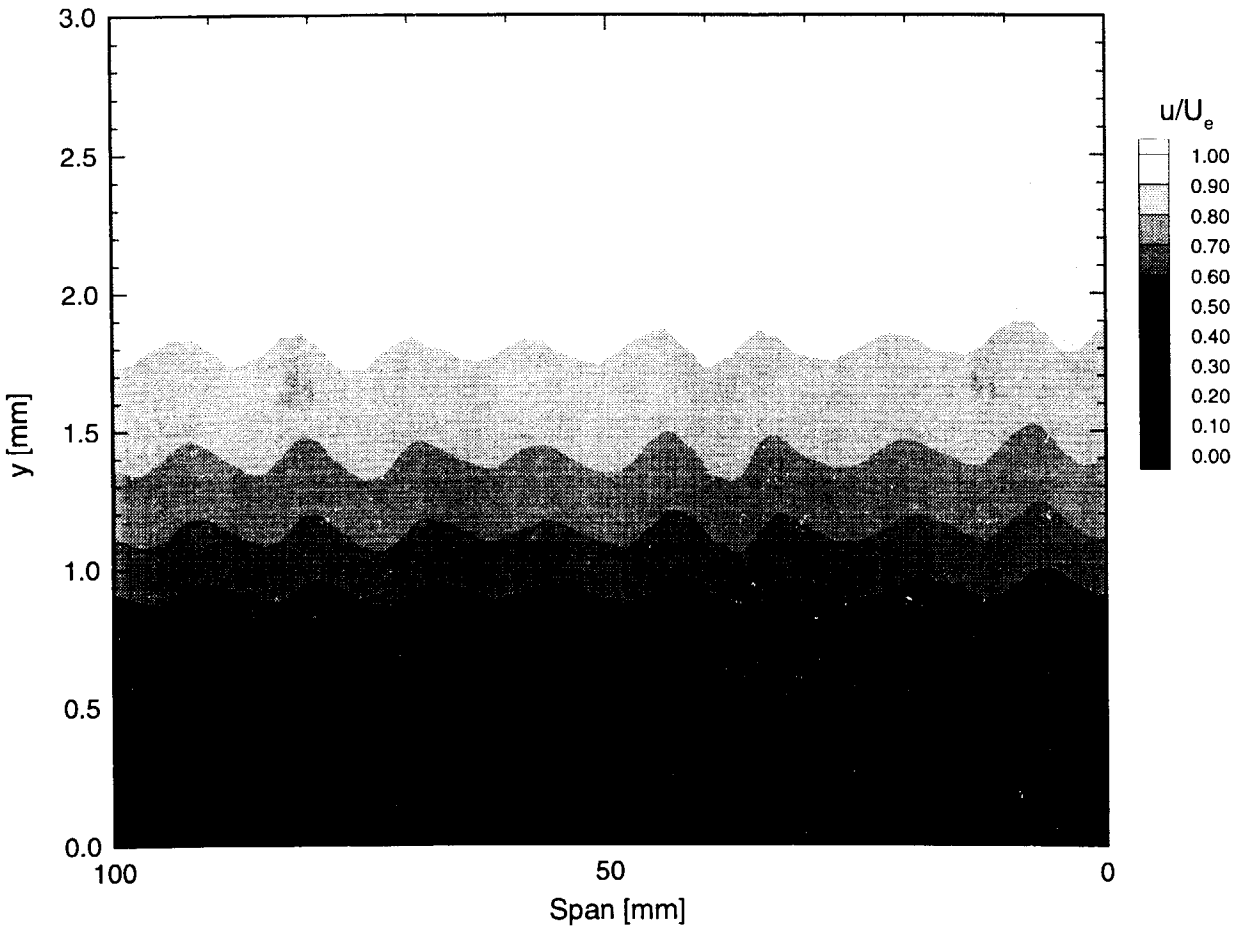

Figure 7.208. Velocity contours for boundary-layer scans at $x/c = 0.50$. A full array of 117 μm roughness with a spacing of 12 mm is at $x/c = 0.005$. $Re_c = 3.0 \times 10^6$. Data set B.

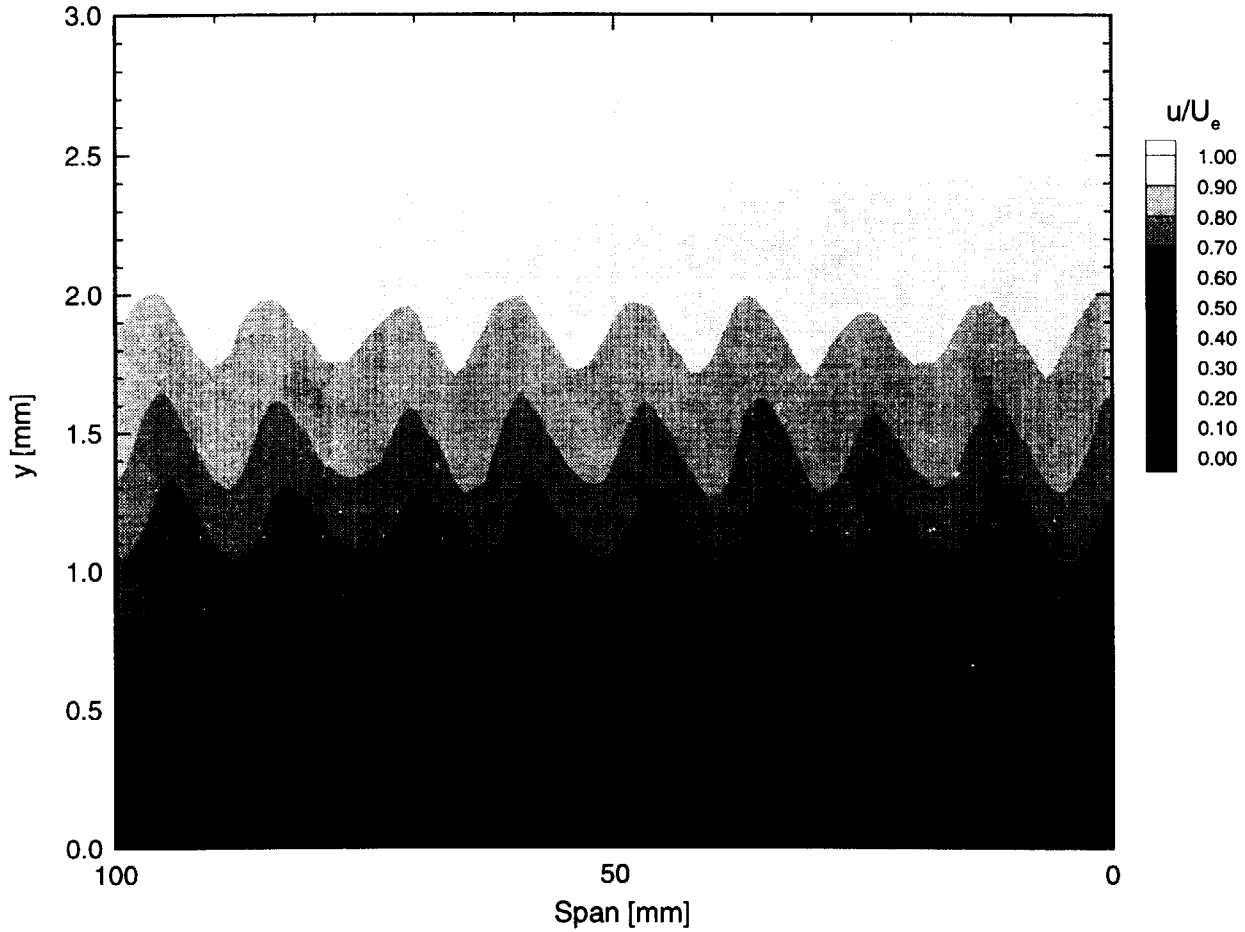

Figure 7.209. Velocity contours for boundary-layer scans at $x/c = 0.60$. A full array of 117 μm roughness with a spacing of 12 mm is at $x/c = 0.005$. $Re_c = 3.0 \times 10^6$. Data set B.

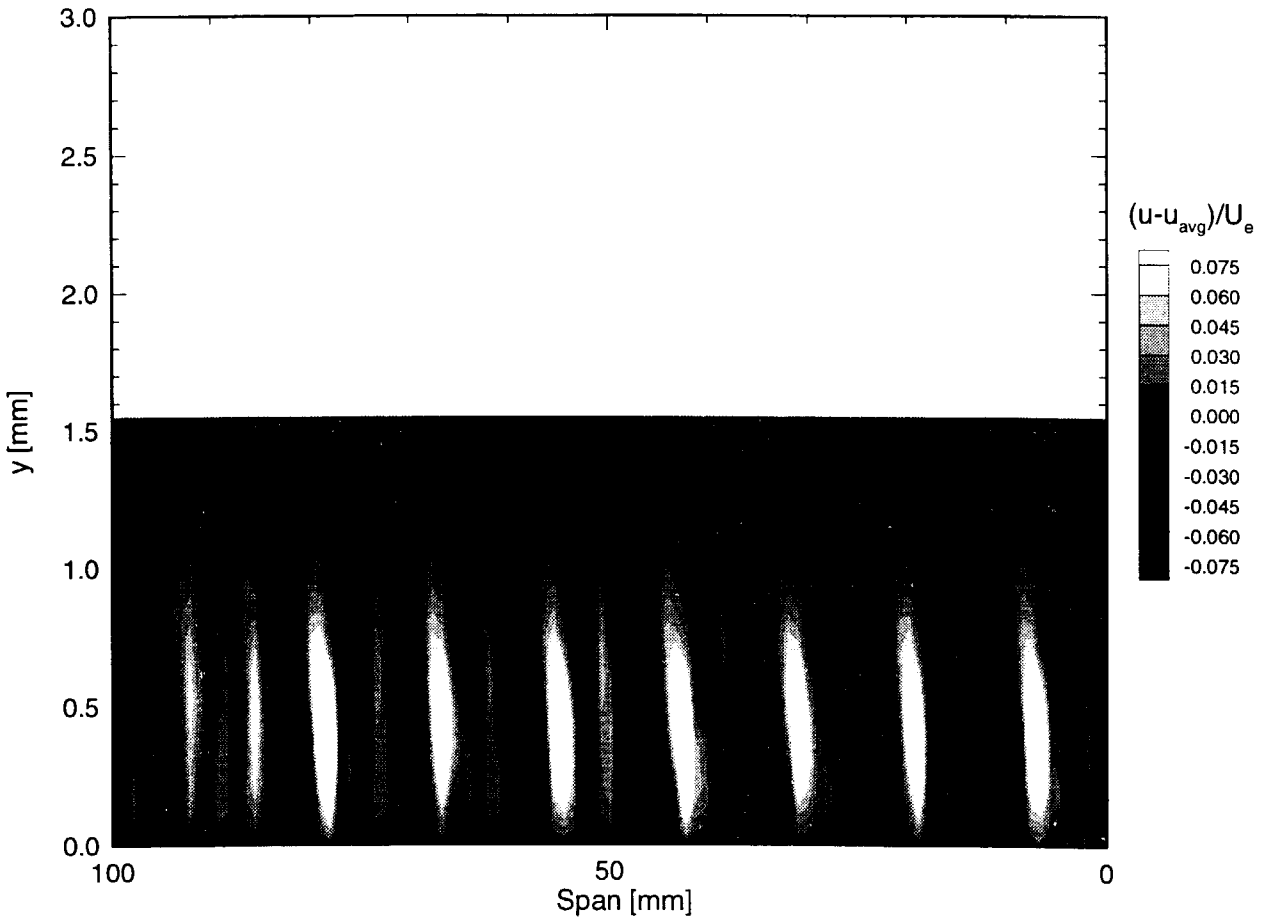

Figure 7.210. Disturbance contours for boundary-layer scans at $x/c = 0.05$. A full array of 117 μm roughness with a spacing of 12 mm is at $x/c = 0.005$. $Re_c = 3.0 \times 10^6$. Data set B.

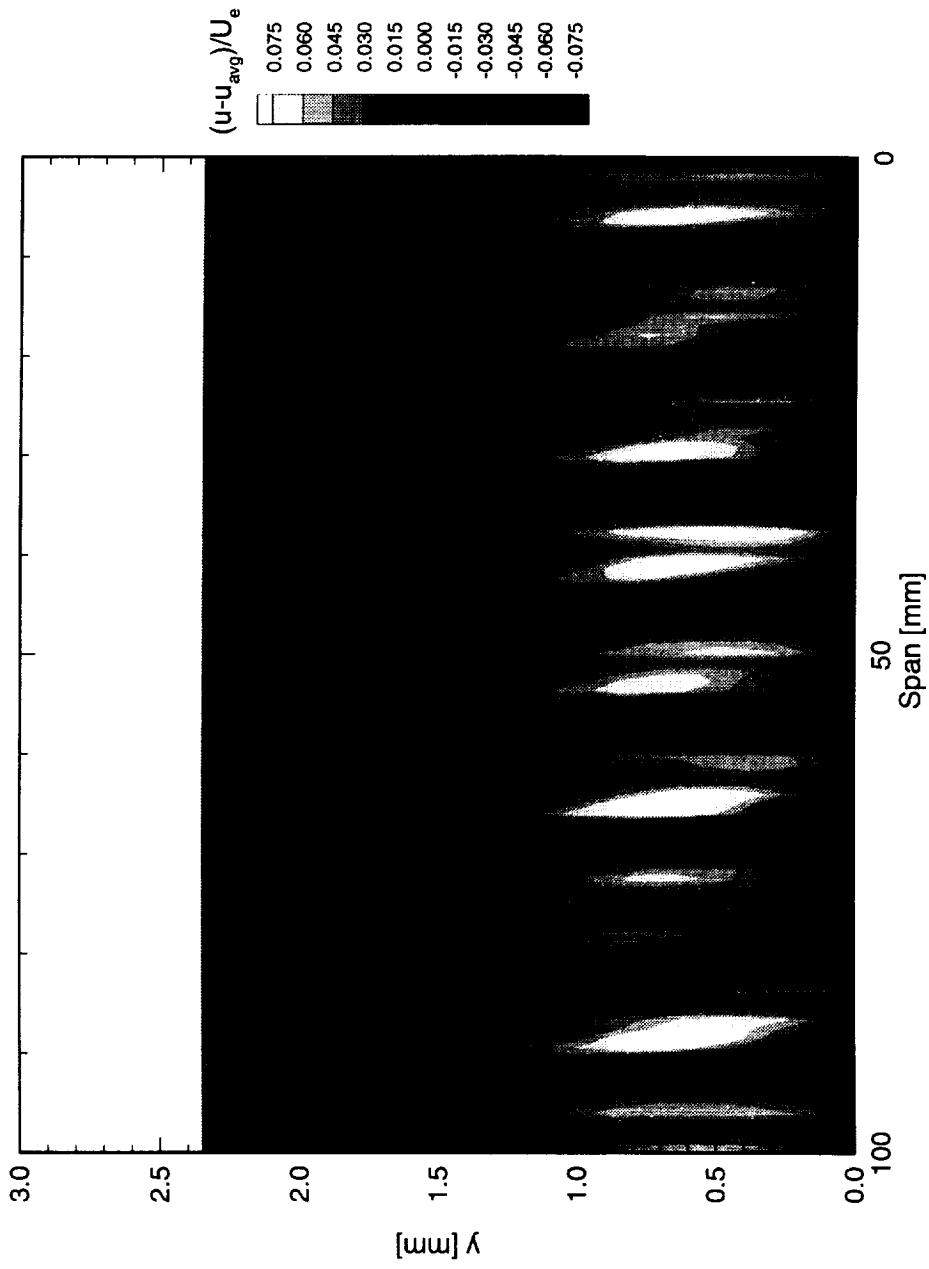

Figure 7.211. Disturbance contours for boundary-layer scans at $x/c = 0.10$. A full array of 117 μm roughness with a spacing of 12 mm is at $x/c = 0.005$. $Re_c = 3.0 \times 10^6$. Data set B.

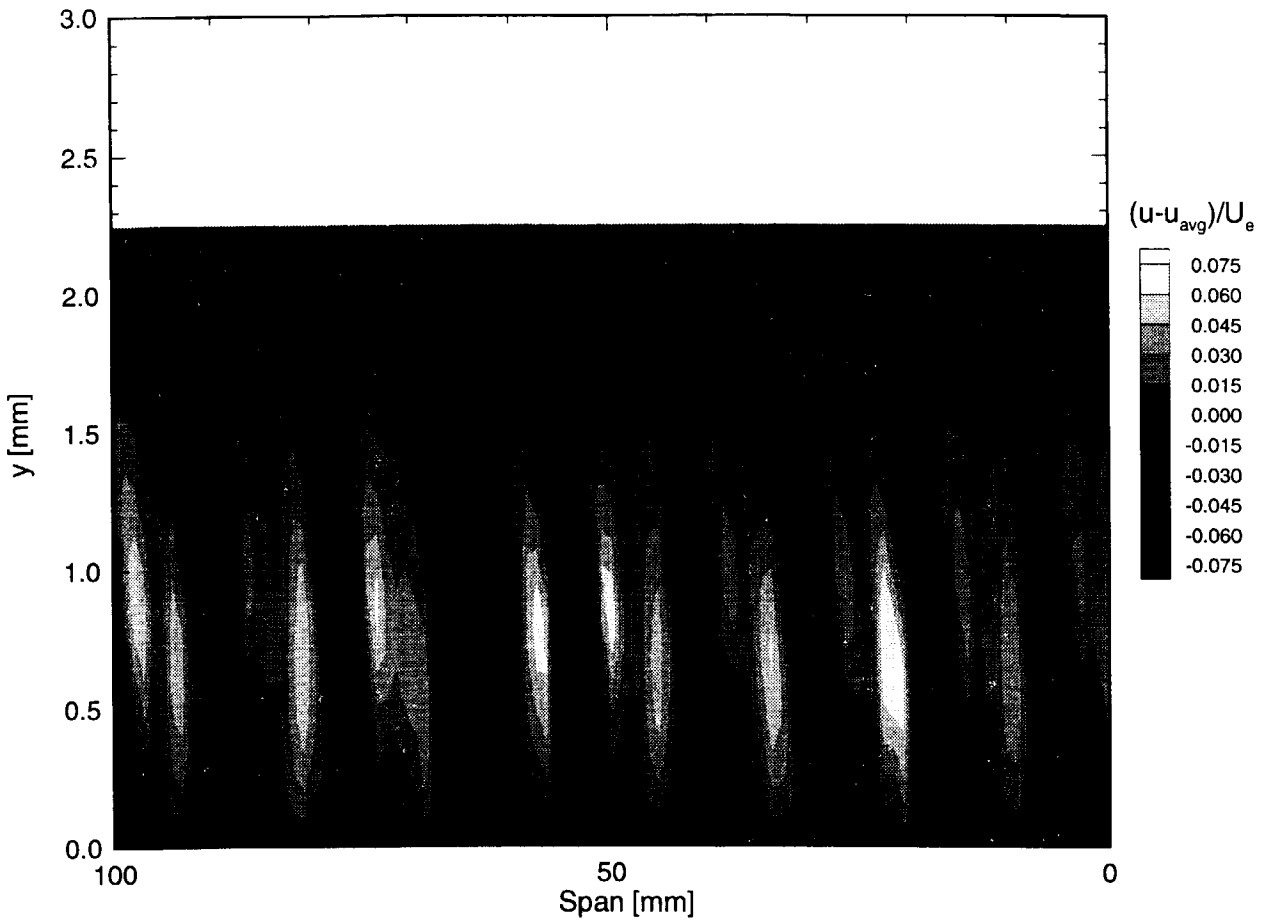

Figure 7.212. Disturbance contours for boundary-layer scans at $x/c = 0.15$. A full array of 117 μm roughness with a spacing of 12 mm is at $x/c = 0.005$. $Re_c = 3.0 \times 10^6$. Data set B.

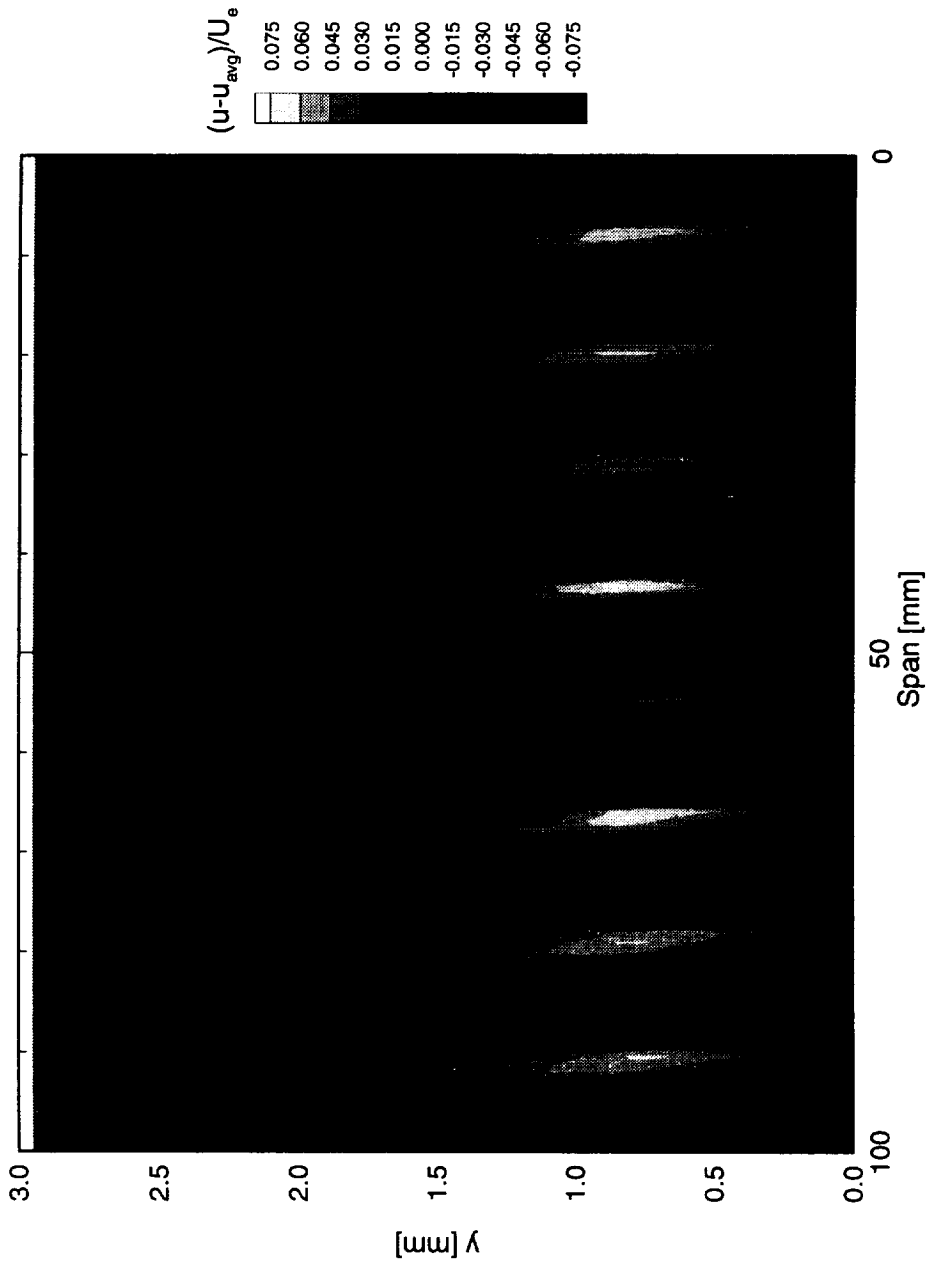

Figure 7.213. Disturbance contours for boundary-layer scans at $x/c = 0.20$. A full array of 117 μm roughness with a spacing of 12 mm is at $x/c = 0.005$. $Re_c = 3.0 \times 10^6$. Data set B.

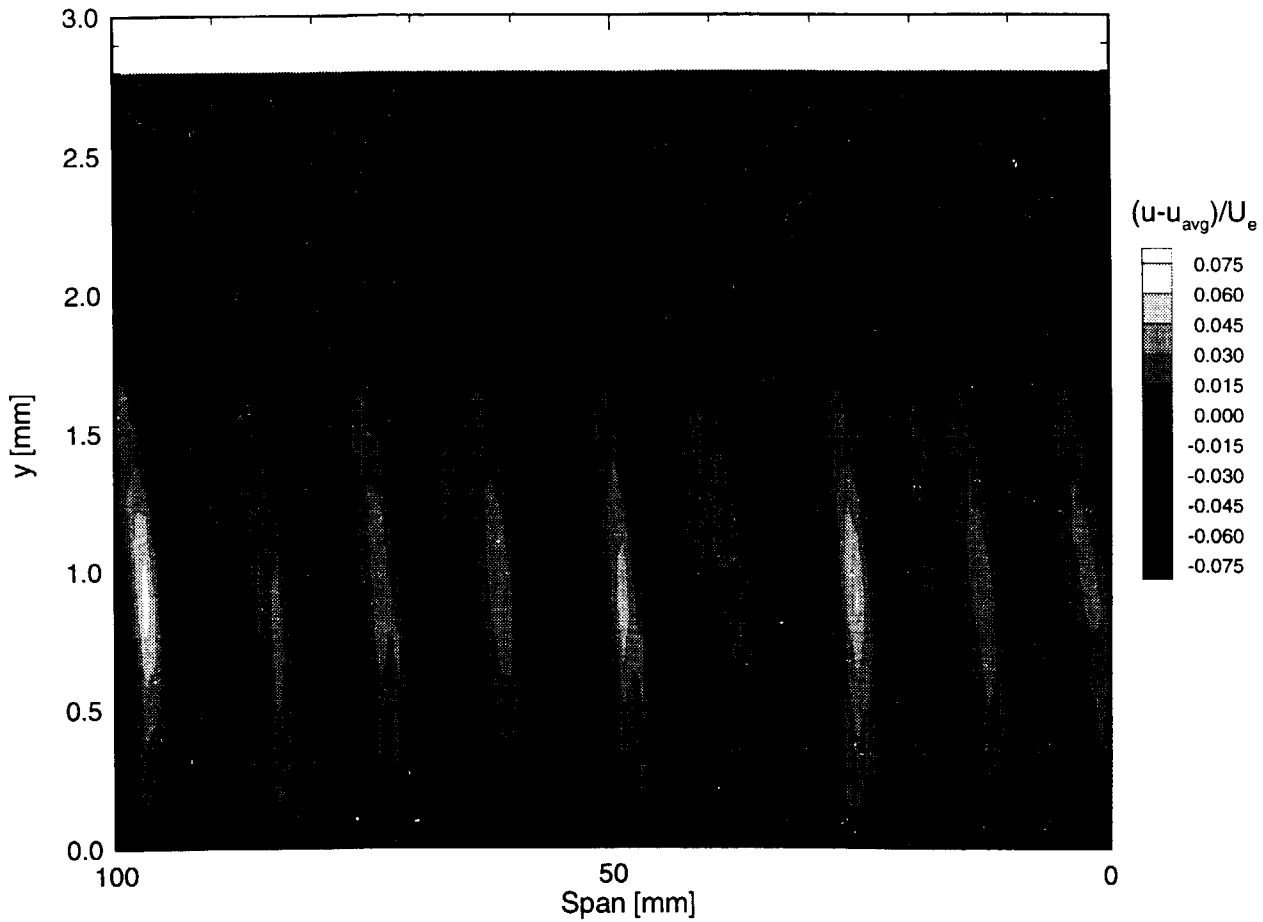

Figure 7.214. Disturbance contours for boundary-layer scans at $x/c = 0.25$. A full array of 117 μm roughness with a spacing of 12 mm is at $x/c = 0.005$. $Re_c = 3.0 \times 10^6$. Data set B.

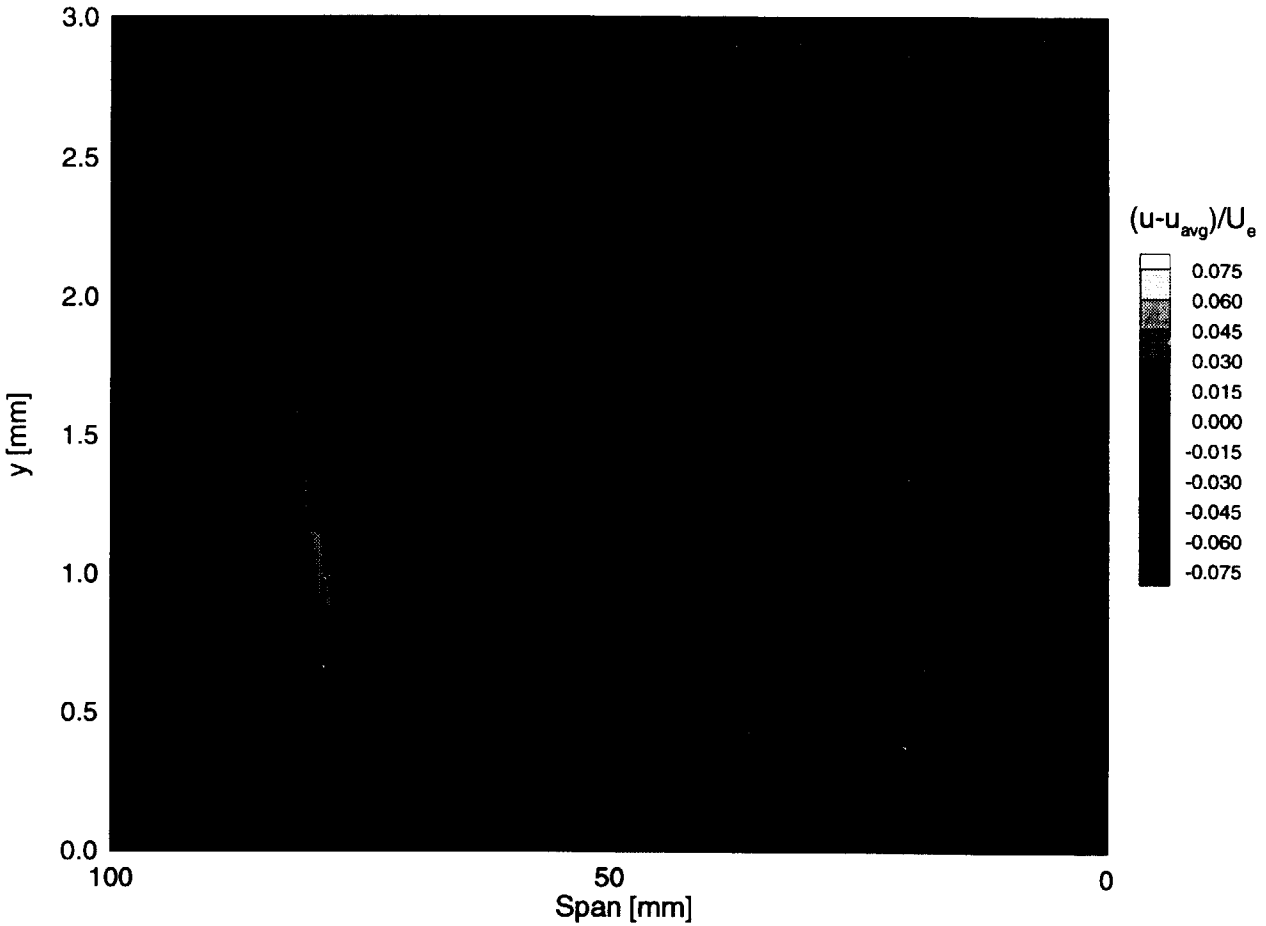

Figure 7.215. Disturbance contours for boundary-layer scans at $x/c = 0.30$. A full array of 117 μm roughness with a spacing of 12 mm is at $x/c = 0.005$. $Re_c = 3.0 \times 10^6$. Data set B.

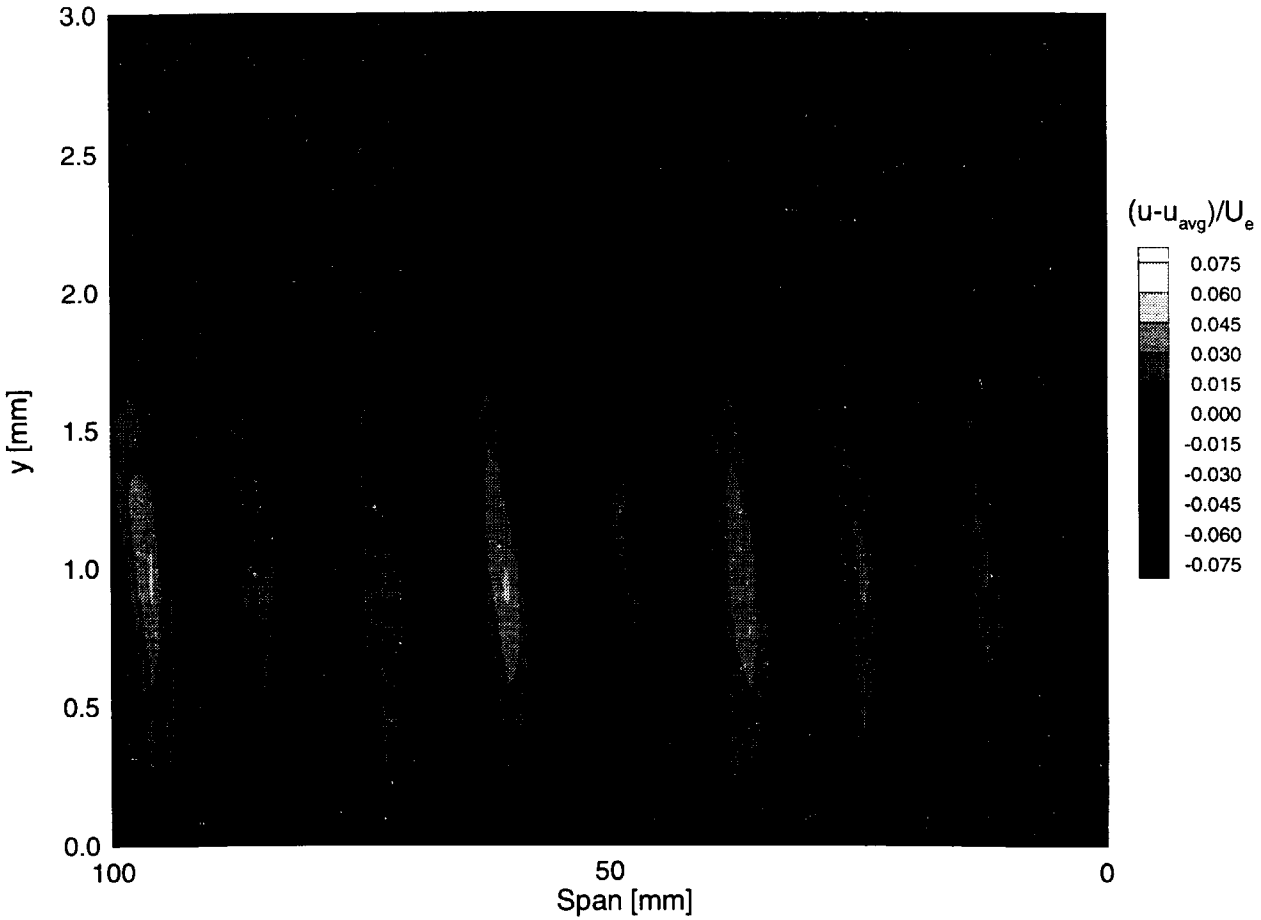

Figure 7.216. Disturbance contours for boundary-layer scans at $x/c = 0.35$. A full array of 117 μm roughness with a spacing of 12 mm is at $x/c = 0.005$. $Re_c = 3.0 \times 10^6$. Data set B.

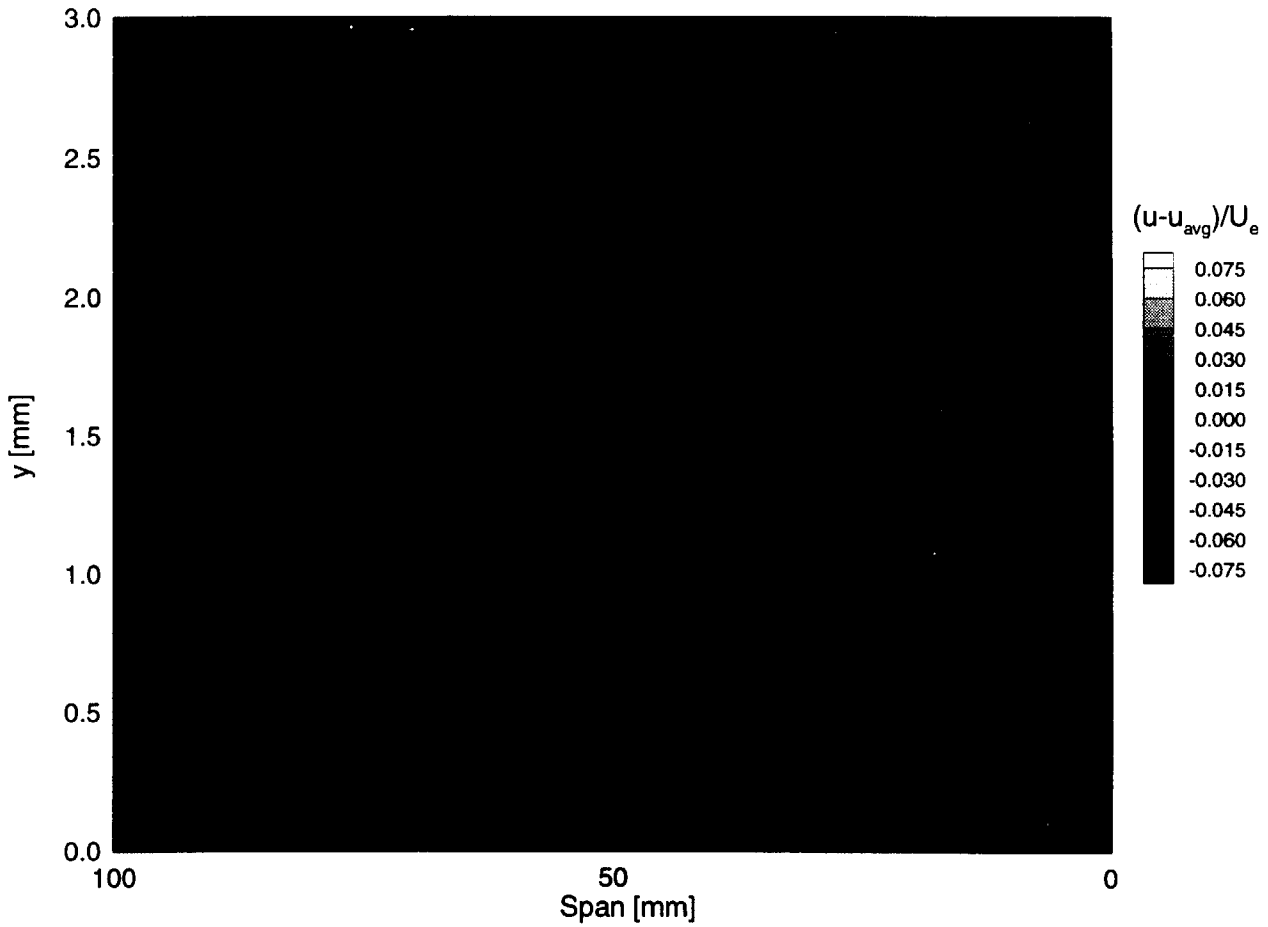

Figure 7.217. Disturbance contours for boundary-layer scans at $x/c = 0.40$. A full array of 117 μm roughness with a spacing of 12 mm is at $x/c = 0.005$. $Re_c = 3.0 \times 10^6$. Data set B.

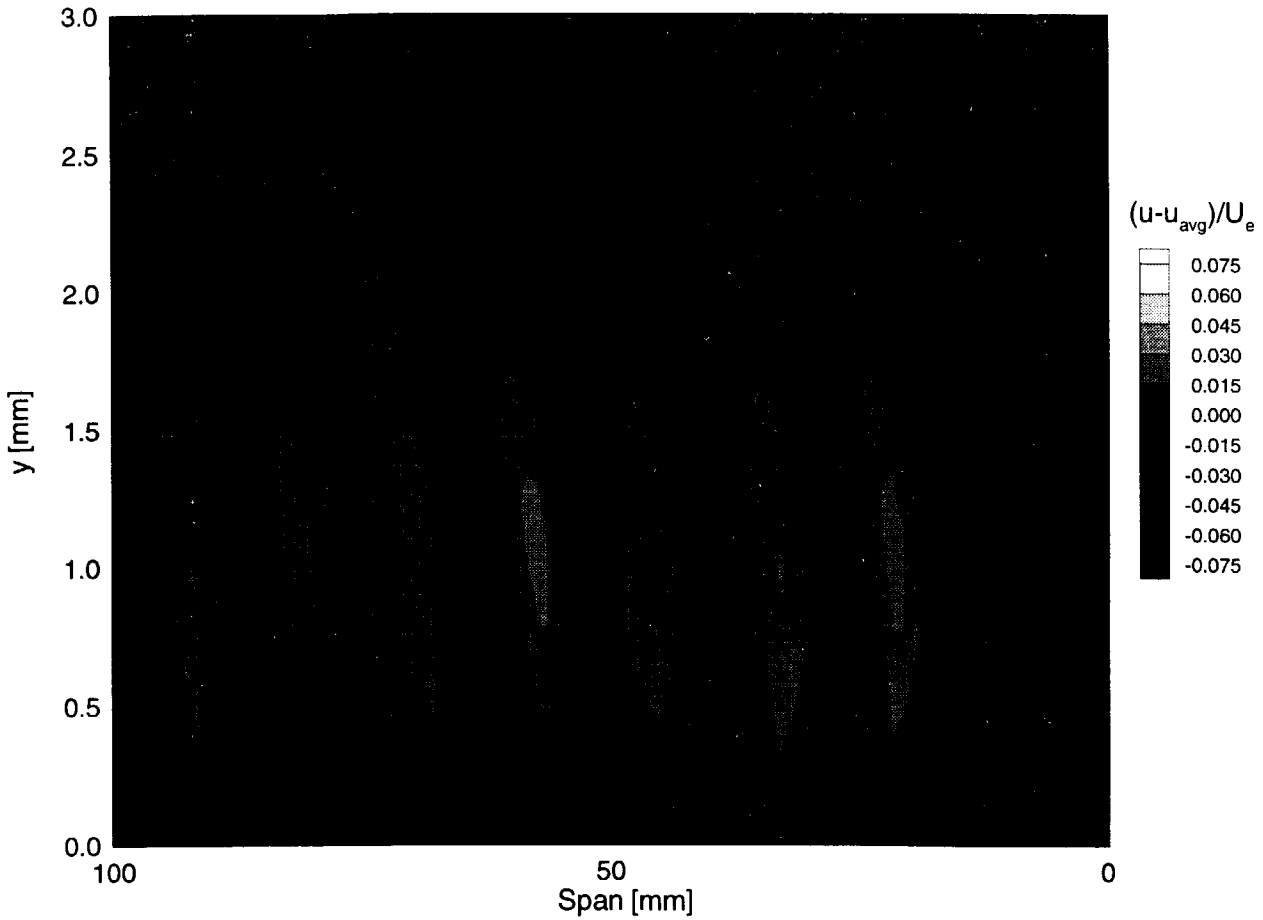

Figure 7.218. Disturbance contours for boundary-layer scans at $x/c = 0.45$. A full array of 117 μm roughness with a spacing of 12 mm is at $x/c = 0.005$. $Re_c = 3.0 \times 10^6$. Data set B.

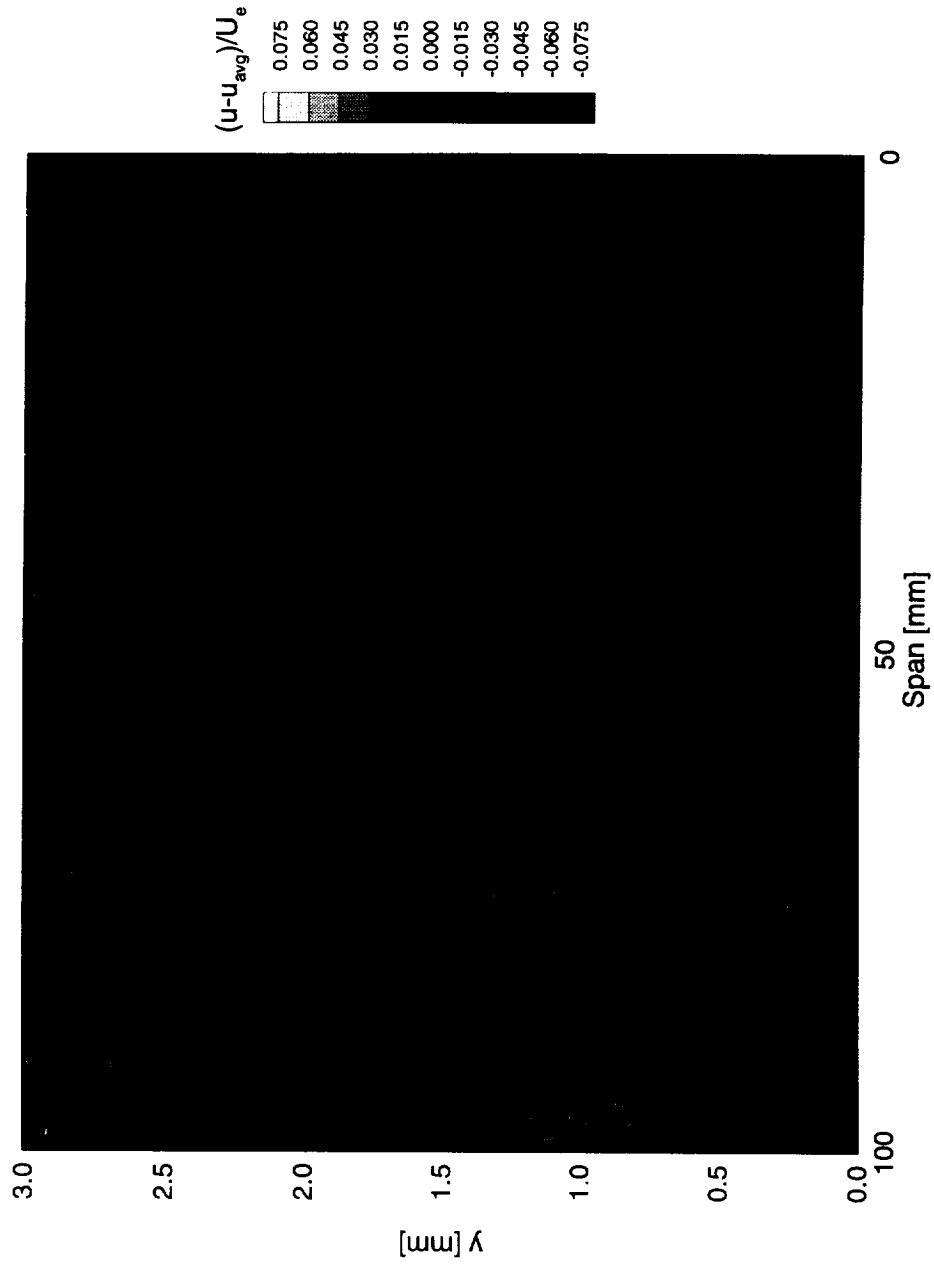

Figure 7.219. Disturbance contours for boundary-layer scans at $x/c = 0.50$. A full array of 117 μm roughness with a spacing of 12 mm is at $x/c = 0.005$. $Re_c = 3.0 \times 10^6$. Data set B.

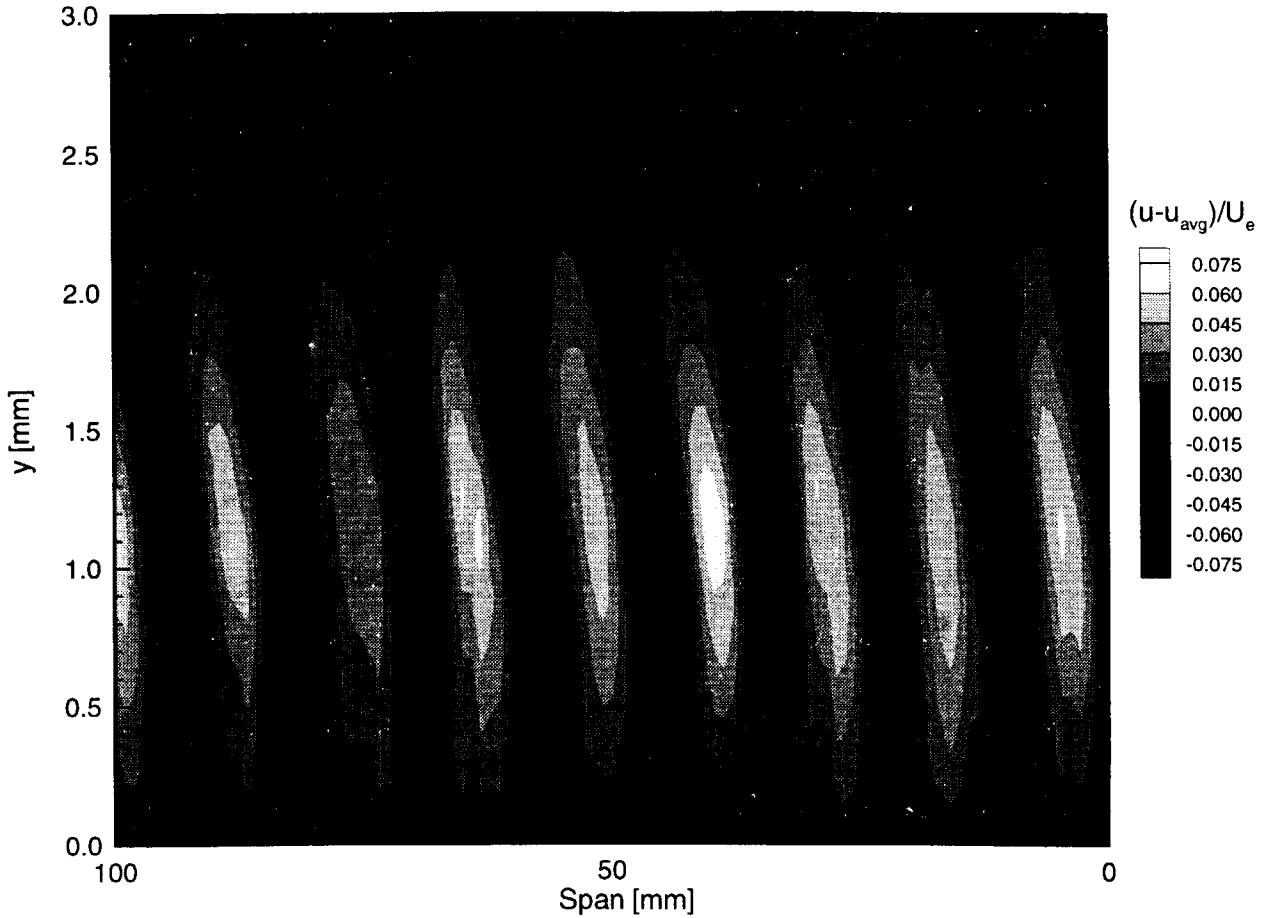

Figure 7.220. Disturbance contours for boundary-layer scans at $x/c = 0.60$. A full array of 117 μm roughness with a spacing of 12 mm is at $x/c = 0.005$. $Re_c = 3.0 \times 10^6$. Data set B.

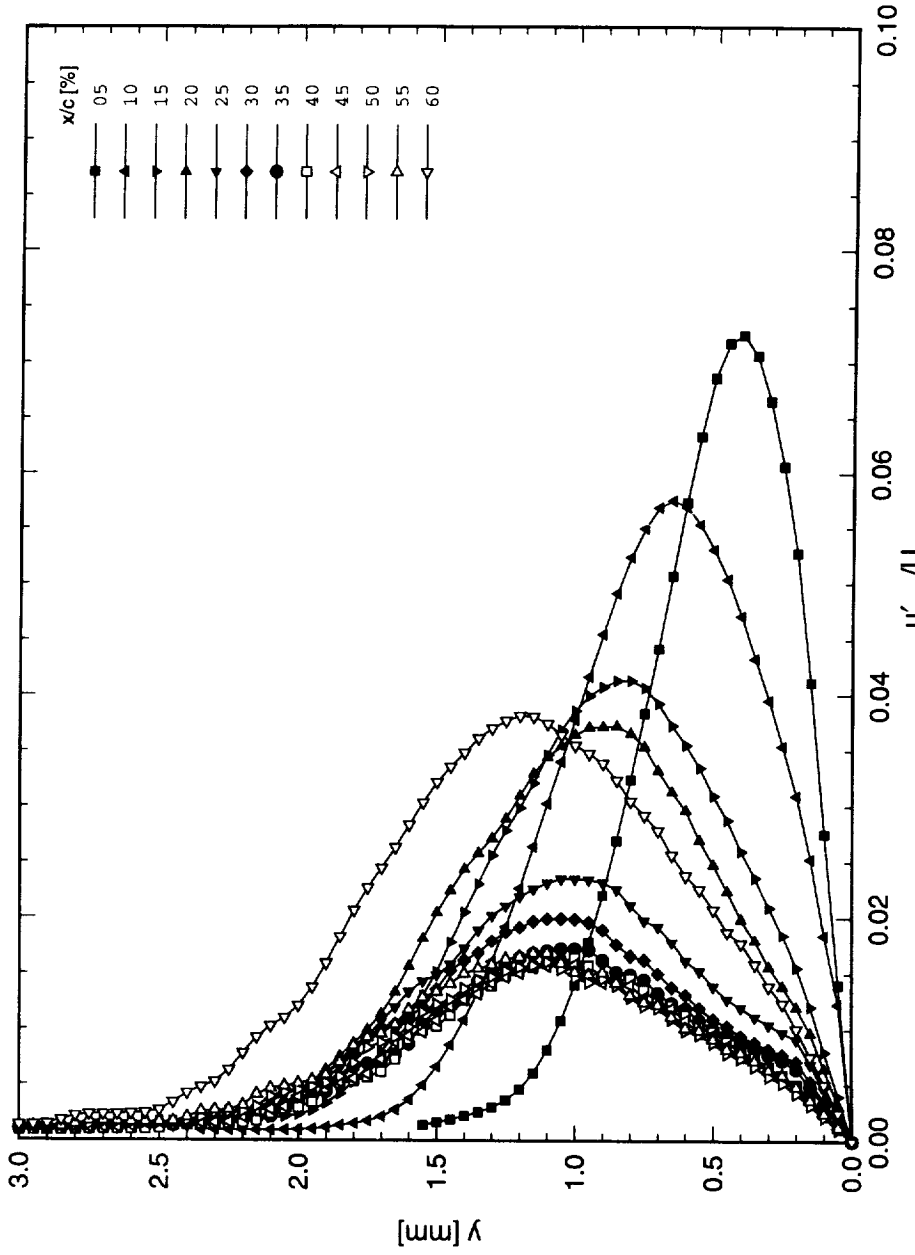

Figure 7.221. Stationary crossflow mode shapes for data set B, using rms method. $Re_c = 3.0 \times 10^6$, $\alpha = 0°$.

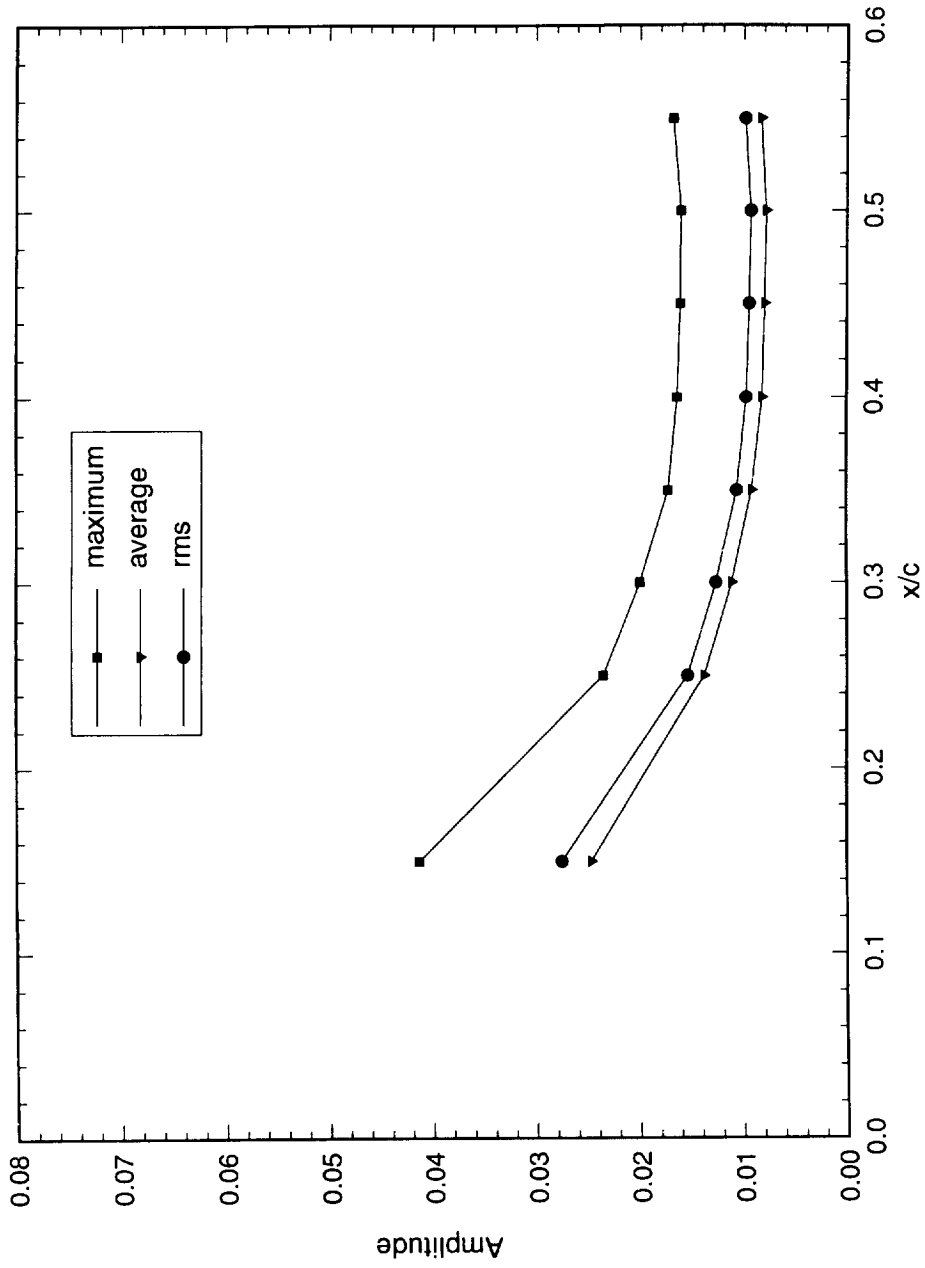

Figure 7.222. Stationary crossflow amplitudes for data set B. $Re_c = 3.0 \times 10^6$, $\alpha = 0°$.

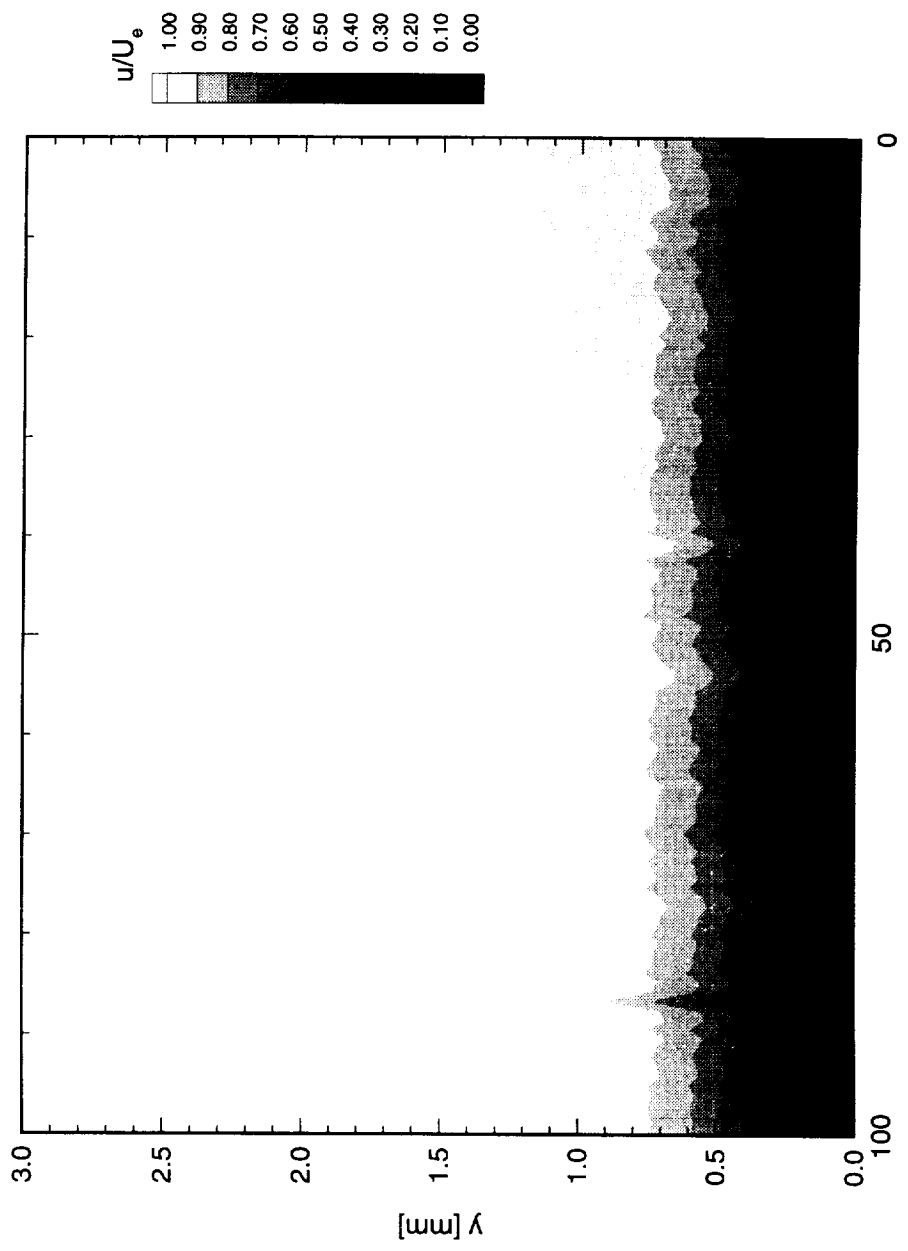

Figure 7.223. Velocity contours for boundary-layer scans at $x/c = 0.05$. A full array of 73 μm roughness with a spacing of 12 mm is at $x/c = 0.005$. $Re_c = 3.0 \times 10^6$. Data set C.

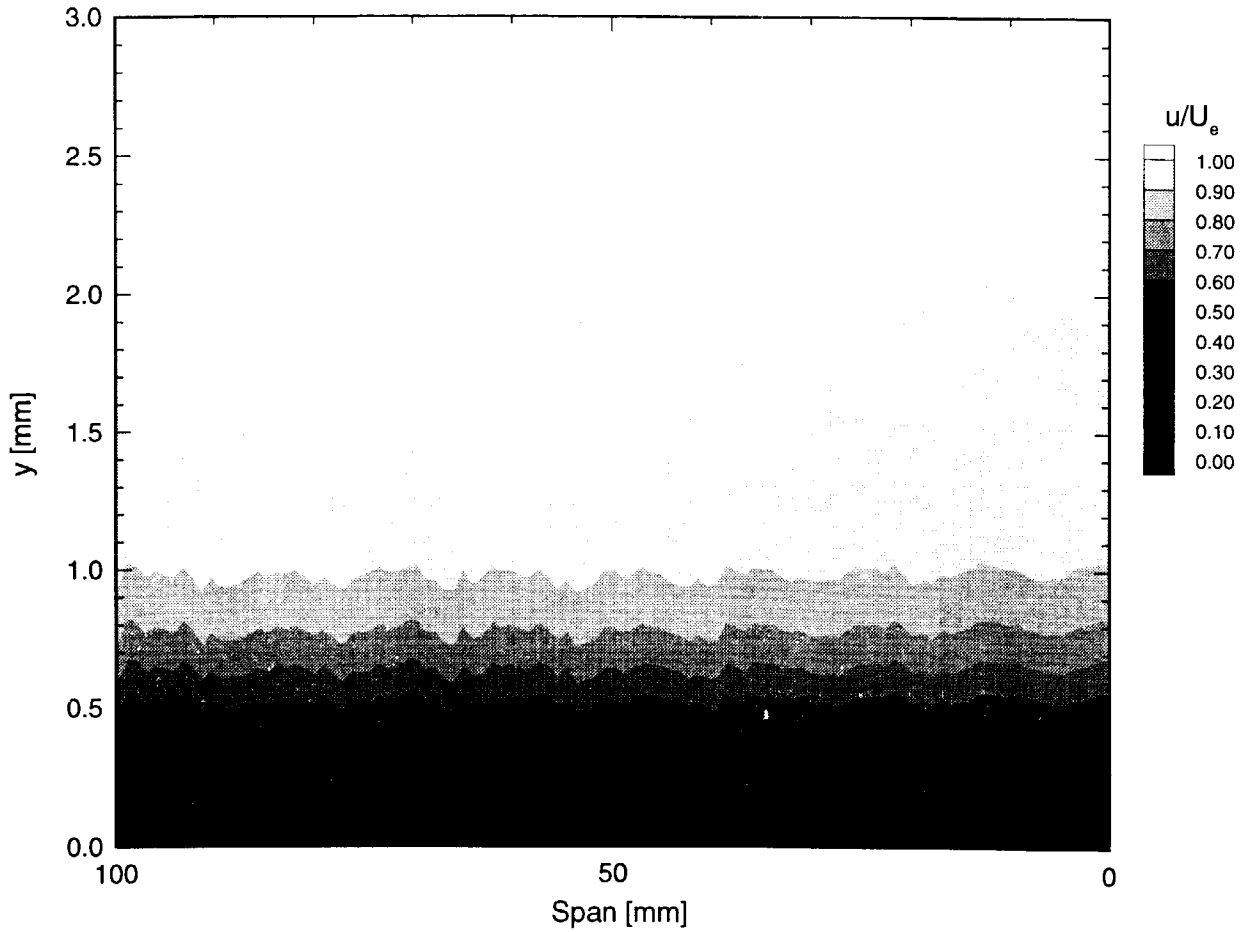

Figure 7.224. Velocity contours for boundary-layer scans at $x/c = 0.10$. A full array of 73 μm roughness with a spacing of 12 mm is at $x/c = 0.005$. $Re_c = 3.0 \times 10^6$. Data set C.

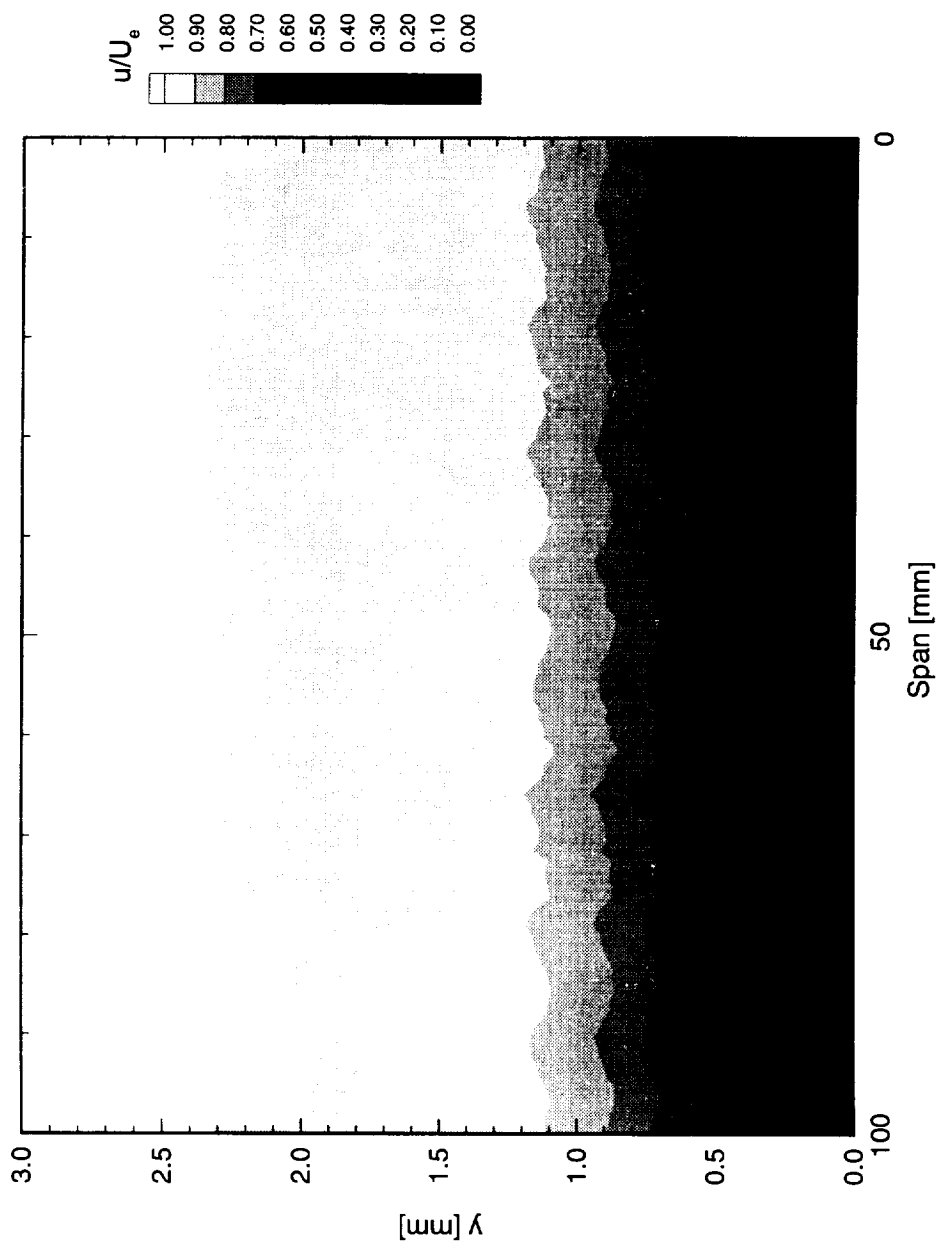

Figure 7.225. Velocity contours for boundary-layer scans at $x/c = 0.15$. A full array of 73 μm roughness with a spacing of 12 mm is at $x/c = 0.005$. $Re_c = 3.0 \times 10^6$. Data set C.

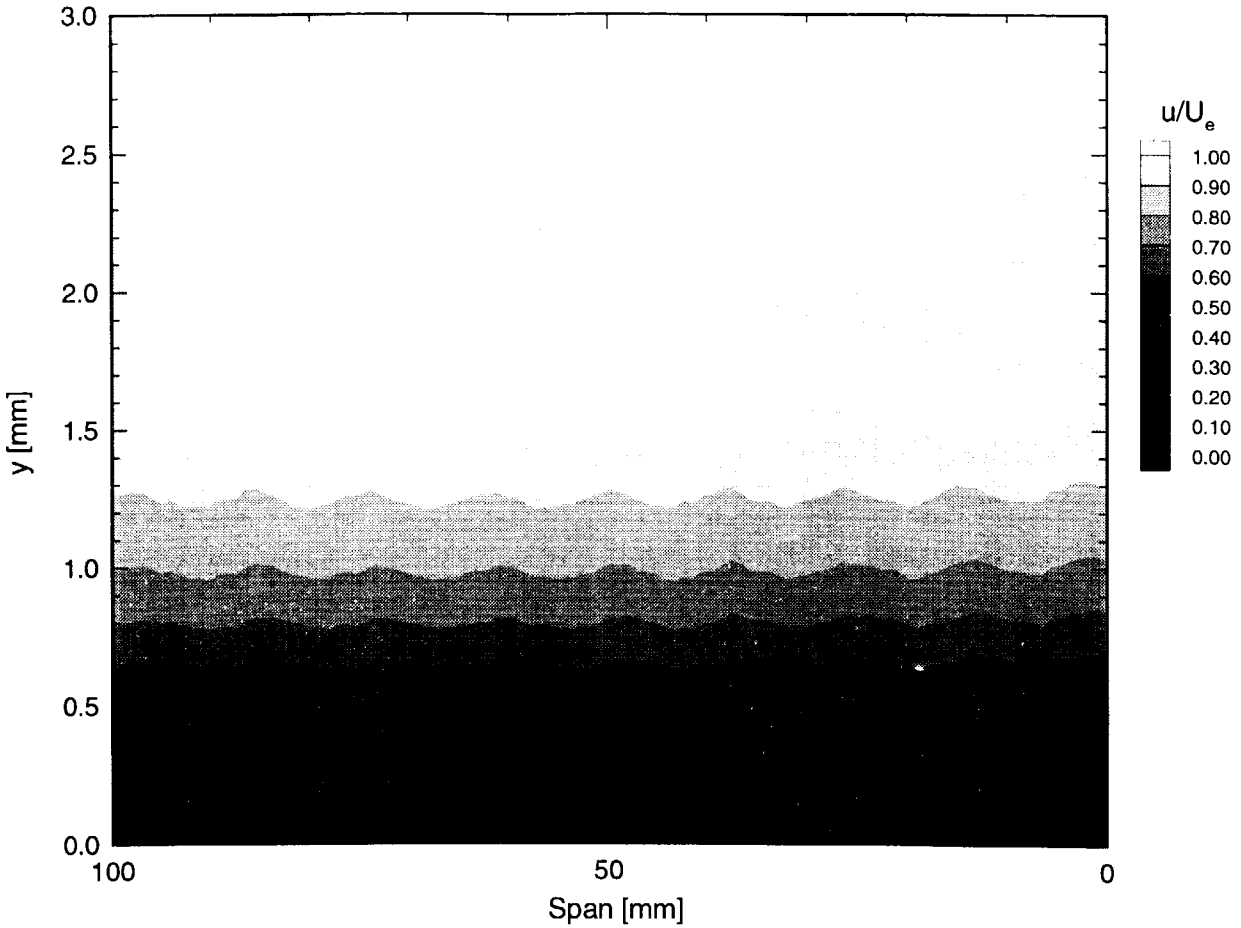

Figure 7.226. Velocity contours for boundary-layer scans at $x/c = 0.20$. A full array of 73 μm roughness with a spacing of 12 mm is at $x/c = 0.005$. $Re_c = 3.0 \times 10^6$. Data set C.

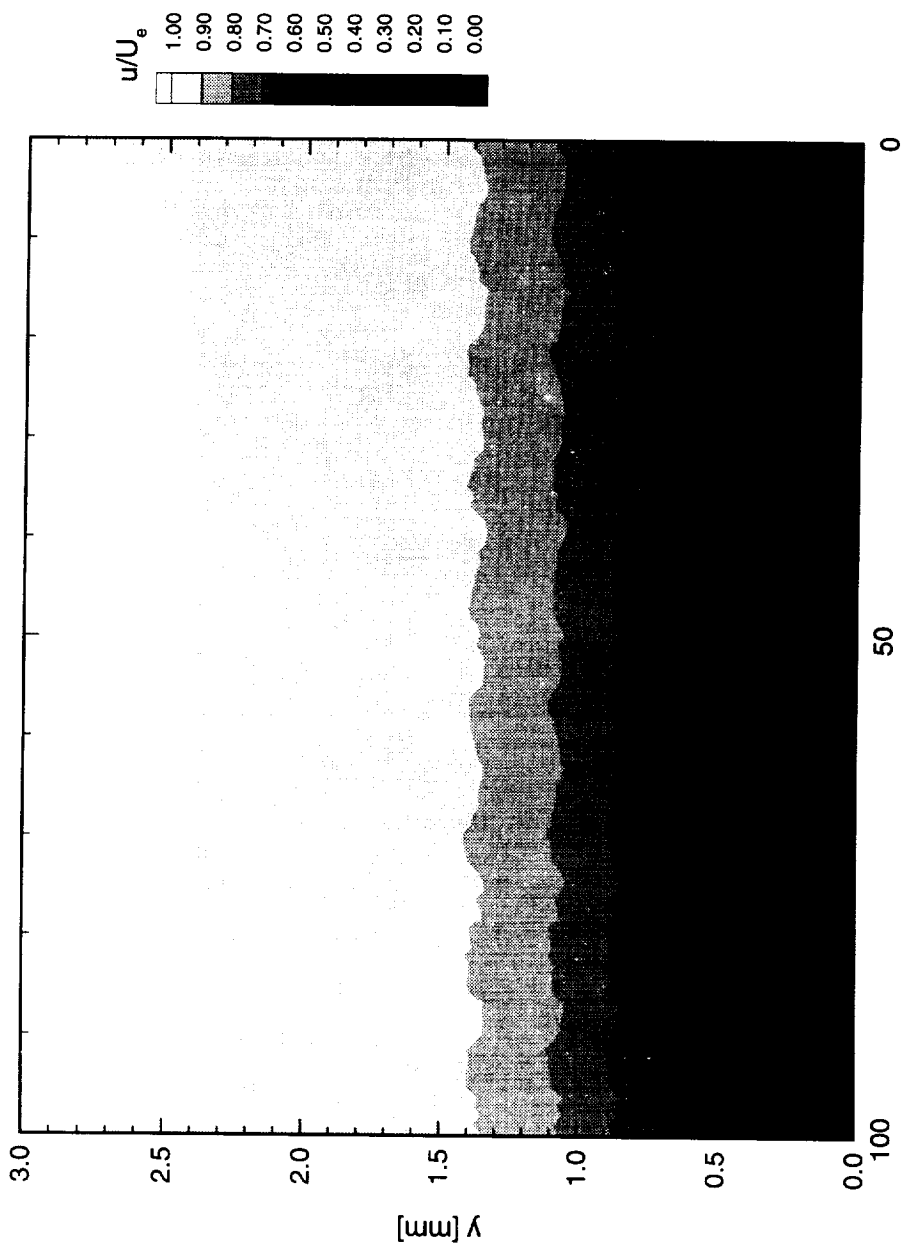

Figure 7.227. Velocity contours for boundary-layer scans at $x/c = 0.25$. A full array of 73 μm roughness with a spacing of 12 mm is at $x/c = 0.005$. $Re_c = 3.0 \times 10^6$. Data set C.

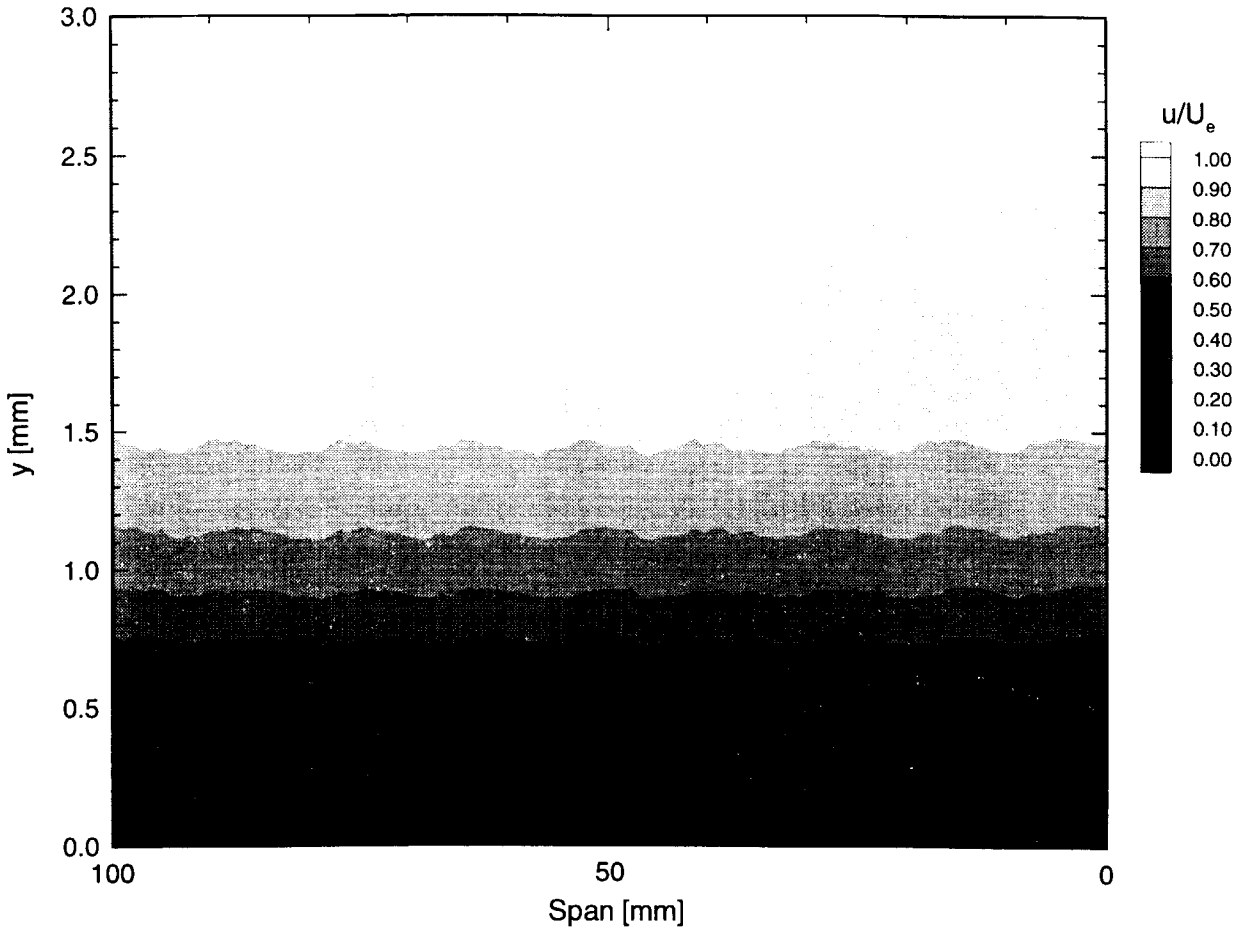

Figure 7.228. Velocity contours for boundary-layer scans at $x/c = 0.30$. A full array of 73 μm roughness with a spacing of 12 mm is at $x/c = 0.005$. $Re_c = 3.0 \times 10^6$. Data set C.

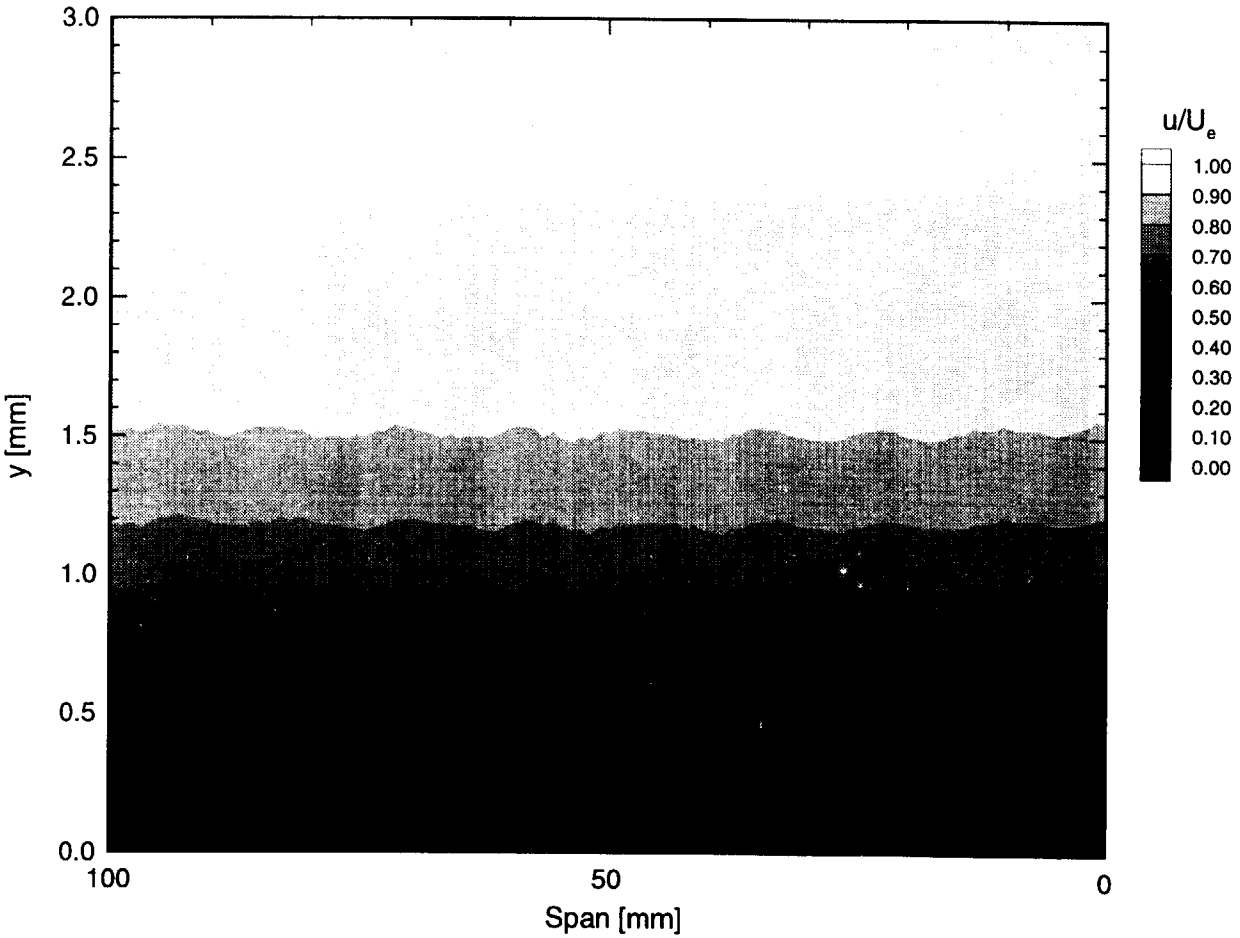

Figure 7.229. Velocity contours for boundary-layer scans at $x/c = 0.35$. A full array of 73 μm roughness with a spacing of 12 mm is at $x/c = 0.005$. $Re_c = 3.0 \times 10^6$. Data set C.

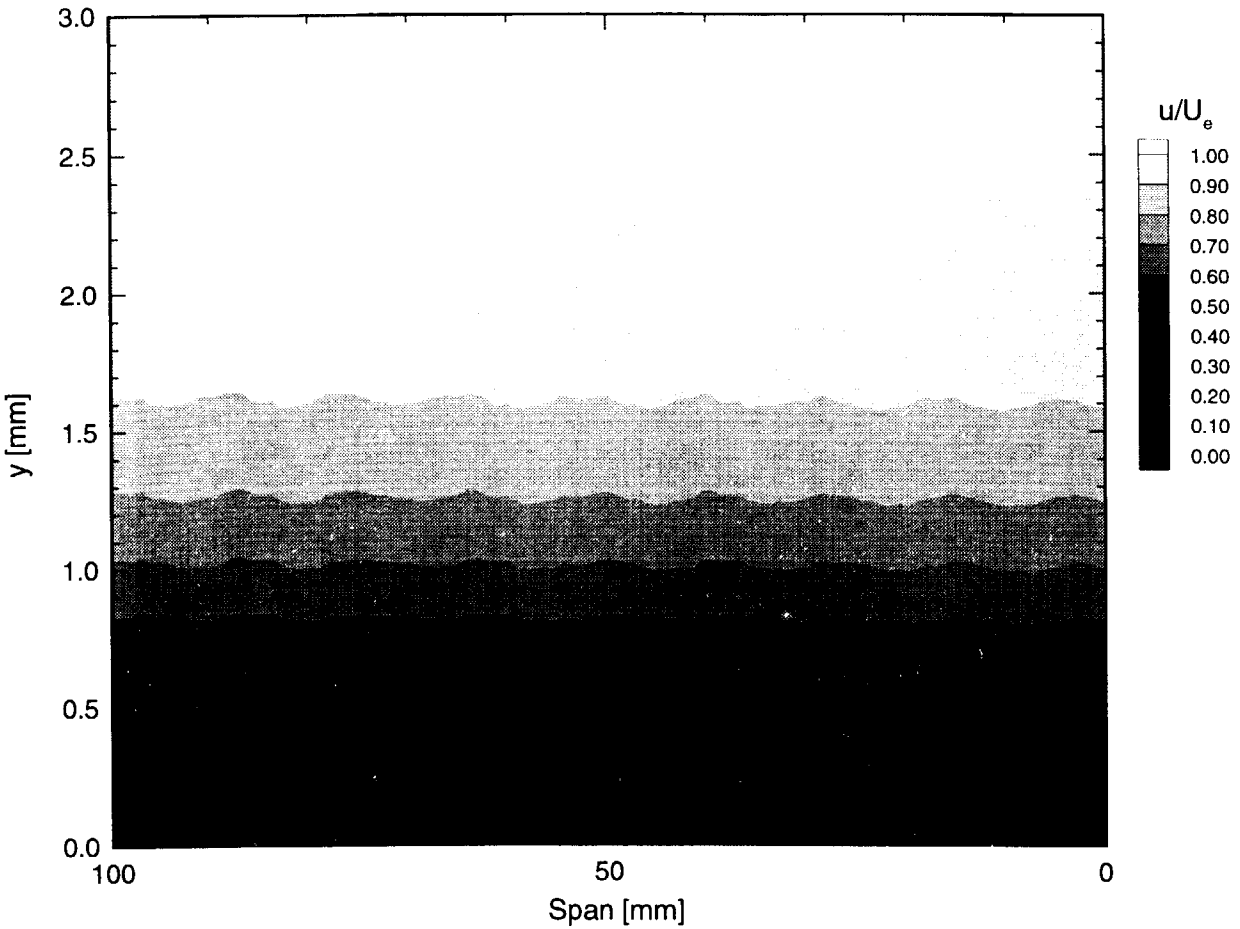

Figure 7.230. Velocity contours for boundary-layer scans at $x/c = 0.40$. A full array of 73 μm roughness with a spacing of 12 mm is at $x/c = 0.005$. $Re_c = 3.0 \times 10^6$. Data set C.

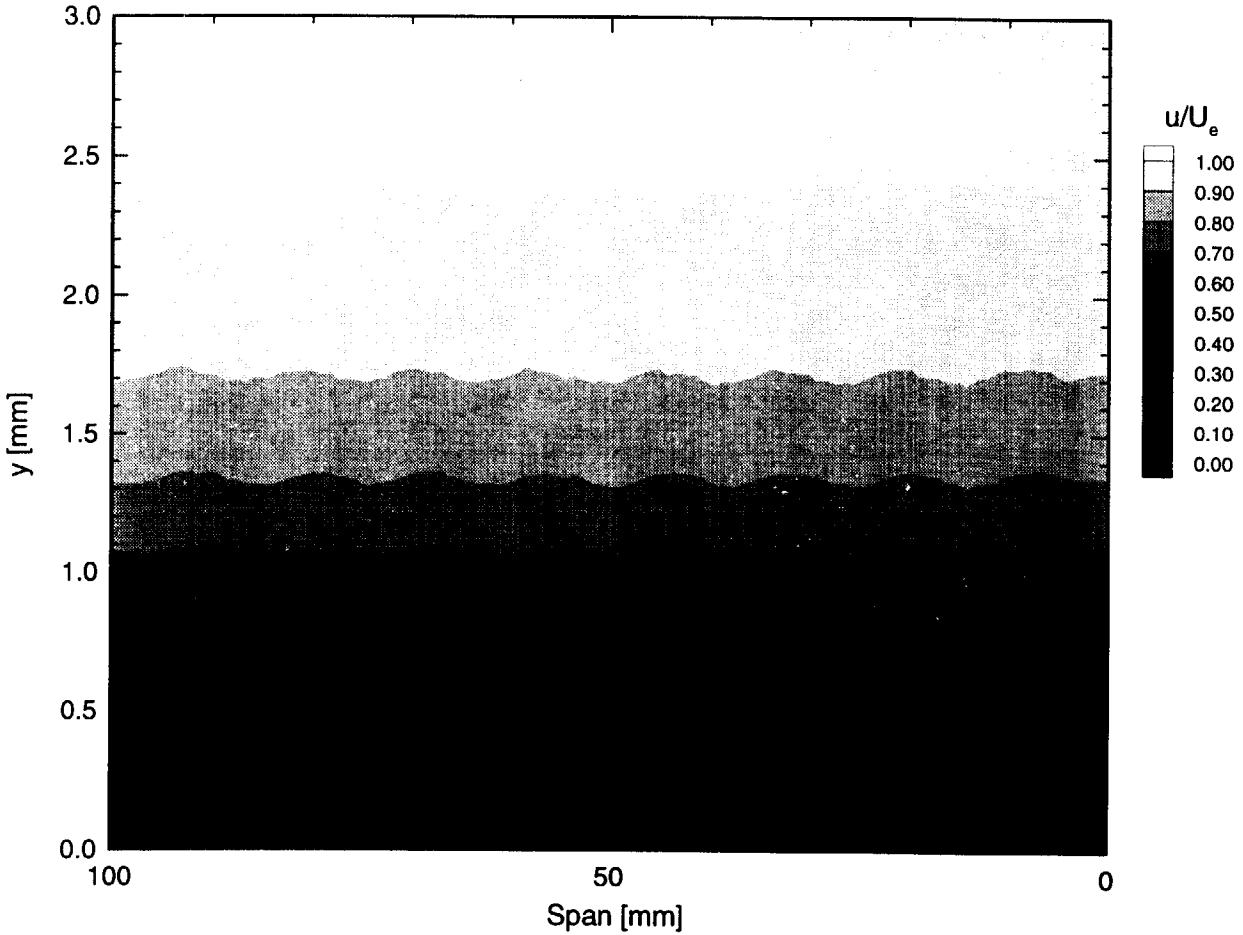

Figure 7.231. Velocity contours for boundary-layer scans at $x/c = 0.45$. A full array of 73 μm roughness with a spacing of 12 mm is at $x/c = 0.005$. $Re_c = 3.0 \times 10^6$. Data set C.

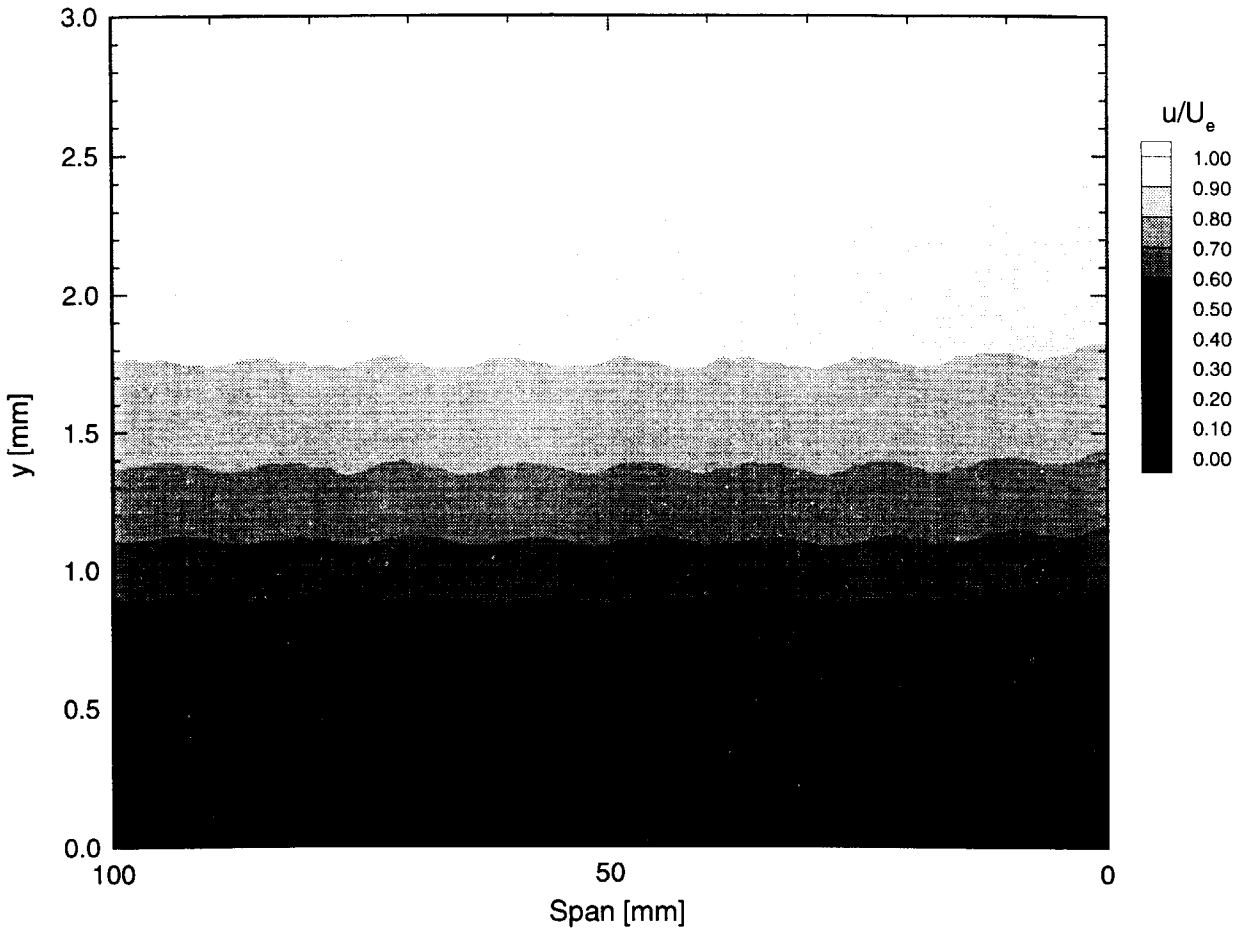

Figure 7.232. Velocity contours for boundary-layer scans at $x/c = 0.50$. A full array of 73 μm roughness with a spacing of 12 mm is at $x/c = 0.005$. $Re_c = 3.0 \times 10^6$. Data set C.

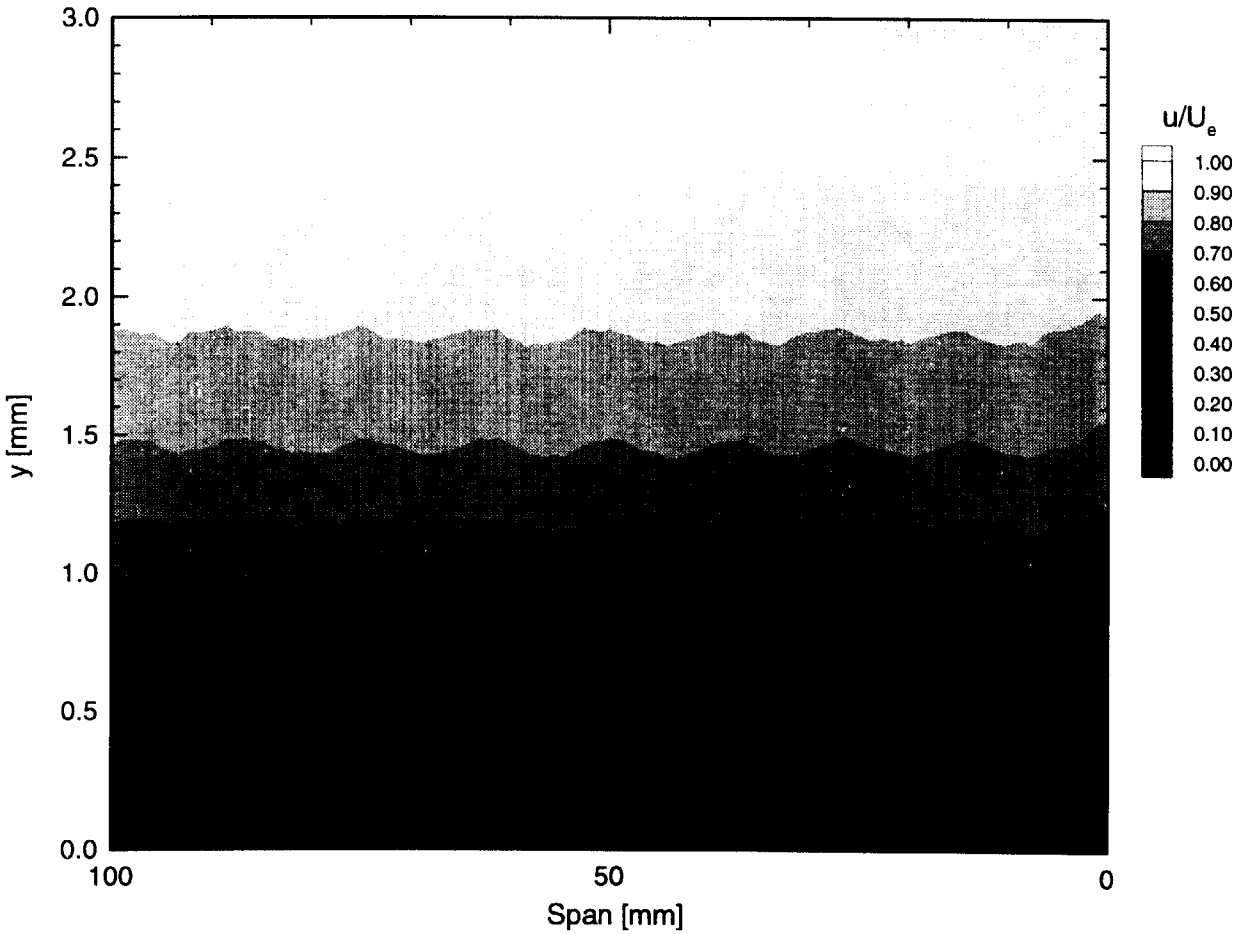

Figure 7.233. Velocity contours for boundary-layer scans at $x/c = 0.55$. A full array of 73 μm roughness with a spacing of 12 mm is at $x/c = 0.005$. $Re_c = 3.0 \times 10^6$. Data set C.

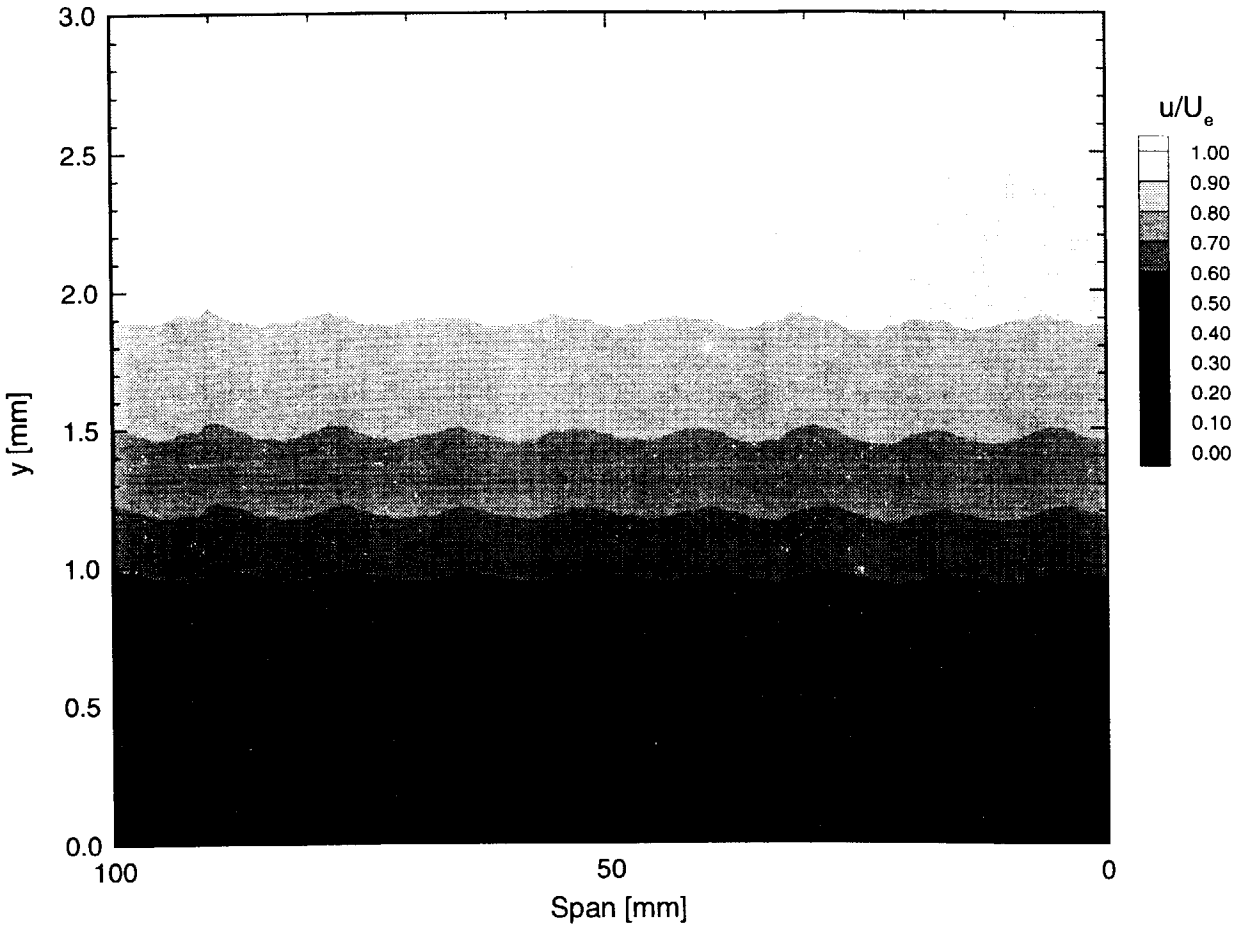

Figure 7.234. Velocity contours for boundary-layer scans at $x/c = 0.60$. A full array of 73 μm roughness with a spacing of 12 mm is at $x/c = 0.005$. $Re_c = 3.0 \times 10^6$. Data set C.

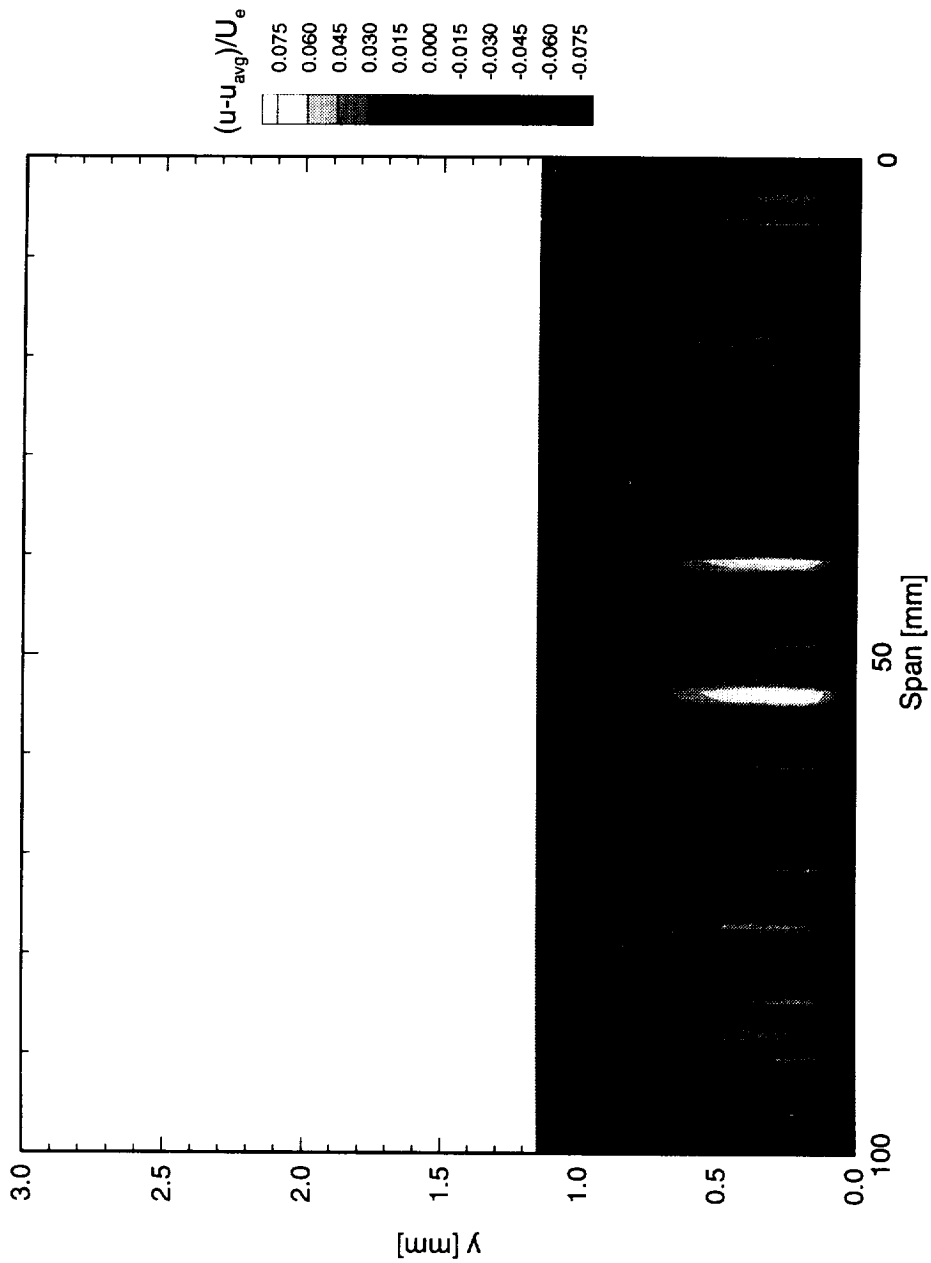

Figure 7.235. Disturbance contours for boundary-layer scans at $x/c = 0.05$. A full array of 73 μm roughness with a spacing of 12 mm is at $x/c = 0.005$. $Re_c = 3.0 \times 10^6$. Data set C.

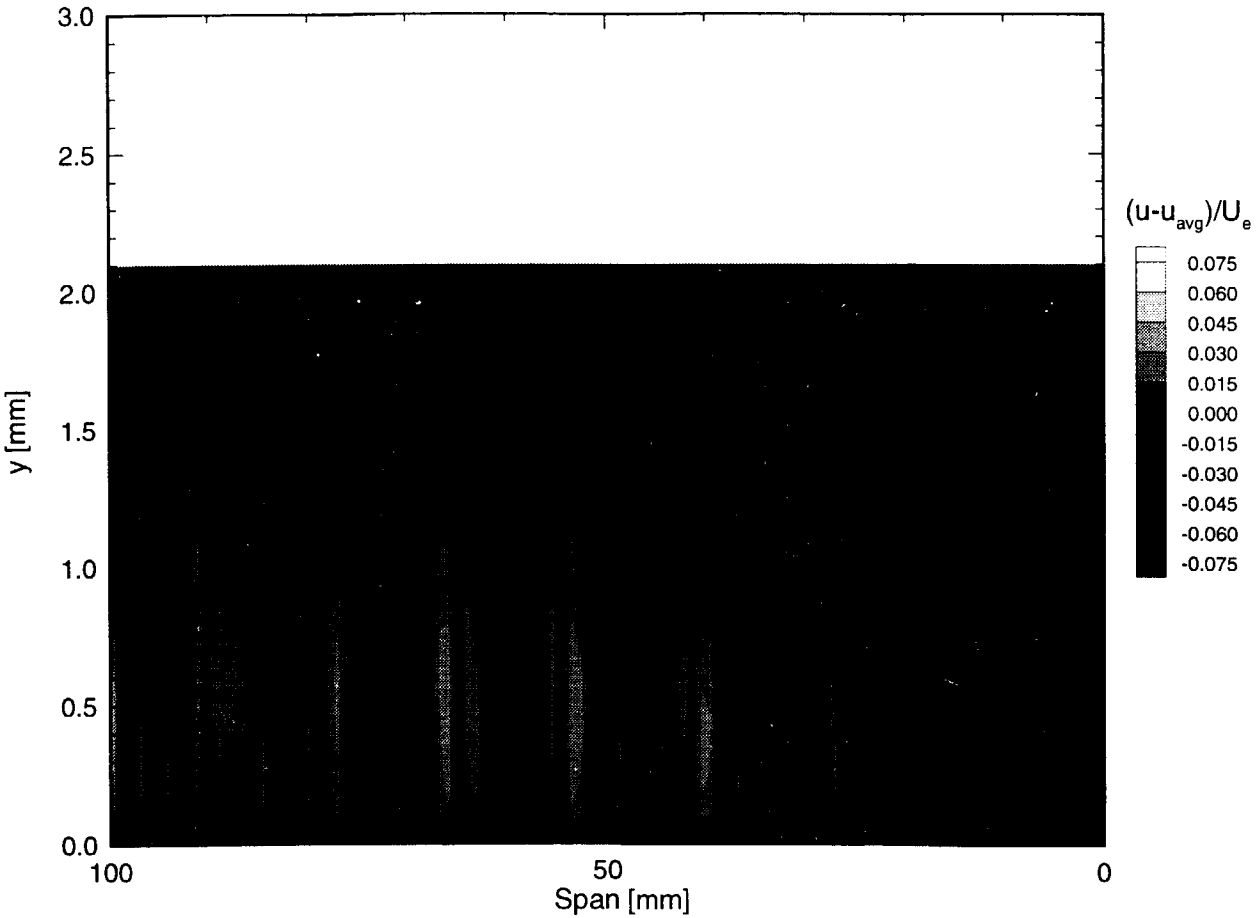

Figure 7.236. Disturbance contours for boundary-layer scans at $x/c = 0.10$. A full array of 73 μm roughness with a spacing of 12 mm is at $x/c = 0.005$. $Re_c = 3.0 \times 10^6$. Data set C.

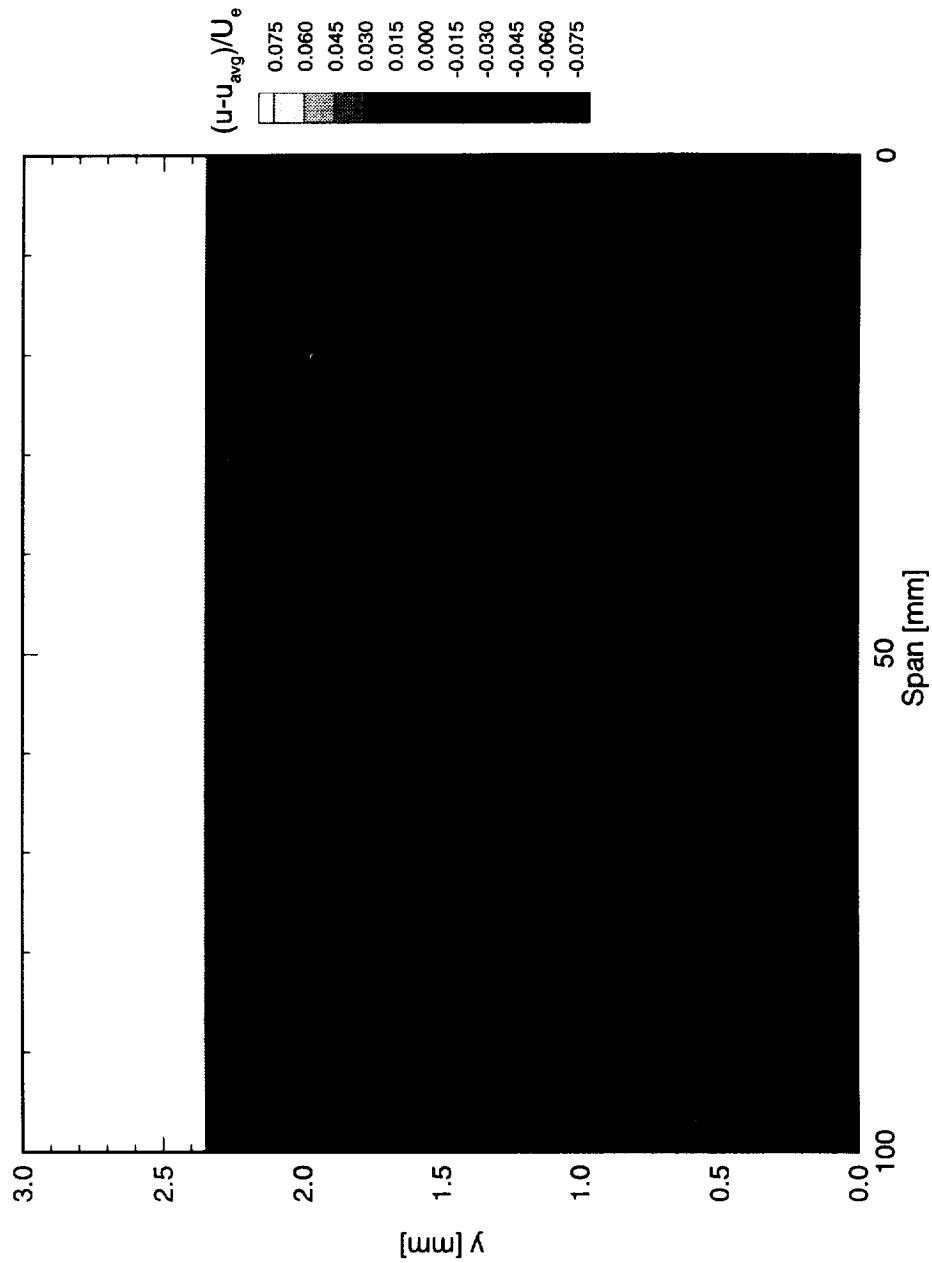

Figure 7.237. Disturbance contours for boundary-layer scans at $x/c = 0.15$. A full array of 73 μm roughness with a spacing of 12 mm is at $x/c = 0.005$. $Re_c = 3.0 \times 10^6$. Data set C.

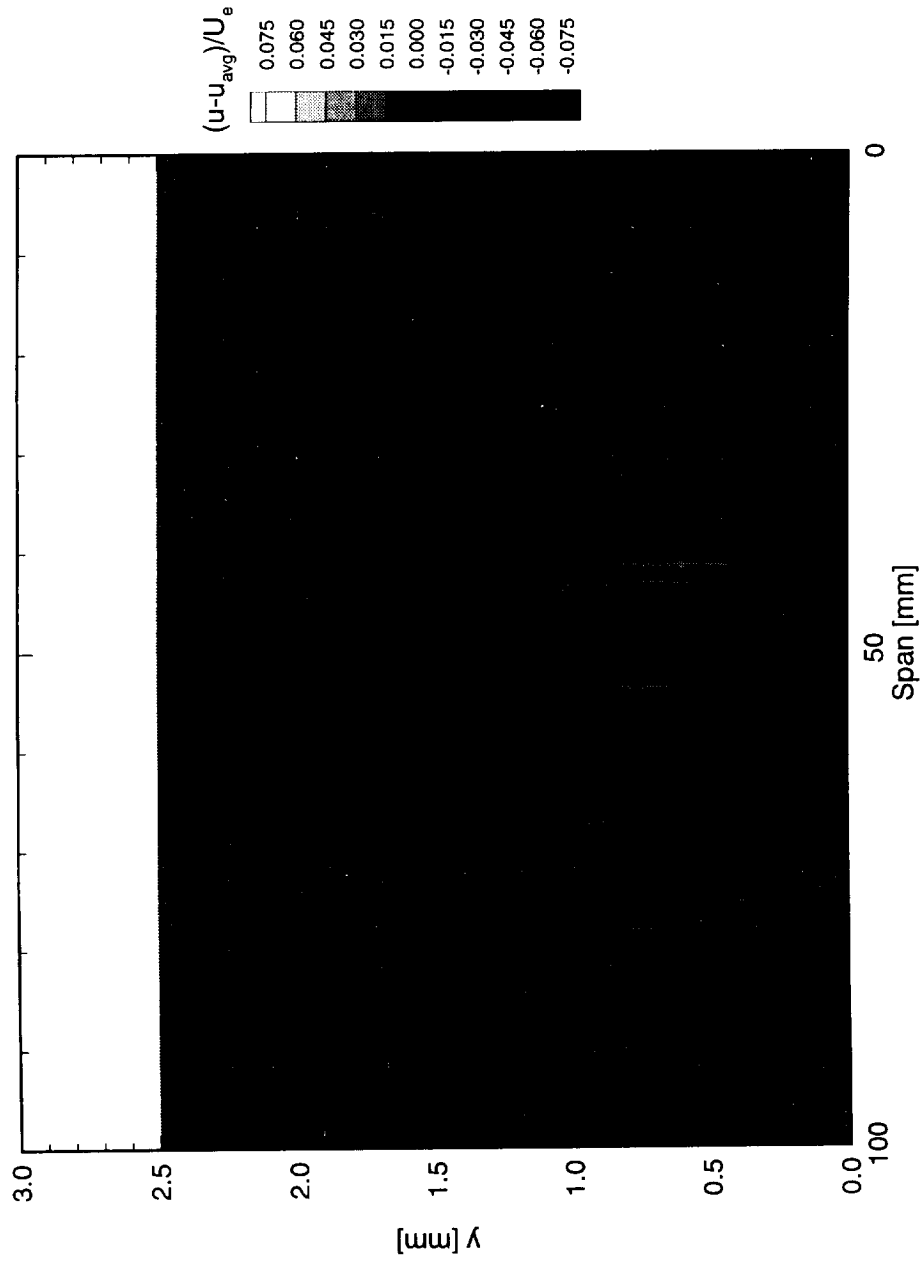

Figure 7.238. Disturbance contours for boundary-layer scans at $x/c = 0.20$. A full array of 73 μm roughness with a spacing of 12 mm is at $x/c = 0.005$. $Re_c = 3.0 \times 10^6$. Data set C.

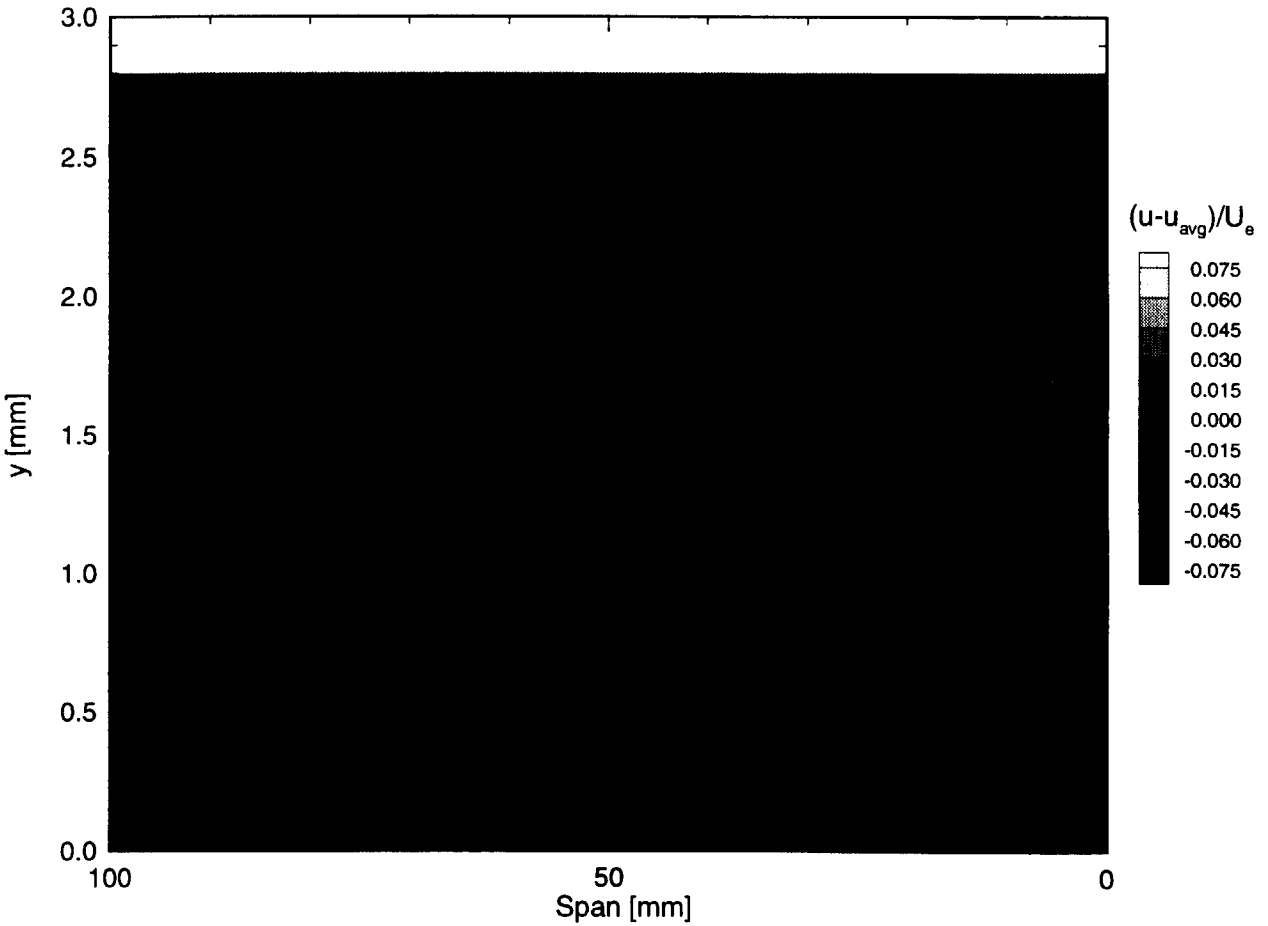

Figure 7.239. Disturbance contours for boundary-layer scans at $x/c = 0.25$. A full array of 73 μm roughness with a spacing of 12 mm is at $x/c = 0.005$. $Re_c = 3.0 \times 10^6$. Data set C.

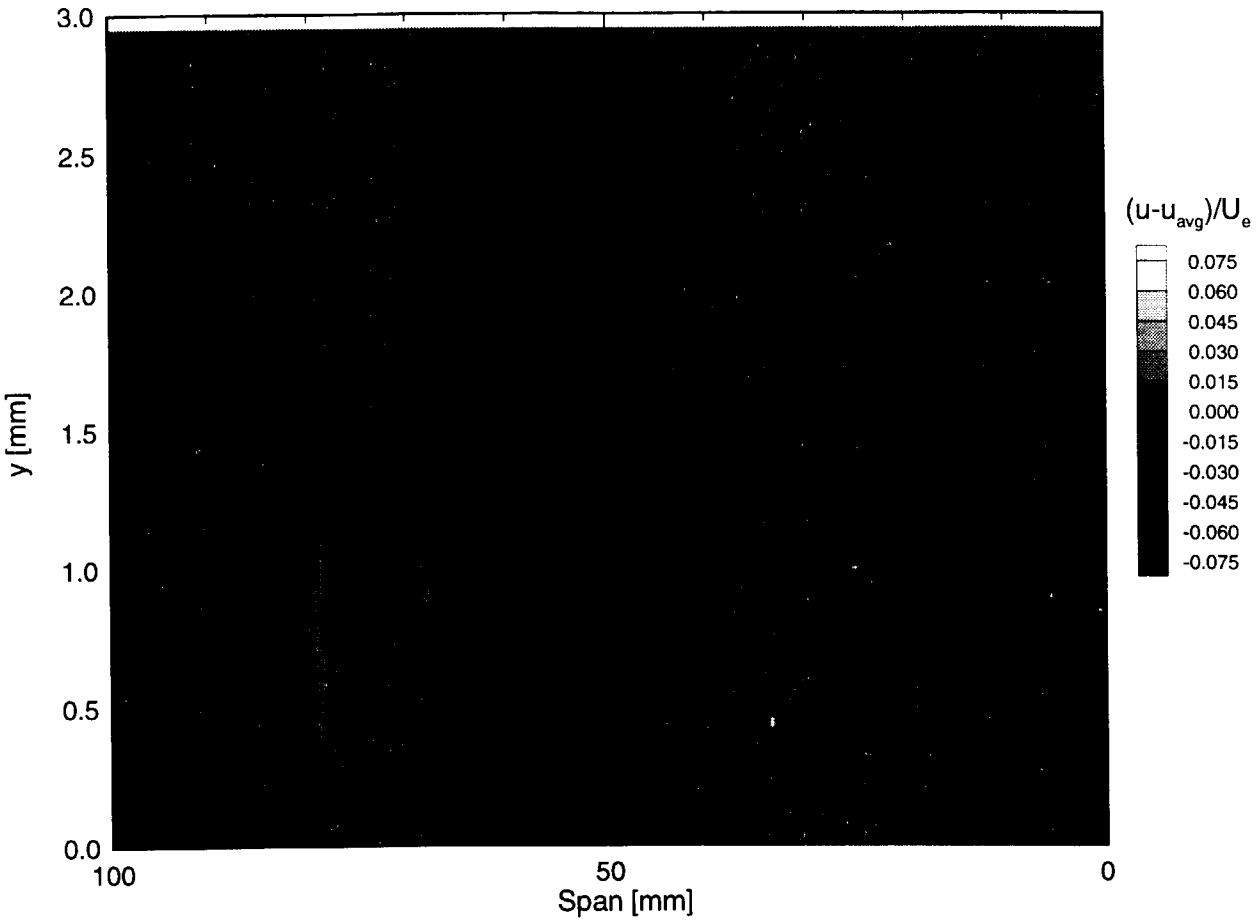

Figure 7.240. Disturbance contours for boundary-layer scans at $x/c = 0.30$. A full array of 73 μm roughness with a spacing of 12 mm is at $x/c = 0.005$. $Re_c = 3.0 \times 10^6$. Data set C.

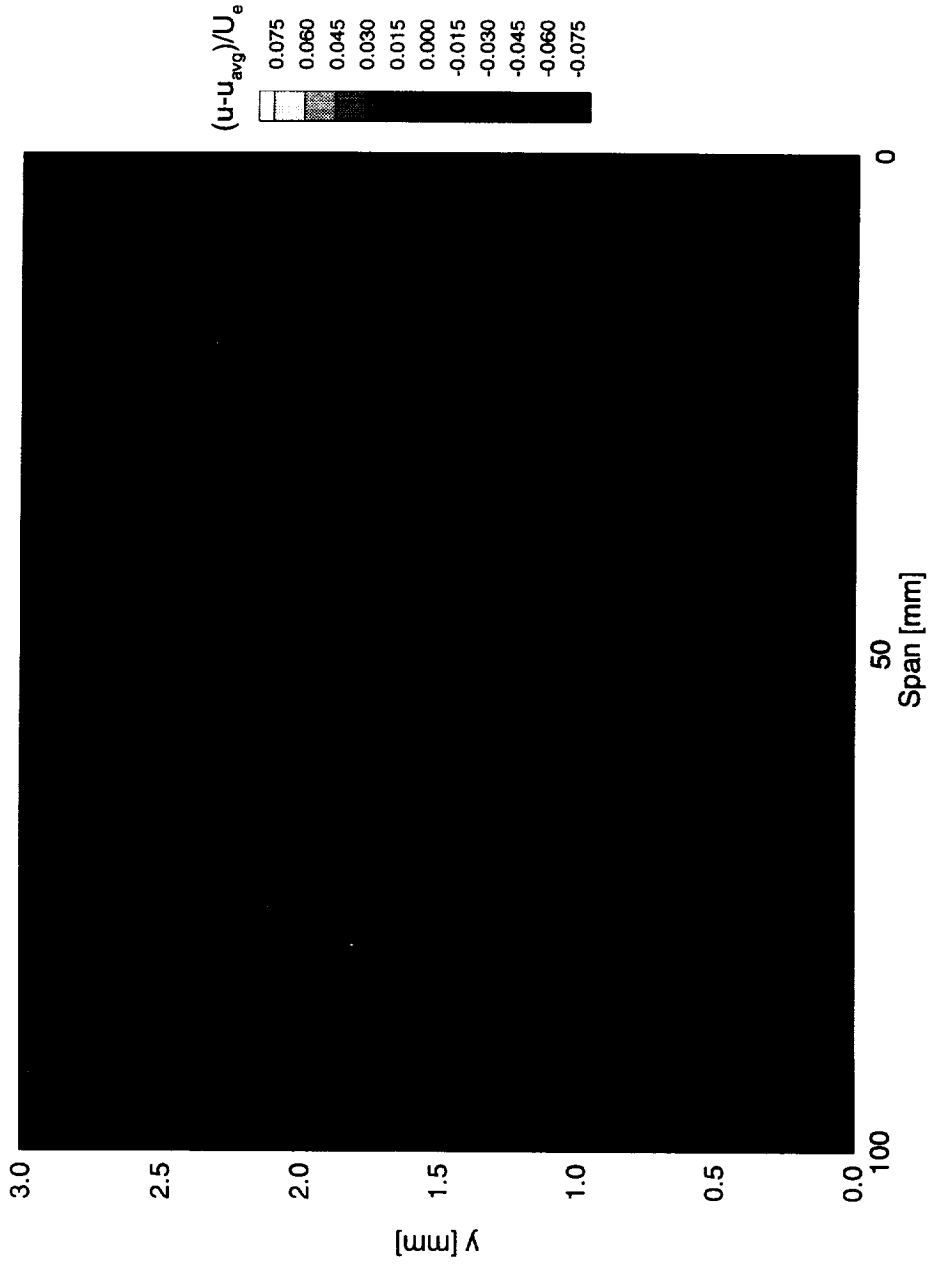

Figure 7.241. Disturbance contours for boundary-layer scans at $x/c = 0.35$. A full array of 73 μm roughness with a spacing of 12 mm is at $x/c = 0.005$. $Re_c = 3.0 \times 10^6$. Data set C.

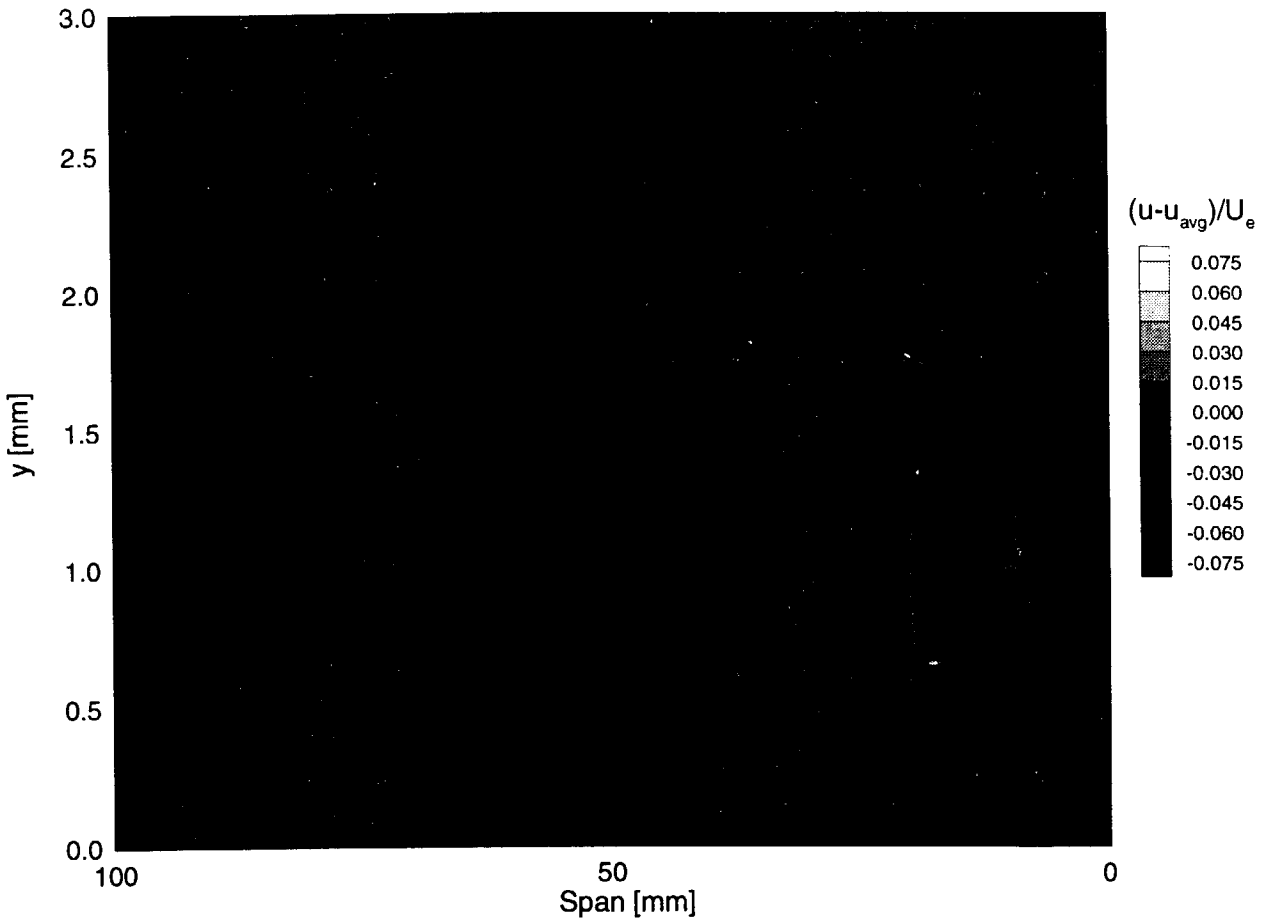

Figure 7.242. Disturbance contours for boundary-layer scans at $x/c = 0.40$. A full array of 73 μm roughness with a spacing of 12 mm is at $x/c = 0.005$. $Re_c = 3.0 \times 10^6$. Data set C.

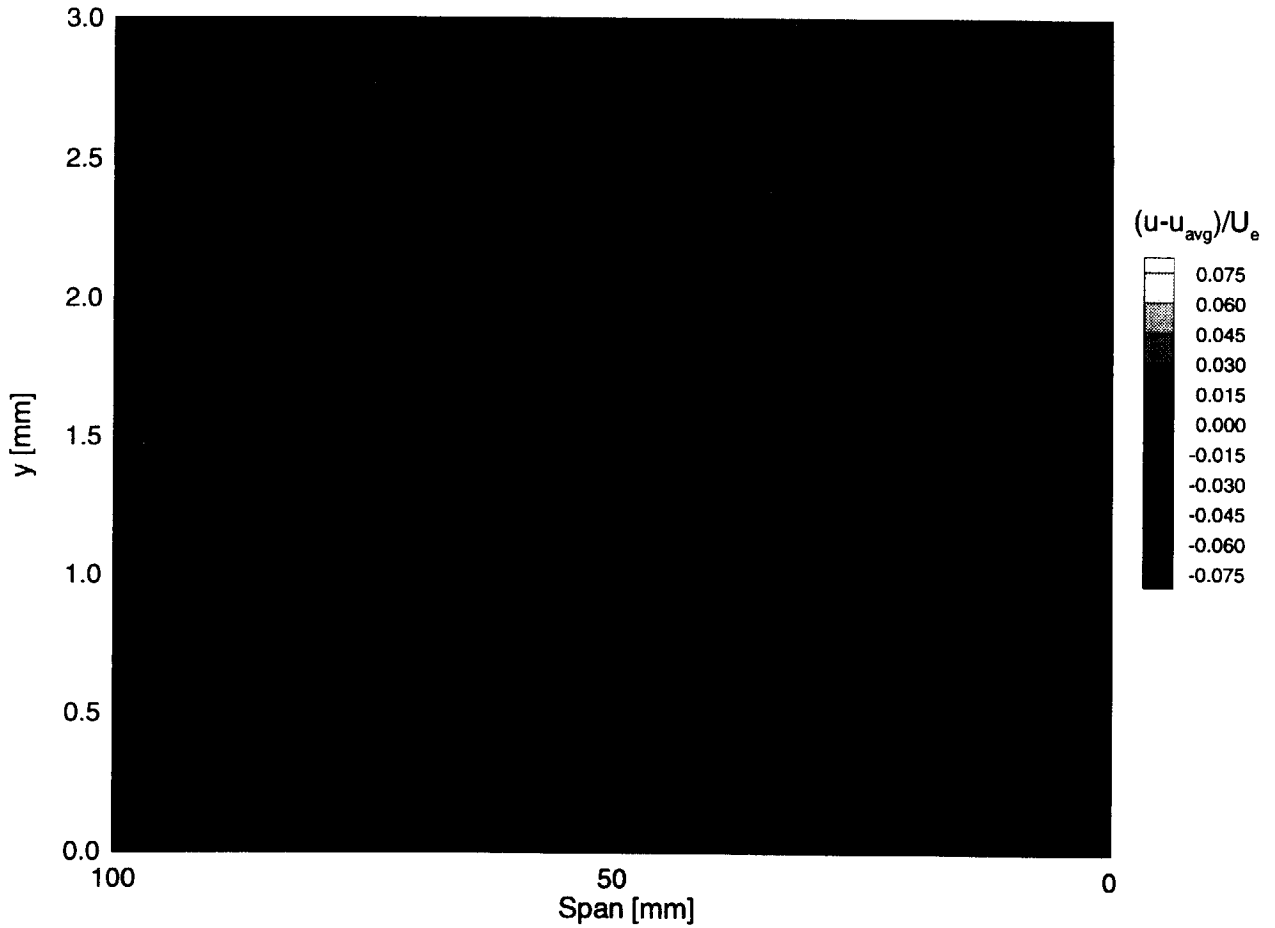

Figure 7.243. Disturbance contours for boundary-layer scans at $x/c = 0.45$. A full array of 73 μm roughness with a spacing of 12 mm is at $x/c = 0.005$. $Re_c = 3.0 \times 10^6$. Data set C.

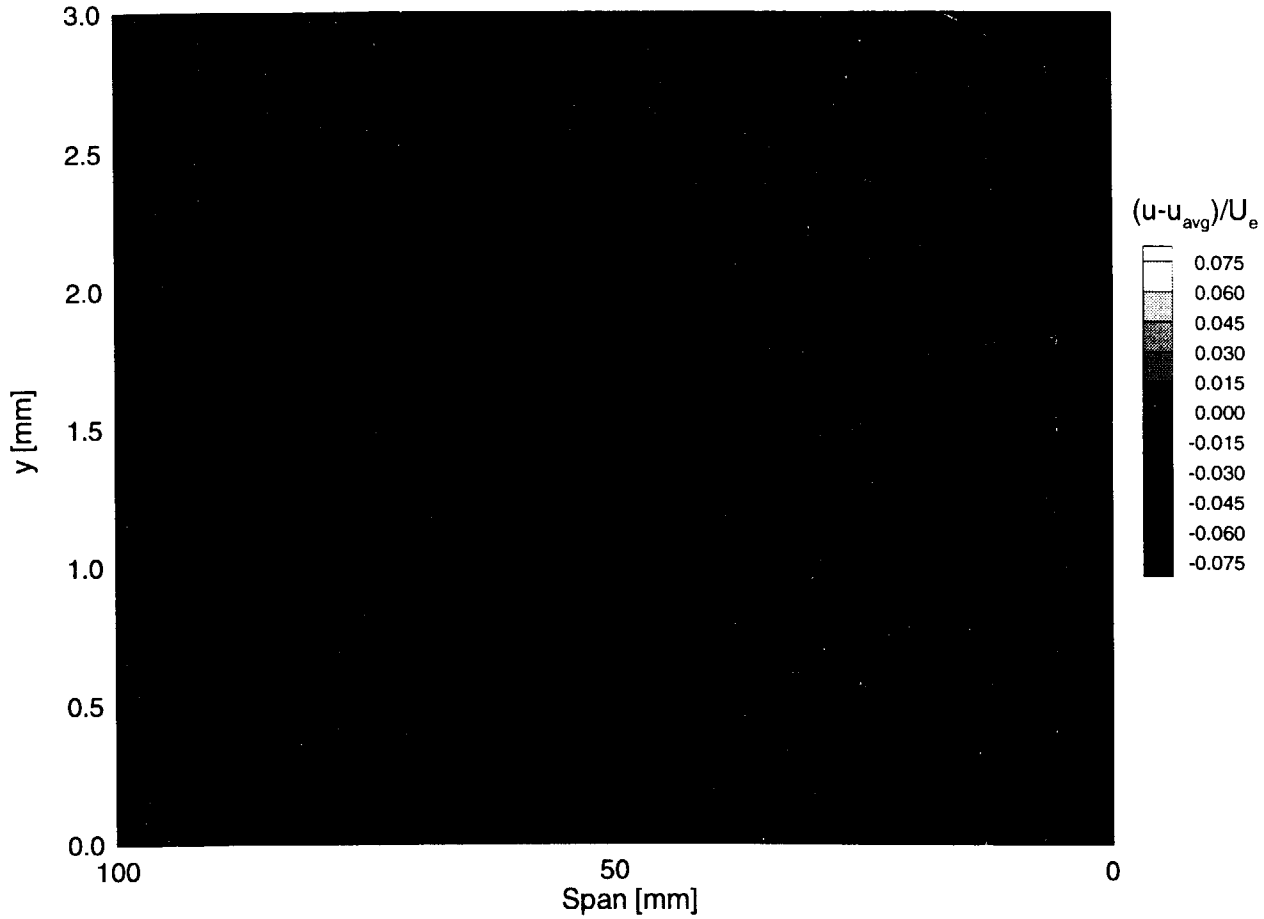

Figure 7.244. Disturbance contours for boundary-layer scans at $x/c = 0.50$. A full array of 73 μm roughness with a spacing of 12 mm is at $x/c = 0.005$. $Re_c = 3.0 \times 10^6$. Data set C.

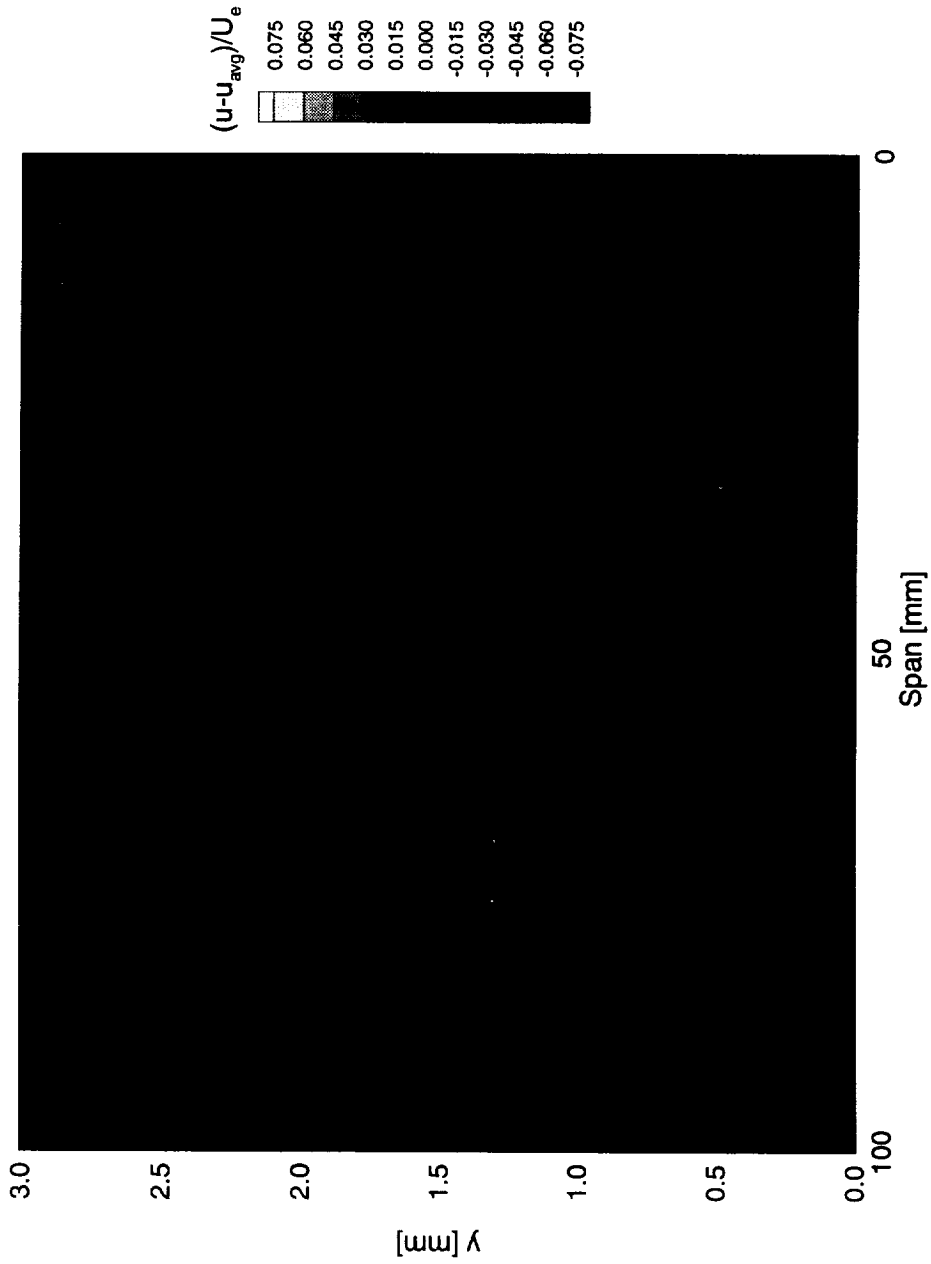

Figure 7.245. Disturbance contours for boundary-layer scans at $x/c = 0.55$. A full array of 73 μm roughness with a spacing of 12 mm is at $x/c = 0.005$. $Re_c = 3.0 \times 10^6$. Data set C.

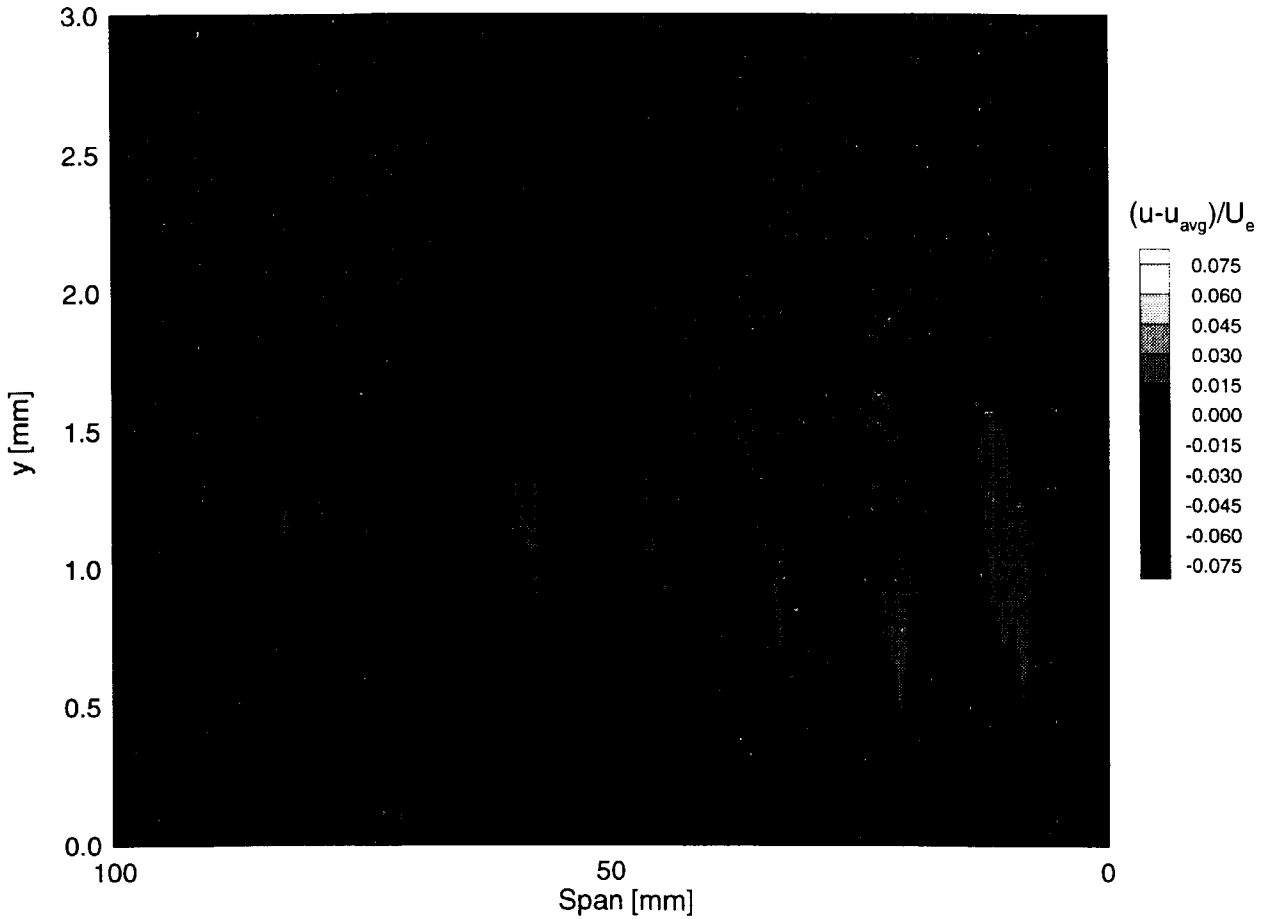

Figure 7.246. Disturbance contours for boundary-layer scans at $x/c = 0.60$. A full array of 73 μm roughness with a spacing of 12 mm is at $x/c = 0.005$. $Re_c = 3.0 \times 10^6$. Data set C.

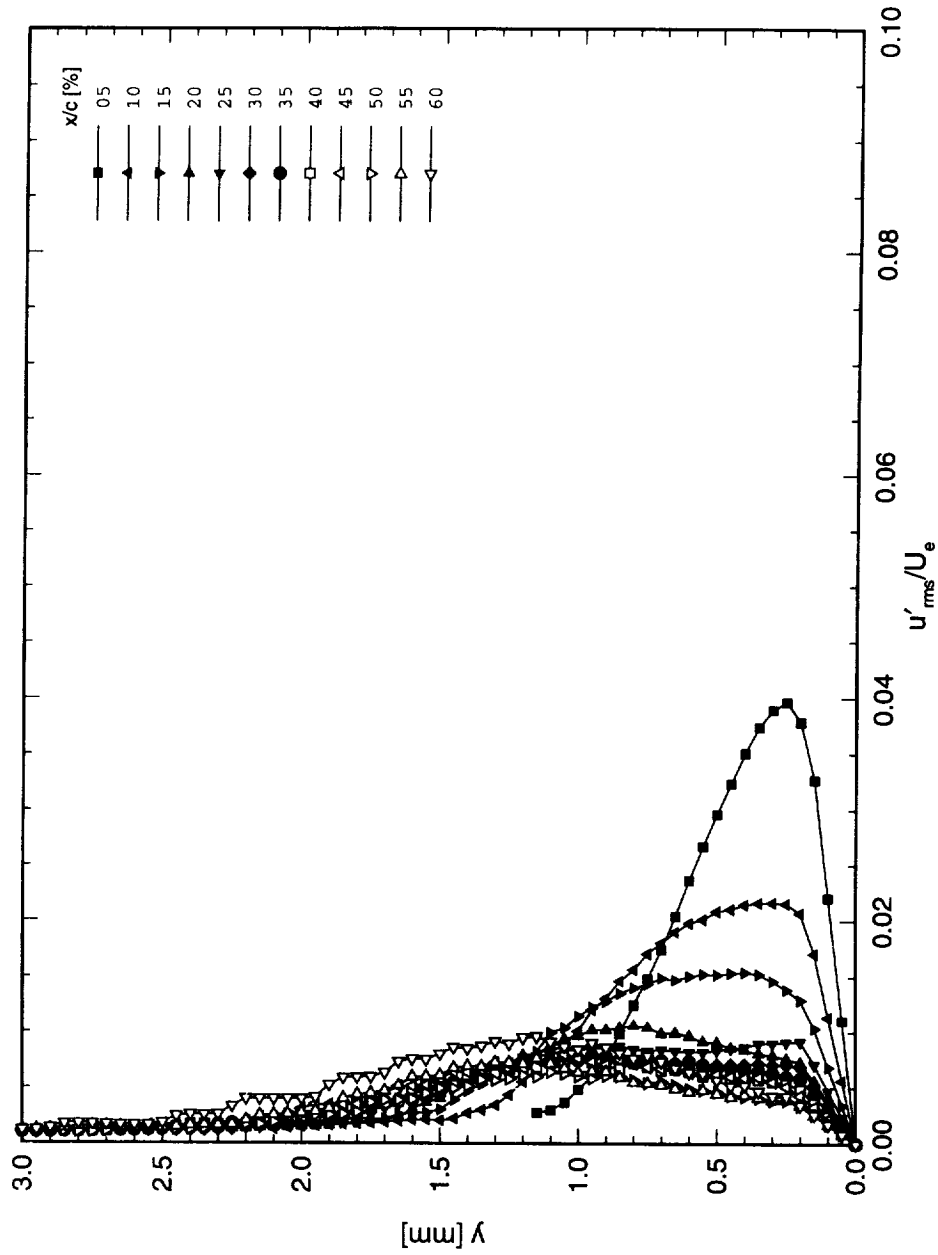

Figure 7.247. Stationary crossflow mode shapes for data set C, using rms method. $Re_c = 3.0 \times 10^6$, $\alpha = 0°$.

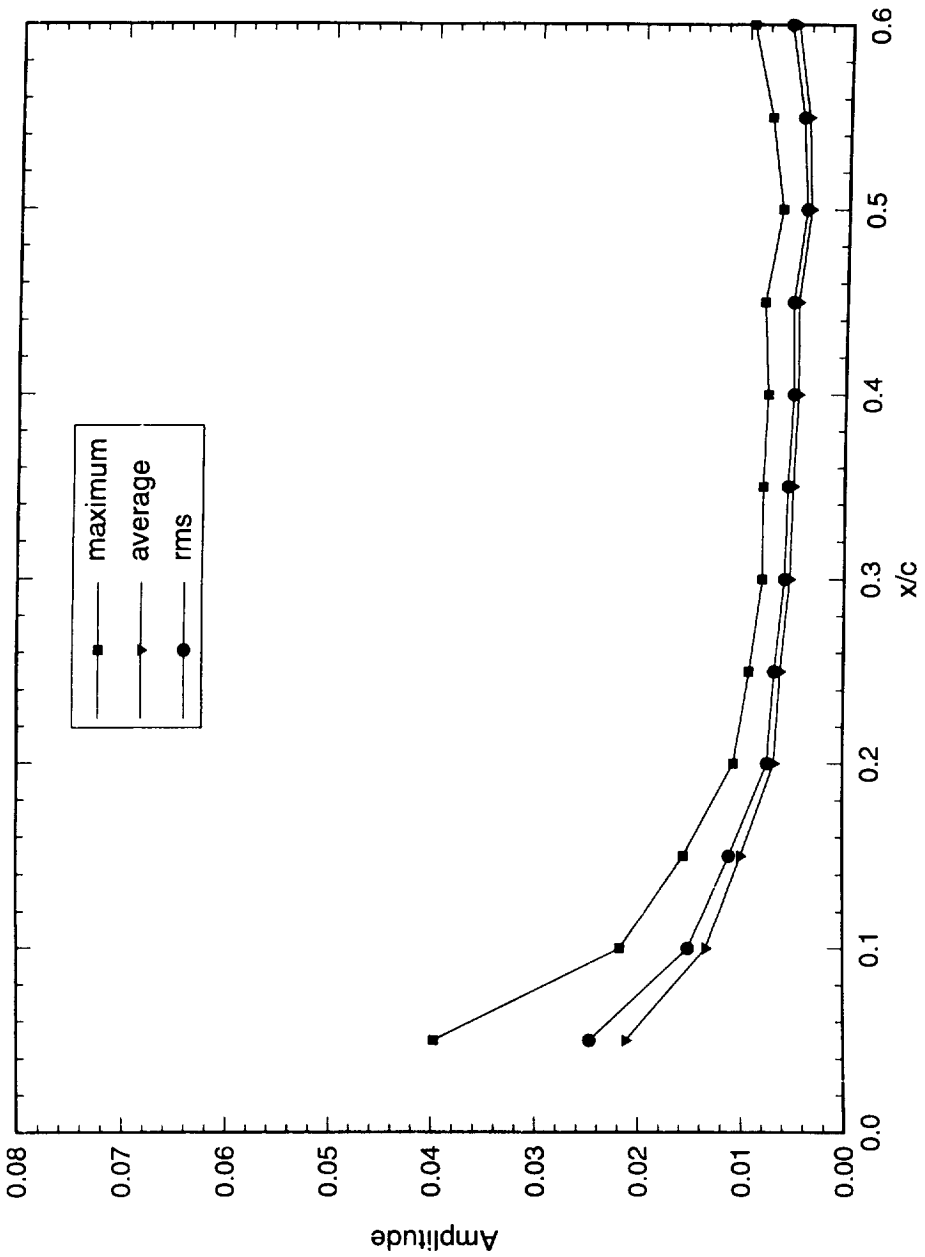

Figure 7.248. Stationary crossflow amplitudes for data set C. $Re_c = 3.0 \times 10^6$, $\alpha = 0°$.

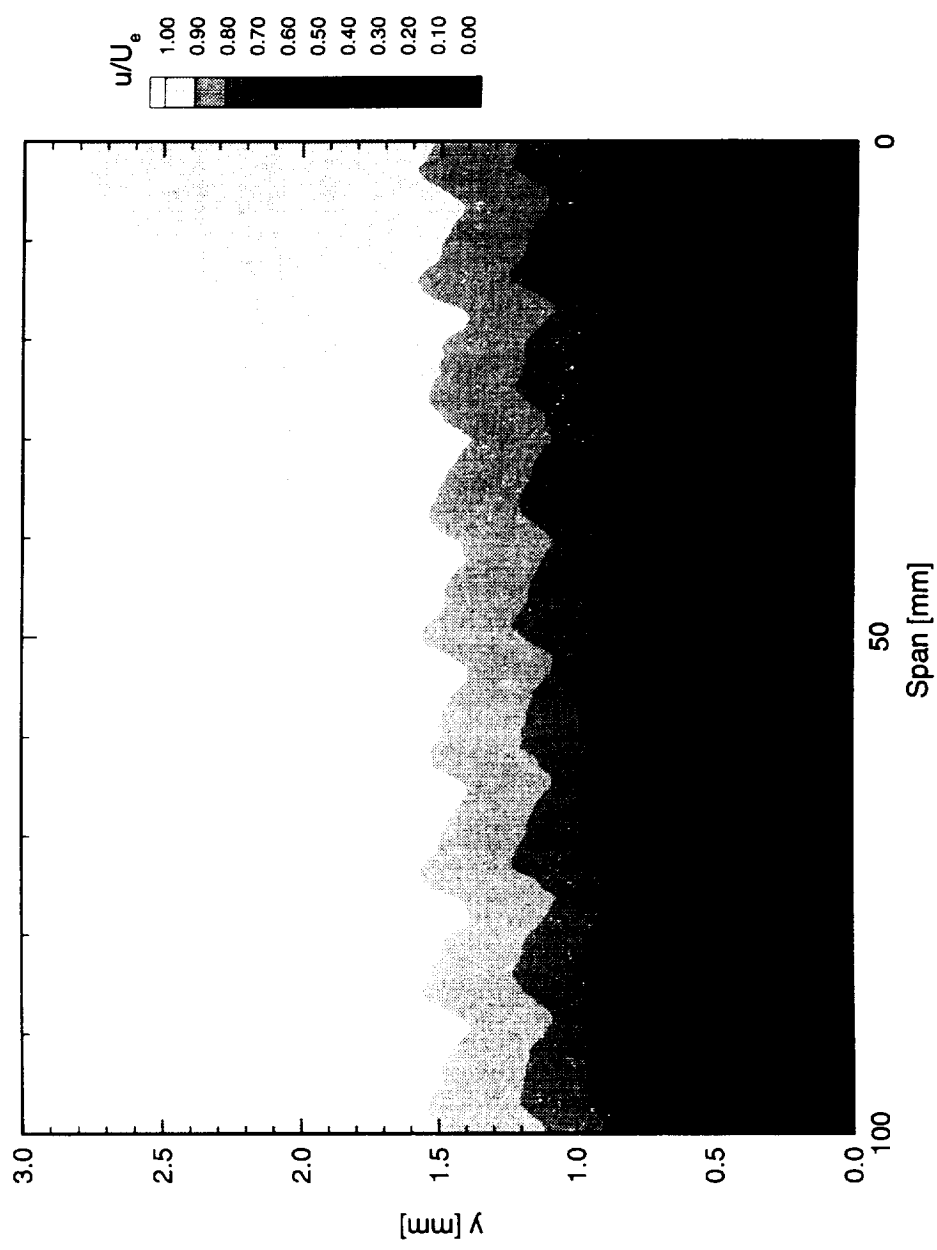

Figure 7.249. Velocity contours for boundary-layer scans at $x/c = 0.30$. A full array of 146 μm roughness with a spacing of 12 mm is at $x/c = 0.005$. $Re_c = 3.0 \times 10^6$. Data set D.

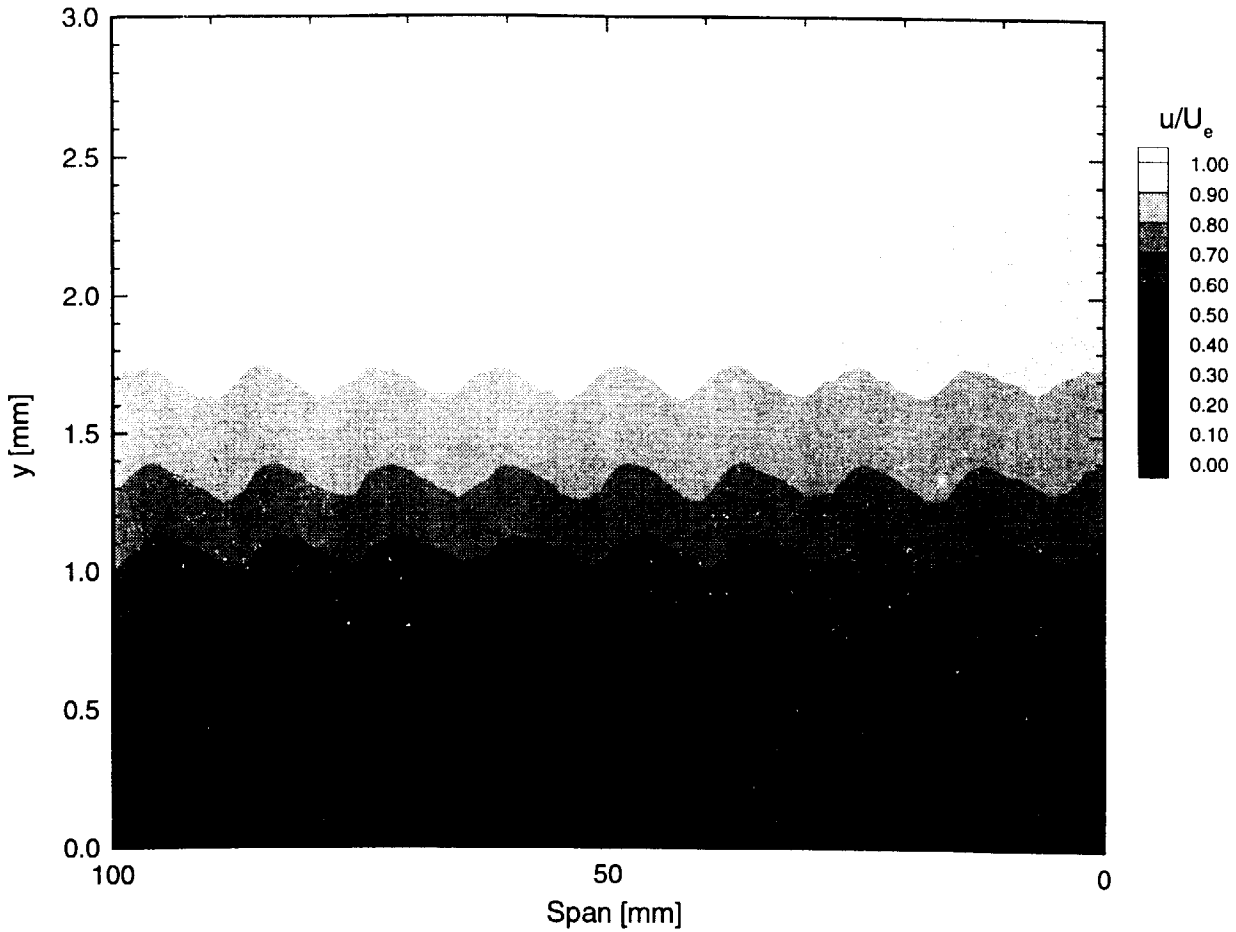

Figure 7.250. Velocity contours for boundary-layer scans at $x/c = 0.40$. A full array of 146 μm roughness with a spacing of 12 mm is at $x/c = 0.005$. $Re_c = 3.0 \times 10^6$. Data set D.

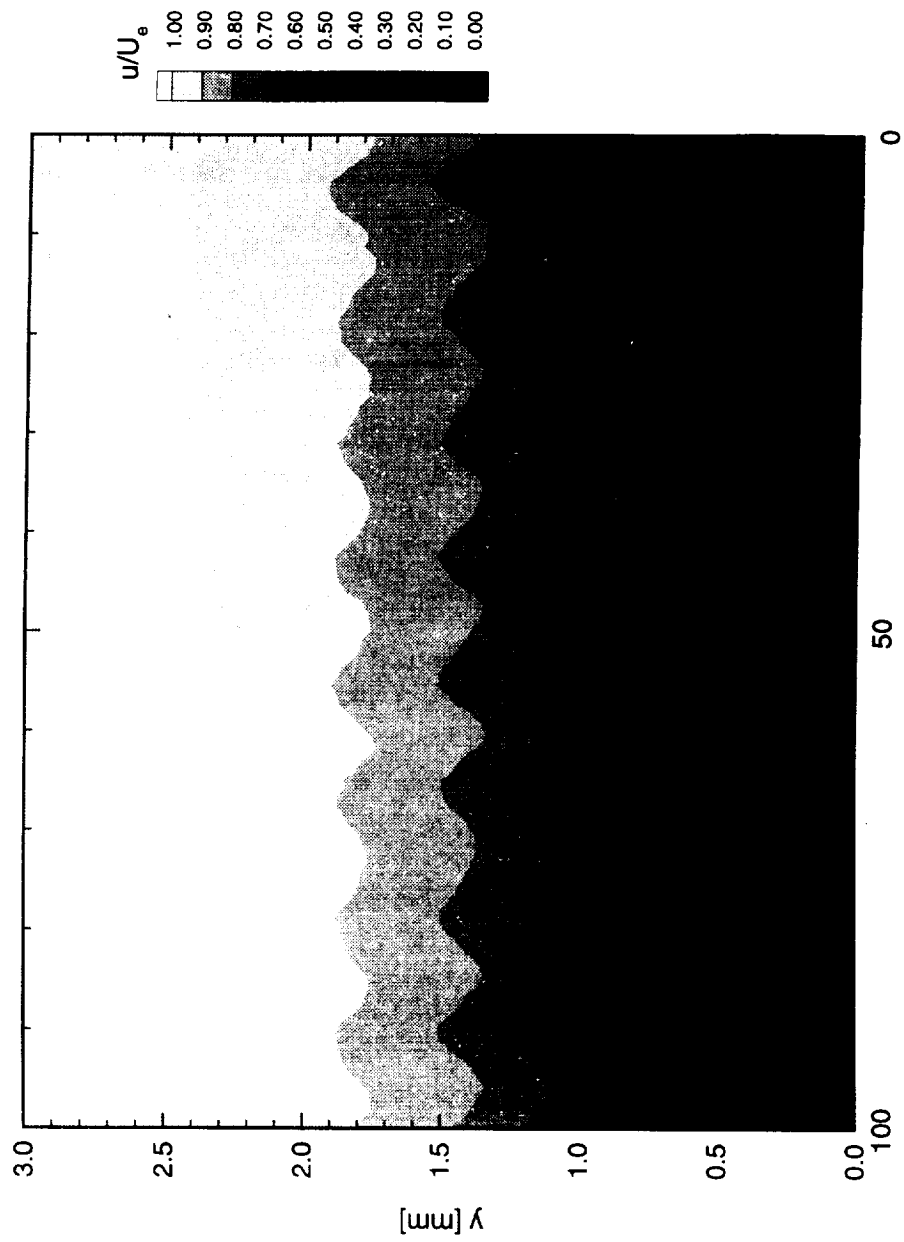

Figure 7.251. Velocity contours for boundary-layer scans at $x/c = 0.50$. A full array of 146 μm roughness with a spacing of 12 mm is at $x/c = 0.005$. $Re_c = 3.0 \times 10^6$. Data set D.

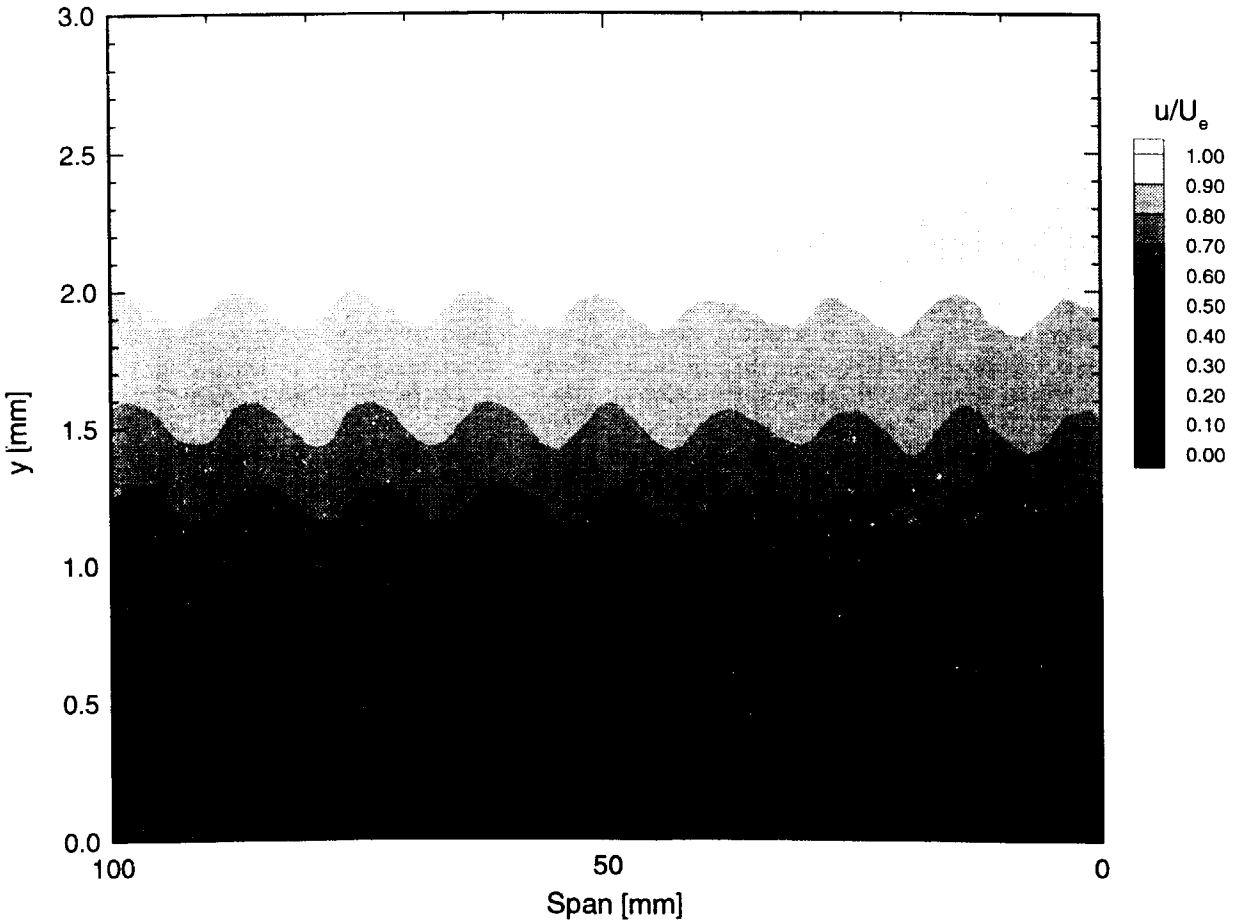

Figure 7.252. Velocity contours for boundary-layer scans at $x/c = 0.60$. A full array of 146 μm roughness with a spacing of 12 mm is at $x/c = 0.005$. $Re_c = 3.0 \times 10^6$. Data set D.

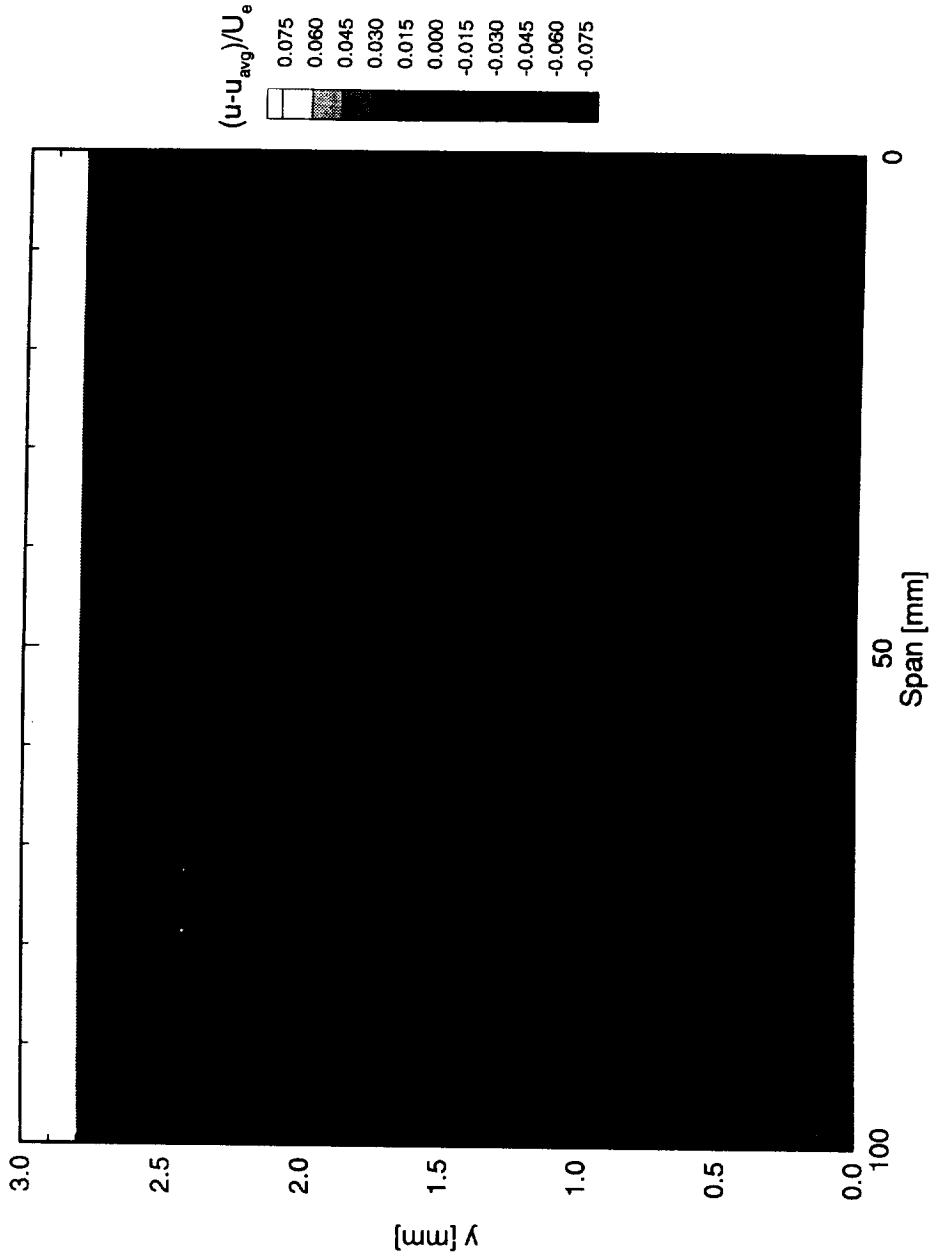

Figure 7.253. Disturbance contours for boundary-layer scans at $x/c = 0.30$. A full array of 146 μm roughness with a spacing of 12 mm is at $x/c = 0.005$. $Re_c = 3.0 \times 10^6$. Data set D.

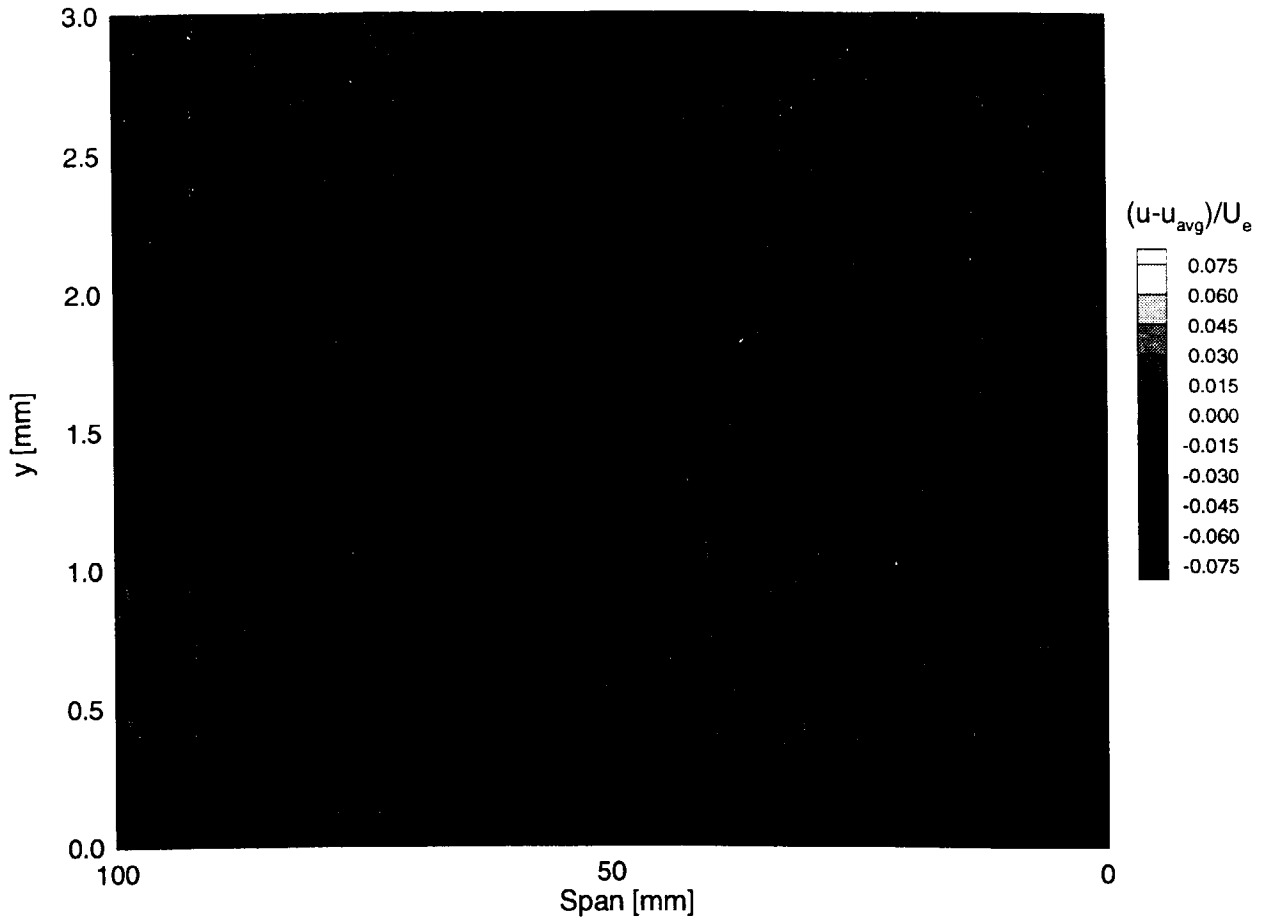

Figure 7.254. Disturbance contours for boundary-layer scans at $x/c = 0.40$. A full array of 146 μm roughness with a spacing of 12 mm is at $x/c = 0.005$. $Re_c = 3.0 \times 10^6$. Data set *D*.

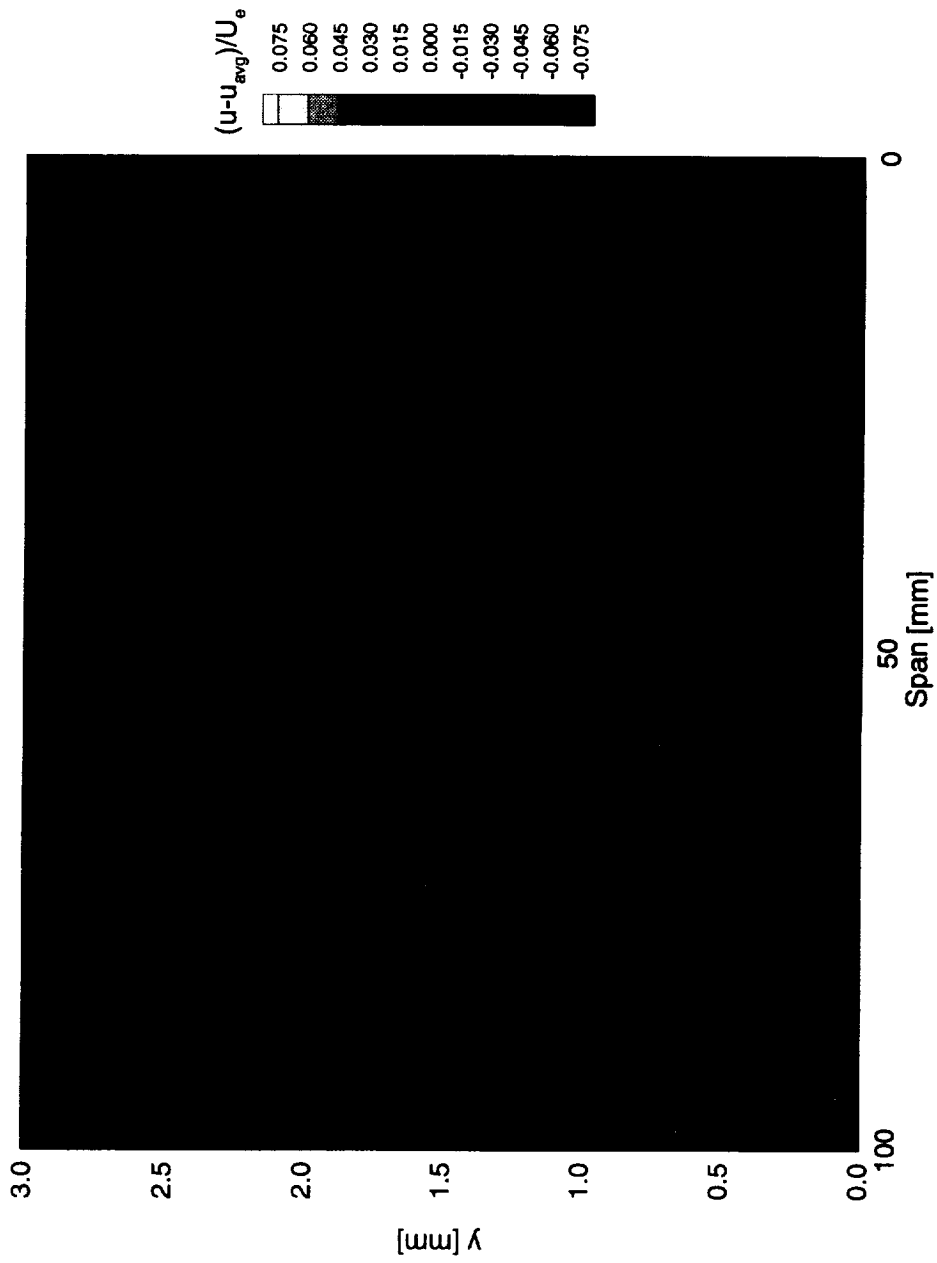

Figure 7.255. Disturbance contours for boundary-layer scans at $x/c = 0.50$. A full array of 146 μm roughness with a spacing of 12 mm is at $x/c = 0.005$. $Re_c = 3.0 \times 10^6$. Data set D.

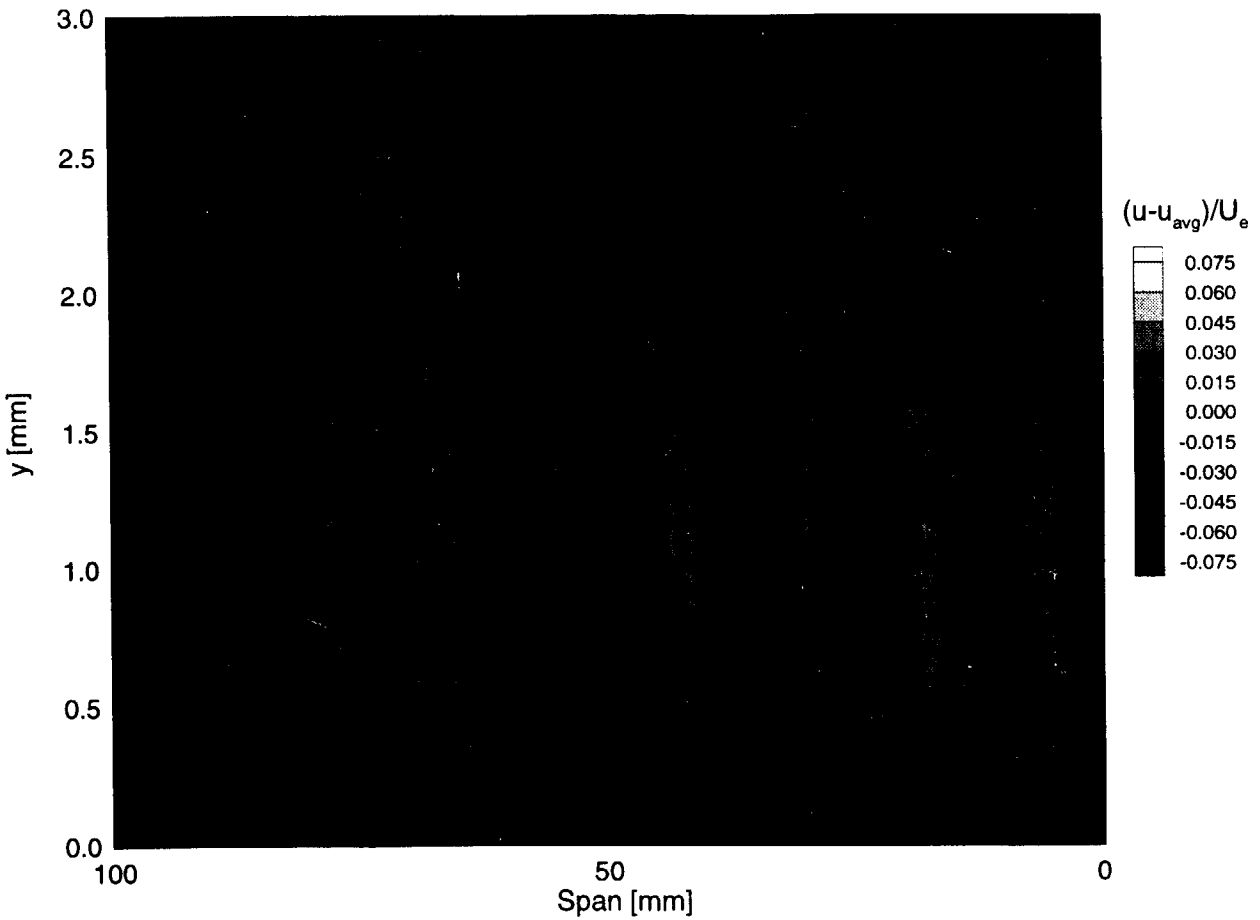

Figure 7.256. Disturbance contours for boundary-layer scans at $x/c = 0.60$. A full array of 146 μm roughness with a spacing of 12 mm is at $x/c = 0.005$. $Re_c = 3.0 \times 10^6$. Data set D.

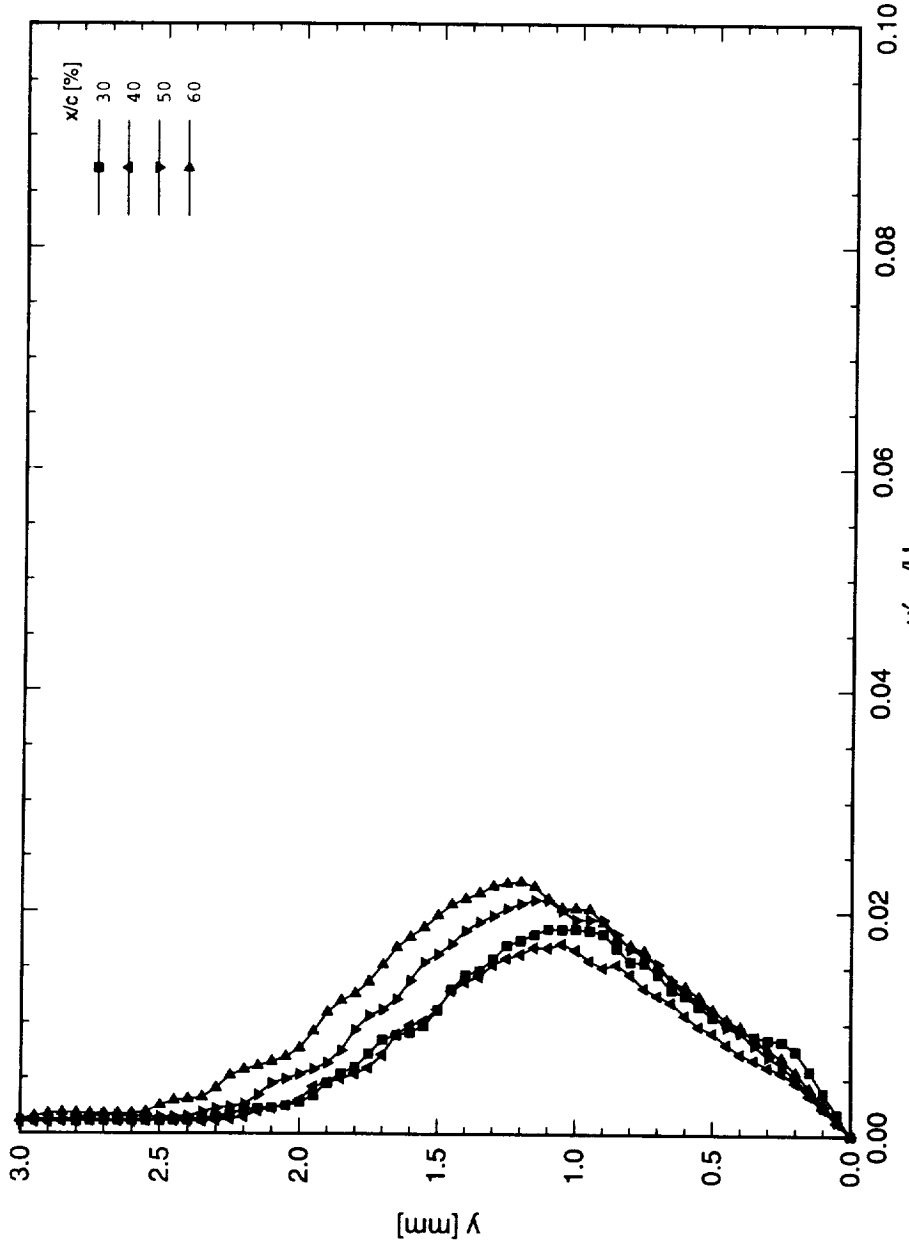

Figure 7.257. Stationary crossflow mode shapes for data set D, using rms method. $Re_c = 3.0 \times 10^6$, $\alpha = 0°$.

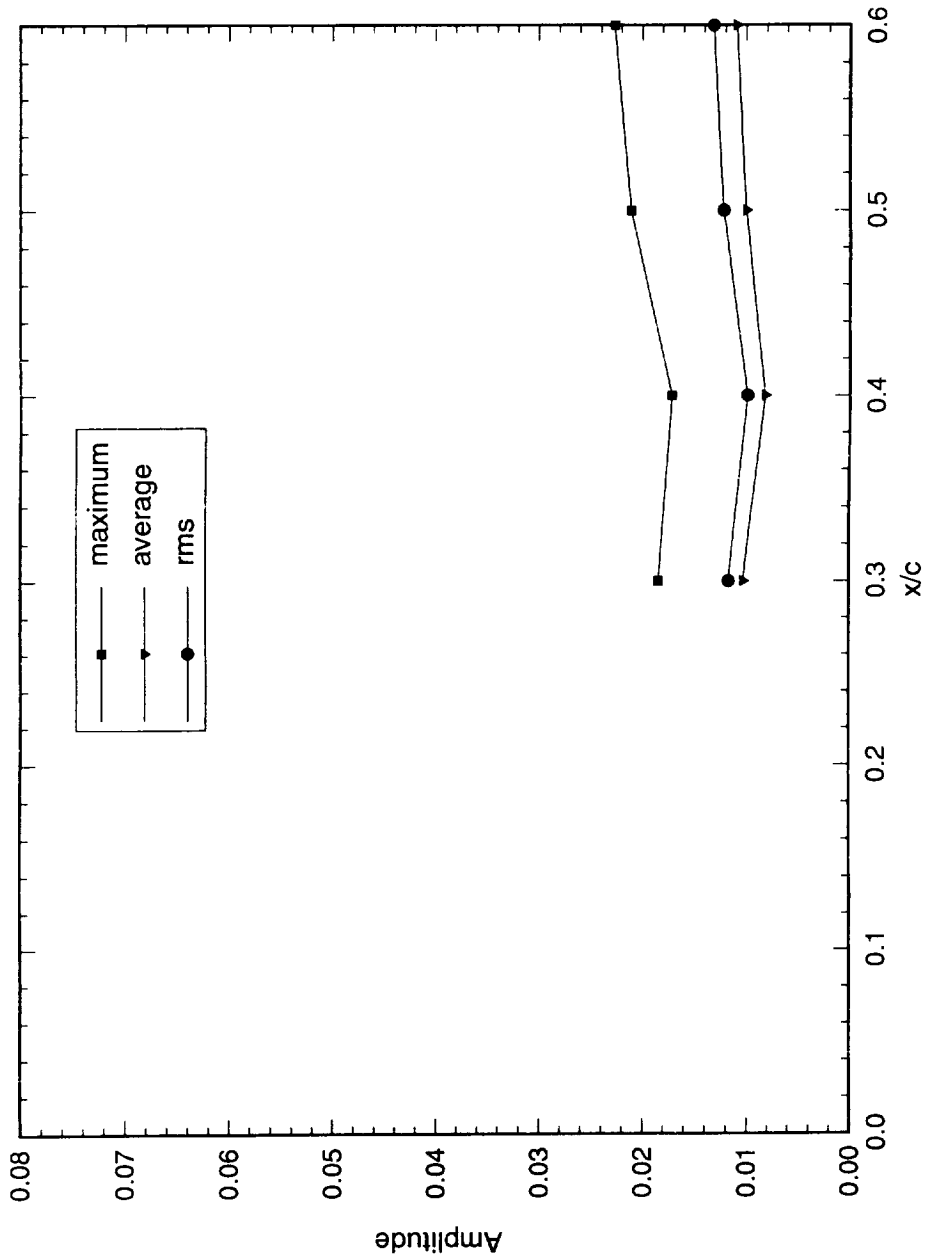

Figure 7.258. Stationary crossflow amplitudes for data set D. $Re_c = 3.0 \times 10^6$, $\alpha = 0°$.

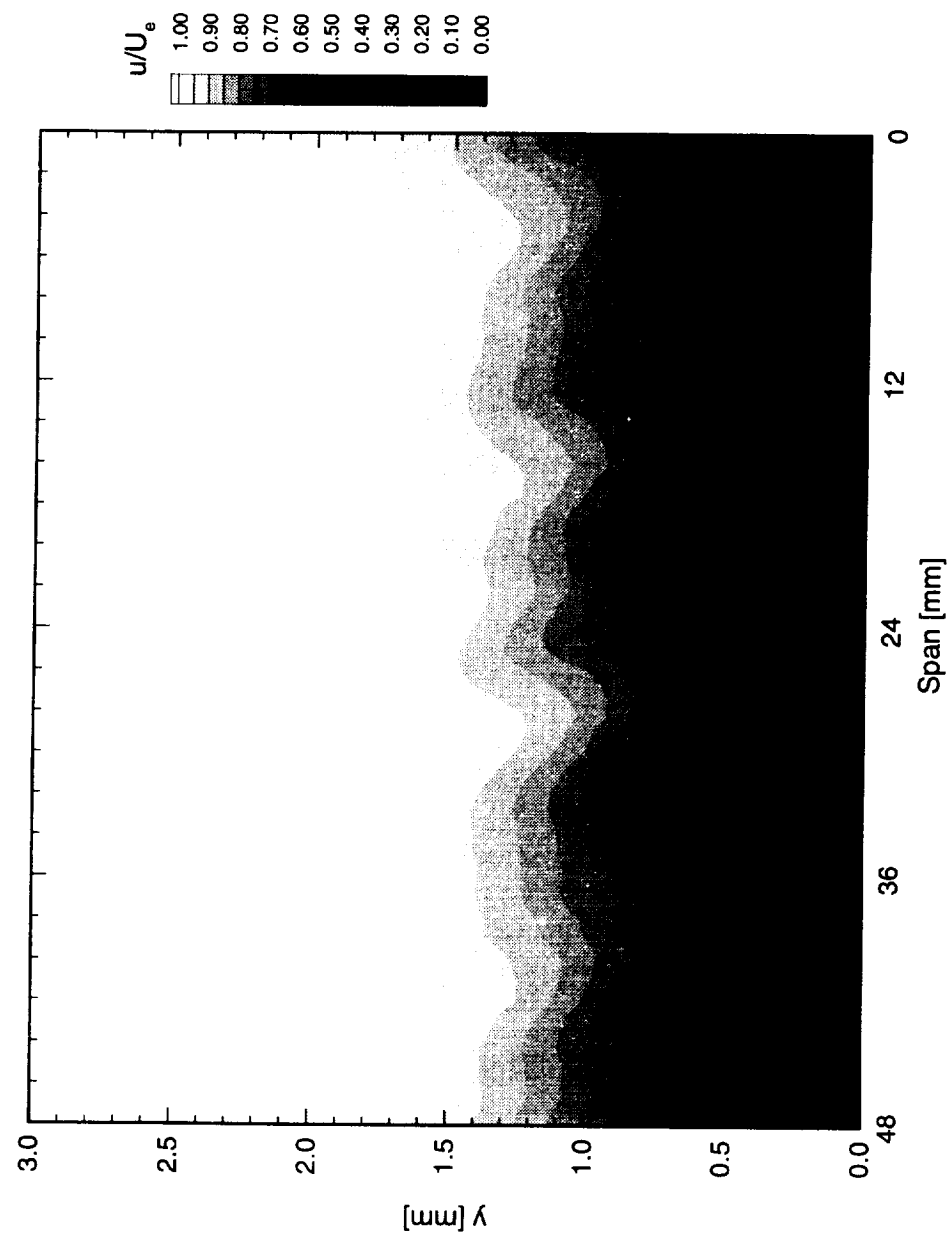

Figure 7.259. Velocity contours for boundary-layer scans at $x/c = 0.30$. A full array of 146 μm roughness with a spacing of 12 mm is at $x/c = 0.005$. $Re_c = 3.6 \times 10^6$. Data set J.

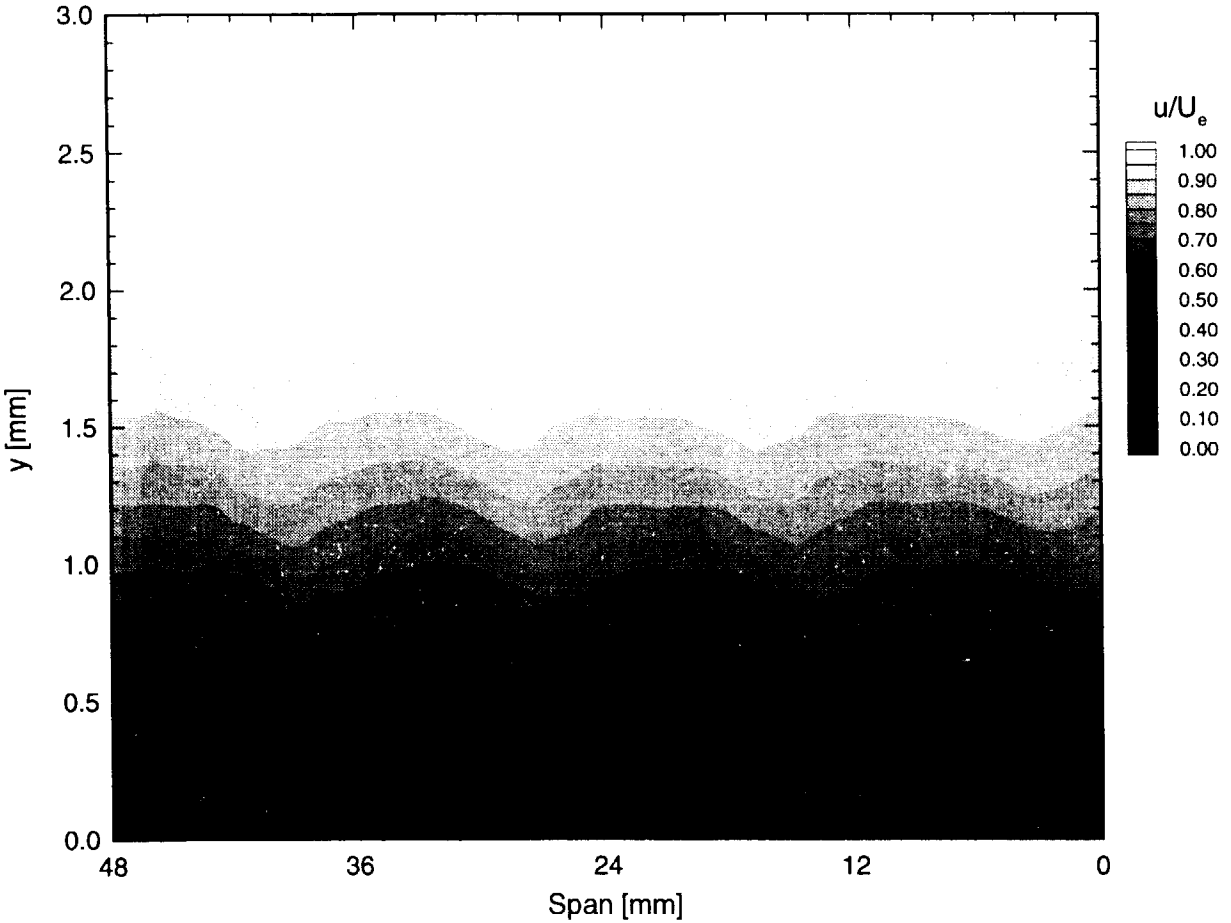

Figure 7.260. Velocity contours for boundary-layer scans at $x/c = 0.40$. A full array of 146 μm roughness with a spacing of 12 mm is at $x/c = 0.005$. $Re_c = 3.6 \times 10^6$. Data set J.

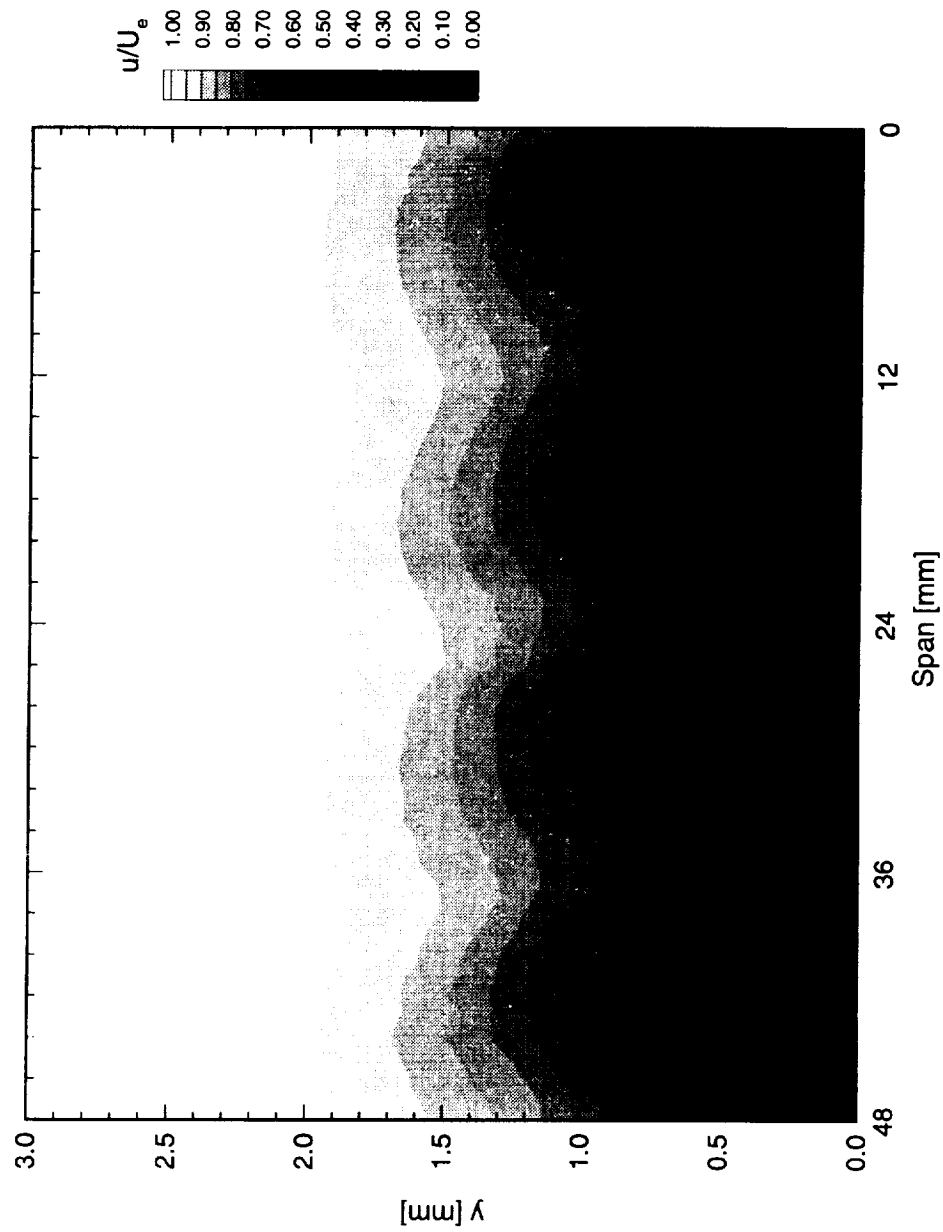

Figure 7.261. Velocity contours for boundary-layer scans at $x/c = 0.50$. A full array of 146 μm roughness with a spacing of 12 mm is at $x/c = 0.005$. $Re_c = 3.6 \times 10^6$. Data set J.

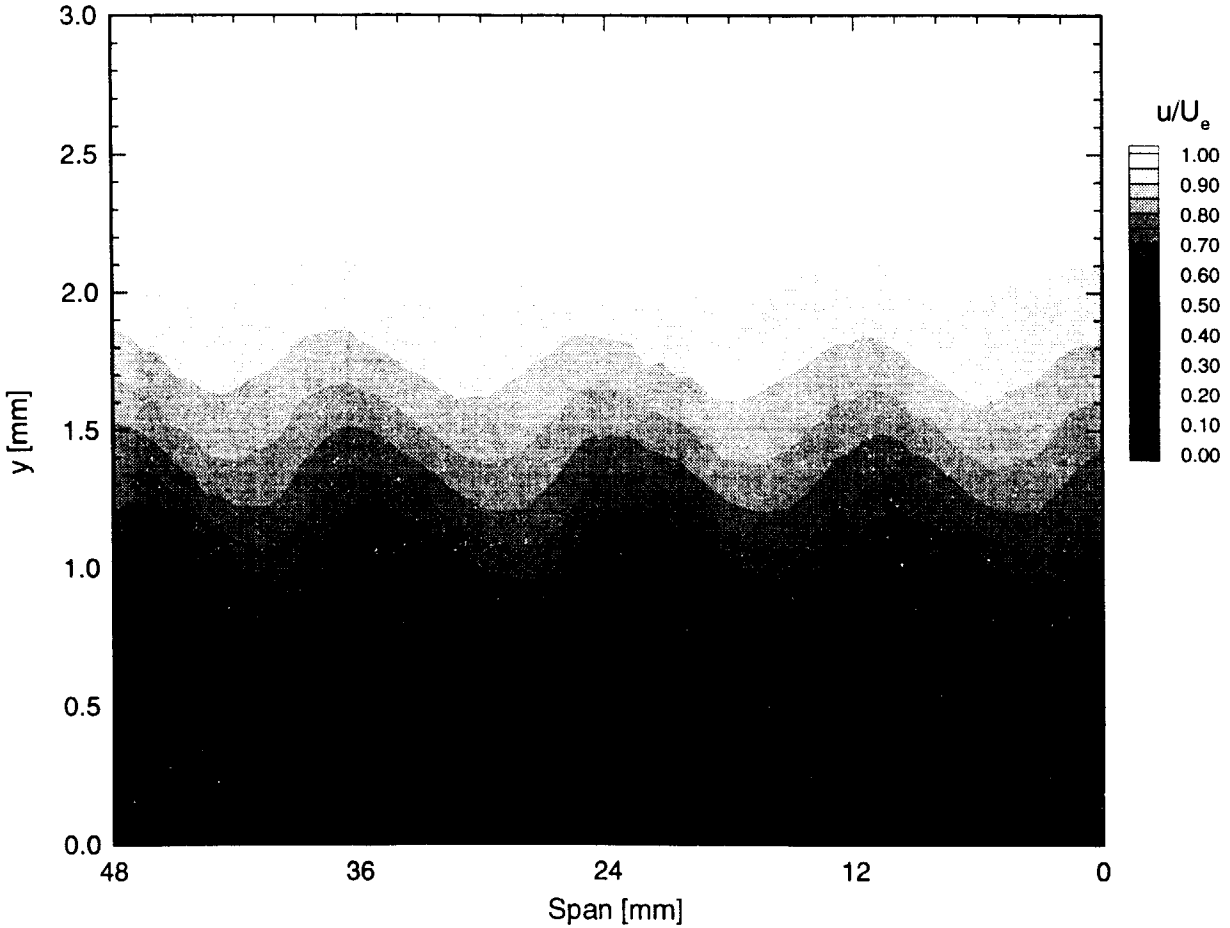

Figure 7.262. Velocity contours for boundary-layer scans at $x/c = 0.60$. A full array of 146 μm roughness with a spacing of 12 mm is at $x/c = 0.005$. $Re_c = 3.6 \times 10^6$. Data set J.

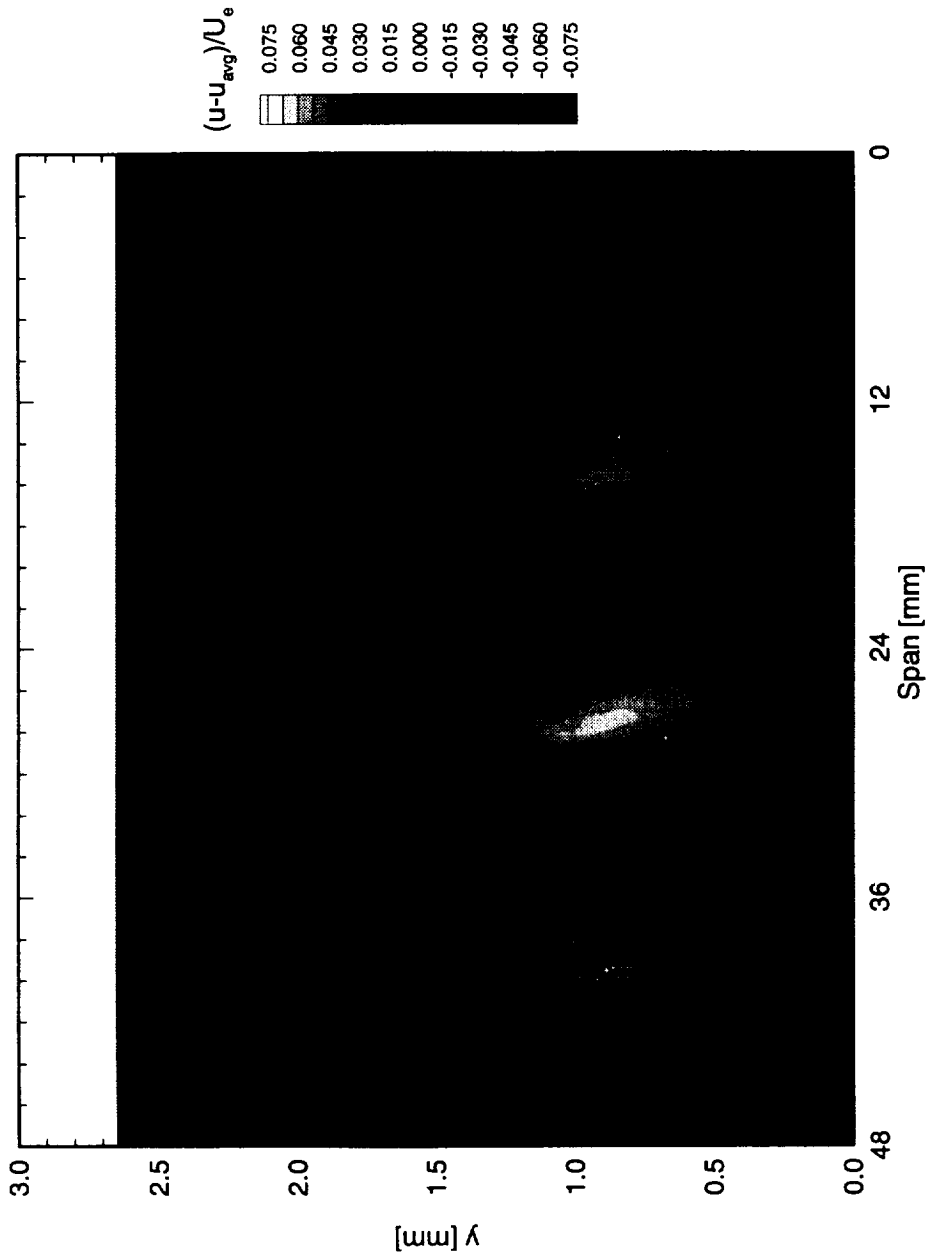

Figure 7.263. Disturbance contours for boundary-layer scans at $x/c = 0.30$. A full array of 146 μm roughness with a spacing of 12 mm is at $x/c = 0.005$. $Re_c = 3.6 \times 10^6$. Data set J.

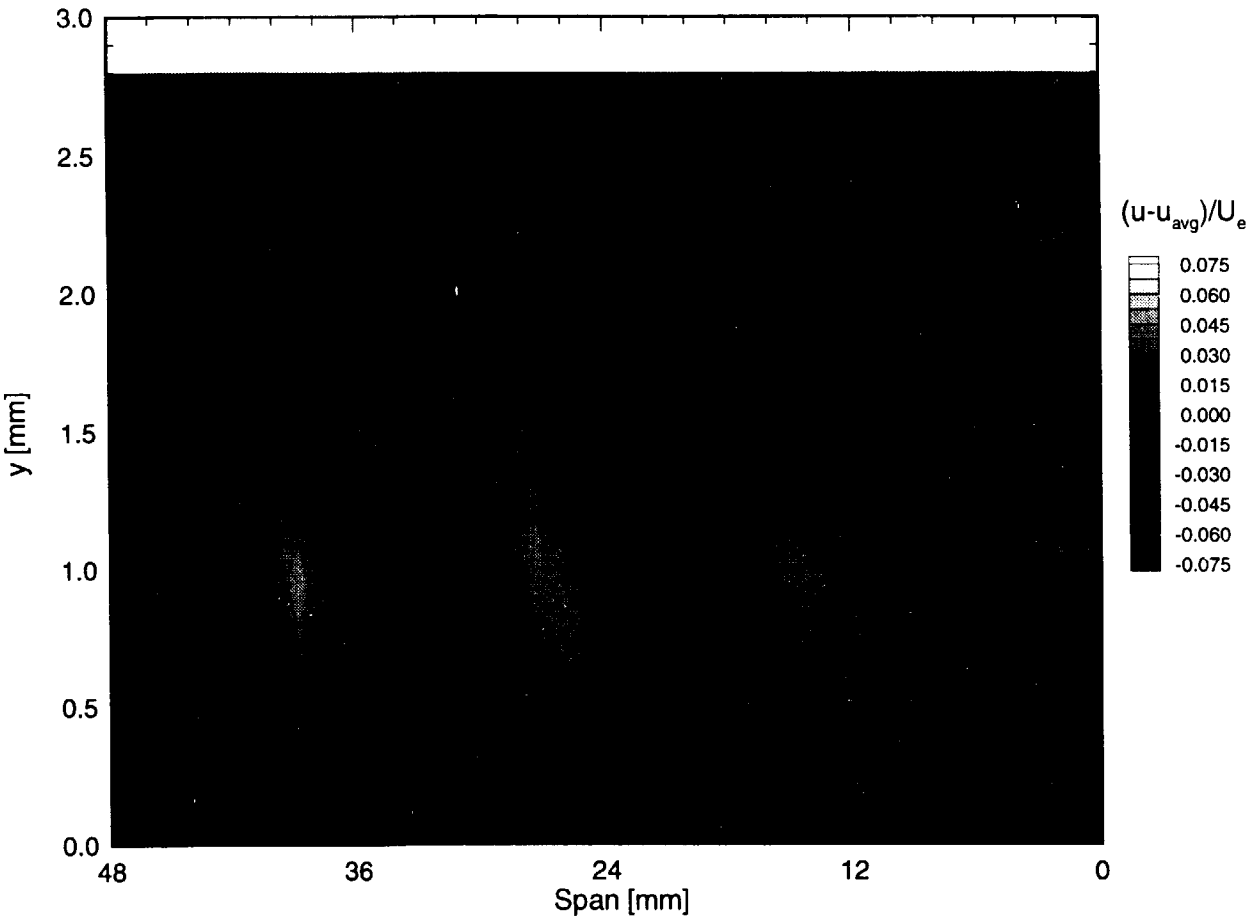

Figure 7.264. Disturbance contours for boundary-layer scans at $x/c = 0.40$. A full array of 146 μm roughness with a spacing of 12 mm is at $x/c = 0.005$. $Re_c = 3.6 \times 10^6$. Data set J.

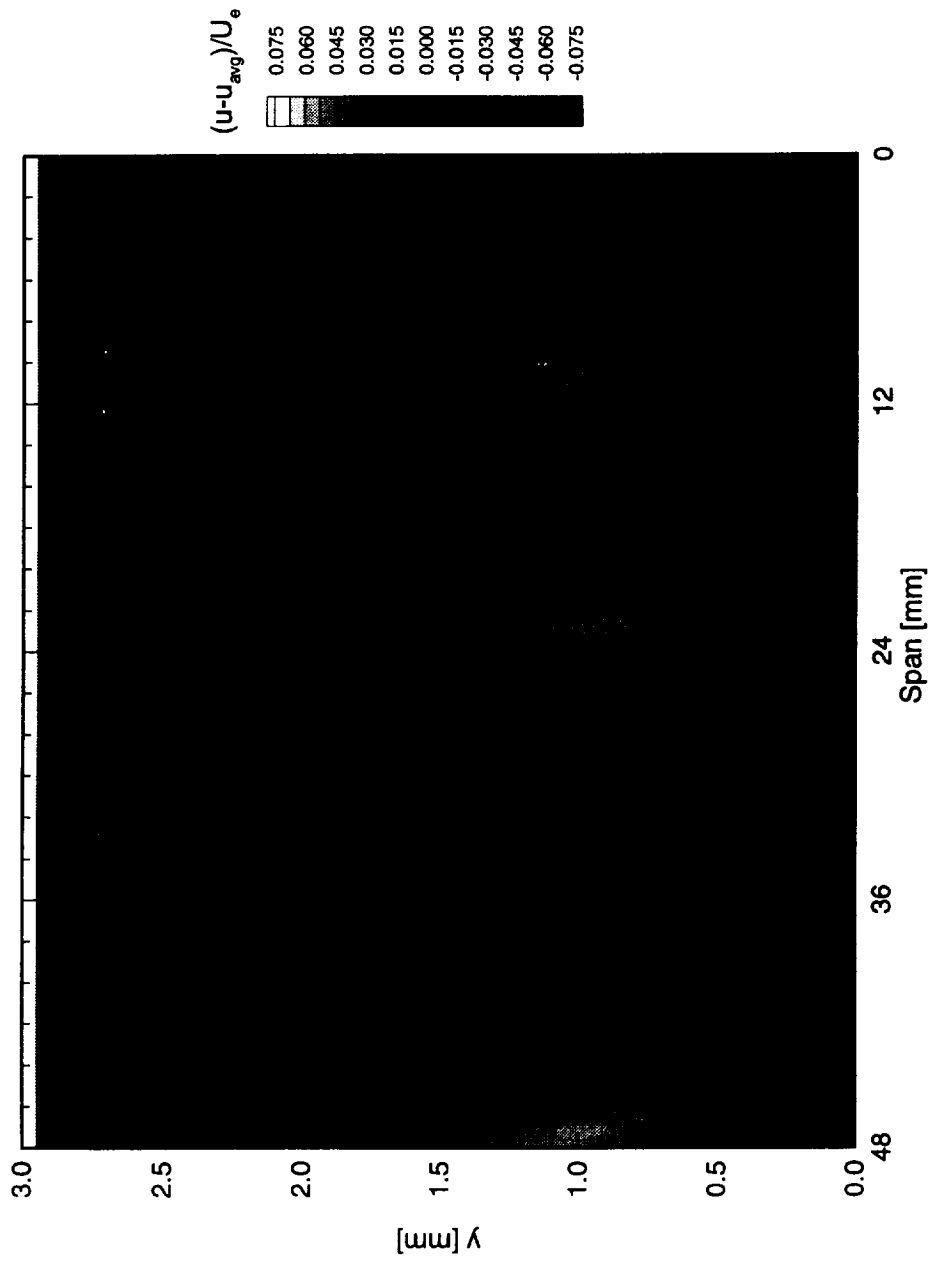

Figure 7.265. Disturbance contours for boundary-layer scans at $x/c = 0.50$. A full array of 146 μm roughness with a spacing of 12 mm is at $x/c = 0.005$. $Re_c = 3.6 \times 10^6$. Data set J.

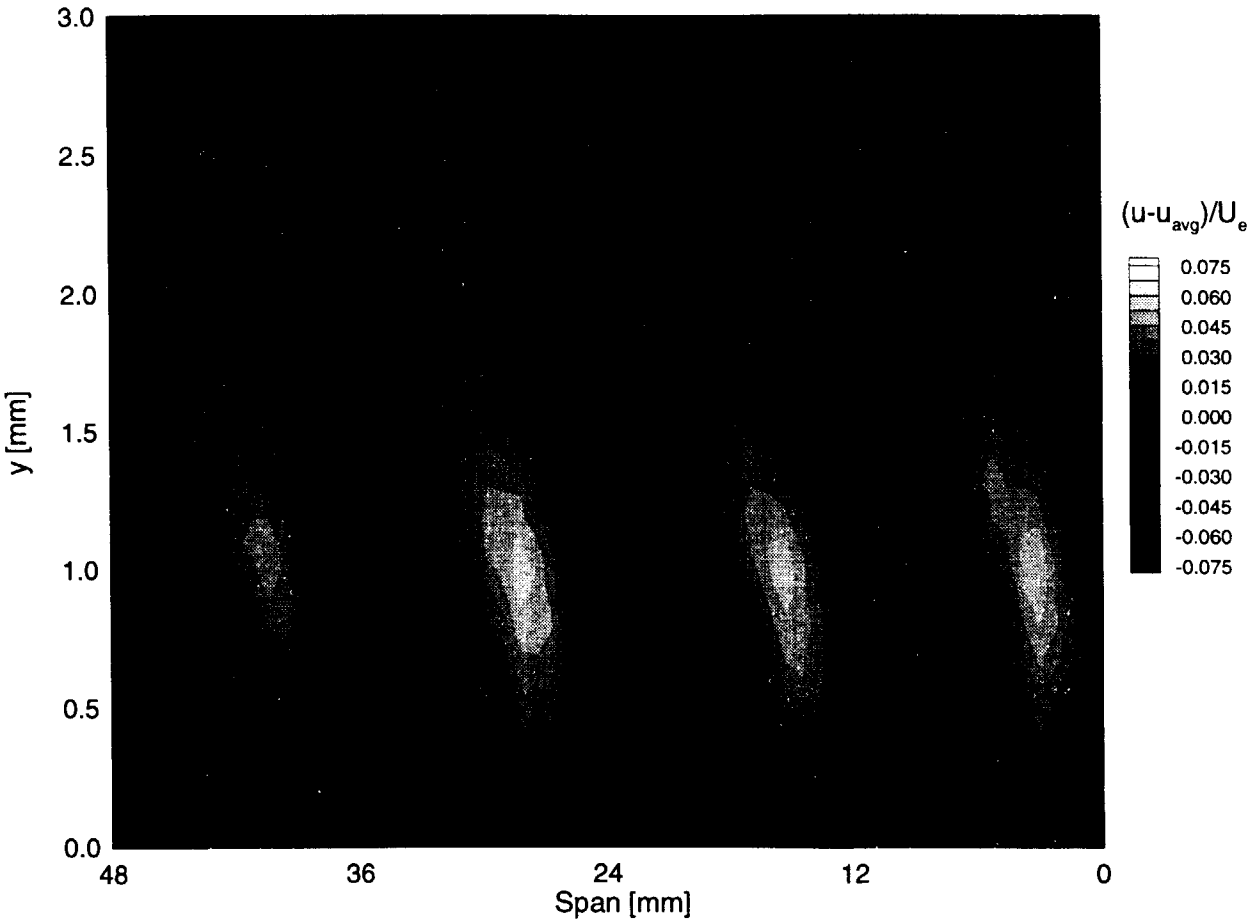

Figure 7.266. Disturbance contours for boundary-layer scans at $x/c = 0.60$. A full array of 146 μm roughness with a spacing of 12 mm is at $x/c = 0.005$. $Re_c = 3.6 \times 10^6$. Data set J.

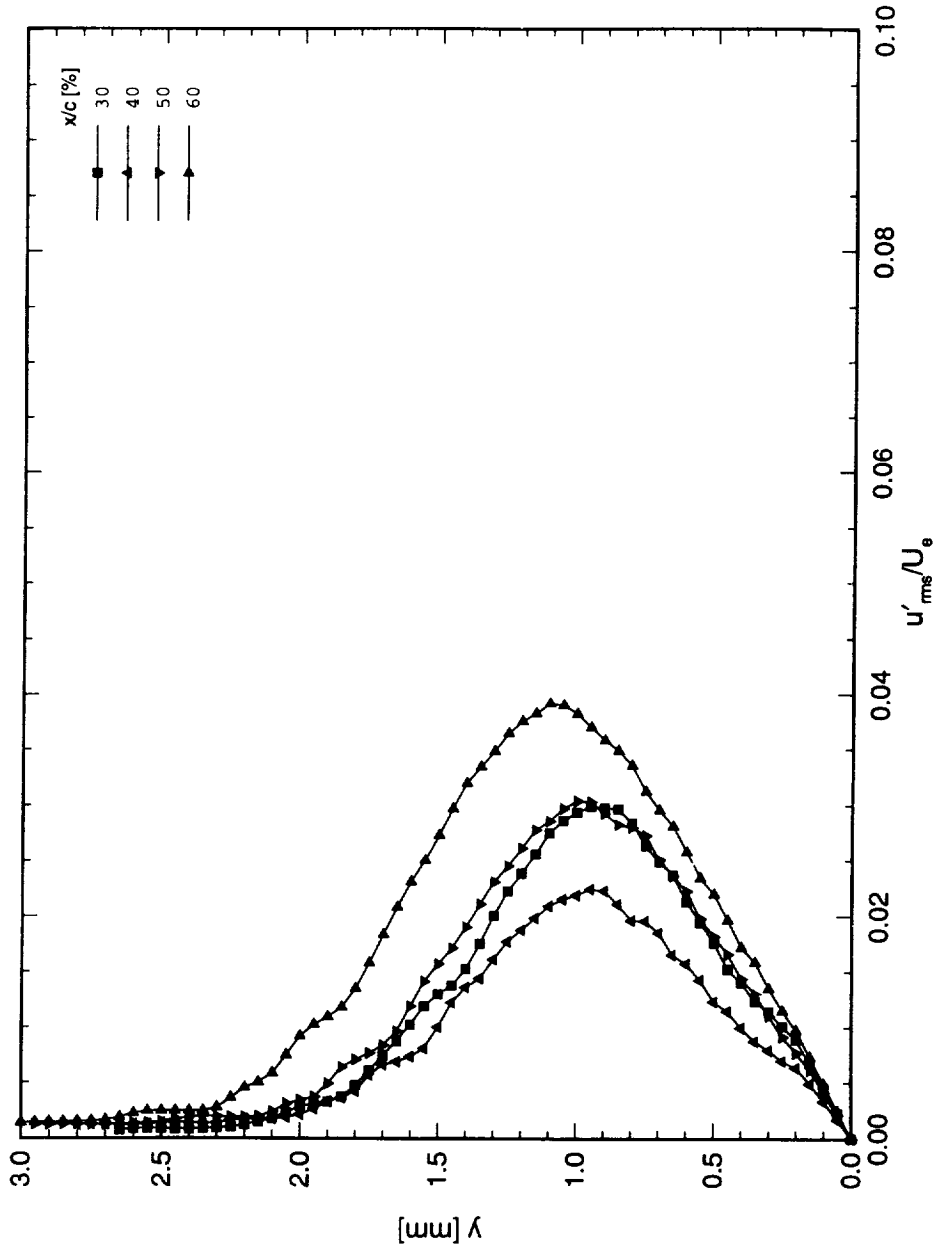

Figure 7.267. Stationary crossflow mode shapes for data set J, using rms method. $Re_c = 3.6 \times 10^6$, $\alpha = 0°$.

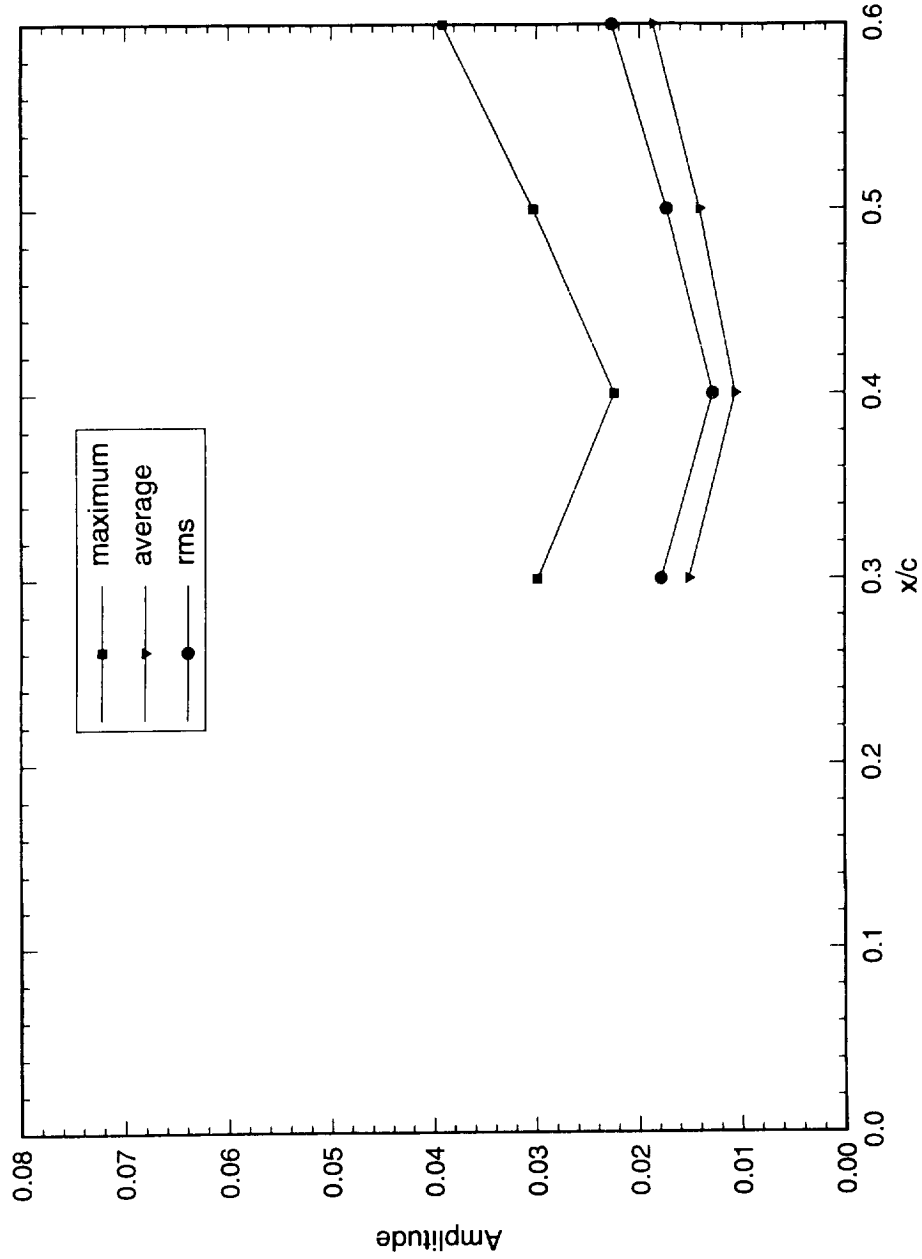

Figure 7.268. Stationary crossflow amplitudes for data set *J*. $Re_c = 3.6 \times 10^6$, $\alpha = 0°$.

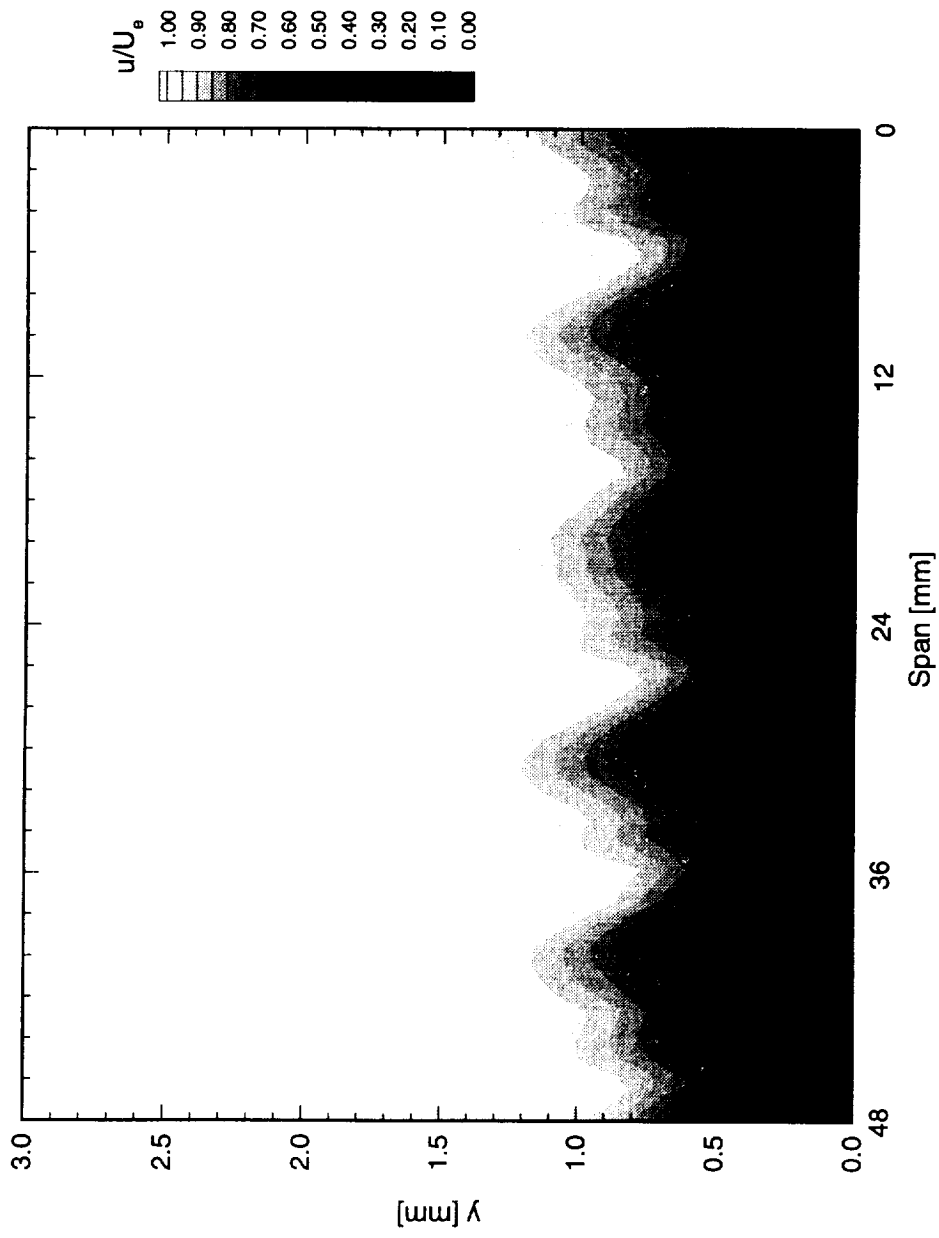

Figure 7.269. Velocity contours for boundary-layer scans at $x/c = 0.10$. A full array of 146 μm roughness with a spacing of 10 mm is at $x/c = 0.005$. $Re_c = 3.0 \times 10^6$. Data set L.

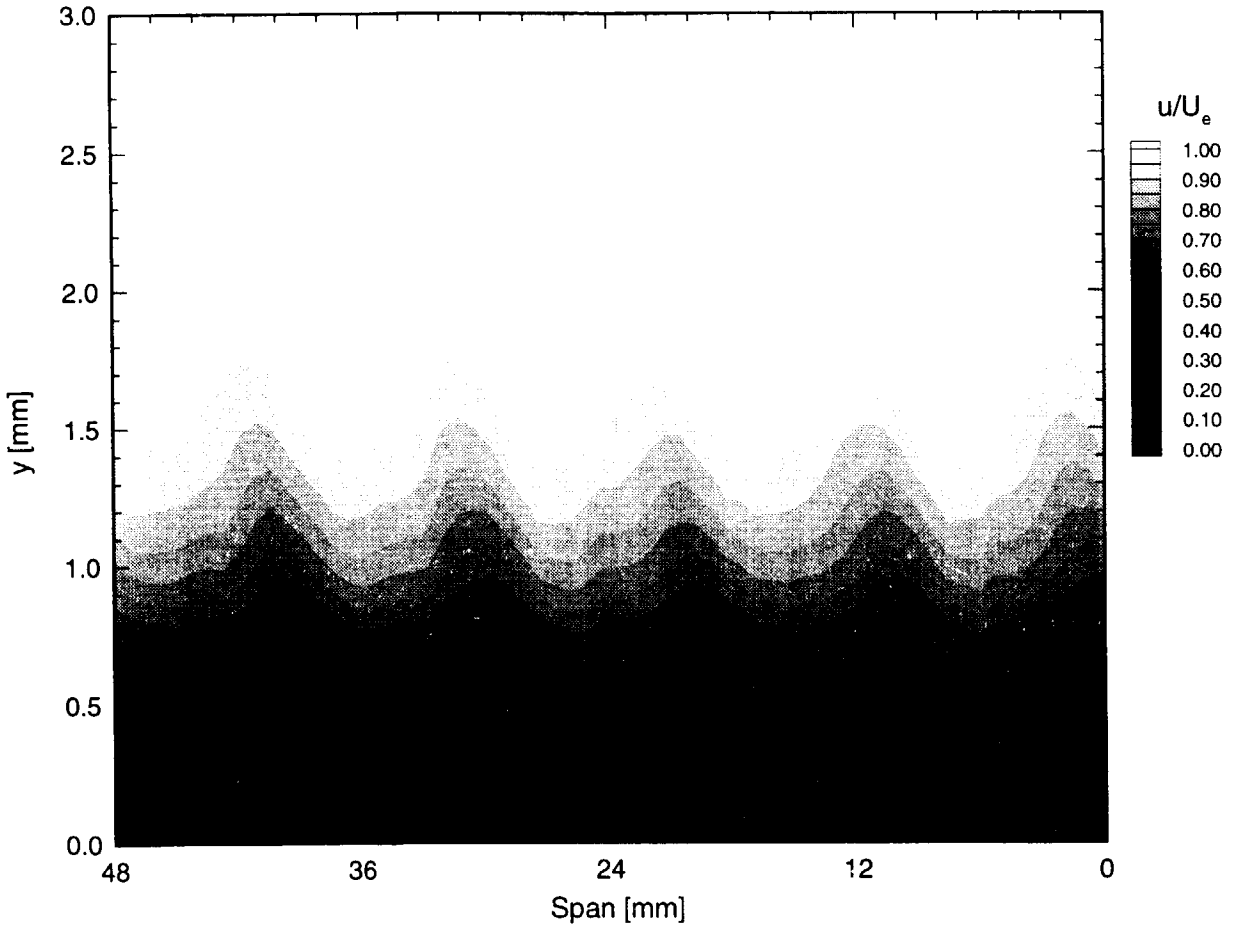

Figure 7.270. Velocity contours for boundary-layer scans at $x/c = 0.20$. A full array of 146 μm roughness with a spacing of 10 mm is at $x/c = 0.005$. $Re_c = 3.0 \times 10^6$. Data set L.

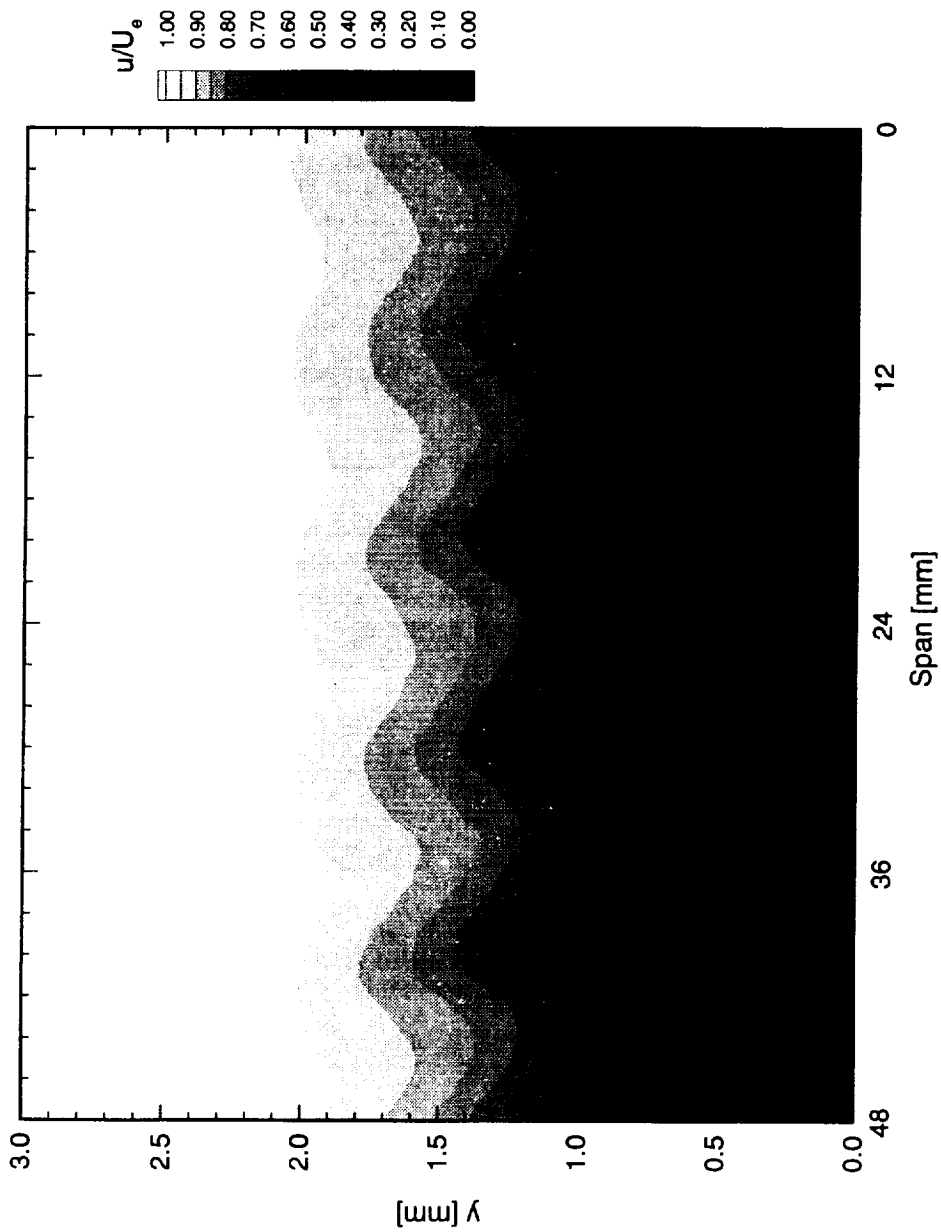

Figure 7.271. Velocity contours for boundary-layer scans at $x/c = 0.40$. A full array of 146 μm roughness with a spacing of 10 mm is at $x/c = 0.005$. $Re_c = 3.0 \times 10^6$. Data set L.

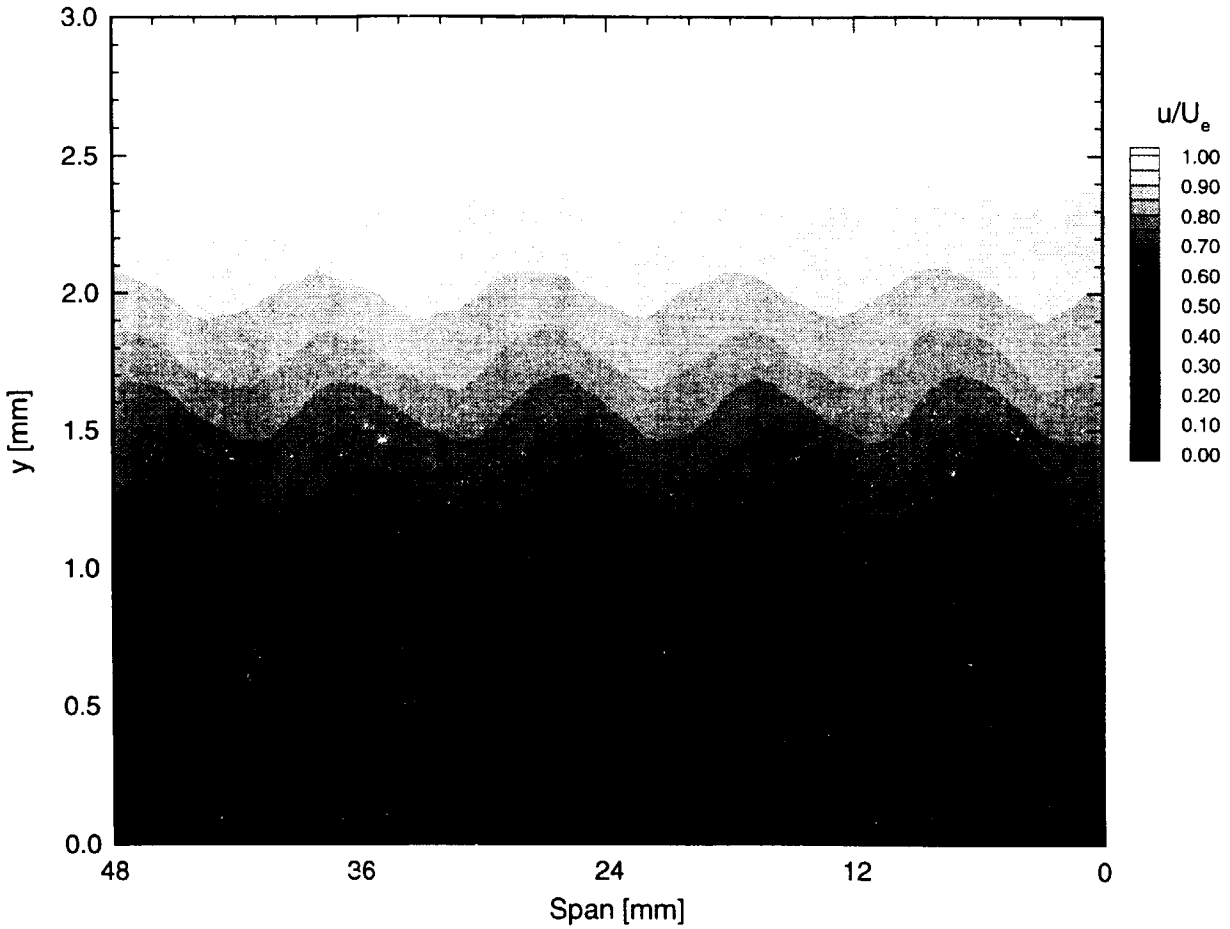

Figure 7.272. Velocity contours for boundary-layer scans at $x/c = 0.60$. A full array of 146 μm roughness with a spacing of 10 mm is at $x/c = 0.005$. $Re_c = 3.0 \times 10^6$. Data set L.

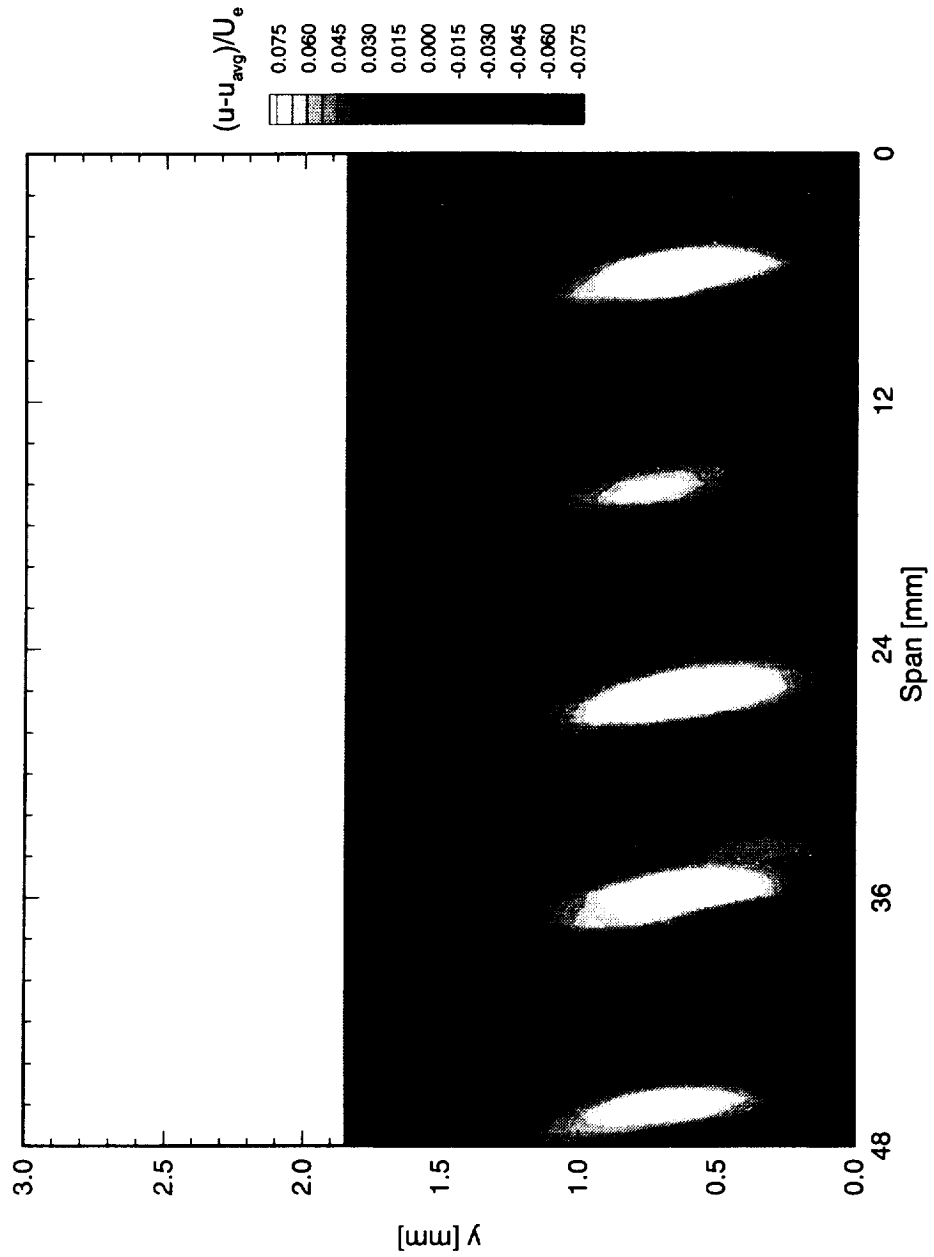

Figure 7.273. Disturbance contours for boundary-layer scans at $x/c = 0.10$. A full array of 146 μm roughness with a spacing of 10 mm is at $x/c = 0.005$. $Re_c = 3.0 \times 10^6$. Data set L.

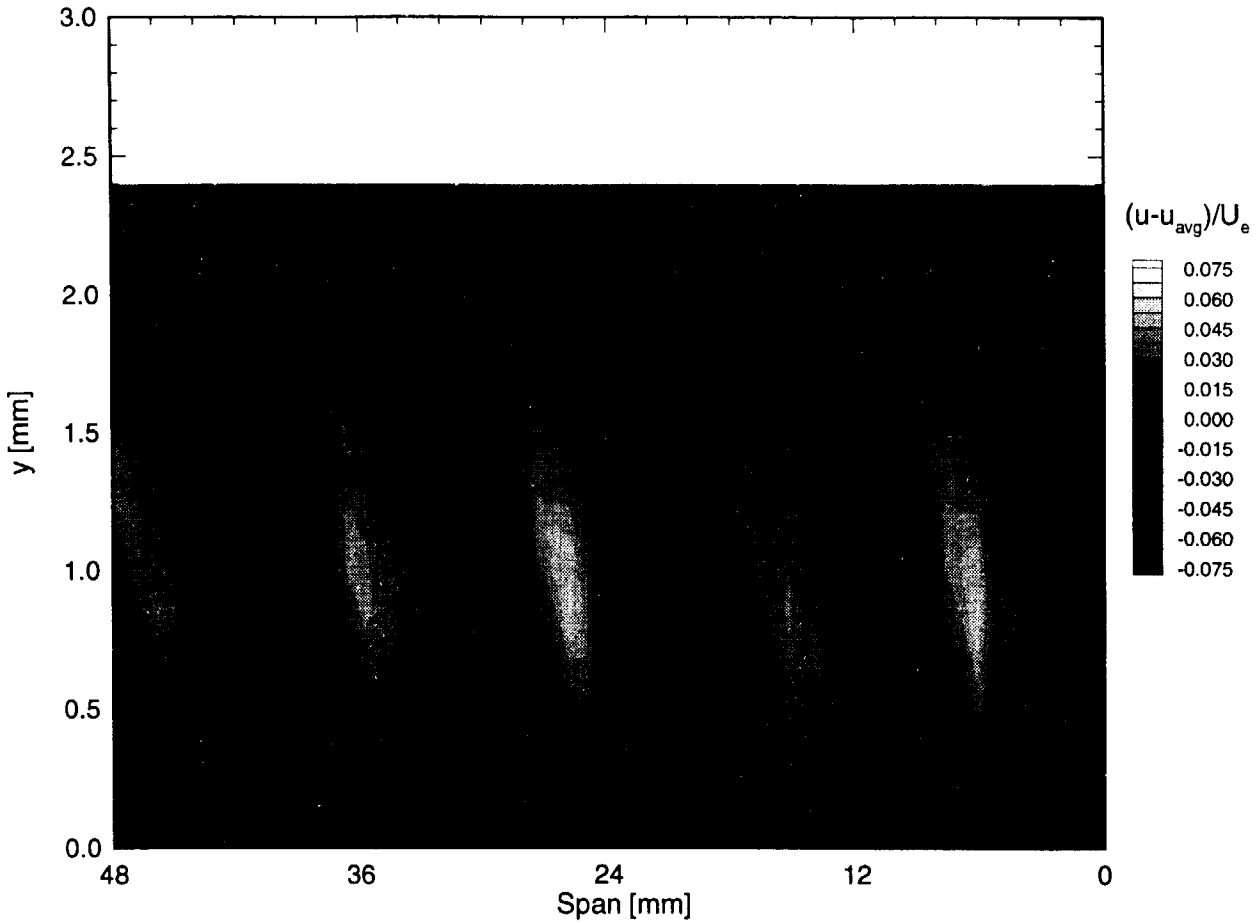

Figure 7.274. Disturbance contours for boundary-layer scans at $x/c = 0.20$. A full array of 146 μm roughness with a spacing of 10 mm is at $x/c = 0.005$. $Re_c = 3.0 \times 10^6$. Data set L.

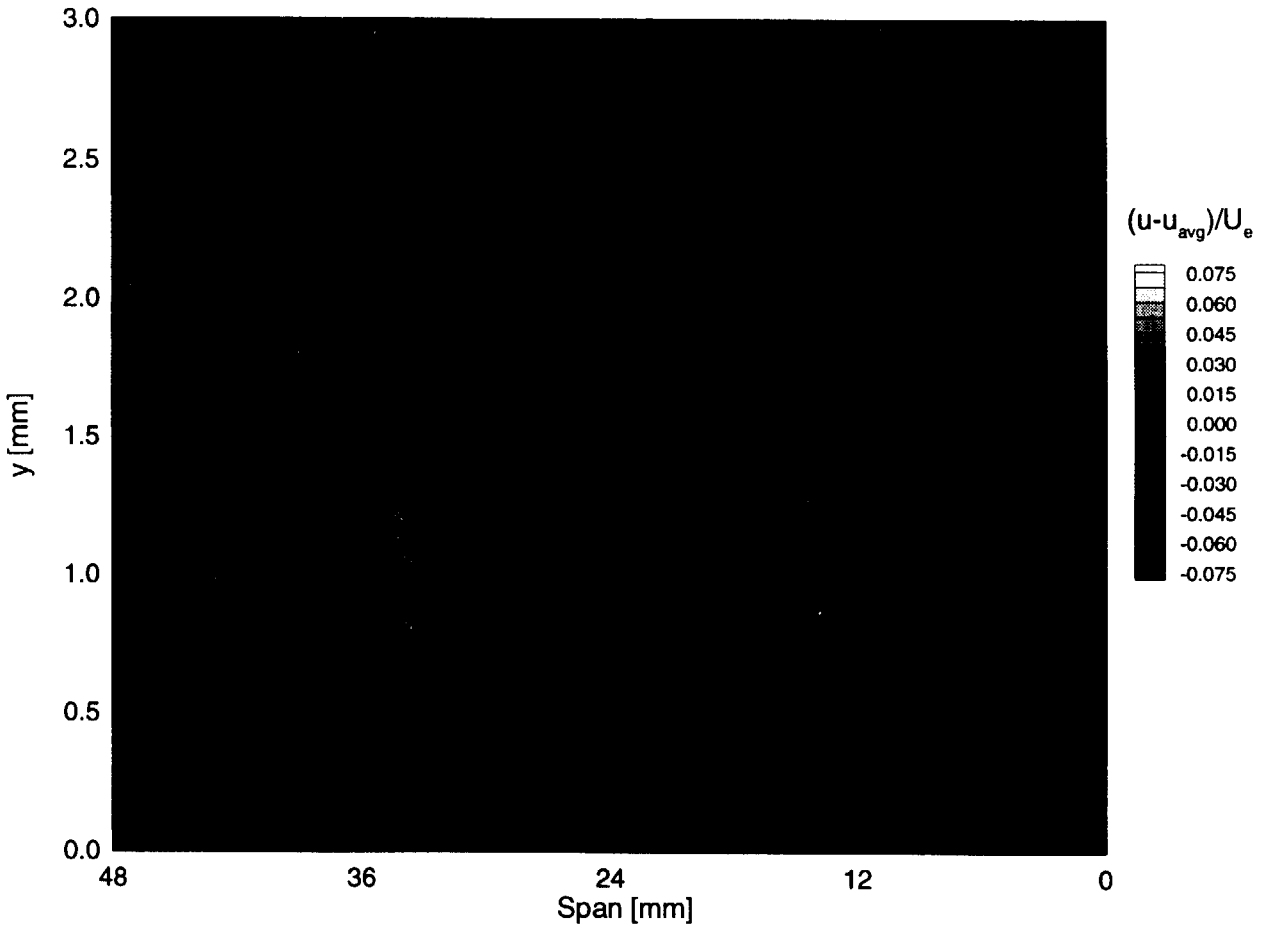

Figure 7.275. Disturbance contours for boundary-layer scans at $x/c = 0.40$. A full array of 146 μm roughness with a spacing of 10 mm is at $x/c = 0.005$. $Re_c = 3.0 \times 10^6$. Data set L.

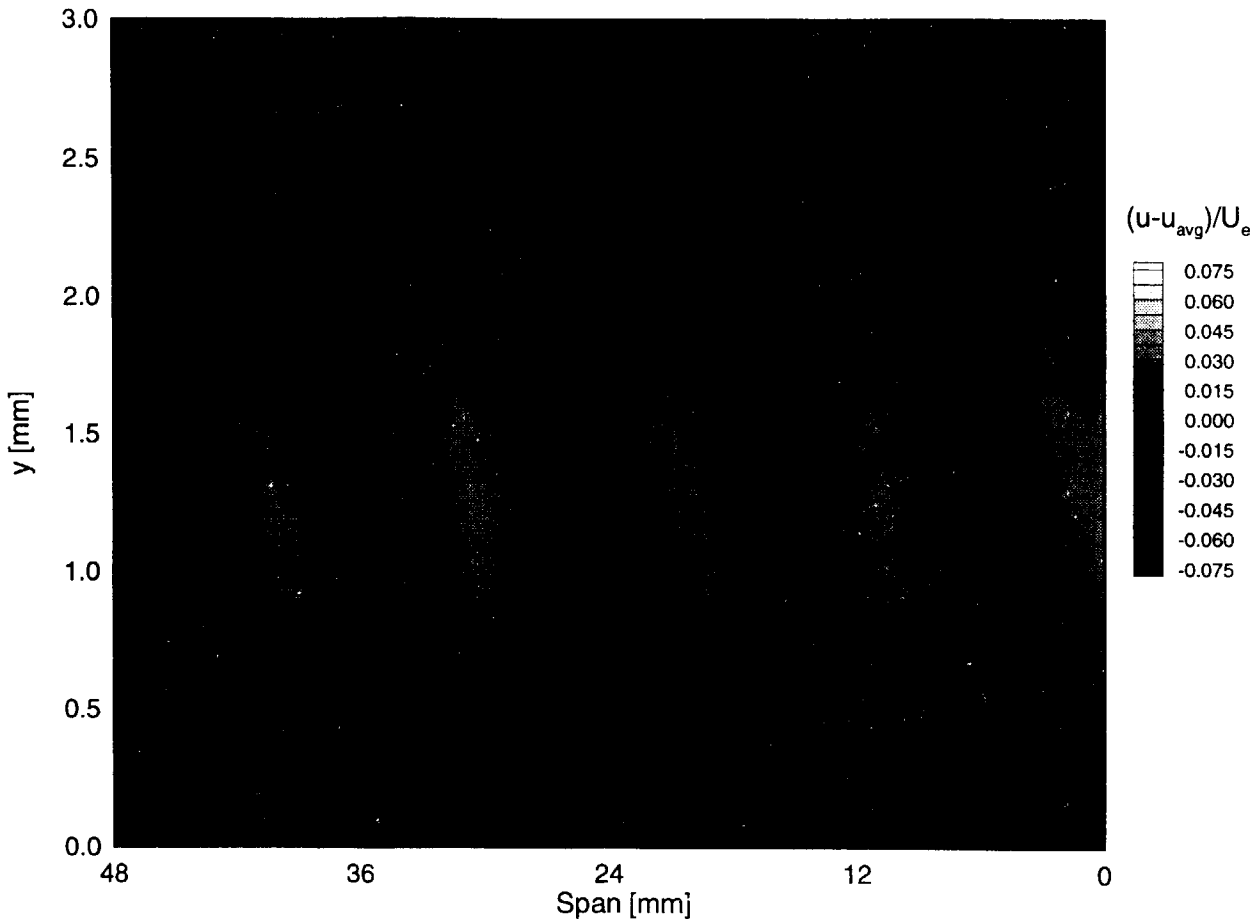

Figure 7.276. Disturbance contours for boundary-layer scans at $x/c = 0.60$. A full array of 146 μm roughness with a spacing of 10 mm is at $x/c = 0.005$. $Re_c = 3.0 \times 10^6$. Data set L.

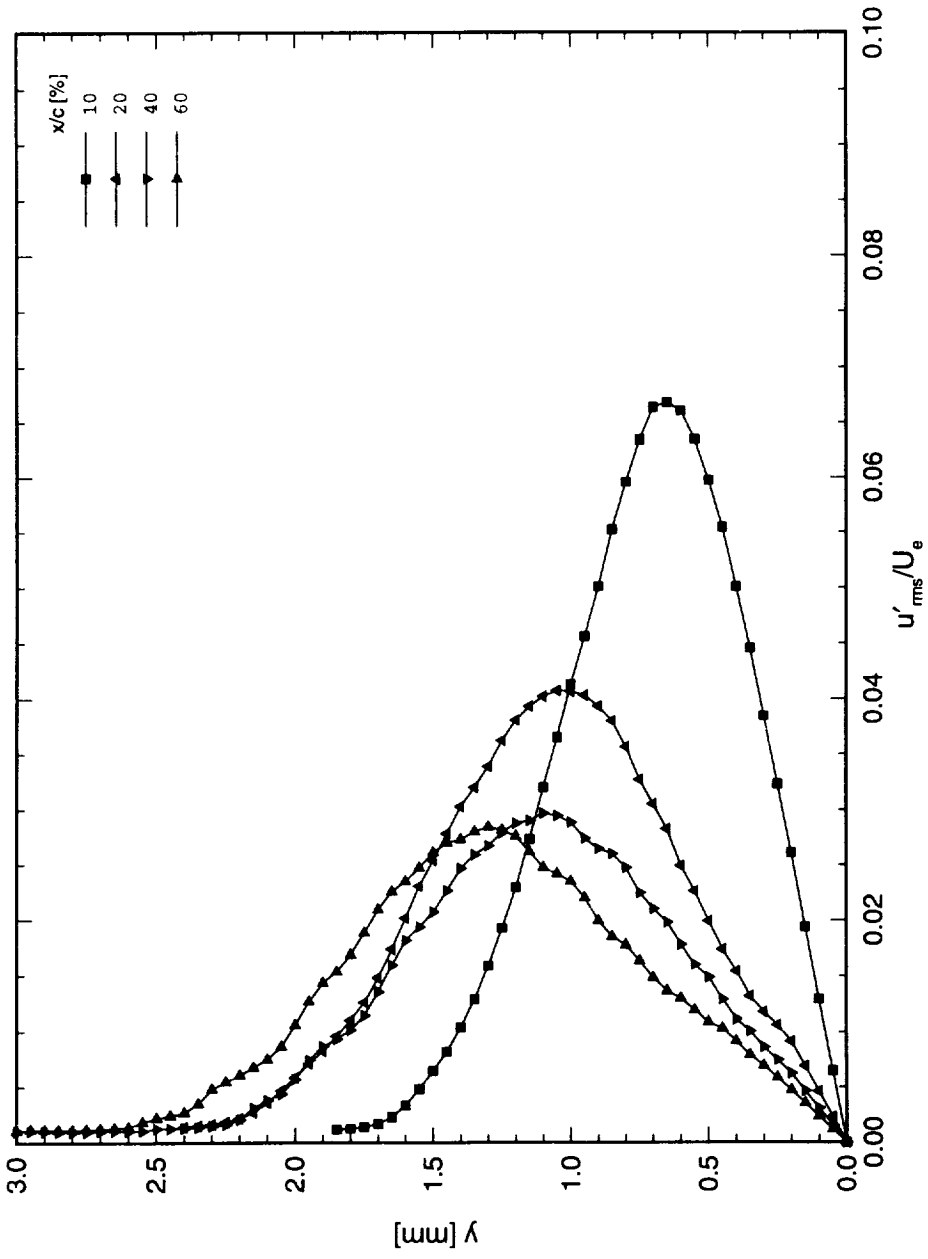

Figure 7.277. Stationary crossflow mode shapes for data set L, using rms method. $Re_c = 3.0 \times 10^6$, $\alpha = 0°$.

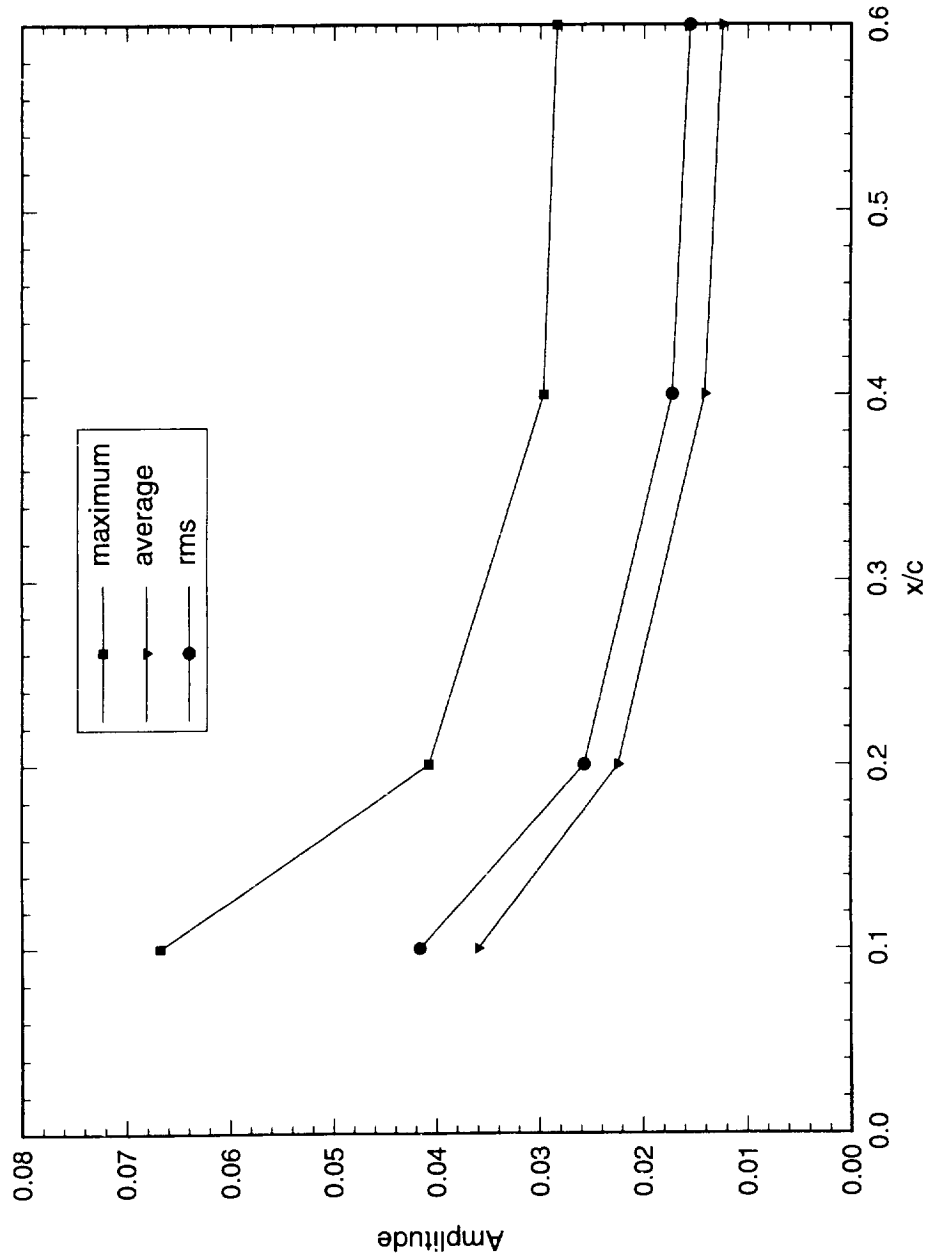

Figure 7.278. Stationary crossflow amplitudes for data set L. $Re_c = 3.0 \times 10^6$, $\alpha = 0°$.

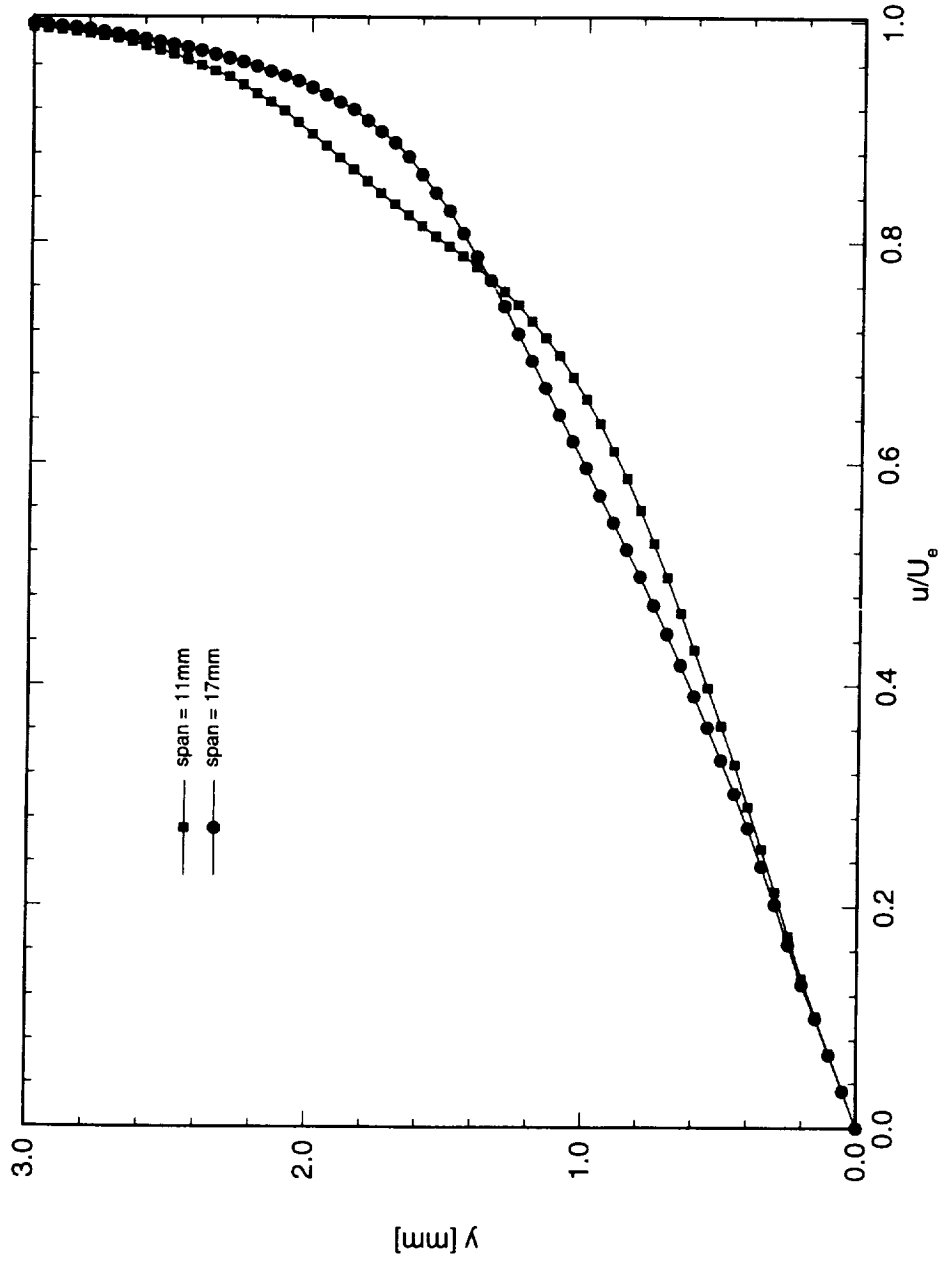

Figure 7.279. Boundary-layer profiles from data set A. Spanwise separation is 6 mm. $Re_c = 3.2 \times 10^6$, 10-element array of 117 μm roughness with 12 mm spacing at $x/c = 0.005$.

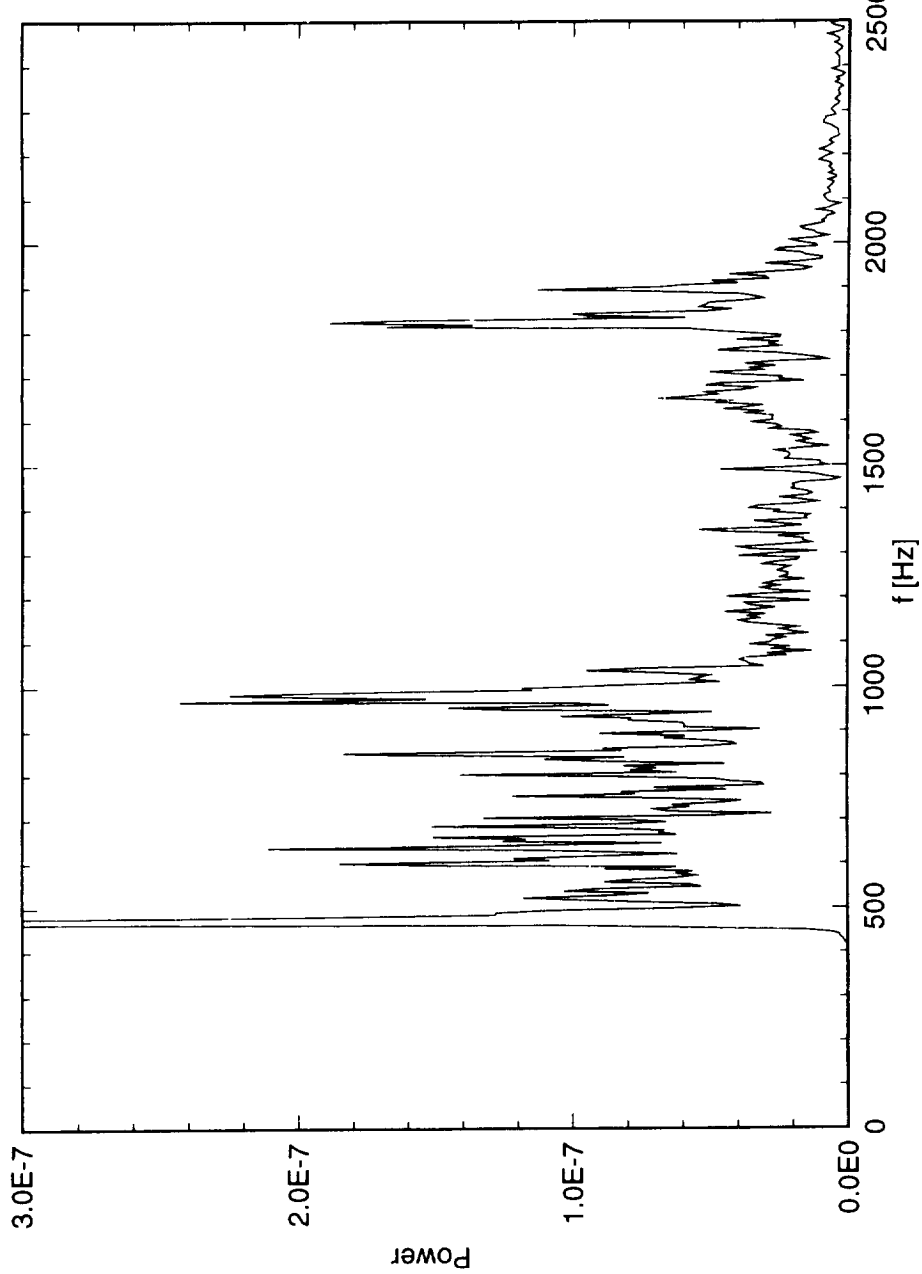

Figure 7.280. FFT power spectrum of time-dependent velocity component at $x/c = 0.6$. Data obtained at $u/U_e = 0.3$ in region with decelerated mean profile.

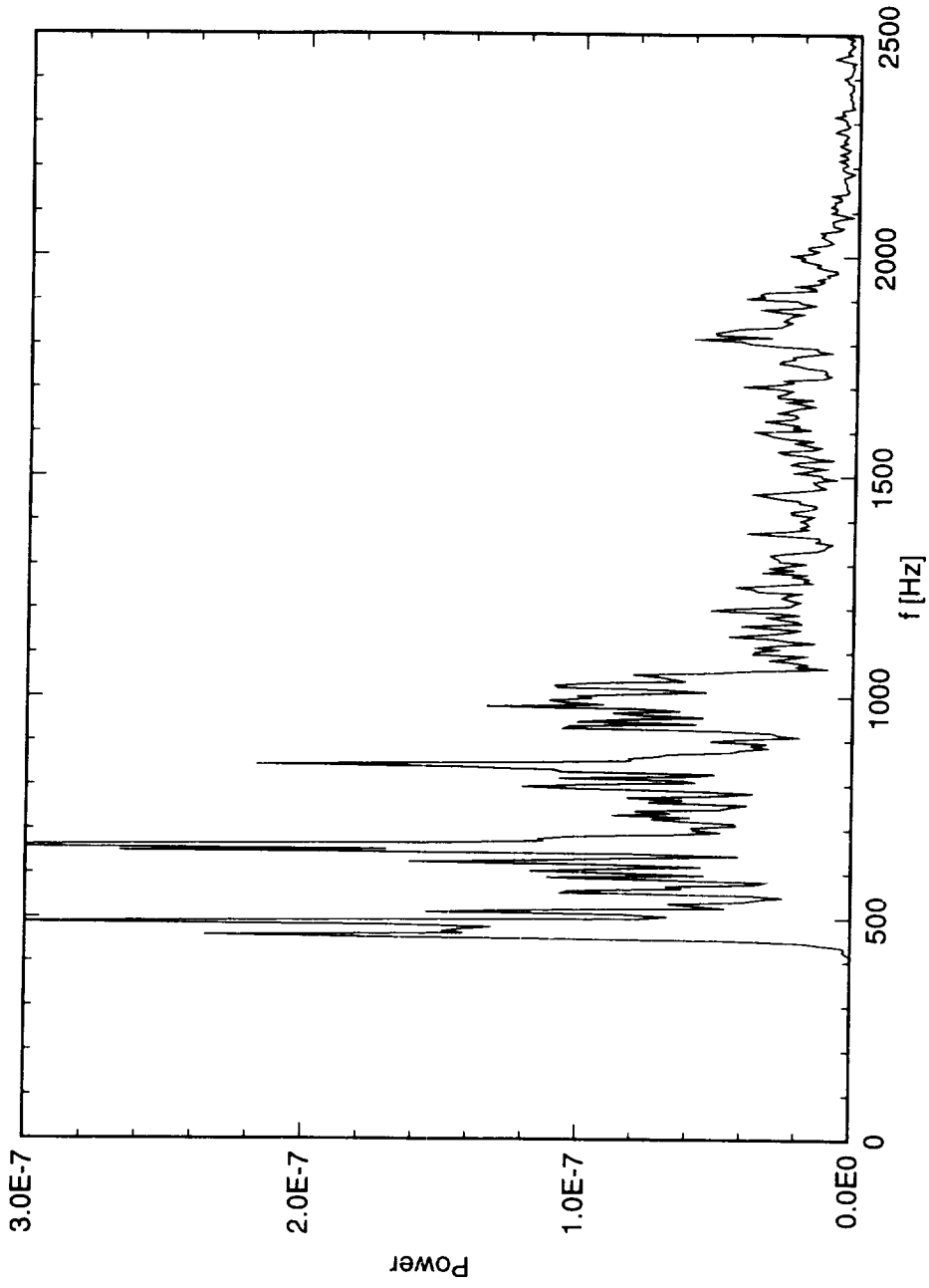

Figure 7.281. FFT power spectrum of time-dependent velocity component at $x/c = 0.6$. Data obtained at $u/U_e = 0.3$ in region with inflected mean profile.

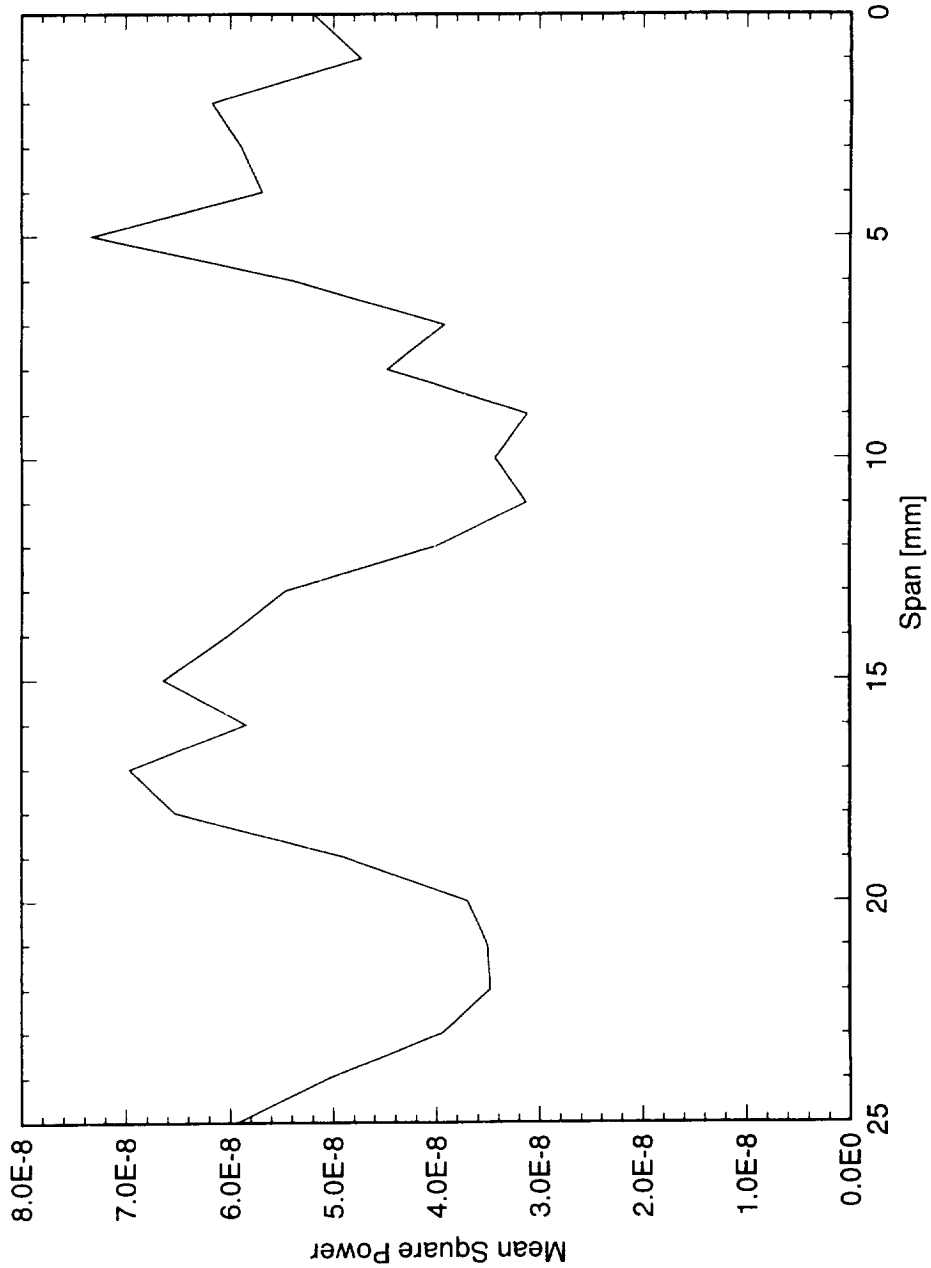

Figure 7.282. Spanwise variation of high-frequency disturbance at $x/c = 0.6$ in the presence of mean-flow distortions due to stationary vortices.